Lecture Notes in Mechanical Engineering

Nicolas Gascoin
E. Balasubramanian *Editors*

Innovative Design, Analysis and Development Practices in Aerospace and Automotive Engineering

Proceedings of I-DAD 2020

Springer

Lecture Notes in Mechanical Engineering

Lecture Notes in Mechanical Engineering (LNME) publishes the latest developments in Mechanical Engineering—quickly, informally and with high quality. Original research reported in proceedings and post-proceedings represents the core of LNME. Volumes published in LNME embrace all aspects, subfields and new challenges of mechanical engineering. Topics in the series include:

- Engineering Design
- Machinery and Machine Elements
- Mechanical Structures and Stress Analysis
- Automotive Engineering
- Engine Technology
- Aerospace Technology and Astronautics
- Nanotechnology and Microengineering
- Control, Robotics, Mechatronics
- MEMS
- Theoretical and Applied Mechanics
- Dynamical Systems, Control
- Fluid Mechanics
- Engineering Thermodynamics, Heat and Mass Transfer
- Manufacturing
- Precision Engineering, Instrumentation, Measurement
- Materials Engineering
- Tribology and Surface Technology

To submit a proposal or request further information, please contact the Springer Editor of your location:

China: Dr. Mengchu Huang at mengchu.huang@springer.com
India: Priya Vyas at priya.vyas@springer.com
Rest of Asia, Australia, New Zealand: Swati Meherishi at swati.meherishi@springer.com
All other countries: Dr. Leontina Di Cecco at Leontina.dicecco@springer.com

To submit a proposal for a monograph, please check our Springer Tracts in Mechanical Engineering at http://www.springer.com/series/11693 or contact Leontina.dicecco@springer.com

Indexed by SCOPUS. The books of the series are submitted for indexing to Web of Science.

More information about this series at http://www.springer.com/series/11236

Nicolas Gascoin · E. Balasubramanian
Editors

Innovative Design, Analysis and Development Practices in Aerospace and Automotive Engineering

Proceedings of I-DAD 2020

Springer

Editors
Nicolas Gascoin
INSA Centre Val de Loire
University of Orléans
Bourges, France

E. Balasubramanian
Department of Mechanical Engineering
Vel Tech Rangarajan Dr. Sagunthala R&D
Institute of Science and Technology
Chennai, India

ISSN 2195-4356 ISSN 2195-4364 (electronic)
Lecture Notes in Mechanical Engineering
ISBN 978-981-15-6618-9 ISBN 978-981-15-6619-6 (eBook)
https://doi.org/10.1007/978-981-15-6619-6

This Springer imprint is published by the registered company Springer Nature Singapore Pte Ltd.
The registered company address is: 152 Beach Road, #21-01/04 Gateway East, Singapore 189721, Singapore

Preface

Design and development are the aspirations of tomorrow's technologies for aero and auto industries to be alive in the competitive world, where cost-effective solutions, improvements in greenhouse environment, longevity/life cycle, eco-friendly materials and manufacturing, certification and government legislation demands are becoming stringent. The aerospace/automotive industries are looking for prominent solutions to improve their performance in air/road. Both the industries have come to symbolize the essence of utilizing the state-of-the-art and cutting edge technologies for satisfying the customer demands. Perhaps more than any other single icon, it is associated with a desire for independence and freedom of movement; an expression of economic status. For the next decades, they are marching towards a new concept designs, analysis and manufacturing technologies, where more swing is for improved performance through specific and/or multifunctional linguistic design aspect to downsize the system, improve the weight-to-strength ratio, fuel efficiency, make better the operational capability at room and elevated temperatures, reduce wear and tear, NVH aspects while balancing the challenges of beyond Euro VI emission norms, greenhouse effects and recyclable materials. The conference covered the research areas such as additive manufacturing, aerodynamics, CAD, CFD, cryogenics, design engineering, environment, finite element method, fuels and energy source, hybrid and electric vehicles, instrumentation and sensors, modeling and simulation, manufacturing, materials, NVH, optimization technologies, product development, propulsion systems, quality, reliability and durability, safety and risk assessment, sustainable manufacturing, UAVs and autonomous systems and vehicle dynamics and control. The conference aimed at addressing these issues of tomorrow where academia—industry—R&D partnerships and collaborative programs can be shared and implemented. The organizers of the 4th International Conference on Innovative Design, Analysis and Development Practices in Aerospace and Automotive Engineering (I-DAD 2020) wish to provide a platform for deliberations on design engineering, numerical methods, analysis/optimization techniques, life cycle engineering, system engineering, configuration managements, advanced

materials, novel manufacturing/prototyping, vibration and health monitoring, propulsion system and quality and reliability in the aerospace and automotive fields. The response to the conference was overwhelming on both national and international fronts.

Chennai, India

Prof. Nicolas Gascoin
Prof. E. Balasubramanian

Contents

About the Editors

Dr. Nicolas Gascoin is Director at INSA Centre Val de Loire (Institut National des Sciences Appliquées, ex ENSI Bourges), France. He holds a Ph.D. in the area of Scramjet cooling by endothermal reactive fuel from MBDA–EADS, Bourges (France). He has published more than 50 papers in international, peer-reviewed journals and attended 90 international conferences. He has also served as an advisor for postdoc and research engineers since 2007. Dr. Gascoin has coordinated numerous major research projects

Dr. E. Balasubramanian completed his Ph.D. in Robotics and Control at Concordia University, Montreal, Canada. He has more than fifteen years of research experience and conducted various funded projects under the aegis of DST, DRDO and ISRO, Government of India. He has collaborated with scientists in Taiwan, Canada and Korea in the development of flapping and rotary wing UAVs for diverse applications, including inspection of bridges, heritage structures, telecom towers, power line cables, monitoring of traffic signals, environment and water quality inspections. He also developed a test rig to measure aerodynamic forces of ornithopters and powder-based additive manufacturing systems. He has won several national and international competitions. He is in editorial board member and reviewer for various journals. His research interests include UAVs, robotics, rapid prototyping, control and sensors with online data acquisition. He has published more than 100 research papers, two books and filed many patents.

3D Digitizing Practice-Advantage in Reverse Engineering with Accuracy Boost

C. J. Thomas Renald, S. Yuvaraj, and J. David Rathnaraj

Abstract 3D Digitizing is the way toward copying an article practically and dimensionally by Reverse Engineering procedures. In current mechanical situation, three-dimensional-geometry recuperation was finished using estimation of the segment directly with the measures else using structure up of physical models or replication using the assistance of computer numerical control systems which result low precision. This work distinguishes the means associated with the Reverse Engineering procedure and 3D information securing method, which is inline for creating CAD models. The three-dimensional digitizing systems were demonstrated as a significant device for the three-dimensional-geometry recuperation, which is financially savvy and of good precision. Endeavors are made to distinguish a practical way to deal with recuperate 3D state of items by utilizing a coordinate measuring machine (CMM). To affirm the method, complicated state of IC motor cylinder is digitized by utilizing a CMM. Examined crude information is spared in point document arrangement and it is moved to CAD virtual products to create cloud focuses. Smooth parametric surfaces were gotten with the help of fitting of B-splines bends converted as surfaces which is accessible in business CAD software, Pro/E wildfire 2.0 package. This strategy for copy the total 3D model demonstrates a reduction in information misfortunes while recovering the 3D picture that will be spared as a correct information position for other CAD/CAM needs.

Keywords Computer numerical control (CNC) · Three-dimensional digitizing techniques · Coordinate measuring machine (CMM) · Piston

C. J. Thomas Renald (✉) · S. Yuvaraj · J. David Rathnaraj
Aeronautical Engineering Department, Sri Ramakrishna Engineering College, Coimbatore, Tamil Nadu 641022, India
e-mail: thomsi_reni2000@yahoo.co.in

S. Yuvaraj
e-mail: Yuvaraj.shanmugam@srec.ac.in

N. Gascoin and E. Balasubramanian (eds.), *Innovative Design, Analysis and Development Practices in Aerospace and Automotive Engineering*, Lecture Notes in Mechanical Engineering, https://doi.org/10.1007/978-981-15-6619-6_1

1 Introduction

Use of Reverse Engineering (RE) is to construct up the fresh item dependent on copying a current article. RE is generally utilized in different regions of item advancement; the target of the huge ventures, for example, vehicle, aviation and assembling businesses, is to set up PC coordinated data frameworks to control their tasks. These businesses utilize RE procedure, as manual or PC supported frameworks to copy a current article or destroyed parts.

Page et al. [1] worked on approaches, developments on robotizing making sense of (RE) through cutting edge imaging and PC vision. Xu et al. [2] suggested a plan making sense of system and portrayed the improvement of a changed making sense of structure wherein a three-dimensional digitiser (MicroScribe-3DX) was fused with a PC helped computer-aided design structure (Pro/E). Puntambekar et al. [3] suggested a framework for manufacturing CAD models of solid parts by digitizing a present thing, making a PC model and after that using it to create the portion. Abella et al. [4] depicted on human aptitudes leveraging in RE. Lee et al. [5] stated a algorithm for laser clear organizing of free-form surface. Chang [6] developed an electronic Reverse Engineering. Chang et al. [7] advanced toward a preliminary examination of digitizing factors on uncertainty with coordinate measuring machine. Eduardo et al. [8] presented a virtual reality instrument for viewing computed-aided design models. Varady et al. [9] gave the idea to reproduce surface model, from a physical model, which rely upon the sort and accurate values of the purposeful point data, similarly as the sort of assessing device. Martin et al. [10] utilized RE for three-dimensional model upgrades. Broacha et al. [11] made methods for appropriate parametric shell patches to three-dimensional position data. Chivate et al. [12] pushed toward the appropriate parametric surface patches to three-dimensional position data for the geometric locals that are used range from clear planes and chambers. Sarkar et al. [13] made for appropriate parametric surface patches to three-dimensional position data. The geometric locals used range since direct planes and chambers to piecewise smooth surface parametric surface patches. Piegl [14] considered on NURBS. Lounsbery [15] made parametric surface interposition. Hoppe et al. [16] made surface redoing from untidy core interests. Hoppe et al. [17] considered triangular arrangement as a midway depiction. Hoppe et al. [18] stated objectwise smooth surface revamping. Joris et al. [19] made RE for geometry mix in Industrial Engineering. Groover [20] depicted on 'Motorization, manufacturing System, and CIM.' At last, this model was used to create computer numerical control machine part program to make the component on CNC machine.

2 Problem Definition

In industry, assembling of IC motor cylinder is finished by Reverse Engineering process. The client would not give the IC motor cylinder model or illustrations, just the wax or pitch model of cylinder is being given, in light of the fact that the cylinder

is a segment which takes fundamental job in a motor execution, the illustration subtleties are kept up secret. By replicating the shape of the gum or wax formed chamber with the aid of computer numerical control machine and it is altered by setting the object to be machined to achieve the chamber profile, this framework is followed in industry to create chambers. By this present Reverse methodology, the worth and surface finishing of chamber is somewhat beneath normal but not prepared to make a virtual model or a computer-aided design data base. So it makes a way to deal with under go investigate in this area to success extraordinary value, incredible surface fruition and accurate crown profile of chambers and besides to make a virtual chamber to keep up the CAD data base.

3 The Planned Reverse Engineering Method

The planned RE method utilizes a coordinate measuring machine to digitize the cylinder, implicit strong cylinder model can be created by utilizing this framework and deviation examination of the cylinder is additionally assessed. This procedure will defeat the current framework. Precision of the cylinder is likewise expanded and surface completion is prevalently great.

3.1 Digitizer Fixing Method with CMM

CMM is utilized to digitize the cylinder also the directions are set to any of the nearby orientation. The Renishaw contact trigger test was utilized to digitize the directions. The precision of the directions depends on the kind of surface, framework exactness, part unpredictability and rate of estimation. The test takes one information position at once by contacting a section or by examining a surface by illustration the test along the item Fig. 1. The CMMs as a rule play out this sort of digitizing. While digitizing a cylinder contains almost 1500–2000 points, it takes about a large portion of an hour to digitize a piston Table 1.

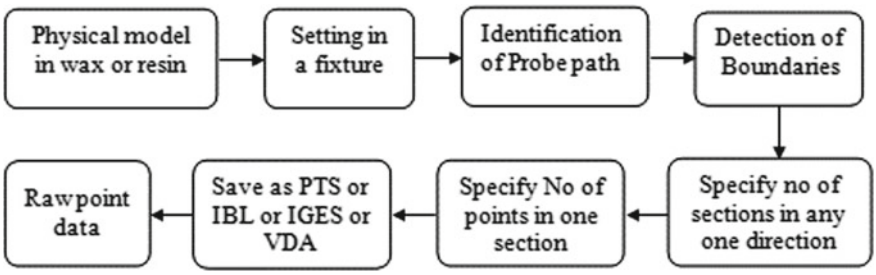

Fig. 1 Digitizing technique with CMM

Table 1 Sample of digitized value of the piston-experimented using CMM

Cartesian coordinates		
x	*y*	*z*
0.000000	0.0000000	−23.0000000
0.0000000	77.0000000	−23.0000000
−18.3303030	0.0000000	−17.0000000
−15.4919330	0.0000000	−17.0000000
15.4919330	0.0000000	−17.0000000
18.3303030	0.0000000	−17.0000000
−18.3303030	44.9142220	−17.0000000
−16.2249810	44.9142220	−17.0000000
16.2249810	44.9142220	−17.0000000
18.3303030	44.9142220	−17.0000000
16.2249810	45.0857780	−17.0000000
18.3303030	45.0857780	−17.0000000
−18.3303030	45.5686220	−17.0000000
−16.2249810	45.5686220	−17.0000000
−19.9474600	47.5674040	−15.0697990
−18.0319480	47.5674040	−15.0697990
−20.0000000	2.0000000	−15.0000000
−17.4355960	2.0000000	−15.0000000
17.4355960	2.0000000	−15.0000000
20.0000000	2.0000000	−15.0000000
−20.0000000	22.0000000	−15.0000000
−17.4355960	22.0000000	−15.0000000
17.4355960	22.0000000	−15.0000000
20.0000000	22.0000000	−15.0000000
−20.3030090	42.4157450	−14.5872490
−18.4244990	42.4157450	−14.5872490
18.4244990	42.4157450	−14.5872490
20.3030090	42.4157450	−14.5872490
18.4244990	47.5842550	−14.5872490
20.3030090	47.5842550	−14.5872490
−22.6300000	42.1581310	−7.2101510
−22.3800000	42.1581310	−7.2101510
22.3800000	42.1581310	−7.2101510
22.6300000	42.1581310	−7.2101510
−22.6300000	47.8418690	−7.2101510
−22.3800000	47.8418690	−7.2101510
22.3800000	47.8418690	−7.2101510

(continued)

Table 1 (continued)

Cartesian coordinates		
x	*y*	*z*
22.6300000	47.8418690	−7.2101510
−22.3800000	42.1566720	−7.1683750
22.3800000	42.1566720	−7.1683750
−22.3800000	42.7944620	−7.1683750
22.3800000	42.7944620	−7.1683750
−22.3800000	47.2055380	−7.1683750
22.3800000	47.2055380	−7.1683750
−22.3800000	47.8433280	−7.1683750
22.3800000	47.8433280	−7.1683750
−24.0000000	30.0000000	−7.0000000
−21.9089020	30.0000000	−7.0000000

3.2 Surfaces Generation

The Pro-E programming was utilized to create the strong virtual model of the cylinder from the digitized focuses Fig. 2.

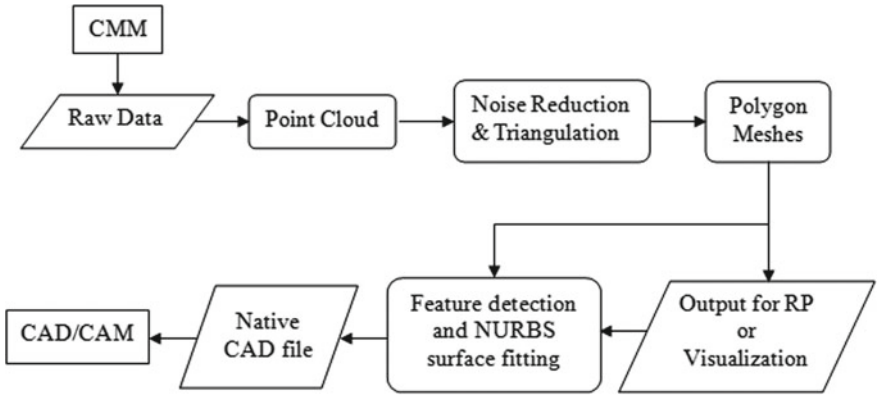

Fig. 2 Virtual prototype generation from scanned data point by Pro-E

4 Comparison of Planned Method Over Already Available Method

Virtual solid cylinder geometry was made. Because of smaller being developed and fixed with precision moving contact bearing and hydrostatic air-bearing, there is no dialog of vibrations in coordinate measuring machine.

- Surface consummation is incredible.
- The accuracy of the CMM is more.
- Precision is about, up to 0.5 micron.
- Computer-aided design data base can be kept up (Figs. 3 and 4).
- To run a coordinate measuring machine for digitizing, least proportion of electrical imperativeness is eaten up than the computer numerical control machine.
- By using little range tests, better precision and extraordinary surface finish of chamber can be practiced.
- Two-dimensional representations will be created for the shop floor reason.

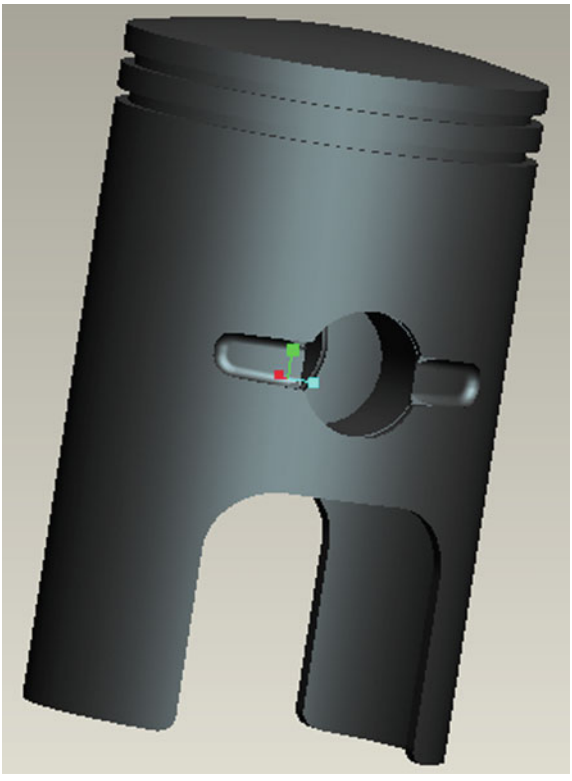

Fig. 3 Snapshot of 3D shape of the piston in Pro\Engineer

Fig. 4 Newly manufactured piston through proposed reverse engineering technique

5 Results and Discussions

5.1 Variation Examination of the Experimental Data

To decide the precision of the surface which was produced from the digitized focuses, variation examination was finished utilizing Pro\Engineer deviation investigation Fig. 5.

The examined position cloud information was amassed with the surface which was created and variations were checked. In the event that the variations are inside the worthy resistance level, at that point the test need not be rehashed. The mistake can be redressed by amending the limit bends.

6 Conclusion

This research suggests the innovative making sense of methods using the coordinate measuring machine exhibited to be a improved digitizing framework using ideal precision over a computer numerical control manufacturing. Measuring and endorsement was done using Pro-E variation examination. The conclusions from the deviational assessment were of best precision over the present structure and besides monetarily insightful. Thusly high precision, extraordinary quality and incredible

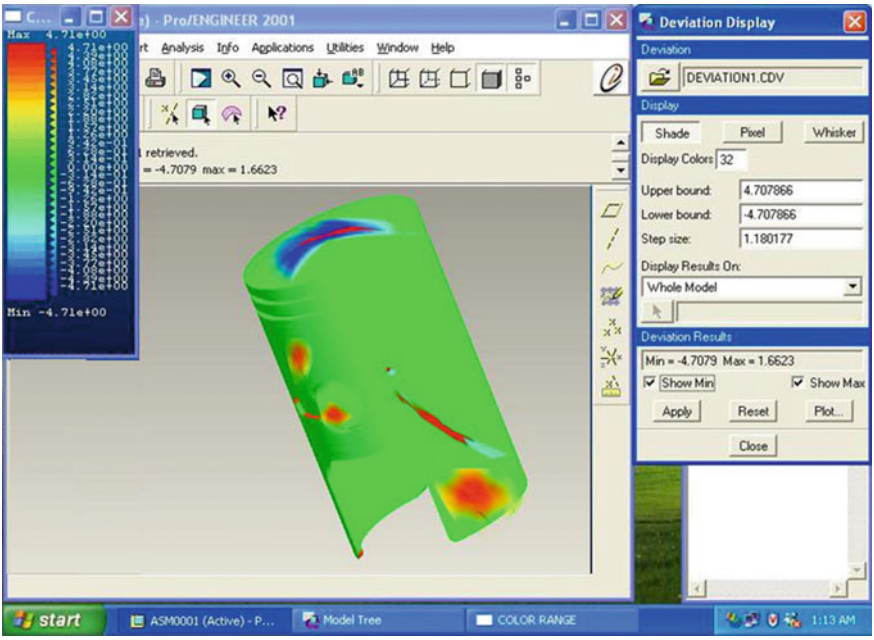

Fig. 5 Snapshot of piston digression analysis done in Pro\Engineer

surface fulfillment of the chamber were made with the present workplaces by using this strategy in a shorter time.

References

1. Page D et al (2007) Methodologies and techniques for reverse engineering—the potential for automation with 3-D laser scanners. Springer Series in Advanced manufacturing, pp 11–32
2. Xu XW et al (2006) Development of an integrated reverse engineering system. Int J Comput Appl Technol 25(1):9–14
3. Puntambekar NV et al (1994) Unified review of 3D model generation for reverse engineering. Comput Integr Manuf Syst 7(4):259–268
4. Abella R et al (1991) Human skills interface in reverse engineering. Comput Ind Eng 21(10):495–502
5. Lee KH et al (2001) A framework for laser scan planning of freeform surface. Int J Adv Manuf Technol 17:171–180
6. Feng C-X (Jack) et al (2002) Experimental study of digitizing parameters on digitizing un certainly with CMM. Int J Prod Res 40(3):683–697
7. Feng C-X (Jack) (2002) Internet based reverse engineering. Int J Adv Manuf Technol
8. Eduardo TL et al (2004) A VR Tool for the visualization of CAD models, http://www.tecgraf.puc-rio.br
9. Varady T et al (1997) Reverse engineering of geometric models—an introduction. Comput Aided Des 29(4):255–268

10. Martin RR et al (1997) Special issue: reverse engineering of geometric models. Comput Aided Des 29(4):253–254
11. Broacha R et al (1995) Getting from points to products. Comput-Aided Eng
12. Chivate PN et al (1993) Solid-model generation from measured point data. Comput-Aided Des
13. Sarkar B et al (1991) Smooth-surface approximation and reverse engineering. Comput Aided Des 23:623–628
14. Piegl L (1991) On NURBS: a survey. IEEE Comput Graph Appl 55–70
15. Lounsbery M et al (1992) Parametric surface interpolation. IEEE Comput Graph Appl
16. Hoppe H et al (1992) Surface reconstruction from unorganized points. In: Computer graphics, SIGGRAPH '92, vol 26
17. Hoppe H et al (1993) Mesh optimization. In: Computer graphics, SIGGRAPH '93, vol 27
18. Hoppe H et al (1994) Piecewise smooth surface reconstruction. In: Computer graphics, SIGGRAPH '94, vol 28
19. Joris SM et al, Reverse engineering for shape synthesis in industrial engineering, http://www.2.io.tudelft.nl
20. Mikell P et al (2002) Automation, production system and computer integrated manufacturing, 2nd edn. Indian reprint. Pearson education Asia, low price edition

Cell Arrangement Measurement—A Perfect Usage of Cell Fabricating Framework in an Industry

C. J. Thomas Renald, S. Yuvaraj, and J. David Rathnaraj

Abstract Advantages of cell producing framework rely upon central point to be specific the plan of equipment cells and part group, setup period and technique for task. CMS become a disappointment when these components are not appropriately utilized. This work consolidates three exhibit-based grouping calculations specifically Altered-Single Linkage Clustering strategy (MOD-SLC), Direct Clustering Analysis (DCA) and Rank Order Clustering-2 (ROC-2) for investigating continuous assembling delay with assembling cell development. In the investigation, Modified-Single Linkage Clustering technique beats the other two strategies, paying little mind to the measure utilized, independent of any extra commonness of outstanding components in the informational index. The outcomes are approved with continuous assembling frameworks information

Keywords Part family · Cell manufacturing system (CMS) · Machine cell · Setup time · Cell formation · Algorithms and performance measures

1 Introduction

Assembling businesses are under extraordinary weight from the undeniably focused worldwide commercial center. Shorter item lifecycles, period-to-advertise and different client aids have provoked makers to improve the proficiency and efficiency of its creation exercises. Assembling frameworks must almost certainly yield items with low creation expenses and high caliber as fast as conceivable so as to convey the items to clients on schedule. What's more, the frameworks ought to have the option to

C. J. Thomas Renald (✉) · S. Yuvaraj · J. David Rathnaraj
Department of Aeronautical Engineering, Sri Ramakrishna Engineering College, Coimbatore, Tamil Nadu 641022, India
e-mail: thomsi_reni2000@yahoo.co.in

S. Yuvaraj
e-mail: Yuvaraj.shanmugam@srec.ac.in

N. Gascoin and E. Balasubramanian (eds.), *Innovative Design, Analysis and Development Practices in Aerospace and Automotive Engineering*, Lecture Notes in Mechanical Engineering, https://doi.org/10.1007/978-981-15-6619-6_2

modify or react rapidly to changes in item structure and item request without significant speculation. Conventional assembling frameworks, for example, work shops and stream lines are not equipped for fulfilling such necessities.

DCA is among the mainstream bunch investigation-based MCF issue arrangement strategies [1–3]. Various sorts exhibit-based strategies and progressive techniques were created and proposed in the prior periods [1, 2, 4–12]. These techniques have the hindrance of not framing item and machine cells all the while; so extra strategies should be utilized to finish the plan of the framework. Gathering efficiency (GE) is one of the critical parameters to be considered in cell arrangement frameworks [13, 14]. Chart deterioration issue is to machine cells and part bunches for a fixed number of social occasions with limits on cell measure [15]. Kumar et al. [17] built up a comparable methodology for deciding parts to be subcontracted so as to acquire an ideal square askew structure. These techniques are observed to rely upon the underlying turn component decision. Co et al. [18] built up a three-arrange technique to frame cells and tackled a three-task issue to allot occupations to machines. Seifoddini [8] analyzed the SLC and ALC strategies. Gunasingh et al. [19] defined a whole number programming issue to gathering machines and items for cell fabricating frameworks. Chandrasekharan et al. [20] examined the presentation of the gathering effectiveness in assessing the arrangement characteristics of a lot of well-organized and badly organized issues. Proposed a compelling calculation to distinguish part-groups and bottleneck-parts, given machine groupings. Prabbahakaran et al. proposed another ordinal creation information likeness coefficient dependent on the succession of activities and the clump size of the parts. While directing the point by point writing overview, it has been discovered that numerous cell development strategies have been utilized to lessen the level of remarkable components (PE) and to expand the grouping efficiency (GE). The aftereffect of the writing review shows the nonattendance of an investigation on cell arrangement strategies utilizing the constant information to foresee the exhibition. In this work, three previously mentioned cell arrangement calculations are approved utilizing constant information got from an assembling organization.

The fundamental issue looked by the organization is that their current design is utilized to produce the parts for a wide range of the siphons, for example, monosquare, stream siphon and submersible siphon and so forth, which causes a clogged stream and bottlenecks. The organization needed to make the submersible siphons in a different plant. M/s CRI Pumps Ltd., a main siphon assembling organization chose to plan a cell format for their submersible siphons division,

- To figure the machine necessities for the new format.
- To create programs for each sort of cell development calculations to process the outcomes naturally.
- To analyze the different cell arrangement calculations and to locate the most appropriate calculation for the given issue.
- To plan a cell design from the best outcome acquired among the most appropriate calculation.

- To think about the presentation of the cell format with the customary design as far as profitability improvement, decrease in material taking care of separation and decrease in floor space prerequisites.

1.1 Evaluation Parameter

The four main parameters were used to evaluate the cells formed are

1. **Exceptional elements (PE)**

$$\mathrm{PE} = e_0 \tag{1}$$

2. **Voids (v)**
   Voids shows that all components assigned to the cell will not require any machine assigned to a cell. Leads to huge, ineffective cells and will potentially supports to low utilizations.
3. **Efficiency (η)**

$$\eta = w\eta_1 + (1 - w)\eta_2 \tag{2}$$

$$\eta_1 = \frac{o - e}{o - e + v} \tag{4}$$

$$\eta_2 = \frac{\mathrm{MP} - o - v}{\mathrm{MP} - o + e - v} \tag{5}$$

4. **Efficacy (τ)**
   GC solves the problem of choosing w and the fixing range of GE. GC has the requisite properties like non-negativity, 0–1 limits and is not disturbed by the size of the MCIM, i.e., the quantity of components or machine is not considered (Fig. 1).

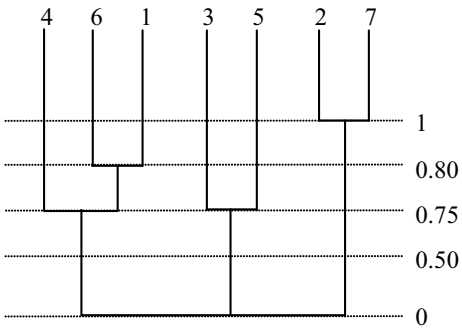

Fig. 1 MOD-SLC dendogram

Grouping efficacy:

$$\tau = \frac{o - e}{o + v} \tag{6}$$

where

o Quantity of 1's in the matrix
e Quantity of exceptional elements
v Quantity of voids.

$\tau = 1$ implies 0 voids and 0 exceptional elements (perfect clustering)

$\tau = 0$ implies all 1's are outside the diagonal blocks.

w Weight factor
o Amount of 1's in matrix
e Amount of exceptional elements
v Quantity of voids
M Quantity of machines
P Quantity of components

$\eta = 1$ implies 0 voids and 0 outstanding elements (perfect clustering)

e_0 number of exceptional elements.

2 Results and Discussions

From the solutions obtained, it is conformed that altered-one link clustering method gives the better performance for the above problem. The result has two exceptional elements, three voids, grouping efficiency is 91.33% and grouping efficacy is 82.14%. Weighing factor was selected as 0.412, given by Mukhopadhyay et al. [36]. Thus, it was identified that MOD-SLC formulae gives better result than the other two in this case study. The results obtained from the three-cell formation algorithms are drawn graphically from Figs. 2, 3, 4, 5 and 6. Table 1 shows the computational results (Figs. 7, 8 and 9).

3 Graphical Results of Algorithm Versus Evaluating Parameters

1. Fig. 2 shows the improved performance of MOD-SLC algorithm than ROC-2 and DCA and gives smaller number of exceptional elements of 2.
2. From Fig. 3, it is clear that MOD-SLC provides minimum number of voids than other two algorithms.

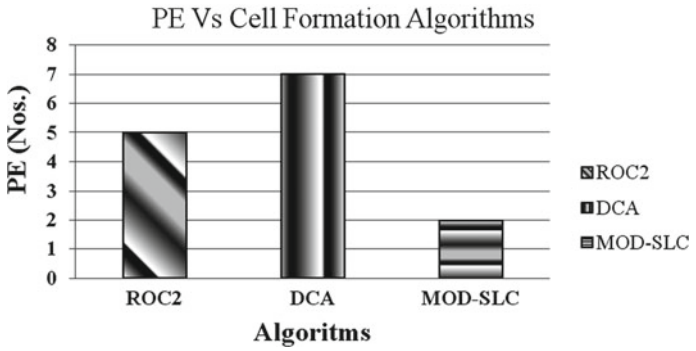

Fig. 2 Exceptional elements versus cell formation algorithms

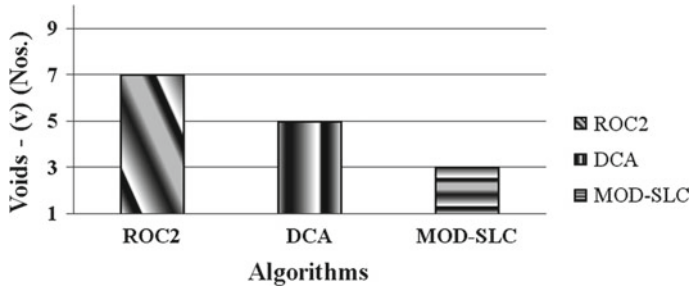

Fig. 3 Voids versus cell formation algorithms

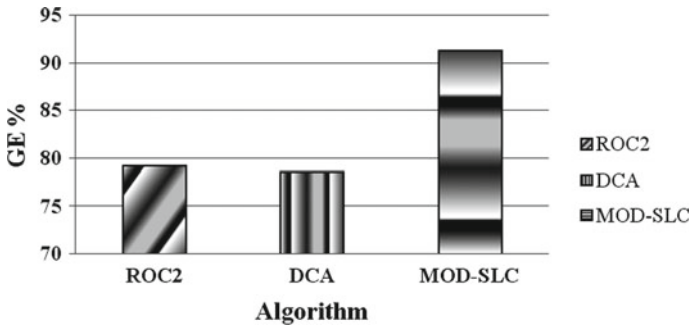

Fig. 4 Grouping efficiency versus cell formation algorithms

3. Improved grouping efficiency of 91.33% when comparing with other two algorithms is shown in Fig. 4.
4. Increased grouping efficacy of 82.14% when compared with other ROC-2 and DCA algorithms is shown in Fig. 5.

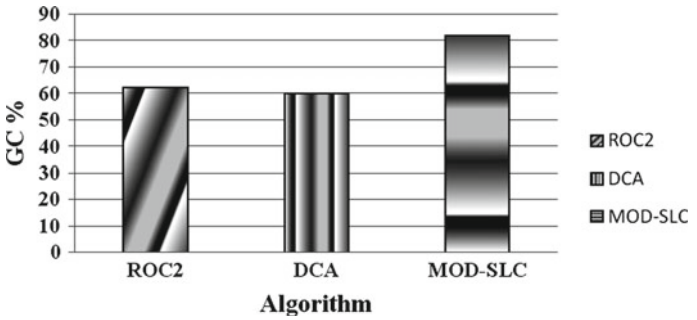

Fig. 5 Grouping efficacy versus cell formation algorithms

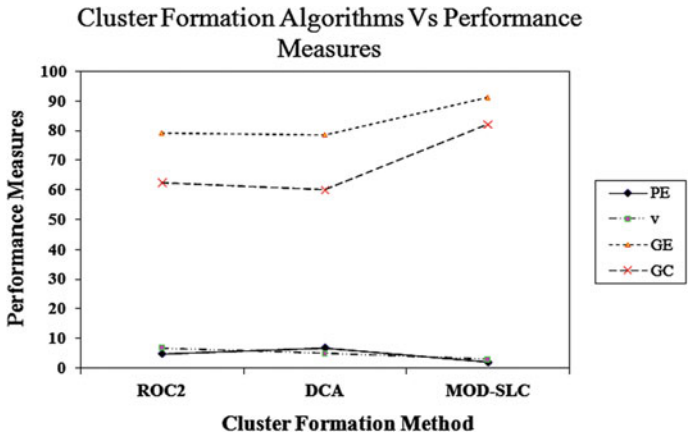

Fig. 6 Overall comparisons of cell formation algorithms and performance measures

Table 1 Numerical results cell formation algorithms

Performance measures	Algorithms		
	ROC2	DCA	MOD-SLC
PE (nos.)	5	7	2
Voids (nos.)	7	5	3
GE %	79.18	78.56	91.33
GC %	62.5	60	82.14

5. The overall comparison of performance measures such as PE, v, GE and GC is shown in Fig. 6.

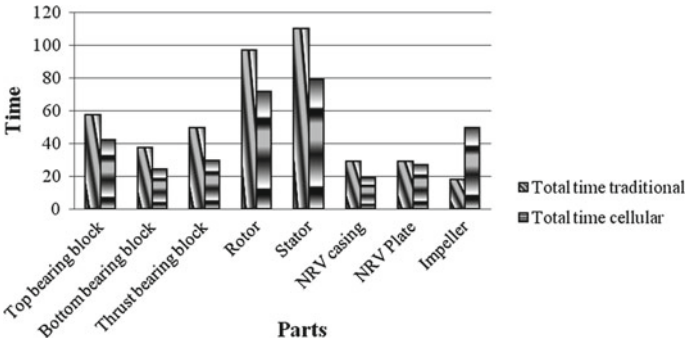

Fig. 7 Total production time

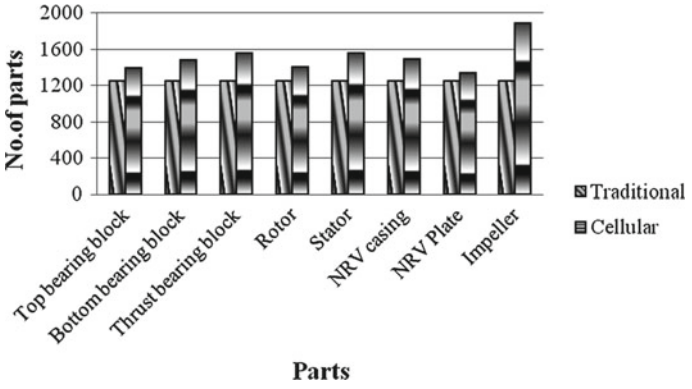

Fig. 8 Productivity

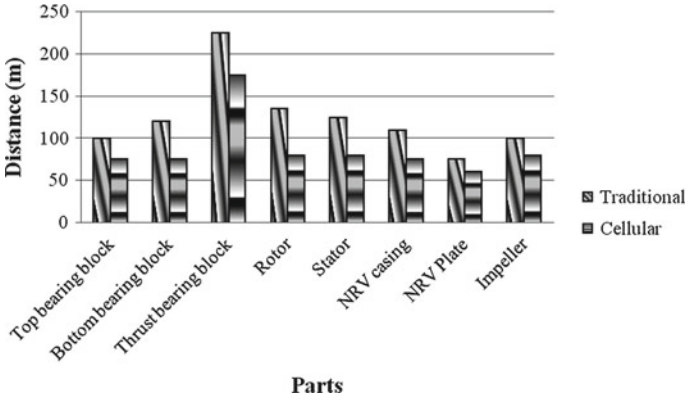

Fig. 9 Total traveling distance

4 Conclusion

In this work, the reaction improvement in the business on assembling of submersible siphon by utilizing Cellular Manufacturing Systems has been inspected. Uncommon elements, voids, group efficiency and group efficacy measures were utilized to assess the three bunching calculations ROC-2, DCA, MOD-SLC. MOD-SLC brought about fewer uncommon components (2), voids (3) higher gathering productivity of 91.33% and higher gathering viability of 82.14%. The consequences of bunching demonstrate that MOD-SLC is more viable than ROC-2 and DCA dependent on the broke down exhibition measures. Cell layout model has been planned dependent on the chose MOD-SLC calculation. The current regular framework model and the phone fabricating framework model were analyzed under various criteria, for example, efficiency and material dealing with separation. The outcomes from the correlation show that the Cellular Manufacturing System can diminish material taking care of separation by 51.25% and can improve profitability by 29.04%. This prompts a quicker reaction than the present framework. Cell manufacturing additionally expands generation precision that yields all the more opportune reactions and progressively focused business capacity.

References

1. King JR (1980) Machine-component group formation in group technology. OMEGA 8:193–199, and also Machine-component grouping in production flow analysis: an approach using a rank order clustering algorithm. Int J Prod Res 18:213–232
2. King JR, Nakornchai V (1982) Machine-component group formation in group technology: review and extension. Int J Prod Res 20:117–133
3. Chan HM, Milner DA (1982) Direct clustering algorithm for group formation in cellular manufacture. J Manuf Syst 1:65–75
4. Gongaware TA, Ham I (1991) Cluster analysis applications for group technology manufacturing systems. In: Proceedings: Ninth North American manufacturing research conference, pp 503–508
5. Mosier CT, Taube L (1985) The facets of group technology and their impacts on implementation—a state of the art survey. Omega 13(5):381–391
6. Mosier CT, Taube L (1985) Weighted similarity measure heuristics for the group technology machine clustering problem. Omega 13(6):577–583
7. Gupta T, Seifoddini H (1990) Production data based similarity coefficient for machine-component grouping decision in the design of a cellular manufacturing system. Int J Prod Res 28(7):247–269
8. Seifoddini HK (1989) A note on the similarity coefficient method and the problem of improper machine assignment in group technology problem. Int J Prod Res 27(7):1161–1165
9. Seifoddini HK (1989) Duplication process in machine cells formation in group technology. IIE Trans 21(4):382–388
10. Khan M, Islam S, Sarker B (2000) A similarity coefficient measure and machine-parts grouping in cellular manufacturing systems. Int J Prod Res 38(3):699–720
11. Yasuda K, Yin Y (2001) A dissimilarity measure for solving the cell formation problem in cellular manufacturing. Comput Ind Eng 39(1):1–17

12. Dimopoulos C, Mort N (2001) A hierarchical clustering methodology based on genetic programming for the solution of simple cell-formation problems. Int J Prod Res 39(1):1–19
13. Chandrasekharan MP, Rajagopalan R (1986) An ideal seed non-hierarchical clustering algorithm for cellular manufacturing. Int J Prod Res 24(2):451–464
14. Chandrasekharan MP, Rajagopalan R (1986) MODROC: an extension of rank order clustering for group technology. Int J Prod Res 24(5):1221–1233
15. Kumar KR, Kusiak A, Vannelli A (1986) Grouping of parts and components in flexible manufacturing systems. Eur J Oper Res 24:387–397
16. Vannelli, Kumar KR (1986) A method for finding minimal bottle-neck cells for grouping part-machine families. Int J Prod Res 24(2):387–400
17. Kumar KR, Vannelli A (1987) Strategic subcontracting for efficient disaggregated manufacturing. Int J Prod Res 25(4):1715–1728
18. Co HC, Araar A (1988) Configuring cellular manufacturing systems. Int J Prod Res 26:1511–1522
19. Gunasingh KR, Lashkari RS (1989) The cell formation problem in cellular manufacturing systems—a sequential modeling approaches. Comput Ind Eng 16(4):469–476
20. Chandrasekharan MP, Rajagopalan R (1989) Groupability: an analysis of the properties of binary data matrices for group technology. Int J Prod Res 27(6):1035–1052

Exploratory and Numerical Examination of Blending of Four Planar Parallel Planes

C. J. Thomas Renald, K. Karthikeyan, S. Yuvaraj, and J. David Rathnaraj

Abstract Blending of fly streams is one of the basic issues that can be investigated in the field of liquid elements which has a ton of utilization esteem in different burning and impetus frameworks. Modern/household gas burners, fuel infusion frameworks, short separation take off and arriving of planes are a portion of the spots where fly blending plays a crucial job in the perspective on proficient ignition and toxin scattering. In this examination, obstruction and collaboration of four parallel planar planes have been dissected both numerically and tentatively for different stream conditions. The business CFD programming bundle, Fluent 6.3.26, has been used to foresee the stream parameters for different stream conditions. In accumulation, to help the numerical examination, an exploratory method utilizing pitot cylinder has been created to research the issue of intrigue. Just the mean stream field is featured in this examination. The outcomes acquired from both test and numerical strategies have been contrasted and found with be concurred. A couple of symmetrical stable vortices has been shaped. The union point and the consolidated point have been found to happen on the hub of symmetry. The situation of union point and the joined point changes conversely as for the separation between the planes.

Keywords Mixed jet flow · Four planar parallel jets · Position of merge point · Combined point

C. J. Thomas Renald (✉) · S. Yuvaraj · J. David Rathnaraj
Department of Aeronautical Engineering, Sri Ramakrishna Engineering College, Coimbatore, Tamil Nadu 641022, India
e-mail: thomsi_reni2000@yahoo.co.in

K. Karthikeyan
Department of Mechanical Engineering, Sri Ramakrishna Engineering College, Coimbatore, Tamil Nadu 641022, India

N. Gascoin and E. Balasubramanian (eds.), *Innovative Design, Analysis and Development Practices in Aerospace and Automotive Engineering*, Lecture Notes in Mechanical Engineering, https://doi.org/10.1007/978-981-15-6619-6_3

1 Introduction

enlargethispage-24ptBlending of fly streams is one of the significant issues utilized in a wide assortment of building applications, for example, gas turbine combustors, fast flies, farming substance sprayers, short separation take off and arriving of aero planes, turbine spouts, air foil limit layer control, ventilation framework fumes, warming and cooling frameworks, modern/local burners, contamination fumes stacks and power boilers. There are essentially three methodologies that are utilized to take care of issues in liquid elements. These strategies are: (1) trial approach; (2) hypothetical methodology; and (3) numerical methodology. The primary methodology appeared in the seventeenth century. It includes just trial techniques to tackle the issues. This methodology was first received in England and France. This methodology is in all respects exorbitant and bulky. The emergence of various theories in the field of fluid engineering leads to the second approach called as the theoretical approach. This concept came into existence in the eighteenth century. The theoretical method uses the flow administering conditions, for example, Navier--Stokes, Prandtl conditions and so on, to take care of a liquid stream issue.

enlargethispage-24ptLin et al. [1] led investigates estimating mean speed parts, mean stream bearings, fierce powers and Reynolds shear pressure utilizing split film test of hotwire anemometer to examine the stream field produced by two indistinguishable planes of air issuing from a typical divider. Because of affectability of the split movie test to the stream heading, the turnaround stream in the uniting area was recognized and stream perception was made. David et al. [2] led tests for estimating mean speed mean stream heading, typical tempestuous shear pressure and mean static weight for sub-sonic field, produced by two indistinguishable planes of air from a typical divider and blending with encompassing air. Their form maps plainly uncover the sub-air static weight trough that records for stream assembly, a free stagnation point on the plane of symmetry. They have made between the advancement of stream, both in district of fly union and the locale of joined fly stream. Robert et al. [3] made research on the three-dimensional limited planes which are generally utilized in assortment of building applications like turbine edges, gas turbine combustors and so forth; they have made examination on blending of limited planes with contiguous planes or with their surroundings, and this incorporates investigation of planes limited by free surfaces and strong dividers, the planes being of different designs. Jyne et al. [4] made examination on various planes which are broadly utilized in fields of compound building procedures of blending. Division and transport among species can be escalated utilizing a progression of planes rather than a solitary stream which has improved the impetus and commotion level.

2 Problem Specification

Dimensions:

Trial 1:

Diameter of the jet: 10 mm

Distance between the jets: 20 mm

Flow field size: 100 mm × 100 mm × 100 mm

Flow field size: 100 mm × 100 mm × 100 mm

Trial 2:

Diameter of the jet: 10 mm

Distance between the jets: 30 mm

Flow field size: 100 mm × 100 mm × 100 mm

Trial 3:

Diameter of the jet: 10 mm

Distance between the jets: 40 mm

Flow field size: 100 mm × 100 mm × 100 mm.

Fig. 1 Experimental set-up

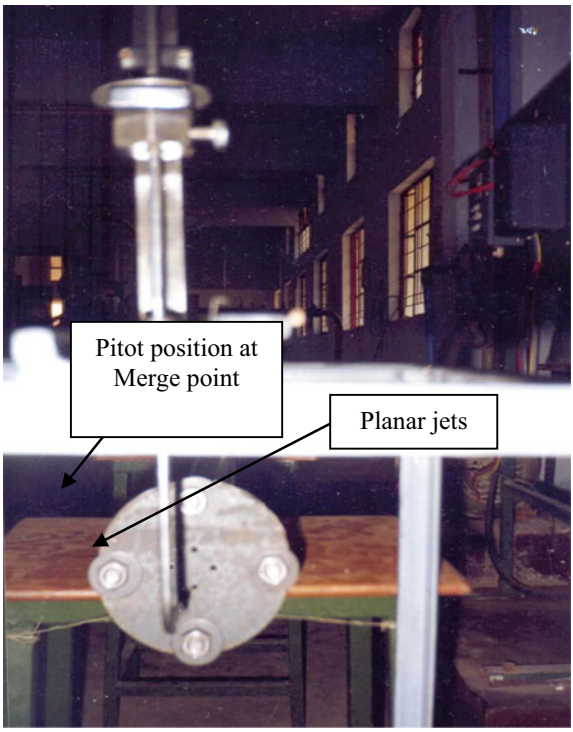

Fig. 2 Jet configuration and pitot tube alignment in the experimental setup

3 Experimental Set-up

The average exploratory set-up is appeared in Fig. 1. Figure 2 demonstrates the design of four planar flies on the fly plate.

Air from the blower is released into the pipe utilizing an enlarger since the cross-sectional region of conduit is greater than the blowers outlet pipe. The channel is furnished with a rib which can suit a wide assortment of stream plates. By utilizing PVC pipe, a comparative stream example of air inside the pipe can be guaranteed.

4 Methodology

At the point when the weight in the blower achieves the ideal esteem, the ball valve is opened. A weight of about 1.5 bar is kept up at the bay. Readings at various positions were taken by navigating the pitot tube in the guide ways. Relating manometric readings were taken from the mercury manometer. The readings were organized for various X/D proportions.

5 Governing Equations

Head (h)

$$H = y \times \left(S_{\text{hg}}/S_{\text{air}}\right) - 1 \tag{1}$$

where

y difference in manometer reading
S_{hg} specific gravity of mercury
S_{air} specific gravity of air.

Velocity (V)

$$V = \sqrt{2\text{gH}} \tag{2}$$

where

g acceleration due to gravity in m/s^2
H head.

6 Results and Discussions

In spite of various results obtained, the contour representation displays the effects predominantly. So, contours of velocity magnitude and velocity vector, numerical and graphical illustrations for various pitch circle diameter while jets diameter d_j = 10 mm and at inlet velocity V_i = 315 m/s have been provided in the following sections.

EFFEC From Figs. 3, 4 and 5, unmistakably the impact of pitch circle dia (PCD) is ruling over the forms of speed size. Following a similar pattern, the impact of PCD is progressively prevailing close to the divider locale of fly plate and delivering consolidation focuses and joined focuses at short separations for expanding the estimations of PCD.

Figures 6, 7 and 8 demonstrate the speed vector for various PCDs. The union focuses and joined focuses can be seen clearly for expanding estimations of pitch circle dia (PCD).

6.1 Graphical Illustrations

Speed extents for various PCDs when width of planes d_j = 10 mm are acquired numerically and they are outlined graphically through Figs. 9, 10 and 11. It is

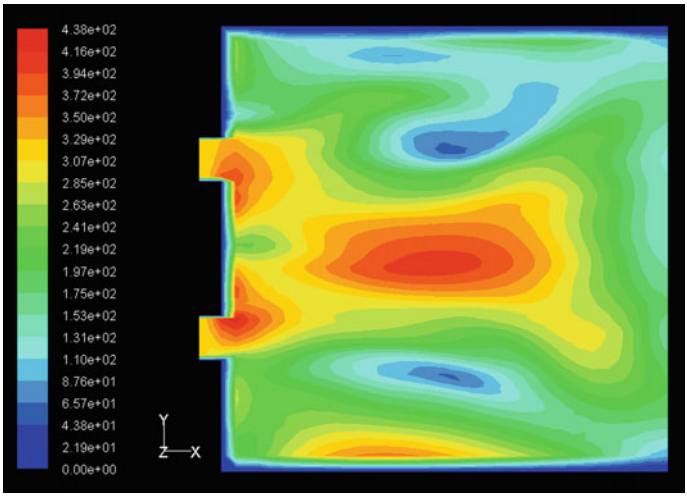

Fig. 3 Contour of velocity magnitude velocity PCD 30 mm

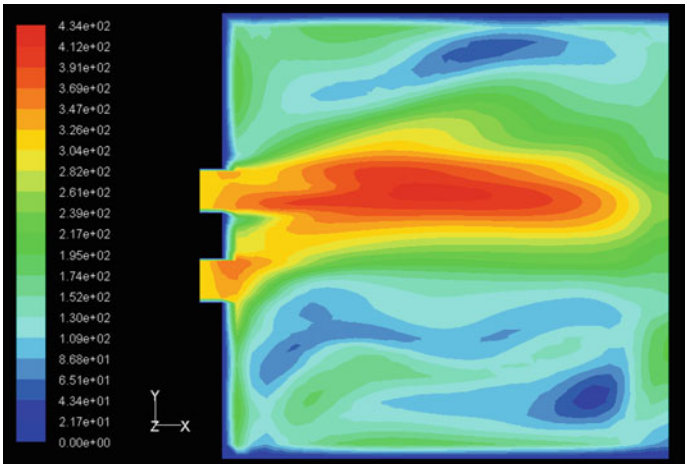

Fig. 4 Contour of magnitude for PCD 20 mm

construed from every one of these assumes that the impact of expanding PCD of the planes diminishes the separation of event of union point and consolidated point. At the point when the PCD of the planes = 20 mm, the union point happens at $1 < X/D, Y/D, Z/D < 3$ and the consolidated point happens at $3 < X/D, Y/D, Z/D < 4$ at hub of symmetry both tentatively and numerically. At the point when the PCD of the planes = 30 mm, the union point happens at $1 < X/D, Y/D, Z/D < 3$ and the joined point happens at $3 < X/D, Y/D, Z/D < 4$ at hub of symmetry both tentatively and numerically. At the point when the PCD of the planes = 40 mm, the consolidation

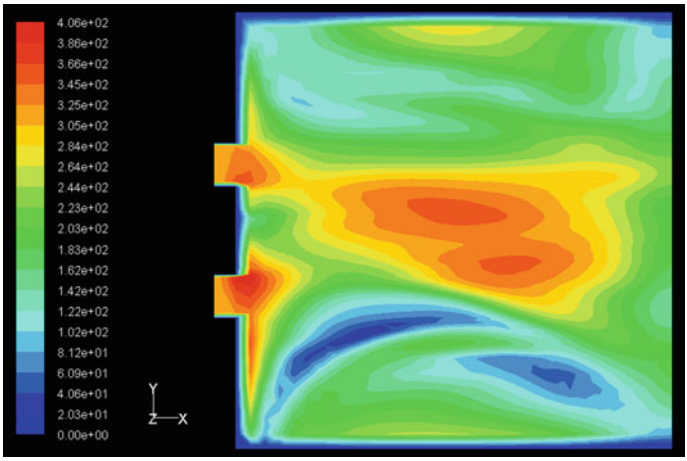

Fig. 5 Contour of velocity magnitude for PCD 40

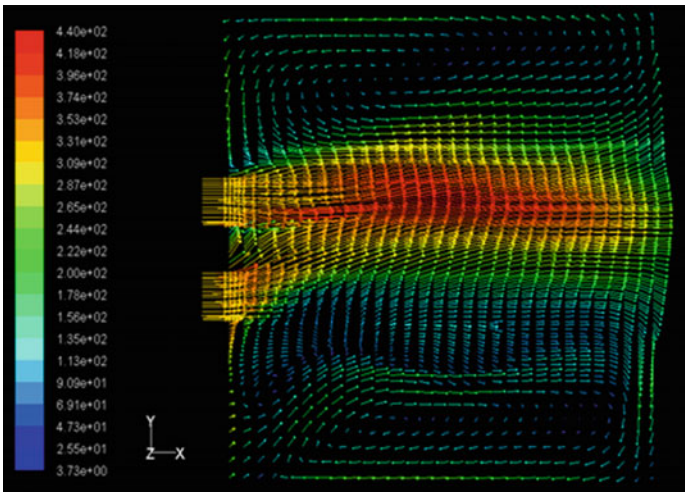

Fig. 6 Velocity vector for PCD = 20 mm

point happens at $1 < X/D, Y/D, Z/D < 2$ and the joined point happens at $2 < X/D, Y/D, Z/D < 3$ at pivot of symmetry both tentatively and numerically.

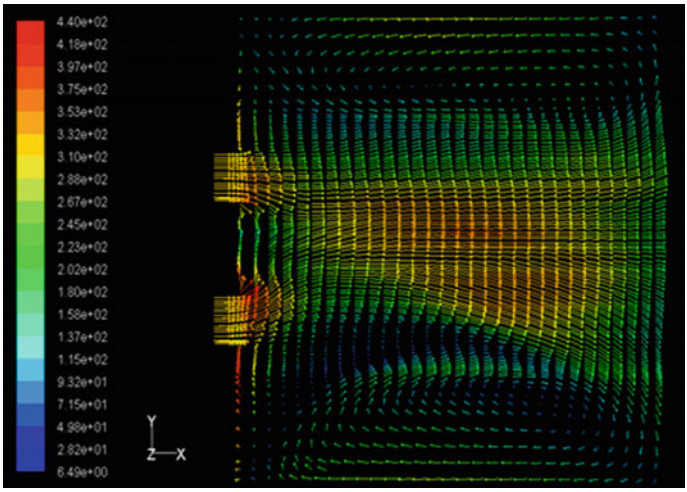

Fig. 7 Velocity vector for PCD = 30 mm

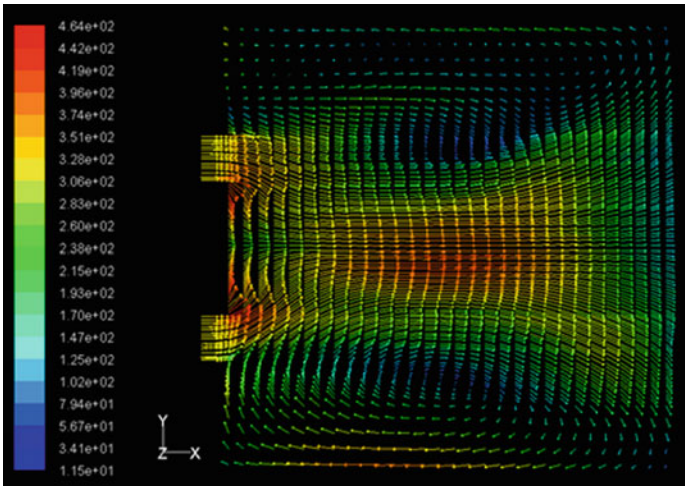

Fig. 8 Velocity vector for PCD = 40 mm

7 Conclusions

From all the above Results and Discussions, the accompanying ends are arrived and they are abridged as pursues:

(1) From the test and hypothetical examinations on the communication of four planar parallel planes, it very well may be seen that the four planar planes collaboration creating like a circle at a downstream separate. (2) At far downstream separate it

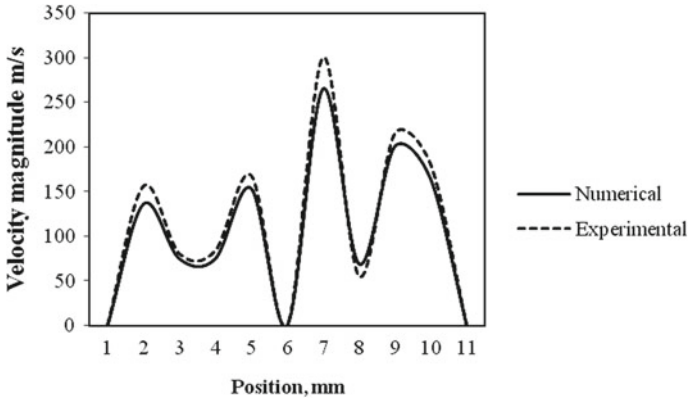

Fig. 9 Position of jets versus velocity magnitude for PCD = 20 mm

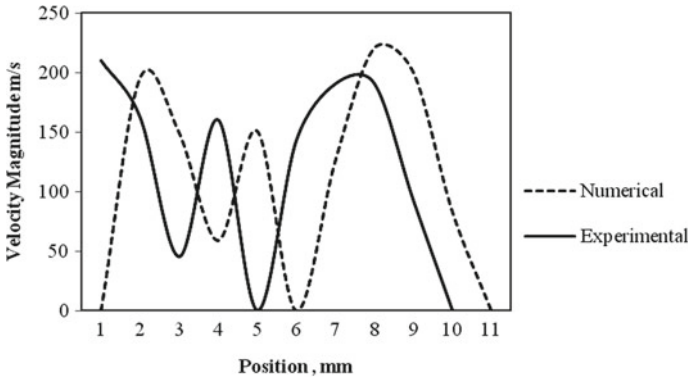

Fig. 10 Position of jets versus velocity magnitude for PCD = 30 mm

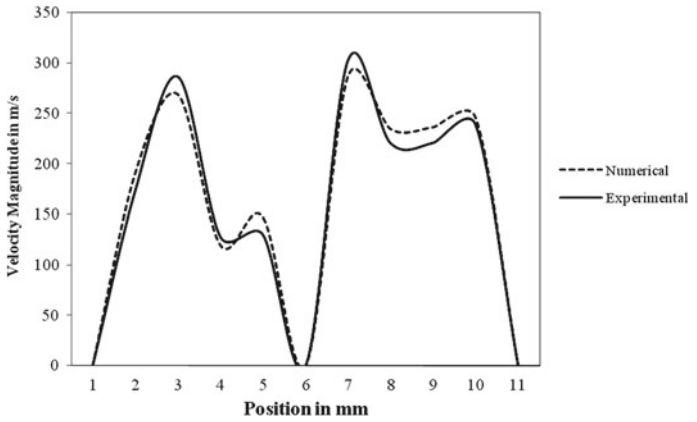

Fig. 11 Position of jets versus velocity magnitude for PCD = 40 mm

is viewed as that the fly is formed into a round fly. (3) A locale of sub-climatic static weight between the merging planes represents their union. (4) A pair of symmetrical stable vortices was framed and the overly climatic static weight diverts the combining plane streams in a typical downstream bearing. (5) The examination of speed profiles of exploratory and numerical qualities uncovers that the outcomes got are acceptable, for different stream conditions. (6) The position of consolidation point and joined point differs contrarily as for the PCD of the planes.

References

1. Lin YF, Sheu MJ (1990) Investigation of two plane parallel unventilated jets. AIAA J Fluid Mech
2. Miller DR, Comings EW (1999) Force momentum fields in a dual-jet flow. J Fluid Mech
3. Kunz RF (2001) LDV measurement of confined jet mixing. ASME J Fluid Mech
4. Okamoto T (1985) Interaction of twin turbulent circular jet. JSME J Fluid Mech

Clutch Operating Mechanism for Disabled People with Leg Amputee

Ravi Kumar Gupta, Deepak Goyal, and Akhilesh Kumar Sharma

Abstract Motor vehicles have become essential and important part of our daily life when it comes to mobility. It is necessary to own a car as it reduces distances. But disabled persons who are physically incapacitated always face difficulty when it comes to mobility. As per census year 2011, out of 1.21 billion population, 26.8 million are disabled which is 2.21% of the total population. Commercially available products offer control of clutch to the user by means of hand interface, however these products are expensive and invasive. Thus, it is needed to develop a better mechanism for disabled (people with one leg disability) person which is more cost-effective and agronomical. In this paper, a mechanism is developed which provides control of clutch at two points by hand instead of leg. Modelling, assembly and simulation using CATIAV5 and structural analysis using ANSYS workbench are presented. Design, fabrication and working of the developed mechanism are explained.

Keywords Automobile · Product development for disabled · Clutch operation · Leg amputee

1 Introduction

As per census 2011, in India, out of 1.21 billion population about 26.8 million people are disabled which is 2.21% of the total population. 20% of disabled persons

R. K. Gupta (✉) · D. Goyal
Mechanical Engineering Department, Faculty of Engineering, Manipal University Jaipur, Jaipur-Ajmer Express Highway, Dehmi Kalan, Jaipur 303007, India
e-mail: ravikumar.gupta@jaipur.manipal.edu

D. Goyal
e-mail: deepakgoyal925@gmail.com

A. K. Sharma
Information Technology Department, Faculty of Engineering, Manipal University Jaipur, Jaipur-Ajmer Express Highway, Dehmi Kalan, Jaipur 303007, India
e-mail: akhileshkumar.sharma@jaipur.manipal.edu

N. Gascoin and E. Balasubramanian (eds.), *Innovative Design, Analysis and Development Practices in Aerospace and Automotive Engineering*, Lecture Notes in Mechanical Engineering, https://doi.org/10.1007/978-981-15-6619-6_4

are having disability in movement, 19% are with disability in seeing and other 19% are with disability in hearing. 8% of the population has multiple disabilities [1]. Disabled persons who are physically incapacitated always face difficulty when it comes for a driving. For a conventional car, control by legs such as accelerator, clutch and brake cannot be operated by persons having lower disability. Today, there are many commercial manufacturers in the market who modify vehicles for people with double leg amputees. The vehicles with automatic gear control are available which do not require clutch operation but these vehicles with automatic gear control are very expensive and cannot be adopted to exiting vehicles and manual gear control cars. Hence, when it comes to provide mobility solutions, it is necessary that driving assistant mechanism(s) for disabled persons should be provided. There are some serious safety concerns when the driver leaves the steering wheel unmanned. The main safety concerns that need to be investigated are emergency manoeuvres, defensive driving and operating the vehicle in a panic situation. Disabled drivers are put into trial by forcing them to drive with one hand, which is quite dangerous in present day congested roads and especially during cornering.

The work presented in this paper is intended to give a mobility solution to paraplegic persons. The conventional clutch operating system (in exist car—Maruti Suzuki 800) is modified using mechanical linkages and steel wire. The major components of mechanism include force lever, pulleys, bearings and flexible wire. The developed mechanism has two points control of clutch by hand instead of leg so that the driver (person with one leg disability) can easily steer with both the hands and can control clutch with one hand (left hand with the left-hand drive cars) at same time. Out of two controls for the clutch one is at the gear knob and other is under the steering column. The amount of force required to press the clutch pedal has been reduced in order to be operated by hand. This mechanism is cost-effective and can be used in most of the cars with very little modification.

2 State of the Art

Ferro Equip and Alfred Bekker are some of the commercial manufacturers who modify cards for paraplegic persons [2, 3]. But the designs available in the market for hand control pedals have some shortcomings. For example, the design of Alfred Bekker has single lever mounted on either side of steering wheel which is used for engagement and disengagement of clutch. For changing the gear, the driver needs to (i) release the accelerator lever, (ii) disengage the clutch, (iii) shift to the required gear, (iv) engage the clutch and (v) again press the accelerator. All these five tasks to be carried out with at least one hand on steering wheel [4] which is not possible by the design of Alfred Bekker. Abdullah et al. [5] present a design of steering control of a vehicle for disabled driver as shown in Fig. 1. A degree of rotation is measured by the potentiometer and input to the microcontroller. The motor amplifies the rotation to the lower steering shaft to transfer the movement to the rack and pinion directly to the tires. The arrangement of the steering wheel, potentiometer, DC motor, rack

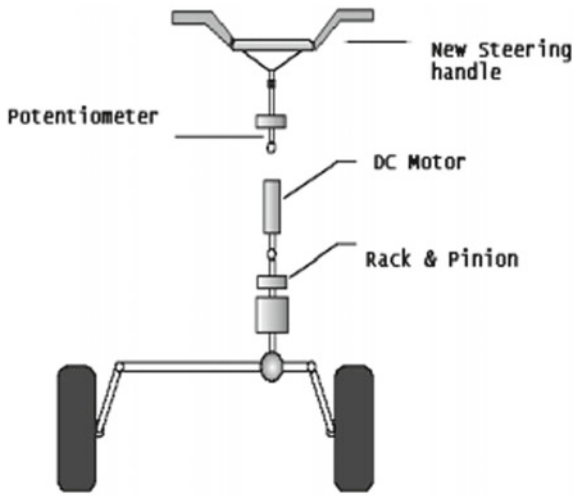

Fig. 1 Steering control of a vehicle for disabled driver

and pinion with the wheels' axle is shown in Fig. 1. Mechanical steering system was modified to mechatronics-based system by replacing mechanical linkages with motor and PIC microcontroller whereas operation of clutch is not included in the paper [5].

Therefore, it is required to develop vehicle control system in order to be driven by a disabled person. The main controlling operations are steering, acceleration, braking, clutching and gearing. Based on the type of disabilities, these five operations need to be managed by fully functional limbs. The work presented in this paper is focused on the development of clutch operation in an existing four-wheeler for lower limbs disabled people (legs are not functional). The developed clutch operating mechanism can be fitted in an existing four-wheeler without modification (very little adjustments) and does only include mechanical components. The development of such a mechanism is explained in the following section.

3 Clutch Operating Mechanism for Disabled People

The study of existing designs, commercially available and explained in literature, has been conducted and picked out the pitfalls so that they could be avoided in our design. Some of the pitfalls are explained in section: literature review. Design for the clutch operating mechanisms was iteration-based, i.e. for making the foot pedals hand controlled, various ideas were put forward and based on that idea's ideation, sketches were created and then feasibility of each design was checked. This methodology will not only keep errors out but will also reduce time resulting in a better design. Outcomes of this project are totally based on the innovation and ideas generated. The present invention is intended to provide a mobility solution by

modifying the manual transmission vehicles (manual control of gear and clutch) so that people with disability can also drive the vehicle without difficulty. The initial design has been filled for the patent [6]. The enhanced clutch operating mechanism and its operation are explained in this paper. The development of the Force Tuner used in the developed mechanism is also explained.

A mechanism has been designed in order to realize controlling the clutch simultaneously at two points. This mechanism named as "Force Tuner" has two points control of clutch by hand instead of leg so that the driver (person with one leg disability) can easily steer with both the hands and can control clutch with one hand (left hand with the left-hand drive cars) at same time. One of the controls for clutch is provided at the gear knob which can be used while shifting the gear and another one with the steering column so that it can be used while in traffic or speed breakers. Dual clutch control mechanism (Fig. 2) shows the mechanism to be used for two points control of clutch. Frame (number 1 shown in Fig. 2) is used for the explanation but the frame is not required in fitting the mechanism in the vehicle. The component numbers used in the explanation are shown in Fig. 2. Special analysis is carried out for checking the interference among components and the movement of the required components.

Figure 2 consists of 14 components which are used for the explanation of the working of the developed mechanism for two points control of clutch by one hand. Component 1 is a square tube frame (fixed as representation of a vehicle space used) which is used to hold the assembly. Component 12 is the clutch (as representation of clutch in a vehicle) which is mounted on the frame 1 and is free to rotate about the circular rod. The clutch is connected to the Force Tuner (component 11, also referred

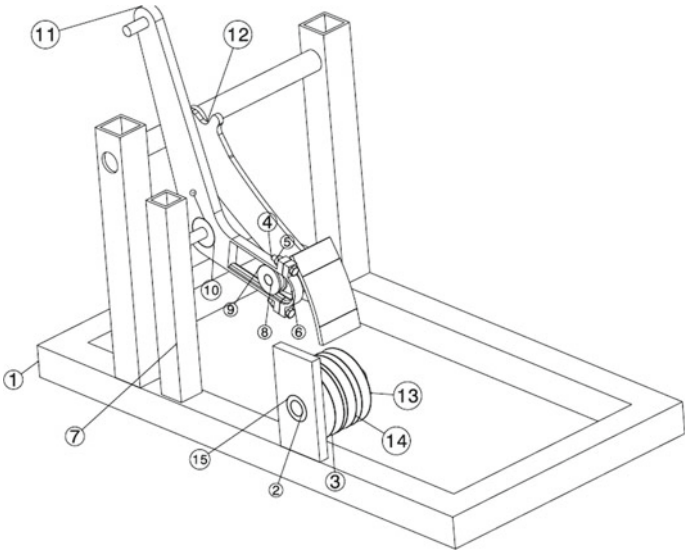

Fig. 2 Dual clutch control mechanism (isometric view of the assembly)

as Force Tuner lever) with the help of rod 8 and roller 9. The rod 8 is welded with the clutch near to the clutch pedal pad. The rod 8 is fixed in the inner bore of the bearing of the roller 9 so that the roller 9 can easily rotate about the rod axis. The roller rolls and slides over the slot provided in the Force Tuner lever so that the clutch and the Force Tuner can maintain the same arc during the operation of clutch engagement and disengagement.

The Force Tuner serves as the most essential component in the assembly. It provides mechanical advantage to the assembly so as to reduce the force required to press the clutch pedal. The shape and size of the Force Tuner, developed for Maruti 800, are shown in Fig. 3. In the Force Tuner, a slot has been provided in which the roller 9, as in Fig. 2, rolls so as to compensate the differences in arcs made by the clutch and Force Tuner. The mechanical advantage is calculated as the ratio of output force to the input force. Here, input force (F) is the force required to press the clutch pedal which is around 200 N as required to push the clutch pedal by leg [7]. Effort required (E) to pull the Force Tuner is calculated by the moment balance Eq. (1).

$$F * e_1 = E * e_2 \tag{1}$$

where F = Force required to press clutch pedal; E = Effort required to pull the Lever; e_1 (distance between the axis of the roller 9 to the axis of rotation of the lever) = 10 cm; e_2 (distance between the point where effort is applied on the lever to the axis of rotation of the Lever) = 20 cm. The required effort (E) is calculated as 100 N. Therefore, mechanical advantage (MS) is calculated by Eq. (2). Thus, the mechanical advantage helps the driver to easily pull the handle with one hand.

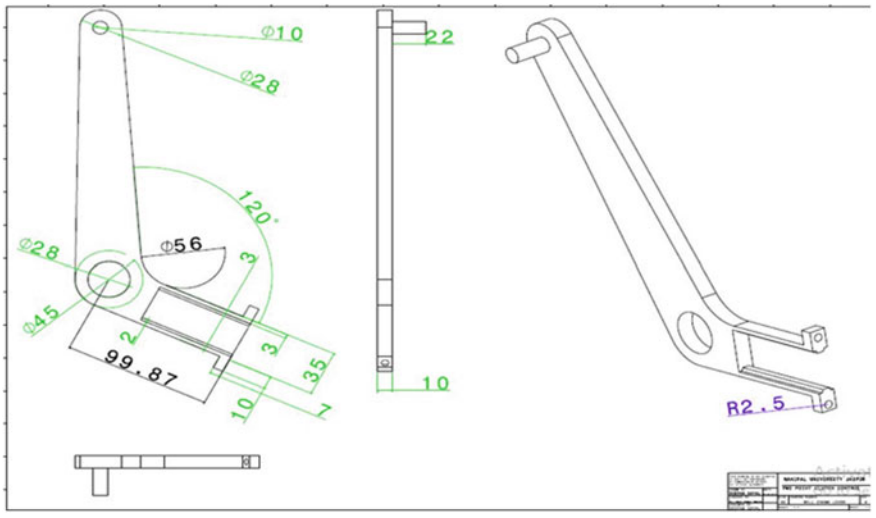

Fig. 3 Shape and size of force turner (all dimensions are in mm)

$$MA = F/E \tag{2}$$

The lever 11 is connected to pulley 13 by flexible steel wire. The pulley 13 is fixed with the rod 2 which in turn is mounted in inner bore of bearing 15 and is free to rotate about its axis. The pulleys 14 and 13 on the rod 2 are connected to the control handles with the help of cable. When the driver releases the handle, the clutch tends to move upwards due to restoration force of spring and the clutch wire until it reaches its initial position.

3.1 Finite Element Analysis (FEA)

The finite element analysis was conducted to check the required size, shape and martial used for the fabrication of the lever. The finite element analysis of the lever has been conducted to find out the risk-prone areas in it and improve the design if needed. The axis of rotation of the lever is fixed where bearing is going to be fitted. Two forces are applied on the lever as shown in Fig. 4. The applied force is exerted when the lever moves down and roller rolls on the red area as shown in Fig. 4a. This force exerted is chosen as 250 N which is greater than the force required to press the clutch pedal by foot so as take safer side. The second position of force was at top of Force Tuner as shown in Fig. 4b where the cable is going to be attached and pulls the lever. The top part can also face some deformation due to pulling action of cable hence it was necessary to carry out analysis for that part also.

Mesh analysis was performed on the various element sizes from 4 to 0.6 mm. It has been found that changes in deformation have been reduced to negligible from 0.0 to 0.6 mm (as shown in deformation graph in Fig. 5) and hence results become mesh independent at this element size. Hence, optimum mesh size has been taken as 0.6 mm. Details of element for the final iteration in FEA have been provided in Fig. 6.

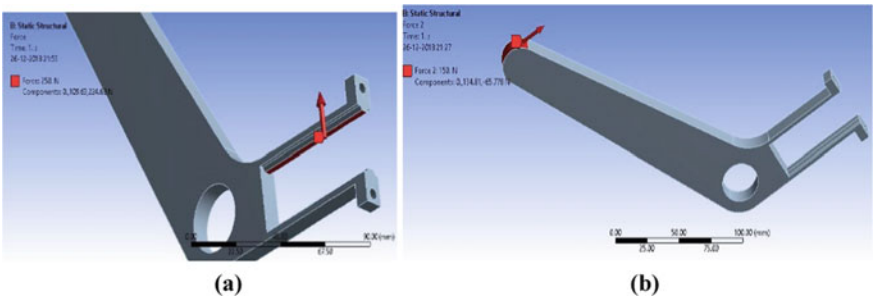

Fig. 4 Forces applied on the lever

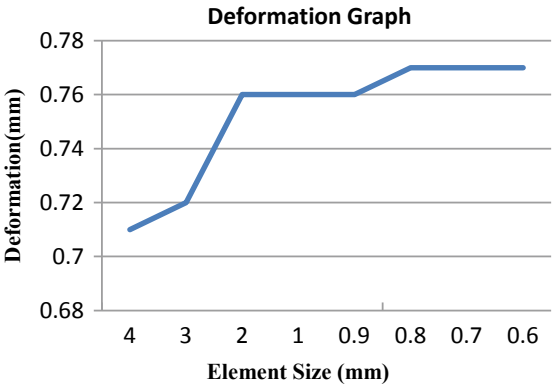

Fig. 5 Deformation with respect of the element size used in FEA

Fig. 6 Element details of the final iteration in FEA

Element Type	SOLID 187
Element Size	0.6 mm
Nodes	1339846
Elements	897102

3.2 Simulation and Results

The simulation results are presented in Fig. 7. Two factors were evaluated namely equivalent stress and deformation. Figure 7a shows the deformation in "Force Tuner". The red area (Fig. 7a) indicates the highest deformation. It is noticed that the sliding portion faces maximum deformation as roller will be sliding on that portion when Force Tuner is in motion, hence maximum force will be experienced by that portion only. The maximum deformation goes only up to 0.75 mm which is under safety

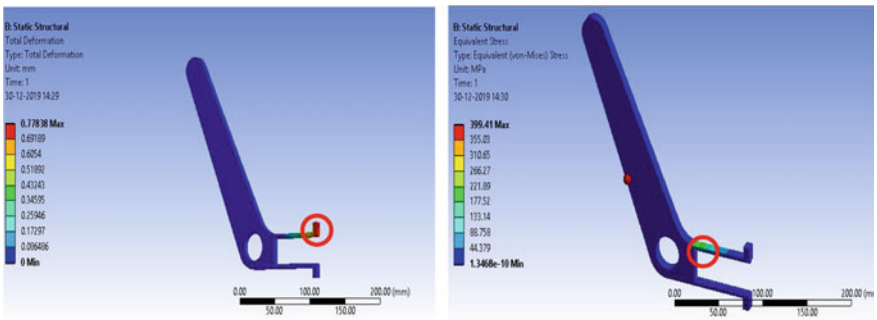

(a) (b)

Fig. 7 Simulation results for the applied forces on the lever

limit. Figure 7b shows the equivalent von Mises stress in the Force Tuner. The circle marked indicates the maximum stress area as it is nearest to the bearing which is fixed; hence, its motion is restricted and therefore faces the maximum stress.

The mechanism was successfully fabricated. Some of the parts like clutch pedal, bearings and mild steel sheet were purchased from the market. The lever was fabricated in-house. Assembly and welding were done in-house and experimented in the laboratory environment.

4 Discussion

The developed clutch operating mechanism for disabled people allows the driver to control the clutch from the two points which are provided at the gear knob and under the steering column. So, when driver meets any panic situation, he/she could just press the handle located under the steering column and avoid any fatal consequences. The other purpose providing the two controls is to allow the driver to control clutch and shift gear simultaneously. While shifting the gear, the driver can use the clutch handle provided at the gear knob to shift the gear. While in traffic, the driver can use the clutch handle provided under the steering column to control the clutch. This will not only make the hill climbing easier but also assist the driver in traffic. Force required to press clutch pedal varies with the different cars. Some cars require high amount of force to press the clutch pedal. In our invention, we have developed a special part "Force Tuner lever" which reduces the force required to press the clutch pedal to half by providing mechanical advantage to the device. This MA will assist the driver to press the clutch handle with feeble amount of force avoiding any strain in hands. The developed mechanism has very limited no. of components and has used cables instead of long rods and levers; hence, there is a lot of space available for the comfort sitting of the driver. Also, a small number of components make the system more reliable and safer. The developed mechanism does not require any electronic equipment and sensors and is completely mechanically operated, hence its cost is also very low as compared to that of electronic/electromagnetic devices.

5 Conclusion

The presented mechanism was developed to provide a mobility solution by modifying the manual transmission vehicles (manual control of gear and clutch) so that people with disability can also drive the vehicle without difficulty. A device named dual clutch control is developed which has two points control of clutch by hand instead of leg so that the driver (person with one leg disability) can easily steer with both the hands and can control clutch at same time. The device enables the user to actuate the complete range of motion of the pedal by hand control. The developed mechanism not only reduces the force required to press the clutch pedal but also saves the space by

eliminating long rods which were used in commercially available devices. Its design is done in such a manner such that it contains maximum strength at with low weight. Its strength has been tested in the FEA and deformation is just 0.77 mm which is very meagre. The mechanism "dual clutch control" can be easily installed in the car which makes it more versatile. The mechanism uses only mechanical components. The fabrication cost of the devices is 1000 INR (14 USD) approximately.

References

1. India Census 2011, http://mospi.nic.in/
2. Ferro Equip Hand Controls, http://www.mobilityenhanced.com/
3. Hand Controls for Disabled Drivers, http://alfredbekker.com
4. Sumit S, Vaibhav B, Amit C, Subodh D, Chinmay S (2017) Modifications in the driving system of a conventional Car for paraplegic people. Int Res J Eng Technol 04(04):1939–1948
5. Abdullah KAR, Mohammed Ali JS, Tuan Kamaruddin TNA, Md Saufi SJ (2010) Design and development of driving system for disabled driver. In: Conference on aerospace and mechanical engineering—world engineering congress 2010, 2–5 Aug 2010, Kuching, Sarawak, Malaysia
6. Gupta RK, Goyal D (2018) Four wheeler (car) driving assistant system for disabled people (one leg disability). Intellectual Property India
7. DiLullo G, Kocienski S, Zopatti D (2013) Development of zero-leg input manual transmission driving interface. Worcester Polytechnic Institute, MIRAD Laboratory, Project Number: MQF-MQP 3310

Optimization and Analysis of Front Telescopic Suspension for Electric Bike to Have Comfortable Ride: India Perspective

Yogendra L. Jain, V. U. Garud, S. Dubal, and S. Arole

Abstract As per current government directives, every automobile OEM has to come up with EV model by 2020. But current Indian road conditions demand variation in torque requirement which leads to uncomfortable ride and so affecting the battery life of electric bike. So there is a need to optimize existing traditional suspension system to experience better and comfortable ride with electric bike which may lead to extend battery life. With this objective, present research and development work initiated to design, develop, and analyze traditional suspension system specifically for an electric bike on bumpy roads using simulation behavior of the spring and damper. The study involves development of solid CAD model of two inverted telescopic spring and damper systems, viz. primary and secondary and virtual simulation of the CAD model in ADAMS software. Spring and damper systems are joined together with different set of attachments and classified them as traditional and optimized one to achieve the desired objectives. To compare the traditional and optimized suspension system, transmissibility analysis at bump size of 10 cm and 3 cm is carried out and corresponding stress developed in shackle plate and fork body is also analyzed to make sure that stresses are within permissible limit of material.

Keywords Front suspension · Electric bike · Virtual simulation · ADAMS

Y. L. Jain (✉) · V. U. Garud · S. Dubal · S. Arole
School of Automobile, Symbiosis Skills and Open University, Kiwale, Pune, India
e-mail: yogendrajain884@gmail.com

V. U. Garud
e-mail: vicky_garud100@yahoo.co.in

S. Dubal
e-mail: sdubal1585@gmail.com

S. Arole
e-mail: Sanjay.arole@ssou.ac.in

N. Gascoin and E. Balasubramanian (eds.), *Innovative Design, Analysis and Development Practices in Aerospace and Automotive Engineering*, Lecture Notes in Mechanical Engineering, https://doi.org/10.1007/978-981-15-6619-6_5

1 Introduction

While developing EVs for Indian market, OEMs must take into consideration the irregular road conditions such as steps and bumps and so in recent years, the focus is also being shifted to have better and comfortable ride with higher segment vehicles. Wide research has already been carried out for higher segment vehicle in order to have maximum possible mileage at desired torque on bumpy or irregular roads and it was observed that economy level drops down on irregular roads [1].

Also, due such irregularities, trend of torque requirement on such roads is shown in Fig. 2. Coefficient of rolling resistance is tested as per standard defined by SAE J1269, SAE J2452, and by ISO 18164:2005 (Europe). As per these standards, allowable coefficient of rolling resistance (CRR) is 0.007–0.014 for new tires. From Fig. 1, it is clear that at as the tire pressure goes down, CRR is exceeding 0.014. Now relating this with electric vehicle, coefficient of rolling resistance is directly proportional to battery consumption or event of battery recharging. It is clear that, to have better battery life or having less event of battery recharging, we must either focus on proposing and developing better roads or developing and optimizing the traditional suspension system. The traditional telescopic suspension systems designed with low cost have less maintenance and durable but it is insensitive to low height bumps. It is observed with telescopic suspension system developed for two wheelers first time in 1939 by BMW in USA [2]. Since then very few design modifications are seen in mid-range bikes in front suspension. Nowadays, vehicles not only differ in engine power or mileage but also in suspension characteristics [1]. Many two-wheeler manufacturers have developed their own technology for front telescopic suspension which is of inverted type. The optimum behavior of this type of suspension is obtained by changing the governing parameters [1]. Looking at variation in Indian road condition, it is required to incorporate inverted telescopic suspensions in for electric bike as it reduces the unsprung mass which leads to better and comfortable ride [3]. The springs in front suspension are preloaded to have desired stability. Preload also helps in maintaining the height of the suspension to adjust vehicle weight. This preloading makes the spring insensitive to road reactions and having lower value than the prestress given to suspension springs [3].

Even after development of conceptual design of suspension system, question is "how to evaluate or compare the performance with existing suspensions"? Experimental validations is one such process in development of suspension system which completely relied on the rider perceptions of comfort and evaluation techniques [4]. Static and dynamic analysis/behavior with the help of parameters such as kinetic energy, displacements, and velocities can be obtained with respect to change in time [5]. The main objective of this study is to reduce the response/vibration or displacement level at bike handle which occurs due to road irregularities to have better and comfortable ride. Current paper is focusing on optimization in existing suspension system. Simplified model was developed in ADAMS for dynamic analysis and the same is done on the conceptual model using ADAMS. Response level was recorded at bike handle bar as displacement in Y-direction and recorded in the form of graphs

Fig. 1 Status of Indian road profiles

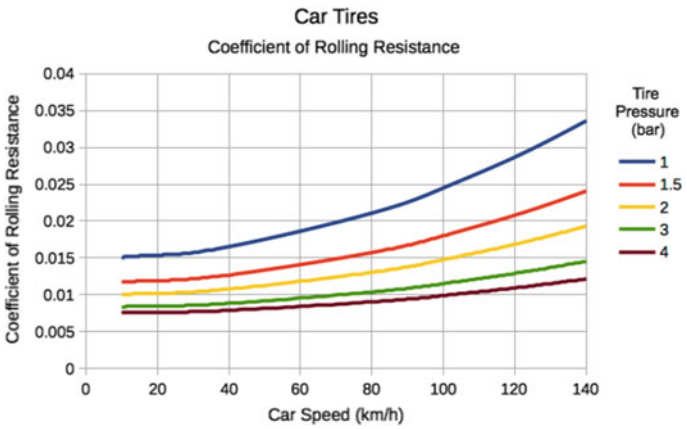

Fig. 2 Rolling resistance versus car speed (courtesy of "engineeringtoolbox.com")

for various conditions. Similarly, graphs for transmission of energy are also plotted. To have minimum transmissibility at different excitation, some parameters such as spring stiffness, damping coefficient, and geometry of the attachment have been changed or modified. This modification is to achieve vehicular ride comfort.

2 Methodology

The conceptual solid model prepared using SolidWorks software by following bottom-up approach of assembly. Traditional suspension (a) wherein primary and secondary tubes are not always parallel while riding on bumpy roads and the same has taken into considerations as shown in Fig. 3, whereas in optimized parallel

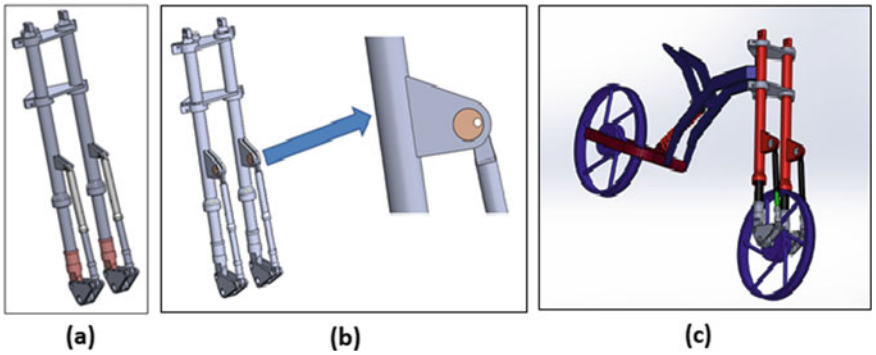

Fig. 3 Conceptual model with traditional and optimized suspension

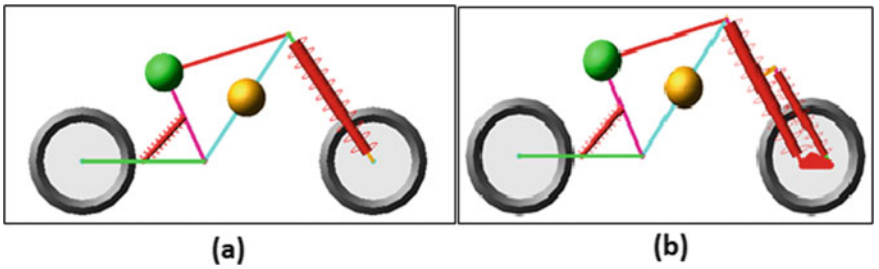

Fig. 4 Bike model with traditional suspension (**a**) and optimized suspension (**b**)

suspension system (b) has shown wherein the tubes and so the springs are parallel to each other irrespective of road conditions.

As a part of model optimization, the maiden attempt is executed which is to constrain secondary fork body to primary body with eccentric attachment (c). This is just to minimize response level or possible displacement at bike handle even if small irregularity comes. The frame of the vehicle is modeled by taking approximate dimensions as that of a commonly used electric bikes as shown in Fig. 4c.

3 Simulation and Analysis

Simplified model of bike with traditional Fig. 4a and optimized Fig. 4b suspension system is modeled in ADAMS. Figure 4b shows modified design with shackle plate in upright position and shackle plate mounted such a that both the suspension forks will have contact point below the axle level. Some design parameters are as in Table 1.

Overall parameters are kept constant for traditional as well as for optimized model. *Y*-displacement in cm of bike handle bar has measured from post-processing menu. From this, transmissibility of front suspension can be calculated. Motion is given to

Table 1 Design parameters of bike

S. No.	Design parameter	Value	S. No.	Design parameter	Value
1	Caster angle	30°	9	Kerb weight of vehicle	50 kg
2	Wheel base	1.5 m	10	Rider weight	100 kg
3	Front tire radius	245 mm	11	Link material	Steel
4	Rear tire radius	245 mm	12	Unsprung mass of vehicle on rear and front link	10 and 5 kg
5	Handle level	950 mm	13	Tire and road models implemented as available in ADAMS library	
6	Bump height	100 mm	14	Vehicle and rider weight are considered as point load on frame	
7	Span of bump	77 cm			
8	Vehicle speed	10, 15, 20 km/h			

Table 2 Simulation results of ADAMS software

Location	Stiffness (K) (N/mm)	Damping coefficient (C) (N s/mm)	Preload (kg)
Traditional suspension			
Front (each leg)	20	0.6	30
Rear	70	3	50
Optimized suspension			
Front primary (each leg)	18	1	20
Front secondary (each leg)	2	0.1	3
Rear	70	3	50

the revolute joint between rear axle and rear tire. The input is varied to have average speed of vehicle as 10, 15, 20 km/h. Simulation results for traditional and optimized suspension are given in Table 2.

4 Result and Discussions

With reference to simulation results for traditional and optimized suspension listed in Table 2, graph for displacement in Y-direction is plotted against time. For dynamic analysis, simulation was ran for 2.5 s with steps of 1500. Vehicle undergoing bump can be seen in graph between 1.5 and 2.0 s on X-axis.

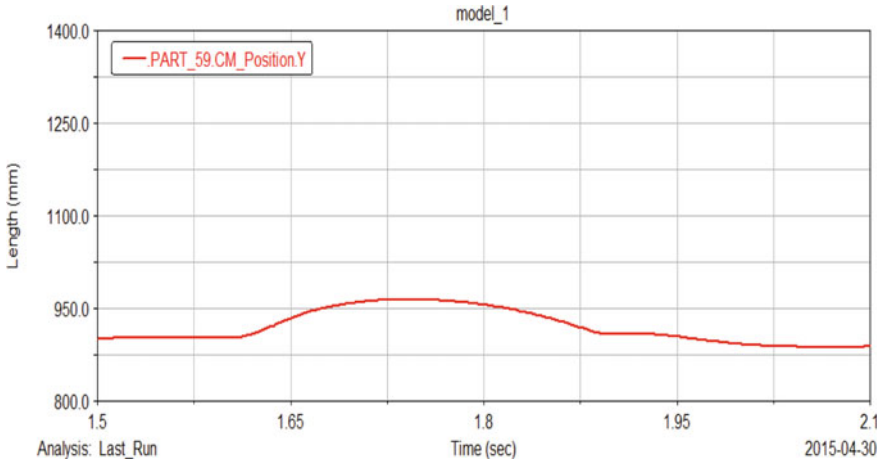

Fig. 5 Displacement in *Y*-direction at 15 kmph

4.1 Traditional Suspension

See Fig. 5.

4.2 Optimized Suspension

Test for transmissibility is carried out for variable vehicle speeds. Displacement in *Y*-direction is measured for bump size of 10 and 3 cm. The transmissibility thus obtained for traditional and optimized suspension is listed in Table 3. Kinetic and potential energy is measured at handle bar. For comparison purpose, a superimposed graph is plotted against time in Figs. 6 and 8. From above graph, it is observed

Table 3 Transmissibility analysis

Vehicle speed (kmph)	Displacement at handle bar (mm)	
	Bump size of 10 cm	Bump size of 3 cm
Traditional suspension		
10	73	17
15	65	17
20	70	21
Optimized suspension		
10	68	14
15	61	13
20	69	20

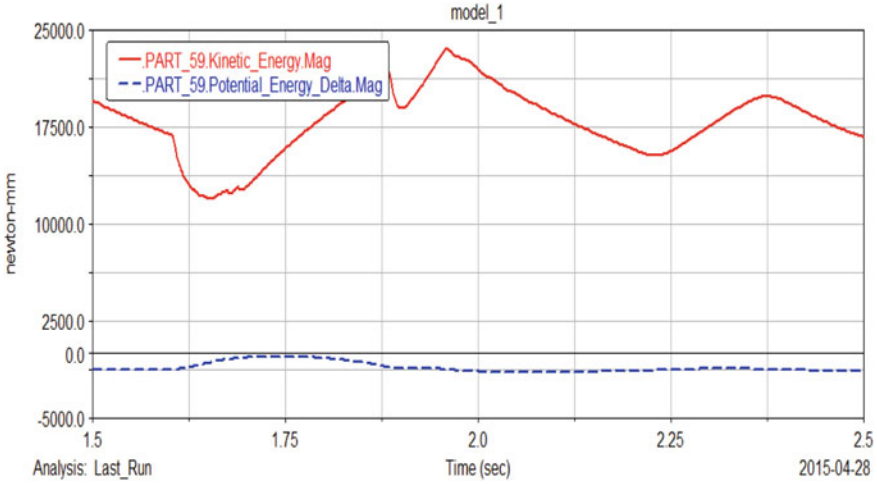

Fig. 6 Kinetic and potential energy at 15 kmph

that when the vehicle is passing over the bump, kinetic energy decreases whereas potential energy increases and attains maximum value at 1.65 s. After this point, potential energy decreases and kinetic energy increases. These changes validate the phenomena of energy transfer (Fig. 7).

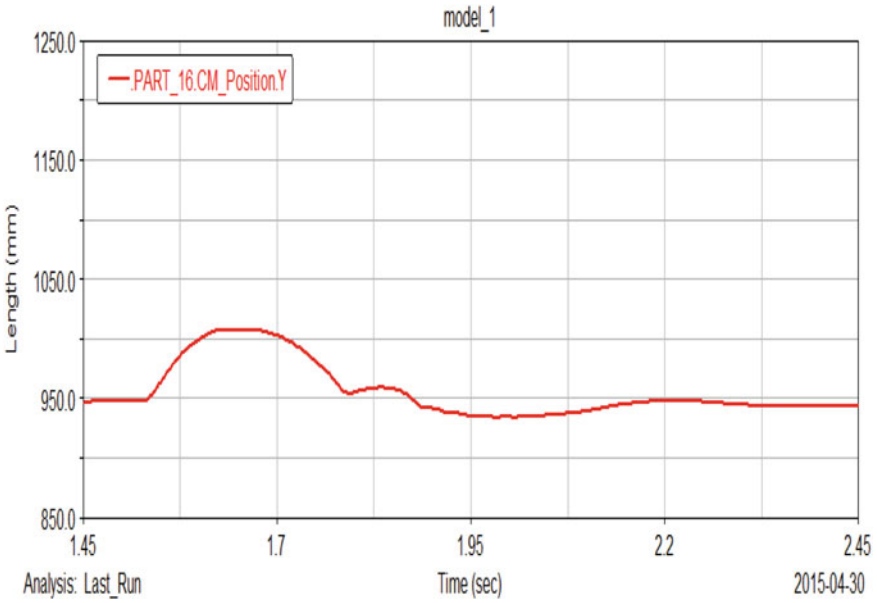

Fig. 7 Displacement in *Y*-direction at 15 kmph

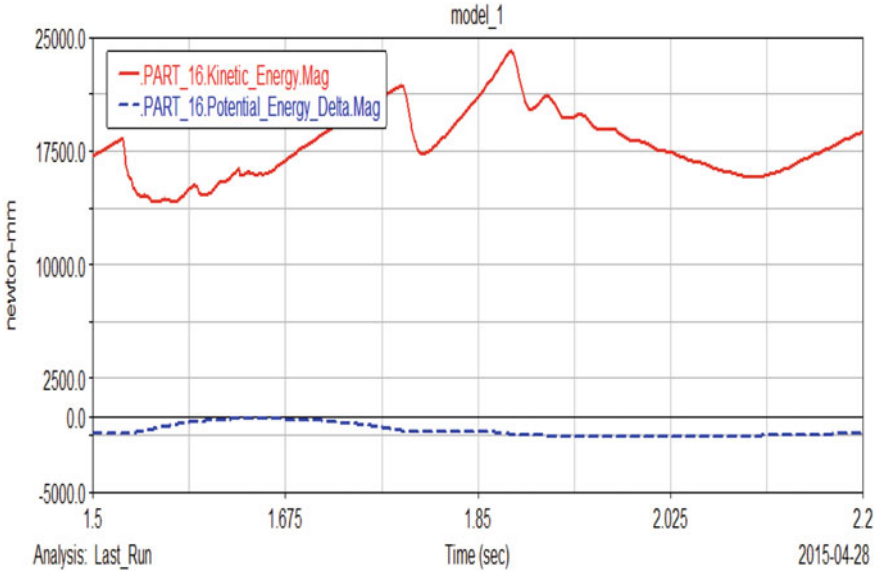

Fig. 8 Kinetic and potential energy at 15 kmph

For clear understanding and comparison purpose, graphs are plotted for traditional and improved suspension subjected to same bumping conditions (Figs. 9 and 10).

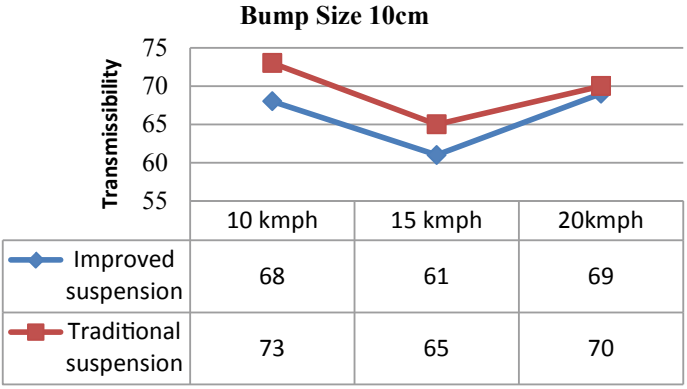

Fig. 9 Transmissibility versus bike speed

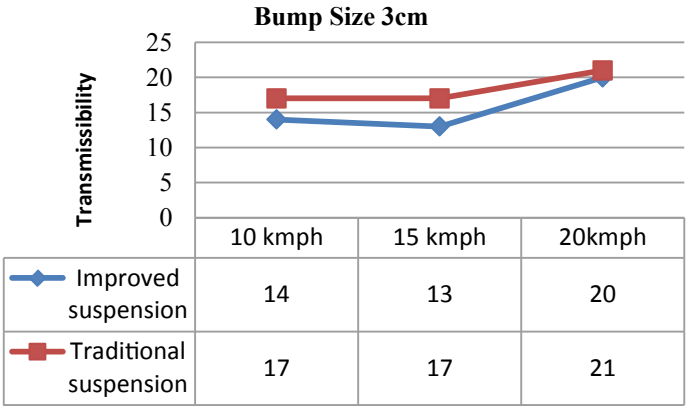

Fig. 10 Transmissibility versus bike speed

4.3 Structural Analysis

Due to irregular road profile, various stresses are also induced in the shackle plate and fork body. For structural analysis and to reduce complexity in calculations, reactions on front and rear tires are assumed to be 40% for front and 60% for rear wheel. Hence, total load on front suspension is approximately 100 kg. For analysis, coarse mesh is selected with following parameters,

- Material for shackle plate: steel.
- Density of the material = 7850 kg/m^3.
- Yield strength of the material = 0.25 × 10^3 MPa.
- Young's modulus = 200 GPa.

From ADAMS post-processing module, forces transmitted through tires are measured. Longitudinal and vertical forces are considered for design of fork body keeping other material parameter as that of shackle plate analysis. Deformation analysis of shackle plate is carried out by fixing inner face of the bottom slot of shackle plate. Load of 500 N is applied to inner surfaces of the shackle plate through holes where suspension forks are mounted and maximum stress in the shackle plate is found to be 09.38 Mpa as shown in Fig. 11.

Outer face of the fork body is constrained as fixed support. Load of 1000 N is applied to inner surface of the plate where the eye of secondary fork body is to be attached and maximum developed stress were found to be under safe stress limit as shown in Fig. 12.

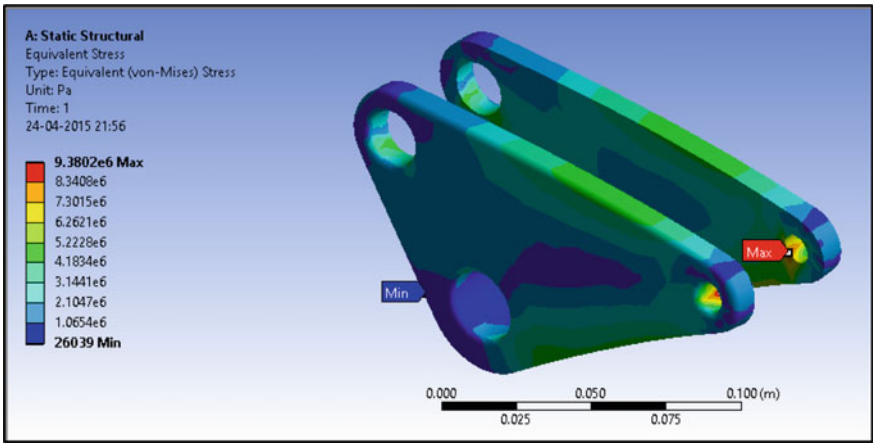

Fig. 11 Maximum stress in shackle plate

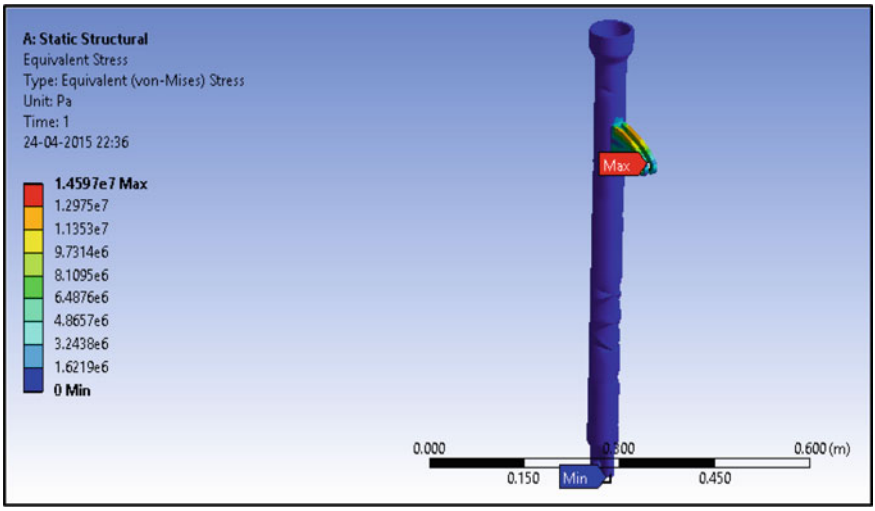

Fig. 12 Average stress in fork body

5 Conclusion

Comparing transmissibility for both traditional as well as optimized suspension model, it is concluded that there is decline trend of transmissibility for optimized suspension system at both bump size, i.e., 10 and 3 cm also for the same set up, transmissibility found to be minimum for vehicle speed of 15 kmph. Also, due to bump or irregular road profile, whatever stresses are induced in components are

within permissible limit of the material which is clearly observed in structural analysis. Though the difference in performance is not significant, efforts can be made to decrease transmissibility of optimized suspension system by working on other parameters such as spring behavior and damper geometry. The same can be achieved by prototyping the model for different setups. Considering these concluding remarks, optimized suspension system can be implemented for upcoming electric bike and if required further modifications and optimization can be done on trial and error basis.

References

1. Tholeti RK, Parimi A, Sheikh PBAM, Yogaraja V (2013) To optimize motorcycle ride comfort and handling parameters for inverted telescopic suspension, 2013-26-0149 2013 SIAT India
2. Croccolo D, De Agostinis M, Motorbike suspensions modern design and optimization. Springer Publication. ISSN 2191-530X
3. Cossalter V, Lot R, Massaro M, Motorcycle dynamics
4. Subbu R, Samy BA, Sharma P (2014) Two wheeled vehicle ride comfort evaluation and optimization using bump test rig in virtual simulation and validation through actual testing, 2014-01-0078
5. Vinogradov O, Fundamentals of kinematics and dynamics of machines and mechanisms. CRC Press. ISBN 0-8493-0257-9

Design and Analysis of Aluminium Matrix Composite Aircraft Wing Structure

M. Saleem, Nishant Kumar Raj, Shreshth Gupta, and Yogesh Kumar

Abstract Reduction of weight ratio seems to be a very challenging thing in aerospace industries as it improves the performance and efficiency of an aircraft wing. Isotropic properties of composites are used to make highly efficient aircraft structures for meeting the performance requirements. Focusing on better properties metal matrix composites are giving high strength, reduction of weight ratio, low density and high thermal conductivity when compared to any other composites. MMCs are used in automotive, civil and aerospace industries for increasing the production. This research work deals with MMCs which is reinforcement as LM6 and fly ash matrix material. Sir casting process is used to produce the MMCs. Mechanical characterisation of the composites are tested with ASTM D 638 standard. The main aim of this paper is to design the composite aircraft wing structure by CATIA. Structural, dynamic analysis was performed by ANSYS software and results has been validated.

Keywords LM6 · Fly ash · High strength · Aircraft wing · Dynamic loading

M. Saleem · N. K. Raj (✉) · S. Gupta · Y. Kumar
Department of Aeronautical Engineering, Vel Tech Rangarajan Dr. Sagunthala R&D Institute of Science & Technology, Chennai, India
e-mail: rajnishant3627@gmail.com

M. Saleem
e-mail: strokesaleem1@gmail.com

S. Gupta
e-mail: shreshthg@hotmail.com

Y. Kumar
e-mail: yogeshdewangan684@gmail.com

N. Gascoin and E. Balasubramanian (eds.), *Innovative Design, Analysis and Development Practices in Aerospace and Automotive Engineering*, Lecture Notes in Mechanical Engineering, https://doi.org/10.1007/978-981-15-6619-6_6

1 Introduction

Wing is considered as the main part of the aircraft for generating lift and make it fly [1–3]. Many kinds of loads act over and underneath the wing which can create structural damage easily. The composite materials have many advantages in order to increase the strength without loading much weight. In aerospace industries, composites are always in demand for a lightweight, high thermal conductivity, high strength and high stiffness applications. As the metal matrix composites in which metal is used as a matrix for reinforcing, have low density, high compression and high tensile strength and good processability, it is used in aerospace applications. MMC's are an economically great solution for the demand for lightweight material with good structural properties when compared to other composite materials such as laminated composite.

The reinforcement matrix interfaces are important to choose accurately because the selected alloy may have a different set of physical, chemical properties [4, 5]. The reinforcement material is inserted into the matrix to enhance or reduce their properties like wear resistance, hardness, density, porosity, mechanical strength etc. The reinforcement may be done in a continuous manner or discontinuous. By the stir casting process, MMC can be produced. In this process, mechanical stirring is used to mix dispersed phase like short fibres or ceramic particles and molten matrix. It is a cheap and best way in liquid state fabrication. The LM6 and fly ash matrix material is considered a good combination for aircraft wing structure [6]. Aluminium matrix composites can provide good strength in case of elevated temperatures also and it also has high stiffness. Other properties like lower density, excellent abrasion resistance, good thermal conductivity, etc. made the composite popular in automotive and mechanical field.

Aircraft wing has to be analysed for suitable lift generation with its strength [7–9]. The design and analysis of aircraft wing allows comparing different results in various aspects to get the desired result.

2 Material Selection

Material selection plays a very major and vital role in making of aircraft wing as well as whole aircraft structure. Aluminium (LM6) and fly ash have been reinforced together for obtaining a new material which can meet the need for better strength, High thermal conductivity and low weight. As these parameters are essential for fabricating the aircraft, by keeping these parameters in mind material has been selected. Aluminium (LM6) and fly ash have been taken in different constituents and has been tested. It has been found that by increasing the fly ash weight percentage strength and toughness of the material is also increased. 15% of Fly ash has been found suitable for reinforcing with Aluminium.

3 Design and Analysis of Wing

NACA0012 airfoil has been chosen for designing and analysing the wing of the aircraft. Basic Calculations has been done for knowing different parameters of the wing. Literature survey has been done and many values have been taken from that. Table 1 shows some of the parameters taken from the literature survey.

From all the above values, wing has been designed in CATIA. Figure 1 shows the basic design of NACA0012 airfoil and Fig. 2 shows designed CATIA modal of the wing of the aircraft.

After designing the wing, it has been analysed in ANSYS. Finite element analysis and flow analysis has been performed on the wing. Density of the material has been given as 2.93. Toughness was found to be 75 J/m, Hardness was found to be 82 HRA and Ultimate strength was 725 Mpa. Figure 3 shows the mesh modal of the wing that has been done in ANSYS.

Fine meshing has been done in the wing. 1,334,493 nodes and 25,536 elements have been created over the whole model. Refinement has been done over whole wing.

Table 1 Parameters of wing

S. No.	Parameters	Value
1	Wing area (m^2)	41.94
2	Aspect ratio	7.3
3	Wing span (m)	17.73

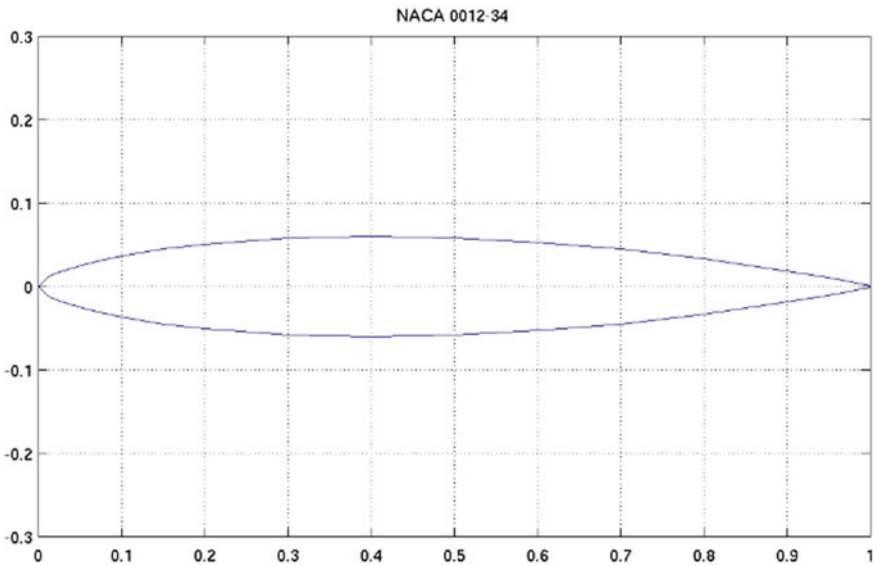

Fig. 1 Design of NACA0012

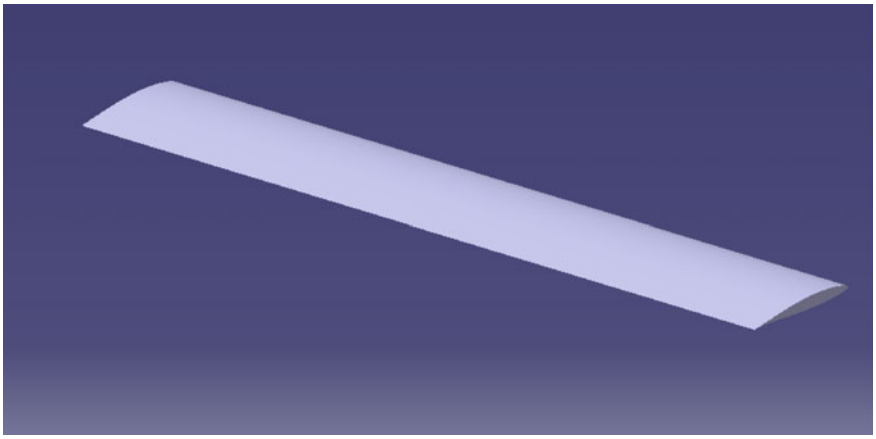

Fig. 2 CATIA model of wing

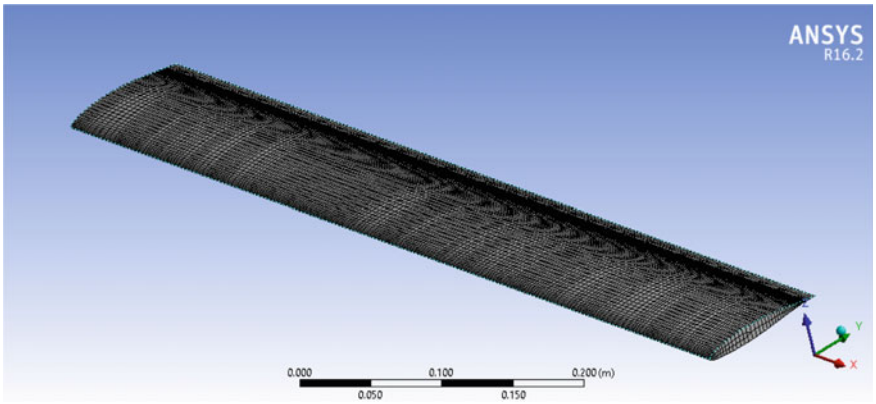

Fig. 3 Meshed model of wing in ANSYS

After meshing, one side of the wing has been fixed supported and load of 20,000 N has been applied on the other side of the wing as shown in Fig. 4.

Analysis has been done on the wing and various parameters like Von-misses stress, Von-misses strain and deformation has been found out. After finite element analysis, flow visualsation has also been done on the airfoil. Velocity of 10 m/s has been given as inlet velocity and SST K-w turbulence modal and energy equation modal has been used for analysis. Ideal gas has been used for further analysis. Gauge pressure has been kept as 0. Coefficient of lift and coefficient of drag monitors has been created in monitors. Pressure and velocity contours have been found from the flow analysis as well as C_l and C_d value have also been found out. Figure 5 shows the parameters taken in materials.

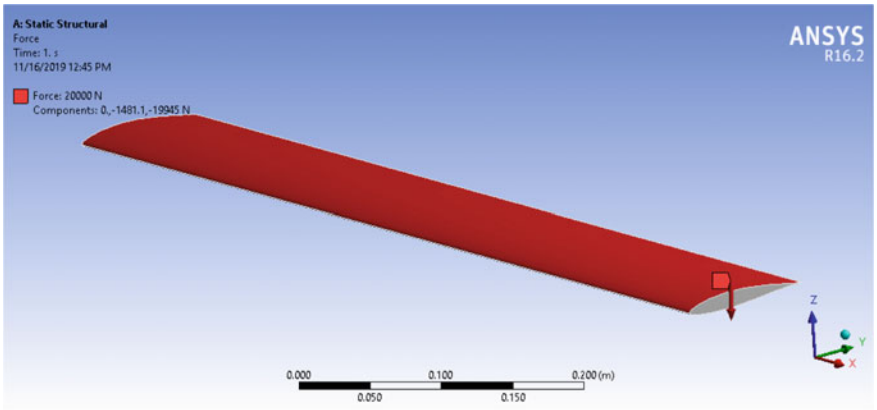

Fig. 4 Force applied on the wing

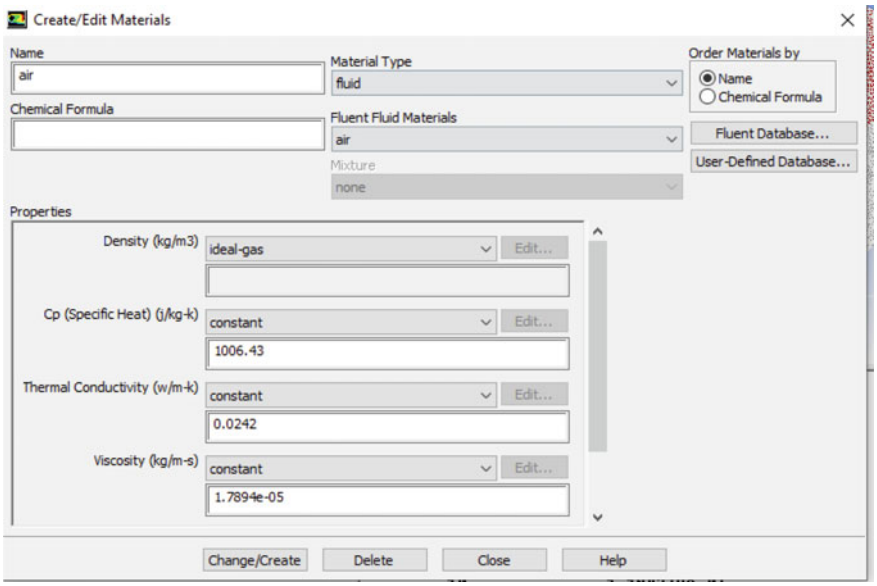

Fig. 5 Fluid parameters

4 Results and Discussion

Finite element analysis and flow analysis has been performed on the wing. From the finite element analysis shear stress, shear strain and deformation distribution have been seen all over the surface of the wing. Figure 6 shows deformation analysis of the wing. Maximum deformation was found to be 0.679 m at the side of the wing.

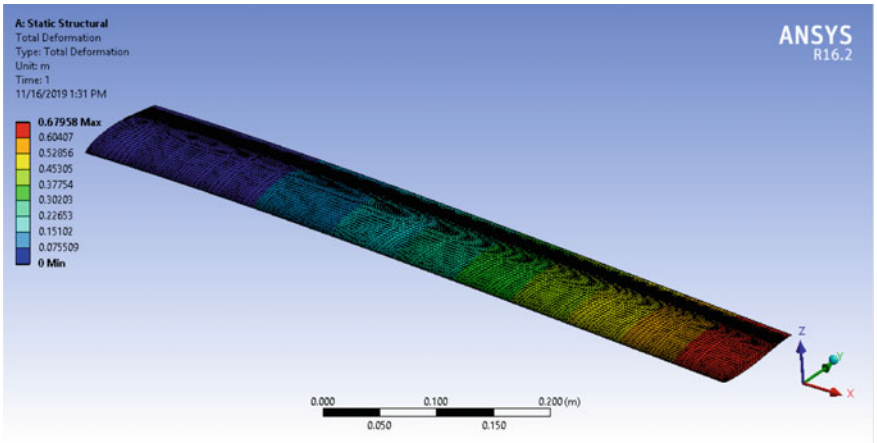

Fig. 6 Total deformation of wing

Figures 7 and 8 show Von-misses stress and strain distribution over the wing. It is seen that maximum stress and strain is acting at the fixed side of the wing.

From the flow analysis velocity and pressure, contour has been found. Figures 9 and 10 show velocity and pressure contour over the surface of the airfoil. It has been found that lowest amount is velocity is found over the surface of the wing. But overall flow is smooth and streamline. From the pressure contour, it is seen that maximum pressure found near the surface of the wing is 4.714e+001 pa. It has also seen that pressure value is very less at the leading edge of the airfoil.

C_l/C_d value has also been found out to be 19 at 5° angle of attack from the flow analysis.

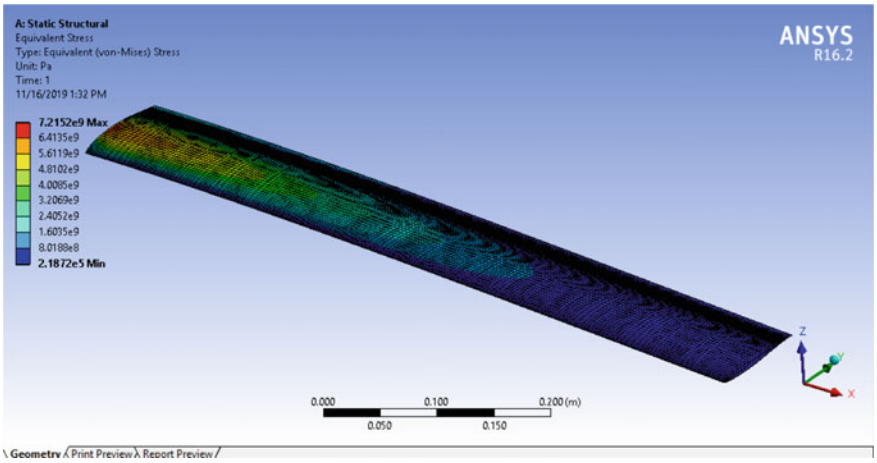

Fig. 7 Von-misses stress

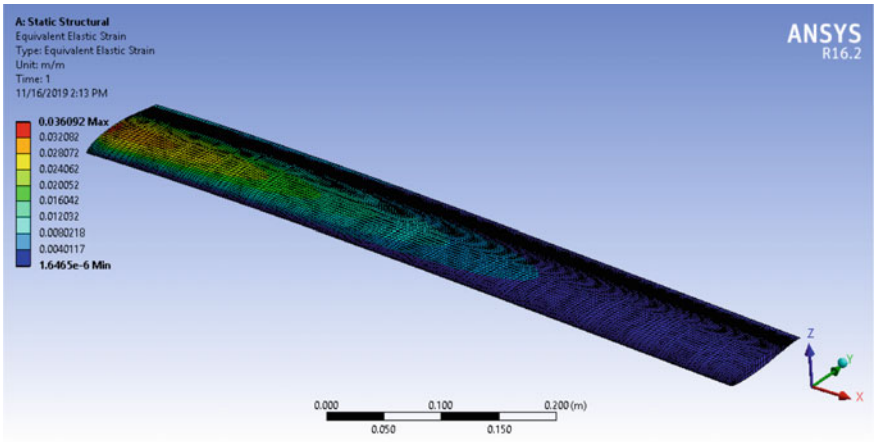

Fig. 8 Von-misses strain

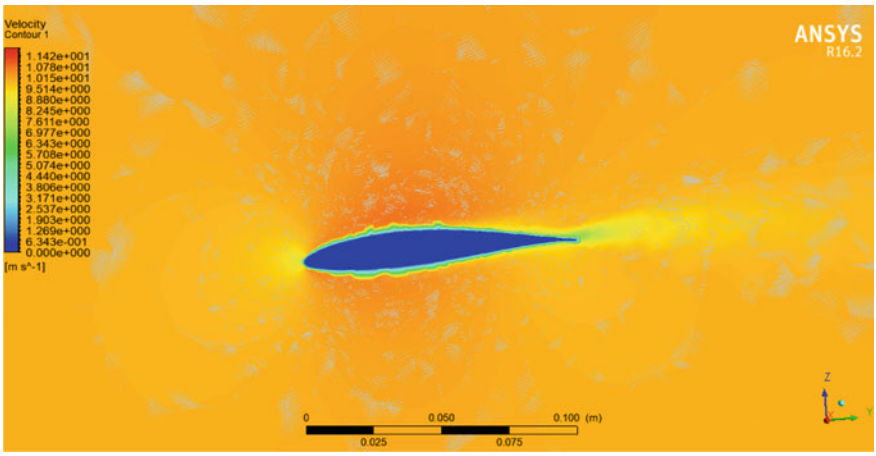

Fig. 9 Velocity contour over the wing

5 Conclusion

As per the design requirements, a wing has been modelled in CATIA. Material properties of LM6 and fly ash has been given to it. The structural analysis and flow analysis was carried out in ANSYS. Wing has been analysed in finite element analysis and has been found that maximum deformation acting over the wing for the load of 20,000 N is 0.679 m. Similarly, stress and strain distribution have also been seen in finite element analysis. It has been seen that maximum strain was found to be 0.036 m/m and maximum stress was 7.25e9 pa.

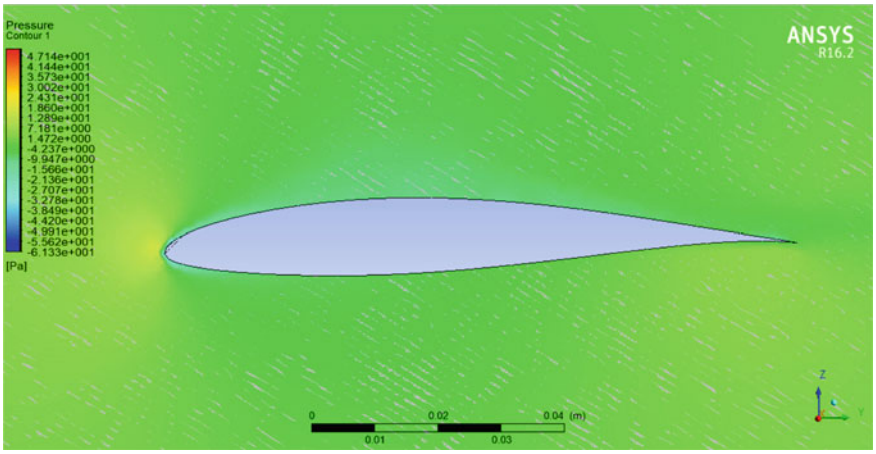

Fig. 10 Pressure contour over the wing

From the flow analysis velocity and pressure contour has been found. From the velocity contour, we have seen that the flow travelling through the surface of the wing is smooth and streamline. C_l/C_d value has also been calculated from the flow analysis as 19 at 5° angle of attack.

References

1. Baughn TV, Packman PF (1986) Finite element analysis of an ultralight aircraft. J Aircr 23(1):82–86
2. Kesavulu A, AnandRaju F, Deva Kumar MLS (2014) Properties of aluminium fly ash metal matrix composite. 3(11). ISSN: 2319-8753
3. Pawara PB, Utpat AA (2014) Analysis of composite material aircraft wing under static loading condition. Elsevier
4. Rajappan R, Pugazhenthi V (2013) Finite element analysis of aircraft wing using composite structure. IJES 2(2)
5. Mayurkymarkevadiya (2013) CFD Analysis of pressure coefficient for NACA 4412
6. Anderson JD Jr (2007) Introduction to flight, 5th edn. The McGraw-Hill Companies
7. Roskam J, Chuan-Tau (1997) Airplane aerodynamics and performance
8. Murugesan P, Thirumurugan P, Analytical and numerical investication of critical buckling analysis of composite wing. Int J Modern Eng Res (IJMER)
9. Jones RT (2013) The spanwise distribution of lift for minimum induced drag of wings having a given lift and a given bending moment. Int J Innov Res Sci Eng Technol 2(6). Tech. Rep. TN-2249, NASA, Dec 1950

CFD Analysis on Extrusion of Slurry in Direct Ink Writing

E. Balasubramanian, Yogesh Kumar, Nishant Kumar Raj, S. Smruthi, and P. Vikram

Abstract Direct ink writing (DIW) is one of the additive manufacturing (AM) technologies being widely utilized to produce functional parts from a complex three-dimensional (3D) computer-aided design (CAD) model without the need of dies, molds, jigs, fixtures and other expensive tools. Recently, screw-type extruder become very vital to handle high viscosity slurry and uniform dispersion of material from the micronozzle for achieving high-dimensional accuracy is extremely essential to fabricate parts using DIW. In this article, computational fluid dynamic (CFD) analysis is performed to simulate the extrusion behavior of the slurry having viscosity in the order of 50,000 poise. Through varying the inlet velocity of slurry for various viscosities, CFD analysis is carried out to determine the maximum pressure developed at the top of feed zone. In addition, extrusion behavior is studied for the cases of increase in the speed of screw spindle and varying mass flow rate. Experiments are performed to measure the viscosity of the slurry with respect to shear rate. Theoretical calculations are compared with CFD analysis results and they are in good agreement in predicting the inlet pressure.

E. Balasubramanian (✉)
Department of Mechanical Engineering, Vel Tech Rangarajan Dr. Sagunthala R&D Institute of Science & Technology, Chennai, India
e-mail: balasubramaniane@veltech.edu.in

Y. Kumar · N. K. Raj · S. Smruthi · P. Vikram
Department of Aeronautical Engineering, Vel Tech Rangarajan Dr. Sagunthala R&D Institute of Science & Technology, Chennai, India
e-mail: vtu8155@veltechuniv.edu.in

N. K. Raj
e-mail: vtu8056@veltechuniv.edu.in

S. Smruthi
e-mail: vtu10147@veltechuniv.edu.in

P. Vikram
e-mail: vikram.veeran@gmail.com

N. Gascoin and E. Balasubramanian (eds.), *Innovative Design, Analysis and Development Practices in Aerospace and Automotive Engineering*, Lecture Notes in Mechanical Engineering, https://doi.org/10.1007/978-981-15-6619-6_7

Keywords Direct ink writing · Slurry · Screw extruder · Viscosity · CFD · Additive manufacturing

1 Introduction

Direct ink writing is the novel additive manufacturing technique (AM) [1–3] which is being utilized over a large area of range to fabricate functional parts swiftly. Compared to other existing AM techniques [4], it does not need any high cost lasers, support structures, and filaments for extrusion. DIW uses simple screw-type extruder to extrude high viscosity slurry of the order of more than 50,000 poise [1] which is very much needed to make components with clay and solid propelleants.

The extrusion technology using screw has become a basic processing technique to produce various products starting from food processing to rubber and plastics and nowadays, it is applied to various fields like injection molding, fiber spinning, compounding, etc. [5]. There are many existing extrusion techniques like piston extruders, roller-type extruders, screw extruders, plunger extruders, etc. In comparison of plunger extruder, the quality of the ceramic green sample found significantly better in screw extruder with high surface accuracy and better control of amount of discharge while changing printing direction [6].

In the production of complex three-dimensional structure, the extrusion technique plays very important role. The fabrication of complex three-dimensional ceramic components (up to tens of centimeters) can be done by using freeform extrusion-based additive manufacturing technique known as Ceramic On-Demand Extrusion (CODE). It provides density near to the theoretical density (>98%). Advantage of using binder content in small amount is to reduce the post-processing [7]. Also the Extrusion-On-Demand (EOD), which is termed for precise control on extrusion flow rate, is used in freeform fabrication of high dense complex geometry. The non-Newtonian behavior of aqueous ceramic pastes make the extrusion more difficult to control and different methods of EOD can be useful [8]. Considering the green manufacturing approach, manufacturing of ceramic-based components can be done in eco friendly way by using the aqueous-based extrusion fabrication (ABEF) method. Water is used as the medium and it is useful for high solid loading ceramic pastes. The dynamic response of aqueous-based ceramic extrusion process is very low as compared to incompressible fluid [9].

Recently, utilization of extruders with single screw has progressed significantly. Single screw extruder with complex screw geometry can be designed and computationally analyzed quickly by applying Hele-Screw approximation of spreading flow in two dimensions. Solving the Naiver-Stoke equations for the flow starting from barrel wall provides simulation result in a very short time as compared other techniques [10]. In case of solid propellant extrusion using single screw, it may be flammable or explosive. The analysis of rheological state of propellant allow to set operation parameters to avoid accidents. Increase in rotational speed of the screw leads to linearly increase in pressure of solid propellant fluid. [11]. Measurement

of the extrusion pressure is an essential task, which can be predicted using artificial neural network (ANN) model with three-layer feed-forward system and this model provides mean extrusion pressure satisfactorily as compared to experimental result. The pressure gradient developed in the extrusion process of slurry through the single screw extruder can be predicted by using a general model which can be developed by volume conservation equation and further solving for pressure and a special case also found for this model [12]. It is suggested to use high viscosity materials [13] such as synthesized Cu paste for screw extruder in fabrication of metal structures using 3D printing, which decreases the shrinkage factor [14].

In this article, DIW technique is discussed to produce complex three-dimensional CAD models and to simulate the extrusion behavior of slurry through varying the screw spindle speed, viscosity, and mass flow rate, CFD analysis has been performed. In addition, experimental measurement of viscosity of slurry with respect to shear rate is carried out. Theoretical calculations are performed and compared with CFD analysis results.

2 CFD Analysis of Slurry Extrusion

2.1 Meshing and Boundary Conditions

The conceptual slurry extruder has been modelled in CATIA V5 platform and simulations are carried out by ANSYS FLUENT V16.2. To perform an internal fluid flow simulation, the fluid domain has been filled inside the extruder. The assumption made as incompressible fluid flow analysis and pressure-based solver are chosen with second-order upwind discretization for convective and diffusive terms. Simulations are performed in the convergence criteria of 1×10^{-05} for better accuracy. The moving reference frame is created in the extruder screw section to accomplish the rotary motion. It took around 3500 simulations for software to converge (Figs. 1 and 2).

The flow domain is meshed with tetrahedral element using ANSYS ICEM tool. The total number of elements which has been generated in computational grid is approximately 800,000. The mesh refinement was tested by using orthogonality and skewness test. The most of the elements are lying in the region of 0.80–0.95 in orthogonality and skewness values of 0.02–0.033. Thus, the mesh refinement is pretty good to observe the flow characteristics of extruder. Grid independence test is conducted to accurately predict the pressure.

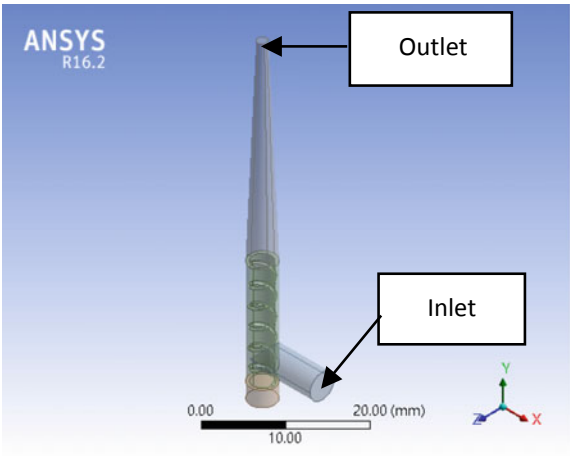

Fig. 1 3D model of extruder

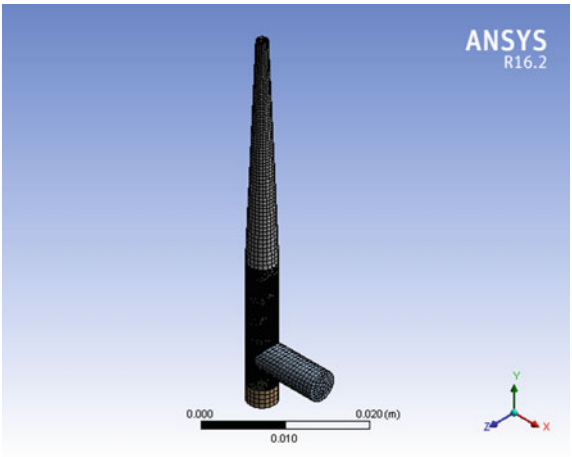

Fig. 2 Meshed model of extruder

2.2 Case(i): Effect of Varying the Screw Speed

By varying the screw spindle speed of extruder, CFD analysis is performed to determine the developed inlet pressure. Simulations are performed for the inlet velocity of 0.028 m/s and varying the spindle speed from 5 to 30 rpm. It is observed from Fig. 3 that, increase in speed leads to have proportional increase in pressure. Based on our experimental measurements, 20 rpm is considered to be optimal speed at which the extrusion of slurry is smoother. The simulation results suggested that, at 20 rpm, the pressure developed at the inlet region of ext ruder is about 0.015 MPa which will not have any effect on damaging the extruder. The pressure distribution across the nozzle is shown in Fig. 4 and it is observed that, maximum pressure occurs at the inlet

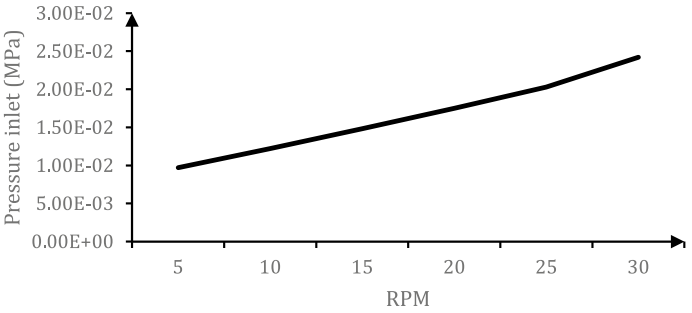

Fig. 3 Measurement of inlet pressure by varying the screw spindle speed

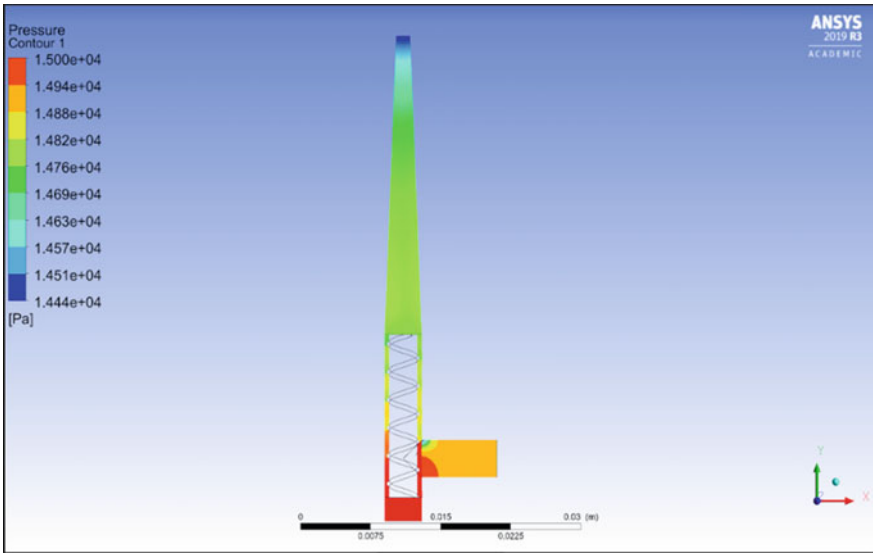

Fig. 4 Pressure contour for spindle of 25 rpm

region and other regions have uniform pressure which leads to smoother dispersion of slurry without any interrupted flow (Fig. 5).

2.3 Case(ii): Effect of Varying the Viscosity

Through varying the viscosity from 150 to 225 Pa s, the inlet pressure is determined by performing CFD analysis. The liner relationship holds between pressure and viscosity as seen from Fig. 6. The pressure contour shown in Fig. 7 and 8 indicates

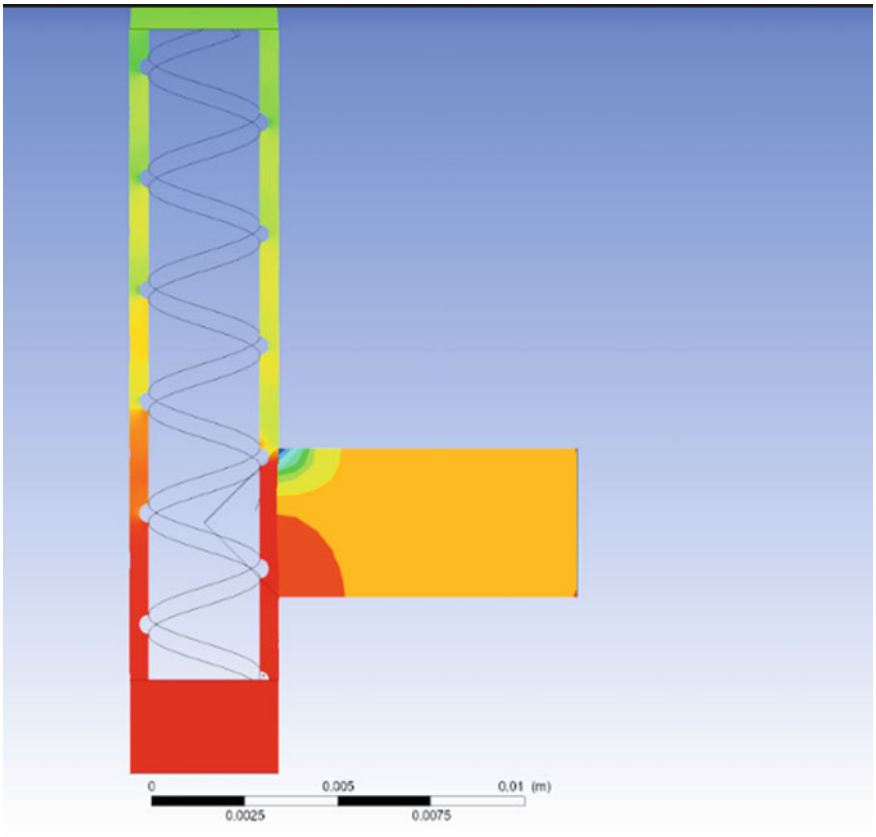

Fig. 5 Pressure contour for inlet section of spindle of 25 rpm

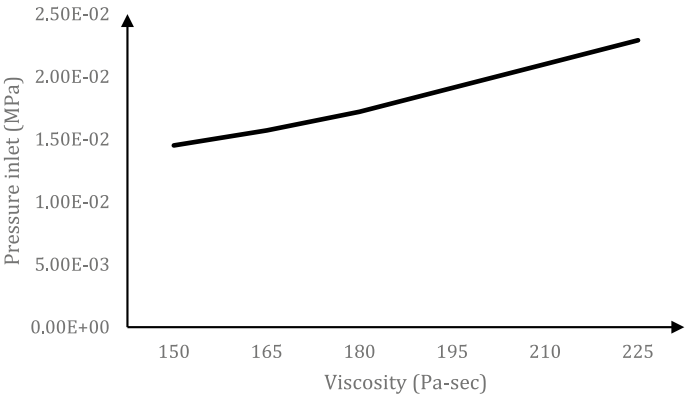

Fig. 6 Measurement of inlet pressure by varying viscosity

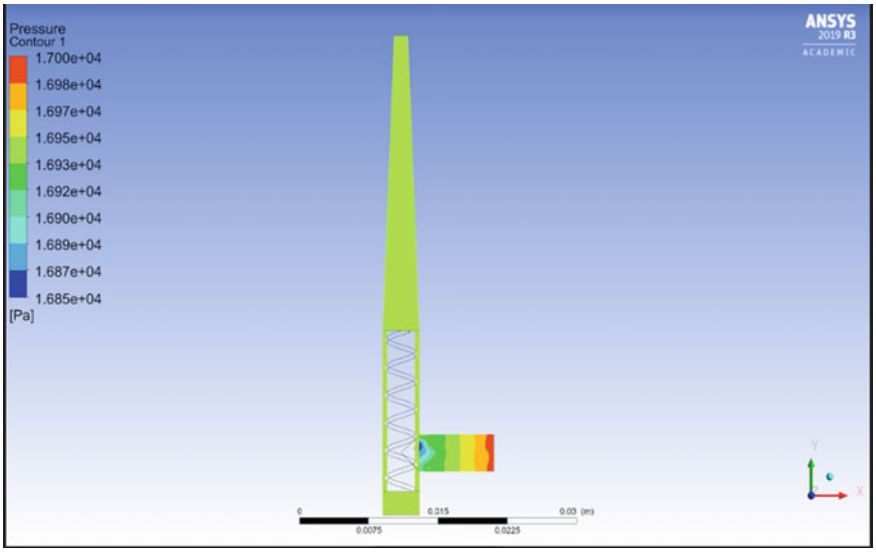

Fig. 7 Local pressure contour at viscosity of 180 Pa s

that, there is high pressure at inlet region of nozzle and uniform pressure across other sections of extruder is experienced.

2.4 Case(iii): Effect of Varying the Mass Flow Rate

The mass flow rate has been diversified from 0.033 to 0.0611 kg/h (for the inlet velocity 0.001–0.003 m/s) and at 25 rpm, CFD analysis is performed. The increase of mass flow rate resulted in increase of pressure as shown in Fig. 9. Due to flow conditions at the top of screw, more pressure is generated as seen from Fig. 10 and it is decreased gradually across the screw region (Figs. 8 and 11).

3 Analytical Approach

3.1 Shear Rate

The shear rate of the extruder screw channel is calculated using the following relation,

$$\gamma(\text{Screw channel}) = \frac{\pi \times D \times N}{h} \tag{1}$$

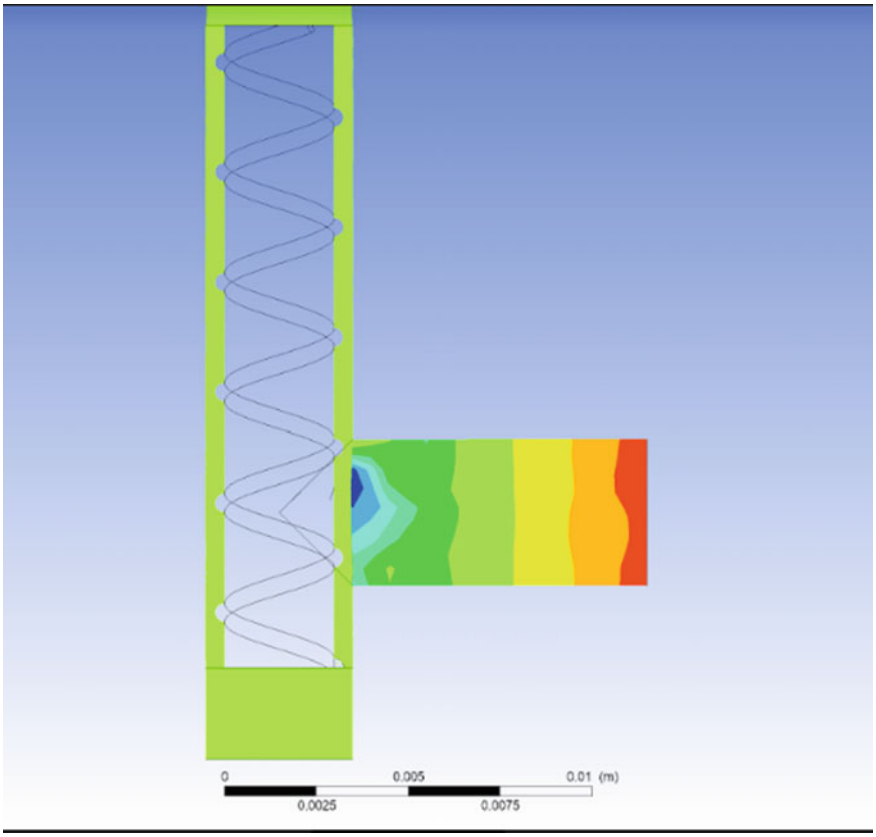

Fig. 8 Inlet section at viscosity of 180 Pa s

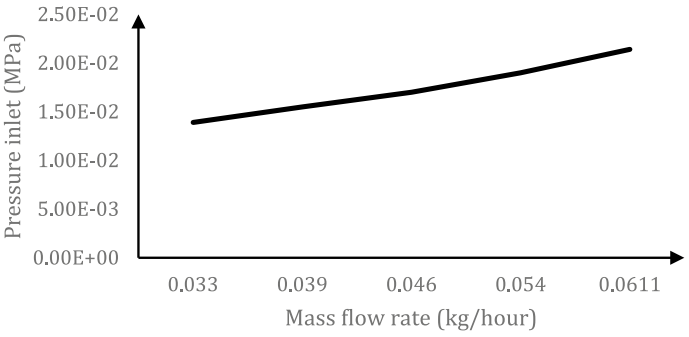

Fig. 9 Measurement of inlet pressure by varying mass flow rate

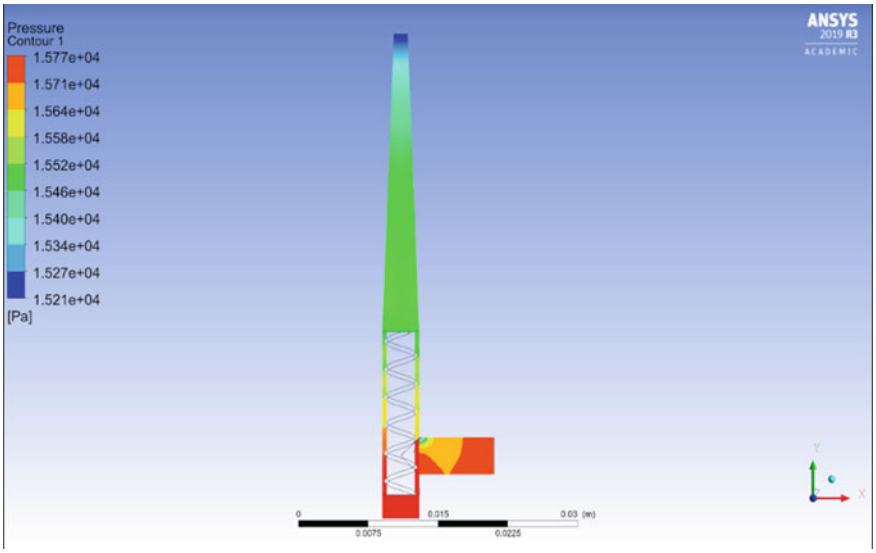

Fig. 10 Local pressure contour at mass flow rate of 1.1055×10^{-5} kg/s

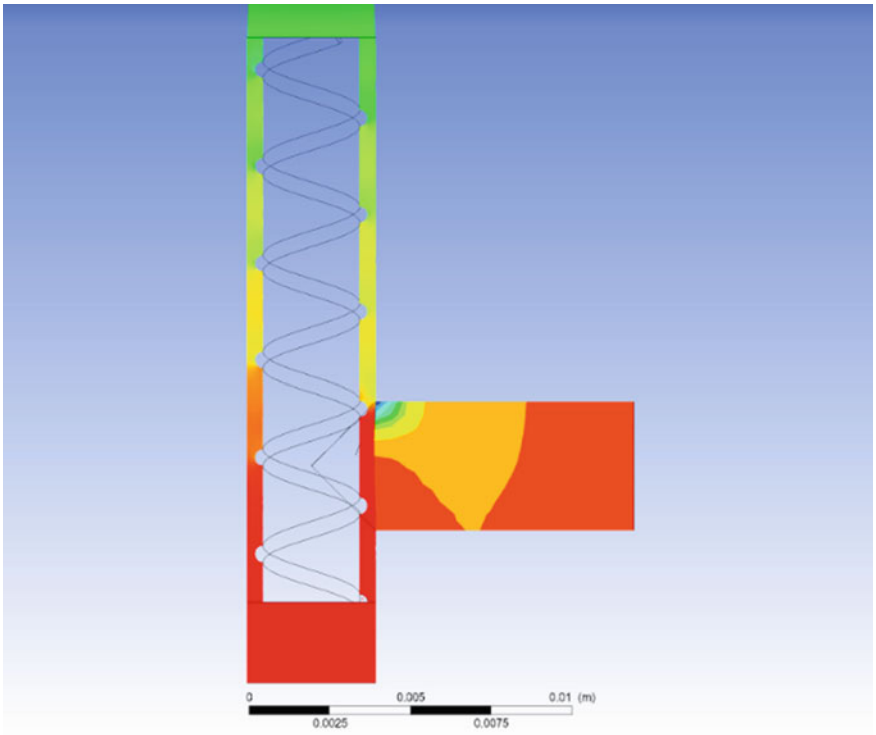

Fig. 11 Inlet section at mass flow rate of 1.1055×10^{-5} kg/s

where, γ = shear rate in screw channel in s^{-1}, D is diameter of the screw, N is speed of the screw and h is the channel depth [15].

In a round die channel (rod or strand for compounding), the shear rate is obtained using the following Eq. (2),

$$\gamma(\text{Round channel}) = \frac{4 \times Q}{\pi \times R^3} \tag{2}$$

where, γ is the shear rate in the screw channel, R is the radius of the channel, and Q is the volumetric flow rate.

Based on the preliminary experiments, the volumetric flow rate has been calculated as 9.06287×10^{-9} m^3/s for the radius of the channel 0.00075 m, the corresponding shear rate is determined as 24.78 s^{-1}. Similarly, for the value of volumetric flow rate of 9.06287×10^{-9} m^3/s and radius of the channel 0.00155 m, shear rate in the screw channel at inlet is calculated as 3.0987 s^{-1}.

3.2 Viscosity

The instantaneous viscosity of the slurry was measured using Bohlin Gemini II Rheometer and it is plotted with respect to shear rate which is shown in Fig. 12.

The instantaneous viscosity at the outlet nozzle and screw is obtained as:

$$\eta_{\text{nozzle}} \approx 51\,\text{Pas} \quad \text{and} \quad \eta_{\text{screw}} \approx 180\,\text{Pas}.$$

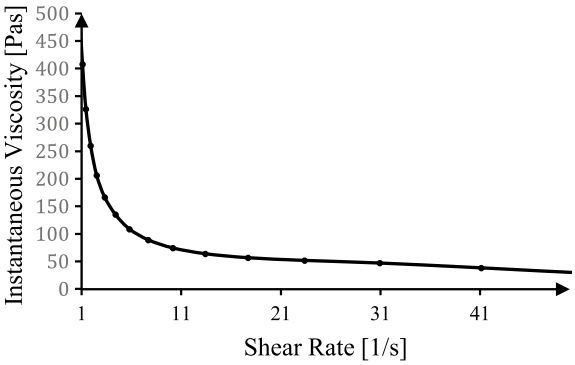

Fig. 12 Determination of shear rate from experiments

3.3 Inlet and Outlet Pressures

The volumetric flow rate is calculated using the following relation [15],

$$Q(\text{Round channel}) = k \times \frac{\Delta P}{\eta} = \frac{\pi \times R^4}{8 \times L} \times \frac{\Delta P}{\eta} \tag{3}$$

where, k is resistance factor, L is channel length, ΔP is pressure drop across the channel, η is the polymer viscosity, and R is radius of the channel.

The pressure drop can be obtained by re-arranging Eq. (3) as follows:

$$\Delta P = \frac{Q \times 8 \times L \times \eta}{\pi \times R^4} \tag{4}$$

For volumetric flow rate of 9.06287×10^{-9} m^3/s, total length of the 0.01632 m, radius of the channel has been taken as 0.00075 m and viscosity of 180 Pa s, the inlet pressure drop across the channel was calculated as 0.015 Mpa which is similar to the CFD analysis results.

3.4 Inlet Velocity

The volumetric flow rate is calculated by,

$$Q = v \times A \tag{5}$$

where, v is the flow velocity; A is the cross-sectional area.

For the value of volumetric flow rate of 9.06287×10^{-9} m^3/s and cross-sectional area 3.14159×10^{-6} m^2, inlet velocity is calculated as 0.00288 m/s.

4 Conclusion

To predict the inlet pressure of the extruder, the CFD analysis was performed through varying the screw spindle speed (5–30 rpm), viscosity (150–225 Pa s), and the mass flow rate (9.03×10^{-6} kg/s–1.69×10^{-5} kg/s). The simulation results suggested that, the maximum developed pressure is about 0.015 MPa in all the cases and distribution of pressure is uniform across the screw extruder. The theoretical calculations also confirmed that, the pressure at the inlet is of the same order and it will not affect the flow conditions and uniform dispersion of the slurry is achieved. In addition,

viscosity measurements under varied shear rate using Bohlin Gemini II Rheometer predicted the instantaneous viscosity for the outlet of nozzle as 51 Pa s and screw inlet as 180 Pa s.

References

1. Lewis JA (2006) Direct ink writing of 3D functional materials. Adv Func Mater 16(17):2193–2204
2. Abdulhameed O, Al-Ahmari A, Ameen W, Mian SH (2019) Additive manufacturing: challenges, trends, and applications. Adv Mech Eng 11(2):1687814018822880
3. Nguyen N, Melamed E, Park JG, Zhang S, Hao A, Liang R (2017) Direct printing of thermal management device using low-cost composite ink. Macromol Mater Eng 302(10):1700135
4. Rueschhoff L, Costakis W, Michie M, Youngblood J, Trice R (2016) Additive manufacturing of dense ceramic parts via direct ink writing of aqueous alumina suspensions. Int J Appl Ceram Technol 13(5):821–830
5. Sakai T (2013) Screw extrusion technology–past, present and future. Polimery 58
6. Vlachopoulos J, Polychronopoulos N, Tanifuji S, McMaster University, Hamilton, ON, Canada, Computational analysis and design of single screw extruders having screws of complex geometry with mixing elements
7. Ghazanfari A, Li W, Leu MC, Hilmas G (2016) Novel extrusion-based additive manufacturing process for ceramic parts
8. Li YY, Bridgwater J (2000) Prediction of extrusion pressure using an artificial neural network. Powder Technol 108(1):65–73
9. Ji H, Zhang X, Huang X, Zheng L, Ye X, Li Y (2019) Effect of extrusion on viscoelastic slurry 3D print quality: numerical analysis and experiment validation. SN Appl Sci 1(9):1036
10. Li W, Ghazanfari A, Leu MC, Landers RG (2015) Methods of extrusion on demand for high solids loading ceramic paste in freeform extrusion fabrication. In: Solid freeform fabrication symposium, Austin, TX
11. He ZQ, Zhou K, Yin SP (2014) Security analysis on single-screw extrusion process of solid propellant by numerical simulation. In: Advanced materials research, vol 997. Trans Tech Publications, pp 605–609
12. Botten AJ, Burbidge AS, Blackburn S (2003) A model to predict the pressure development in single screw extrusion. J Mater Process Technol 135(2–3):284–290
13. Mason MS, Huang T, Landers RG, Leu MC, Hilmas GE (2009) Aqueous-based extrusion of high solids loading ceramic pastes: Process modeling and control. J Mater Process Technol 209(6):2946–2957
14. Hong S, Sanchez C, Du H, Kim N (2015) Fabrication of 3D printed metal structures by use of high-viscosity cu paste and a screw extruder. J Electron Mater 44(3):836–841
15. Giles HF Jr, Mount EM III, Wagner JR Jr (2004) Extrusion: the definitive processing guide and handbook. William Andrew

Experimental and Numerical Study on Temperature Distribution of Infrared Heater Used for Curing Solid Propellant Slurries

K. Tesfaye, M. Silambarasan, L. M. Manova, E. Balasubramanian, and A. S. Praveen

Abstract The combustion rate of solid propellants is strongly influenced by its shape and geometry. The use of conventional casting and forming methods to produce complex-shaped solid propellants is tedious and requires skilled manpower intervention, which greatly increases the production time and costs. Now a day, the application of the additives manufacturing process simplifies the production of complex-shaped parts from the slurries composition, but the curing process of the parts is still carried out by placing the printed slurry in the furnace with uniform heating for a long time. To shorten the extended curing time, layer by layer curing scheme with curved ceramic infrared heater (FTE serious) was implemented in this study. The capability of the heater to produce uniform temperature distribution over the printed part was measured with thermal camera (i.e., FLIR duo r). Moreover, ANSYS Fluent software was used to develop a numerical model based on the control volume method and to simulate the temperature distribution of the part. The simulation results and the thermal imaging measurement value showed good agreement.

Keywords Ceramic infrared heater · Curing · Surface temperature measurement · Control volume method · Additive manufacturing

K. Tesfaye · E. Balasubramanian (✉) · A. S. Praveen
Department of Mechanical Engineering, Vel Tech Rangarajan Dr. Sagunthala R&D Institute of Science and Technology, Chennai, Tamil Nadu 600062, India
e-mail: balasubramaniane@veltech.edu.in

M. Silambarasan · L. M. Manova
Department of Aeronautical Engineering, Vel Tech Rangarajan Dr. Sagunthala R&D Institute of Science and Technology, Chennai, Tamil Nadu 600062, India

N. Gascoin and E. Balasubramanian (eds.), *Innovative Design, Analysis and Development Practices in Aerospace and Automotive Engineering*, Lecture Notes in Mechanical Engineering, https://doi.org/10.1007/978-981-15-6619-6_8

1 Introduction

Solid propellant is a highly energetic elastomer material composed of different chemicals ingredients like binder, fuel, cross-linking agent, oxidizing agent, curing agent and stabilizer [1]. The proportion of the chemical ingredients ratio of the propellant composition slurry is reflected in its intended physical and chemical properties. Furthermore, the burning rate of solid propellants also depends on their shape and geometry, but traditional production techniques (i.e., casting and extrusion paste through a die) are not flexible enough to produce complex shapes. On top of that, the method requires the preparation of mold and mandrel for production of different shapes, which needs skilled manpower and increases the time and cost of production. In order to manufacture solid propellant with a complex shape with precise geometry, a new flexible production process, i.e., additive manufacturing (AM) is required. The additive manufacturing process is able to produce a flexible custom product with reduced cost and production time [2, 3]. This manufacturing process produces parts in the layered manufacturing process, wherein the manufacturing process is controlled from a computer model [4]. Production flexibility and freedom of AM processes have attracted much attention in various manufacturing sectors, such as the automotive [5], aeronautics [6], food [7], medical [8], construction [9], etc.

Nowadays, the adoption of additive manufacturing in the production of solid propellant paved the way to produce a complex shape with less intervention of manpower, and researches have been still conducting in this area to further optimize the quality of the product. In the recent past, the production of solid propellant comes into effect. In 2012 [10], Casting of hybrid rocket fuel grains was fabricated using additive manufacturing techniques, which was served as mechanical support. The printing slurry of the additively manufactured grains was prepared by homogeneously mixing Acrylonitrile-butadiene-styrene with paraffin wax. A few years later [11], a direct slurry extrusion-based additive manufacturing technique called fused deposition modeling (FDM) was applied to cast fuel grains that could be applicable for hybrid rocket motors and the authors further recommend the technique for production of composite propellant grain in order to improve the design flexibility. In 2018 [12], the fabrication attempt of composite propellant grain geometries using fused deposition modeling (FDM) became successful. The peculiar characteristic of this manufacturing method was able to customize the part geometry of composite propellant grains, which is highly improved the burning rates. McClain [13] and his colleagues developed a new additive manufactured method viz. direct write system, which has the ability to fabricate low-void propellants with complex geometry.

All the work done so far has focused only on the solid fuel printing process of the solid propellant and the curing process of the printed parts was done by placing the final printed part in the furnace just like traditional production techniques. But these curing techniques take a long time, which increases the speed and cost of manufacturing. To deal with this problem, the printing and curing process was synergistically integrated into the presented work. The curing process was applied

after the production of each layer instead of bulk curing which reduce the curing time radically. To make this curing approach effective, the infrared heater should provide uniform thermal energy over the printed layer. Therefore, in this study, the capability of FTE serious ceramic infrared heater to deliver uniform temperature was evaluated through the experimental and numerical approach.

2 Experimental Method

2.1 Slurry Synthesis

Owning high cost and the flammable nature of the solid propellant seeks extraordinary safety measures during curing. The main intention of this work is to examine the feasibility of uniform heating of each layer of the cured part that cured layer by layer fashion by FTE serious ceramic infrared heater. Therefore, ordinary home salt viz. NaCl was used as a solid loading powder during the preparation of printer slurry, which tremendously minimizes the raw materials and process cost of experimental investigation of this work. The preparation of slurry was started by uniform mixing 15.6 wt% of Hydroxyl-terminated polybutadiene (HTPB) acts as a binder, 2.2 wt% of Diacetyl adipate (DOA) as a plasticizer and 0.03 wt% ferric acetylacetonate acts as burn rate modifier for ten minutes. Next, 80 wt% of NaCl powder with particle size range from 50 to 100 μm, which acts as solid loading, was added in the solution and mixed for another ten minutes. Finally, 2.2 wt% curing agent namely Toluene diisocyanate (TDI) was mixed with the slurry solution for ten minutes again.

2.2 Experimental Setup

Although the purpose of this study is to integrate the curing system into the printing system, which simplifies the temperature distribution measurement process. However, in this study, two separate experimental settings were arranged: one is intended for the printing process and the other is for the curing and temperature distribution measurement process of each layer. The composition slurry is extruded over the part build bed through a syringe with an internal nozzle diameter of 1.55 mm. As shown in Fig. 1, the printing system was based on a modified desktop fused deposition modeling (FDM) 3D printer and its slurry extrusion were driven by compressed air supply. The ceramic infrared heater (FTE serious) was applied to build the heating system as presented in Fig. 2. Precise temperature control was achieved by integrating closed-loop temperature control into the heating system, which consists of PID autonics tcn4s temperature controller, RTD P100 temperature sensor, and FOTEK SSR-25 DA solid state relay. In addition, the system is also equipped with a single-phase AC supply synchronized with a wattmeter to set the required heater

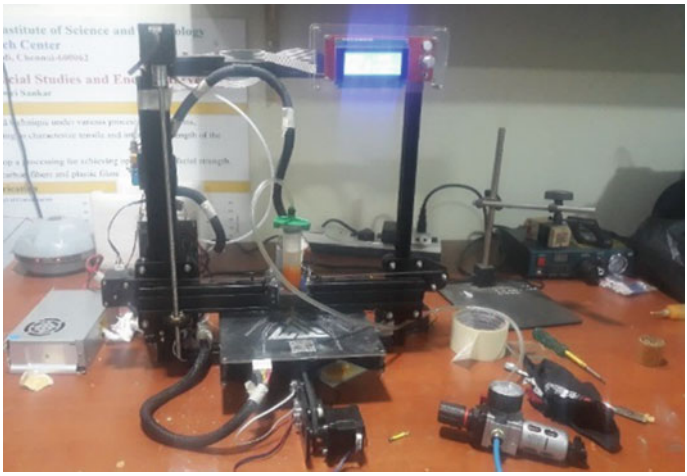

Fig. 1 3D printer system

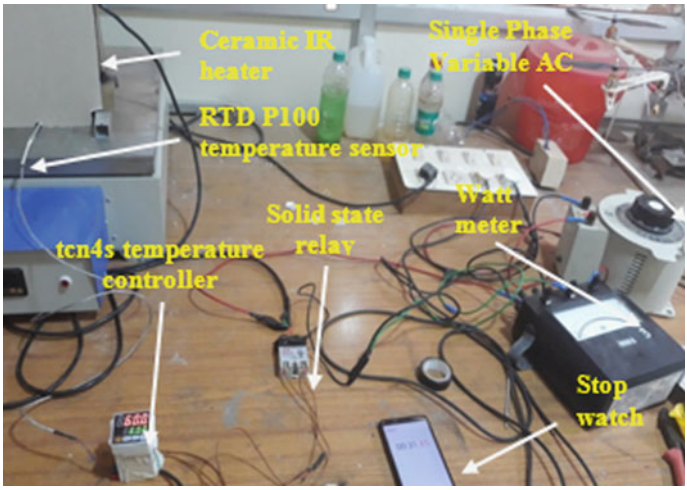

Fig. 2 IR heating system

power. In this study, the curing process was done for each layer by setting heater temperature 60 °C for 15 min. The process of printing each layer in printing system and curing it for 15 min in heater system must continue until the entire part is built.

Table 1 Printed material properties

Properties	Values
Coefficient of thermal expansion ($°C^{-1}$)	4.45×10^{-5}
Thermal conductivity [W/m °C]	6.15
Specific heat [J/kg °C]	871
Young's modulus [Pa]	3.27×10^{10}
Poisson's ratio	0.203
Bulk modulus [Pa]	1.835×10^{10}
Shear modulus [Pa]	1.3591×10^{10}

3 Numerical Method

The irradiance, is the absorbed heat flux by the cured surface of printed part, consider as the source of heat for temperature distribution for simulation in ANSYS 19.2 version software. At the beginning of the numerical work, a three-dimensional part with dimensions of $3.2 \times 12.7 \times 125$ mm was modeled using the geometric modeling tool of ANSYS. Since approximately 80% of the printed parts were made of NaCl, the engineering material properties of the modeled parts were considered to be NaCl material properties only (see Table 1). Then, the model has meshed with 3960 pieces of rectangular elements and 21,149 nodes. The stable-state thermal simulation was carried out by applying heat flux boundary conditions of 60 kW/m^2 at the top of the part surface, and the rest of the surface was exposed to an ambient temperature of 26 °C.

4 Result and Discussion

The temperature distribution over the surface of cured parts was measured at a different heating time using the high-resolution thermal camera (flir duo pro r) and the thermal images were analyzed with flir-tool software, as shown in Fig. 3. According to the analyzed thermal images, the measured temperature variation at a different location of the surface of the part is insignificant. This might be happened due to the heat transfer rate through radiation is fast, which made the FTE serious ceramic infrared heater was capable to deliver its heat energy with minimum temperature variation (i.e., $59.7 \approx 60$ °C). In addition, the influence of heating time on the temperature distribution over the surface was negligible.

The steady-state analysis of surface temperature distribution for the modeled part can be observed from Fig. 4. Based on the energy absorption simulation result of the cured part, the temperature distribution over the cured surface becomes uniform with top surface temperature of 57.22 °C and gradually decreases from the top surface to bottom surface. Fast heat transfer by infrared radiation and low thermal conductivity of parts play a significant role in achieving uniform temperature on the upper surface.

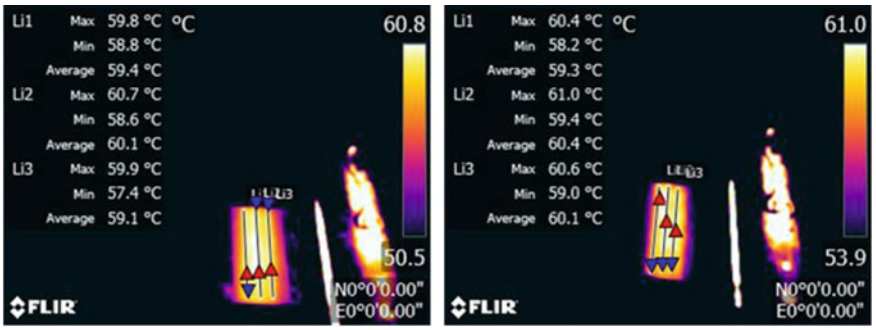

Fig. 3 Temperature distribution contour measured by thermal camera

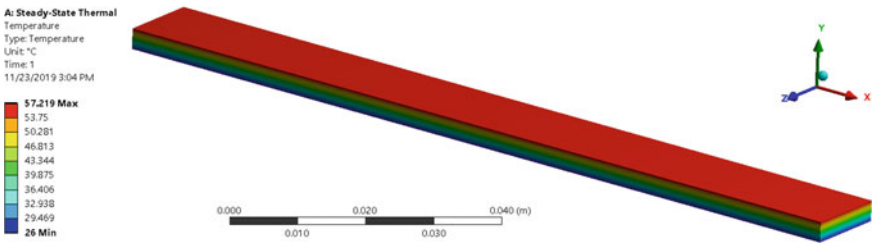

Fig. 4 Temperature distribution contour simulated by ANSYS

The CFD model validation is crucial to validate the simulation results. Minimum measurement error (i.e., 4.2%) was observed between the numerical and average experimental values.

5 Conclusion

The temperature distribution over the cured surfaces, heated at 60 °C using a ceramic infrared-based fast heating system, was investigated by experimental measurement and thermal module of ANSYS simulation. Based on the simulation result, a uniform temperature of 57.22 °C was observed on the upper surface of the model and was gradually reduced from the upper surface to the lower surface. Furthermore, the temperature distribution on the top surface of the cured part was measured with a high-resolution thermal camera, and the measured values agreed well with the simulation results. Therefore, the experimental and simulation results clearly show that the FTE serious ceramic infrared heater is feasible to heat the printed slurry with almost the targeted (i.e., 60 °C) temperature during the curing process.

References

1. Beckstead MW, Derr RL, Price CF (1970) A model of composite solid-propellant combustion based on multiple flames. AIAA J 8(12):2200–2207
2. Weller C, Kleer R, Piller FT (2015) Economic implications of 3D printing: market structure models in light of additive manufacturing revisited. Int J Prod Econ 164:43–56
3. Garrett B (2014) 3D printing: new economic paradigms and strategic shifts. Glob Policy 5(1):70–75
4. Ngo TD, Kashani A, Imbalzano G, Nguyen KTQ, Hui D (2018) Additive manufacturing (3D printing): a review of materials, methods, applications and challenges. Compos Part B Eng 143:172–196
5. Leal R et al (2017) Additive manufacturing tooling for the automotive industry. Int J Adv Manuf Technol 92(5–8):1671–1676
6. Coykendall J, Cotteleer M, Holdowsky J, Mahto M (2014) 3D opportunity in aerospace and defense: additive manufacturing takes flight. [Report], vol 1, pp 1–28
7. Lipton JI, Cutler M, Nigl F, Cohen D, Lipson H (2015) Additive manufacturing for the food industry. Trends Food Sci Technol 43(1):114–123
8. Gibson I, Srinath A (2015) Simplifying medical additive manufacturing: making the surgeon the designer. Procedia Technol 20:237–242
9. Bos F, Wolfs R, Ahmed Z, Salet T (2016) Additive manufacturing of concrete in construction: potentials and challenges of 3D concrete printing. Virtual Phys Prototyp 11(3):209–225
10. Mcculley JM (2012) Design and testing of digitally manufactured paraffin acrylonitrile-butadiene-styrene hybrid rocket motors. In: 48th AIAA/ASME/SAE/ASEE joint propulsion conference & exhibit, p 81
11. Bauer C et al (2016) Application of additive manufacturing in solid and hybrid rocket grain design. In: 52nd AIAA/SAE/ASEE joint propulsion conference, pp 1–13
12. Chandru RA, Balasubramanian N, Oommen C, Raghunandan BN (2018) Additive manufacturing of solid rocket propellant grains. J Propul Power 34(4):1090–1093
13. McClain MS, Gunduz IE, Son SF (2019) Additive manufacturing of ammonium perchlorate composite propellant with high solids loadings. Proc Combust Inst 37(3):3135–3142

Experimental Investigation on Geometric Error in Single-Point Incremental Forming with Dummy Sheet

Vikas Sisodia, Shailendra Kumar, Rahul Jagtap, and Kiran More

Abstract Single-point incremental forming (SPIF) process is an emerging sheet metal forming process in which constraint of using dedicated press tools is eliminated. Some process limitations like poor surface finish, longer forming time, higher geometrical error, and uneven wall thickness distribution restrict its applicability in sheet metal industry. But SPIF process with dummy sheet has the capability to overcome some of the prevailing limitations of SPIF process. In the present paper, influence of dummy sheet thickness, step size, wall angle, and feed rate on geometrical error in terms of root-mean-squared error (RMSE) of formed part is investigated. Box Behnken design is used to design the experiments. From the analysis of experimental result, it is found that dummy sheet thickness, step size, and wall angle are significant process parameters influencing RMSE. No significant influence of feed rate on RMSE is observed. RMSE increases with increase in dummy sheet thickness and wall angle, while it decreases with increases in step size. As feed rate increases, there is nominal decrease in RMSE which is desirable. So higher feed rate is recommended to reduce forming time. Further, empirical model is developed to predict RMSE. Also, optimization of process parameters is performed to minimize RMSE. Confirmation experiments were performed in order to check the accuracy of developed predictive model and it is found that predicted results are in good agreement with experimental results.

Keywords Single-point incremental forming (SPIF) process · Wall angle · Step size · Geometric error · Root-mean-squared error (RMSE) · Dummy sheet

V. Sisodia (✉) · S. Kumar · K. More
Mechanical Engineering Department, Sardar Vallabhbhai National Institute of Technology, Surat, Gujarat 395007, India
e-mail: vikas.singh619@gmail.com

R. Jagtap
School of Mechanical Engineering, MIT World Peace University, Pune, Maharashtra 411038, India

N. Gascoin and E. Balasubramanian (eds.), *Innovative Design, Analysis and Development Practices in Aerospace and Automotive Engineering*, Lecture Notes in Mechanical Engineering, https://doi.org/10.1007/978-981-15-6619-6_9

1 Introduction

Single-point incremental forming (SPIF) process is emerging sheet metal forming process which is capable producing complicated sheet metal parts without dedicated press tools. The part is directly made from computer-aided design (CAD) geometry, thus eliminating the requirement of molds, fixture, punch, and die setup. It is a flexible process [1]. The process is a carried on three-axis conventional computerized numerically controlled (CNC) milling machine without investing on new equipment and tooling [2]. Tool path can be simulated and optimized on simple CNC simulator software. Due to the above-mentioned benefits, the cost of machine setup and tooling in SPIF process is much lesser relative to conventional sheet metal forming processes which requires dedicated press and press tools [3]. If there is any design change in existing part, then it requires whole new or modified die and punch setup. But in SPIF process, any change design of part can be quickly and easily incorporated.

Due to incremental deformation characteristics, forming force required during forming operation is less. In this process, sheet is held between the clamping plate and the backing plate while the tool is given desired motion along with the small steps in Z-axis (vertically downward direction) on the blank as show in Fig. 1. The tool may be given rotation or can be held still while following the contour of the predefined tool path. For such reasons, this process is nowadays preferred by researchers for prototypes and customized products [5]. Despite such numerous advantages of the process, it is yet not accepted in sheet metal industries. One of the main reasons for this is poor geometrical accuracy. Geometric accuracy of industrial sheet metal parts typically lies within the range of ± 0.2 mm while the geometric accuracy with SPIF process lies within ± 2 mm (approximately) [6]. The geometrical error is termed as the difference in target profile and the profile obtained after forming operation. Allwood et al. [7] categorized profile accuracy in the SPIF process into (i) Profile error due to clamping of sheet, (ii) profile error arises when formed part is unclamped

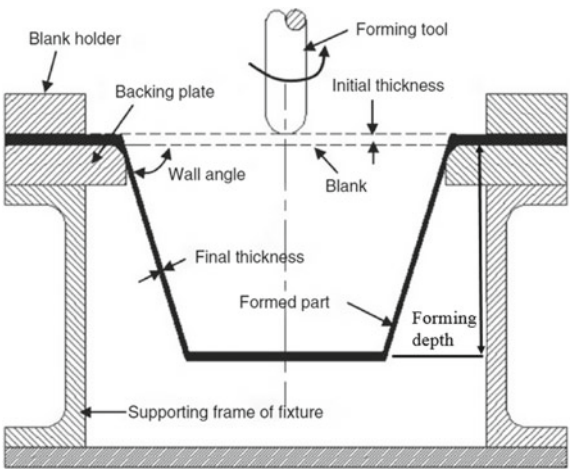

Fig. 1 Single-point incremental forming process [4]

accuracy, and (iii) final accuracy of formed part. Further, Micari et al. [8] subdivided the shape accuracy as (a) bending of sheet along the clamped edges from where the plastic deformation initiates, (b) spring-back in formed part after tool/punch is raised after forming operation, and (c) pillow effect. If a simple truncated conical shape is to be deformed, these three different errors can be detected on it after forming operation. Bending of sheet along the clamped edges is normally solved simply by the use of backing plate. Secondly, when the tool/punch is relaxed after forming the deformed sheet, metal part slightly rises upward and the final forming depth of part is lesser than target depth. Finally, pillow defect can be seen as central undeformed concave region.

Worldwide researchers have made efforts to improve geometric accuracy and proposed various different strategies for enhancing it. For example, Ceretti et al. [9] proposed SPIF process with and without full die to form some complex part shapes. They reported that considerable improvement in geometric accuracy of part was achieved by using die as compared to the part formed without die. They suggested to fabricate the die using cheap and easily available material to reduce the tooling cost. Hirt et al. [10] focused on two main process limitation, namely maximum formable wall angle and poor geometrical accuracy. It was observed that multi-stage forming approach is capable of forming steep flanges of the order of 81° while an improvement algorithm helps to reduce profile deviation. Ambrogio et al. [11] studied the influence of process parameters, namely tool diameter, step size, wall angle, forming depth, and sheet thickness on profile deviation of the truncated cone formed by SPIF process. It was observed that the profile deviation measured along the corners was mainly influenced by thickness of sheet and forming depth while pillow effect which was at the middle of the base was majorly influenced by the size of tool and forming depth. Ambrogio et al. [12] have made efforts to improve industrial suitability of SPIF process by studying influence of high feed rate on geometric accuracy. Higher forming time was identified as major limitation and it was suggested that it can be overcome by using high feed rates. It was found that with smaller tool diameter good geometrical precision is obtained. Bambach et al. [13] have formed sheet metal fender of car using SPIF process. They used multi-stage forming process to improve the accuracy of asymmetrical component. They suggested that the geometric error of formed part could increase if the part is trimmed after forming operation due to presence residual stresses. To overcome this limitation, stress-relief annealing combined with multi-stage forming process was used. It was observed that multi-stage forming results in higher accuracy as compared to single-stage forming process. But accordingly, the forming time is increased, making multi-stage forming slower than single-stage forming. Ziran et al. [14] have investigated tool geometry (hemispherical and flat ended tool) on profile accuracy (or geometric error) in SPIF process. It was reported that with flat-end tool, low geometric error is observed and lower forming force is recorded as compared to hemispherical-ended tool. Gottmann et al. [15] proposed new setup for laser-assisted SPIF process. Two main limitations of asymmetric incremental sheet forming (ASIF) (i.e., low geometrical accuracy and low formability) at room temperature were studied. It is reported that formability and profile deviation of formed component of Ti grade

5 sheet metal can be improved with local laser heating system. Rauch et al. [16] investigated the influence of tool path strategy, feed rate, and axial increment on profile accuracy, forming force and maximum forming depth of formed part. They proposed a dedicated tool path technique to reduce the geometric error. Fiorentino et al. [17] analyzed the influence of step decrements on forming forces, formability, geometric deviation and thinning in SPIF process, and two-point incremental forming (TPIF) process. Good geometric accuracy was observed in parts formed with TPIF process. Radu et al. [18] studied the effect of process parameters on residual stresses and profile deviation of formed parts. They reported that large tool diameter and pitch result in poor geometric accuracy whereas large feed rate and spindle speed form accurate parts. Residual stresses increase with increase in pitch and feed rate. Behera et al. [19] proposed a methodology to map the influence of different factors on the geometric error of part formed by SPIF process. Partial tool path strategy that records the geometric error of particular feature in the formed part was also presented. It was reported that the maximum geometrical deviation in the formed part is significantly reduced by optimized tool path strategy. Lu et al. [20] reported that geometric accuracy increases by decreasing the step size. Lu et al. [21] developed a model predictive control algorithm to compensate the tool position in both horizontal and vertical directions in SPIF and TPIF process to reduce the geometric error of formed component. The developed algorithm is able to reduce the geometric error. Wang et al. [22] investigated the influence of tool path strategies, namely squeezing and reverse bending in double-sided incremental forming process (DSIF) to improve the geometric accuracy of parts. They reported that spring-back in DSIF technique is reduced using reverse bending and squeezing. Researchers have reported that poor geometric accuracy in SPIF process is due to minimum constraints on the blank sheet. The main reasons for high geometric error in SPIF process are absence of supporting die, spring-back (combined local and global), bending of sheet at the clamped edges, and presence of residual stress in formed part. To improve the geometric accuracy of parts, methods such as stress relieving techniques [19, 23–25] and use of partial support or double-sided incremental forming [25, 26] were used. From the critical review of literature, it is clear that very less research efforts have been made to study the geometric error of formed part in SPIF process. Different strategies have been proposed by researchers to improve geometric error but most of them is either very complex in nature or time consuming. Also, no work has been reported in studying geometric error in SPIF process with dummy sheet. Therefore, objective of present work is to investigate the effect of process parameter on geometric error (RMSE), develop mathematical model, and optimize significant process parameters to minimize RMSE.

2 Experimental Plan and Methodology of Present Work

In the present experimental investigation, influence of dummy sheet thickness (t_d), step size (Δz), wall angle (φ), and feed rate (f) on geometric error (in terms of root-mean-squared error) is studied. Table 1 represents the designated process parameters and their levels. Box behnken design of experiments (BBD) is used to create experimental run order matrix. Totally, 29 experiments were performed. The experimental setup is depicted in Fig. 2. The experimental investigation was done in the following order:

1. Selection of sheet material, sheet thickness, and tool material.
2. Identification of major process parameters influencing geometric error.
3. Determination of range and level of identified and finalised process parameters.
4. Selection of appropriate response surface method (RSM) for designing the experiments.
5. Conducting experiments as per obtained design matrix.

Table 1 Process parameters with their levels

S. No.	Process parameters	Unit	Level 1	Level 2	Level 3
1	Wall angle (φ)	degree	40	52.5	65
2	Step size (Δz)	mm	0.35	0.65	0.95
3	Feed rate (f)	mm/min	2200	3300	4400
4	Dummy sheet thickness (t_d)	mm	0.51	0.71	0.91

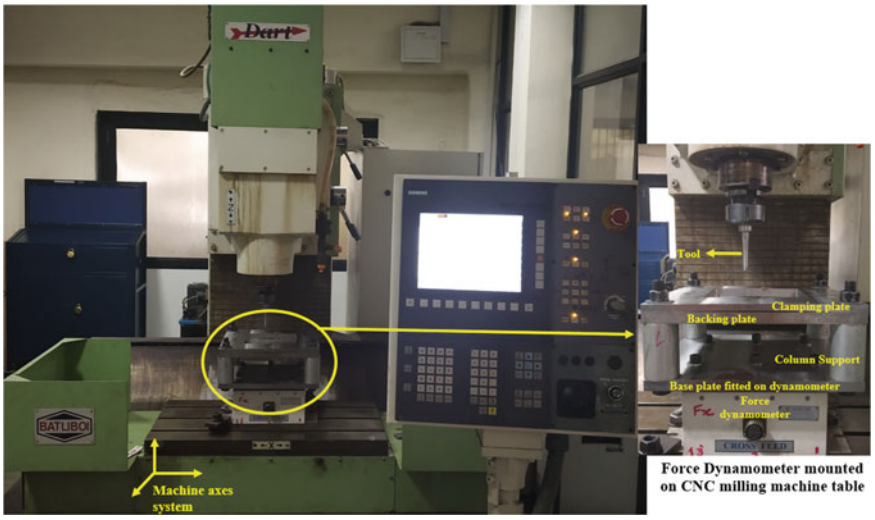

Fig. 2 Experimental setup for SPIF with dummy sheet

6. Generation of point cloud data by scanning the formed part using 3D laser scanner.
7. Import the point cloud data in SolidWorks software and measure the geometric error in formed profile with target profile.
8. Interpretation of result, analysis of variance, development of mathematical model.
9. Conducting the confirmation experiments for inspecting the adequacy of developed model.
10. Optimization of process parameters to minimize geometric error (RMSE).

For the present work, tool diameter of 9 mm is used. It is hemispherical-ended tool made of high-speed steel (HSS). Table 2 lists the values of parameters kept constant. Root-mean-squared error (RMSE) is selected as response. For measurement of geometrical error, first, the part is sprayed with Magnaflux make SKD-S2 developer spray to make the surface of formed part less reflective and facilitate accurate generation of point cloud. After that, the part is kept inside the 3D laser scanner for scanning purpose. The scanner used for present work is Roland make Dr. Picza 3D laser scanner. It generates the point cloud of the part. The sprayed formed part is depicted in Fig. 3a and the point cloud data generated by the scanner is shown in Fig. 3b. The truncated pyramid is formed using SPIF process with dummy sheet. The depth of formed part with wall angle 40° is 35 mm while with 52.5° and 65° wall

Table 2 Process parameter kept constant

Process parameter	Unit	Value
Tool path type	NA	Spiral
Spindle speed	rpm	0
Target sheet thickness	mm	0.91
Dimensions of square pyramid	mm	110 × 110
Tool material	NA	HSS
Tool size	mm	9

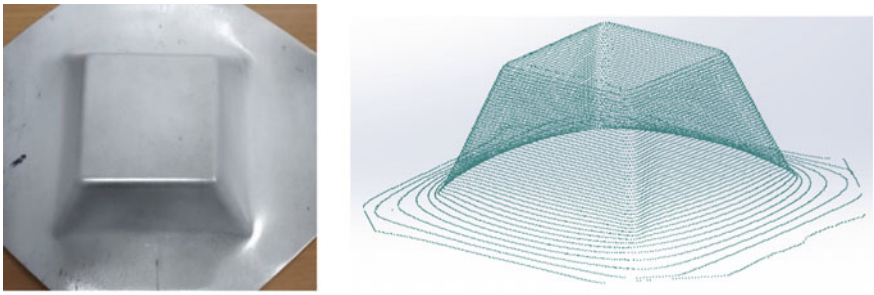

Fig. 3 **a** Formed part sprayed for scanning; **b** point cloud data obtained from 3D point laser scanner

angle have depth of 50 mm. From preliminary tests and observations, it is seen that the bending is more in the top region of pyramid. This is due to absence of proper support to the sheet. This contributes in severe geometric error.

To overcome this, a height allowance of (say 10–20 mm) from top of square pyramid is considered. Thus, the effective height of 52.5° wall angle square pyramid is around 40 mm. Minor post-processing work may be required to cut maximum bending region from the formed part. This facilitates the removal of bending zone which contributes in geometric error. This is done by designing the part geometry in such a way that after cutting the bending region, cut-out part is the desired part with required dimensions (i.e., by considering height allowance). This extra 10–12 mm height can be removed with the help of abrasive water jet machining, wire electro discharge machining, or laser machining process.

3 Results and Discussion

With respective experimental run order, the value of geometrical error is measured and selected as response, i.e., geometric accuracy is evaluated in terms of root-mean-squared error (RMSE). The value of geometrical error (RMSE) is calculated using Eq. (1). The RMSE varies within the range of 0.78–1.854 mm. ANOVA for RMSE is depicted in Table 3. It is used to quantify the influence of process controlling variables on response characteristic. In the present study, step size, dummy sheet thickness, and wall angle are significant model terms while feed rate is insignificant.

Table 3 ANOVA table for RMSE

Source	SOS	DoF	MS	F-value	p-value	
Model	1.58	4	0.3947	15.52	<0.0001	Significant
A-Dummy sheet thickness (t_d)	0.6841	1	0.6841	26.90	<0.0001	
B-Step size (Δz)	0.6974	1	0.6974	27.43	<0.0001	
C-Wall angle (ϕ)	0.1933	1	0.1933	7.60	0.0110	
D-Feed rate (f)	0.0041	1	0.0041	0.1599	0.6928	
Residual	0.6102	24	0.0254			
Lack of fit	0.5800	20	0.0290	3.84	0.1003	Not significant
Pure error	0.0302	4	0.0076			
Cor total	2.19	28				
Model summary						
R^2	0.7212					
Adjusted R^2	0.6748					

$$\text{Root Mean Squared Error (RMSE)} = \sqrt{\frac{\sum_{i=1}^{n}(x_i - x_o)^2}{n}} \quad (1)$$

where x_i = target value; x_o = observed value and n = number of observations.

Figure 4 depicts the perturbation plot. From the ANOVA (Table 3), it is found that dummy sheet thickness (t_d), step size (Δz), and wall angle (φ) are significant parameter while feed rate is found to be insignificant. As dummy sheet thickness increases, RMSE increases. It is because as dummy sheet thickness increases, virtual tool size [27] increases and as tool size (in terms of tool diameter) increases, geometric error increases. This observation is in agreement with the findings of previous researchers [11, 12, 18]. The amount of plastic deformation accomplished by small diameter tool is large compared to that of large virtual size tool (at constant step size). More plastic deformation accomplished at lesser thickness of dummy sheet due to small virtual tool size. At small tool size, projected contact area between tool and sheet interface is small, resulting more plastic deformation due to highly concentrated forces. Thus, the sheet deforms plastically at such magnitude of concentrated forming forces.

As dummy sheet thickness increases, virtual tool size also increases and it contributes in more bending deformation and small plastic work resulting in considerable elastic recovery as compared to small tools. As step size (Δz) increases, geometrical error (RMSE) decreases. Since the tool path is spiral, there is gradual increase of vertical increment in every loop as compared to sudden rise of step size in contoured/incremental tool path. This gradual rise in Δz creates plastic deformation and enhances the geometric accuracy and reduces the error. Also, in contoured/incremental tool path, the tool tries to indent the sheet at higher step size.

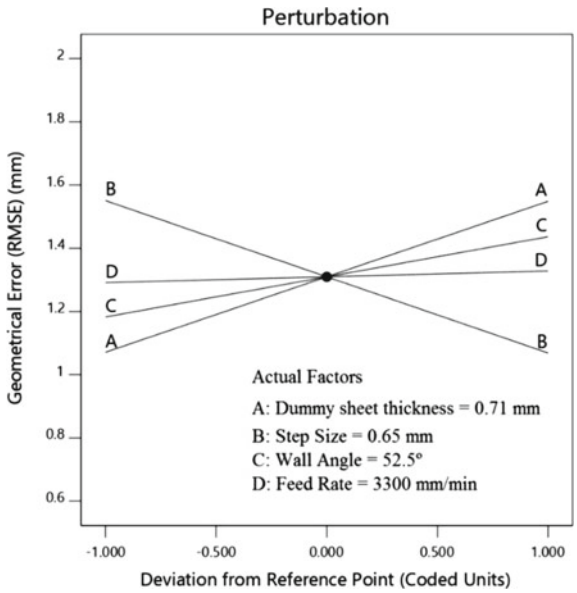

Fig. 4 Perturbation plot for geometrical error (RMSE)

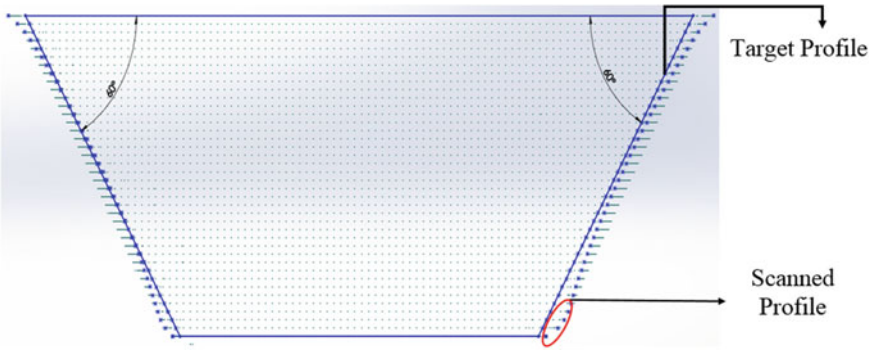

Fig. 5 Point cloud data of 60° wall angle pyramid imported in SolidWorks software

This results in more stretching of sheet with relatively more elastic recovery. Thus, there is more spring-back at large step size in case of contoured/incremental tool path which is not the case in spiral tool path. As the wall angle increases, RMSE increases. This is because, at high wall angle, elastic recovery is more which leads to increased spring-back. Since, at higher wall angle, stretching is predominant and high localized deformation takes place which results in more spring-back. Since feed rate has no significant influence on RMSE. Therefore, high feed rate can be used to reduce forming time. In fact, there is slight decrease in RMSE as feed rate increases which is desirable. This is due to the fact that frictional heat which is generated due to sliding contact between the tool and sheet metal blank, which softens the material and plastic deformation takes place with less elastic recovery. So, as feed rate increases, RMSE decreases. Figure 5 shows the point cloud data of 60° wall angle pyramid which is imported in SolidWorks software and the difference between scanned and target profile.

4 Predictive Model for Geometrical Error (RMSE)

Using experimental results, an empirical relation is proposed to represent the geometrical error (RMSE). It is given by Eq. (2) in actual factors.

$$\text{Geometrical Error (RMSE)} = \{0.4 + (1.2 \times t_d) - (0.8 \times \Delta z) + (0.01 \times \varphi) + (0.000017 \times f)\} \quad (2)$$

where t_d = dummy sheet thickness; Δz = step size, φ = wall angle; f = feed rate. Confirmation tests are carried out in order to verify adequacy and suitability of developed mathematical model. Process parameters settings are randomly finalized within range of design space. Results of confirmation experiments are given in Table 4.

Table 4 Confirmation test results for geometric error

Conf. test no.	Dummy sheet thickness	Step size	Wall angle	Feed rate	Predicted RMSE	Measured RMSE	% error
1	0.51	0.4	45	2500	1.2	1.389	14.72
2	0.71	0.45	50	3000	1.44	1.698	15.01
3	0.91	0.7	55	3600	1.54	1.706	9.543
4	0.51	0.8	60	4000	1.04	1.22	14.75

Table 5 Criteria for optimization

S. No.	Process parameter and responses	Goal	Lower limit	Upper limit	Optimized value
1	Dummy sheet thickness	In range	0.51	0.91	0.5162
2	Step size	In range	0.35	0.95	0.936
3	Wall angle	In range	40	65	41.537
4	Feed rate	In range	2200	4400	2225.41
5	Geometric error (RMSE)	Minimize	0.783	1.854	0.718

5 Optimization of Geometric Error (RMSE)

The optimized set of process parameters is selected to reduce the geometric error (RMSE). The optimized values of process parameters are listed in Table 5. The obtained vale for desirability is "1" and hence can be accepted.

6 Conclusion

In the present work, influence of process parameters on geometric error (in terms of RMSE) of formed part in SPIF process with dummy sheet has been studied. Following are the conclusions drawn from the present experimental study:

1. Step size, dummy sheet thickness, and wall angle are significant process parameters influencing RMSE. No significant influence of feed rate is observed.
2. Geometric error increases with increase in dummy sheet thickness and wall angle, while it decreases with the increase in step size.
3. As feed rate increases, there is nominal decrease in geometric error which is desirable. So high feed rate is recommended to reduce forming time.

Based on analysis of results, a mathematical model for RMSE has been proposed. Adequacy and accuracy of developed mathematical model for RMSE have been validated by performing confirmation experiments. The obtained experimental results

are in good agreement with predicted results. Further optimization of RMSE based on desirability function has been performed. The findings of present work are useful in forming parts with good accuracy by using SPIF process with dummy sheet.

References

1. Manco GL, Ambrogio G (2010) Influence of thickness on formability in 6082-T6. Int J Mater Form 3(1):983–986
2. Matsubara S (2001) A computer numerically controlled dieless incremental forming of a sheet metal. Proc Inst Mech Eng Part B J Eng Manuf 215(7):959–966
3. Franzen V, Kwiatkowski L, Martins PAF, Tekkaya AE (2009) Single point incremental forming of PVC. J Mater Process Technol 209(1):462–469
4. Kurra S, Rahman NH, Regalla SP, Gupta AK (2015) Modeling and optimization of surface roughness in single point incremental forming process. J Mater Res Technol 4(3):304–313
5. Ambrogio G, Costantino I, De Napoli L, Filice L, Fratini L, Muzzupappa M (2004) Influence of some relevant process parameters on the dimensional accuracy in incremental forming: a numerical and experimental investigation. J Mater Process Technol 153:501–507
6. Allwood JM, King GPF, Duflou J (2005) A structured search for applications of the incremental sheet-forming process by product segmentation. Proc Inst Mech Eng Part B J Eng Manuf 219(2):239–244
7. Allwood JM, Braun D, Music O (2010) The effect of partially cut-out blanks on geometric accuracy in incremental sheet forming. J Mater Process Technol 210(11):1501–1510
8. Micari F, Ambrogio G, Filice L (2007) Shape and dimensional accuracy in single point incremental forming: state of the art and future trends. J Mater Process Technol 191(1–3):390–395
9. Ceretti E, Giardini C, Attanasio A (2004) Experimental and simulative results in sheet incremental forming on CNC machines. J Mater Process Technol 152(2):176–184
10. Hirt G, Ames J, Bambach M, Kopp R (2004) Forming strategies and process modelling for CNC incremental sheet forming. CIRP Ann 53(1):203–206
11. Ambrogio G, Cozza V, Filice L, Micari F (2007) An analytical model for improving precision in single point incremental forming. J Mater Process Technol 191(1–3):92–95
12. Ambrogio G, Filice L, Gagliardi F (2012) Improving industrial suitability of incremental sheet forming process. Int J Adv Manuf Technol 58(9–12):941–947
13. Bambach M, Araghi BT, Hirt G (2009) Strategies to improve the geometric accuracy in asymmetric single point incremental forming. Prod Eng Res Dev 3(2):145–156
14. Ziran X, Gao L, Hussain G, Cui Z (2010) The performance of flat end and hemispherical end tools in single-point incremental forming. Int J Adv Manuf Technol 46(9–12):1113–1118
15. Göttmann A, Diettrich J, Bergweiler G, Bambach M, Hirt G, Loosen P, Poprawe R (2011) Laser-assisted asymmetric incremental sheet forming of titanium sheet metal parts. Prod Eng Res Dev 5(3):263–271
16. Rauch M, Hascoet JY, Hamann JC, Plenel Y (2009) Tool path programming optimization for incremental sheet forming applications. Comput Aided Des 41(12):877–885
17. Fiorentino A, Attanasio A, Marzi R, Ceretti E, Giardini C (2011) On forces, formability and geometrical error in metal incremental sheet forming. Int J Mater Prod Technol 40(3–4):277–295
18. Radu C, Tampu C, Cristea I, Chirita B (2013) The effect of residual stresses on the accuracy of parts processed by SPIF. Mater Manuf Process 28(5):572–576
19. Behera AK, Lauwers B, Duflou JR (2014) Tool path generation framework for accurate manufacture of complex 3D sheet metal parts using single point incremental forming. Comput Ind 65(4):563–584

20. Lu HB, Li YL, Liu ZB, Liu S, Meehan PA (2014) Study on step depth for part accuracy improvement in incremental sheet forming process. In: Advanced materials research. Trans Tech Publications, vol 939, pp 274–280
21. Lu H, Kearney M, Wang C, Liu S, Meehan PA (2017) Part accuracy improvement in two-point incremental forming with a partial die using a model predictive control algorithm. Precis Eng 49:179–188
22. Wang H, Zhang R, Zhang H, Hu Q, Chen J (2018) Novel strategies to reduce the springback for double-sided incremental forming. Int J Adv Manuf Technol 96(1–4):973–979
23. Behera AK, Lu B, Ou H (2016) Characterization of shape and dimensional accuracy of incrementally formed titanium sheet parts with intermediate curvatures between two feature types. Int J Adv Manuf Technol 83(5–8):1099–1111
24. Vanhove H, Carette Y, Vancleef S, Duflou JR (2017) Production of thin shell clavicle implants through single point incremental forming. Procedia Eng 183:174–179
25. Attanasio A, Ceretti E, Giardini C, Mazzoni L (2008) Asymmetric two points incremental forming: improving surface quality and geometric accuracy by tool path optimization. J Mater Process Technol 197(1–3):59–67
26. Formisano A, Boccarusso L, Capece Minutolo F, Carrino L, Durante M, Langella A (2017) Negative and positive incremental forming: comparison by geometrical, experimental, and FEM considerations. Mater Manuf Process 32(5):530–536
27. Martins PAF, Bay N, Skjødt M, Silva MB (2008) Theory of single point incremental forming. CIRP Ann 57(1):247–252

Numerical Investigation on Optimized Convergent Divergent Nozzle in 3S Separator Device

L. Prabhu, N. Kiran Jadediya, P. Gangadhar Venkata Ramana, and J. Srinivas

Abstract In this work, the optimal parameters required to develop the shock at a specified location of a convergent-divergent nozzle in the 3S supersonic separator are obtained using a meta-heuristic algorithm in conjunction with the surrogate model. Here, the study is carried over the air. Initially, a non-conventional optimization scheme firefly algorithm is employed to obtain the optimal parameters of convergent-divergent nozzle such as area ratio and operating pressure ratio to develop the normal shock at a specific location of a nozzle in 3S device. The operating pressure ratio limit is imposed as a constraint in the problem. The mathematical modelling of a nozzle is based on the one-dimensional flow governing equations. To reduce the computational cost, mathematical modelling is replaced by a neural network-based surrogate model. Then, using the optimal parameters obtained from an optimization scheme, the nozzle is modelled and simulated in ANSYS Fluent to validate it by identifying the shock location in the divergent portion of nozzle.

Keywords Supersonic separator · Firefly algorithm · 3S device · Normal shock wave · Condensation

1 Introduction

The supersonic swirling (3S) separator is a device used to separate the undesirable components in natural gas. A convergent-divergent (CD) nozzle is used to accelerate the flow to supersonic speed and to generate normal shockwave. The 3S device shown in Fig. 1 removes the unwanted materials from the natural gas by reducing the fluid

L. Prabhu (✉) · N. Kiran Jadediya · P. Gangadhar Venkata Ramana
Department of Aerospace Engineering, Lakireddy Bali Reddy College of Engineering, Mylavaram, Andhra Pradesh 521230, India
e-mail: prabhu@lbrce.ac.in

J. Srinivas
Department of Mechanical Engineering, National Institute of Technology Rourkela, Rourkela, Odisha 769008, India

N. Gascoin and E. Balasubramanian (eds.), *Innovative Design, Analysis and Development Practices in Aerospace and Automotive Engineering*, Lecture Notes in Mechanical Engineering, https://doi.org/10.1007/978-981-15-6619-6_10

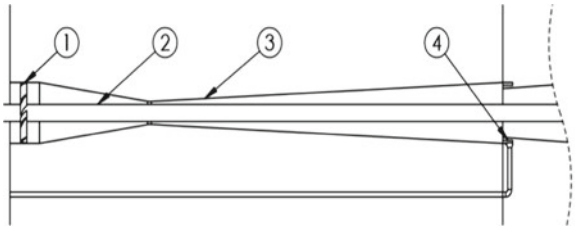

S.no	Name
1	Static guide vanes
2	Mandrel
3	Convergent-Divergent nozzle
4	Drain

Fig. 1 Supersonic swirling separator

properties to the dew point. After the condensation, condensate is to be separated via the drain pipe. Hussaini [1] proposed a theoretical method for an identification of the normal shockwave location using the adiabatic flow equations. Niknam et al. [2] predicted the normal shockwave location using the artificial neural networks and coined an iterative process for identification of normal shockwave location.

Gangadhar Venkata Ramana and Prabhu [3] identified the optimal nozzle parameters such as area ratio (*AR*) and operating pressure ratio (*OPR*) to develop the normal shock at the known location in a 3S device using a genetic algorithm optimization scheme. Shooshtari and Shahsavand [4] studied the effect of diverging angles on shock location, pressure recovery coefficient (*PRC*), and the condensation conditions. Numerical simulation was carried out to study the phase change and fluid properties of the undesired components of natural gas in a supersonic separator [5]. Jinnah [6] identified the turbulence parameters due to the presence of shockwave in the nozzle divergent. Shooshtari and Shahsavand [7] designed an optimal 3S device for efficient separation of condensed liquid and increased *PRC*. Bian et al. [8] identified the pressure and temperature distribution of a flow in a separator device. Cao and Yang [9] studied the influence of PRC on a dew point depression.

In this work, the optimal parameters required to develop the shock at a specified location in a CD nozzle of a 3S device are obtained using a meta-heuristic algorithm in conjunction with the surrogate model. The source used is air. Initially, a non-conventional optimization scheme firefly algorithm is employed to obtain the optimal parameters AR and OPR of CD nozzle with PRC as the constraint to produce the shock at a specified location. To reduce the computational cost, mathematical modelling is replaced by a neural network-based surrogate model. Finally, to validate the optimal parameters obtained from an optimization scheme, the nozzle is modelled and simulated in ANSYS Fluent.

2 Mathematical Modelling

The mathematical modelling of a nozzle is based on the one-dimensional flow governing equations [1]. Figure 2 shows a convergent-divergent nozzle. By developing a pressure difference across the nozzle, flow accelerates in the convergent section and decelerates in the divergent section. If the pressure difference is increased, the nozzle achieves a choke condition and further increment leads to normal shockwave.

The distance between throat to condensate drain is represented as '*C*.' If the normal shockwave is at a location '*S*' from the throat and length of the divergent section is '*L*,' then the non-dimensional shock location is expressed as follows:

$$X_s = \frac{S}{L} = \frac{(\mathrm{AR}(M_s))^{0.5} - 1}{\left(\mathrm{AR}\left(M_{\mathrm{sup}}\right)\right)^{0.5} - 1} \tag{1}$$

The *AR* as a function of Mach number (*M*) is given as follows:

$$\frac{A}{A^*} = \mathrm{AR}(M) = \left(\left(\frac{2}{\gamma+1}\right) \times \left(1 + \frac{(\gamma-1) \times M^2}{2}\right)\right)^{\frac{\gamma+1}{2(\gamma-1)}} \times M^{-1} \tag{2}$$

where M_{sup}, M_s, γ, A and A^* are supersonic Mach number, Mach number before the shock, a ratio of specific heats of fluid, exit area, and throat area, respectively. The operating pressure ratio (*OPR*) is expressed as:

$$\mathrm{PR}(M) = \frac{P}{P_O} = \left(1 + \left(\frac{\gamma-1}{2} \times M^2\right)\right)^{\frac{-\gamma}{(\gamma-1)}} \tag{3}$$

where p is the static pressure and p_o is the stagnation pressure.

The (p_{nsr}) static and (*PRC*) stagnation pressure ratio across the normal shockwave is obtained as follows:

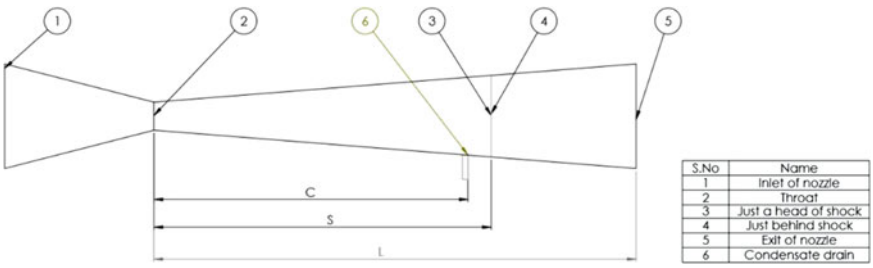

Fig. 2 Schematic diagram of convergent-divergent nozzle

$$p_{\text{nsr}}(M) = \left(1 + \left(2\gamma \times \frac{(M^2) - 1}{\gamma + 1}\right)\right)^{-1} \tag{4}$$

$$\text{PRC}(M) = \left(1 + \left(2\gamma \times \frac{(M_s^2) - 1}{\gamma + 1}\right)\right)^{-\frac{1}{\gamma - 1}} \times \left(\left(\frac{M_s^2(\gamma + 1)}{(\gamma - 1)M_s^2 + 2}\right)^{\frac{\gamma}{\gamma - 1}}\right) \tag{5}$$

For every *AR*, there are two possible pressure ratios, the first pressure ratio is the minimum pressure ratio to choke the nozzle and the second one is the pressure ratio required to place the shock at the exit of the nozzle. These pressure ratios are written as given below:

$$\text{OPR1} = \text{PR}(M_{\text{sub}}); \quad \text{OPR2} = \left(p_{\text{nsr}}\left(M_{\text{sup}}\right) \times \text{PR}\left(M_{\text{sup}}\right)\right)^{-1} \tag{6}$$

where M_{sub} is the subsonic Mach number of *AR*.

2.1 Firefly Algorithm

Firefly algorithm is a nature-inspired algorithm formulated as all fireflies are unisexual and they are attracted to the attractive firefly [10]. Attractive is proportional to the brightness level of the individual. Initially, fireflies are spread randomly in the solution domain of the problem. The intensity of every firefly is calculated using the objective or intensity function. The firefly algorithm is shown in Fig. 3. The movement of the firefly depends on attractiveness $\beta(r)$ which is given as follows:

$$\beta(r) = \beta_o \text{e}^{(-\mu r^2)} \tag{7}$$

where r and α_o are the distance between any two fireflies and randomization control, respectively. β_o is attractiveness or intensity at $r = 0$, and μ is the light absorption coefficient.

If 'n' is the total number of simulations and at simulation 't,' the movement of less intensity firefly 'j' is expressed as follows:

$$X_j^{t+1} = X_j^t + \beta_i(r) \times \left(X_i^t - X_j^t\right) + \alpha_o \theta^t \in \tag{8}$$

where θ and $\in$ are randomness reduction and random parameter, respectively.

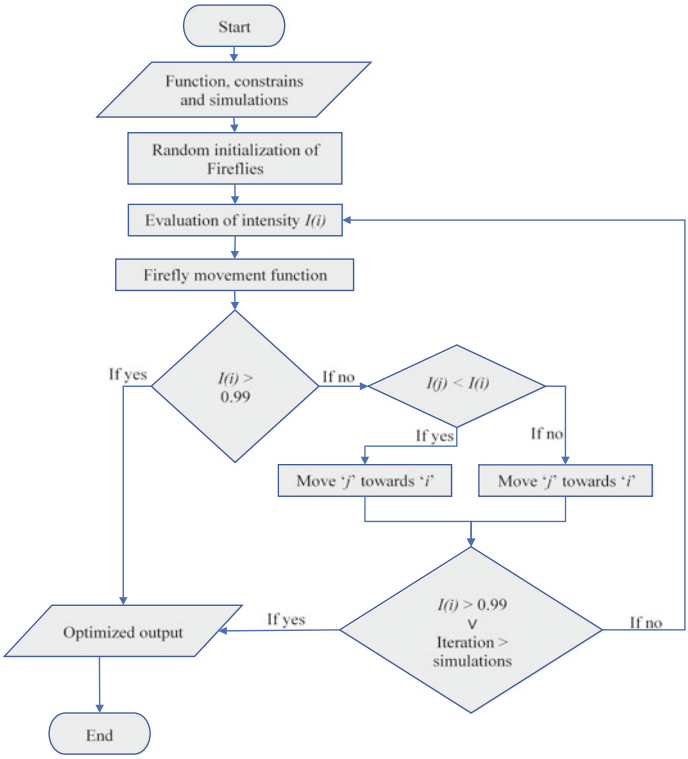

Fig. 3 Flowchart of firefly algorithm

2.2 Surrogate Model

Artificial intelligence is widely used in engineering applications. It is similar to the human neural system. The backpropagation neural network model consists of three layers, they are input, hidden, and output layer, and it is used as a surrogate model. The computations are passed forward from the input to output layers; calculated errors are propagated backward to update the weights. After a number of training sessions, the weight reaches optimum values, which gives the outputs close to the targets.

3 Numerical Simulation

In-house, MATLAB code is written to carry out the computational work. Initially, the data is generated from mathematical modelling, and it is used to train the neural network. The output of NN models are compared with mathematical modelling.

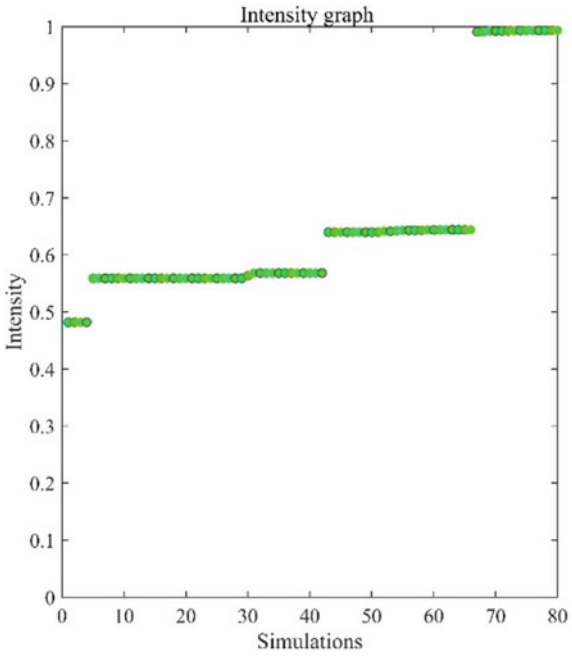

Fig. 4 Intensity versus simulation graph

The errors are within the acceptable range, and now, NN models are substituted as surrogate models in optimization schemes to identify the optimal parameters.

Values of *PRC* and X_s are taken as 0.532 and 0.532, respectively, in the optimization scheme to find the optimal parameter *AR* and *OPR*. A number of simulations n are considered as 80, and the problem is defined to achieve the intensity greater than 0.99. Light absorption coefficient μ, randomization control α_o and randomness reduction θ are taken as 1,1 and 0.9 respectively. The lower and upper limits of two variables are taken as: AR $\in$ [2 25], OPR $\in$ (0 1].

After running the algorithm for several times, the optimal parameters are identified to be AR = 4.25, which has the OPR limits from 0.9868 to 0.2804, and the obtained OPR = 0.505. The simulations--intensity graph is shown in Fig. 4.

3.1 Computational Flow Analysis

The nozzle is modelled with optimal parameters obtained from the optimization scheme. The convergent and divergent angles are taken as 10° and 5°, and convergent and divergent length of the nozzle are 0.0735 m and 0.148 m, respectively. The inlet and exit diameters of the nozzle are considered to be equal. A quadrilateral mesh element is used, and the generated mesh in the computational domain is shown in

Fig. 5. Operating conditions are set to the atmosphere, and the inlet absolute operating pressure and the exit pressure are set to be 200 kPa and atmosphere, respectively, as predicted by the firefly algorithm.

To proceed further, the grid independence test is carried out and found that mesh points of 8000 is optimum. The density-based solver with *k-ω SST* a turbulence model is used. The centerline Mach number of CD nozzle is shown in Fig. 6a, and the respective Mach contour is shown in Fig. 6b. The shockwave location is identified as 0.073 m from the divergent section, and the ratio of shockwave location to divergent length X_s is 0.5 which is close to shockwave location used in the firefly optimization scheme.

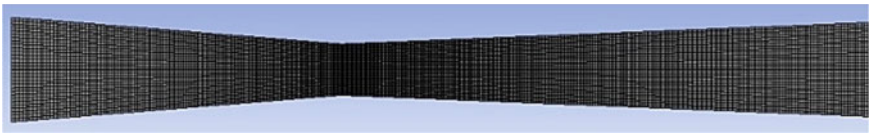

Fig. 5 2D computational domain with mesh

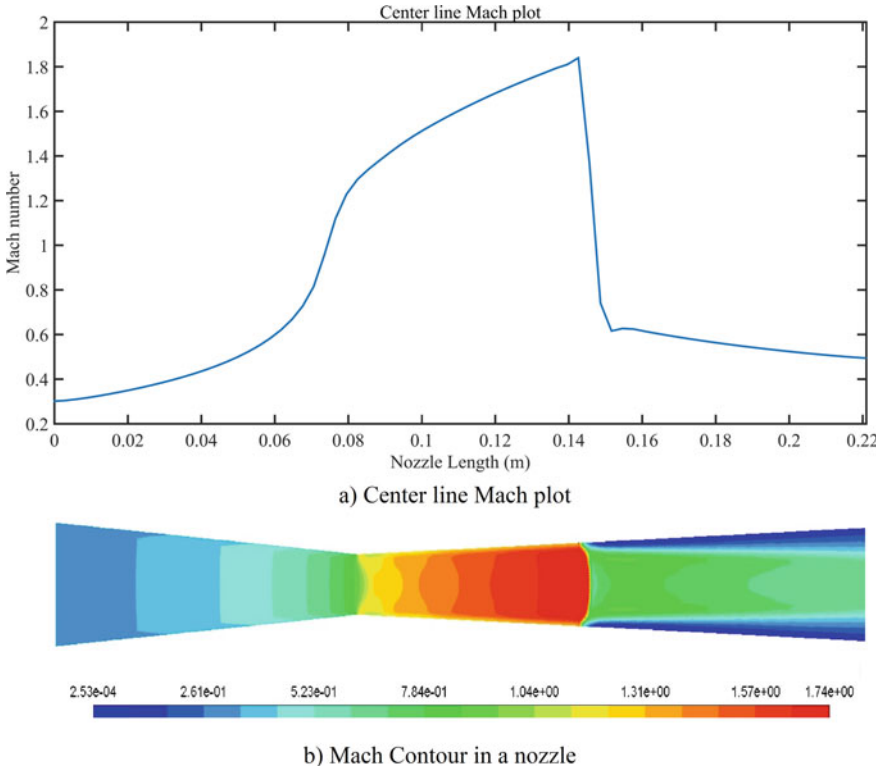

Fig. 6 Numerical simulation

4 Conclusion

Identification of an optimal parameters area ratio and operating pressure ratio of a nozzle to place the normal shock at a specific location in a 3S device is carried out using meta-heuristic optimization scheme. Initially, for a shockwave location, the optimal parameters with pressure recovery coefficient as a constraint were identified using a nature-inspired firefly algorithm. The surrogate model using a neural network was deputed in the optimization scheme to compute the parameters with a less computational cost. Finally, the convergent-divergent nozzle was designed using the optimal parameters identified by the firefly algorithm, and flow analysis was carried out. The shock location from the flow analysis was found to be very close to the shockwave location used in the optimization scheme. This shows the effective working of the firefly optimization in the design of a nozzle in the 3S device. In the future, the experimental investigation of the nozzle design with optimal parameters will be carried out to validate further.

References

1. Hussaini AA. Gas dynamics. http://uotechnology.edu.iq/dep-MechanicsandEquipment
2. Niknam PH, Mokhtarani B, Mortaheb HR (2016) Prediction of shockwave location in supersonic nozzle separation using self-organizing map classification and artificial neural network modeling. J Nat Gas Sci Eng 34:917–924
3. Gangadhar Venkata Ramana P, Prabhu L (2020) Identification of nozzle parameters in 3S device using artificial intelligence and meta-heuristic optimization scheme. American Inst Phy Conf Proc 2204:030004
4. Shooshtari SHR, Shahsavand A (2017) Maximization of energy recovery inside supersonic separator in the presence of condensation and normal shock wave. Energy 120:153–163
5. Niknam PH, Mortaheb HR, Mokhtarani B (2018) Dehydration of low-pressure gas using supersonic separation: experimental investigation and CFD analysis. J Nat Gas Sci Eng 52:202–214
6. Jinnah MA (2013) Numerical simulation of shock induced turbulence in a nozzle flow. J Inst Eng India Ser C 94:229–237
7. Shooshtari SHR, Shahsavand A (2018) Optimal operation of refrigeration oriented supersonic separators for natural gas dehydration via heterogeneous condensation. Appl Therm Eng 139:76–86
8. Bian J, Cao X, Yang W, Edem MA, Yin P, Jiang W (2018) Supersonic liquefaction properties of natural gas in the Laval nozzle. Energy 159:706–715
9. Cao X, Yang W (2015) The dehydration performance evaluation of a new supersonic swirling separator. J Nat Gas Sci Eng 27:1667–1676
10. Yang X-S (2014) Nature-inspired optimization algorithms. Elsevier, Amsterdam, Boston

Thermal Distribution on Gas Turbine Blade Using Thermal Paint

P. L. Rupesh and Arulprakasajothi

Abstract Thermal life of any hot surface depends on its surface temperature measurement. Turbines and combustors are the main components of a gas turbine system which are subjected to high thermal stress due to flow of combustible gases. Higher exposure of these components to the maximum temperature leads to thermal stress; hence, the measurement of temperature at different locations of these components is necessary. Measurement of temperature through thermal paints is the latest development in the field of surface temperature detection. The present study deals with the design, fabrication and surface temperature evaluation of gas turbine blades. The colour change observed at different locations of blades corresponds to different temperature. A computational analysis of these blades has been performed. The observed experimental results hold in good agreement with the computational results.

Keywords Thermal images · Irreversible colour · Thermal stress

1 Introduction

Gas turbine is a power plant, which creates a lot of vitality for its size and weight. The gas turbine has discovered expanding administration in the previous 40 years in the power production. Its smallness, low weight and numerous fuel applications make it a characteristic power plant for seaward stages [1]. Today, there are gas turbines, which run on petroleum gas, diesel fuel, naphtha, methane and biomass gas. Gas turbine motor progressed as a fundamental part and the most capable driving force unit for aircrafts. It is directly used in for all intents and purposes the whole of the voyager flying machines worldwide with different assortments [2].

P. L. Rupesh (✉) · Arulprakasajothi
Department of Mechanical Engineering, Vel Tech Rangarajan Dr. Sagunthala R&D Institute of Science and Technology, Chennai, Tamil Nadu 600062, India
e-mail: rupeshkumar221@gmail.com

Arulprakasajothi
e-mail: mapj08@gmail.com

N. Gascoin and E. Balasubramanian (eds.), *Innovative Design, Analysis and Development Practices in Aerospace and Automotive Engineering*, Lecture Notes in Mechanical Engineering, https://doi.org/10.1007/978-981-15-6619-6_11

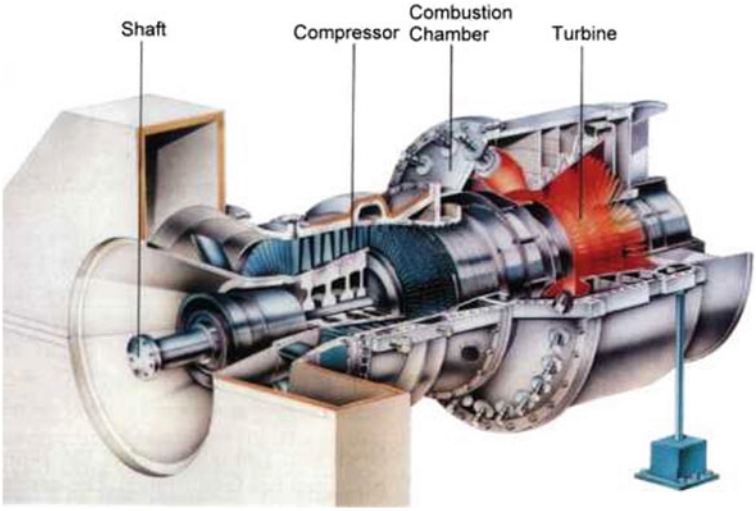

Fig. 1 Gas turbine components (*Courtesy* AutomationForum.Co)

The gas turbine engine works on the Brayton cycle, which starts with pressure, heat expansion and ends in extension. The admission air is packed in a blower and conveyed through the diffuser to the combustor, where fuel is infused and consumed to raise the gas temperature [1]. The hot high-pressure burning gases at that point grow through the pivoting turbines, where work is removed to create shaft power, propulsive push or the mix of these two. The development of gas turbine with its segments has been delineated in Fig. 1, and the working rule of gas turbine has been appeared in Fig. 2.

Work can be delivered from a gas at a greater intake pressure to bring down back weight by permitting it to course through a turbine. In a turbine as the gas goes through, it extends. The work done by the gas is equal to the difference in its enthalpy. Some portion of the vitality of the gas during extension is changed over into kinetic energy in the stream nozzles [1, 3]. The gas leaves these stationery spouts at a moderately higher speed, and afterwards it is made to encroach on the sharp edges over the turbine rotor or wheel. Energy granted to the cutting edges turn the wheel.

The vitality yield of gas turbine might be augmented through the ascent in turbine passage or intake temperature. Increment in turbine channel temperature from 1700 to 2200 K may prompt high warm proficiency and increment in power yield [4]. Increment in turbine section temperature additionally expands the warmth burden to the turbine edge. As an outcome, the turbine sharp edge material may experience warm worry as it surpasses the dissolving temperature of cutting edge material. Temperature mapping is basic for the well-being observing of gas turbine sharp edge.

Turbine sharp edges are one of the most significant parts in a gas turbine power plant. It is the mode of move of vitality from the gases to the turbine rotor. The sharp

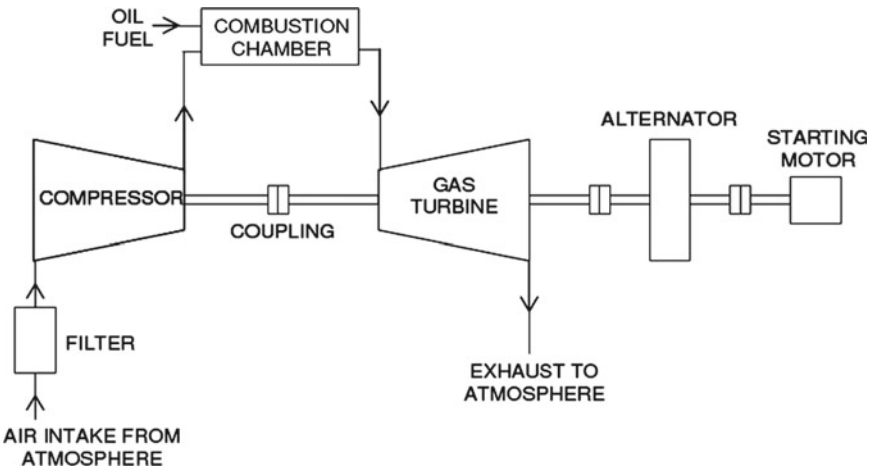

Fig. 2 Block diagram---gas turbine working

edge is exposed to countless forces, for example, rotor main thrust, hub power and so forth [1] notwithstanding these powers it is likewise exposed to differential warm anxieties which hamper cutting edge's smooth working. Sharp edge materials are additionally chosen depending on their security at high temperature. Steels, titanium combination and nickel-based compound are the most widely recognized materials utilized for the assembling of sharp edges.

Materials working under high pressure and high temperature have a specific scope of creep. Prolongation keeps on expanding with time and temperature and edges slowly decrease the first hole gave at their tips. Along these lines contacts with packaging bring about failure.

Temperature plays a vital role in the selection of materials for blades as the material should possess good strength at high temperatures and should have structural stability when exposed to varying temperature [1]. Definite information of the wall temperature is imperative to decide an ideal cooling wind current. Moreover, numerical reproductions are commonly applied for the improvement of gas turbines. To assess and improve the dependability of numerical forecasts, extensive informational collections are required in fact pertinent flares under raised weights with well-characterized limit conditions. A significant parameter in this regard is the temperature of the combustor wall. Expanding consideration has been attracted late years to warm misfortune to the restriction and the impact on fire adjustment [2].

In order to evaluate the thermal stress impressed on turbine blades (or) for the selection of materials for turbine blades such that they should withstand high temperature, the temperature contours of the turbine blade surface should be evaluated. This work concentrates on experimental evaluation of temperature contours for the turbine blades using thermal paints.

2 Thermal Paint

2.1 Significance of Thermal Paint

The most typically used methodology for testing gas turbine sections in mechanical application is the use of temperature demonstrating paints which grants overall mapping of allocation of zenith temperatures on the sharp edges of turbine and jars of combustor which keep up a key good ways from challenges looked with usually used electrical and electronic-based temperature indicating sensors. The undeniable shading changes are the outcome of engineered reactions that these one of a kind paint mixes involvement with explicit raised temperatures [5]. The essential interest of using thermal paints to show the scattering of temperature over a surface is the ability to get an overall temperature profile of the portion under evaluation, where thermocouples and other such systems can simply give point temperatures [6].

Application. These TIPs have discovered its one of a kind situation in the accompanying reasonable applications

- Usage of TIPs for combustor and turbine segments to realize the temperature profiles since late 1950s by Rolls-Royce;
- Testing of gas turbine and numerous air motors for the approval and affirmation of the motor and its part's plan;
- TIP assumes a significant job in warm mapping of segments during hypersonic flight tests.

Cameron [7] sketched out further that the adjustment in shade of a thermal paint is time-dependent and quick temperature increments in brief time allotments are not adequate to change the shading, however may actuate the synthetic response that causes the shading change. In this way, the study states that estimations will be helpful for transient reactions later on with further investigation. In this way, this undertaking intends to set up the test technique for examination of a chemical--colour relationship as a full compound investigation necessitates that the steady-state response be known before applying the strategy for a transient reaction. Mandavkar et al. [8] concentrated the well-being observing of gas turbine blades through centring the basic zone and problem area along the temperature circulation utilizing thermal paints. Mandavkar et al. [8] also observed that the temperature mapping for well-being observing of gas turbine is fundamental as current gas turbine exposed to exceptionally high temperature applications and gas turbines is utilized widely for airplane drive, land-based power age and modern applications. Improvements in turbine cooling innovation assume a basic job in expanding the thermal efficiency and power yield of advanced gas turbines. The work introduced by Lempereur et al. [9] demonstrates an image processing technique in which the value of RGB is converted into HLS and an exact estimation of temperature from shading is created by thermal paint TP96. Yang and Zhi-Min [10] have watched the temperature profile of the hot end segments through the judgment of shading change of thermal paint films. The

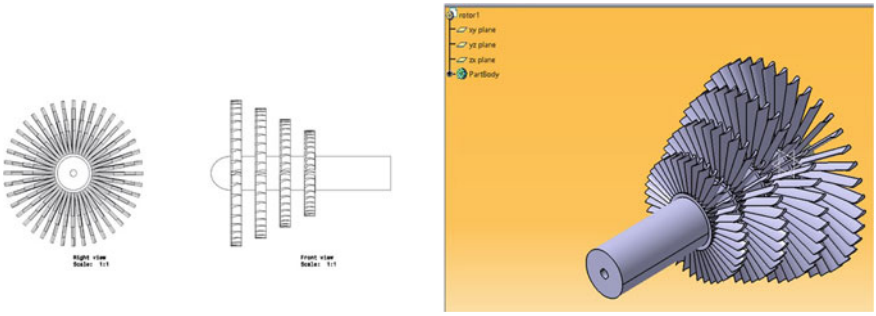

Fig. 3 2D and 3D model of turbine blades with rotor shaft

creator has made another thermal paint with an exceptional equation structure and has clarified the planning and painting process. Girish Prasad et al. [11] reveal that the blades are cooled with removed air from the blower of the motor. Since this extraction brings upon a punishment on the thermal efficiency and the power yield of the engine, it is essential to comprehend and advance the cooling innovation for a given turbine blade geometry under experimental conditions.

3 Design and Fabrication

3.1 Design of Blades

A runner shaft fixed with the turbine blades has been modelled and has been designed using Pro-E package. The 2D model and 3D model of the turbine blades with rotor shaft are shown in Fig. 3 and the same sketch which has been designed in 3D is shown in Fig. 3.

3.2 Blade Fabrication

In this research work, blades are manufactured using forging where a piece of metal is impacted to give it a certain shape. The material selected for the blade is steel. Steel blades are produced by coating with a thin layer of nickel and forging at 1100 °C. The nickel is necessary to prevent decarburization by the reducing atmosphere and to act as a lubricant [12]. The nickel layer is stripped off after forging. The blade is then heated to about 1050 °C to dissolve the hardening metals. The distortions are removed by cold coining operations. Then, the blade is rapidly cooled and tempered to give the required hardness [13]. The blades are then checked and polished by blasting or barrelling as shown in Fig. 4.

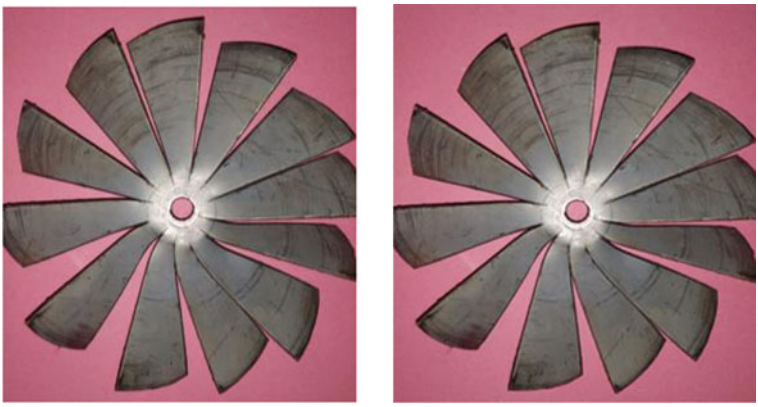

Fig. 4 Fabricated turbine blades

The cutting edges of a gas turbine are to be fitted cautiously to the plates [14, 15]. This is served by the edge root which is either welded or fixed to the circle circuit. The temperature consequences for the sharp edge and the plate ought not to cause extension because of high temperature and ought not prompt any detachment or disfigurement of the connection.

4 Experimentation

The experimentation has been carried out using the fabricated blades painted with the selected thermal paint and it is exposed to a constant heat source.

4.1 Selection of Thermal Paint

A multichange thermal paint MC 350-8 has been selected for the analysis of surface temperature. The initial colour of the paint is red and colour changes when the paint is exposed to temperature more than 3500 °C. The colour change of the paint at different elevated temperatures is shown in Fig. 5.

4.2 Painting of Blades

The fabricated blades shown in Fig. 4 have been sprayed with MC 350 as shown in Fig. 6. The initial colour of the paint is red. The painting of the blades is done by nozzle spray in order to maintain the thickness of the paint film within 0.5 μm (or)

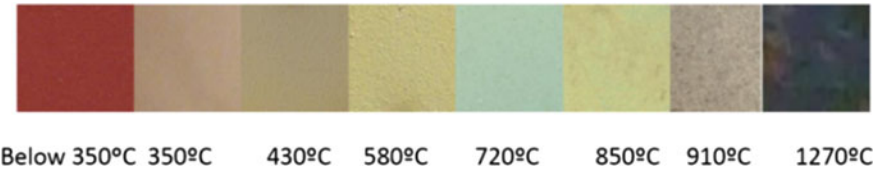

Fig. 5 MC 350-8 colour change

Fig. 6 Thermal paint sprayed blades

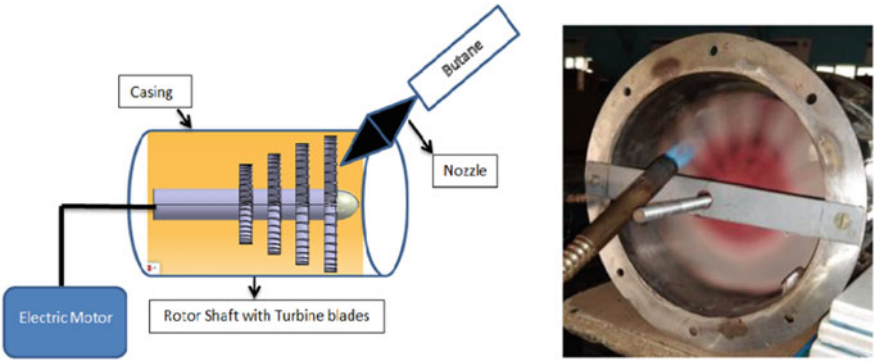

Fig. 7 Experimental set-up---block diagram

microns. The paint should not adhere to the surface firmly as the paint can be removed easily from the blade in order to repeat the experiments at different conditions.

4.3 Experimental Test Rig

The painted blades have been placed inside the shaft and the set-up is kept inside the casing. The shaft is connected to the electric motor in order to drive the shaft initially

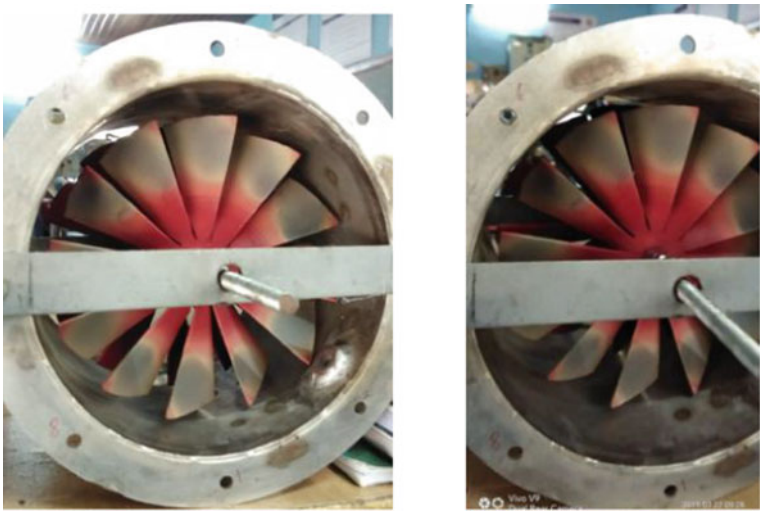

Fig. 8 Exposed turbine blades to high flame gas

and the turbine blades are rotated with a regulated speed of 15000 rpm. Butane gas is used as an fuel to produce high flame gas through a nozzle. The nozzle is placed in such a way that it is inclined at 45° to the tip of the blade. The whole experimental set-up as described above is shown in Fig. 8, and the exposure of blades to high flame is shown in Fig. 7.

5 Results and Discussion

5.1 Experimental Results

Employment of high-temperature gas in gas turbine requires materials which can withstand the effects of high temperature operation [16–18]. Further, high-temperature operations affect all the components in the engine with varying degree. On the off chance that a turbine sharp edge is warmed quickly to a high temperature it causes lopsided temperature circulation, and therefore, extreme warm anxieties are created inside the material. Beyond certain temperature (650–800 °C) the blade material does not remain elastic and continues to stretch under the applied forces and this is called as creep. If this phenomenon exists for a long time, fracture can occur.

The turbine blades fixed on the shaft is exposed to the high flame gas with temperature of 1400 °C. The colour of the blades changes with respect to time and as well as with temperature. The colour of the blade changes from root to end of the blade as depicted in Fig. 9. The colour of the blade changes from red to brown (blackish) from 10 mm from the root. The brown colour indicates temperature of 1100 °C. This

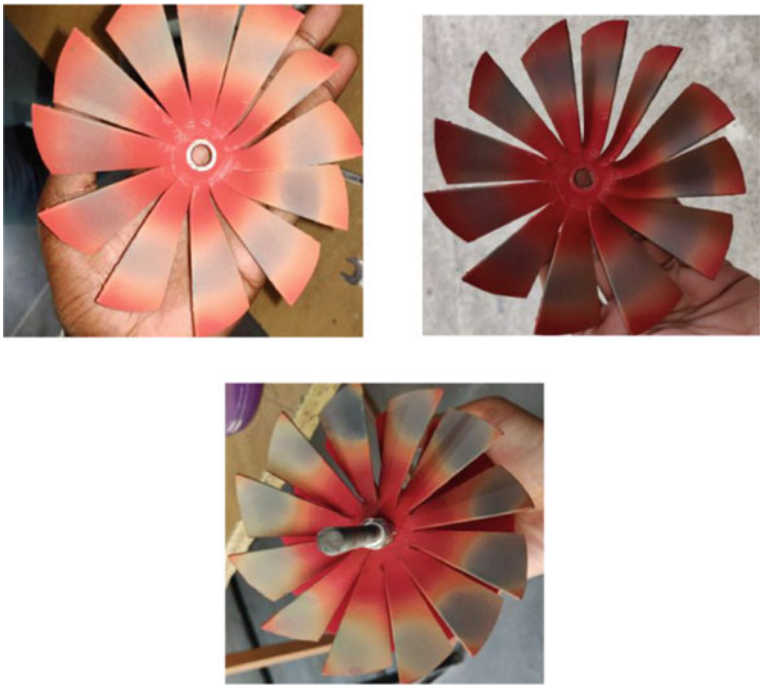

Fig. 9 Colour change of blades at different time interval

temperature is achieved after the exposure of blade to butane gas for 1 h (3600 s). The colour of the blade surface at the distance of 10 mm from the root has been changed at different time intervals. The change in surface temperature has been depicted experimentally through remarkable colour change.

The above graph shown in Fig. 10 indicates the change of temperature with respect to length of the blade. The temperature of the blade is changed from root to tip of the blade. The maximum temperature is recorded at the distance of 10 mm from the root.

The graph shown in Fig. 11 depicts the variation of temperature on the blade surface at different time interval. The initial time was taken as 900 s, and with the interval of 900 s, the experimentation has been done. The experimental results depict that the surface temperature at the distance of 10 mm from root of the blade has been increased linearly and it has reached 1100 °C from 800 °C.

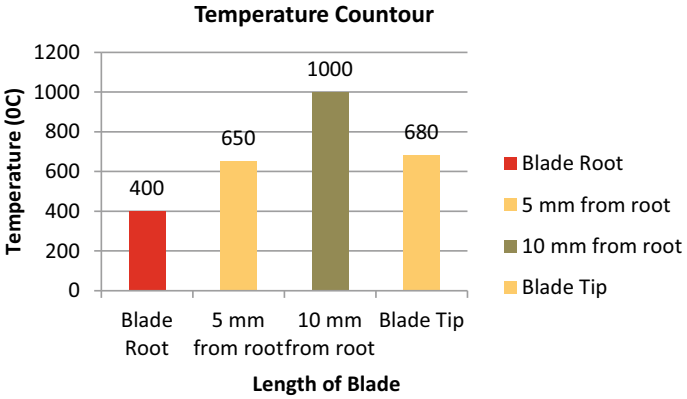

Fig. 10 Temperature versus blade length

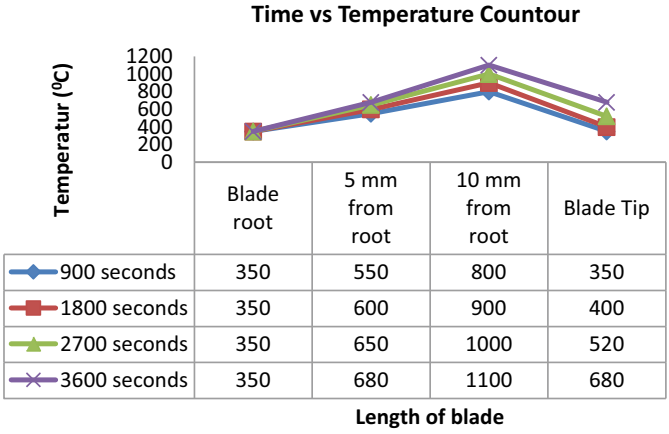

	Blade root	5 mm from root	10 mm from root	Blade Tip
900 seconds	350	550	800	350
1800 seconds	350	600	900	400
2700 seconds	350	650	1000	520
3600 seconds	350	680	1100	680

Fig. 11 Temperature versus time

5.2 Computational Results

A steady-state thermal analysis of a gas turbine blade has been done by using a software package ANSYS R16.2. The temperature contour on the blade surface is depicted in Fig. 12

The blade surface has been undergone convection (a mode of heat transfer) with the high flame gas of temperature 1200 °C and a steady-state thermal analysis has been performed. The results of temperature distribution over the blade surface have been depicted in Fig. 12. The above figure indicates that the tip of the blade attains maximum temperature of 1160 °C and the base of the blade attains 350 °C. The same analysis has been performed on series of blade of a rotor and the results have been

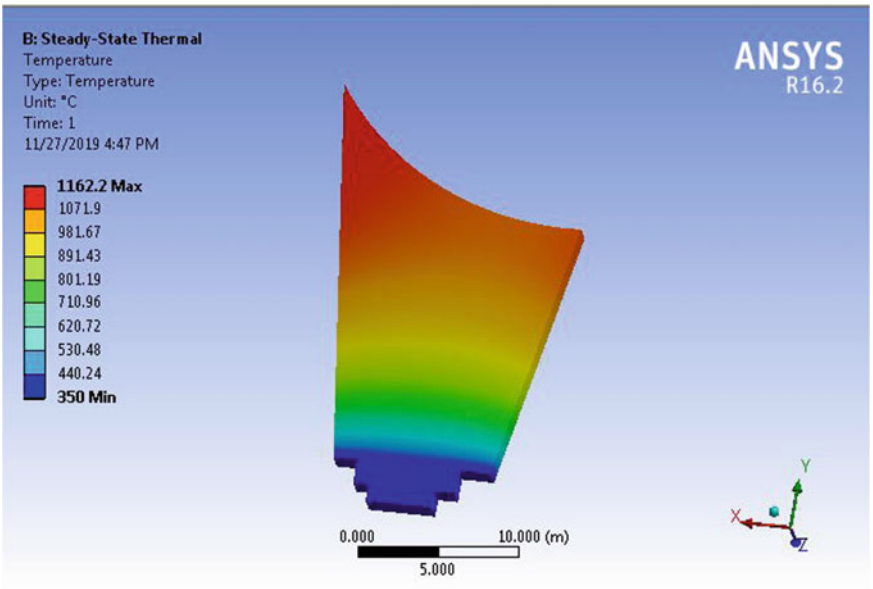

Fig. 12 Steady-state thermal analysis of a gas turbine blade

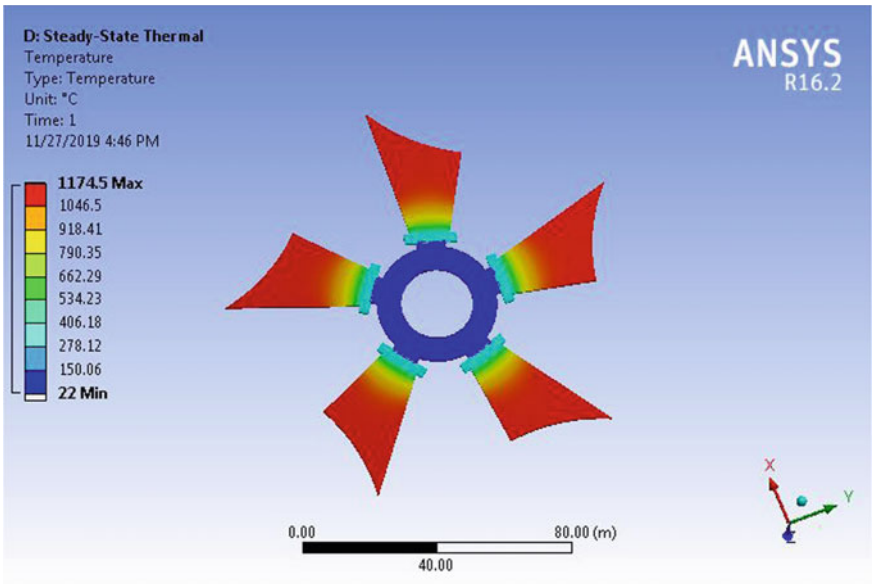

Fig. 13 Steady-state thermal analysis of a gas turbine rotor

depicted in Fig. 13. The results shown in Fig. 13 also show that the temperature has been increased from root to tip of the blade.

6 Conclusion

The above results shown in the present work shows that the thermal paint is a powerful technique for thermal mapping in geometry of a gas turbine blade. The experimental results obtained in the above study reveal that the temperature contour of a blade surface can be obtained experimentally. These results help in health monitoring of the blade and the selection of material for blade. The creep of the blade can be decreased based on the observation of peak temperature occurred due to irreversible change of colour in temperature indicating paint. The experimental results also hold in relation with the computational results.

References

1. Ganesan V (2003) Gas turbines, 2nd edn. Tata McGraw Hill Publication, New York
2. Nau P, Yin Z, Lammel O, Meier W (2018) Wall temperature measurements in gas turbine combustors with thermographic phosphors. J Eng Gas Turbines Power 141(4)
3. Saravanamuttoo HIH, Cohen H, Rogers GFC (2001) Gas turbine theory, 5th edn. Pearson Education Ltd, UK
4. Boyce MP (2002) Gas turbine engineering handbook, 2nd edn. Gulf Professional Publishing Company, Houston
5. Mark CP, Selwyn A (2016) Design and analysis of annular combustion chamber of a low bypass turbofan engine in a jet trainer aircraft. Propul Power Res 5(2):97–107
6. Rupesh PL, Prakasajothi MA, Chandrasekhar U, Mycherla R, Teja MB (2019) Study on temperature indicating paint for surface temperature measurement—a review. In: Innovative design, analysis and development practices in aerospace and automotive engineering (I-DAD 2018), Lecture notes in mechanical engineering
7. Cameron HE. Calibration for thermal paint chemistry. ZEIT 4500 aeronautical engineering project, thesis and practical experience. School of Engineering & Information Technology
8. Mandavkar PS, Sawane SM, Dongre DG (2008) Study of thermal mapping for health monitoring of gas turbine blade. Int J Res Sci Eng 1(2)
9. Lempereur C, Andral R, Prudhomme JY (2008) Surface temperature measurement on engine components by means of irreversible thermal coatings. Meas Sci Technol 19(10):105501
10. Yang L, Zhi-Min L (2015) The research of temperature indicating paints and its application in aero-engine temperature measurement. In: Asia-Pacific International Symposium on Aerospace Technology (APISAT2014). Procedia Eng 99:1152–1157
11. Girish Prasad M, Ravitej M, Shanmuga Priya (2016) Thermal analysis of aero gas turbine blade. Int J Mech Prod Eng 4(7). ISSN: 2320-2092
12. Gallardo JM, Rodriguez JA, Herrera EJ (2002) Failure of gas turbine blades. Wear 252(3–4):264–268
13. Naeem MT, Jazayeri SA, Rezamahdi N (2008) Failure analysis of gas turbine blades. In: Proceedings of the IAJC-IJME international conference
14. Munktell M (2008) Cooling of combustion chamber. Letebvre AH (1983) Gas turbine combustion. Chapter 8: heat transfer

15. Dedekind MO, Harris LE (1996) Evaluation of premature failure of a gas turbine component. Int J Press Vessel Pip 66(1–3):59–76
16. Chmielniak T, Lepszy S, Rulik S (2011) Algorithm for design calculation of axial flow gas turbine compressor-comparison with GTD-350 compressor design. Mech Mech Eng 15(3):207–216
17. Bhalerao SV, Pawar AN (2012) Thermal analysis of an aero-gas turbine compressor blade and vane using temperature sensing thermal paints. Int J Adv Sci Res Technol 2(2):286–292
18. Lee JJ, Dutton JC, Jacobi AM (2007) Application of temperature-sensitive paint for surface temperature measurement in heat transfer enhancement applications. J Mech Sci Technol 21:1253–1262

Development and Experimental Assessment of a Fluid Flow Monitoring System Using Flow Sensor and Arduino Interface

Sharad S. Mulik, Abhishek D. Patange, R. Jegadeeshwaran, Sujit S. Pardeshi, and Aditi Rahegaonkar

Abstract The flow monitoring has been a priority in fluid handling industry for controlling and regulating various parameters. Any change in flow dimension directly affects the output parameters in the domain of heat transfer, fluid mechanics, fluid power, etc. This may lead to huge economical and quality loss which is totally unbearable. The traditional fluid flow measurement methodologies are time consuming, bulky and affected by pressure, temperature, and viscosity with self-draining characteristics. It also requires appropriate observation followed by theoretical calculations. This motivates developing a flow management system incorporating integration of flow meters with the electronic control system. In the generation of open-source instrumentation, it is quite easy to implement such in-house built systems. This paper presents development of a fluid flow monitoring system using flow sensor YF-DN50 and Arduino interface. The algorithm is designed in ARDUINO IDE and is communicated to Microsoft Excel through PLX DAQ. The experimentation is carried out on centrifugal pump to measure the outlet discharge by conventional method and with use of developed system. The comparison of outlet discharge measured by both approaches has been plotted for calibration purpose. The advocated approach is efficient, reliable, inexpensive, and flexible particularly for academic research. Additionally, the system may perhaps be implemented in stand-alone special purpose industries and for laboratories at engineering institutes.

Keywords Fluid flow monitoring · Flow meter · Arduino · PLX DAQ · Centrifugal pump

S. S. Mulik
Rasiklal M. Dhariwal Sinhgad School of Engineering, Pune, India

A. D. Patange (✉) · S. S. Pardeshi · A. Rahegaonkar
College of Engineering Pune, Pune, India
e-mail: abhipatange93@gmail.com

R. Jegadeeshwaran
Vellore Institute of Technology, Chennai, Tamil Nadu 600127, India

N. Gascoin and E. Balasubramanian (eds.), *Innovative Design, Analysis and Development Practices in Aerospace and Automotive Engineering*, Lecture Notes in Mechanical Engineering, https://doi.org/10.1007/978-981-15-6619-6_12

1 Introduction

The flow monitoring is essential for assessing the movement of fluid. A lot of measurement techniques are used to monitor the flow. The positive displacement flow measurement technique is based on principle that it collects a fixed volume of fluid and measures time enquired. On the other hand, some flow measurement methods are based on forces generated by the flowing fluid as it conquers known constraints, to indirectly measure the flow. The flow can be monitored by measuring the velocity of fluid over a known area. For voluminous flows, the flow rate is calculated from the change in concentration of a dye or radioisotope [1–3]. The traditional instrumentation like flow meter, venturi meter, orifice plate, and Pitot tube are well known from decades. Advancement in the technology has adopted reforms in flow measurement too. The flow meters triggered by magnetic field are assembled with an electronic circuit. The impeller magnets of a positive displacement flow meter triggers the latched circuit in sensor, which in turn emits and sends a square wave pulse to a controller or any other monitoring devices [4]. Castaner et al. [5] used an economical hot wire flow meter where it does not get exposed by the flow but, however, due to the pins in the lead frame where thermic contact is provided. Ramyaa et al. [6] developed a system which measures the pipes of the hose fluids flow rate, and system made is also economical. The system comprises of PIC 16F877A microcontroller, detectors, fluid injectors, a power source, display, etc. This system can be used in the farm which will prevent it from damaging the crops and also it is easily accessible in the market and also economical than the other products. Sood et al. [7] designed water flow meter system which saves water as well as the energy while supplying water to the crops. In the system which consists of detectors called Hall effect sensor, the rotation varies with the flow of water. These detector measures output voltage which is relative to a magnetic strength of the input in the microcontroller. Hao and Garcia [8] developed a system which stored the kinetic energy in a capacitor from a fluid which can be used expeditiously. Cai and Toral [9] presented a research on measuring the individual phases in a hybrid network model where the fluid flow is in the horizontal direction pipelines by the network that are neural (KSOFM: The Kohonen self-organizing features map and MBPN: Multilayer back propagation network). These techniques are used to categorize it by variation of the fluids or the deviation of pressure values of various fluid flow regimes. Characteristics are retrieved from the variation and deviation of pressure values that are unique to the individual phase flow rates in multiphase flow. It is reviewed that the traditional fluid flow measurement methodologies are time consuming, bulky and affected by pressure, temperature, and viscosity with self-draining characteristics. It also requires appropriate observation followed by theoretical calculations. Also the modern techniques are based on costlier proprietary software-hardware tools [10–13]. This motivates developing a flow management system incorporating integration of low-cost flow sensor YF-DN50 with the electronic control system built using open-source instrumentation, i.e., Arduino, IDE, PLX DAQ. This system serves as

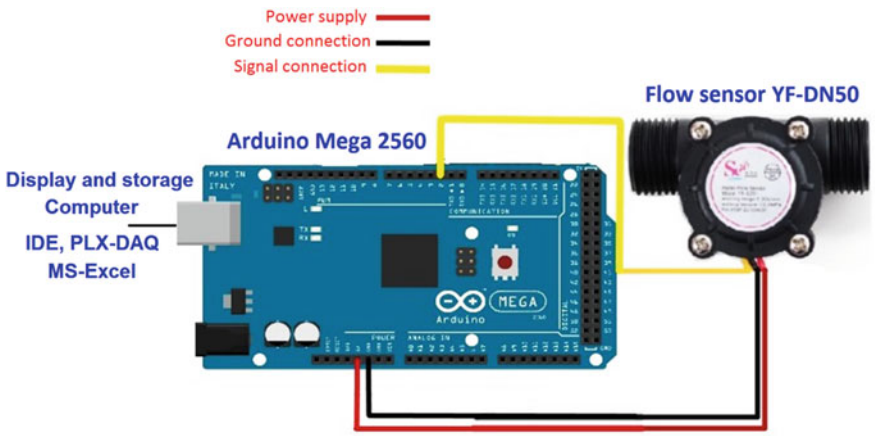

Fig. 1 System layout and mechatronic integration circuit

a data acquisition system to acquire, process, display, and store data which can be used further for analysis if any.

2 System Design, Mechatronic Integration, and Design of Algorithm

An innovative approach for development of a fluid flow monitoring system was formulated using YF-DN50 flow sensor and Arduino Mega 2560 microcontroller. The provision of integration of multichannels of flow sensors at a time can be made. The core flow sensor, i.e., YF-DN50, consists of turbine which is placed inside plastic envelope upon which a magnet is placed. As the turbine blades rotate, the fluid flows; hence, the magnetic fluctuation obstructs hall sensor, the degree of interference is being subjected to the velocity of flow, and therefore, the sensor emits pulse signal, which is used to estimate the water volume [14]. Arduino ATMega2560 has 16 analog inputs, 54 digital input/output pins, 16 MHz crystal oscillator, power supply cord, and USB connection. This system can be connected with the USB cable and further connected to a computer. Figure 1 shows system layout and circuit diagram. The algorithm was designed in Arduino IDE, and it is integrated with MS Excel through PLX DAQ. The flowchart of the algorithm is given in Fig. 2.

3 Experimentation and Testing

The objective of the experimentation is to evaluate the performance of developed fluid flow monitoring system and validating it with conventional experimental method.

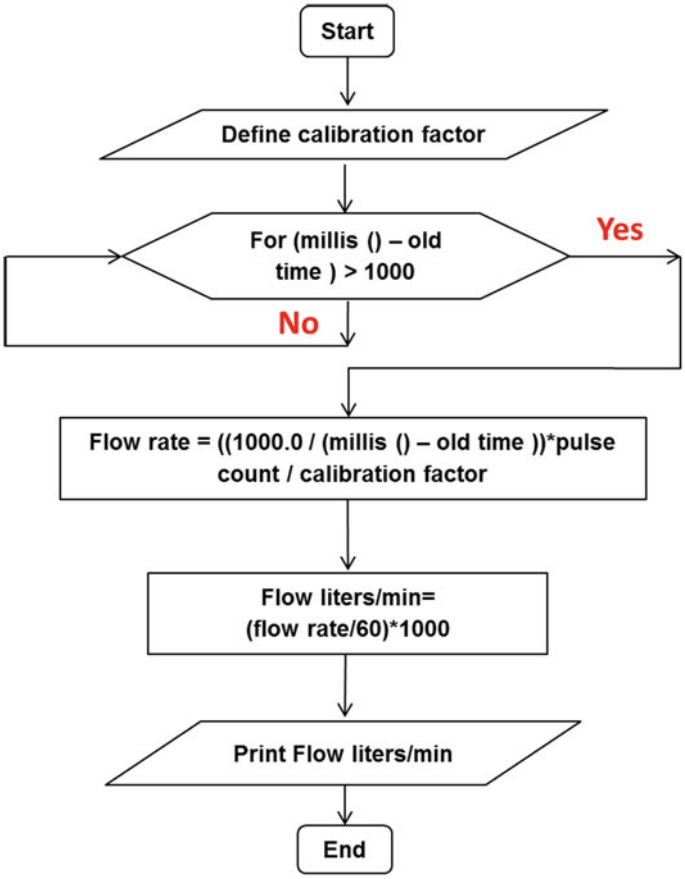

Fig. 2 Flowchart for algorithm

Experimentation is carried on a centrifugal pump (KCFM-302 centrifugal pump test rig) at various speeds. Suction and delivery pressures are measured using pressure gauge. The discharge time is recorded for 10 cm rise in water level in measuring tank. Then discharge was calculated using formula $Q =$ Volume collected/time required. Then, for same conditions, the discharge was measured using developed system. Figure 3 shows the experimental setup.

4 Results, Validation, and Discussion

Figure 4 represents the results displayed in MS Excel. The pump speed varied from 1600 to 3254 rpm. It shows variation in discharge w.r.t. change in pump speed. Outlet discharge varies linearly as pump speed increases. The head, output power, overall

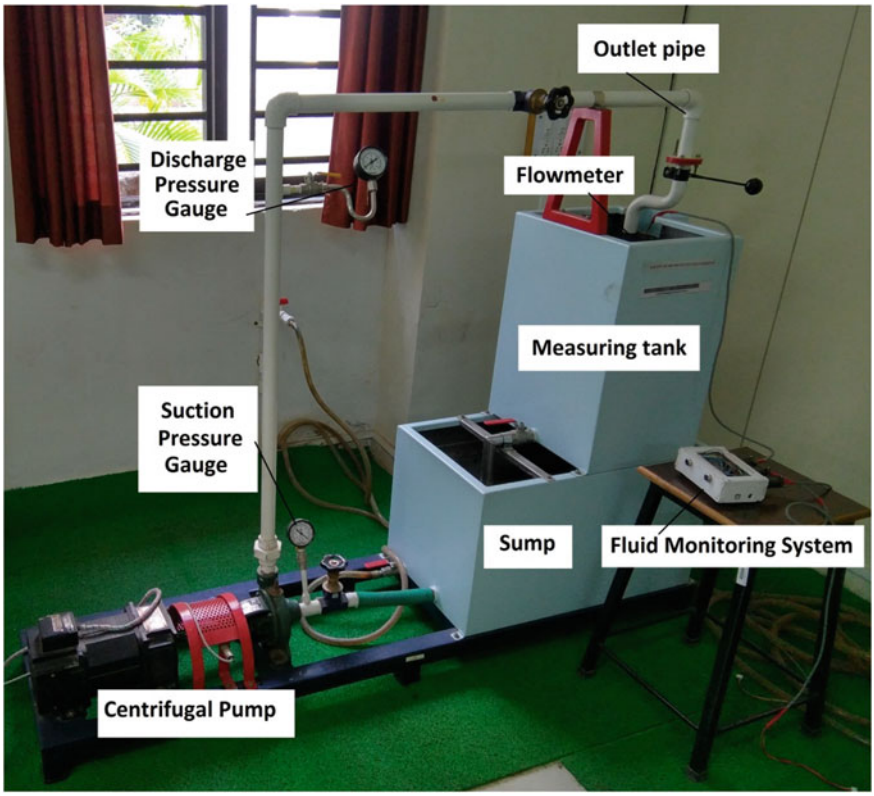

Fig. 3 Experimental setup

efficiency, and pump efficiency can be plotted. PLX DAQ software enables to read, store, and display results in MS Excel.

The graph in Fig. 5 shows comparison of discharge measured by both ways. Experimental method shows good agreement with discharge measured using developed system.

The pump characteristics plotted for the experimentation is carried out here. Figure 6 shows variation of head, output power, and efficiency with respect to discharge.

The developed system is more compatible as compared to the existing fluid flow measurement systems which are time consuming, bulky and affected by pressure, temperature, and viscosity with self-draining characteristics. The existing systems also require appropriate observation followed by theoretical calculations. Hence, the developed system incorporates flow management system integration of flow meters with the electronic control system. In the generation of open-source instrumentation, it is quite easy to implement such in-house built systems. The advocated approach is efficient, reliable, inexpensive, and flexible particularly for academic research.

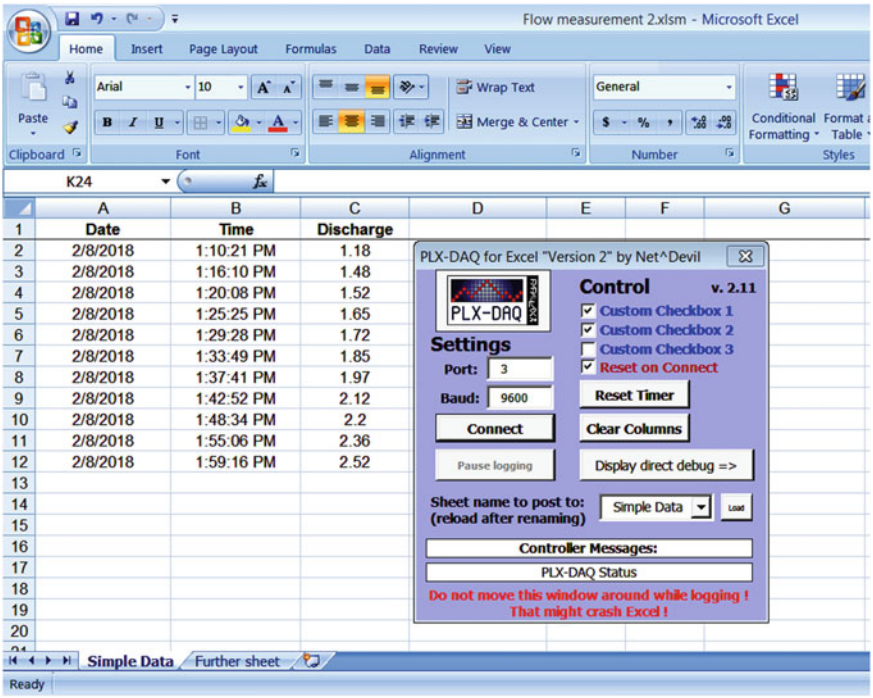

Fig. 4 Results on MS Excel using the developed system

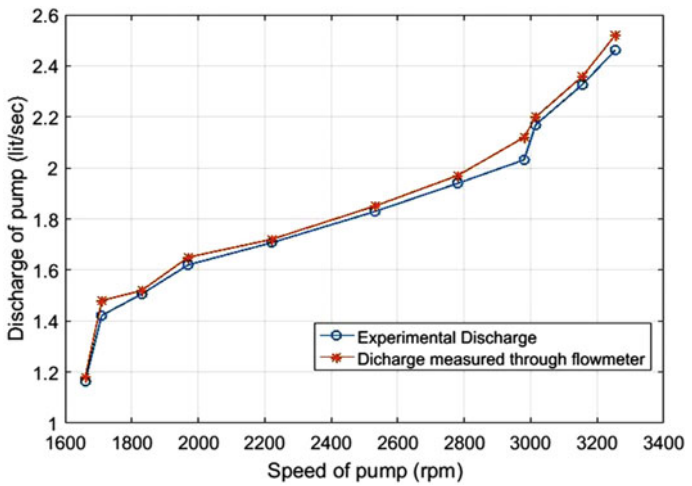

Fig. 5 Comparison of results RPM versus discharge

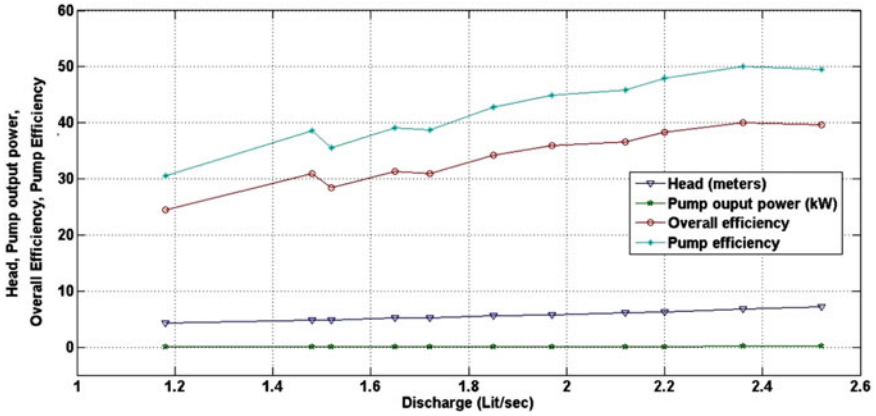

Fig. 6 Comparison of results RPM versus discharge

5 Conclusion

A novel fluid flow monitoring system incorporating integration of low-cost flow sensor YF-DN50 with the electronic control system built using open-source instrumentation, i.e., Arduino, IDE, PLX DAQ was developed. This system serves as a data acquisition system to acquire, process, display, and store data can be used further for analysis if any. The control system was designed to develop mechatronic interfacing of sensor and microcontroller. The algorithm was designed in ARDUINO IDE and is communicated to Microsoft Excel through PLX DAQ. The experimentation was carried out on centrifugal pump for monitoring and measuring outlet discharge by conventional method and with use of developed system. The comparison graph of outlet discharge measured by both the methods has been plotted and found to have good accuracy. The total price of prototype is near about Rs. 1000/- which is most affordable to all. The advocated approach is efficient, reliable, inexpensive, and flexible particularly for academic research. Additionally, the system may perhaps be implemented in stand-alone special purpose industries and for laboratories at engineering institutes.

References

1. Nakayama Y (1999) Introduction to fluid mechanics, 1st edn. Butterworth-Heinemann, An imprint of ELSEVIER, UK
2. James AF (1994) Introduction to fluid mechanics. MIT Press, Cambridge
3. Fox, Mcdonald (2011) Introduction to fluid mechanics, 8th edn. Wiley, Hoboken
4. Britton TC, Stewart RA, O'Halloran KR (2013) Smart metering: enabler for rapid and effective post meter leakage identification and water loss management. J Clean Prod 54:166–176
5. Castaner L, Jimenez V, Dominguez M, Masana F, Rodriguez A (1997) Design and fabrication of a low cost water flow meter. In: Solid state sensors and actuators. ISBN: 0-7803-3829-4

6. Ramyaa S, Alekhya D, Balachander (2016) Design and development of automatic water flow meter. Int J Adv Technol Innovative Res 08(04):0732–0735. ISSN: 2348-2370
7. Sood R, Kaur M, Lenka H (2013) Design and development of automatic water flow meter. Int J Comput Sci Eng Appl 3(3)
8. Hao WS, Garcia R (2014) Development of a digital and battery-free smart flowmeter. Energies 7:3695–3709
9. Cai S, Toral H (1993) Flowrate measurement in air-water horizontal pipeline by neural networks. In: Proceedings of international joint conference on neural networks, vol 2
10. Shewale MS, Mulik SS, Deshmukh SP, Patange AD (2018) A novel health monitoring system. In: Proceedings of 2nd international conference on data engineering and communication technology. Advances in intelligent systems and computing. Springer, Singapore, pp 461–468
11. Patange AD, Jegadeeshwaran R (2019) Milling cutter condition monitoring using machine learning approach. IOP Conf Ser Mater Sci Eng 624
12. Nalavade SP, Patange AD (2019) Development of 12 channel temperature acquisition system for heat exchanger using MAX6675 and arduino interface. Innovative design, analysis and development practices in aerospace and automotive engineering (I-DAD 2018). Lecture notes in mechanical engineering. Springer, Singapore. https://doi.org/10.1007/978-981-13-2697-4_13
13. Shewale MS, Razban A (2020) Characterization and system identification of XY flexural mechanism using double parallelogram manipulator for high precision scanning. In: ICCCE 2019. Lecture notes in electrical engineering. Springer, p 570. https://doi.org/10.1007/978-981-13-8715-9_47
14. Datasheet, YF-DN50 G2" inch water flow meter sensor flowmeter caudalimetr counter indicator water flow system gauge device, 10-200L-min/2114.10010108.1000013.4

A Study on the Performance and CO_2 Mitigation Potential of an Advanced Micro-gasifier Cookstoves for Sustainable Development

D. Sakthivadivel, P. Ganesh Kumar, G. Praveen Kumar, P. Raman, Ranko Goic, and S. Iniyan

Abstract Cooking is an essential part of life as food is indispensable for the persistence of human beings. Cooking of food requires heat energy and which can be met through electric cookstoves and LPG in developed countries. But the developing countries still depend on the combustion of biomass fuels such as wood, crop residues, dung cake, charcoal to meet up with their cooking and heating demands. The biomass is abundantly existing everywhere in the world and can be burnt directly in the cookstoves. Attention has been increased all over the globe in dipping the consumption of household energy and indoor air pollutants. Advanced micro-gasifier cookstoves (AMGCS) has been a topic of recent research, but still, 3 billion people cook over inefficient means of cookstoves though the number of initiatives has been taken by the government and non-government agencies to encourage the energy-efficient

D. Sakthivadivel (✉) · G. Praveen Kumar
School of Mechanical Engineering (SMEC), Vellore Institute of Technology, Vellore, Tamil Nadu, India
e-mail: sakthi2energy@gmail.com

G. Praveen Kumar
e-mail: praveen2energy@gmail.com

P. Ganesh Kumar · S. Iniyan
Department of Mechanical Engineering, Anna University, Chennai, Tamil Nadu, India
e-mail: selgan.cad@gmail.com

S. Iniyan
e-mail: iniyan777@hotmail.com

P. Raman
The Energy and Resources Institute, Darbari Seth Block, IHC Complex, Lodhi Road, New Delhi, India
e-mail: raman03@gmail.com

R. Goic
Faculty of Electrical Engineering, Mechanical Engineering and Naval Architecture, University of Split, Split, Croatia
e-mail: rgoic@fesb.hr

N. Gascoin and E. Balasubramanian (eds.), *Innovative Design, Analysis and Development Practices in Aerospace and Automotive Engineering*, Lecture Notes in Mechanical Engineering, https://doi.org/10.1007/978-981-15-6619-6_13

biomass cookstove. In this paper, an effort has been made to discuss the AMGCS with its recent advancements, performance, CO_2 mitigation and payback period.

Keywords Advanced cookstoves · CO_2 mitigation · Emissions · Economics

Nomenclature

LPG	Liquid Petroleum Gas
ASTM	American Society for Testing and Materials
IEC	International Electrotechnical Commission
BIS	Bureau of Indian Standards
SPP	Simple Payback Period
C_{ACS}	Investment cost of an AMGCS
C_{TCS}	Investment cost of a TCS
S_t	Saving in spending for fuel during period "t"

1 Introduction

Fossil fuels are considered to be a significant focus in meeting global energy demand after the industrial revolution. However, world fuel reserves are limited and their large-scale use is associated with environmental deterioration. Emission of pollutants such as carbon dioxide (CO_2) due to burning of the conventional fossil fuels are the major cause of global warming subsequently climate change. These facts have encouraged the use of renewable energy (RE) worldwide due to deteriorating fossil fuel reserves [1]. The various form of RE technologies based on Solar, Wind, Hydro power, Biomass and Geothermal are very clean and sustainable. Hence, it is necessary for the developing countries like India to move towards the use of RE resources. One form of chemical energy stored as hydrocarbon with presence of sunlight during photosynthesis process is known as biomass. The stored energy contains 50% of cellulose, 25% of hemicellulose and rest of the 25% is lignin with an average chemical composition of $CH_{1.4}O_{0.6}$, with minor deviations [2].

Cooking is one of the significant parts of life; food is being a basic need for human [3]. The people around the world use solid biomass fuels [4–6] for example wood, charcoal, crops and other agricultural residues, cow dung, shrubs/straw, etc. for cooking. More than 3 billion people on every corner of the world cook and warm their home using solid biomass fuels in an open three stone fires and poor efficient improved cookstoves (ICS). The above said people are economically weaker, and they live in poor (low income) and middle income countries. The cookstoves used by them create extreme level of health hazards by generating indoor air pollution (IAP)

which includes smaller size of soot particles or particulate matter (PM) that pearce deep into the lungs.

Bruce et al. [7] indicates the combustion of biomass over the period of a day increased indoor air pollution between 300 and 3000 $\mu g/m^3$. During cooking, in houses of Africa, Asia or Latin America, this may raise up to 10,000 $\mu g/m^3$ [7]. The report [7, 8] also says that more than 10 million children below the age of 5 die in an year due to indoor air pollution by biomass cooking. According to World Health Organization [9], 99% of them are from developing countries like India, South Africa and Brazil. World Bank states that 730 MT of biomass used for cooking in developing countries emit greater than a billion tonnes of CO_2 into the atmosphere. World Bank says each family needs approximately 2 tonnes of biomass fuel every year; [10] women and children spend great effort to collect firewood by going deep into forests, travelling more than 2 km every day as stated by Laximi et al. [11]. Women and children employ themselves up to 5–8 h every day to perform cooking actions, with 20% of the said time dedicated to the gathering of biomass fuel [12]. According to World Health Organization (WHO), burning of biomass indoors leads to poor eyesight. More than 2.5 million women become visionless [13] Chronic Obstructive Pulmonary Disorder (COPD) among women alone kills about 1.5 million worldwide.

In this present work, the performance and CO_2 mitigation potential study for an AMGCS have been conducted and compared with the traditional cookstoves (TCS) using different biomass fuels. Furthermore, a simple payback period was determined and explained for AMGCS.

2 Advanced Micro-gasifier Cookstoves (AMGCS)

AMGCS are well engineering designed, fabricated by acquiring with recent technologies and materials, cutting edge manufacturing techniques and universal standards such as ASTM, IEC, BIS, etc., for the whole systems to furnish higher efficiency, reduced emissions, self-produced electricity to power its system accessories such as air supply fan, battery charger, etc., and to fulfill the user needs in terms of power generation ad supply without compromising safety [10, 14–19]. These modern AMGCS have its own features like primary (gasification) and secondary (combustion) air by blowers or fan [19–21]. AMGCS also designed to produce electricity by extracting waste heat in the system using thermoelectric generators [22]. Even though the system efficiency is very high and emission of pollutants is low over TCS and ICS, still better way ahead to compete with LPG stoves [23, 24]. Gasifier-type AMGCS models include Oorja, Philips, TERI SPT-0610 and IES-18 cookstoves in India [18, 19, 25–27] shown in Fig. 1.

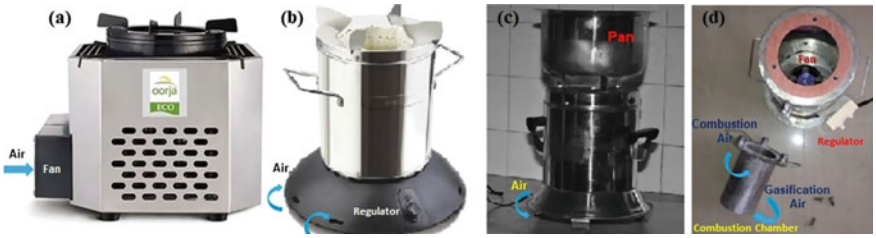

Fig. 1 AMGCSs. **a** OORJA plus. **b** PHILIPS and **c** TERI SPT-0610. **d** IES-18

3 Assessment of CO_2 Emissions Mitigation/Reduction Potential

The CO_2 emissions reduction potential using AMGCS for household cooking has been projected. The cost benefits of mitigating CO_2 emissions by the AMGCS also has been estimated. By utilising the data obtained by conducting the repeated experiments and the numerical evaluation presented in this study, the results of some typical workouts are projected and deliberated. The year around mitigation potential for CO_2 emissions using an AMGCS instead of a TCS can be evaluated using the following equation [28]:

$$\text{CO}_2 \text{ mitigation} = \left(\frac{365 \times E_{\text{th}}}{CV_{\text{fuel}}}\right) \times \left(\frac{1}{\eta_{\text{TCS}}} - \frac{1}{\eta_{\text{AMGCS}}}\right) \times C_{\text{i}} \times \left(\frac{\text{M}_{\text{CO}_2}}{\text{M}_{\text{C}}}\right) \quad (1)$$

The performance comparison of AMGCS and TCS using WBT 4.2.3, and the values of input parameters used to evaluate the CO_2 emissions mitigation potential of AMGCS is given in Fig. 2 and Table 1.

The performance comparison in terms of firepower (FP), fuel-burning rate (FBR) and specific fuel consumption (SFC) using WBT 4.2.3 of AMGCS and TCS are depicted in Fig. 2. The average per capita of the daily useful energy demand of the household is 520 kcal and the average daily useful energy consumption per household for basic cooking is approximately 12 MJ [21, 30]. The annual mitigation potential of CO_2 emissions for AMGCS has been calculated for different fuels ranging from 350 to 500 metric tonnes (MT) [19]. These values are comparatively good with the annual mitigation potential of CO_2 emissions of ICS is about 212.3 MT [28] and even better than TCS.

4 Economic Analysis

Payback period was the term used here, as the period of time needed for the AMGCS to recover the investment cost by self-produced heat or thermal energy. The maximum level of financial benefits can be anticipated, if the payback period is minimum. The

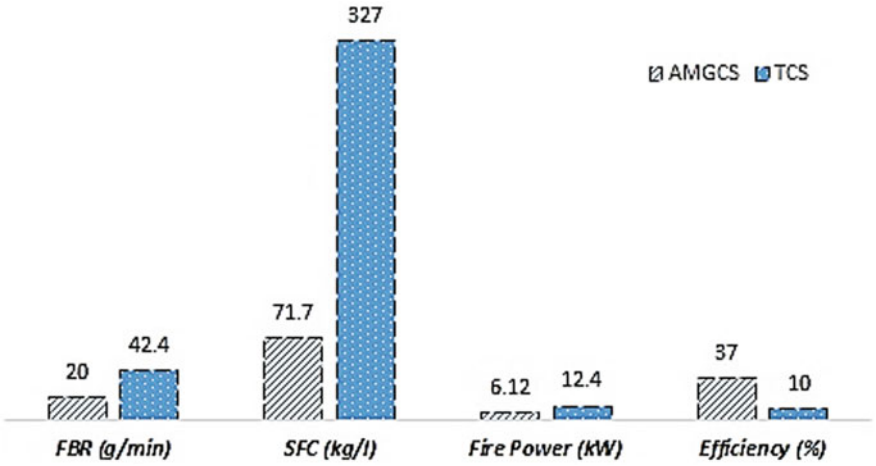

Fig. 2 Performance of the AMGCS [19] and TCS [32]

Table 1 The input parameters for estimating CO_2 emissions mitigation potential

Parameter	Character	Unit	Value
Thermal energy required for cooking	E_{th}	MJ/day	15
Capital cost of TCS stove	–	₹	400
Capital cost of ICS stove	–	₹	1000
Capital cost of AMGCS stove	–	₹	4500
Useful lifespan of AMGCS stove [29]	–	Years	5
Fraction of carbon in different biomass fuels	–	Fraction	45–55
Calorific value of fuels	CV_{fuel}	MJ/kg	15–20
Efficiency of TCS stove	η_{TCS}	Fraction	0.1
Efficiency of ICS stove	η_{ICS}	Fraction	0.16
Efficiency of AMGCS [19, 21, 22]	η_{AMGCS}	Fraction	0.36–0.38

below formula is taken to compute the payback period [31]:

$$\text{SPP} = \frac{(C_{\text{ACS}} - C_{\text{TCS}})}{S_t} \tag{2}$$

Cost analysis of the AMGCS developed in the laboratory was determined and comparison was made on the cost of energy generated by the conventional TCS. The payback period for different fuels used in AMGCS was found to be from 2 to 5 months for four-member family. Also, higher the annual working hours will results in lower the payback period.

5 Conclusions and Way Forward

The analysis of the performance comparison of AMGCS and TCS was carried out in terms of FBR, FP, SFC and efficiency using WBT 4.2.3. The annual CO_2 mitigation potential of AMGCS has been estimated at about 350–500 MT for different fuels and found these values are comparatively better than ICS and TCS. A simple payback period for different fuels was calculated between 2 and 5 months for four members family. Greenhouse gas mitigation, cost, robustness and cultural fit are mostly important in this regard are fulfilled by AMGCS.

Any technology extends the grassroots only when everyone is conscious of that particular concept and its implications. Hence, AMGCS system should be put to use in schools and college laboratories, for the creation of awareness of the technology among the people and should be disseminated to every household in rural areas. The financial support or government subsidies can be offered for scaling up the AMGCS and branding the technology as inexpensive. Direct user subsidy is desirable for ensuring the use of AMGCS and the sustainability of operations. Microfinance with repayment opportunities can help to make this technology affordable allowing further number of households and commercial cooking communities to move towards advanced smart cookstoves.

References

1. Kucuk MM, Demirbas A (1997) Biomass conversion processes. Energy Convers Manag 38(2):151–165
2. Mukunda HS (2011) Understanding clean energy and fuels from biomass. Wiley India, New Delhi
3. Prasanna UR (2010) Modeling, optimization and design of a solar thermal energy transport system for hybrid cooking application. Indian Institute of Science
4. WHO (2017) Household air pollution and health. Available from: http://www.who.int/mediacentre/factsheets/fs292/en/
5. User guide for India's 2047 energy calculator cooking sector 2013. India Energy. Available from: http://www.indiaenergy.gov.in/docs/Cooking.pdf. Accessed on: 30 July 2017
6. Bhattacharya SC (2015) Wood energy in India: status and prospects. Energy 85:310–316
7. Bruce N, Perez-Padilla R, Albalak R (2000) Special theme—environment and health. Bull World Health Organ 78(9):1078–1092
8. Arbex MA, Martins LC, de Oliveira RC, Pereira LAM, Arbex FF, Cancado JED (2007) Air pollution from biomass burning and asthma hospital admissions in a sugarcane plantation area, Brazil. J Epidemiol Commun Health 61(5):395–400
9. WHO (2006) Fuel for life: household energy and health 23. Available from: http://www.who.int/indoorair/publications/fuelforlife.pdf. Accessed on: 30 July 2017
10. The World Bank (2011) Household cookstoves, environment, health, and climate change, a new look at an old problem. Washington, DC. Available from: http://cleancookstoves.org/resources_files/household-cookstoves.pdf
11. Laxmi V, Parikh J, Karmakar S, Dabrase P (2003) Household energy, women's hardship and health impacts in rural Rajasthan, India: need for sustainable energy solutions. Energy Sustain Dev 7(1):50–68

12. Varunkumar S (2012) Packed bed gasification-combustion in biomass based domestic stoves and combustion system. Indian Institute of Science
13. WHO (2009) Women and today's evidence tomorrow's agenda. World Health Organization. ISBN 9789241563857
14. Venkataraman C, Sagar AD, Habib G, Lam N, Smith KR (2010) The Indian national initiative for advanced biomass cookstoves: the benefits of clean combustion. Energy Sustain Dev 14:63–72
15. Sakthivadivel D, Vigneswaran VS, Iniyan S. Advanced self driven micro-gasifier cook stove. IN 7025/CHE/2015
16. Raman P, Murali J, Sakthivadivel D, Vigneswaran VS (2013) Evaluation of domestic cookstove technologies implemented across the world to identify possible options for clean and efficient cooking solutions. J Energy Chem Eng 1(1):15–26
17. Raman P, Murali J, Sakthivadivel D, Vigneswaran VS (2013) Performance evaluation of three types of forced draft cook stoves using fuel wood and coconut shell. Biomass Bioenergy 49:333–340
18. Sakthivadivel D, Balakumar A, Iniyan S (2017) Development of advanced cook stove with optimum air mixture using CFD. Asian J Res Soc Sci Humanit 7(2):384–392
19. Sakthivadivel D (2018) Performance enhancement of an advanced micro-gasifier cookstove. Anna University, Chennai, p 277
20. Sakthivadivel D, Iniyan S (2019) Computational modeling and performance evaluation of an advanced micro-gasifier cookstove with optimum air injection. Biofuels. https://doi.org/10.1080/17597269.2019.1573606
21. Sakthivadivel D, Iniyan S (2018) Experimental design and 4E (Energy, Exergy, Emission and Economical) analysis of a fixed bed advanced micro-gasifier stove. Environ Prog Sustain Energy 37(6):2139–2147
22. Sakthivadivel D, Manikandan S, Kumaraselvan R, Ganesh Kumar P, Iniyan S (2019) Energy and exergy analysis of an advanced cookstove-based annular thermoelectric cogeneration system [Online First]. IntechOpen. http://doi.org/10.5772/intechopen.84237
23. Sakthivadivel D, Iniyan S (2017) Combustion characteristics of biomass fuels in a fixed bed micro-gasifier cook stove. J Mech Sci Technol 31(2):995–1002
24. Sakthivadivel D, Iniyan S (2018) Characterization, density and size effects of fuels in an advanced micro-gasifier stove. Biofuels 31(2):995–1002
25. Mukunda HS, Dasappa S, Paul PJ, Rajan NKS, Yagnaraman M, Ravikumar D (2010) Gasifier stoves—science, technology and field outreach. Curr Sci 98:627–638
26. Mukhopadhyay R, Sambandam S, Pillarisetti A, Jack D, Mukhopadhyay K, Balakrishnan K (2012) Cooking practices, air quality, and the acceptability of advanced cookstoves in Haryana, India: an exploratory study to inform large-scale interventions. Glob Health Action 5:19016
27. Jetter J, Zhao Y, Smith KR, Khan B, Yelverton T, DeCarlo P (2012) Pollutant emissions and energy efficiency under controlled conditions for household biomass cookstoves and implications for metrics useful in setting international test standards. Environ Sci Technol 46:10827–10834
28. Purohit P, Kumar A, Kandpal TC (2002) Renewable energy technologies for domestic cooking in India: estimation of CO_2 emissions mitigation potential. Int J Ambient Energy 23(3):127–135
29. Rapp VH, Caubel JJ, Wilson DL, Gadgil AJ (2016) Reducing ultrafine particle emissions using air injection in wood burning cookstoves. Environ Sci Technol 50:8368–8374
30. ABE (1985) Towards a perspective on energy demand and supply in India in 2004/05. Advisory Board on Energy (ABE), Government of lndia
31. Sakthivadivel D, Ganesh Kumar P, Vigneswaran VS, Meikandan M, Iniyan S (2019) Performance study of an advanced micro-gasifier stove with coconut shell. Eur J Sustain Dev Res 3(4):em0101
32. Rasoulkhani M, Ebrahimi-Nik M, Abbaspour MH, Rohani FA (2018) Comparative evaluation of the performance of an improved biomass cook stove and the traditional stoves of Iran. Sustain Environ Res 28(6):438–443

Experimental and Numerical Investigation of Non-reacting Flow in Can Combustor for Microgas Turbine Engine

V. Kirubakaran and David S. Bhatt

Abstract Generally, microgas turbines are in the range of 30–200 kW. So, here it is proposed to develop a microgas turbine engine with a capacity of 3 kW which will have applications in unmanned aerial vehicle (UAV) and standalone power generation for domestic use. In this study, the behavior of non-reacting flow pattern inside a swirl stabilized can combustor is studied. Total pressure loss, which is an important performance parameter, is predicted numerically and compared with that from experiments. Good agreement is achieved between experimental and numerical results. The combustor total pressure drop was found to be negligible; in the range of 0.002–0.06% at an inlet velocity ranges from 1.7 to 10.19 m/s. Flow pattern indicates strong vortex formation due to secondary air entrainment inside the flame tube.

Keywords CFD · Can combustor · Total pressure loss

1 Introduction

The microgas turbines are more suitable for compact power generation; the engines are classified on power ranges less than 200 kW. It has advantages futures like high power density, fuel flexibility, low emission, less maintenance and operational costs [1–4]. In literature, more emphasis is given for the development of engines more than 30 kW. However, for domestic power generation and UAVs, small engines of capacity from 1 to 10 kW are needed. So, it is aimed to develop such an engine. At the outset, the focus is to develop a small can combustor for this type of engine. The development of microgas turbine combustor is a challenging task similar to large gas turbine combustor. The combustor is one of the important components which decide the

V. Kirubakaran · D. S. Bhatt (✉)
Department of Aeronautical Engineering, Vel Tech Rangarajan Dr. Sagunthala R&D Institute of Science and Technology, Chennai, Tamil Nadu 600062, India
e-mail: davidbhatt@gmail.com

V. Kirubakaran
e-mail: kirubakaranvijayakumar@gmail.com

N. Gascoin and E. Balasubramanian (eds.), *Innovative Design, Analysis and Development Practices in Aerospace and Automotive Engineering*, Lecture Notes in Mechanical Engineering, https://doi.org/10.1007/978-981-15-6619-6_14

overall performance of an engine. The flow field inside the combustor is very complex in nature because of its turbulent flow field. The gas turbine combustor has number of sub-components like diffuser, snout, swirler, flame tube and annulus. Because of this complex flow pattern inside the combustor, there is a need for detailed non-reacting flow analysis before dealing with reacting mixture for a better understanding of combustion physics. In literature, the non-reacting flow analysis in the gas turbine combustor was carried out by numerous researches [5–13]. Among this, a notable work has been carried by Anand et al., wherein detailed 3D flow has been simulated inside an annular combustor using a 20° sector for analysis. The k-ε RNG model was used to model turbulence. The total pressure loss of the combustor varied from 4.41 to 9.87% for a given set of input velocity 158.8–238.20 m/s. Most of the previous studies are on a large scale combustor employed in high power gas turbines. Using the same principles, a small swirl combustor of 3 kW thermal capacity is designed. In this present study, the focus is to investigate a cold flow analysis to study the flow pattern inside the newly designed small size can combustor and measure the pressure loss.

2 Combustor Geometry

An in-house designed can combustor includes diffuser, snout, swirler, flame tube and annulus. The conical diffuser with 24.2° divergence angle is used in the present study. The snout has a divergence angle of 24.8°; the axial swirler has 8 flat vanes inclined at an angle of 45°. The flame tube has 265 mm length and 46 mm diameter; it has primary zone having 88 number of 2 mm holes arranged in 4 rows, secondary zone having 60 number of 3 mm holes arranged in 4 rows and dilution zone having 24 number of 2 mm holes arranged in 3 rows. The outer annulus has 300 mm of length with 72 and 44 mm of inlet and outlet diameter. The overall thickness of can combustor is maintained as 2 mm thickness. The dimensional detail of can combustor is given in Fig. 1.

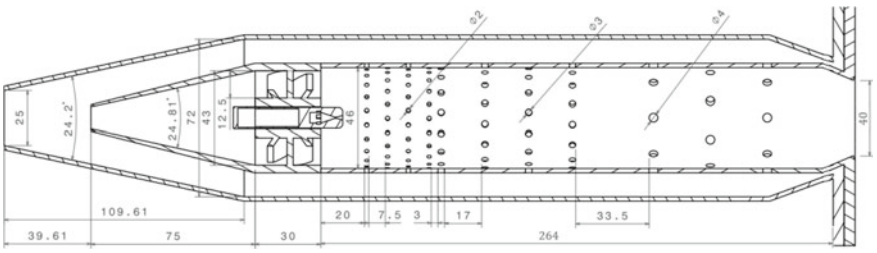

Fig. 1 Dimension details of can combustion chamber (all dimensions are in mm)

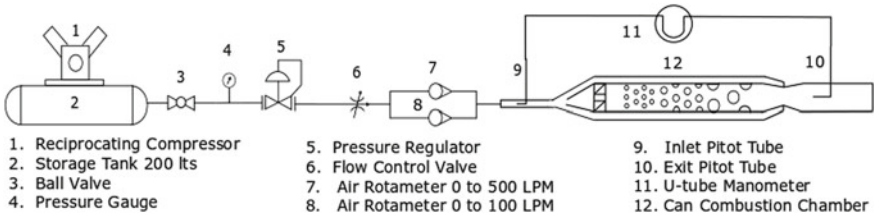

Fig. 2 Gas turbine combustor experimental setup

3 Experimental Study

The pressure loss across the combustor is measured using pitot tubes connected to a U-tube water column manometer (Fig. 2). The compressed air at 5 bar is passed through the combustor. The air mass flow rate is determined using rotameters.

4 Numerical Study

The numerical simulation is performed to predict the detailed flow field characteristics of the combustor. Here, the three-dimensional models of 90° sector are taken for analysis. The combustor flame tube wall thickness is assumed as zero, to minimize the complexness of the geometry. The turbulence modeling has been done using k-ε RNG model. The combustor inlet is specified as a velocity boundary. The outlet of the geometry is specified as a pressure outlet boundary. The inlet and outlet of snot, swirler, primary ports, secondary ports and dilution ports are specified as a interior. The sectional plane of the sector model is specified as a periodic boundary. The remaining faces of the combustor model are specified as a wall. The computational domain taken in the present study is given in Fig. 3.

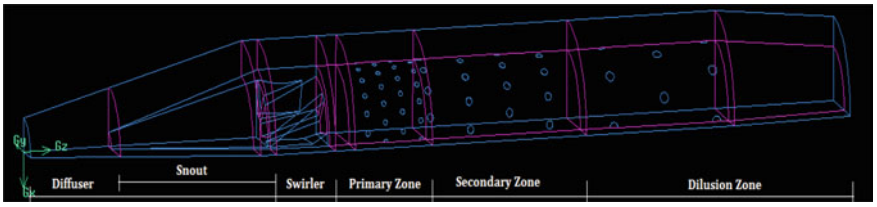

Fig. 3 90° sector can combustor computational domain

4.1 Grid-Independent Study

The unstructured grid has been employed due to the complexity of combustor geometry. The grid-independent study is carried out for four different grid sizes. The mass-weighted average of differential pressure is compared with Grid-D. The results were obtained numerically at 10.19 m/s inlet velocity. As can be seen from Table 1, almost similar results were obtained with the Grid-B and Grid-C. When grid size is increased further as in Grid-D, small difference is observed.

Alternately, the center line velocity across the combustor length for different grids (Fig. 4) is also considered. From the plot, it can be seen that the velocity profile matches closely for all grids considered. Hence, considering the optimality, Grid-B is adopted in the study.

5 Results and Discussion

The flow field inside an can combustor has been analyzed for a 90° sector model under non-reacting flow conditions. Expect flame tube wall thickness, the other blockages in geometry like snout wall, swirler wall, and fuel injector were included in this analysis. The performance characteristics of the combustor for non-reacting flow

Table 1 Grid study for four different grid sizes for 10.19 m/s inlet velocity case

Description	Grid type	Elements	Differential pressure [Pa]	Difference [%]
Grid-A	Tetrahedral	2,018,026	51.90	4
Grid-B	Tetrahedral	2,687,636	48.81	2
Grid-C	Tetrahedral	4,009,738	48.37	2
Grid-D	Tetrahedral	5,942,049	46.03	–

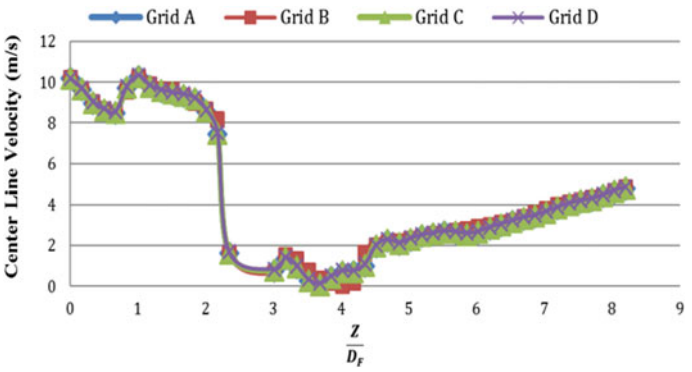

Fig. 4 Combustor center line velocity variation for 10.19 m/s inlet velocity

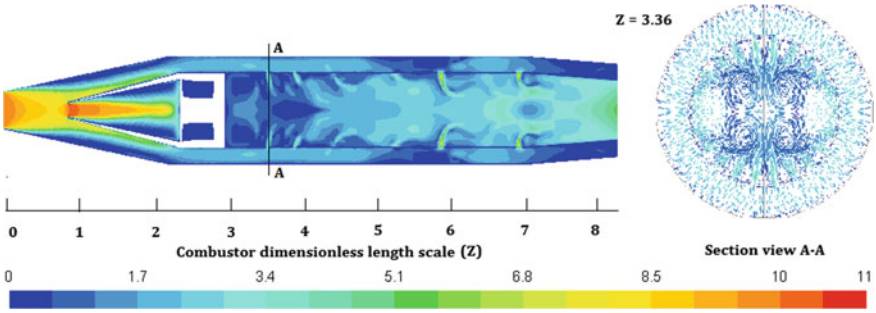

Fig. 5 Contour of velocity magnitude for inlet velocity of 10.19 m/s case

conditions with inlet velocity ranges from 1.7 to 10.19 m/s with corresponding to a Reynolds number of 2874–17,243 were evaluated.

5.1 Velocity Distribution Inside the Combustor

Figure 5 shows the reconstructed velocity contour along the length of the combustor on the symmetric plane of the 90° sector combustor. As the compressed air enters the diffuser, the flow decelerates due to area enlargement. Further, when the flow reaches the snout, the amount of air entering the snout accelerates and further decelerates due to area enlargement. Alternately, the secondary flow also decelerates due to constriction caused due to liner and blockage at the exit. When flow passes through swirler, a sudden decrease in axial velocity of the flow is seen (Fig. 4), because the swirler converts the axial component of velocity to radial and tangential components. The swirling flow helps the flame stabilize by creating a recirculation zone in the downstream. Past the swirler, the secondary air enters the combustion chamber via three zones: primary, secondary and dilution zone. The velocity of entrainment is so high that it creates a strong vortex as seen from the vector plot along the cross-section A-A at $z = 3.36$ (Fig. 5). This rotational flow would be useful in stabilizing the flame even at ultra-lean mixtures. Further downstream, as the entrainment from subsequent ports increases the net mass flow, which increases flow velocity.

5.2 Total Pressure Loss Along the Combustor

The total pressure loss across the combustor is calculated from the numerical simulation for 16 cases having velocities in the range of 1.7–10.19 m/s. These results are shown in Fig. 6 along with values obtained from the experimental study. It is seen that the pressure loss increases linearly with inlet mass flow from 0.002 to 0.06%

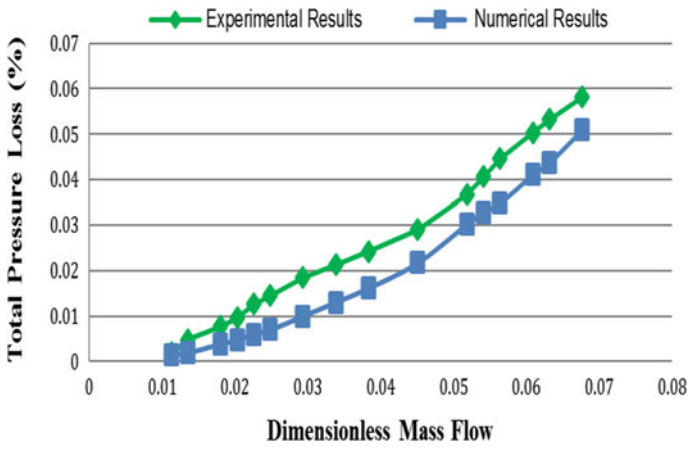

Fig. 6 Total pressure loss of combustor for various non-dimensional mass flow

as velocity is varied from 1.7 to 10.19 m/s. The good agreement found between experimental and numerical results.

6 Conclusions

The typical non-reacting flow inside the can combustor is studied experimentally as well as numerically. A swirler creates a strong recirculation zone due to the effect of radial pressure and the interaction of opposing primary jets. This would create a strong mixing of air and fuel and achieve a distributed flame region inside the combustor. The flame is also expected to be stabilized even at low equivalence ratio. The combustor total pressure drop was found to be negligible; in the range of 0.002–0.06% at an inlet velocity ranges from 1.7 to 10.19 m/s. As the inlet mass flow is increased, the total pressure loss across the combustor also increases.

References

1. Xiao G, Yang T, Liu H, Ni D, Ferrari ML, Li M, Luo Z, Cen K, Ni M (2017) Recuperators for micro gas turbines: a review. Appl Energy 197:83–99
2. Pilavachi PA (2014) Mini- and micro-gas turbines for combined heat and power. Appl Therm Eng 22(18)
3. Chiaramonti D, Rizzo AM, Spadi A, Prussi M, Riccio G, Martelli F (2013) Exhaust emissions from liquid fuel micro gas turbine fed with diesel oil, biodiesel and vegetable oil. Appl Energy 101:349–356
4. Malmquist A (2016) Modeling and simulation of an externally fired micro-gas turbine for standalone polygeneration application. J Eng Gas Turbines Power 138:1–15

5. Hall BF, Chana KS, Povey T (2013) Design of a non-reacting combustor simulator with swirl and temperature distortion with experimental validation. In: Proceedings of the ASME turbo expo: turbine technical conference and exposition. Volume 3C: heat transfer. San Antonio, Texas, USA. June 3–7, 2013. V03CT17A010. ASME
6. Gouda P, Srinivasan K, Sivaramakrishna G, Shashishekar KS (2016) CFD analysis of gas turbine combustor primary zone using different axial swirler configurations. Int J Mech Prod Eng 4(6)
7. Karuppannan S, Sondur VM, Sivaramakrishna G, Navindgi RD, Muthuveerappan N (2017) CFD analyses of combustor-diffuser system of marine gas turbine engine. In: Proceedings of the ASME gas turbine india conference. Volume 1: compressors, fans and pumps; turbines; heat transfer; combustion, fuels and emissions. Bangalore, India. V001T04A013. ASME
8. Crocker DS, Nickolaus D, Smith CE (1999) CFD modeling of a gas turbine combustor from compressor exit to turbine inlet. ASME J Eng Gas Turbines Power 121(1), 89–95
9. Ananda Reddy G, Ganesan V (2004) Non-reacting flow analysis from combustor inlet to outlet using computational fluid dynamics code. Defence Sci J 54(4), 455–467
10. Dzida M, Kosowski K (2015) Experimental investigations of pressure drop in the combustion chamber of gas turbine. ASME. Turbo expo: power for land, sea, and air. Volume 3: coal, biomass and alternative fuels; combustion and fuels; oil and gas applications. V003T06A001
11. Knight MA, Walker RB (1957) The component pressure losses in combustion chambers. Aeronautical Research Council R and M 2987, UK
12. Zhou D, Wang T (1998) Cold flow computations for the diffuser-combustor section of an industrial gas turbine. ASME 96-GT-513, Presented at the international gas turbine and aero engine congress and exhibition, Birmingham, UK
13. Lefebvre AH, Ballal DR (2010) Gas turbine combustion

Effect of Number of Inlet Tangential Ports and Their Angle on Spray Characteristics of Plug Type Swirl Injector

Sri Nithya Mahottamananda, D. N. Dilli Babu, and P. N. Kadiresh

Abstract Fuel atomization is a critical process. Swirl injector is used in gas turbine combustion chamber, rocket thrust chamber and hybrid rocket motor, etc., because of its efficient atomization process. This paper focuses on an experimental study on spray characteristics of plug type swirl injector using three injector configurations namely SW1, SW2, and SW3. The objective of the study is to analyze the spray characteristics like liquid sheet break up length, spray cone angle, discharge coefficient, and volumetric flow of plug type swirl injector for three chosen configurations. The injection pressure got varied from 1 to 2 bars and water was used as working fluid. The experimental data shows that for all injection pressures, SW1 configuration gives 43–49% lesser breakup length, 39–51% higher spray cone angle, lesser discharge coefficient, and 1–6% lesser volume flow rate compared to SW3 injector. It is also observed that SW1 configuration gives 7–11% lesser breakup length, 1–3% higher spray cone angle, 1–2% lesser discharge coefficient, and 3–6% lesser volume flow rate compared to SW2 configuration. The observed results of lesser breakup length and spray cone angle make the plug type swirl injector of SW1 configuration best suited for the short combustor.

Keywords Plug type swirl injector · Swirl cone angle · Break up length · Number of inlet tangential port effect · Inlet port tangential angle effect

Nomenclature

L_b Liquid sheet break up length
L Break up length of liquid sheet along streamwise direction

S. N. Mahottamananda (✉) · D. N. Dilli Babu · P. N. Kadiresh
Department
of Aerospace Engineering, B.S. Abdur Rahman Crescent Institute of Science & Technology, Chennai, India
e-mail: mahottamananda@gmail.com

N. Gascoin and E. Balasubramanian (eds.), *Innovative Design, Analysis and Development Practices in Aerospace and Automotive Engineering*, Lecture Notes in Mechanical Engineering, https://doi.org/10.1007/978-981-15-6619-6_15

θ Spray cone angle
C_d Discharge coefficient
m Mass flow rate of water
d_0 Outer diameter of the plug type swirl nozzle exit
$\mathrm{d_i}$ Inner diameter of the plug type swirl nozzle exit
ρ_f Density of working fluid
ΔP Pressure drop across the injector

1 Introduction

Swirl injector atomization process is a critical performance parameter of gas turbine combustion chamber as well as various liquid and hybrid rocket combustion chambers. The advantage of using swirl injectors is the reduction of boundary layer thickness of combustion chamber walls and increasing the stay time of the injecting fluid, leading to good mixing and efficient combustion [1]. The atomization process of swirl injector is evaluated by various parameters namely liquid sheet break up length, spray cone angle, discharge coefficient, and volumetric flow of injector. Over the years, many experimental and numerical studies were carried out on swirl injector. The number of inlet tangential ports has a direct effect on spray characteristics. Yule et al. [2] did experiments on spray characteristics of swirl injectors with different numbers of inlet tangential ports. They discovered that the injector with two inlet tangential ports reduces the droplet size than a single inlet injector with constant inlet area. Hamid [3]. done research on the effect of inlet slot number on spray cone angle. They found six inlet slot injector produces a higher spray cone angle compared with other injectors. Mat Rashid et al. [4]. carried out experimental work on the effect of inlet slot number on discharge coefficient and spray cone angle. They discovered that the effect of injection pressure on spray cone angle is more prominent at a lower range of injection pressure and higher number of inlet slots. The lesser number of inlet slots and higher injection pressure of inlet slots lead to less discharge coefficient.

Present experimental study focuses on the effect of number of inlet tangential ports and their port angle on spray characteristics like liquid sheet breakup length, spray cone angle, discharge coefficient, volumetric flow. Spray characteristics of swirl injector have a direct influence on combustion chamber design parameters like combustion chamber length and diameter. Three plug type swirl injector configurations are used namely SW1, SW2, and SW3. The comparison is made between SW1and SW2 as well as SW1 and SW3, to evaluate the effect of number of tangential port and tangential port angle on spray characteristics.

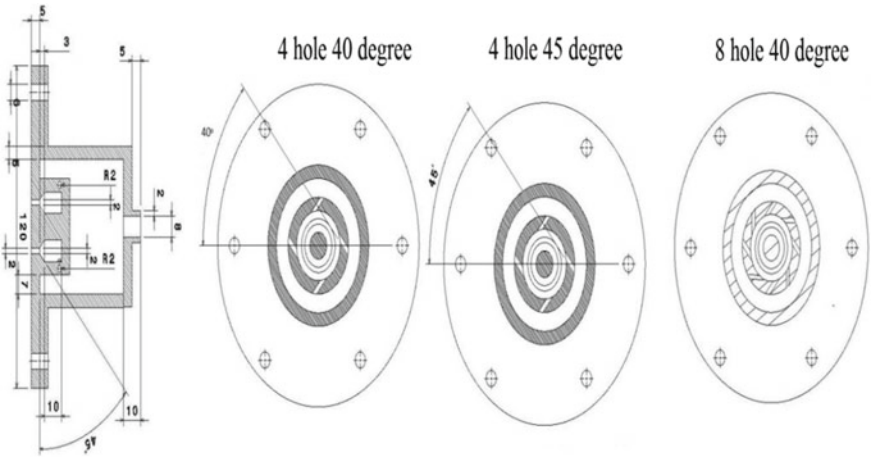

Fig. 1 Schematic geometry of three configurations of plug type swirl injector

Table 1 Plug type swirl injector geometrical specification

Swirl injector configuration type	Number of tangential port	Tangential port angle (°)
SW1	4	40
SW2	4	45
SW3	8	40

2 Experimentation

2.1 Plug Type Swirl Injector

The effect of swirl injector's geometrical parameters on spray characteristics is very important. Schematic of plug type swirl injector is given in Fig. 1. It consists of an injector plate and a reservoir chamber. The reservoir chamber is cup-shaped and all relevant dimensions are shown. It is attached with an injector flange of 120 mm PCD. Three injector plate configurations are fabricated. Tangential port of diameter 2 mm and liquid sheet thickness of 2 mm are maintained constant for all injectors. The details of three injector plate dimensional details are given in Table 1.

2.2 Swirl Injector Cold Flow Test Facility

The swirl injector test facility is shown in Fig. 2. It consists of a water reservoir tank, a piston pump (Inter Pump Model No FE 5108), and a swirl injector. A pressure regulator and rotameter are fitted to control the flow at pump outlet and to measure

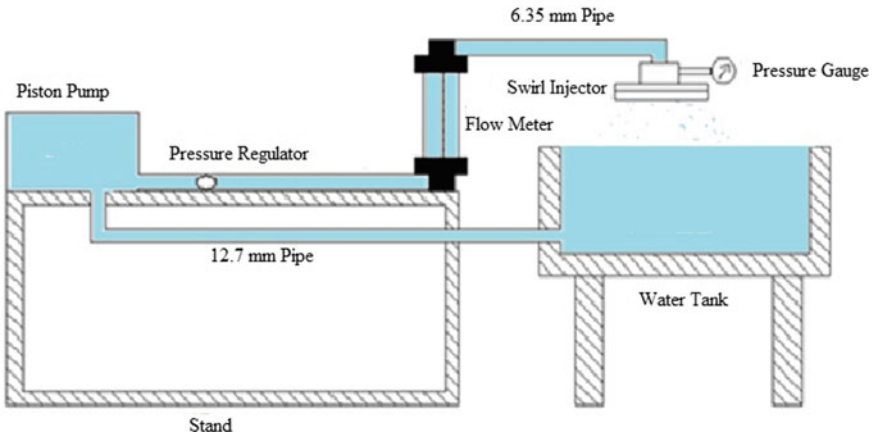

Fig. 2 Schematic of experimental setup for cold flow test

the mass flow, respectively. A pressure gauge (Baumer Technologies) with a range of 0–8 bar is fitted at the injector reservoir chamber to measure the injection pressure. Calibration of pressure regulators also been carried out.

2.3 Test Procedure

Figure 3 shows a schematic of the experimental setup. Swirl injector is fixed with 6.35 mm pipe vertically. The piston pump is switched on. Water gets pumped from tank to swirl injector. Pressure regulator supplies a set pressure flow and the corresponding mass flow is noted through the rotameter. The spray patterns are obtained

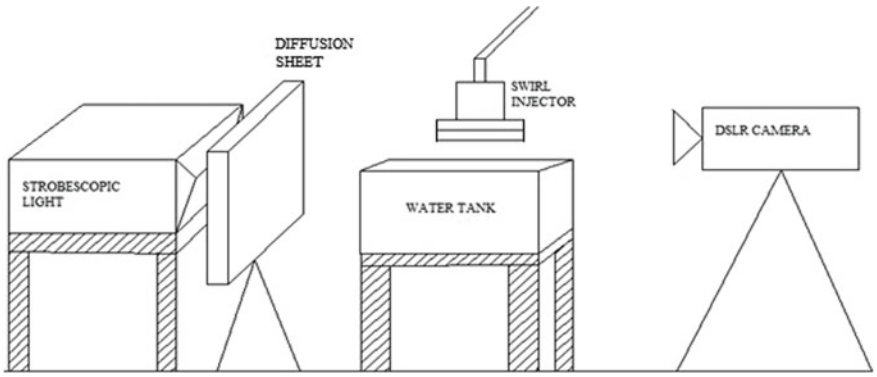

Fig. 3 A schematic of the experimental setup with diffused backlight system

by capturing images of liquid spray using photographic techniques. A Nikon D5100 digital camera with diffused backlighting system is used to take photographs of the spray. The pixel resolution of the camera is 4928 × 3264. A zoom lens (Nikon AF Zoom-NIKKOR 70–300 mm f/4–5.6G) is employed with the camera to capture good quality pictures of liquid sheet breakup. The measurements of spray cone angle, liquid sheet breakup length are obtained from the analysis of digital images using Image J software [5]. Photos of the liquid spray discharging from swirl injectors are shown in Fig. 4.

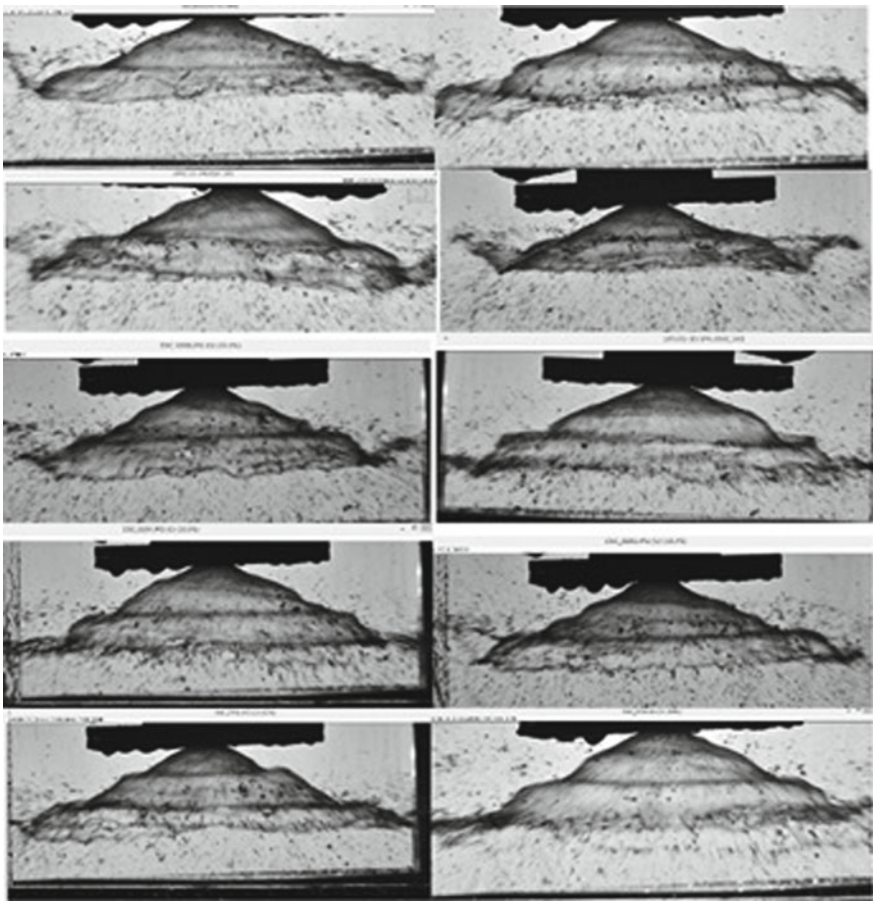

Fig. 4 Photos of the liquid spray discharging from SW2 injector configuration at a pressure of 1 bar

3 Results and Discussion

3.1 *Effect of Number of Inlet Tangential Ports and Their Angle on Liquid Sheet Breakup Length*

In a plug type swirl injector, unstable growth of sinuous waves on the surface of liquid sheet causes liquid sheet breakup. The breakup length of liquid sheet L_b is measured as the distance from the exit of injector to where the liquid sheet breaks up along the spray axis, illustrated in Fig. 5. For every injection pressure, more than 20 photos of the spray are taken at different runs and are used to calculate the average value of L_b.

The determination of breakup length L_b of plug type swirl injector liquid sheet in the axial direction is expressed as [6],

$$L_b = L\cos\left(\frac{\theta}{2}\right) \tag{1}$$

The effect of number of inlet tangential ports on breakup length L_b is presented in Fig. 6. The trend of decreasing breakup length with increasing pressure is observed. Higher injection pressure is resultant in higher axial velocity component. Higher resultant axial velocity component increases the tendency of earlier disintegration of the liquid film [7]. A decrease in liquid sheet breakup length L_b leads to a decrease in the length of the combustion chamber. It is also observed that for all injection pressures, SW1 injector configuration gave 43–49% lesser breakup length compared to SW3 injector configuration. The effect of inlet tangential port angle on liquid sheet breakup length is shown in Fig. 6. It is observed that for each injection pressure SW1 injector gave 7–11% lesser breakup length compared to SW2 injector configuration. This is because of SW2 injector is having higher tangential port angle compared to

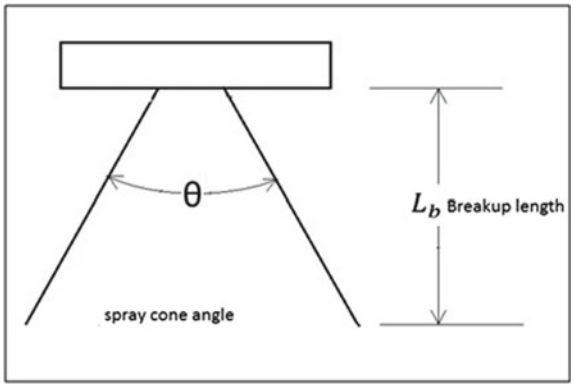

Fig. 5 Definitions of spray cone angle and breakup length

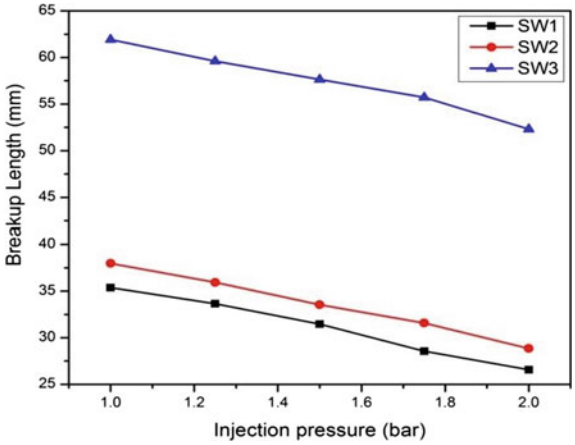

Fig. 6 Effect of number of inlet tangential ports and their angle on liquid sheet breakup length

SW1. Higher port angle present in SW2 injector leads to higher azimuthal velocity in swirl chamber resulting in higher breakup length.

3.2 Effect of Number of Inlet Tangential Port and Tangential Angle on Spray Cone Angle

The spray cone angle is another important parameter to account for the efficient atomization process. The effect of number of inlet tangential port on spray cone angle and injection pressure is presented in Fig. 7. The trend of increasing cone angle with increasing pressure is observed here. This observation matches well with literature findings by Datta et al. [8] and Halder et al. [9]. Moreover, with the increase in injection pressure, spray cone angle varies nearly linearly. This graph also represents that spray formation becomes broader with increasing injection pressure. It is also observed that for each injection pressure, SW3 injector configuration produced 39–51% lesser spray cone angle compared to SW1 injector configuration. The effect of inlet port tangential angle on spray cone angle is shown in Fig. 7. From this graph, it is observed that for each injection pressure, SW2 injector configuration formed 1–3% lesser spray cone angle compared to SW1 injector configuration. This is because more number of inlet ports produces higher azimuthal velocity in swirl chamber resulting in higher spray cone angle.

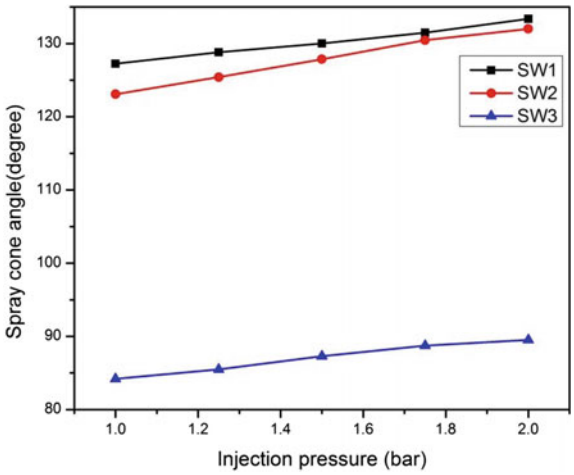

Fig. 7 Effect of number of inlet tangential ports and their angle on spray cone angle

3.3 Effect of Number of Inlet Tangential Port and Tangential Angle on Discharge Coefficient

The discharge behavior of the plug type swirl injector is quantified from the experimental measurements of mass flow rate of liquid and injector pressure drop ΔP across the injector. The discharge coefficient C_d of the injector is expressed as [6],

$$C_d = \frac{4m}{\pi\left(d_0^2 - d_i^2\right)\sqrt{2\rho_f \Delta P}} \tag{2}$$

The effect of number of inlet tangential ports on discharge coefficient is presented in Fig. 8. From the plot, it is observed that C_d value is initially higher and decreases for higher injection pressures. This study helps us in understanding the swirl strength effect inside the plug type injector. At low injection pressures, strength of the swirl controls the flow inside the plug type injector causing resistance to the total flow resulting in increased discharge coefficient. At higher injection pressures swirl strength will be decreased resulting in low discharge coefficient. And more friction in the plug type swirl injector is also causing a gradual decrease in the discharge coefficient at higher injection pressures. It is also observed that in SW1 injector configuration C_d changes from 0.1 to 0.6 and for SW3 injector configuration C_d changes from 0.11 to 0.13. This is because more inlet port configuration is having higher discharge coefficient compared to less no. of inlet port. The effect of tangential inlet port angle on discharge coefficient is shown in Fig. 8. It is observed that SW2 configuration produced 1–2% higher discharge coefficient compared to SW1 injector configuration.

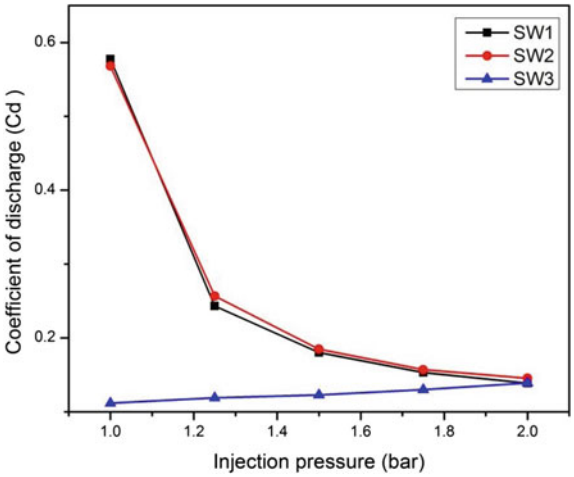

Fig. 8 Effect of number of inlet tangential ports and their angle on discharge coefficient

3.4 Effect of Number of Inlet Tangential Port and Tangential Port Angle on Volume Flow Rate

The effect of number of inlet tangential ports on volume flow rate is shown in Fig. 9. From this plot, an increase in volume flow rate with an increase in injection pressure is observed. The pressure difference between the atmospheric pressure and injection pressure may lead to this trend. Pressure difference is directly proportional to the volume flow rate for incompressible fluids. So any increase in the injection pressure,

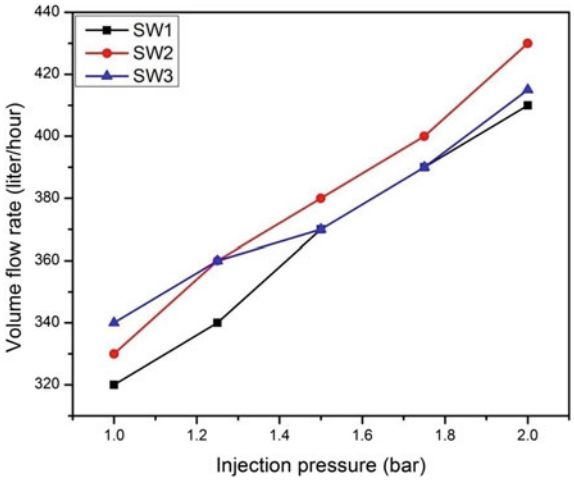

Fig. 9 Effect of number of inlet tangential ports and their angle on volume flow rate

the pressure variation between the atmospheric and injection pressure, also increases higher flow rate. It is also observed that for varying injection pressures SW3 injector configuration delivered 1–6% higher volume flow rate compared to SW1 injector configuration. The effect of tangential inlet port angle on volume flow rate is shown in Fig. 9. It is observed that SW2 injector delivered 3–6% higher volume flow rate compared to SW1 swirl injector configuration.

4 Conclusion

The spray characteristics of plug type swirl injectors configuration are experimentally analyzed and the effect of number of inlet tangential ports and tangential port angles on spray characteristics are studied. The summary of the findings is given below.

- It is observed that for all injection pressures, SW1 injector configuration produced 43–49% lesser breakup length compared to SW3 injector configuration.
- It is observed that for all injection pressures, SW1 injector configurations, produced 7–11% lesser breakup length compared to SW2 injector configuration.
- It is also observed that at all injection pressures, SW1 injector configuration formed 39–51% higher spray cone angle compared to SW3 injector configuration.
- It is observed that at all injection pressures, SW1 injector formed 1–3% higher spray cone angle compared to SW2 injector configuration.
- It is also observed that for SW1 injector configuration C_d varies from 0.1 to 0.6 and for SW3 injector configuration C_d varies from 0.11 to 0.13.
- It is observed that SW2 configuration gave 1–2% higher discharge coefficient compared to SW1 injector configuration.
- It is also observed that at all pressures, SW3 injector delivered 1–6% higher volume flow rate compared to SW1 injector configuration.
- It is observed that SW2 injector configuration delivered 3–6% higher volume flow rate compared to SW1 swirl injector configuration.

From the above results, it is concluded that SWI injector configuration gives lesser breakup length and spray cone angle compared to other configurations. These spray characteristics of SW1 injector configuration feature aids in a shorter combustor.

References

1. Mahottamananda SN, Rafnaz M, Kadiresh PN (2018) Spray characteristics of plug type swirl injector. In: Advances in science and engineering technology international conference. IEEE Conference Publication, pp 1–6. https://doi.org/10.1109/ICASET.2018.8376804
2. Yule AJ, Widger IR (1996) Swirl atomizers operating at high water pressure. Int J Mech Sci 38:981–999. https://doi.org/10.1016/0020-7403(95)00095-X
3. Hamid AHA (2011) Spray cone angle and air core diameter of hollow cone swirl rocket injector. IIUM Eng J 12. https://doi.org/10.31436/iiumej.v12i3.66

4. Rashid MSFM, Hamid AHA, Sheng OC, Ghaffar ZA (2012) Effect of inlet slot number on the spray cone angle and discharge coefficient of swirl atomizer. Procedia Eng 41:1781–1786. https://doi.org/10.1016/j.proeng.2012.07.383
5. Mahottamananda SN, Joshi PC (2016) Combustion study of HTPB–sugar hybrid fuel with gaseous oxygen. J Therm Anal Calorim 123(3):1927–1934
6. Sivakumar D, Vankeswaram SK, Sakthikumar R, Raghunandan BN (2015) Analysis on the atomization characteristics of aviation biofuel discharging from simplex swirl atomizer. Int J Multiph Flow 72:88–96. https://doi.org/10.1016/j.ijmultiphaseflow.2015.02.009
7. Hamid AHA, Atan R (2009) Spray characteristics of jet–swirl nozzles for thrust chamber injector. Aerosp Sci Technol 13:192–196. https://doi.org/10.1016/j.ast.2008.10.003
8. Datta A, Som SK (2000) Numerical prediction of air core diameter, coefficient of discharge and spray cone angle of a swirl spray pressure nozzle. https://doi.org/10.1016/s0142-727x(00)00003-5
9. Halder MR, Dash SK, Som SK (2004) A numerical and experimental investigation on the coefficients of discharge and the spray cone angle of a solid cone swirl nozzle. Exp Thermal Fluid Sci 4:297–305. https://doi.org/10.1016/S0894-1777(03)00110-9

Hybrid Incremental Forming: Investigation on Localized Thinning and Thickness Distribution in Formed Parts

Rahul Jagtap, Vikas Sisodia, Kiran More, and Shailendra Kumar

Abstract In the present experimental work, hybrid incremental sheet forming (HISF) process comprising stretch forming followed by single point incremental sheet forming (SPIF) is developed for forming conical frustum. Experimental investigation is done to find the influence of process parameters on thickness distribution and localized thinning in the formed parts. Experimental result reveals that stretching has a substantial effect on localized thinning in formed parts. Small improvement in the thickness distribution and localized thinning is found in formed parts. Experimental investigation on the influence of preform tool shape is also done to further improve thickness distribution. It is observed that the geometry of preform tool and amount of stretching has a great influence on thinning and thickness distribution. It is found that intermediate preform tool size and small amount of preforming results in forming conical frustum having uniform thickness distribution. Also, a considerable reduction in forming time using developed HISF process is observed as compared to SPIF process alone.

Keywords Hybrid incremental sheet forming · Stretch forming · Single point incremental forming · Thickness distribution · Localized thinning

R. Jagtap (✉)
School of Mechanical Engineering, MIT World Peace University, Pune 411038, India
e-mail: rkjagtap20@gmail.com

V. Sisodia · K. More · S. Kumar
Department of Mechanical Engineering, Sardar Vallabhbhai National Institute of Technology, Surat, Gujarat 395007, India
e-mail: vikas.singh619@gmail.com

S. Kumar
e-mail: skbudhwar@med.svnit.ac.in

N. Gascoin and E. Balasubramanian (eds.), *Innovative Design, Analysis and Development Practices in Aerospace and Automotive Engineering*, Lecture Notes in Mechanical Engineering, https://doi.org/10.1007/978-981-15-6619-6_16

1 Introduction

Incremental forming (ISF) process is a novel, flexible sheet metal forming process. It is also called as a die-less forming process because it does not require a dedicated die for forming sheet metal parts [1]. Virtually, any part shape can be formed using ISF process with minimum tooling setup, as parts using ISF are formed using a numerically controlled machine such as CNC milling machine or a numerically controlled robot arm [2]. It has a short setup time as well as lower production cost for producing small number of different part shapes [3]. It offers many advantages over conventional sheet metal forming method such as improved material formability, small forming forces, die-less forming, short changeover time from one part shape to other and design changes are quickly and easily carried out [4]. ISF has already been used to form a variety of parts such as aircraft cowling [5], different aerospace components [6], human prosthesis reconstruction [7], cranial implant [8], knee joint [9], solar cooker [10], and car exterior skin part [11].

Despite its advantages over conventional sheet metal forming process, ISF is not popular in industries due to its key shortcomings such as low geometric precision, uneven thickness along walls of formed component, localized thinning and long forming time. Many researchers such as Ambrogio et al. [12] have studied and investigated the influence of parameters on thinning, formability and surface quality. Some researchers used techniques such as tool path optimization [13], use of secondary support [14], use of closed-loop control systems [15] and different tool geometries [16] etc. to improve the geometric accuracy of formed parts. Researchers such as Störkle et al. [17] also used robots instead of using CNC machined for forming. The current ISF process development does not meet the quality of parts which is acceptable in industries. Hence, some researchers [18, 19] studied and developed a combined ISF process with some allied process called a HSIF process to improve the quality of incrementally formed parts. As HISF process is in its early development stage, only a few researchers such as Araghi et al. [19], Lu et al. [5] and Shamsari et al. [20] have applied research efforts to study the HISF process comprising SPIF combined with stretch forming process. It has reported by Araghi et al. [16], Lu et al. [5], and Kumar and Kumar [21] that the HISF process is capable of improving forming time, thickness distribution and thinning as compared to SPIF process. Hence, there is stern need to apply more research efforts to develop a reliable HISF process which can produce sound parts with uniform thickness distribution and reduced thinning in short forming cycles.

The present study aims to develop HISF process comprising preforming and SPIF process. Material flow in ISF and stretch forming are completely different, hence it can be used to improve the thickness distribution and reduce thinning in formed parts. Further, stretch forming is considerably faster than SPIF process, hence total forming time can be reduced using SPIF and stretch forming. Figure 1 illustrates the schematic representation of the proposed hybrid forming process. A simple and low-cost tooling setup is developed for forming conical frustums using proposed HISF process. The objectives of the present experimental investigation are as follows:

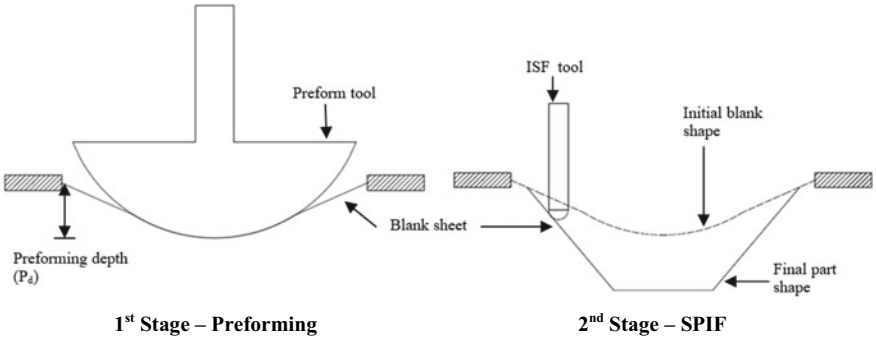

Fig. 1 Schematic representation of proposed HISF process

1. Development of HISF process for forming conical frustum of wall angle 50°.
2. Investigation on the effect of different parameters on sheet thinning and thickness distribution in the formed part.
3. Investigation on the preform tool shape to improve thickness distribution along the formed surface.

2 Materials and Methodology

2.1 Experimental Setup

All the experiments were performed on a 3 axis CNC milling machine (Batliboi DART). A modular fixture is fabricated for holding the blank sheet on the work table. Backing plate is provided to support to blank sheet and avoid further undesired bending during the forming process. The blank sheet in the present HISF process is aluminium Al 1050. Al 1050 is pure aluminium alloy which is well known for its high ductility and excellent corrosion resistance. The blank sheet is cut in rectangular sections of 200 mm × 300 mm from a 1.24 mm thick sheet metal stock. The

Table 1 Mechanical properties of blank sheet

Material property	Unit	Value
Density	kg/m^3	2700
Young's modulus	GPa	63.45
Ultimate tensile stress	MPa	146.144
% Elongation	–	5.8
Strain hardening exponent	–	0.301
Strength coefficient	MPa	133.64

mechanical properties of blank sheet (Table 1) are measured using uniaxial tensile testing method according to ASTM standards (ASTM M8).

2.2 Design of Forming Tools

Preform tool of hemispherical shape having 50 mm radius is used for the stretching process and it is made of wood. SPIF tools are also hemispherical in shape and are made of high carbon high chromium (HCHCr) die steel. Figure 2a depicts the preform tool and Fig. 2b depicts the SPIF tools used for experimental work.

Three process parameters namely preforming depth (P_d), SPIF tool diameter (d) and pitch (P) are considered for experimental work. The process parameters and their levels as given in Table 2 are selected based on the literature review and available machine capabilities.

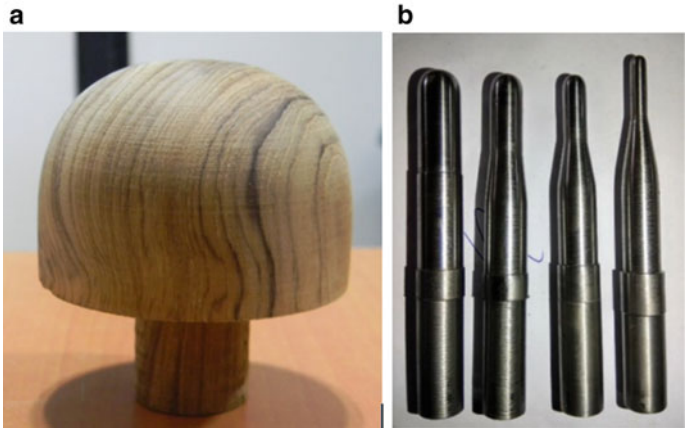

Fig. 2 **a** Wooden preforming tool. **b** SPIF tools

Table 2 Process parameters and their levels

Parameter	Unit	Actual values					Coded values				
Preforming depth (P_d)	mm	10	12	14	16	18	−2	−1	0	1	2
Tool diameter (d)	mm	4	6	8	10	12	−2	−1	0	1	2
Pitch (P)	mm	0.2	0.4	0.6	0.8	1	−2	−1	0	1	2

2.3 Experimental Plan

The experimental campaign in present work is planned using Taguchi's orthogonal arrays. Two sets of experiments are performed using Taguchi's L_{25} orthogonal array. Thickness along the formed surface is measured using Mitutoyo's digital point micrometre. Minimum thickness is used as response for statistical analysis.

3 Result and Discussion

The statistical tool analysis of variance (ANOVA) is used for the analysis of experimental results. Results are analysed using Minitab software at 95% confidence level. Table 3 is ANOVA table for minimum thickness ($T_{\min}$). ANOVA table decomposes the variability and significance of the process parameters. It is observed that preforming depth is significant process parameter affecting minimum thickness in formed parts.

3.1 Influence of Factors on Minimum Thickness (T_{min})

Figure 3a shows the main effects plot of thickness with respect to preforming depth. It is observed that increase in amount of preforming depth reduces the wall thickness ($T_{\min}$). As preforming is a plastic deformation process, it results in thickness reduction. Hence, increase in amount of preforming further reduces the wall thickness as depicted in Fig. 3a. In the second stage of HISF process, SPIF process forms the final part shape, which further reduces the thickness in formed part. Hence as amount of stretching increases, considerable reduction in wall thickness of formed part is observed. Figure 3b depicts the graph of preforming depth versus S/N ratio. It is observed from the graph that small preforming depth results in high S/N ratio ensuring better product quality (in this case improved thinning).

Table 3 ANOVA table for $T_{\min}$

Source	DF	Seq SS	Adj SS	Adj MS	F	P
Preforming depth (P_d)	4	0.020496	0.020496	0.005124	39.21	0.000
Pitch	4	0.001096	0.001096	0.000274	2.10	0.144
Tool diameter	4	0.000456	0.000456	0.000114	0.87	0.508
Residual error	12	0.001568	0.001568	0.000131		
Total	24	0.023616				

$R^2 = 0.934$; Adjusted $R^2 = 0.867$

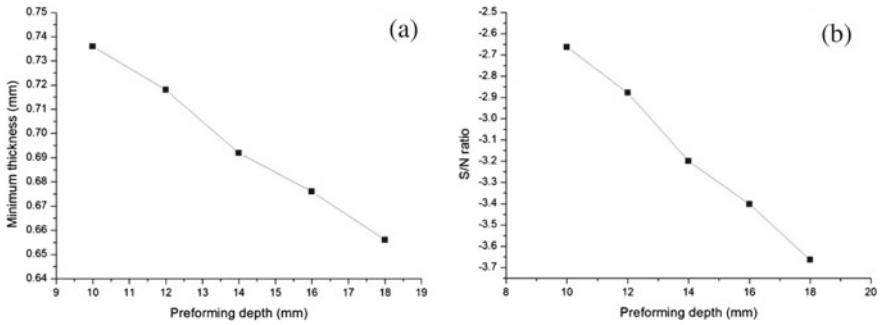

Fig. 3 **a** Preforming depth versus minimum thickness. **b** Preforming depth versus S/N ratio for $T_{\min}$

It is observed from Fig. 4 that thinning band appears near clamped edge in SPIF process as described by Young and Jeswiet [22]. It is seen in the thickness profiles of preformed sheet that preforming causes plastic deformation at the tool-sheet contact area and bending deformation surrounding the plastic deformation. Small amount of stretching results in small amount of plastic deformation. The deformation results in improvement in the thickness at thinning band as seen from thickness profiles of conical frustum. As the amount of stretching increases from 10 to 14 mm, considerable improvement in thickness reduction at thinning band is observed. But an increase in preforming depth leads to more thickness reduction near the apex of conical frustum. Further increase in preforming depth from 14 to 18 mm shows no signs of thinning band near clamped edge. Instead, large amount of thickness

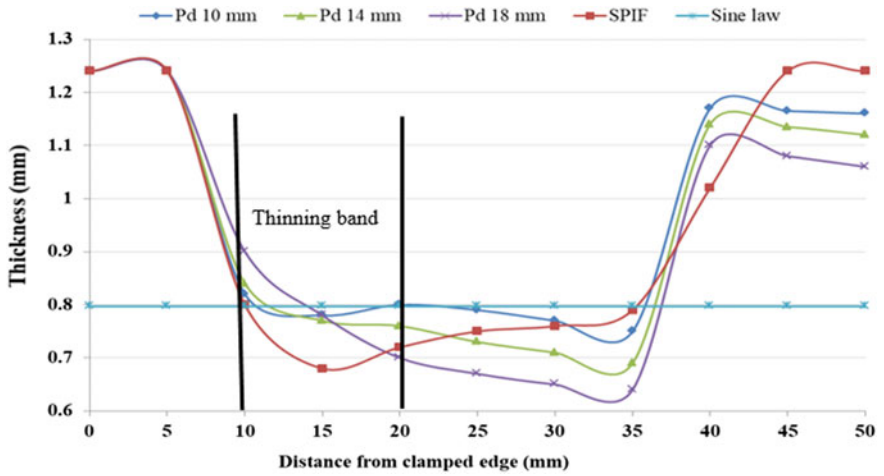

Fig. 4 Thickness profiles of conical frustum formed using SPIF and HISF process at different preforming depth

reduction as compared to thinning band is observed near apex of cone. Thickness reduction takes place according to hemispherical bulging as discussed in Sect. 2.2 and is identical to thickness distribution reported by Santos et al. [23]. Hence, minimum thickness reduction at thinning band and uniform thickness distribution along formed surface are obtained using 10 mm preforming depth.

3.2 Influence of Tool Shape on Thinning and Thickness Distribution

As discussed in the previous section that preforming using 10 mm stretching results in slight enhancement in the thickness distribution and thickness reduction at thinning band. The preforming process also accounts for the thickness reduction near the apex of conical frustum which leads to uneven thickness distribution. As the shape of preforming tool is hemispherical, thickness reduction in the first stage of preforming follows hemispherical bulging. According to the hemispherical bulging process, maximum thickness reduction takes place at the centre of hemispherical bulge as discussed in materials and methodology Sect. 2.1. Hence experimental investigation on the influence of preform tool shape is carried out to optimize the tool shape in order to improve thickness distribution and localized thinning. In previous experiments, preform tool having a radius of 50 mm is used. Hence, more tools are designed using preform tool radius as shape function as depicted in Fig. 5. Full factorial design of experiments (DoE) plan is used for planning the experimental campaign.

Experiments are carried out to rectify the influence of preform tool shape in terms of preform tool radius and stretching amount using full factorial design of experiments plan. Table 4 gives the process parameters and their levels.

Result of the full factorial experiments is analyzed using ANOVA at 95% confidence interval. The ANOVA table shows the variability of preform tool radius and preforming depth on thickness ($T_{\min}$). Table 5 is ANOVA table for minimum thickness using full factorial design of experiments plan.

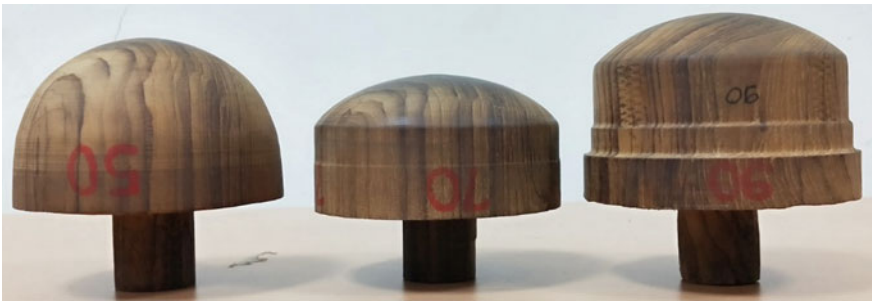

Fig. 5 Wooden preforming tools having radius of 50 mm, 70 mm and 90 mm respectively

Table 4 Process parameters and their levels for full factorial design

Parameters	Levels		
	−1	0	+1
Preform tool radius (P_r) (mm)	50	70	90
Preforming depth (P_d) (mm)	10	14	18

Table 5 ANOVA table for T_{min} using full factorial design of experiment plan

Source	DF	Seq SS	Adj SS	Adj MS	F	P
P_r	2	0.0014889	0.0014889	0.0007444	7.88	0.041
P_d	2	0.0029556	0.0029556	0.0014778	15.65	0.013
Residual Error	4	0.0003778	0.0003778	0.0000944		
Total	8	0.0048222				

R^2= 0.9217; Adjusted R^2= 0.8433

Preforming is a plastic deformation process. Hence increase in preforming or stretching results in increased plastic deformation and reduced thickness of blank sheet as discussed in Sect. 3.1. As preform tool radius increases, improvement in minimum thickness is observed as shown in Fig. 6. It is observed from the thickness profiles of preformed sheet and conical frustum that, while using preform tool radius of 50 mm, plastic deformation is localized and bending deformation is spread over a small area. Hence, slight improvement in the thickness reduction is observed in conical frustum along with more uniform thickness distribution as compared to SPIF process. It is observed that minimum thickness reduction along the formed surface is obtained at 10 mm preforming depth. It is observed that as the preform tool radius increases to 70 mm, the area of contact between tool and sheet increases. Therefore, more bending is observed near clamped edge where thinning band appears. Increased bending due to 70 mm preform tool radius causes improvement in minimum thickness near clamped edge, hence uniform thickness distribution is observed along the formed surface as shown in Fig. 7. Further, as the preform tool radius increases to 90 mm, the

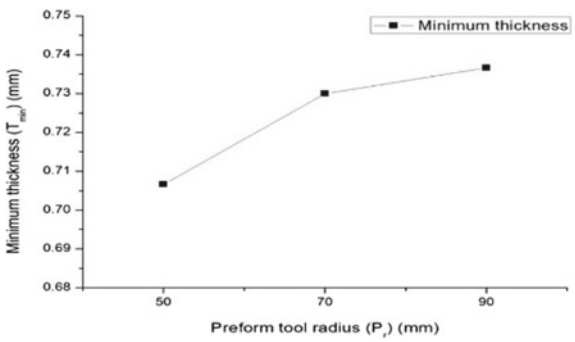

Fig. 6 Preform tool radius versus minimum thickness

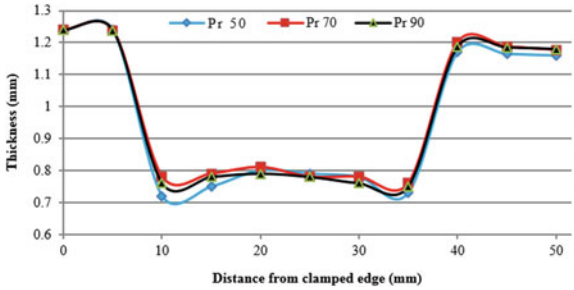

Fig. 7 Thickness profiles of conical frustum formed at 10 mm P_d

plastic defamation is spread over large area as compared bending deformation due to 70 mm preform tool radius. The bending deformation causes thickness reduction in the 1st stage of HISF process. In the second stage, more thickness reduction due to SPIF process is observed.

Finally, it is observed that the developed HISF process forms parts in short time period as compared to SPIF process. In HISF process, preforming operation forms the partial shape of the part to be formed. Hence, HISF requires slightly less time to form the part.

4 Conclusion

In present experimental work, a hybrid incremental sheet metal forming method is developed for forming conical frustums. Findings of present work are summarized as follows:

1. Stretching has considerable influence on thickness distribution and localized thinning in formed parts. More stretching induces more plastic deformation, which results in increased local thinning.
2. HISF process results in improved thickness at thinning band which appears near clamped edge.
3. Preform tool radius has a significant influence on thickness distribution of parts formed using HISF process. 70 mm stretching tool radius and 10 mm stretching results in reduction in minimum thickness as well as results in uniform thickness distribution in the formed part.
4. Process combination of preforming and SPIF process leads to short forming cycles as compared to SPIF alone.

References

1. Matsubara S (2001) A computer numerically controlled dieless incremental forming of a sheet metal. Proc Inst Mech Eng Part B J Eng Manuf 215:959–966
2. Belchior J, Guillo M, Courteille E et al (2013) Off-line compensation of the tool path deviations on robotic machining: application to incremental sheet forming. Robot Comput Integr Manuf 29:58–69. https://doi.org/10.1016/j.rcim.2012.10.008
3. Jeswiet J, Micari F, Hirt G et al (2005) Asymmetric single point incremental forming of sheet metal. CIRP Ann—Manuf Technol 54:88–114
4. Echrif SBM, Hrairi M (2011) Research and progress in incremental sheet forming processes. Mater Manuf Process 26:1404–1414
5. Lu B, Zhang H, Xu DK, Chen J (2014) A Hybrid flexible sheet forming approach towards uniform thickness distribution. Procedia CIRP 18:244–249. https://doi.org/10.1016/j.procir.2014.06.139
6. Gupta P, Jeswiet J (2019) Manufacture of an aerospace component by single point incremental forming. Procedia Manuf 29:112–119
7. Vanhove H, Carette Y, Vancleef S, Duflou JR (2017) Production of thin shell clavicle implants through single point incremental forming. Procedia Eng 183:174–179. https://doi.org/10.1016/j.proeng.2017.04.058
8. Duflou JR, Behera AK, Vanhove H, Bertol LS (2013) Manufacture of accurate titanium craniofacial implants with high forming angle using single point incremental forming. Key Eng Mater 549:223–230
9. Oleksik V, Pascu A, Deac C et al (2010) Experimental study on the surface quality of the medical implants obtained by single point incremental forming. Int J Mater Form 3:935–938
10. Jeswiet J, Duflou JR, Szekeres A, Lefebvre P (2005) Custom manufacture of a solar cooker—a case study. Adv Mater Res 6–8:487–492
11. Scheffler S, Pierer A, Scholz P et al (2019) Incremental sheet metal forming on the example of car exterior skin parts. Procedia Manuf 29:105–111
12. Ambrogio G, Filice L, Gaudioso M, Manco GL (2010) Optimised tool-path design to reduce thinning in ISF process. Int J Mater Form 3:959–962
13. Bambach M, Cannamela M, Azaouzi M et al (2007) Computer-aided tool path optimization for single point incremental sheet forming. Adv Methods Mater Form, 233–250
14. Silva MB, Martins PAF (2013) Two-point incremental forming with partial die: theory and experimentation. J Mater Eng Perform 22:1018–1027
15. Hao W, Duncan S (2011) Optimization of tool trajectory for incremental sheet forming using closed loop control. In: IEEE international conference on automation science and engineering. IEEE, pp 779–784
16. Vanhove H, Carette Y, Duflou JR (2019) An explorative study on, the influence of an elliptical tool on incremental forming. Procedia Manuf 29:74–79
17. Störkle D, Altmann P, Möllensiep D et al (2019) Automated parameterization of local support at every toolpath point in robot-based incremental sheet forming. Procedia Manuf 29:67–73
18. Fan G, Gao L, Hussain G, Wu Z (2008) Electric hot incremental forming: a novel technique. Int J Mach Tools Manuf 48:1688–1692
19. Araghi BT, Manco GL, Bambach M, Hirt G (2009) Investigation into a new hybrid forming process: Incremental sheet forming combined with stretch forming. CIRP Ann—Manuf Technol 58:225–228
20. Shamsari M, Mirnia MJ, Elyasi M, Baseri H (2018) Formability improvement in single point incremental forming of truncated cone using a two-stage hybrid deformation strategy. Int J Adv Manuf Technol 94:2357–2368
21. Kumar Y, Kumar S (2019) Experimental and analytical evaluation of incremental sheet hydroforming strategies to produce high forming angle sheets. Heliyon 5:2–5. https://doi.org/10.1016/j.heliyon.2019.e01801

22. Young D, Jeswiet J (2004) Wall thickness variations in single-point incremental forming. Proc Inst Mech Eng Part B J Eng Manuf 218:1453–1459
23. Santos AD, Teixeira P, Barata Da Rocha A, Barlat F (2010) On the determination of flow stress using bulge test and mechanical measurement. AIP Conf Proc

Influence of Seam Threading of a Cricket Ball on Its Trajectory

K. S. Vepa and N. V. S. S. Sagar

Abstract Like other sports, cricket is also a sport where the perfection of the player decides the outcome of the game. One of the key areas that influence the game is bowling. Seam on the cricket ball helps a bowler in achieving the expected trajectory of the ball. This paper focuses on modelling the flow around the ball with its seam upright and travelling in air. This is the phase during which the ball movement is completely under the influence of aerodynamic loads. This is an important phase during its flight since this will decide the course of the ball after it hits the ground. In order to model this, three different models of cricket balls are taken viz., a smooth sphere, a sphere with a plain seam and a sphere with threaded seam. All the three models are subjected to numerical simulation of wind tunnel tests and the results are compared with the existing results. It is observed that the threading on the seam plays an important role and hence should not be neglected while modelling. It is also observed that the computational cost associated with the modelling of threading on the seam is high.

Keywords Cricket ball · Trajectory · Wind tunnel · CFD

1 Introduction

Cricket is a sport where the accuracy of the bowler in pitching the ball at the expected location can yield favourable results. There are four aspects of bowling that are influencing the trajectory of a ball viz., (a) seam, (b) asymmetric tear, (c) speed and (d) bowling action. Lot of work has already been done in the area of asymmetric tear and bowling action [1, 2]. Many experimental studies have been carried out to understand

K. S. Vepa (✉)
GITAM (Deemed to Be University), Hyderabad, India
e-mail: Sridhar.v.k@gmail.com

N. V. S. S. Sagar
Vel Tech Rangarajan Dr. Sagunthala R&D Institute of Science and Technology, Chennai, India
e-mail: nvsssagar@gmail.com

N. Gascoin and E. Balasubramanian (eds.), *Innovative Design, Analysis and Development Practices in Aerospace and Automotive Engineering*, Lecture Notes in Mechanical Engineering, https://doi.org/10.1007/978-981-15-6619-6_17

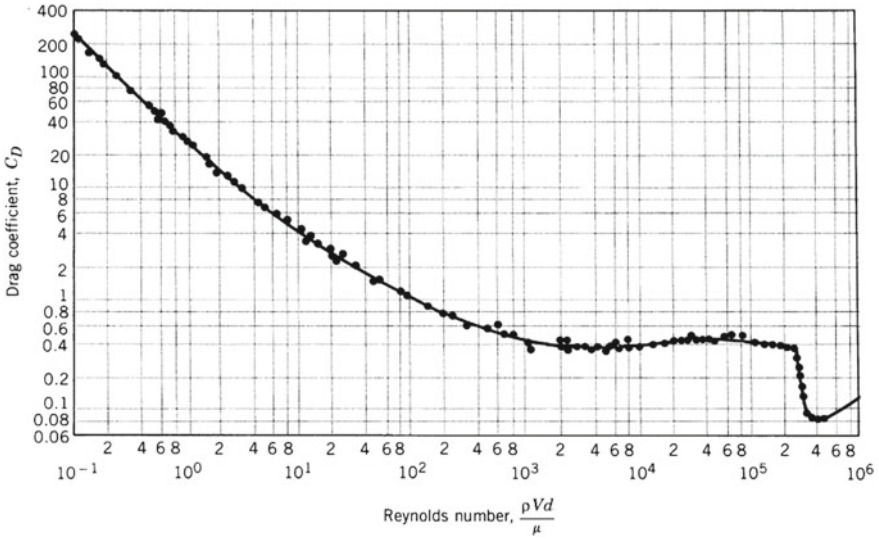

Fig. 1 Effect of Reynolds number on the drag coefficient of a smooth sphere [12]

the physics behind movement of the ball, i.e. its swing [3–5]. A preliminary CFD analysis of cricket ball to test its swing has also been studied earlier [6]. Another aspect of the cricket ball that is very effective in achieving the desired result by the bowler is its speed. Many researchers in the past have established the link between the point of release and its speed [7–11]. In this work, the focus is both on the seam and speed of the ball. To understand this influence of seam and speed, numerical simulations of wind tunnel tests have been carried out on different sphere geometries. Wind tunnels are widely used for simulating flow around a body and calculation of drag force is one example for that. As shown in Fig. 1, drag coefficient does not change much for the flows with a Reynolds number between 10^3 and 2×10^5. Hence, the same can be inferred about the cricket ball which also spherical in shape. But the presence of threading rows on the ball can influence the drag coefficient/drag force. This influence of threading on the drag force is studied in this work.

2 Ball Models

2.1 Plain Sphere (PS)

Figure 2a shows a sphere of 72 mm diameter which is the diameter of a conventional cricket ball. The main emphasis in this paper is to compare the drag force values for understanding the movement of the ball. Also, aspects like flow separation and stagnation point are very important for understanding the boundary flow behaviour.

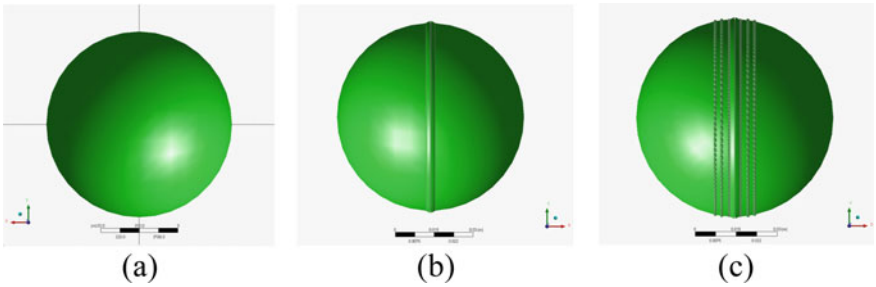

Fig. 2 CAD models of the spheres used

Flow around a smooth sphere is widely studied by multiple authors [13–16]. A comparison with the theoretical values is done (i) to prove the results are mesh converged and (ii) to calculate the margin of error while evaluating the coefficient of drag for a perfectly smooth sphere.

2.2 Sphere with Seam (SS)

Figure 2b shows a two-piece ball (sphere) with seam. Diameter of the sphere is the same as that of the plain sphere. A groove is marked to represent two-piece ball. Also, extra thickness is provided near the groove to represent the seam. Since the coefficient of drag is not available for this shape, results from the simulation are used to calculate it.

2.3 Two-Piece Sphere with Seam and Threading (SST)

Figure 2c shows the CAD model of a two-piece ball (sphere) with seam and threading modelled with the same diameter as the previous models. Also, a groove is marked to represent two-piece ball along with the extra thickness for the seam. Three different crests are modelled on this geometry to represent three different types of threading. A total of 65 stitches are modelled in each row over the circumference of the ball. The distance between any two rows of threading is 3 mm. Based on the literature survey, diameter of the thread is taken 1 mm [17]. Since coefficient of drag is not available for this shape, results from the simulation are used to calculate it.

3 Numerical Model and Boundary Conditions

3.1 Numerical Model

Numerical model for studying the behaviour of a cricket ball with and without seam and threading is done by carrying out CFD simulations for the fluid flow around the ball using Finite Volume Method. Figure 3 shows numerical domain with all the boundary conditions mentioned. The flow over (a) plain sphere, (b) sphere with seam and (c) Sphere with seam and threading with a base diameter of 72 mm is simulated in a 600 × 600 × 800 mm enclosure with flow direction being in negative Z direction. All the three models are created in DesignModeler and then exported to CFX-Pre for applying boundary conditions. All the sphere models are considered rigid. Hence, only the fluid domain surrounding the spheres are meshed and considered for the simulation. Table 1 gives the mesh details for the three flow regimes.

All the three-sphere models are treated as walls with no slip. Fluid in the domain is taken as air. Average pressure at the outlet is given as 1 atm. Three different inlet

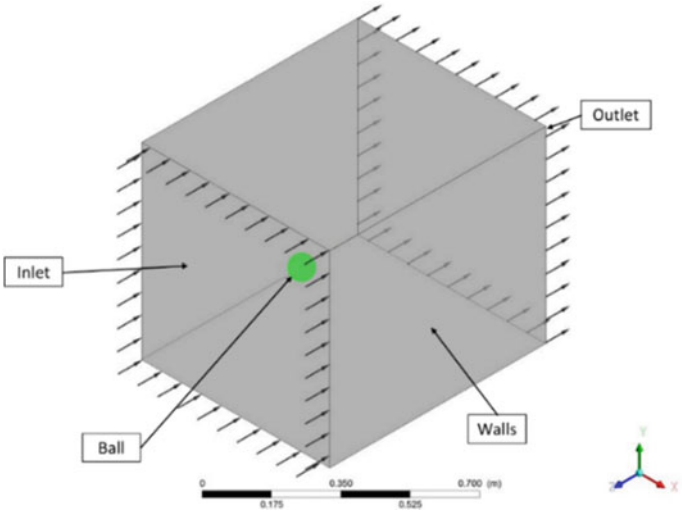

Fig. 3 Numerical model with boundary conditions

Table 1 Mesh details for the three mesh regimes

Ball type	Number of elements	Types of elements	Element size (m)	Mesh Defeaturing size (m)
PS	7,593,244	Tetrahedrons	0.006122	0.0000306
SS	10,854,469	Tetrahedrons	0.00613	0.0000306
SST	17,335,900	Tetrahedrons	0.00613	0.0000306

velocities viz., 80, 100 and 120 km/h are simulated which yields a Reynolds number range of 1×10^5 to 1.5×10^5.

A steady-state simulation with pressure correction algorithm (SIMPLE) is setup. Velocity and pressure residuals are set to 0.00001. In the case of the model with seam and threading, three different sizes of threading are modelled on the sphere to represent a two-piece cricket ball as closely as possible.

4 Results

Two aspects viz., (a) flow around the sphere models and (b) drag coefficient for different geometries.

4.1 Flow Around Sphere Models

Figure 4 shows the velocity contours for plain sphere and sphere with seam models at the centre of the models for an inlet velocity of 80 kmph. We can observe multiple vortex shedding flows initiated in case of sphere with seam. Point of flow separation and peak velocities are not much different for both the cases. Similar observations were made for the other two inlet velocities as well.

Figure 5 shows the velocity contours for sphere with seam and threading at the centre of the sphere as well as on the first threading plane for an inlet velocity of 80 kmph. Unlike plain sphere and sphere with seam, oscillating flow originates at circumference of the sphere and continues to be in the ring rather than converging (like plain sphere). This clearly proves the influence of threading on the vortex shedding pattern and hence the trajectory of the ball.

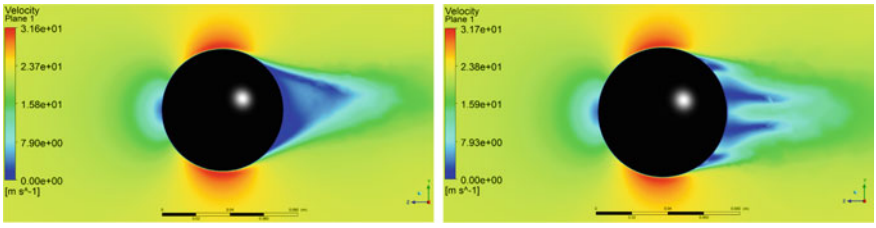

(a) Plain sphere (b) Sphere with seam

Fig. 4 Velocity contours

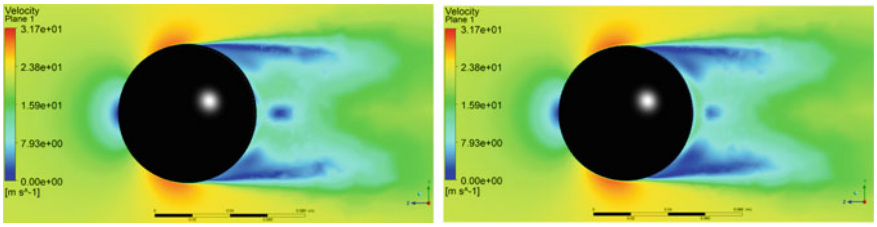

(a) At the centre (b) At the first threading

Fig. 5 Velocity contours for sphere with seam and threading

Table 2 Computational time

Model	CPU time
Plain sphere	4 h 56 min
Sphere with seam	6 h 59 min
Sphere with seam and threading	12 h 35 min

4.2 Computational Time

Table 2 gives us the computational cost associated with each of the simulations. All the simulations have been carried out on Intel® Xeon® CPU with 6 cores with 16 GB DDR3 RAM. It is observed in Table 1 that the number of elements needed to model the ball with threading is more compared to plain sphere. Hence the computational cost associated with simulating two-piece cricket ball is higher compared that of the other two models.

4.3 Drag Force

Drag force is considered as a performance measurement in aviation industry. In the case of cricket as a sport, drag will define the trajectory of the ball. Table 3 gives the results of drag calculations on different ball configurations and velocities. Drag coefficient values for the plain sphere match with that of the theoretical values as

Table 3 Drag force and drag coefficient results

Speed (km/h)	Drag force (N)			Drag coefficient
	Plain sphere	Sphere with seam	Sphere with seam and threading	Plain sphere
80	0.536	0.727	1.554	0.450
100	0.853	1.166	2.329	0.459
120	1.248	1.721	3.547	0.466

observed in the literature [3]. In comparison to plain sphere, drag force on the cricket ball with threading is approximately three folds higher. The percentage increase in cross-sectional area due to seam and threading is only 0.2%. As the drag force is directly proportional to the area of cross-section, the reason is not just the increase in the area of cross-section. Because of the threading provided on the cricket ball, an increase in the vortex shedding is observed which in turn is the cause for increased drag force (Fig. 5).

5 Conclusions

From the results discussed in the previous section, it may be concluded that the threading on the cricket ball has an influence on the drag force and vortex shedding of the models which in turn will have an impact on the trajectory. When compared to the plain sphere, sphere with seam and sphere with seam and threading models gave higher drag. These simulations also differentiate between the influence of seam as well as the threading. For all the velocities simulated, the percentage increase in the drag because of seam is ranging between 35.6 and 37.9 whereas the percentage increase in the drag from sphere with seam to sphere with seam and threading is ranging from 99.7 to 113.7. But the increase in the area of cross-section between the sphere with seam and the sphere with seam and threading is negligible. Hence the influence of cross-section area in defining the drag force is negligible. Also, vortex shedding has a superior role to play in the increased drag force. This goes on to prove that the threading has higher influence on the drag force than the seam.

In the simulations, the shape of the thread is considered to be cylindrical. This may not be true in the real case scenario. But the perfect cylinder case gives a more conservative result than other shapes similar to an ellipse. Distance between the threading rows and the size of each stitch will also have an influence on the result. Simulations carried out in this work are based on the threading currently available in the commercial space. A further study into this aspect can help the cricket boards to design threading on the ball that suits their home conditions.

References

1. Mehta RD (2005) An overview of cricket ball swing. Sports Eng 8(4):181–192
2. Mehta RD, Koga DJ (2000) Cricket ball aerodynamics: myth versus science
3. Mehta R et al (1983) Factors affecting cricket ball swing. Nature 303(5920):787–788
4. Barton N (1982) On the swing of a cricket ball in flight. Proc R Soc Lond A Math Phys Sci 379(1776):109–131
5. Scobie JA et al (2013) Fluid dynamics of cricket ball swing. Proc Inst Mech Eng Part P J Sports Eng Technol 227(3):196–208
6. Penrose J, Hose D, Trowbridge E (1996) Cricket ball swing: a preliminary analysis using computational fluid dynamics. Eng Sport, 11–19

7. Worthington PJ, King MA, Ranson CA (2013) Relationships between fast bowling technique and ball release speed in cricket. J Appl Biomech 29(1):78–84
8. King MA, Worthington PJ, Ranson CA (2016) Does maximising ball speed in cricket fast bowling necessitate higher ground reaction forces? J Sports Sci 34(8):707–712
9. Marshall R, Ferdinands R (2003) Cricket: the effect of a flexed elbow on bowling speed in Cricket. Sports Biomech 2(1):65–71
10. Portus MR et al (2004) Cricket: technique factors related to ball release speed and trunk injuries in high performance cricket fast bowlers. Sports Biomech 3(2):263–284
11. Loram L et al (2005) Determinants of ball release speed in schoolboy fast-medium bowlers in cricket. J Sports Med Phys Fitness 45(4):483
12. Munson B, Young D, Okiishi T (1998) Fundamentals of fluid mechanics
13. Taneda S (1956) Experimental investigation of the wake behind a sphere at low Reynolds numbers. J Phys Soc Jpn 11(10):1104–1108
14. Jones DA, Clarke D (2008) Simulation of flow past a sphere using the fluent code. DST organization Victoria (Australia) maritime
15. Sadikin A et al (2014) Numerical study of flow past a solid sphere at moderate Reynolds number. Appl Mech Mater
16. Lee S (2000) A numerical study of the unsteady wake behind a sphere in a uniform flow at moderate Reynolds numbers. Comput Fluids 29(6):639–667
17. Lanjewar R et al (2007) Design and development of an ingenious cricket ball decorative stitching machine

Numerical Modeling and Analysis of a Multi-rotor UAS

K. S. Vepa, N. V. S. S. Sagar, Balasubramanian Esakki, and Chandrasekhar Udayagiri

Abstract Unmanned Aircraft Systems (UASs) are gaining a lot of importance due to their inherent advantage of operating the aircraft with no onboard pilot. Though there are single and multi-rotor UASs, the later one is a popular choice for operations like surveillance and seed sowing in agriculture. This work emphasizes on carrying out computational fluid dynamic (CFD) simulations for investigating the flow around a quadcopter (UAS with four rotors) for different angles of attack (AoAs). Phenomena such as vortex formations and wake regions are studied. Quadcopter chosen for this work is a topology optimized 3D printed model. Numerical wind tunnel simulations are carried out for different wind velocities. Influence of relative propeller motion on each other is also studied. Stability of the quadcopter during lift and hovering stages is examined. From the results, it is observed that the stability of the quadcopter is dependent on the combination of AoA and velocity. Further, at lower ground clearances, the quadcopter is more stable than at higher altitudes because of the flow pattern.

Keywords Computational fluid dynamic · Wind tunnel · 3D printed quadcopter frame · Aerodynamic performance

K. S. Vepa (✉)
GITAM (Deemed to Be University), Hyderabad, India
e-mail: Sridhar.v.k@gmail.com

N. V. S. S. Sagar · B. Esakki
Vel Tech Rangarajan Dr. Sagunthala R&D Institute of Science and Technology, Chennai, India

C. Udayagiri
IIT Bombay, Mumbai, India

N. Gascoin and E. Balasubramanian (eds.), *Innovative Design, Analysis and Development Practices in Aerospace and Automotive Engineering*, Lecture Notes in Mechanical Engineering, https://doi.org/10.1007/978-981-15-6619-6_18

1 Introduction

Unmanned Aircraft Systems (UASs) are widely used in various applications due to its major advantage of operating without onboard pilot [1, 2]. There are three types of UASs, i.e., fixed wing, flapping wing, and rotary wing. Rotary wing UASs have better hovering characteristics as the aerodynamic behavior of rotors have greater significance in controlling and maneuvering the vehicles. Information exchange at the interface between the rotor and fluid domains is a challenging task. Computational fluid dynamic (CFD) analysis helps in addressing this problem. Using CFD analysis, wake region, formation of vortex, shift of tip vortex to turbulence regimes and multi-rotor interactions can be studied [3]. Considerable research is available in the field of CFD [4–6] and multi-rotor dynamics [7, 8]. The forces acting on quadcopter opposite to the direction of motion affect its performance. The force that opposes the forward motion is drag and it affects the endurance. The value of drag varies with the angle of attack and the present study investigates the performance of quadcopter on varied angles of attack.

Filippone and Michelsen [9] estimated the drag on the structure of a helicopter for several configurations and respective center of pressure regions are determined. Also, wind tunnel tests are conducted for various geometries to understand the flow fields for asymmetric flow conditions. More recently, Yoon et al. [10] studied the effect of the distance between the rotors and fuselage during hovering condition. It has been observed that as the distance decreases, the efficiency of the UAS also decreases. Felismina [11] analyzed the aerodynamic behavior of UAV assembled with seeder mechanism and drag force is computed using CFD analysis. Lopez et al. [12] used SA and K-ω models to study the flow field around propeller of a quadcopter. With the use of Lattice-Boltzmann and LES turbulence methodology, Thibault et al. [13] simulated the vortex phenomena for a quadcopter. In line with the existing studies, an off-the-shelf structural model is considered for examining its aerodynamic behavior. The UAS chosen for this analysis is a quadcopter. The topology of the frame is optimized to reduce its weight, but the resulting frame is complex in geometry with intricate flow fields. Hence, we aimed to calculate the value of drag during the hovering phase and forward motion for various angles of attack.

2 Design of Quadcopter UAS

The conceptual model of UAS is an off-the-shelf model of a commercially available quadcopter frame. The model is designed and developed to carry an all-up weight of 2 kg load. The process of designing the model is carried out in ANSYS Design Modeler and CFD simulations are carried out using ANSYS CFX. The model considered for the analysis is very complex which involves various spline curves, hence the model is manufactured using Fused Deposition Modelling (FDM) technology [14].

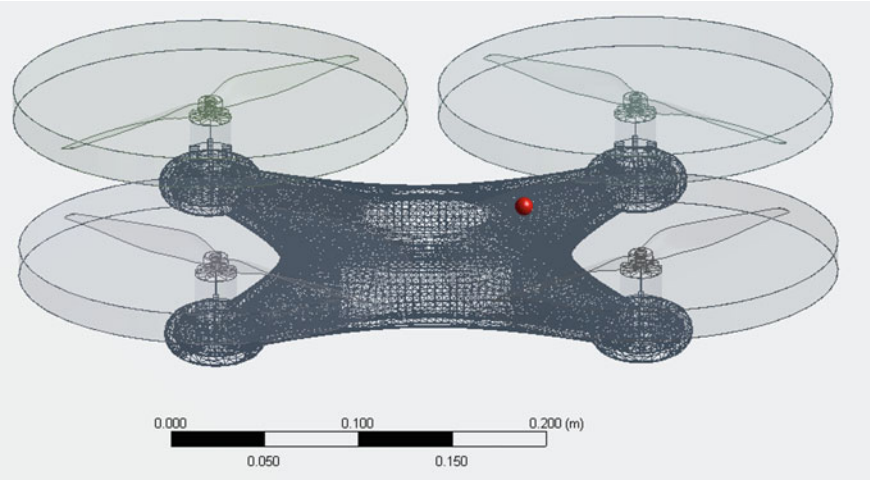

Fig. 1 UAS with MRF domain

The frame is printed using ABS material to accommodate all the parts of quadcopter. Factor of safety for the design is considered as 2, therefore thrust-to-weight ratio of 2 is chosen. Hence, the maximum thrust required to lift the vehicle is 40 N. The Fuselage shown in Fig. 1 has a diagonal length of 330 mm and height of 50 mm with a total weight of 0.338 kg.

Four motors with suitable propellers are selected to produce approx. 1 kg thrust each. Based on frame dimensions and estimated thrust, propellers of 8 × 4.5 inches are selected. For 1 kg thrust motor, brushless motor 935 kV emax 2213 is used. Figure 2 shows the physical assembly of the quadcopter.

3 Numerical Approach or Modeling

Computational domain is modeled based on the wind tunnel used for the analysis. Figure 3 shows the computational domain with the model and its moving rotational frames.

3.1 Mesh Generation

In simulations, mesh quality always plays a prominent role in obtaining results. Quality of the mesh depends mainly on the skewness and orthogonality of the elements in it. Hence the skewness and orthogonality values for the mesh are controlled using element sizing option. From the calculations, it is observed that

Fig. 2 Quadcopter assembly

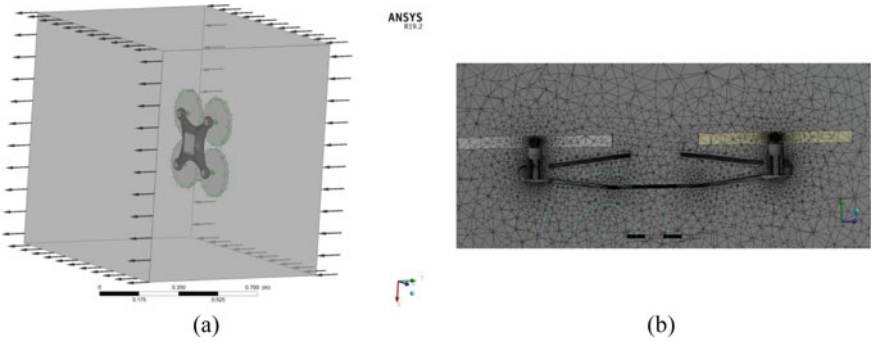

Fig. 3 Computational domain and the mesh around the quadcopter

the mesh quality is good enough to produce accurate results as shown in Fig. 4. A total of 1,988,470 tetrahedral elements are generated in the computational grid. For attaining convergence in solution, each simulation took about 1000 iterations.

3.2 Hovering Phase

Quadcopter attains the hovering phase when over-all thrust matches with the downward force (gravitational weight). Hence in the hovering phase, each rotor will be provided with the same rpm to attain stability at a certain height. In hovering phase simulations, two parallel faces that are in the YZ plane (see Fig. 3) are given "opening"

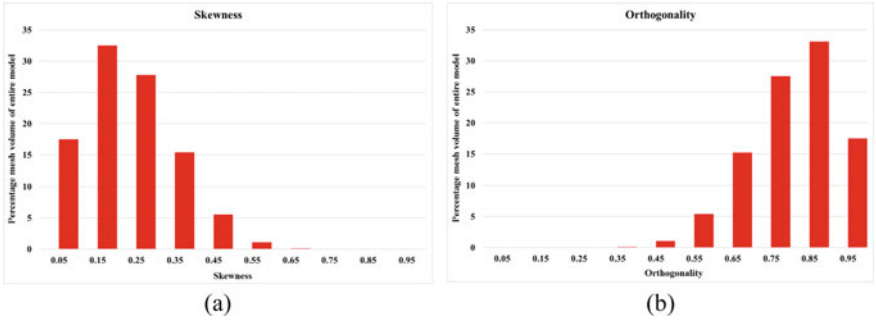

Fig. 4 Mesh quality **a** skewness and **b** orthogonality

boundary condition and the other four faces are given "wall" boundary conditions for simulating the flow field. It is observed that there is a recirculating flow that helps the quadcopter stay horizontal/flat. Figure 5 shows the flow field for zero degrees angle of attack.

Similar flow fields with varying peak pressures and maximum velocities are observed for other angles of attack which are summarized in Table 1. It may be observed that the maximum velocity in the MRF region decreases initially and then increases. Since the parameters like density and free stream velocities remain constant, the best angle of attack lies in between 4° and 8°.

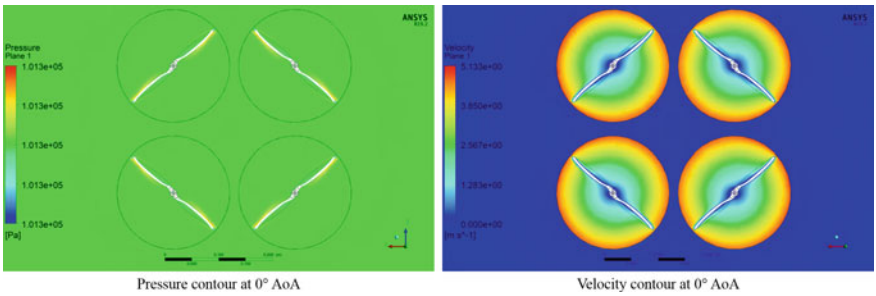

Fig. 5 Pressure and velocity flow fields in the MRF region (hovering)

Table 1 Maximum pressure and velocities for different angles of attack (hovering)

Angles of attack (°)	Max. pressure (Pa)	Propeller tip velocity (m/s)
0	101,333	5.133
4	101,335	5.109
8	101,334	5.190
12	101,340	6.148

3.3 *Forward Phase*

In the case of forward motion, quadcopter will move against the wind. Such a scenario is simulated by keeping the quadcopter in the same position and wind is blown at 5 m/s. Simulations are performed for different angles of attack. Figure 6 shows the flow field for zero degrees angle of attack. Similar flow fields with varying peak pressures and maximum velocities are observed for other angles of attack which are summarized in Table 2. It may be observed that the maximum velocity in the MRF region decreases initially and then increases which is the same trend is observed in the hovering phase. Since the parameters like density and free stream velocities remain constant, the best angle of attack lies between 8° and 12°.

4 CFD/Experimental Analysis Using Wind Tunnel

Wind tunnel facility used for the current research work is a subsonic speed open-circuit wind tunnel. It has mainly three divisions, an inlet division, nozzle and test division, and a diffuser division. Figure 7 shows the actual wind tunnel and its test division views. Velocity of the flow is noted from an inclined tube manometer. The wind tunnel is equipped with a six-component force balance. The strain data from

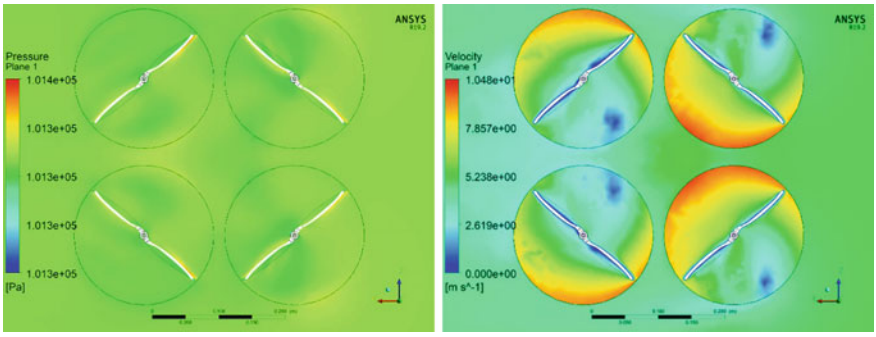

Pressure contour at 0° AoA Velocity Contour at 0° AoA

Fig. 6 Pressure and velocity flow fields in the MRF region (forward motion)

Table 2 Maximum pressure and velocities for different angles of attack (forward motion)

Angles of attack (°)	Max. pressure (Pa)	Propeller tip velocity (m/s)
0	101,364	10.4759
4	101,365	10.1698
8	101,365	10.1613
12	101,381	11.3034

Fig. 7 Wind tunnel **a** equipment, **b** test division with model

the force balance equipment is used to extract the forces and moments in the three directions.

4.1 Validation Through Numerical and Experimental Comparison

A comparison between the experiments and simulations is done for the generated drag when placed in upright position (by considering the upward motion of the quadcopter as shown in Fig. 7). Figure 8 shows the streamlines with velocity contours for the simulation. Table 3 gives the comparison of the drag force value as seen in the wind

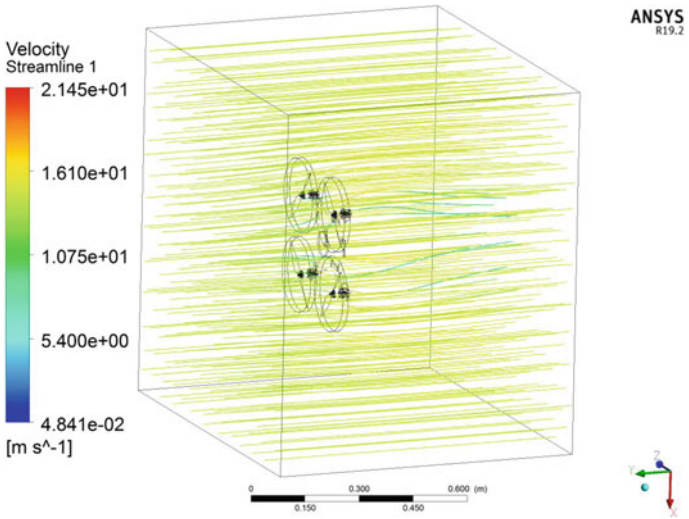

Fig. 8 Drag flow simulation of the quadcopter

Table 3 Comparison of experimental and numerical drag force results

Speed (m/s)	Numerical	Experimental
4.788	1.5762 N	1.52873 N

tunnel tests and the simulations for a wind speed of 4.788 m/s which are equivalent to 165 RPM in the wind tunnel. From the comparison, it is observed that there is only a relative error of approximately 3% between the two.

5 Conclusions

In the present work, an unmanned aircraft system is considered for CFD simulation to study its aerodynamic performance. The frame of the UAS is optimized for its mass and structural strength. Due to its geometrical complexity, it is fabricated using FDM technology. Flow field around the quadcopter and the drag forces generated are analyzed. For validation, numerical simulations and wind tunnel experiments are compared which shows they are in good agreement with each other. Simulations are carried out during hovering and forward motion for various angles of attack. Minimum drag is experienced between 4° and 8° during hovering and 8° and 12° during forward motion (at a speed of 5 m/s). Based on the comparison of numerical and experimental results, it is concluded that the drag is dependent on the AoA as well as the wind velocity.

References

1. Hassanalian M, Abdelkefi A (2017) Classifications, applications, and design challenges of drones: a review. Progr Aerosp Sci 91:99–131
2. Yan R-j et al (2010) Development and missions of unmanned surface vehicle. J Mar Sci Appl 9(4):451–457
3. Domenge PXC, Ilie M (2010) Numerical study of helicopter blade–vortex mechanism of interaction using the potential flow theory. Appl Math Model 36(7):2841–2857
4. Dwivedi Y, Jagadish D, Sridhar V (2016) Aerodynamic analysis of corrugated winglet for improved MAV performance
5. Sridhar V, Dwivedi Y (2017) Effect of peak shape in bio inspired corrugated wing. In: International conference on advances in thermal systems, materials and design engineering (ATSMDE2017)
6. Dwivedi Y et al (2017) Computational study of fluid flow behavior over bio-inspired corrugated airfoil for micro aerial vehicles. In: International conference on advances in thermal systems, materials and design engineering (ATSMDE2017)
7. Esakki B et al (2018) Design of amphibious vehicle for unmanned mission in water quality monitoring using internet of things. Sensors 18(10):3318
8. Ganesan S, Esakki B (2019) Design and development of unmanned hovercraft
9. Filippone A, Michelsen J (2001) Aerodynamic drag prediction of helicopter fuselage. J Aircr 38(2):326–333

10. Yoon S, Lee HC, Pulliam TH (2016) Computational analysis of multi-rotor flows. In: 54th AIAA aerospace sciences meeting
11. Felismina R et al (2017) Study on the aerodynamic behavior of a UAV with an applied seeder for agricultural practices. In: AIP conference proceedings. AIP Publishing
12. Lopez OD, Escobar JA, Pérez AM (2017) Computational study of the wake of a quadcopter propeller in hover. In: 23rd AIAA computational fluid dynamics conference
13. Thibault S et al (2017) CFD simulation of a quad-rotor UAV with rotors in motion explicitly modeled using an LBM approach with adaptive refinement. In: 55th AIAA aerospace sciences meeting
14. Sagar N, Vepa K (2018) Experimental investigations for improving the strength of parts manufactured using FDM process. In: Innovative design, analysis and development practices in aerospace and automotive engineering (I-DAD 2018). Springer, pp 307–313

Multistage Mass Optimization of a Quadcopter Frame

N. V. S. S. Sagar, Balasubramanian Esakki, Chandrasekhar Udayagiri, and K. S. Vepa

Abstract Unmanned aerial vehicles (UAVs) are swiftly achieving their distinction in the fields of defence and agriculture. Of all the UAVs, quadcopters are widely used due to their inherent advantages like easy control and manoeuvrability. The need to operate for a longer duration under suitable payload is perhaps an exacting task. The flight time and efficiency of quadcopter typically rely on its weight. Among all the parts of a UAV, frame is the structural member that takes up the entire load. Since it constitutes up to 30% weight of the UAV, optimization of the UAV frame is highly recommended. To study this, weight of an off-the-shelf model is optimized using numerical schemes in two stages. In the first stage, optimization is done for the shape of the frame using Design of Experiments (DoEs). In the second stage, optimization is carried out for mass using topology optimization. Despite the considerable reduction of mass in the design of experiments, mass is further reduced in the second stage, i.e. topology optimization. Topology optimization yielded a complex-shaped model that is difficult to manufacture using traditional methods hence the optimized model is redesigned and validated using static structural finite element analysis.

Keywords Static structural analysis · Design of experiments · Topology optimization and quadcopter frame

N. V. S. S. Sagar (✉) · B. Esakki
Vel Tech Rangarajan Dr. Sagunthala R&D Institute of Science and Technology, Chennai, India
e-mail: nvsssagar@gmail.com

B. Esakki
e-mail: esak.bala@gmail.com

C. Udayagiri
Wipro 3D, Bengaluru, India
e-mail: rapidchandra@gmail.com

K. S. Vepa
GITAM (Deemed to Be University), Hyderabad, India
e-mail: sridhar.v.k@gmail.com

N. Gascoin and E. Balasubramanian (eds.), *Innovative Design, Analysis and Development Practices in Aerospace and Automotive Engineering*, Lecture Notes in Mechanical Engineering, https://doi.org/10.1007/978-981-15-6619-6_19

1 Introduction

The research in the area of unmanned aerial vehicles (UAVs) (also known as drones) is significantly increasing due to its huge potentiality in discrete applications. Usually, the aerodynamic performance of the drone depends both on its mass and shape. Of all the types of UAVs, owing to its need for less regulation, quadcopters with four motors and four propellers are widely used. Hence, it is aimed to design a lightweight quadcopter structure by integrating the concepts of design optimization, topology optimization and fused deposition modelling.

In the first stage of optimization, design optimization is carried out to identify the optimum set of input parameters that define the shape and mass of the quadcopter viz., shell thickness, frame height and arm width using Design of Experiments (DoE). Non-dominated Sorted Genetic Algorithm (NSGA) is used to identify the optimum set of parameters. Eventually, in the second stage, the mass is further optimized using topology optimization. The geometry obtained from topology optimization is rough and uneven. Hence, the model is modified and validated before fabrication. Because of its advantages like time compression [1] and design flexibility [2], widely used additive manufacturing technology Fused Deposition Modelling (FDM) [3] is used. Entire design procedure is presented in the flow chart given in Fig. 1.

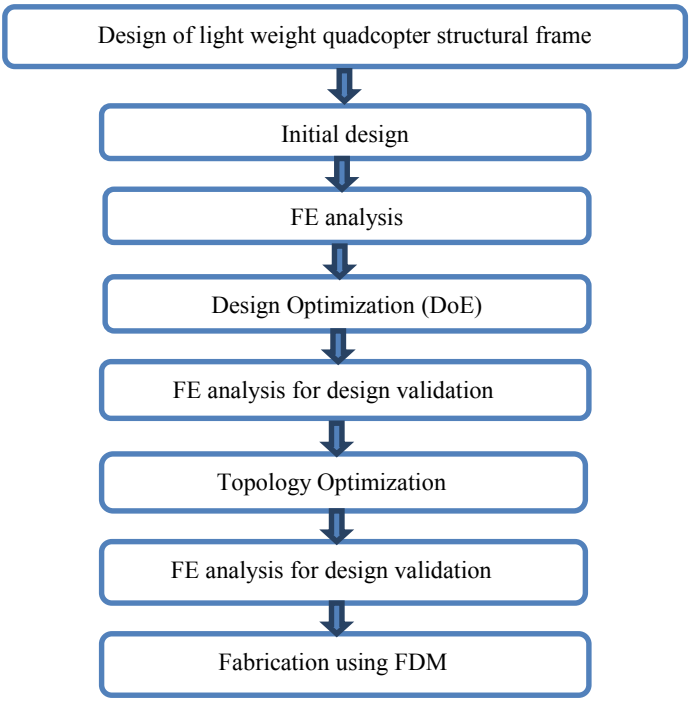

Fig. 1 Flow chart for multistage optimization

2 Design and Modelling of Quadcopter Structure

The conceptual model considered for the analysis is an off-the-shelf quadcopter frame. DoE requires input variables that define the frame size and shape. Hence, parametric modelling is carried out using ANSYS design modeler. Initial geometry is modelled with a frame height of 50 mm, diagonal length of 330 mm and a thickness of 5 mm as shown in Fig. 2. Acrylonitrile Butadiene Styrene (ABS) [4] is chosen as material by considering its manufacturability and production cost. The material used for the existing quadcopter is also thermoplastic polystyrene. A comparison of mechanical properties between the two materials is given in Table 1. The existing material has a lower density making it a lighter frame for the same dimensions. But the superior mechanical properties of the new material, i.e. ABS allows for the optimization of the design. Allowable deformation is calculated based on the percentage elongation to break and the dimensions of the arm [5].

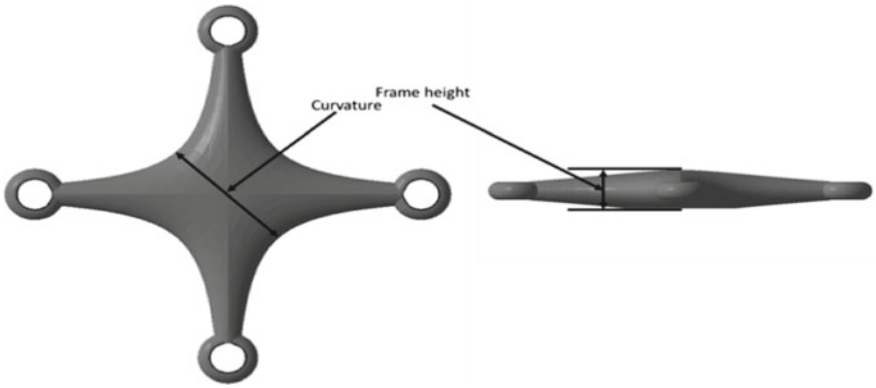

Fig. 2 Initial geometry

Table 1 Mechanical properties of quadcopter frame materials

Property	Existing (thermoplastic polystyrene)	New design (ABS)
Density (kg/m^3)	1040	1050
Young's Modulus (MPa)	1550	2500
Allowable stress (MPa)	22 MPa	40
Allowable deformation (mm)	0.0825	0.1237

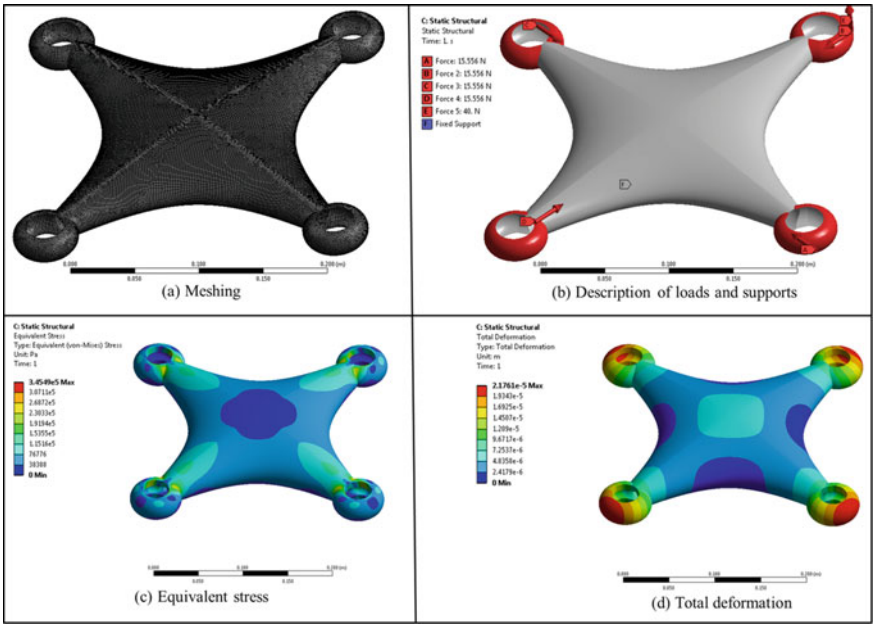

Fig. 3 Static structural analysis for the basic model

3 FE Analysis

During motion, structural elements of quadcopter are subjected to thrust forces and gravitational forces [6]. For the finite element analysis, the designed parametric model is imported and meshed using an element size of 0.02 mm. Static structural finite element analysis is carried out to check the model for its strength for an all-up weight of 2 kg. From the results, maximum equivalent stress of 0.3 MPa and maximum deformation of approximately 0.02 mm is observed as shown in Fig. 3.

4 Structural Optimization

4.1 Design Optimization

Design Optimization aims at modifying the input parameters that satisfy the given constraints for achieving the required objective. Hence, three parameters namely frame height, curvature and shell thickness are taken as input parameters for the optimization problem as mentioned in the Table 2. Minimization of mass and deformation with limiting stress of 10 MPa are taken as objective functions. Hence, a factor of safety of 4 is utilized while defining the optimization problem.

Table 2 Design variables

Parameter	Lower bound	Upper bound
Frame height (mm)	45	55
Curvature (mm)	80	150
Shell thickness (mm)	5	8

Optimization method used for this simulation is an adaptive multi-objective method which is a variant of the popular Non-dominated Sorted Genetic Algorithm (NSGA). From the results, a set of three combinations is suggested by the optimization tool that is the best. Since the priority is to identify the sample that yields the least mass, the sample in Table 3 is chosen. The model generated from the selected combination is as shown in Fig. 4.

The optimized model is validated using finite element analysis with the same loading and boundary conditions. From the results, it is observed that the maximum equivalent stress is 0.81 MPa and the maximum deformation is 0.055 mm. Though the stress and deformations are within the limits, the mass of the model seems to be high and there is scope for further optimization. Hence, the model is considered for topology optimization to reduce its mass.

Table 3 Optimum input parameter combination

Frame height (mm)	Curvature (mm)	Shell thickness (mm)
50	140	5

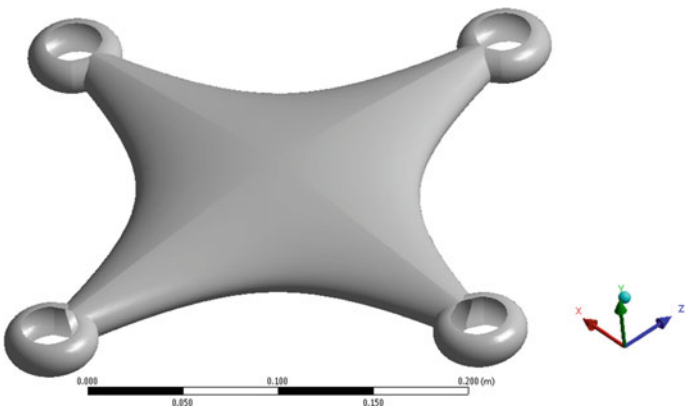

Fig. 4 Design optimized model

4.2 Topology Optimization

The model is optimized further using the topology optimization tool, by considering mass minimization as objective function and allowable maximum stress as response constraint. Topology optimization resulted in geometry as shown in Fig. 5 with lowest possible weight and capable of lifting an all-up weight 2 kg. Finally, topology optimized model is verified and validated using static structural finite element analysis.

Figure 5 shows the results of topology optimization. It is observed that the shape is uneven and rough, which is very difficult to manufacture. Hence the design is remodelled as shown in Fig. 6.

For validation, the remodelled geometry is analyzed with the same loading and boundary conditions. From the results, maximum stress of 0.8 MPa and maximum

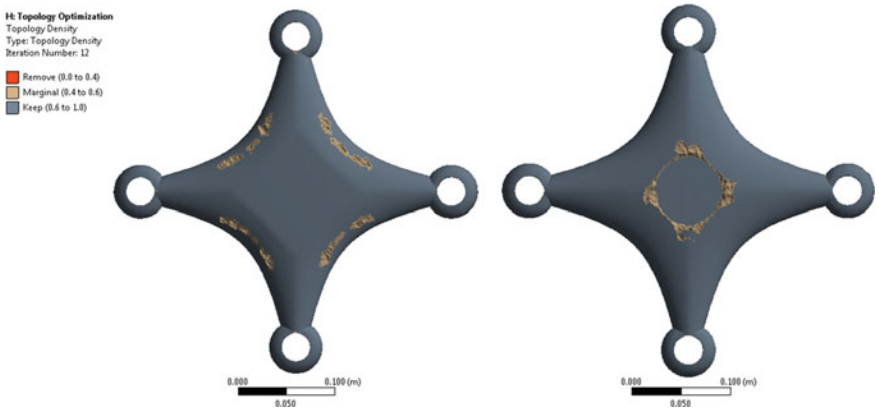

Fig. 5 Topology optimized model

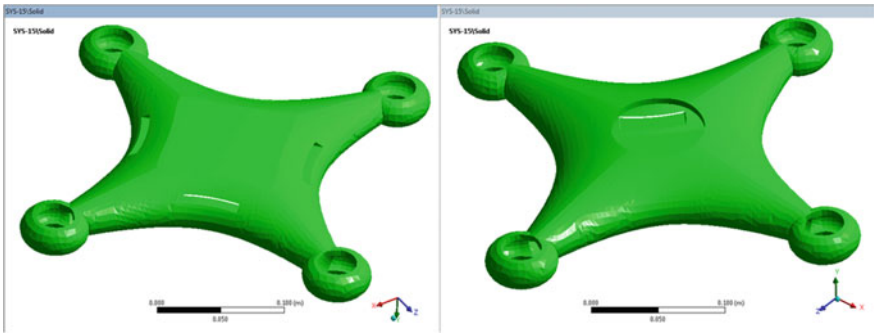

Fig. 6 Remodelled geometry

Fig. 7 FDM Fabricated model

Table 4 3D printing parameters

Parameter	Value
Layer thickness (mm)	0.1
Orientation	XY
Infill percentage	100

deformation of 0.56 mm is observed. Both the stress and deformations are within the permissible limits as mentioned in Table 1.

5 Fabrication of Frame Using FDM

Off-the-shelf model chosen for optimization was manufactured using injection molding process. But the resulting model of optimization is complex and its manufacturing using injection molding is always a challenging task. Since the goal of this work is to provide a design and manufacturing process that can suit any optimized geometry, FDM is recommended as the manufacturing process. FDM is cost-effective and versatile when compared to other additive manufacturing techniques. The final model is fabricated using FDM technology as shown in Fig. 7, with the parameters shown in Table 4. Choice of the parameters is based on the previous research was done by the authors in this area [5].

6 Final Results and Conclusions

Structural optimization integrated with additive manufacturing technology is realized for designing a lightweight quadcopter structure that can carry an all-up weight

Table 5 Multistage Mass Optimization

Model	Frame mass (kg)	von Mises stress (MPa)	Max. principal stress (MPa)	Total deformation (mm)
Initial geometry	0.756	0.345	0.391	0.0217
Design optimized model	0.460	0.807	0.923	0.0549
Topology optimized model	0.434	0.809	1.127	0.0568

of 2 kg. It resulted in a geometry of least possible weight and capable of withstanding the payload while satisfying all the loading and boundary conditions. Utilization of design optimization reduced the weight of the frame by 39.2% and topology optimization reduced it further by 5.64% while retaining its strength and potential. The final redesigned and remodelled geometry yielded a mass of 434 g as against 756 g of initial design. From the results as mentioned in the Table 5, it is proved that stresses and deformations are within the acceptable limits throughout the part. Thus, it can be concluded that the integration of structural optimization with additive manufacturing is a promising approach in reducing the weight of quadcopter structure.

References

1. Kun K (2016) Reconstruction and development of a 3D printer using FDM technology. Procedia Eng 149:203–211
2. Esakki B et al (2019) Development of 3D-printed floating Quadrotor for collection of algae in remote water bodies. Comput Electron Agric 164:104891
3. Goh G et al (2017) Additive manufacturing in unmanned aerial vehicles (UAVs): challenges and potential. Aerosp Sci Technol 63:140–151
4. Sagar N, Esakki B, Udayagiri (2019) Design of monocoque quadcopter structure through integration of additive manufacturing and topology optimization
5. Sagar NVSS, Vepa KS (2018) Experimental investigations for improving the strength of parts manufactured using FDM process. In: Chandrasekhar U, Yang LJ, Gowthaman S (eds) Innovative design, analysis and development practices in aerospace and automotive engineering (I-DAD 2018). Lecture Notes in Mechanical Engineering. Springer, Singapore
6. Balasubramanian E et al (2019) Development of light weight multi-rotor UAV structures through synergistic application of design analysis and fused deposition modelling. Int J Mater Prod Technol 59(3):229–238

Comparative Study of Response of Vibrations for Circular and Square Defects on Components of Cylindrical Roller Bearing Under Different Conditions

Sushant M. Patil, R. G. Desavale, Prasad V. Shinde, and Vijay R. Patil

Abstract Rolling element bearing is the crucial constituent in many revolving equipments. For effective performance of the machine, it is necessary to precisely predict the effect of various parameters and operating conditions on the machine's behavior. In this paper, the dynamic responses of a rotor-bearing system are studied. The presence of defect in bearing may lead to failure hence bring to a standstill of machinery. The solution of this problem is to discover these defects in earlier stages to avoid any damage to system. In this paper, the effect of speed load and defect is studied. The circular and square defects are produced by using electro discharge machine on inner race, outer race, and rolling element. In experimentation, vibration amplitudes for various speeds and loads for healthy bearing, circular defect bearing, and square defect bearing are observed. Mathematical model has been developed to predict the

S. M. Patil (✉)
Research Scholar, Department of Mechanical Engineering, Visvesvaraya Technological University, Belagavi 590018, India
e-mail: sushant.rit@gmail.com

S. M. Patil · P. V. Shinde · V. R. Patil
Research Scholar, Department of Automobile Engineering, ADCET, Ashta 416301, India
e-mail: prasadshinde7174@gmail.com

V. R. Patil
e-mail: vijaypatil872@gmail.com

R. G. Desavale
Department of Mechanical Engineering, RIT (Shivaji University, Kolhapur), Islampur 415414, India
e-mail: ramdesavale@rediffmail.com

P. V. Shinde
Research Scholar, Department of Mechanical Engineering, RIT (Shivaji University, Kolhapur), Islampur 415414, India

V. R. Patil
Research Scholar, Department of Mechanical Engineering, BVDU College of Engineering, Pune 411043, India

N. Gascoin and E. Balasubramanian (eds.), *Innovative Design, Analysis and Development Practices in Aerospace and Automotive Engineering*, Lecture Notes in Mechanical Engineering, https://doi.org/10.1007/978-981-15-6619-6_20

effect of defect in terms of the amplitude of vibration. The comparison of experimental analysis and mathematical model for both inner race and outer race shows good agreement. It shows that the vibration amplitude increases as speed and load increases. In addition, it is observed that inner race defect has significant vibration amplitude than outer race defect. Both circular and square defects have dominant effect on rotor bearing system.

Keywords Rolling element bearing · Circular and square defect · Vibration amplitude

1 Introduction

The most widely used component in industry is rolling element bearings. There is a powerful influence of rolling element bearings on dynamic behavior of the rotating machines and on the vibration and noise source. To avoid the catastrophic failure of machinery, need to increases a reliability and performances of a system. Defects in bearings may arise during use or during the manufacturing process. Special methods are used for recognition and diagnosis of bearing imperfections. Mathematical modeling along with experimentation methods provides progressively more exact move toward the prediction of dynamic performance of the systems that include antifriction bearings.

2 Literature Review

Rafsanjani et al. [1] developed a numerical model using non-dynamic behavior of rotor-bearing system for surface defect. Equation of motion has been solved using Newmark time integration technique. Bai et al. [2] developed a 6 DOF rotor dynamic model using Hertzian contact forces, ball bearing nonlinearity, internal bearing clearance, and bending vibration of rotor. Sinou et al. [3] studied a nonlinear behavior of rolling contact bearing by harmonic balance method with a condensation procedure. Ghafari et al. [4] use Hertzian contact theory to represent a stiffness of rolling element bearing using a lumped mass-damper-spring model. Nonato et al. [5] investigated new approach for characterization of the elasto-hydrodynamic lubricated point contacts, coupled lubrication deformation problem, and Newmark-ß integrator of the motion equation for the contact system. Desavale et al. [6] developed empirical model with experimental model based data and artificial neural network for condition monitoring of the rotor system. Authors concluded that speed, defect size, load, clearance, and unbalance affect significantly on the performance of rotor-bearing system. Desavale et al. [7] developed model based on experimentation to highlight the damage in bearing component. This paper suggests that experimental data based model (EDBM) is the tool, which point out the possible defect and size of defect at

early stage. Desavale [8–10] developed different models by using dimensional analysis approach to study different faults in rotor-bearing system, namely looseness, misalignment, defect of various component of bearing, etc.

3 Formulations of Mathematical Model

The dimensional analysis approach is used to develop mathematical model for complex systems containing more number of variables. This paper presents a model proposed by using dimensional analysis to estimate vibration amplitude.

The dimensional groups are obtained in terms of three basic dimensions—*L* length, *T* time and either *M* mass or *F* force. The mathematical model expressed to obtain the dynamic behavior of the system (Table 1).

According to dimensional analysis modeling, each dimensional group consists of terms formed by combining the m variables out of the total n variables with one of the remaining (*n-m*) variables. The functional dependence of vibration characteristics is obtained from dimensional analysis and Buckingham's theorem as shown in Eq. (1).

Table 1 Parameters of the system for dimensional analysis

Parameter	Symbol	Unit	Dimension	Parameter	Symbol	Unit	Dimension
Diameter-bore	D	mm	L	MI of rotor	W_r	kg	$FL^{-1}T^2$
Diameter-ball	d_b	mm	L	MI of shaft	I_s	kg mm^2	FL^2
Diameter-inner race	d_i	mm	L	Damping	c	$\frac{\text{Ns}}{\text{m}}$	$FL^{-1}T^1$
Diameter-outer race	d_o	mm	L	Speed	N_r	rpm	T^{-1}
Diameter-pitch	d_m	mm	L	Load	T	N mm	FL^1
Width	B	mm	L	Bearing deflection	δ	mm	L
Shaft length	L	mm	L	Mass eccentricity	Δ	mm	L
Density of material	ρ	$\frac{\text{kg}}{\text{m}^3}$	$FL^{-4}T^2$	Unbalance	W_u	kg	$FL^{-1}T^2$
Young's Modulus of shaft	E_S	$\frac{\text{N}}{\text{mm}^2}$	FL^{-2}	Defect	R_c	mm	L
Young's Modulus of rotor	E_R	$\frac{\text{N}}{\text{mm}^2}$	FL^{-2}	Vibration amplitude	V	µm	L
Mass of shaft	W_s	kg	$FL^{-1}T^2$	Defect frequency	f_s	Hz	T^{-1}

$$V = f(D, d_b, d_i, d_o, d_m, B, L, \rho, E_S, E_R, W_s, W_r, I_s, I_r, c, \delta, T, \Delta, f_s) \quad (1)$$

The vibration signals are acquired from the system to study effect of speed, clearance, and unbalance mass. All the above variables considered for formulation and dimensionless products are given in Eq. (2)

$$f(\pi_1, \pi_2, \pi_3, \ldots, \pi_m) = 0 \quad (2)$$

In the above mathematical formulation, the total number variables are equal to 26 out of which three variables are not forming dimensionless product; therefore, to formulate the complete set, $23 - 3 = 20$ parameters required.

3.1 System Modeling

The relationship shown in Eq. (1) is modeled with the dimensional analysis; using dimension analysis techniques, dynamic response modeled can be written as

$$\pi_1 = V[R_c]^a[N_r]^b[W_u]^c \quad (3)$$

where a, b, and c represent constants which are obtained from fundamental units, as given in Eq. (4)

$$= LT^{-2}[L]^a\left[T^{-1}\right]^b\left[FL^{-1}T^2\right]^c \quad (4)$$

The balancing of the fundamental units to find constants a, b, and c, may be done as,

$$F^0L^0T^0 = F^cL^{-1+a-c}T^{2+b+2c} \quad (5)$$

The equations may be written as follows

$$c = 0, \quad 1 + a - c = 0, \quad 2 + b + 2c = 0$$

Solving equations, values of a, b and c are

$$a = -1, \quad b = -2, \quad c = 0$$

Hence, the first dimensionless (π_1) group is

$$\pi_1 = V[R_c]^1[N_r]^{-2}[W_u]^0$$

$$\pi_1 = \frac{\ddot{x}}{R_c N^2} \tag{6}$$

Using the similar procedure, Table 2 gives the remaining twenty (20) dimensionless groups,

3.2 Deducing of Dimensionless Groups

It is required to reduce above groups, as there are more variables. It is obtained by products or division of one group by another group. Substituting reduced dimensionless group, Eq. (2) may be obtained as follows

$$\frac{V}{R_c N^2} = f\left(\Psi \times \frac{\rho R_c^4 N_r^2}{E_S} \times \frac{E_S R_c}{C N_r} \times \frac{R_c^3 E_S}{T} \times \frac{f_s}{N_r}\right) \tag{7}$$

Equation (7) shows the exact relationship for getting vibration. The above-derived functional relationship is proposed. By performing experiments, the functional dependency is studied.

4 Experimental Details

An experimental setup is as shown in Fig. 1. Variable speed DC motor drives the shaft, which is supported by two test bearings, one at each end. Vibration signals were obtained with the help of pick up type analyzer.

The FFT technique has been utilized afterwards; here, use of vibration measurement instrument for measuring the vibrations (Displacement pickup type meter). The displacement pickup type meter is as shown in Fig. 2. For the measurement of acceleration, velocity, and displacement, the data acquisition system was used. The vibration signals were measured on the bearing housing of the test bearing by mounting an accelerometer with sensitivity 105.5 mV/g. 43 V data acquisition system had four analog channels and four digital channels as shown in Fig. 3. Specifications of the bearing are as shown in Table 3.

Defects on Bearings Circular and square defects were produced on the rolling element, inner race, and outer race of the bearing by using electronic discharge machining (EDM). Table 4 gives the details of defects produced (Fig. 4).

Table 2 Dimensionless groups

Variable	Dimensionless π-products	Variable	Dimensionless π-products	Variable	Dimensionless π-products
R_c, N_r, W_u and D	$\pi_2 : \frac{D}{R_c}$	R_c, N_r, W_u and L	$\pi_8 : \frac{L}{R_c}$	R_c, N_r, W_u and I_s	$\pi_{14} : \frac{I_s R_c}{W_u N_r^2}$
R_c, N_r, W_u and d_b	$\pi_3 : \frac{d_b}{R_c}$	R_c, N_r, W_u and ρ	$\pi_9 : \frac{\rho R_c^5}{W_u}$	R_c, N_r, W_u *and* $I_r \frac{n!}{r!(n-r)!}$	$\pi_{15} : \frac{I_r R_c}{W_u N_r^2}$
R_c, N_r, W_u and d_i	$\pi_4 : \frac{d_i}{R_c}$	R_c, N_r, W_u and E_S	$\pi_{10} : \frac{E_S R_c}{W_u N_r^2}$	R_c, N_r, W_u and δ	$\pi_{16} : \frac{\delta}{R_c}$
R_c, N_r, W_u and d_o	$\pi_5 : \frac{d_o}{R_c}$	R_c, N_r, W_u and E_R	$\pi_{11} : \frac{E_R R_c}{W_u N_r^2}$	R_c, N_r, W_u and δ	$\pi_{17} : \frac{C}{W_u N_r}$
R_c, N_r, W_u and d_m	$\pi_6 : \frac{d_m}{R_c}$	R_c, N_r, W_u and W_s	$\pi_{12} : \frac{W_s}{W_u}$	R_c, N_r, W_u and T	$\pi_{18} : \frac{T}{W_u N_r^2 R_c^2}$
R_c, N_r, W_u and B	$\pi_7 : \frac{B}{R_c}$	R_c, N_r, W_u and W_r	$\pi_{13} : \frac{W_r}{W_u}$	R_c, N_r, W_u and Δ	$\pi_{19} : \frac{\Delta}{R_c}$
R_c, N_r, W_u and f_s	$\pi_{20} : \frac{f_s}{N_r}$				

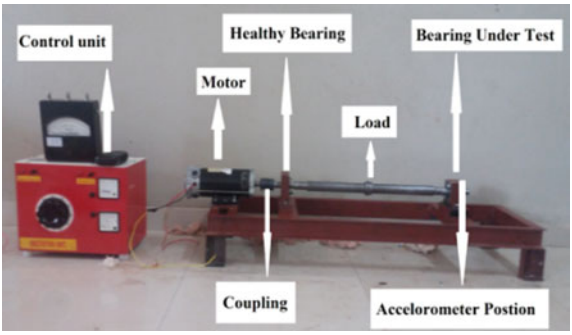

Fig. 1 Experimental setup

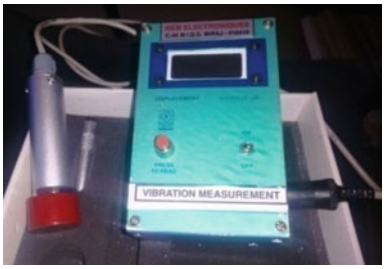

Fig. 2 Vibration meter

Fig. 3 FFT

Table 3 Specifications of bearing

Quantity	Symbol	Specifications
Bearing inner diameter	d	25 mm
Bearing Outer diameter	D	52 mm
Bearing width	B	15 mm
Dynamic load capacity	C	17,700
Static load capacity	Co	15,700
Bearing material	–	52,100 Chrome steel

Table 4 Defects on bearing elements

S. No.	Bearing element	Type of defect	Size
1	Rolling element	Square	1 mm * 1 mm
2	Inner race	Square	1 mm * 1 mm
3	Outer race	Square	1 mm * 1 mm
4	Rolling element	Circular	1 mm ø
5	Inner race	Circular	1 mm ø
6	Outer race	Circular	1 mm ø

(a) Rolling element **(b)** Inner race **(c)** Outer race

(I)

(d) Rolling element **(e)** Inner race **(f)** Outer race

(II)

Fig. 4 Square defect on **a** rolling element, **b** inner race, **c** outer race. Circular defect on **d** rolling element, **e** inner race, **f** outer race

5 Result and Discussion

Experimentation was carried out by changing load and speed for above six defective bearings. Table 5 shows the level of trails with respective load and speed. Using three variables and two levels, a total of eight experiments were designed to obtain amplitude of vibration and defect frequencies.

The repeated experiments were conducted for the experimental data analysis for better evaluation of error. Experimental data were analyzed by using Minitab-16 for response variables. Response amplitude peak values are given in Table 5 for various combinations of defects (Circular and square), speed and load.

Table 5 Taguchi method plan and results

Trial No.	Defect type	1	2	3	Amplitude (Vibrometer) (μm)	Amplitude (FFT) (μm)	Mathematical model
1	Circular	1	1000	10	22	22.932	21.06
2		1	1000	15	24	26.262	24.02
3		1	1500	10	28	30.912	28.50
4		1	1500	15	27	29.532	27.22
5	Square	1 * 1	1000	10	25	27.573	25.64
6		1 * 1	1000	15	24	27.110	24.80
7		1 * 1	1500	10	26	29.110	26.43
8		1 * 1	1500	15	27	29.262	27.00

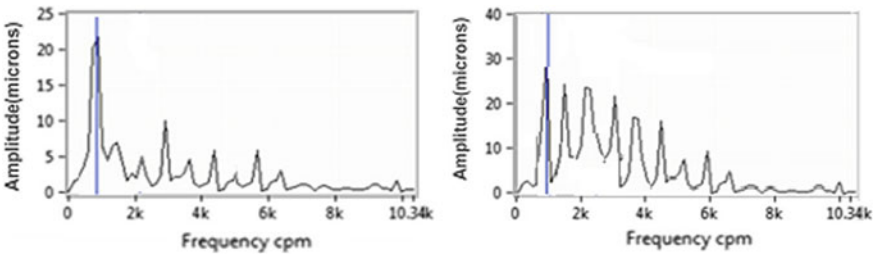

Fig. 5 Amplitude versus frequency plot

Figure 5 shows amplitude of vibration for the circular and square defect on rolling element of bearing only.

Vibration amplitude was calculated by a mathematical model developed using dimensional analysis Eq. (7). The values of amplitude of vibration predicted by the mathematical model and experimental results are shown in Table 5. It is clear that the numerical results and experimental results show good agreement for all eight trials.

6 Conclusion

Summary of outcomes of the investigations:

1. The result obtained using a mathematical model for trial 1 is 22.932 μm and experimental analysis is 21.06 μm matches. Similarly, results in all cases match as shown Table 5.

2. When the rotor-bearing system operates at circular defect level, the system shows periodic behavior. However, when the rotor-bearing system operates at square defect level, the chaos is observed in the system.
3. Vibration level is more for the circular defect (30.912 μm) than that of the square defect (27.110 μm).

References

1. Rafsanjani A, Abbasion S, Farshidianfar A, Moeenfard H (2009) Nonlinear dynamic modeling of surface defects in rolling element bearing systems. J Sound Vib 319:1150–1174
2. Bai C, Zhang H, Xu Q (2013) Subharmonic resonance of a symmetric ball bearing–rotor systems. Int J Non-Linear Mech, 1–10
3. Sinou J-J (2009) Non-linear dynamics and contacts of an unbalanced flexible rotor supported on ball bearings. Mech Mach Theory 44:1713–1732
4. Ghafari SH, Abdel-Rahman EM, Golnaraghi F, Ismail F (2010) Vibrations of balanced fault-free ball bearings. J Sound Vib 329:332–1347
5. Nonato F, Cavalca KL (2010) On the non-linear dynamic behavior of elastohydrodynamic lubricated point contact. J Sound and Vib 329:4656–4671
6. Desavale RG, Kanai RA, Chavan SP (2016) Experimental-based fault diagnosis of rolling bearings using artificial neural network. J Tribol 138:031103-1-9
7. Desavale RG, Chavan SP, Venkatachalam R (2013) Antifriction bearings damage analysis using experimental data based models. J Tribol 135:041105-1-12
8. Desavale RG, Kanai RA, Chavan SP, Venkatachalam R, Jadhav PM (2016) Vibration characteristics diagnosis of roller bearing using the new empirical model. J Tribol 138:011103-1-9
9. Desavale RG, Chavan SP, Venkatachalam R (2014) Experimental and numerical studies on spherical roller bearings using multivariable regression analysis. J Vib Acoust 136:021022-1-10
10. Desavale RG (2019) Dynamics characteristics and diagnosis of a rotor-bearing's system through a dimensional analysis approach: an experimental study. J Comput Nonlinear Dyn 14:014501-1-11

Development of DLP-Based Stereolithography System

Baban Suryatal, Suhas Deshmukh, and Sunil Sarawade

Abstract A low-cost stereolithography (STL) apparatus was developed to produce highly precise, three-dimensional (3D) structures from broad selection of functional materials, especially photopolymer resin. The developed stereolithography apparatus (SLA) utilizes focused light beam of wavelength range (300–700 nm) coming from the DLP projector and passing through the objective lens over the surface of a photocurable resin, which undergoes photopolymerization and forms solid structures. The photopolymer used in this STL system was polyethylene glycol di-acrylate and photoinitiator was Irgacure 784. The Creo 3.0 software was used for modelling of 3D object. A special MATLAB code was developed for slicing of the 3D CAD model. The Creation Workshop software was used to control the z-stage motion with the help of Arduino microcontroller, stepper motor, and ball screw. It also controls time period to display the sliced images through DLP projector and settling period. The experiments were successfully performed to built hexagonal cross-section and pyramid objects with 0.1 mm curing depth and two seconds curing time. The pyramid object with maximum 120 numbers of layers with 12 mm maximum dimension along Z-axis was build.

B. Suryatal (✉)
Mechanical Engineering Department, Sinhgad College of Engineering Vadgaon (Bk.), Savitribai Phule Pune University, Pune, Maharashtra 411041, India
e-mail: bksuryatal@gmail.com

Mechanical Engineering Department, PDEA's College of Engineering, Manjari (Bk.), Pune, Maharashtra 412307, India

S. Deshmukh
Mechanical Engineering Department, Government Engineering College, Karad, Maharashtra 415124, India
e-mail: suhas.deshmukh@gmail.com

S. Sarawade
Mechanical Engineering Department, MES College of Engineering, Pune, Maharashtra 411001, India
e-mail: sunilsarawade36@gmail.com

N. Gascoin and E. Balasubramanian (eds.), *Innovative Design, Analysis and Development Practices in Aerospace and Automotive Engineering*, Lecture Notes in Mechanical Engineering, https://doi.org/10.1007/978-981-15-6619-6_21

Keywords Stereolithography (STL) · Digital light processing (DLP) projector · Photopolymer · Photoinitiator

1 Introduction

Nowadays, rapid prototypes of the different objects are required before its actual manufacturing because one can improve the design before its actual manufacturing. This technology is very fast growing one and can be applicable to all the fields, i.e., engineering as well as non-engineering. The present 3D printers available in the market are very costly one. In this research paper, a low-cost stereolithography apparatus (SLA) was developed which will be affordable to anybody with low cost of printing. Ikuta et al. [1] introduced micro stereolithography technology and also proposed a means of applying micro stereolithography in mass-production using an optical fiber array so that multiple microstructures could be fabricated in a single process. Bertsch et al. [2] developed a micro stereolithography apparatus employing a pattern generator in which a UV laser and dynamic LCD pattern generator were used to generate the cross-section of a 3D structure. While the substrate did not move in the *x*–*y*-direction in the liquid photopolymer, an LCD pattern generation system was necessary. Itoga et al. [3] developed maskless photolithography device by modifying liquid crystal display (LCD) projector optics from magnified to reduced projection. But they arise problems in jagged pattern boundaries due to the liquid crystal panel structure and collapse pattern of the boundary divided on divisional exposure using the auto-XY stage. Hadipoespito et al. [4] developed DMD-based UV microstereolithography system for fabricating 2D and 3D microparts providing reasonable curing speed and good resolution at a low cost. In this method, process optimization is needed to improve the quality of fabricated microparts. Zhou and Chen [5] presented a novel AM process based on the mask video projection. For each layer, a set of mask images instead of a single image is planned based on the principle of optimized pixel blending. Compared to fused deposition modelling (FDM) machines, machines for DLP stereolithography are expensive and thus not available to a broad range of users as it is the case with FDM 3D printers. Gandhi et al. [6] analyzed various optical scanning schemes used for MSL systems by optical simulations and experiments. The mechanical design of the scanning mechanism is carried out to meet requirements of high speed and resolution. The system integration and investigation in process parameters are carried out and large microcomponents with high resolution are fabricated. Valentincic et al. [7] conclude that constrained

surface (illumination through a transparent bottom of the vat) gives better 3D printing accuracy compared to free surface (illumination of the photopolymer surface). The all above-described stereolithography apparatus are very costly which are not affordable to common- or medium-sized industries or vendors who can build their prototypes with a cheaper cost. Therefore, development of a low-cost SLA is necessary and which was the goal of this research.

2 Experimental Setup

2.1 Stereolithography Apparatus (SLA)

A low-cost stereolithography apparatus (SLA) was developed to produce highly precise, three-dimensional (3D) structures from broad selection of functional materials, especially photopolymer resin. The experimental setup is shown in Fig. 1. The developed stereolithography apparatus (SLA) utilizes focused light beam from DLP projector and then through the objective lens over the surface of a photocurable resin, which undergoes photopolymerization and forms solid structures. The lamp of the modified DLP projector works as light source and DMD chip in the DLP projector works as a dynamic pattern generator. The color wheel of the DLP projector was filtering most of the UV light out. Therefore, glass portion of the color wheel was removed so that maximum UV light should focus by the projector which was our requirement for solidification of the photopolymer. Infocus makes DLP projector with display resolution 1024 × 768 was used.

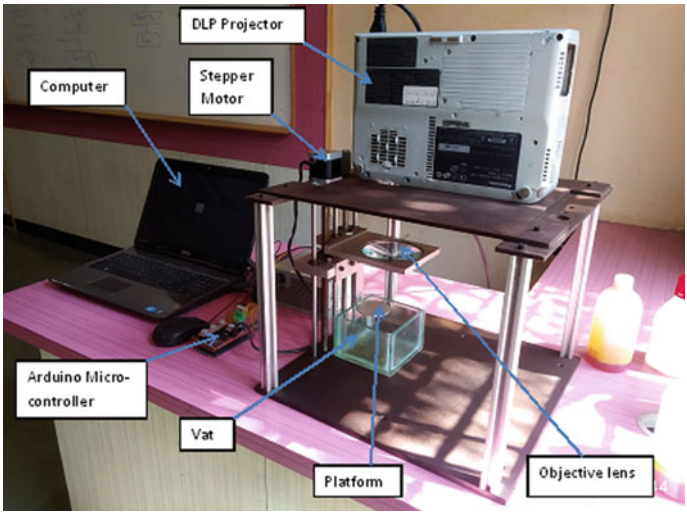

Fig. 1 Experimental setup

The photopolymer used in this experimentation was polyethylene glycol diacrylate and 2% Irgacure 784 as a photoinitiator was added in the photopolymer. The maximum absorbance of the photopolymer was in the range of 315–340 nm. The stepper motor was used to rotate the ball screw which moves the Z-stage platform up and down. The sliced layer image was focused on platform through projector and objective lens. The sliced image consists of black and white portion; the photopolymer on the platform with white portion of the focused image was solidified. The Creo 3.0 software was used for modelling of 3D CAD model. A special MATLAB code was developed for slicing of the 3D CAD model and this sliced 3D CAD model was imported into the Creation Workshop software which was used to control the focusing time period of sliced images through DLP projector. The Creation Workshop software also controls the motion of the Z-stage through Arduino MEGA 2560 microcontroller and NEMA 17 bipolar stepper motor. Finally, the different shape objects are built by curing the aforementioned photocurable resin. The digital microscope was used to measure the dimensions of the built parts. The overall cost of the developed SLA is two lac thirty five thousand Indian Rupees only.

2.2 Slicing of 3D CAD Model

The 3D CAD model of the object which was to be built by using STL process was developed with the help of CREO 3.0 software and then it was saved in .STL file format. The .STL file consists of an unordered list of triangular facets that represent the outside skin of a part. The triangular facets are described by a unit normal vector and a set of X, Y, and Z coordinates for each of the three vertices. The unit vectors indicate the outside of the part. Since the STL model consists of triangular facets, it is an approximate model of the accurate CAD data. .STL file is a simple solution for representing 3D CAD data and it provides small and accurate files for data transfer for specific shapes [8]. After generating the .STL file of the 3D CAD model, then it was sliced into a number horizontal cross-sections with the help of specially developed MATLAB code by using ray tracing method [9]. The sliced CAD model in MATLAB window is shown in Fig. 2. The sliced CAD model was imported in Creation Workshop software and the sliced layers were focused one by one at required time interval with the help of DLP projector through objective lens on the Z-stage platform and finally, the 3D object was built.

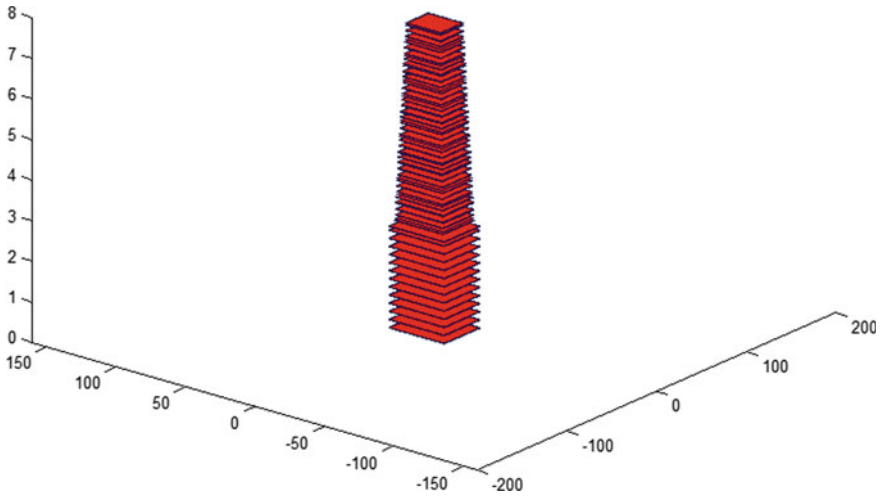

Fig. 2 Sliced CAD model in MATLAB

2.3 ARDUINO Programming

In the Z-stage, we have to control the linear movement of the platform with the help of stepper motor and ball screw. The stepper motors rotational motion was transformed into linear motion with help of ball screw coupled with motor shaft. The rotational movement of the stepper motor was controlled with the help of special Arduino program. The program mainly consists of various commands and statements to control the various parameters like speed, time delay, etc. With the used ball screw and stepper motor, the Z-stage can move with 0.005 mm minimum distance. The Arduino microcontroller with stepper motor was interfaced with Creation Workshop Software to obtain desired motion of Z-stage.

3 Experimental Results and Discussions

The experiments were performed on objects with hexagonal cross-section and pyramid objects with 0.1 mm curing depth along Z-axis. The trials were performed with different exposure time and settling period. The exposure time was varied from 10 to 1 s and it was observed that the objects were best cured for 2 s curing time. The pyramid object with 120 numbers of layers with 12 mm dimension along Z-axis was cured. The maximum area 18 mm $\times$ 16 mm of pyramid object along X-Y plane was cured. The resolution in Z-axis of 0.25 mm creates a fairly coarse surface for medium-sized parts, but for larger models, the layer steps are not too noticeable due to the relative size of larger parts. A resolution of 0.1 mm provides a more favorable surface finish for medium and small parts [10, 11]. Therefore, experiments

were performed with 0.1 mm curing depth along Z-axis. For DMD-based SLA, the maximum model size obtained with 0.1 mm minimum layer thickness in the available literature was 60 mm × 80 mm [11]. Therefore, maximum exposure area of 55 mm × 45 mm in our SLA shows the good agreement to build medium-sized parts. It was observed that as the curing time decreases, the percentage error between the 3D CAD model dimensions and build dimensions was also decreases. The maximum and minimum percentage errors for hexagonal cross-section object were 9.43 and 2.0, respectively. The maximum and minimum percentage errors for pyramid object were 4.5 and 1.77, respectively. The minimum percentage error was observed for 2 s curing time. The maximum percentage error between the CAD models and build components dimensions is also below 10% which shows the good agreement with the results available in the literature [10, 11]. Observed that the resolution of the build components depends upon software imposed parameters like width compensation, .STL file resolution, layer thickness, z compensation, and STL process parameters like light beam size and intensity, light beam focus depth, and layer thickness [12]. The experimental test data for hexagonal cross-section and pyramid objects are given in Table 1. The cured objects are shown in Figs. 3 and 4.

4 Conclusions

A low-cost stereolithography apparatus (SLA) was successfully developed to built 3D components. The trials were performed with different exposure time and settling time. The exposure time was randomly varied from 10 to 1 s and it was observed that the objects were best cured by 2 s curing time. The maximum and minimum percentage errors observed were 9.43 and 1.77, respectively. The percentage error was minimum for 2 s curing time. The pyramid object with maximum 120 numbers of layers with 12 mm dimension along Z-axis was built in 11.0 min. The maximum area 18 mm × 16 mm of pyramid object along X-Y plane was cured. The maximum exposure area obtained in X-Y plane was 55 mm × 45 mm. The objects were built with 0.1 mm curing depth due to limitations of the experimental setup. It is necessary to perform the experiments with values lower than 0.1 mm curing depth so that resolution of object along Z-axis will be improved.

Table 1 Experimentation data of built objects

Object cross-section	Measuring scale	Dimensions (in mm)			Layer thickness (mm)	Number of layers	Exposure time (s)	Settling period (s)	Build time (min)
		x	*y*	*z*					
Hexagon (7 mm side)	CAD model	14	14	10	0.1	100	2.0	3.5	9.17
	Built object	15.32	14.28	10.64					
	% Error	9.43	2.0	6.4					
Pyramid	CAD Model	18	16	12	0.1	120	2.0	3.5	11.0
	Built object	17.68	16.72	11.72					
	% Error	1.77	4.5	2.33					

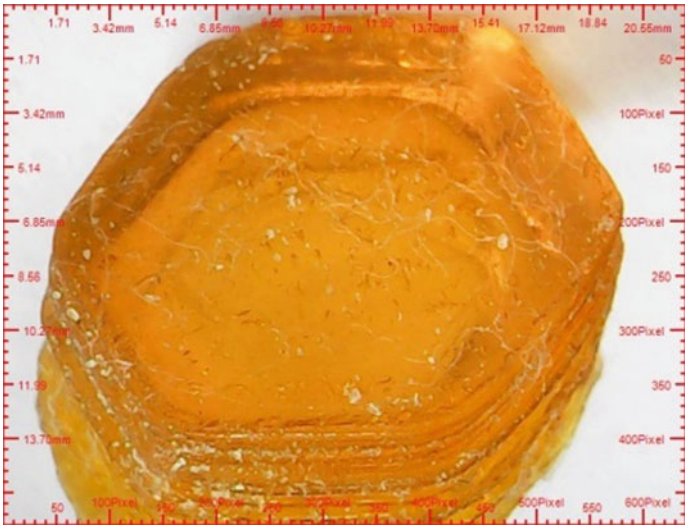

Fig. 3 Hexagonal cross-section object

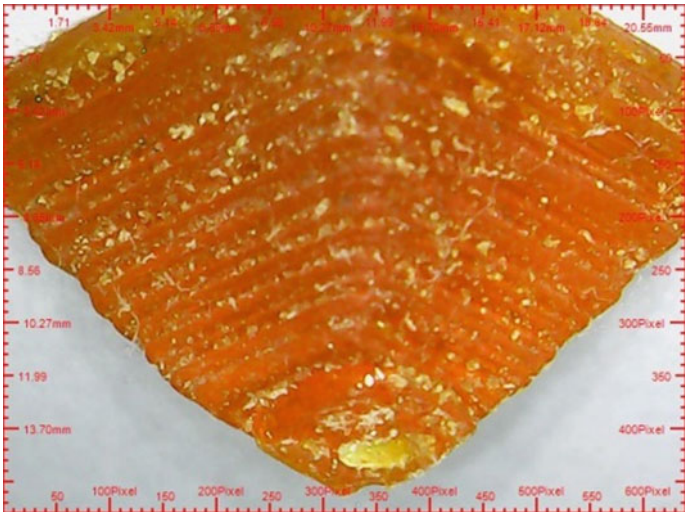

Fig. 4 Pyramid object

Acknowledgements The authors are thankful to the Board of Colleges and University Development (BCUD) of Savitribai Phule Pune University, Pune, Maharashtra, India for funding this research project under the grant number OSD/BCUD/360/122. The authors are also thankful to Management of Pune District Education Association's College of Engineering, Manjari (Bk.), Pune for permitting to carry out this research work.

References

1. Ikuta K, Hirowatari K (1993) Real three-dimensional microfabrication using stereolithography and metal mold. In: Proceedings of IEEE international workshop on micro electro mechanical systems (MEMS'93), pp 42–47
2. Bertsch A, Zissi S, Jezequel J, Corbel S, Andre J (1997) Microstereolithography using liquid crystal display as dynamic mask-generator. Microsyst Technol 3(2):42–47
3. Itoga K, Kobayashi J, Yamato M, Okano T (2010) Development of microfabrication technology with maskless photolithography device using LCD projector. J Robot Mechatron 22(5)
4. Hadipoespito GW, Yang Y, Choi H, Ning G, Li X (2003) Digital micromirror device based microstereolithography for micro structures of transparent photopolymer and nanocomposites. Department of Mechanical Engineering University of Wisconsin-Madison, Madison, WI 53706
5. Zhou C, Chen Y (2011) Additive manufacturing based on optimized mask video projection for improved accuracy and resolution. in: Proceedings of NAMRI/SME, vol 39
6. Gandhi P, Deshmukh S, Ramtekkar R, Bhole K, Baraki A (2013) "On-axis" linear focused spot scanning microstereolithography system: optomechatronic design, analysis and development. J Adv Manuf Syst 12(01):43–68
7. Valentincic J, Perosa M, Jerman M, Sabotin I, Lebar A (2017) Low cost printer for DLP stereolithography. J Mech Eng 63(10):559–566
8. Chua C, Leong K, Lim C (2010) Rapid prototyping: principles and applications, 3rd edn. World Scientific
9. Kwok TH (2019) Comparing slicing technologies for digital light processing printing (ASME). Department of Mechanical, Industrial and Aerospace Engineering Concordia University Montreal, Canada
10. Zyzalo JR (2008) Masked projection stereolithography: improvement of Limaye model for curing single layer medium sized parts. Ph.D. thesis, Massey University, Albany, New Zealand
11. Takahasi K (2001) A new application of DMD to photolithography and rapid prototyping system. In: 8th international display workshops, pp 1339–1342
12. Sager B, Rosen D, Stereolithography process resolution. The George W. Woodruff School of Mechanical Engineering Georgia Institute of Technology, Atlanta, USA

Experimental Investigation on Geometric Accuracy and Surface Roughness of Formed Part in Multistage Single Point Incremental Forming (SPIF) Process

Sunandkumar Gajjar, Vikas Sisodia, Rahul Jagtap, Kiran More, and Shailendra Kumar

Abstract Single point incremental forming (SPIF) process is an advanced dieless sheet metal forming process in which the requirement of a dedicated punch-die setup is eliminated. The dedicated punch-die setup is replaced by a universal blank holding fixture, a punch (or tool), and a backing plate. It has a variety of applications ranging from automotive to biomedical fields. But its limitations such as inability to form steeper wall angle and high geometric error in single-stage restricts its application in sheet metal industries. To overcome this, multistage SPIF process is an alternative to achieve larger wall angles. Formability in multistage SPIF process is increased by providing intermediate stages. Various methodologies have been suggested to enhance the profile accuracy, however, it still remains the major issue. In the present paper influence of process variables namely feed rate, number of forming stages and pitch size on geometric accuracy and surface roughness of formed part is investigated. Taguchi L_{18} orthogonal array is used for design of the experiments. From the analysis of variance (ANOVA), it is found that the number of stages and pitch size have a significant influence on geometric accuracy and surface roughness. Since feed rate is an insignificant parameter. So a higher feed rate can be used to reduce forming time. Further, a mathematical model is developed to predict the geometrical accuracy and surface roughness of the formed part.

Keywords Single point incremental forming (SPIF) process · Multistage · Geometric accuracy · Surface roughness · Wall angle

S. Gajjar
Department of Mechanical Engineering, Parul Institute of Technology, Parul University, Vadodara, Gujarat 391760, India

V. Sisodia (✉) · K. More · S. Kumar
Department of Mechanical Engineering, Sardar Vallabhbhai National Institute of Technology, Surat, Gujarat 395007, India
e-mail: vikas.singh619@gmail.com

R. Jagtap
School of Mechanical Engineering, MIT-World Peace University, Pune, Maharashtra 411038, India

N. Gascoin and E. Balasubramanian (eds.), *Innovative Design, Analysis and Development Practices in Aerospace and Automotive Engineering*, Lecture Notes in Mechanical Engineering, https://doi.org/10.1007/978-981-15-6619-6_22

1 Introduction

Single point incremental forming (SPIF) process is a dieless advanced sheet metal forming technique in which the sheet is deformed to a final shape by deforming series of intermediate shapes. SPİF is especially suitable for small batch production. SPIF process has various benefits over conventional sheet forming processes such as relatively high formability, production of parts directly from the computer-aided design (CAD) file, easy and quick design changes, small forming forces, etc. However, low geometric accuracy is the main disadvantage that restricts the application of SPIF process in the industry.

Figure 1 depicts the layout of SPIF process. In this process, a forming tool is given motion according to a predefined contour at a given vertical depth increment which gradually deforms the sheet metal blank. The formed part with a steep wall with the help of single-stage SPIF process is difficult to achieve because as per sine law if the drawing angle is 90°, the final thickness approaches zero leading to infinite strain. Therefore, the present paper deals with the concept of multi-stage SPIF to resolve unreasonable thinning and prevent crack in forming parts at steep walls. A multistage process is able to achieve the final part with higher wall angle by forming intermediate shapes. Each intermediate shape represents an individual forming stage.

Many researchers have made efforts in the domain of SPIF process. For example, Ham and Jeswiet [2] suggested the methodology to map the forming parameters which are critical in SPIF process and the level to which they influence formability. Echrif and Hrairi [3] investigated the influence of different process variables on surface roughness. They reported that the tool size and the step size are major factors influencing the surface roughness. With large tool size and less step size relatively smoother was obtained. Li et al. [4] reported a significant influence of elastic supports on springback and formability. Profile deviation significantly reduced in order with supports made up of polyurethane, followed by rubber and finally wood. Camara et al. [5] reported that severe necking appears in the parts formed at higher tool diameter. Singh and Kumar [6] and Zhang et al. [7] suggested that springback can be reduced by annealing. Li et al.[8] studied geometric accuracy of formed part and concluded

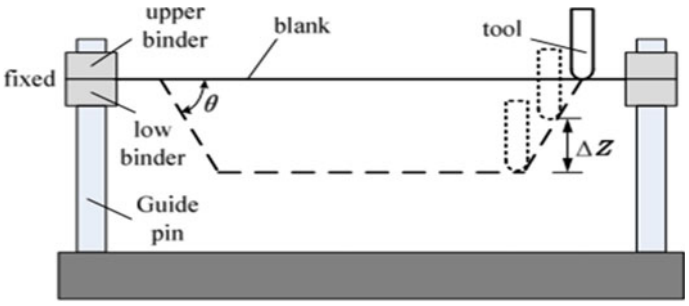

Fig. 1 Layout of SPIF process [1]

that decreasing the step size was effective in improving geometric accuracy. Edwards et al. [9] reported that increase in step size results in reduced spring back. Kumar et al. [10] investigated the influence of process variables such as tool diameter, step size and spindle speed on surface characteristics in SPIF process. İt is reported that surface roughness increase as spindle speed and tool diameter decrease whereas it decreases with the decrease in step size. Salem et al. [11] investigated thickness variation in SPIF process. Continuous thickness reduction is observed that a bending region and thereafter a region of excessive thinning (thinning band) occurs, followed by a steady-state region of constant thickness in formed part. Behera and Ou [12] reported that the pre-forming heat treatment enhanced the average roughness while post-forming heat treatment improved surface and accuracy formed part. Isidore et al. [13] investigated the role of tool shape and tool size on pillow defect (responsible for reducing geometric accuracy). It was observed that influence of changing tip shape of tool hemispherical to flat was more effective than varying tool size. Skjoedt et al. [14] presented the multistage process which is used to produce a cup with a 90° wall angle which has not been possible before. Skjoedt et al. [15] observed that the overall level of strains achieved in multi-stage SPIF process is much higher than the conventional SPIF process. Li et al. [16] investigated the influence of number of stages and step increment in wall angle on the formability in ISF process. Uniform thickness distribution was observed as forming stages increase. Liu et al. [17] reported at smaller wall angle less thinning of sheet occurs. Kurra et al. [18] reported that because of springback effect fracture occurred at the corners so it became necessary for the tool to deform more material in the later stages.

From the literature review, it is found that a multistage SPIF process is a viable option for forming parts of steeper wall angles with uniform wall thickness along with the forming depth. Very less research efforts have been made to study multistage SPIF process. Therefore, in the present work, the influence of the process variables on the geometric accuracy and the surface roughness of the formed part is investigated. Experiments are designed using Taguchi L_{18} orthogonal array. Also, predictive models for geometry accuracy and surface roughness in multistage incremental sheet forming are developed.

2 Experimental Plan and Methodology

İn present work, experiments are designed with the help of Taguchi L_{18} orthogonal array. Experimental investigation has been done by using a 3–axis CNC milling machine. Aluminium alloy AA 1080 of 1.22 mm thickness is used sheet material. A conical frustum with 110 mm base diameter and 70º wall angle with 45 mm upper bound of height is formed. As shown in Fig. 2, the sheet is held along its edges with the help of a fixture and the tool is introduced to deform the sheet into the desired shape. High-speed steel is taken as tool material (Fig. 3).

In multistage forming, number of forming stages and increment angles are important factors influencing geometric accuracy and thickness distribution. Therefore,

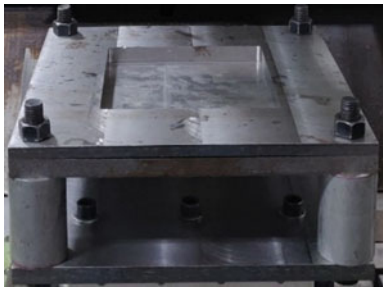

Fig. 2 Fabricated fixture

Fig. 3 Forming tool

experiments are performed using a different number of forming stages (single stage, two stages, three stages). Table 1 shows the number of stages and corresponding wall angles. Figure 4 shows the drawing of desired formed parts with wall angle 40°, 55° and 70°, respectively.

All eighteen experiments are carried out using Taguchi L_{18} orthogonal array. The process variables and their levels are listed in Table 2 and Taguchi design matrix is presented in Table 3. Influence of three process parameters namely number of stages (N), pitch size (P) and feed rate (F) on responses namely geometric accuracy (using RMSE - root mean square error method) and surface roughness (R_a value) is studied.

The response geometric accuracy is measured using RMSE - root mean square error method. Formed parts are masked using Spotcheck's SKD-S2 developer spray and scanned using Dr. PICZA 3D laser scanner and it is as shown in Fig. 5. The part is scanned and the data is processed and saved in point cloud data form which is then imported in SolidWorks modelling software as depicted in Fig. 6. After importing this point cloud data in SolidWorks software an outer profile of the formed part is produced, which is the deformed part profile. This profile is compared with the target part profile. The deviation between target and formed part profile is recorded at 42

Table 1 Forming stages and respective wall angle

Number of forming stages	1	2	3
Respective wall angle (in degrees)	70°	55° and 70°	40°, 55° and 70°

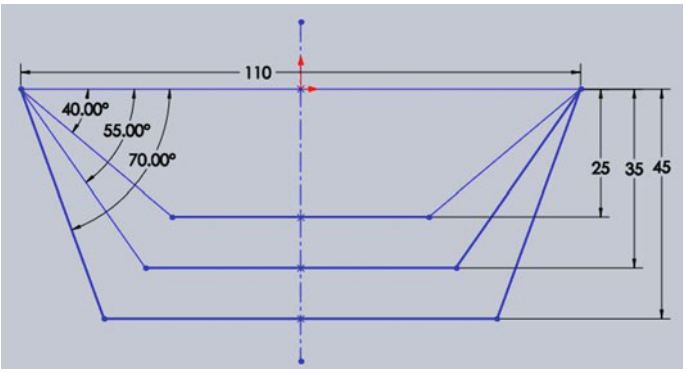

Fig. 4 Part drawings at different wall angles

Table 2 Process variables and their levels

Variables	Unit	Level (1)	Level (2)	Level (3)
Feed rate	mm/min	2400	3600	–
Pitch	mm	0.3	0.65	1
Number of stages	–	1	2	3

Table 3 Taguchi design matrix

Exp. No.	Feed rate (mm/min)	No. of stages	Pitch size (mm)
1	2400	1	0.3
2	2400	1	0.65
3	2400	1	1
4	2400	2	0.3
5	2400	2	0.65
6	2400	2	1
7	2400	3	0.3
8	2400	3	0.65
9	2400	3	1
10	3600	1	0.3
11	3600	1	0.65
12	3600	1	1
13	3600	2	0.3
14	3600	2	0.65
15	3600	2	1
16	3600	3	0.3
17	3600	3	0.65
18	3600	3	1

different points along with the forming depth. This difference in target and formed part profile is geometrical deviation or error. Then this geometric error is converted into root mean square error (RMSE) using Eq. (1).

$$\text{RMSE} = \sqrt{\frac{\sum_{i=1}^{n}(x_i - x_o)^2}{n}} \tag{1}$$

where

x_i Target values;
x_o Observed value.

The surface roughness is measured using Mitutoyo's SJ-310 surface roughness tester (as depicted in Fig. 7). Surface roughness is measured at four places in inner

Fig. 5 **a** Component sprayed for scanning; **b** Dr. Picza 3D laser scanner

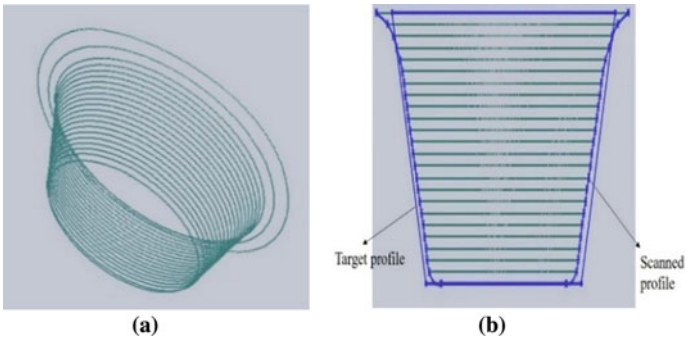

Fig. 6 **a** Scanned point cloud; **b** Comparison of scanned and target profile

Fig. 7 Mitutoyo's surftest SJ-310

Table 4 ANOVA results for geometric accuracy

Source	DF	SS	MS	*F*-Value	*P*-Value	Remarks
Regression	3	2.6615	0.8872	28.78	0.00	Significant
Feed	1	0.0013	0.0013	0.04	0.84	
Stages	1	2.3949	2.3949	77.70	0.00	Significant
Pitch	1	0.2653	0.2653	8.61	0.01	Significant
Error	14	0.4315	0.0308			
Total	17	3.093				
Model summary						
S (Std. deviation)	R^2			R^2 (modified)		
0.175563	86.05%			83.06%		

circular region of the formed shape. Average of these four readings is considered as a response for analysis purposes.

3 Results and Discussion

The results obtained from ANOVA are used to identify the influence of process variables and their interactions on responses (i.e. geometric accuracy and surface roughness) are discussed in this section. The results are analysed using Minitab 18.1 numerical firmware.

3.1 Geometric Accuracy

Table 4 shows the involvement of each factor to the overall variation that indicates the extent of influence on the geometric accuracy in the Analysis of Variance. Table 4 clearly shows that the model's p-value is less than 0.05, therefore model is significant. It is observed that number of stages and pitch sizes are significant process variables and feed rate is insignificant. Thus, all three parameters significantly affect the geometric error except the feed rate.

The R^2 statistics (i.e. R^2 and modified R^2) for the geometric error study are given in Table 4. Values of $R^2 = 86.05\%$ suggest that the model describes 86.05% of the overall variance of the geometric error. Values of R^2 modified $= 83.06\%$ suggest that the model clarified 83.06% of overall variability. Geometric accuracy in terms of RMSE varies within the range from 1.9028 to 3.23085 mm. Based on results a regression formula for geometric error in terms of RMSE is given Eq. 2.

$$\text{Geometric error(RMSE)} = 3.189 - 0.000014 \times F - 0.4467 \times N + 0.425 \times P \tag{2}$$

where

F Feed rate;
N Number of stages;
P Pitch Size.

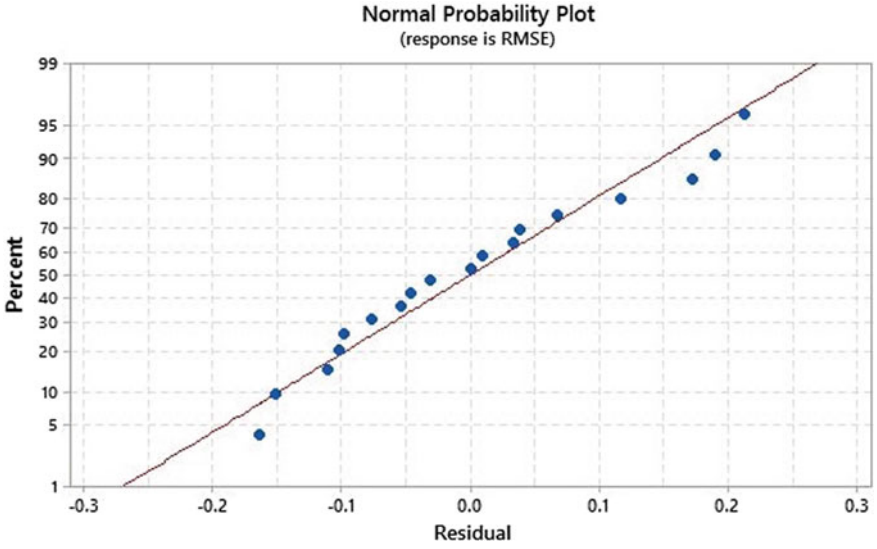

Fig. 8 Normal probability plot for geometric accuracy

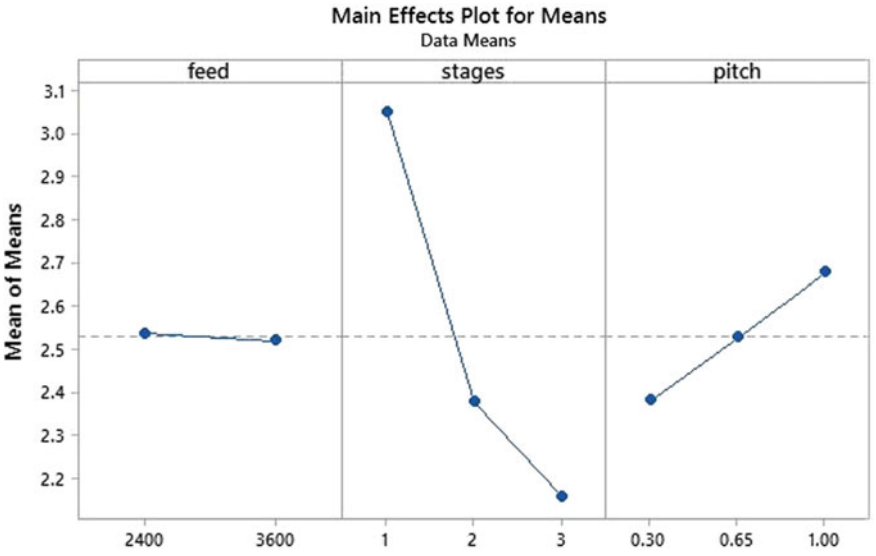

Fig. 9 Main effects plots for geometric accuracy

The normality plot of the residuals in Fig. 8 shows that many residual points fall on a straight line which implies that the error distribution is normal and the residuals follow the normality plot. Figure 9 shows the main effect plot for geometric accuracy. As shown in the graph, feed rate has a small influence on geometric accuracy compared to other parameters. As feed rate increases, the RMSE value decreases but the variation is not significant.

It is observed from the main effect plot that with an increase in pitch size, RMSE value increases. This is because the forming profiles generated are more intense when the pitch value is set at a low value. And also the action of the forming tool is less between two contiguous profiles which provides greater uniform material distribution and plastic deformation along forming depth. Therefore, for better geometric accuracy, a small pitch should be used. It is observed from Fig. 9 that the RMSE value decreases with an increase in the number of forming stages. In the first stage, since undeformed sheet is deformed at wall angle of 40°, the springback is considerable. Therefore, accuracy after first stage is low because of global and local springback. Further, in second stage, 40° wall angle part is deformed (to 55° wall angle) rather than deforming raw sheet. Thus, spring back in second stage is less relative to spring back in first stage and similar is the case with third stage. So, as the number of stages increases, spring back decreases and geometric accuracy increases. It can be observed from main effects plots that maximum geometric accuracy is achieved using three stages, 0.3 mm pitch and 3600 mm/min feed rate. Table 5 shows the resemblance between the RMSE values of experimental and prediction (using the developed mathematical model).

Table 5 Observed and predicted values of RMSE

Exp. Run order	Observed RMSE (mm)	Predicted RMSE (mm)	Error (%)
1	2.9123	2.8362	2.6831
2	3.2309	2.9849	8.2396
3	3.1072	3.1337	0.8456
4	2.4275	2.3895	1.5902
5	2.3084	2.5382	9.0555
6	2.5044	2.6870	6.7957
7	2.0851	1.9428	7.3244
8	2.0016	2.0915	4.3006
9	2.2614	2.2403	0.94184
10	2.7834	2.8194	1.2769
11	3.0504	2.9681	2.7710
12	3.2247	3.1169	3.4585
13	2.1744	2.3727	8.3576
14	2.2165	2.5214	12.094
15	2.635	2.6702	1.3183
16	1.9029	1.9260	1.1994
17	2.3602	2.0747	13.7583
18	2.337	2.2235	5.1045

3.2 Surface Roughness

Analysis process used for geometric accuracy is also performed for surface roughness. The Analysis of Variance for surface roughness is given in Table 6. It is observed that number of stages and pitch size are significant and the feed rate is insignificant. Thus, all three parameters significantly affect the surface roughness except the feed rate.

Table 6 Analysis of variance for surface roughness

Source	DF	SS	MS	*F*-Value	*P*-Value	Remarks
Feed rate	1	0.0055	0.0055	0.17	0.686	
No. of stages	2	0.8884	0.4442	13.89	0.001	Significant
Pitch size	2	0.2833	0.1416	4.43	0.036	Significant
Error	12	0.3837	0.03198			
Total	17	1.5609				
Model summary						
S (Std. deviation)	R^2			R^2 (modified)		
0.178825	75.42%			65.17%		

The R^2 statistics for surface roughness study (i.e. R^2 and modified R^2) are given in Table 6. The values of $R^2 = 75.42\%$ for surface roughness indicate that the model describes 75.42% of overall variation in surface roughness. The modified R^2 is a size-adjusted statistic; that is the number of factors. Values of modified $R^2 = 65.17\%$ suggest that the model clarified 65.17% of overall variability. Surface roughness in terms of R_a obtained is in the range of 0.833–1.7803 μm. From ANOVA analysis, the regression formula for surface roughness in terms of R_a is given in Eq. 3,

$$R_a = 0.410 + 0.00029 \times F + 0.2604 \times N + 0.387 \times P \tag{3}$$

where

F Feed rate;
N Number of stages;
P Pitch Size.

The normality plot of the residuals (Fig. 10) shows that many residual points fall on a straight line. Figure 11 shows the main effect plot for surface roughness. It is observed from the main effect plot that with an increase in pitch, surface roughness increases. The reason behind the worse surface quality is the tool impressions leave on the formed shapes when using higher pitch values (0.65 mm or 1.00 mm). Also, at larger pitch, the scallop height is more, and thus the surface waviness is more. For small pitch value (0.35 mm), the formed surface is much smoother with no-tool impressions on the part. Therefore, for better quality small pitch size should be used.

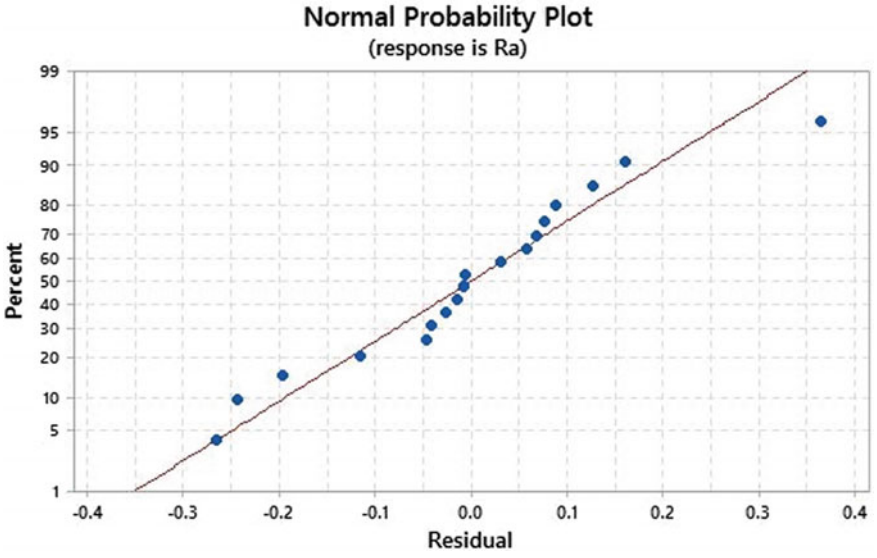

Fig. 10 Normal probability plot for surface roughness

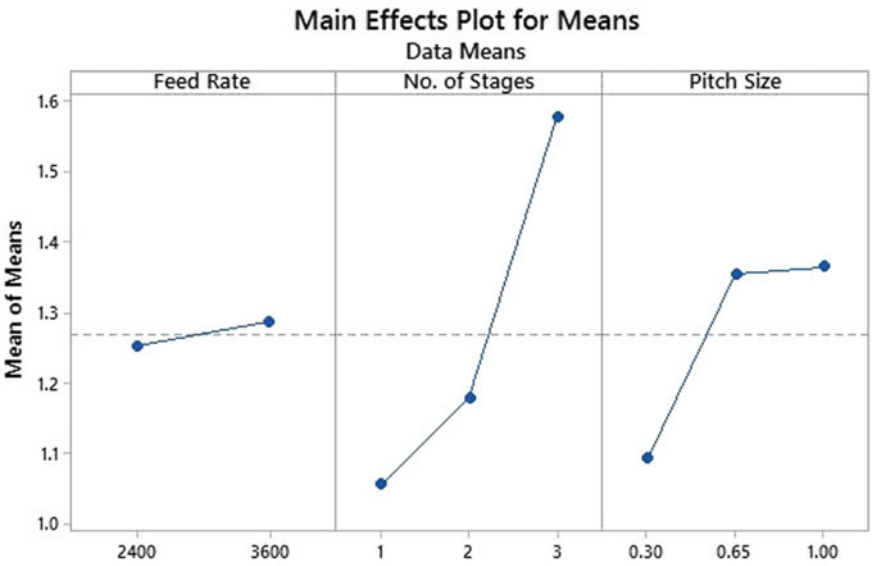

Fig. 11 Main effects plots for surface roughness

It is observed from Fig. 11 that with an increase in the number of forming stages surface roughness increases. It is due to the frequent reprocessing of the formed part (i.e. in intermediate stages) in which tooltip touches the formed shape more than once can result in poorer end surface quality of a component. As feed rate increases the surface roughness decreases. This is because the heat generated due to friction at tool-sheet interface increases. This softens the sheet metal and since the tool is harder it leaves an impression of its movement on sheet metal. This is why the surface roughness increases as feed increases. Table 7 shows the resemblance between the Ra values of experimental and prediction (using the developed mathematical model).

4 Conclusions

In the present work, influence of process variables on geometric accuracy and surface roughness of the part formed by the multistage SPIF process has been investigated. The following conclusions are drawn from the present study.

1. Number of forming stages and pitch size have a significant effect on geometric accuracy. Number of stages is the most significant parameter, followed by pitch size. With an increase in the number of forming stages, RMSE decreases. While part formed at large pitch sizes, values have poor geometric accuracy.

Table 7 Observed and predicted values of R_a (μm)

Exp. Run order	Observed R_a (μm)	Predicted R_a (μm)	Error (%)
1	0.8333	0.8561	2.6691
2	1.2818	0.9916	29.2673
3	1.2195	1.127	8.2076
4	0.9695	1.1165	13.1661
5	1.3015	1.2520	3.9578
6	1.3808	1.3874	0.4793
7	1.1145	1.3769	19.0573
8	1.5258	1.5124	0.8860
9	1.646	1.6478	0.1092
10	0.8873	0.8909	0.4097
11	0.9128	1.0264	11.0683
12	1.1968	1.1618	3.0083
13	0.9713	1.1513	15.6388
14	1.35575	1.28675	5.3623
15	1.09375	1.4222	23.0945
16	1.78025	1.4117	26.1068
17	1.74375	1.54715	12.7072
18	1.6455	1.6826	2.2049

2. Number of forming stages and pitch sizes also have significant effect on surface roughness. As number of forming stages and pitch size is increased, surface roughness increases.
3. As feed rate has no influence on surface roughness and geometric accuracy of formed part, therefore high feed rate should be used to reduce forming time.

Mathematical models for geometric accuracy and surface roughness have been developed which are in good agreement with experimental results. With multistage strategy, geometric accuracy of formed parts improves.

References

1. Li JC, Geng P, Pan JJ (2012) Influences of process parameters on forming performance of sheet metal incremental forming based on numerical simulation. Adv Mater Res 562:294–297
2. Ham M, Jeswiet J (2006) Single point incremental forming and the forming criteria for AA3003. CIRP Ann 55(1):241–244
3. Echrif SB, Hrairi M (2014) Significant parameters for the surface roughness in incremental forming process. Mater Manuf Process 29(6):697–703
4. Li J, Bai T, Zhou Z (2014) Numerical simulation and experimental investigation of incremental sheet forming with an elastic support. Int J Adv Manufact Technol 74(9–12):1649–1654

5. Camara J (2009) Single point incremental forming. Phd Thesis [University—Instituto Superior Técnico]
6. Singh P, Kumar N (2015) Experimental and statistical study on spring- back behavior in incremental sheet metal forming process. Int J Innovat Res Sci Eng Technol 4:8124–8130
7. Zhang Z, Zhang H, Shi Y, Moser N, Ren H, Ehmann KF, Cao J (2016) Springback reduction by annealing for incremental sheet forming. Procedia Manufact 5:696–706
8. Li Y, Lu H, Daniel WJ, Meehan PA (2015) Investigation and optimization of deformation energy and geometric accuracy in the incremental sheet forming process using response surface methodology. Int J Adv Manufact Technol 79(9–12):2041–2055
9. Edwards WL, Grimm TJ, Ragai I, Roth JT (2017) Optimum process parameters for springback reduction of single point incrementally formed polycarbonate. Procedia Manufact 10:329–338
10. Kumar A, Gulati V, Kumar P (2018) Investigation of surface roughness in incremental sheet forming. Procedia Comput Sci 133:1014–1020
11. Salem E, Shin J, Nath M, Banu M, Taub AI (2016) Investigation of thickness variation in single point incremental forming. Procedia Manufact 5:828–837
12. Behera AK, Ou H (2016) Effect of stress relieving heat treatment on surface topography and dimensional accuracy of incrementally formed grade 1 titanium sheet parts. Int J Adv Manufact Technol 87(9–12):3233–3248
13. Isidore BL, Hussain G, Shamchi SP, Khan WA (2016) Prediction and control of pillow defect in single point incremental forming using numerical simulations. J Mech Sci Technol 30(5):2151–2161
14. Skjødt M, Bay N, Endelt B, Ingarao G (2008) Multi stage strategies for single point incremental forming of a cup. Int J Mater Form 1(1):1199–1202
15. Skjødt M, Silva MB, Martins PAF, Bay N (2010) Strategies and limits in multi-stage single-point incremental forming. J Strain Analys Eng Design 45(1):33–44
16. Li J, Geng P, Shen J (2013) Numerical simulation and experimental investigation of multistage incremental sheet forming. Internation J Adv Manufact Technol 68(9–12):2637–2644
17. Liu Z, Li Y, Meehan PA (2013) Vertical wall formation and material flow control for incremental sheet forming by revisiting multistage deformation path strategies. Mater Manuf Processes 28(5):562–571
18. Suresh K, Nasih HR, Jasti NVK, Dwivedy M (2017) Experimental studies in multi stage incremental forming of steel sheets. Mater Today: Proc 4(2):4116–4122

Wear Behavior of Duplex Stainless Steels Sintered and Forged Under Partial Vacuum Atmosphere

C. Rajkumar, J. Udaya Prakash, C. Sarala Rubi, and R. Mariappan

Abstract DSS has a mixture of ferritic and austenitic stainless steel employed in different industrial branches owing to combined mechanical and corrosion properties. DSSs utilization is increasing year after year in the automotive and offshore industries. The main objective of this research is to produce Duplex Stainless Steels through powder metallurgy. In this investigation, two DSSs namely DSS A and DSS B were prepared using pre-alloyed powders such as 310L and 430L together with the addition of elemental powders of chromium, nickel, and molybdenum in correct proportions to obtain the required DSS composition. The powder particles are blended in a pot mill for 12 h to obtain a homogeneous distribution of alloying elements. Using a Universal testing machine, DSS with 15 mm radius and 10 mm thickness was compacted at 550 MPa. After compaction powder preforms were sintered at 1350 °C in a partial vacuum and hydrogen atmospheres. Sintered compacts were forged at 1150 °C and quenched in water. Wear tests were performed using full factorial experiments (L_{16}) and analyzed using Taguchi's Signal to Noise ratio analysis. Forged DSS B sintered under partial vacuum exhibited wear rate of 0.014 mm^3/mm for 20 N loading condition. ANOVA reveals that material has a contribution of 18% towards wear rate, closely followed by a condition.

Keywords Duplex stainless steels · Forging · Partial vacuum · ANOVA · S/N analysis · Wear

1 Introduction

Sintered items fabricated from Duplex Stainless Steels (DSS) are suitable for many applications. Therefore, so many researchers are involving in the development of Duplex Stainless Steels using the powder metallurgy route. Stainless steels are

C. Rajkumar (✉) · J. U. Prakash · C. Sarala Rubi · R. Mariappan
Department of Mechanical Engineering, Vel Tech Rangarajan Dr. Sagunthala R & D Institute of Science and Technology, Chennai, Tamil Nadu 600062, India
e-mail: crajkumartan@gmail.com

N. Gascoin and E. Balasubramanian (eds.), *Innovative Design, Analysis and Development Practices in Aerospace and Automotive Engineering*, Lecture Notes in Mechanical Engineering, https://doi.org/10.1007/978-981-15-6619-6_23

commonly used in automobiles, food, petroleum, power, transportation, paper, and pulp industries. In particular, automotive exhaust systems are one of the major applications of Powder Metallurgy products. Duplex Stainless Steels includes similarly voluminous austenite and ferrite phases, i.e., 50:50. To maintain the equal phases of ferrite and austenite alloying elements are added in the correct proportion. DSS gains the combined advantages of these two phases [1]. Ferritic Stainless Steels are inferior in toughness and weldability than DSS. Similarly, Austenitic Stainless Steels have lower pitting resistance and lower corrosion resistance relative to DSS.

DSS may be manufactured by several methods. But, the fabrication of DSS by powder metallurgy is low cost and near net shape. The first mode of achieving duplex structure was obtained by pre-alloyed powders [2]. The second mode was to combine individual elementary powders including chromium, nickel, and molybdenum with austenitic, ferrite powders in the right proportions to obtain bi-phase microstructure [3]. Elements such as molybdenum, nickel, and chromium present in DSS make it strong and responsible for corrosion and mechanical properties. Undesirable phases such as sigma, secondary austenite has reducing effects on mechanical and corrosion properties of DSS due to embrittlement [4]. Apart from the sigma phase, non-metallic inclusions in steels also have a negative impact on corrosion and mechanical properties [5, 6]. Several researchers reported that sigma phase takes place when steels underwent annealing at less than 1000 °C and it can take away by solution treatment, controls the mixture of austenite and ferrite [7, 8].

The sigma phase (rich in chromium, molybdenum) has enhanced wear resistance of DSS with different manganese contents [9]. From literature, it has been observed that the effects of sintering temperature on the mechanical characteristics of stainless steel products are higher than that of sintering time [10]. Wear Characteristics of DSS have been attempted by some researchers [11, 12]. The friction influenced the mechanical behavior of DSS [13]. The wear properties of aluminum matrix composites depend upon sliding distance and it is the key factor affecting wear behavior of the composites [14]. The wear behavior of DSS mainly depends upon chromium content in DSS [15]. Design of Experiments applies statistical methods so the effect of the variable can be used to determine the outcome of the required process or product reported by Sorrentino et al. [16]. The data for wear behavior of PM DSS using Taguchi's approach is very limited in the literature. So, the main goal of this research work is to make DSS using pre-alloyed powders like 310L and 430L and to test wear properties under different loading conditions and analyzed statistically by Taguchi's Design of Experiments.

2 Materials and Processes

Two atomized powders namely 310 L and 430 L are mixed for 12 h in pot mill (ASE, EIE Instruments Pvt. Ltd.,) with chromium, nickel, molybdenum, and manganese. To consolidate the powders to required shape and size compaction is carried out in Universal Testing Machine (FIE Model, Hitech India) at 550 MPa. In the hot press

Table 1 Chemical constituents of stainless steels powders

Powder grade	Elements (%wt)						
	Cr	Ni	C	Si	Mn	Mo	Fe
310L	24	10	0.02	0.30	2.00	0.3	Balance
430L	16.6	–	0.02	1.20	0.10	–	Balance

Table 2 Chemical constituents of DSS

Composition	Elemental concentration (%wt)									
	Ni	Cr	C	Si	Mn	Mo	Fe	Ni_{eq}	Cr_{eq}	PREN
DSS A	5	20.3	0.02	0.75	1.05	0.15	Bal.	6.1	21.57	20.53
DSS B	8.5	23.3	0.018	0.67	0.945	1.13	Bal.	9.51	25.41	27.01

DSS A: 50% 310L + 50% 430 L
DSS B: 45% 310L + 45% 430 L +4Ni + 5Cr +1 Mo

(BIRSON, 100 T), the green compacts are sintered at a temperature of 1350 °C. Sintered compacts underwent forging operation at 1150 °C and quenched in water immediately. The chemical constituents of 430 L and 310 L powders are shown in Table 1. The chemical constituents of the two DSS are given in Table 2.

The chemical composition of DSS A is 20 Cr-5Ni and DSS B is 23.2Cr-8.5Ni. Wear testing was carried out at room temperature under two different loads 20 N and 30 N with constant sliding velocity and sliding distance of 2 m/s, 750 m, respectively, based on the previous work done in DSS.

2.1 Wear Test—Pin on Disc Machine

A Pin-on-disc wear testing machine (M/s METMECH, Chennai) was used for the research work for finding the sliding wear characteristics of the PM duplex stainless steel preforms. The key variables influencing friction and wear are sliding velocity, sliding distance, load, and temperature conditions.

The wear test machine consists of a rotating spindle connected to the disc by M6 counter bolt. A pivoted hanging arm has the provision for inserting pin and holder to bring them to have access to the track diameter. The pin was firmly fixed in the holder with the help of screw. The arm of the lever made to rest on that disc after confirmation of the track diameter. Loads were added to the arm one after another, after setting the duration of the test.

The pin size was 3 mm in radius and 34 mm in length. Duplex stainless steels were used as the pin material, counterface disc with 32.5 radius and 10 mm thickness was prepared from high carbon high chromium steel (die steel). The disc and the pin were washed through acetone to confirm that the wear tests were done under dry sliding conditions. The hardness of the counter disc is 62 HRC whereas the hardness

for the pin is 70 HRA. The measurement of weight loss was used to calculate the wear rate. The tests were carried out at 20 N and 30 N, respectively. The test has been performed under room temperature.

3 Results and Discussions

3.1 Wear Analysis—Design of Experiments

Table 3 shows the systems parameters and their levels. The wear tests were performed using L_{16} full factorial design and shown in Table 4. Results reveal that forged steels have lesser wear rate compared to sintered steels. The reason for this is more ferrite content in the forged steels. Minitab Statistical Software has been used for all plots and analysis in this study. Columns are assigned the factors and interactions. Response Table 5 shows the average characteristics of the individual factor level. The response

Table 3 Process parameters and their levels

Level	Load	Material	Condition	Atmosphere
1	20	DSS-A	Sintering	Partial vacuum
2	30	DSS-B	Forged	Hydrogen

Table 4 Experimental results

Exp. No.	Load (N)	Material	Condition	Atmosphere	Wear rate (mm^3/m)
1	20	DSS-A	Sintered	Hydrogen	0.044
2	20	DSS-A	Sintered	Partial-Vacuum	0.052
3	20	DSS-A	Forged	Hydrogen	0.065
4	20	DSS-A	Forged	Partial-Vacuum	0.016
5	20	DSS-B	Sintered	Hydrogen	0.037
6	20	DSS-B	Sintered	Partial-Vacuum	0.043
7	20	DSS-B	Forged	Hydrogen	0.040
8	20	DSS-B	Forged	Partial-Vacuum	0.014
9	30	DSS-A	Sintered	Hydrogen	0.051
10	30	DSS-A	Sintered	Partial-Vacuum	0.061
11	30	DSS-A	Forged	Hydrogen	0.076
12	30	DSS-A	Forged	Partial-Vacuum	0.041
13	30	DSS-B	Sintered	Hydrogen	0.042
14	30	DSS-B	Sintered	Partial-Vacuum	0.048
15	30	DSS-B	Forged	Hydrogen	0.014
16	30	DSS-B	Forged	Partial-Vacuum	0.030

Table 5 Response table

Level	Load	Material	Condition	Atmosphere
1	29.19	26.58	26.6	27.51
2	27.67	30.28	30.26	29.35
Delta	1.52	3.7	3.66	1.84
Rank	4	1	2	3

table is based on delta statistics comparing the relative impact magnitude. The delta value for each element is the largest minus the least average. Depending on delta values, ranks are allocated; rank 1 at the highest value, rank 2 at the next higher value, etc. The rank reveals the importance of the individual response to each factor. The response table shows the material is the main cause influencing the wear rate of DSS closely followed by condition. ANOVA table shows that there is no significant contribution by load and atmosphere. This is because of the very less delta value, which shows that the change of levels does not affect the wear rate.

3.2 Selection of Optimum Levels

The response Table 5 shows the average feature of each response for each variable level. The rank indicates the relative importance of the response of each factor. The rank and delta value shows that the main parameters influencing the wear rate followed by load and atmosphere are material and condition. To assess the effect of system variables on the measurement of wear rates ANOVA was performed. Table 6 shows the S/N data for wear rate values. ANOVA table reveals that material has influenced 18% towards wear rate compared to other factors such as load and atmosphere. Figure 1 shows the Response Graphs for Wear Rate. The response graph shows that forged DSS under partial vacuum in 20 N is the optimized one. The response graph also reveals that, wear rate increases with an increase in load. From the interaction plot, it is noticed that there is no factor interaction among each other influencing the wear rate of DSS.

3.3 Confirmation Experiment

Confirmation experiments were conducted. The optimum process parameters for wear rate and their predicted and experimental values are given. The optimum predicted value is 0.0133 mm^3/mm, whereas the experimental value is 0.0140 mm^3/mm. The error is 5%, so the optimization technique holds good for Wear Rate.

Table 6 ANOVA table

Source	DF	SS	MS	F	P	Contribution %
Load	1	9.193	9.1935	0.73	0.432	3.0
Material	1	54.677	54.6771	4.34	0.092	18.0
Condition	1	53.588	53.5877	4.25	0.094	17.6
Atmosphere	1	13.561	13.5608	1.08	0.347	4.5
Load * Material	1	9.35	9.3497	0.74	0.429	3.1
Load * Condition	1	0.366	0.3663	0.03	0.871	0.1
Load * Atmosphere	1	30.865	30.8648	2.45	0.179	10.2
Material * Condition	1	15.027	15.0271	1.19	0.325	4.9
Material * Atmosphere	1	12.628	12.6278	1	0.363	4.2
Condition * Atmosphere	1	41.682	41.6822	3.3	0.129	13.7
Residual error	5	63.062	12.6123			20.7
Total	15	303.999				100.0

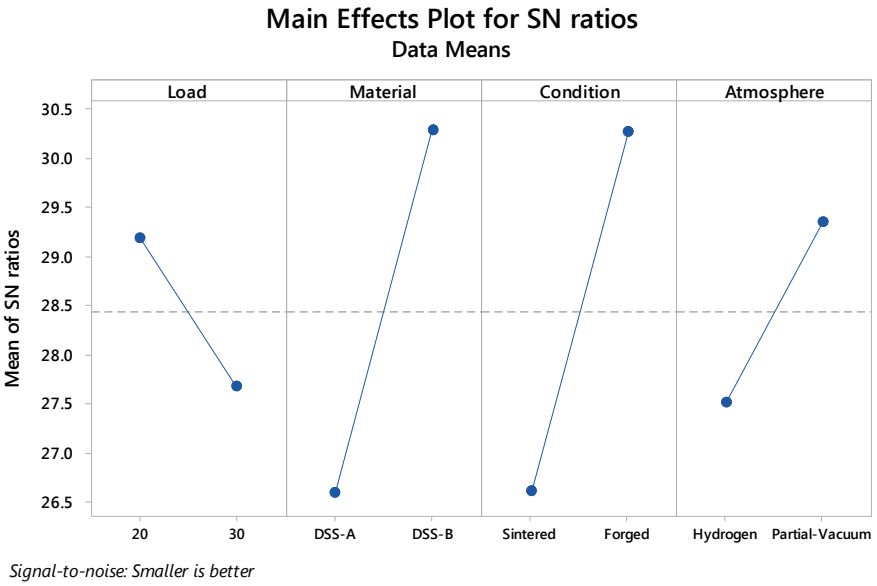

Fig. 1 Response graphs

4 Conclusions

1. Material has influenced 18% towards wear rate compared to other factors such as condition and atmosphere.
2. The rank shows the material is the main cause influencing the wear rate of DSS.

3. The optimum predicted value for forged DSS B under partial vacuum is 0.0133 mm^3/mm, whereas the experimental value is 0.0140 mm^3/mm.

References

1. Lo KH, Shek CH, Lai JKL (2009) Recent developments in stainless steels. Mater Sci Eng: R: Rep 65(4–6):39–104
2. Munez CJ, Utrilla MV, Urena A (2008) Effect of temperature on sintered austeno-ferritic stainless steel microstructure. J Alloy Compd 463(1–2):552–558
3. Smuk O (2004) Microstructures and properties of modern P/M duplex stainless steels, Doctoral Thesis, Department of Mat. Science Engg., Royal Institute of Technology, Swedan, pp 1–5, (2004)
4. Pohl M, Storz O, Glogowski T (2007) Effect of intermetallic precipitations on the properties of duplex stainless steel. Mater Charact 58(1):65–71
5. Tan H, Jiang Y, Deng B, Sun T, Xu J, Li J (2009) Effect of annealing temperature on the pitting corrosion resistance of super duplex stainless steel UNS S32750. Mater Charact 60(9):1049–1054
6. Hwang H, Park Y (2009) Effects of heat treatment on the phase ratio and corrosion resistance of duplex stainless steel. Mater Trans, 0905110767–0905110767
7. Kim HJ, Jeon SH, Kim ST, Lee IS, Park YS, Kim KT, Kim YS (2014) Investigation of the sensitization and intergranular corrosion of tube-to-tube sheet welds of hyper duplex stainless steel using an electrochemical reactivation method. Corros Sci 87:60–70
8. Jeon SH, Kim ST, Lee IS, Park JH, Kim KT, Kim JS, Park YS (2011) Effects of copper addition on the formation of inclusions and the resistance to pitting corrosion of high performance duplex stainless steels. Corros Sci 53(4):1408–1416
9. Lu XC, Li S, Jiang X (2001) Effects of σ phase in stainless steels on corrosive wear behavior in sulfuric acid. Wear 251(1–12):1234–1238
10. Kazior J, Szewczyk-Nykiel A, Pieczonka T, Hebda M, Nykiel M (2013) Properties of precipitation hardening 17-4 PH stainless steel manufactured by powder metallurgy technology. Adv Mater Res 811:87–92
11. Whitefield DJ, Van Bennekom A (1996) Abrasive wear properties of experimental metastable duplex stainless steels. Wear 196(1–2):92–99
12. Straffelini G, Trabucco A (2002) Molinari, a sliding wear of austenitic and austenitic–ferritic stainless steels. Metall Mater Trans 33A:613–623
13. Vignal V, Mary N, Ponthiaux P, Wenger F (2006) Influence of friction on the local mechanical and electrochemical behaviour of duplex stainless steels. Wear 261(9):947–953
14. Udaya Prakash J, Ananth S, Sivakumar G, Moorthy TV (2018) Multi-objective optimization of wear parameters for aluminium matrix composites (413/B4C) using grey relational analysis. Mater Today: Proc 5(2):7207–7216
15. Chinnaraj R, Ramajayam M (2019) studies on mechanical properties of hot-forged duplex stainless steels sintered in hydrogen atmosphere. J Inst Eng (India): Series D, pp 1–8
16. Sorrentino L, Simeoli G, Iannace S, Russo P (2015) Mechanical performance optimization through interface strength gradation in PP/glass fibre reinforced composites. Compos B Eng 76:201–208

Static Analysis of a C-Channel Robot Gripper Arm Using Finite Element Analysis

D. Sakthimurugan, L. Antony Michael Raj, V. Antony Aroul Raj, R. Balaji, K. Thavasilingam, and N. Bharath

Abstract In recent years, increase the demand in automobile companies, and to survive in a competitive world, and to achieve the customer target and satisfaction, the companies going through for automation. So it leads to improvement in quality and brings zero defects and also reduces the process cycle time, manpower cost and bring safety aspects. In our project, two gripper plates (six electromagnets each) are mounted on C-type gripper bracket. These electromagnets are used to hold the face of Clutch Cover plate. For forming process, the clearance between the tool and cover plate is 0.5 mm for avoiding fracture and plastic deformation. Our aim is to find the deformation of gripper bracket at Static condition. The model of robot gripper bracket is established using the SOLIDWORKS software and Finite element analysis (FEA) is done by ANSYS 17.0 and the results are compared with the optimization techniques tool. Different values of loads are applied are compared and prove the design is valid.

D. Sakthimurugan (✉) · V. Antony Aroul Raj · R. Balaji · K. Thavasilingam · N. Bharath
Department of Mechanical Engineering, Easwari Engineering College, Chennai 600089, India
e-mail: skthids@gmail.com

V. Antony Aroul Raj
e-mail: antonyaroulraj@gmail.com

R. Balaji
e-mail: balajimech8148@gmail.com

K. Thavasilingam
e-mail: thavasi.k.89@gmail.com

N. Bharath
e-mail: nbarb1992@gmail.com

L. Antony Michael Raj
Department of Mechanical Engineering, Loyola-ICAM College of Engineering, Chennai, India
e-mail: antonymr@yahoo.com

N. Gascoin and E. Balasubramanian (eds.), *Innovative Design, Analysis and Development Practices in Aerospace and Automotive Engineering*, Lecture Notes in Mechanical Engineering, https://doi.org/10.1007/978-981-15-6619-6_24

Keywords Automation · C-Channel robot gripper arm · Electromagnets · Static condition · ANSYS 17.0 · Finite element analysis (FEA) · Optimization technique tool · Modal analysis

1 Introduction

The world-leading manufacturing company in clutch production goes through automation in the press shop. The robot automation is implemented in forming stage condition to achieve the target volume. The robot automation is implementing for four Press Machine. We involved in the design of the robot arm end effector. The Robotic end-effector is any object attached to the robot flange (wrist) that serves a function [1]. It certainly helps the robot to handle several tools in an operation, and thus makes the multi-tooling function possible [2].

The design guidelines may be as follows [3]:-

1. Gripper weight should be minimized.
2. Grasping of objects should be secure.
3. Grip multiple objects with a single gripper.

The machine die and workpiece have lesser tolerance, i.e., 0.5 mm. So our aim is to reduce the deflection of gripper arm below 0.5 mm. This deflection will not affect the accuracy in operation and prove the design is valid.

The following ways are most often used to minimum deflection [4]:

1. Decrease length of beam.
2. Move one or both supports inward from the end of the beam.
3. Increase beam of the moment of inertia.
4. Share load with other beams.

2 Literature Review

2.1 Gripper

Grippers are the end effectors used for holding the parts or objects. Grippers are devices that can be used for holding or gripping an object. They include might call mechanical hands and also anything like hooks, magnets and suction devices that can be used for holding or gripping [5, 6]. **Applications**:- Machine Loading and unloading, picking and placing of parts on conveyor, material handling.

2.2 Magnets and Application

Magnetic grippers obviously only work on magnetic objects and therefore limited in working with certain metals. For maximum effect, the magnet needs to have complete contact with the surface of the metal to be gripped.

If the magnet is strong enough, a magnetic gripper can pick up an irregular shaped object [7] (Table 1).

3 Arrangement of Layout

In cell 1 for robot automation is implementing for two machines and cell 2 for two machines as shown in Fig. 1. For each cell, the four robots are used which are:

1. Pick and Place robot (KR 30-Payload of 30 kg)—R × 1 and R × 2.
2. Loading and Unloading robots (K 180-Payload of 180 kg)—R1 and R2.

3.1 Process

The blanking material has an input which is placed on the auto trolley bin through crane. The auto trolley bin is operated by servo motor and move near to robot. The R × 1 robot picks the blanking or covers plate from the bin and places it on the table near to R1 as shown in Fig. 1. The R1 robot picks cover forming by using electromagnetic end gripper arm X1 and goes inside the press. The electromagnetic end effectors X1 holding the part in gripper at a similar time, X2 picks the materials from tool inside the press for reducing the cycle time. The robot arm slightly come back from press and material held in the X1 drops the part inside the press. The robot R1 arm end effectors X2 holds the material which comes outside from the press and placed on conveyor. Then press starts and forming take place inside material. The robot R1 arm end effectors X2 holds the material drops in another table near to the robot R2 for the next stage. The finished parts are picked from the table and placed in trolley.

4 Finite Element Analysis

Inputs are:

Material: Structural Steel (ST 42)
Load type: Static Structural
FOS: 1.5
Density: 7850 kg/m^3

Table 1 The type of magnets and their advantage, disadvantages and applications

Parameter	Servo-electric gripper	Pneumatic gripper	Magnetic gripper	Permanent magnet gripper
Working Mechanism	Electric motors control the movement of the jaws using electric input from the robot	Grippers provide their actuation by compressed air into chamber. It converts air pressure into mechanical force [3]	Grippers using are generally powered by DC power for handling material	These kinds of end effectors do not need power to operate. They are separate piece from magnet, by cut electric power
Energy used	Electrical energy	Air-operated actuator	Electrical energy	Electrical energy
Grasping speed	Fast	Relatively speed	Very fast	Fastest
Environmental adapt-ability	These actuators are not suited for all environments	Actuators involve areas of extreme temperatures. A typical temperature range is −40 °F to 250 °F	At some point, affect the magnets due to factors like ohmic heating, core losses [7]	This magnet can not use this type of magnets for hot device applications
Material used	Alloy steel/titanium	Alloy steel	Ferromagnetic material	Ferromagnetic material
Precision	Highly Precise. Range of accuracy is ± 0.00315 inches and repeatability of less than 0.0000394 inch	Pneumatic actuators generate precise linear motion by providing accuracy, within 0.1 inches and repeatability within 0.001 inches	The grasping speed is fast, as the magnet is magnetized, taking 0.5 s	The grasping speed is fast, as the gripper is constantly on pneumatic is used to activate on and off position. Time consumed is 1–1.5 s
Gripping factor	High Gripping factor, due to feedback response	Simple and quick hence high gripping factor	Gripping factor is weak, as it's prone to slippage and if excess oil comes in contact with the surface of magnet (5)	Gripping factor relatively weak, as it's prone to slippage and if excess oil (film thickness > 10 mm) comes in contact with the surface of magnet
Shape of gripper	Jaw type- double and triple, 5 finger type grippers (6)	Claw type, double and triple jaw gripper	Rectangular magnetic, Single long arm, circular magnetic	Rectangular magnetic slab, Single long arm, circular magnetic slab [8]

(continued)

Table 1 (continued)

Parameter	Servo-electric gripper	Pneumatic gripper	Magnetic gripper	Permanent magnet gripper
Application	Machine tending, lab Automation	Grippers for cleanroom applications, domestic purposes	Assembly and automotive industry	Assembly and automotive industry automation

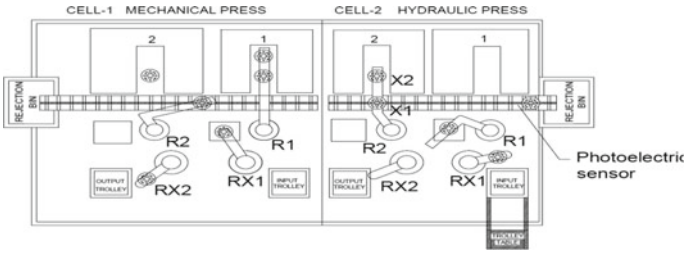

Fig. 1 Design layout for robot automachine

Young Modulus: 2×10^{11} Pa
Poisson ration: 0.3
Tensile ultimate Strength: 410–490 MPa (460 MPa)
Compressive ultimate strength: 1250 Pa
Tensile yield strength: 250 MPa
Compressive yield strength: 250 MPa
Shear Modulus: 7.69×10^{10} Pa
Bulk Modulus: 0.167 GPa.

5 Result and Discussion

Thus the result is found for 29.5, 49, 78.5, 98 and 117.8 N are 0.089, 0.149, 0.23, 0.289 and 0.358 mm by using FEA software [9] as shown in Fig. 2. So the maximum weight of the clutch is 117.8 N gets below 0.5 mm. The deformation for this robot design concept does not affect the operation of press and quality is improved. This operation reduces process cycle time, manpower, and bring safety aspects. So, we save cost 30% of the production cost. Due to short time, we cannot complete the next journal we compared this result with one of the optimization tools.

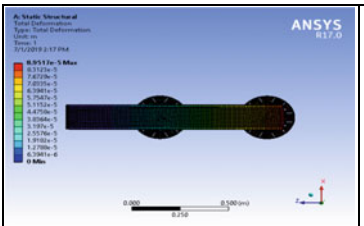	Load Acting = **29.5 N** Resultant Load = **44.145 N** Maximum Deformation (δ_{max}) = **0.089 mm** Minimum Deformation (δ_{min}) = **0 mm**
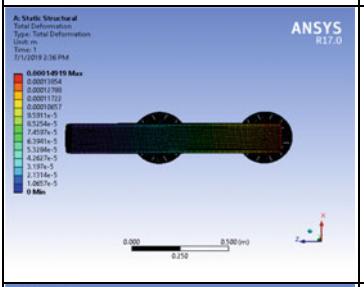	Load Acting = **49 N** Resultant Load = **73.575 N** Maximum Deformation (δ_{max}) = **0.149 mm** Minimum Deformation (δmin) = 0 mm
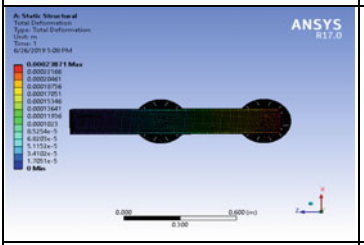	Load Acting = **78.5 N** Resultant Load = **117.72 N** Maximum Deformation (δ_{max}) = **0.23mm** Minimum Deformation (δ_{min}) = **0mm**
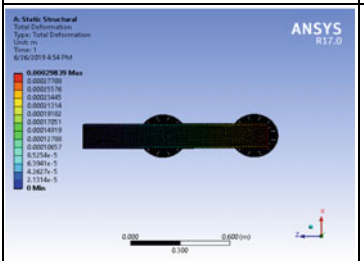	Load Acting = **98 N** Resultant Load = **147.15 N** Maximum Deformation (δ_{max}) = **0.298 mm** Minimum Deformation (δ_{min}) = **0 mm**
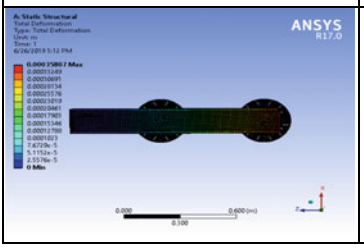	Load Acting = **117.8 N** Resultant Load = **176.58 N** Maximum Deformation (δ_{max}) = **0.358 mm** Minimum Deformation (δ_{min}) = **0 mm**

Fig. 2 Finite element analysis of End effector for various load

References

1. Zaki AM, Mahgoub OA, El-Shafei AM, Soliman AM (2010) Design and implementation of efficient intelligent Robot gripper 9(11)
2. Rishank Reddy G, Krishna V, Eranki P (2016) Design and structural analysis of a robotic arm
3. Yasodharam R (2016) Robot end effector, published on July
4. Naga Prasad CS (2017) Design and analysis of cantilever beam. Int J Adv Technol Innovative Res 09(05):0682–0685. ISSN 2348-2370
5. Lad NA, Ballal YP, Kulkarni PD (2015) Study of end effectors—a review. Int J Trend Res Dev 2(5). ISSN 2394-9333
6. Machine Structure Design (2009) Industrial grippers: history and new innovation. A variable http://machinedesign.com/motioncontrol/industrial-grippers-histroy-and-new-innovation.com in May 2009
7. Grippers for Robots (2016) Robots.com N.p. 2010, web. 12 July 2016. Robot Magnetic Grippers—Robotics Bible—Projects, News, videos, Books, Events, and more. N.p. 2016, web. 6, June 2016
8. Jeevan R (2015) Amar nageswara: modeling and analysis of robot arm using ANSYS. Int J Sci Eng Technol Res 04(33):6692–6697. ISSN 2319-885
9. Frabcis N, Urmila K (2016) Design and analysis of circular and square arm robot. Anveshana's Int J Res Eng Appl Sci 1(11):2455–6300

TLBO and JAYA: Insights into Novel Multi-objective Optimization Techniques

V. Rajashekar and Yeole Shivraj Narayan

Abstract Optimization is an effective tool for optimum utilization of existing resources so as to improve quality, productivity and to reduce the cost. The majority of the real-world situations have multiple objectives that conflict with each other. Hence multiple objectives or criteria need to be optimized effectively and simultaneously for achieving the best output. Hence, many evolutionary algorithms like Pareto Optimization, Non-Sorted Genetic Algorithm (NSGA), Particle Swarm Optimization (PSO), Simulated Annealing (SA), etc. have been developed in the past for this purpose. However, in order to obtain more accurate predictions, these techniques are continuously being modified to make them evolutionary in nature resulting in newer multi-objective optimization techniques. Teaching-Learning Based Optimization (TLBO) and JAYA are two state-of-the-art multi-objective optimization techniques. This paper presents a review of TLBO and JAYA multi-objective optimization techniques with an emphasis on key insights into the methodology and algorithms, followed by their application in different fields. It is observed that these techniques yielded better performance than the existing ones.

Keywords Multi-objective optimization (MOO) · TLBO · JAYA · Evolutionary algorithms

1 Introduction

Optimization is an important aspect to improve the quality, productivity and reduction of the cost. Most of the literature is focused on single objective (SO) optimization, but real-world problems are conflicting in nature. Hence, MOO comes into the picture. Based on decision-making processes MOO classified as no preference-based, priori,

V. Rajashekar · Y. Shivraj Narayan (✉)
VNR Vignana Jyothi Institute of Engineering and Technology, Hyderabad, Telangana 500090, India
e-mail: shivrajyeole@vnrvjiet.in

N. Gascoin and E. Balasubramanian (eds.), *Innovative Design, Analysis and Development Practices in Aerospace and Automotive Engineering*, Lecture Notes in Mechanical Engineering, https://doi.org/10.1007/978-981-15-6619-6_25

posteriori and interactive methods [1–4]. In order to have better prediction and efficiency, TLBO [5] and JAYA [6] are developed by R. Venkata Rao. There is not much literature available on these MOO techniques as they are relatively new. TLBO is further modified as Elite TLBO and Non-Sorted TLBO [7] whereas Jaya is further modified as Self-adaptive Jaya [8], Quasi-Oppositional based Jaya (QO-Jaya) [9] and Self-Adaptive Multi-Population Jaya [10]. This paper aims to provide an overview of significant contributions of new optimization techniques especially TLBO and JAYA in fields like machining, design, shop floor problems, medical and 3D printing.

1.1 Optimization

Optimization is defined as minimization or maximization of performance measurements by obtaining optimum condition (OC) to process parameters. Optimization is done in two steps. They are [3]as follows:

1. Parameter Modelling: To construct the relationship between the input-output and process variables [3].
2. Optimal/Near-Optimal Condition for process parameters was developed by using various optimization techniques [3].

Optimization are classified based on objectives as Single objective optimization and Multi-objective optimization [5, 6, 11].

2 TLBO [5]

TLBO consists of teachers phase and learners phase.

1. Teachers phase: Teacher improves average performance in a particular variable [5]. At each iteration 'i', consider 'm' input variables (number of subjects $j = 1,\ldots m$), 'n' population (number of learners $k = 1,\ldots n$), $M_{i,j}$ be the average outcome particular variable 'j'. The best overall result $X_{\text{total,Kbest},i}$ taking all the variables together obtained in total population can be taken as the outcome of best learner K_{best}. Variation between the existing mean results of each subject and the respective result of the teacher for each variable is given by

$$\text{Differencemean}_{j,k,i} = r_i\left(X_{\text{total,Kbest},i} - T_{\text{F}} M_{i,j}\right)$$

where r_i is random number [0, 1], T_{F} is teaching factor ($T_{\text{F}} = \text{round}\,(1 + r_i\,\{2-1\})$) Then update input variables by using below equation.

$$X'_{j,k,i} = X_{j,k,i} + \text{Difference mean}_{j,k,i}$$

$X'_{j,k,i}$ is accepted if it gives superior functional value than $X_{j,k,i}$ these accepted functional values become input values to the learner's phase.

2. Learners phase. Learners knowledge improved by interacting among themselves. Two learners ($K = 1 \ldots n$) are randomly selected, e.g. 1 and 2, the condition is $X'_{\text{total},1,i} \neq X'_{\text{total},2,i}$

   For minimization:

$$X''_{j,1,i} = X'_{j,1,i} + r_i(X'_{j,1,i} - X'_{j,2,i}) \text{ if } X'_{\text{total},1,i} < X'_{\text{total},2,i}$$
$$X''_{j,1,i} = X'_{j,1,i} + r_i(X'_{j,2,i} - X'_{j,1,i}) \text{ if } X'_{\text{total},2,i} < X'_{\text{total},1,i}$$

   For maximization:

$$X''_{j,1,i} = X'_{j,1,i} + r_i(X'_{j,1,i} - X'_{j,2,i}) \text{ if } X'_{\text{total},2,i} < X'_{\text{total},1,i}$$
$$X''_{j,1,i} = X'_{j,1,i} + r_i(X'_{j,2,i} - X'_{j,1,i}) \text{ if } X'_{\text{total},1,i} < X'_{\text{total},2,i}$$

$X''_{j,k,i}$ is accepted if it gives superior function value than $X'_{j,k,i}$. If this satisfies termination criteria report the solution and stop the process, if not go to the next iteration. The flow chart of TLBO is presented in Fig. 1.

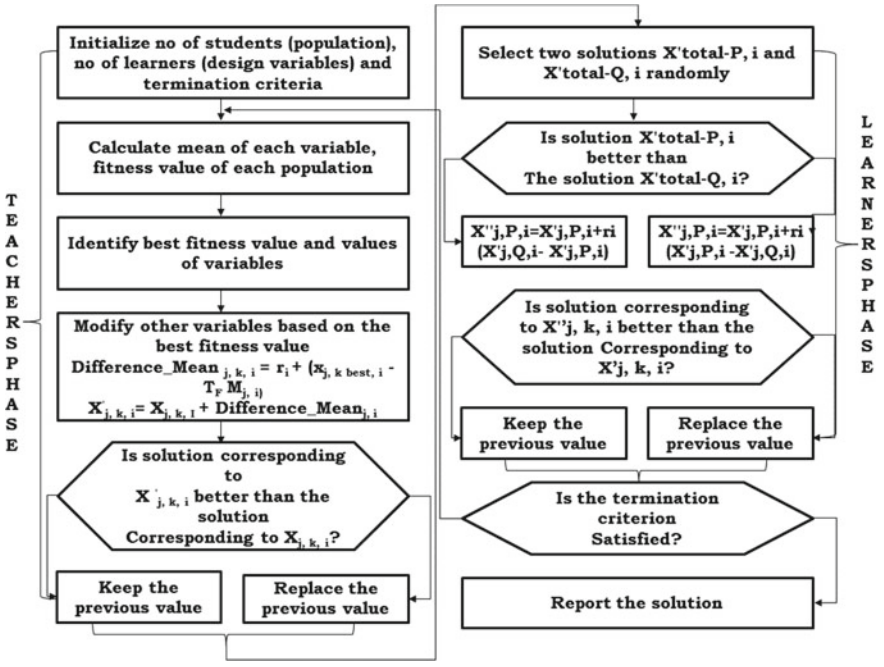

Fig. 1 Flow chart of TLBO algorithm (*Source* Comput. Aided. Des. p. 305)

2.1 Applications of TLBO Algorithm

Wenwen et al. proposed and implemented MOTLBO and GRA in the turning process. Analytical hierarchy process was used to find optimum results (OR) [12]. Rao et al. applied NSTLBO and MOTLBO to 3 different manufacturing processes namely wire EDM, turning and laser cutting process (LCP). In WEDM and turning processes, fewer evaluations are required to get optimum results as compared to NSGA-II. In micro-WEDM and LCP, Pareto solution obtained in NSTLBO is better than PSO and GA [13]. Rao et al. implemented priori-based TLBO in thermoacoustic devices (TAD), namely thermo-acoustic refrigerator (TAR), thermo-acoustic prime-mover (TAP), and thermo-acoustic engine (TAE). TLBO is found to achieve optimum condition in fewer functional evaluations and effective than GAMS and RSM [14]. Saleh et al. applied hybrid TLBO-PSO technique to choose the Associated Genes with Breast Cancer. Hybrid TLBO-PSO technique produces accurate results than TLBO, PSO [15]. Venkata Rao implemented NSTLBO in micro ball-end milling process. NSTLBO results are found to be in good concurrence with FEM [16]. Venkata Rao applied TLBO and NSTLBO in fused deposition modelling process optimization. NSTLBO produced better Pareto fronts in terms of spacing and coverage than NSGA-II [17]. Subhrajyoti et al. applied priori-based TLBO and MIPSO (Mixed Integer Particle Swarm Optimization) in MO power flow problems. TLBO outperforms MIPSO in convergence rate to get OC [18]. Neelesh and Atul applied priori-based TLBO, JAYA and GA to optimize the turning process. Size of population and generations for all algorithms are the same, TLBO and JAYA performed better than GA [19]. Dashuang Li et al. proposed and implemented MITLBO in assembly line optimization. Better Pareto fronts are acquired rapidly in MITLBO than MOTLBO and NSGA-II [20]. Vivek and Vimal proposed TS-TLBO algorithm and applied it to MOP of a sterling heat engine (SHE). It is easily applied in case of high number of variables and objectives [21]. Edmund and Rajesh applied MOTLBO to 4 cases of spur gear design to minimize weight and maximize power. TLBO produced better OR compared GA, SA [22].

3 Jaya Algorithm [6]

Jaya algorithm is completed in one step, by modification of variables using the simple equation given by Rao [6]. At any iteration 'i', consider 'm' input variables (number of subjects $j = 1,\ldots m$), 'n' population (number of learners $k = 1,\ldots n$) the best and worst overall result are $X_{\text{total,KbeFst},i}$ and $X_{\text{total,Kworst},i}$. In Jaya algorithm, '$P$' initial solutions are there. These are updated using the below equation

$$A(i+1, j, k) = A(i, j, k) + r(i, j, 1)(A(i, j, b) - |A(i, j, k)|) - r(i, j, 2)(A(i, j, w) - |A(i, j, k))$$

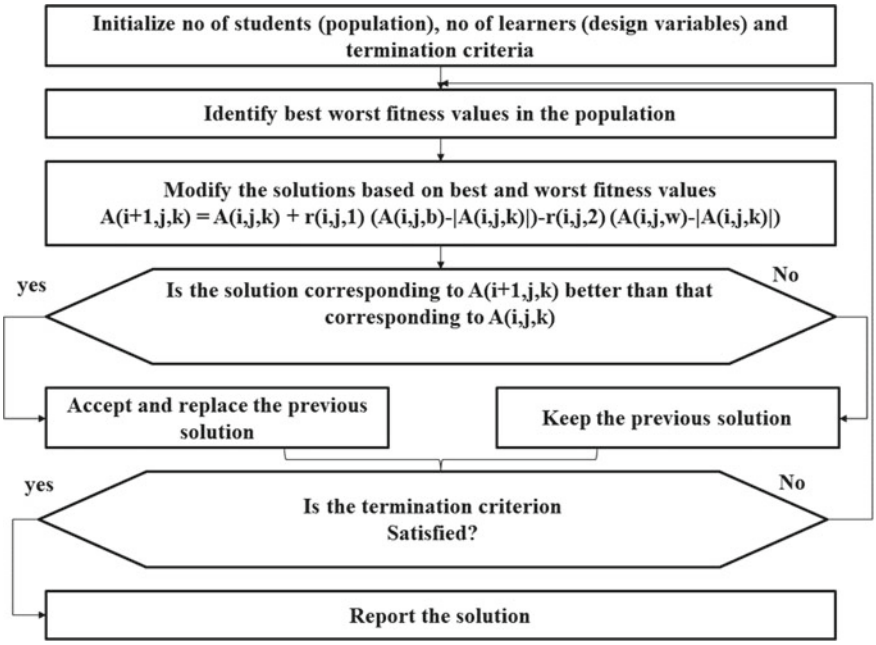

Fig. 2 Flow chart of Jaya algorithm (*Source* Int. J. Ind. Eng, p. 21)

$A\ (i, j, b)$, $A\ (i, j, w)$ are input variable at best, worst functional value. $r\ (i, j, 1)$, $r(i, j, 2)$ are random numbers. Values of input variables are updated, assessed with previous results. Superior results are treated for immediate iteration. Process is continued till termination criteria reached. Flow chart of Jaya is shown in Fig. 2.

3.1 Applications of JAYA Algorithm

Ravipudi et al. proposed and applied MO-SAMP for MOO of design parameters of thermal devices namely two-stage thermoelectric cooler, two-stage irreversible heat pump and plate-fin heat exchanger (PFHE), transcritical CO_2 cycle and irreversible Carnot power cycle. In all thermal devices, superior results are obtained using MO-SAMP algorithm than GA, PSO, TLBO, MOTLBO [23]. Rao et al. implemented Mo-Jaya to machining processes—plasma arc machining (PAM), electro-discharge machining (EDM) and micro-EDM. In PAM optimization, MO-Jaya produces 50 solutions in 8 iterations, EDM process, 50 trade of solutions produced in 20 iterations by MO-Jaya. In micro-EDM process, MO-Jaya has taken 11 iterations to produce 50 trade of solutions [24]. Rao and Ankit implemented Elite Jaya algorithm to different heat exchangers design like STHE and PFHE, both cases Elite Jaya results are comparatively improved than TLBO and GA [25].

Venkata Rao et al. done MOO of abrasive water jet machining (AWJM) and abrasive water jet turning processes (AWJT). MO-Jaya produces more significant OR than GA, PSO, cuckoo search (CS), NSTLBO and NSGA-II. [26]. Warid et al. developed and applied MO-Jaya and QO-Jaya to PFP, IEEE 30-bus system taken as input in all cases, MO-Jaya and QO-Jaya produced better results with efficient and quickly [27]. R. Venkat Rao et al. applied MO-Jaya algorithm in AWJM process. MO-Jaya results are assessed with NSTLBO and NSGA. It produced better Pareto fronts in fewer generations and higher hypervolume metric [28]. R. Venkat Rao et al. implemented adaptive multi term perturbation guiding Jaya (AMTPG Jaya) to three cases of solar dish SHE and solar heat pump. AMTPG Jaya produced better Pareto solutions than TOPSIS and NSGA-II [29]. Singh et al. applied priori-based Jaya to optimize wire EDM process Jaya algorithm do not require specific parameters like other algorithms [30].

4 Conclusions

An overview of novel multi-objective optimization techniques like TLBO and Jaya algorithms is presented. Either priori-based approach or posteriori-based approach is used for MOO. TLBO and Jaya algorithms have been applied for optimization in design, process parameters in manufacturing processes, medical field to find the diseases, assembly line operations to improve line efficiency, and scheduling. In priori-based approach, TLBO and Jaya algorithms have a good convergence rate to reach optimum conditions in fewer functional evaluations as compared to other algorithms like GA, PSO, SA, BBO, TS, CS. In posterior-based approach, NSTLBO, MOTLBO, MO-Jaya, MO-SAMP, and AMTPG-Jaya produced good Pareto fronts, higher hypervolume metrics compared to all other algorithms NSGA, NSGA-II, MOPSO.

References

1. Tamaki H, Kita H, Kobayashi S (1996) Multi-objective optimization by genetic algorithms: a review. Evol Comput 517–522
2. Wang H, Olhofer M, Jin Y (2017) A mini-review on preference modeling and articulation in multi-objective optimization: current status and challenges. J Complex Intell Syst 3(4):233–245
3. Mukherjee I, Kumar Ray P (2006) A review of optimization techniques in metal cutting processes. Comput Ind Eng 50(1–2)15–34
4. Said LB, Bechikh S, Ghédira K (2010) The r-dominance: a new dominance relation for interactive evolutionary multicriteria decision making. IEEE T Evolut Comput 14(5):801–818
5. Rao RV, Savsani VJ, Vakharia DP (2011) Teaching–learning-based optimization: a novel method for constrained mechanical design optimization problems. Comput Aided Des 43(3):303–315
6. Rao R (2016) Jaya: a simple and new optimization algorithm for solving constrained and unconstrained optimization problems. Int J Ind Eng Comput 7(1):19–34

7. Rao R, Patel V (2012) An elitist teaching-learning-based optimization algorithm for solving complex constrained optimization problems. Int J Ind Eng Comput 3(4):535–560
8. Rao RV, More KC (2017) Design optimization and analysis of selected thermal devices using self-adaptive Jaya algorithm. Energ Convers Manage 140:24–35
9. Venkata Rao R, Rai DP (2017) Optimisation of welding processes using quasi-oppositional-based Jaya algorithm. J Exp Theor Artif 29(5):1099–1117
10. Venkata Rao R, Saroj A (2017) A self-adaptive multi-population-based Jaya algorithm for engineering optimization. Swarm. Evol Comput 37:1–26
11. Shivraj Y, Ramesh Nunna N, Banoth BN, Alluru R (2015) Realization of surface morphology and process parameter optimization in MicroEDM hole drilling of maraging steel 300 alloy. In: ASME 2015 international mechanical engineering congress and exposition, pp V02AT02A044–V02AT02A044
12. Lin Wenwen DY, Yu SW, Zhang C, Zhang S, Tian H, Luo M, Liu S (2015) Multi-objective teaching–learning-based optimization algorithm for reducing carbon emissions and operation time in turning operations. Eng Optimiz 47(7):994–1007
13. Venkata Rao R, Rai DP, Balic J (2018) Multi-objective optimization of machining and micro-machining processes using non-dominated sorting teaching–learning-based optimization algorithm. J Intell Manuf 29(8):1715–1737
14. Rao RV, More KC, Taler J Ocłoń P (2017) Multi-objective optimization of thermo-acoustic devices using teaching-learning-based optimization algorithm. Sci Technol Built En 23(8):1244–1252
15. Shahbeig S, Helfroush MS, Rahideh A (2017) A fuzzy multi-objective hybrid Tlbo-Pso approach to select the associated genes with breast cancer. Sig Process 131:58–65
16. Venkata Rao K (2019) Power consumption optimization strategy in micro ball-end milling of D2 steel via TLBO coupled with 3D FEM simulation. Measurement 132:68–78
17. Venkata Rao R, Rai DP (2016) Optimization of fused deposition modeling process using teaching-learning-based optimization algorithm. Int J Eng Sci Technol 19(1):587–603
18. Sahu S, Barisal AK, Kaudi A (2017) Multi-objective optimal power flow with DG placement using TLBO and MIPSO: a comparative study. Enrgy Proced 117:236–243
19. Sahu NK, Andhare AB (2019) Multiobjective optimization for improving machinability of Ti-6Al-4 V using RSM and advanced algorithms. J Comput Des Eng 6(1):1–12
20. Li D, Zhang C, Shao X, Lin W (2016) A multi-objective TLBO algorithm for balancing two-sided assembly line with multiple constraints. J Intell Manuf 27(4):725–739
21. Patel V, Savsani V (2016) Multi-objective optimization of a stirling heat engine using TS-TLBO (tutorial training and self-learning inspired teaching-learning based optimization) algorithm. Energy 95:528–541
22. Maputi ES, Arora R (2016) Multi-objective spur gear design using teaching learning-based optimization and decision-making techniques. Cogent Eng 1665396
23. Rao Ravipudi V, Saroj A, Oclon P, Taler J, Lakshmi J (2018) A posteriori multi objective self-adaptive multi population Jaya algorithm for optimization of thermal devices and cycles. IEEE Access 7:4113–4134
24. Rao R, Rai DP, Ramkumar J, Balic J (2016) A new multi-objective Jaya algorithm for optimization of modern machining processes. Adv Prod Eng Manage 11(4):271
25. Rao RV, Saroj A (2018) Multi-objective design optimization of heat exchangers using elitist-Jaya algorithm. Energ Syst 9(2):305–341
26. Rao RV, Rai DP, Balic J (2018) Optimization of abrasive waterjet machining process using multi-objective jaya algorithm. Mater Today-Proc 5(2):4930–4938
27. Warid W, Hizam H, Mariun N, Wahab NIA (2018) A novel quasi-oppositional modified Jaya algorithm for multi-objective optimal power flow solution. Appl Soft Comput 65:360–373
28. Rao RV, Rai DP, Balic J (2019) Multi-objective optimization of abrasive waterjet machining process using Jaya algorithm and PROMETHEE Method. J Intell Manuf 30(5):2101–2127

29. Rao RV, Keesari HS, Oclon P, Taler J (2019) Improved multi-objective Jaya optimization algorithm for a solar dish Stirling engine. J Renew Sustain Ener 11(2):025903
30. Singh M, Ramkumar J, Rao RV, Balic J (2019) Experimental investigation and multi-objective optimization of micro-wire electrical discharge machining of a titanium alloy using Jaya algorithm. Adv Prod Eng Manag 14(2):251–263

Study of Vehicle Pulling Phenomenon and Various Factors that Influence Vehicle Pull

Kale Shubham, Patil Pramod, Sharma Ankur, Tawade Prasad, and Bhalekar Sahil

Abstract Vehicle pulling is extremely frustrating and perpetually adjusting the steering wheel while driving the vehicle is additionally very unsafe if the person driving the vehicle gets distracted even for several seconds. The pulling issue can begin from different underlying roots. Determination of the proper root cause(s) among many doable choices is very important to rectify the pulling behavior. However, the diagnostic method is very complicated to put in practice due to the functional limitations of the manufacturing processes. In this research, we describe possible causes and remedial actions for the resolution of a vehicle having a drift or pull condition. The study was performed on a batch of vehicles having pulling problems and the wheel alignment values for those vehicles were matched with the defined values. Experiments were carried for understanding the effect of change in the tire conicity values, tire pressure, and many other parameters like road camber and crosswinds. We have proposed a generalized method based on our investigations for examination and resolution of the vehicle pulling problem.

Keywords Vehicle pulling · Camber · Caster · Plysteer · Conicity · Wheel alignment

K. Shubham (✉) · P. Pramod · S. Ankur · T. Prasad · B. Sahil
Mahindra & Mahindra Ltd., Automotive Division, Chennai, India
e-mail: shubham.kale@mahindra.com

P. Pramod
e-mail: patil.pramod3@mahindra.com

S. Ankur
e-mail: sharma.ankur2@mahindra.com

T. Prasad
e-mail: tawade.prasad@mahindra.com

B. Sahil
e-mail: bhalekar.sahil@mahindra.com

N. Gascoin and E. Balasubramanian (eds.), *Innovative Design, Analysis and Development Practices in Aerospace and Automotive Engineering*, Lecture Notes in Mechanical Engineering, https://doi.org/10.1007/978-981-15-6619-6_26

1 Introduction

Vehicle pulling is a motion of vehicles in lateral direction on a straight road and at a constant speed, without application of any load on the steering wheel; it is also known as vehicle residual aligning torque (VRAT) [1]. A vehicle with the pulling issue would require a constant correction of vehicle direction to maintain the vehicle on a straight line. Driving a vehicle that is pulling is not only uncomfortable and irritating for the driver but also dangerous from a road safety perspective [2]. The motivation behind this study is to perform an in-depth analysis of vehicle pulling phenomenon and propose general guidelines to systematically identify the root cause and find corrective measures for its resolution.

Vehicle pull is attributed to different factors. Understanding what can effect it is imperative for resolution of the pulling issue in any vehicle. Major factors that cause vehicle pulling problem are tire conicity, PRAT, road crown, cross camber, cross castor, cross wind, and various other manufacturing constraints [3–5].

This article initially outlines basic vehicle attributes that have an impact on the vehicle pulling. Then, the details of the study that was conducted to check the wheel alignment data for the vehicles that were reported for vehicle pulling from the field with reference to the specified standards in design.

Based on the observations and experiments conducted, a generalized procedure is established for resolution of vehicle pulling issue for the future reference as a guideline.

2 Vehicle Pulling Checking Procedure

Following procedure was followed for checking if the vehicle has a pull or not.

1. Before stesting the test, verified that the tires are original, as provided by the vehicle manufacturer and are set to the inflation pressure as per vehicle specifications.
2. Located a road for testing the vehicle which meets the following criteria.
    a. Road slope not more than 1.7°.
    b. One or a multiple lane road.
    c. Straight road for at least 250 m.
    d. Lane width to be between 3 m and 3.5 m.
3. Cautions ensured:
    a. Conducted the test on a flat amd even road without bumps or grooves.
    b. Did not tested on the roads having an excessive crown.
    c. Conducted the test on uncrowned road and ensured that the safety precautions are ensured.
    d. Ensured that there is no strong cross wind during the testing.

Table 1 Test conditions for pulling test

Case	Condition	Pull criteria
A	Vehicle moves from one edge of the lane to the other (about 1 m)	Time taken is 6 s or less at 65 kmph, or 4.5 s or less at 80 kmph
B	Vehicle moves across one full lane (about 3 m)	Time taken is 9 s or less at 65 kmph, or 7 s or less at 80 kmph

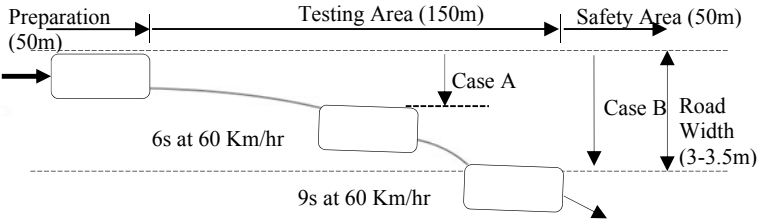

Fig. 1 Vehicle pulling checking procedure

4. Two passes were made to validate the concern at different speeds. Approached the test road section and drove through at 70–80 kmph. Centered the steering wheel, then slightly turned (3°) the steering vehicle to the left and then to the right to get a feel for centeredness. Held the steering wheel with a light touch on center. If the vehicle drove straight but steering wheel is off center, it was required to perform an alignment to correct the condition.
5. Noted the direction toward which the vehicle tends to drift or pull. If the vehicle had a tendency to go left, then place the vehicle on right lane and vice versa. To ensure accuracy, test was repeated with the vehicle traveling in the opposite direction on the same road for multiple times.
6. Two measurements were taken. First, how long it takes for the vehicle to move from one edge to the other edge (case A) and secondly, how long it takes for the vehicle to move across one complete lane (case B). Used the conditions in Table 1 given below to confirm drifting or pulling condition.
7. It was ensured that strong wind was not blowing during the road test (Fig. 1).

3 Pulling Vehicle Wheel Alignment Data Distribution

A regular vehicle model was selected for study with the specifications as shown in the following Table 2.

Based on the vehicle design parameters, the wheel alignment specifications are set and are as shown in Table 3.

For this study, 51 random vehicles are selected with vehicle pulling problem. During the vehicle manufacturing, the wheel alignment is done. This wheel alignment data is recorded for all the production vehicles (Fig. 1).

Table 2 Test vehicle specifications

Vehicle parameter	Specification
Body	SUV, Monocoque
Engine	Four-cylinder diesel 2 L transversal engine, 114 kW, 360 Nm, 4-point engine mounting system
Steering	Hydraulic rack and pinion steering gear
Drive and transmission	FWD, 6 Speed—manual
Suspension (front/rear)	MacPherson Strut/Multi-link
Tires	R18/R17, tire pressure 32 psi

Table 3 Test vehicle wheel alignment specifications

Angle	Wheel side	Specification	Wheel side	Specification
Camber	Front LH	−0° 30′ to 0° 30′	Rear LH	0° to 1°
	Front RH	−0° 30′ to 0° 30′	Rear RH	0° to 1°
Toe-in	Rear LH	0° to 0° 10′	Front LH	0° to 0° 10′
	Rear RH	0° to 0° 10′	Front RH	0° to 0° 10′

To check the effect of the wheel alignment on the vehicle pulling phenomenon, camber and toe angle values set for those sample vehicles are plotted as shown in Figs. 2, 3, 4, 5, 6, 7, 8 and 9. In all figures, the horizontal lines represent the acceptable range of variation.

It is evident from Figs. 2 and 3 that for all the vehicles front LH and RH camber angle, respectively, though on the negative side but all the values are within the specifications as described in Table 3.

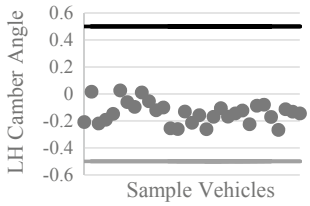

Fig. 2 Front LH camber angle distribution

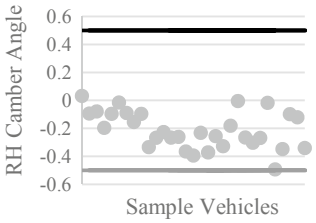

Fig. 3 Front RH camber angle distribution

It is evident from Figs. 4 and 5 that for all the vehicles, rear LH and RH camber angle, respectively, though on the negative side but all the values are within the specifications as described in Table 3.

It is evident from Figs. 6 and 7 that for all the vehicles, rear LH and RH toe angle, respectively, are within the specifications as described in Table 3 with two vehicles having rear RH toe angle value equal to the lower limit of specification.

It is evident from Figs. 8 and 9 that for all the vehicles, front LH and RH toe angle, respectively, are within the specifications as described in Table 3 with two vehicles having front LH toe angle value equal to the lower limit of specification.

Thus, from the data distribution, it can be concluded that the wheel alignment values are not causing the vehicle pull phenomenon.

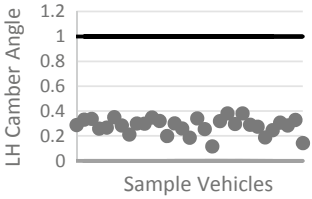

Fig. 4 Rear LH camber angle distribution

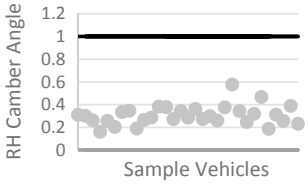

Fig. 5 Rear RH camber angle distribution

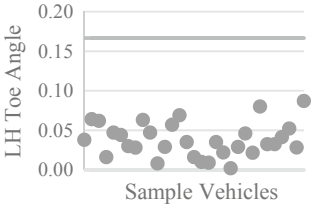

Fig. 6 Rear LH toe angle distribution

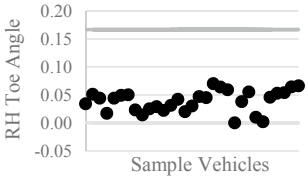

Fig. 7 Rear RH toe angle distribution

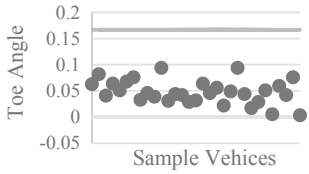

Fig. 8 Front LH toe angle distribution

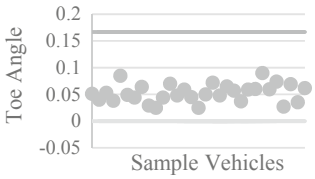

Fig. 9 Front RH toe angle distribution

4 Subjective Evaluation of Vehicles

To find the root cause for the pulling issue, we conducted subjective evaluation of eight vehicles numbered from V1 to V8. These selected vehicles were new vehicles which were not driven for more than 50 km since their manufacturing. The vehicle specifications were same as that mentioned in Table 3.

The test track selected for the subjective evaluation was a flat surface. During the testing, it was ensured that there is no relevant wind speed to eliminate the possibility of any crosswind causing the vehicle to pull in the direction of crosswind and test day was selected to have stable weather conditions. Vehicles were driven in straight line and maximum deviation from the center line along a distance of 750 m was evaluated.

For the subjective evaluation, rating scale was used with 1 indicating almost no deviation, 2 for low deviation, 3 for High deviation, and 4 for very high deviation. Table 4 shows the results obtained during the subjective evaluation.

Table 4 Subjective vehicle evaluation ratings

Vehicle number	Acceleration from 40 to 100 kmph 4th gear	Constant speed 100 kmph 4th gear	Constant speed 100 kmph 6th gear	Coast down clutch depressed 120–60 kmph
V1	1	1	1	1
V2	1	1	1	1
V3	2	1	1	2
V4	3	2	1	2
V5	3	2	2	3
V6	4	2	2	3
V7	4	3	3	4
V8	4	3	3	4

Table 5 Tire swapping effect on subjective vehicle evaluation ratings

Vehicle	Tire set used	New ratings
Good	T5, T6, T6, T8	3
Bad	T1, T2, T3, T4	0
Worst	T1, T2, T3, T4	0

As seen from the subjective ratings given in the table above, the vehicle V1 was showing the best capability to maintain the straight line and the side pull was not noticeable.

For finding the correct cause for the pull, three out of the eight vehicles were selected for further study. Based on the total score of each vehicle we selected V1 which was considered as good vehicle, V7 as a bad vehicle and V8 as a worst vehicle.

To check the effect of tires on the vehicle pull, tire swapping was done between the three selected vehicles and subjective ratings were given again with changed tires. Tires were numbered for the three vehicles as T1 to T4 for good vehicle, T5 to T8, and T 9 to T12. Numbering for the tires was from front right, front left, rear right, and rear left for each vehicle.

Vehicles were evaluated on the same track and pulling was checked during accelerating from 40 to 100 kmph in the 4th gear.

As shown in Table 5 it can be seen that worst vehicle rating changed to zero, which indicates no pulling which by replacing the tires with the good vehicle and similarly, because of replacement of tires form the good vehicle with the bad vehicle pulling phenomenon started to occur in the good vehicle.

Figure 10 shows the change in the subjective evaluation score because of the tire replacement between vehicles.

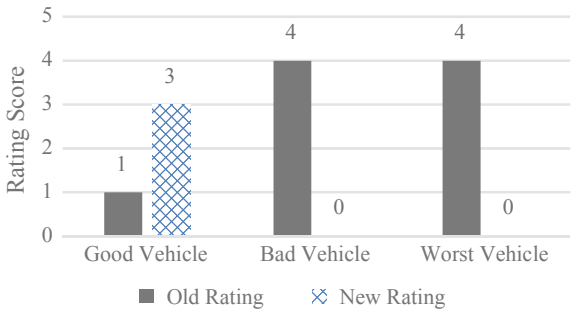

Fig. 10 Rating comparison pre- and post-tire change (lower is better)

5 Results and Discussion

Vehicle pulling problem observed in the vehicles was a major concern in terms of safety hence detailed analysis was required to find the rootcause and identify a corrective action for its rectification. In this study, we have demonstrated the procedure used to identify the vehicles with the pulling issue. Effect of wheel alignment parameters on the vehicle pull is also checked and conducted subjective vehicle tests to identify effect of tire on vehicle pulling.

Wheel alignment being one of the possible cause, we analyzed the alignment values for the vehicles and compared those with the design specifications. However, wheel alignment data analysis for the vehicles with the pulling shows no conclusive trend.

Based on the subjective study conducted, it can be concluded that the effect of pull is caused because of tire.

References

1. Blundell M, Harty D (2014) The multibody systems approach to vehicle dynamics, pp 1–741
2. Gent AN, Walter JD (2006) United States and University of Akron. The pneumatic tire
3. Muthu Siva Sankar T, Sankarganesh P, Amarnath SKP, Becker P (2011) Prediction of tread geometry influence on Ply steer Residual Aligning Torque (PRAT). SIMULA India Regional Users Meeting
4. Manual of Specifications & Standards (2010) Planning commission government of India New Delhi, IRC: SP: 73-2007
5. Gillespie TD Fundamentals of Vehicle Dynamics. University of Michigan-Ann Arbor, 1992-02-01, SAE International

Design and Analyzing Vibration with Acoustic—Structural Coupling of Muffler for Four-Stroke Diesel Engine

T. Sreedhar and B. Nageswara Rao

Abstract Muffler is one of the important devices in the exhaust system. This plays a key role in reducing the exhaust gas noise and pressure, before when they are expelled from the exhaust system. This noise comes from the exhaust manifold which is due to the large pressure in the difference between atmosphere and exhaust gases. For quite operation Muffler is used. In this paper, a muffler with selective sound-absorbing material like carbon fiber and rockwool was used. Two different mufflers (original and modified) are designed and modelled Creo2.0. Acoustic—structural simulation is done for the two different models of muffler along with two assigned sound-absorbing materials. The simulation results are explained that the acoustic power level (dB) and frequencies are reduced for the modified model than the original model when the Rockwool material is used.

Keywords Muffler · Carbon fiber · Rockwool · Creo2.0 and ansys

1 Introduction to Muffler

A muffler (silencer) is a very important noise controlling part for reduction of tackle exhaust noise, fan noise, and unusual noise sources involving the flow of gases. The reduction levels of those kinds of the muffler are enthusiastic about the frequency of the noise supply. Investigations on absorption mufflers have indicated that these have fairly smart noise decrease. The muffler is arranged in the middle of the engine exhaust pipe and outlet pipe. In muffler, exhaust gases are permitted to increase

T. Sreedhar (✉)
Department of Mechanical, VFSTR, Guntur, Andhra Pradesh, India
e-mail: sreedharthotti@gmail.com

B. Nageswara Rao
Department of Mechanical & Director IES, VFSTR, Guntur, Andhra Pradesh, India
e-mail: director_ies@vignan.ac.in

N. Gascoin and E. Balasubramanian (eds.), *Innovative Design, Analysis and Development Practices in Aerospace and Automotive Engineering*, Lecture Notes in Mechanical Engineering, https://doi.org/10.1007/978-981-15-6619-6_27

slowly and to cool in the muffler. In various designs, the outer most shells of the mufflers are made with an oval shape to allow sufficient clearance with the ground. Most of the mufflers are provided with little channel gaps in the outside shell to drain out the condensate from the exhaust gases and to oppose corrosion [1].

1.1 Types of Mufflers

- Baffle type
- Wave cancellation type
- Resonance type
- Absorber type
- Combined resonance and absorber type.

1.2 Rockwool Insulation

Rockwool was discovered on the islands of Hawaii, wherever it happens naturally as a by-product of volcanic activity at the start of the twentieth century. Dielectric in its manufactured state has non-directional fiber orientation and also the distinctive characteristics of the stone. Dielectric is synthetic from liquefied rock in a chamber through that a stream of an air temperature of concerning around 160 °C. The ultimate product generates a mass of fine free fibers which have a loose-leaf folder and oil to reduce dusting. Once ironed into reels and pieces their capability to partition air makes them outstanding heat insulators and sound absorber.

2 Literature Survey

In Chen et al. [2], the compression ratio is altered to 17.5, the intake pipe and valve are changed to 45 mm and 3°CA (backwards), the timing of the exhaust valve is changed 3°CA (forward), and now, the new muffler is assembled. The results show for the modified modelled and simulated that intake noise decreases 1.1–1.4 dB and exhaust noise decreases 2.6–3 dB. Md. In Nasir et al. [3], the experiments on the muffler tested with a 500KW load and 1800 RPM. It frequently causes duct ion of exhaust gas flow noise. In Asutosh Prasad et al. [4], the experimental results are stated that 2.5 dB minimum exhaust pressure is obtained at the tailpipe of the reactive muffler and respective to the higher conduction loss of 90 dB which is obtained with frequency 1350 Hz. In Crocker et al. [5], the coherence model has allowed a rigorous determination of the attenuation (frequency response function Hi) between individual cylinder pressures and engine noise. Previous attempts at this must be regarded as approximate at best since only an “average” attenuation

could be deduced. Previous attempts must assume that each cylinder pressure is incoherent and equal in magnitude and is thus suspect in the low-frequency range where the signals are coherent. In Meiling et al. [6], it is constructed on a finite-volume method of the Navier–Stokes equations and solved with flux-difference splitting and an explicit formulation. In Gen et al. [7], acoustic performance and existing problems on muffler are analyzed, and the acoustic performance analysis methods like one-dimension acoustic transfer matrix, finite element method, and boundary element method using on muffler design are discussed. Based on the actual working characteristics of a muffler, point out that the influence of airflow and temperature on muffler acoustic performance cannot be neglected. In Vijayaraj et al. [8], the measurements data explains that engine noise is highly associated with engine speed and that the produced noise variation (nearly 10 dB) was high enough to permit the evaluation of the potential of both approaches for noise assessment during transients.

3 Boundary Conditions

- The muffler design and dimensions are taken from standard data book from Ashok Leyland.
- Velocity of air = 20 m/s [1],
- Rockwool and carbon fiber mechanical properties are taken from the matweb.com.
- In 3D modelling software (CREO 2.0), the assembly of a muffler is designed, and 2D drawings are given below (Fig. 1).

4 Results and Discussions

The assembly file is converted into step file in Creo 2.0 and imported to the ANSYS Fluent (Fig. 2; Table 1).

The observation found in Fig. 3a and b is acoustic power level (dB) for the original and modified model. In this, the (dB) level is less for the modified model because of the holes and material is used for the simulation is carbon fiber. In this, for the modified model, the acoustic is reduced compared to original due to holes are arranged in the area of exhaust gas flow. By conducting the FST technique in ANSYS and with harmonic analysis, the frequencies (Hz) versus amplitude (mm) and phase angle versus frequency (Hz) for an original and modified model with both materials are observed.

Amplitude is always inversely proportional to frequency. Frequency is measured in Hertz. Small waves have less energy, and large waves have high energy. In Fig. 4, the frequency response is shown for the original model for the carbon material. In this, at 560 Hz of frequency obtained, the maximum amplitude (8.68e−6 mm) and minimum (1.37e−8 mm) at 875 Hz were obtained. In Fig. 5, the maximum amplitude is obtained at 440 Hz when the rockwool material is assigned to the original model.

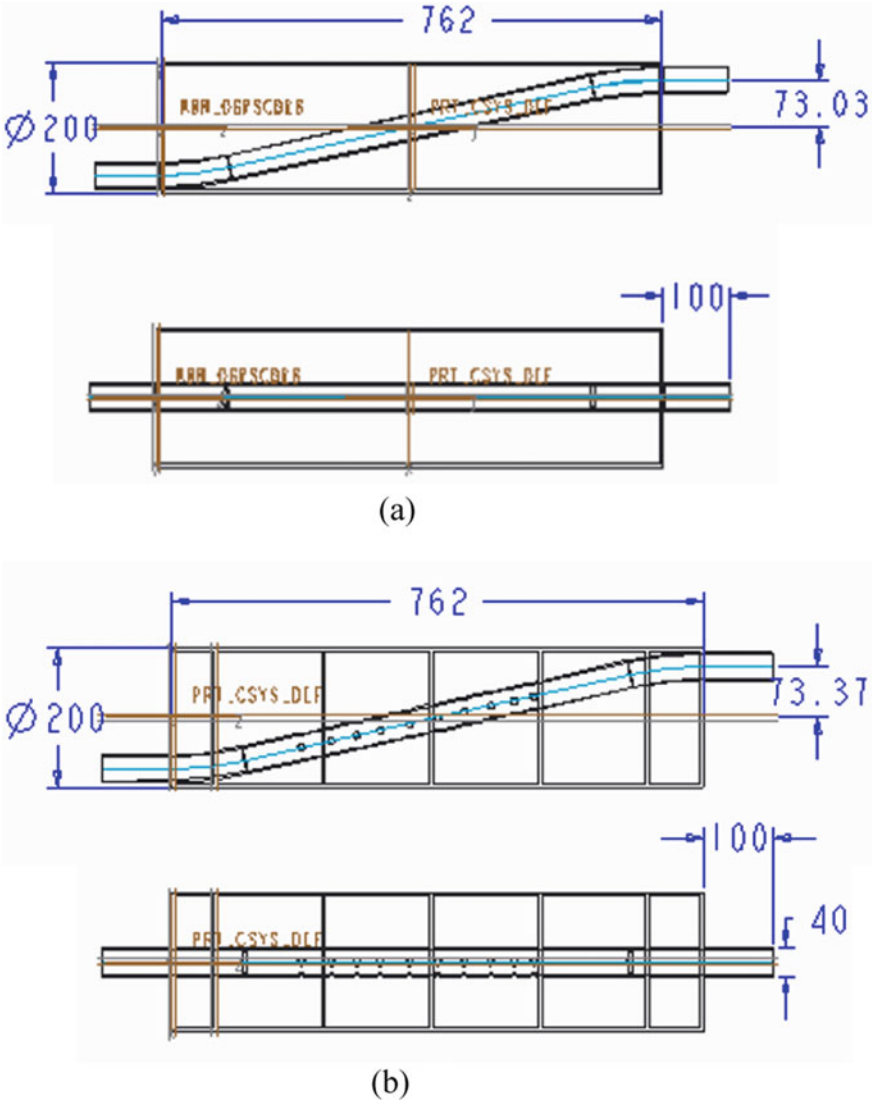

Fig. 1 **a** 2D wire frame drafting–original, **b** 2D wire frame drafting–modified with holes

The maximum energy levels are obtained for the carbon fiber material and minimum for the rockwool.

In Fig. 6, the frequency response is shown for a modified model for the carbon material. In this, at 1.16 e+3 Hz of frequency obtained, the maximum amplitude (3.01e−2 mm) and minimum (9.64e−4 mm) at 770 Hz are obtained. Similarly, in Fig. 7, the maximum amplitude is obtained at 357 Hz when the rockwool material is assigned to the modified model. The maximum energy levels are obtained for the

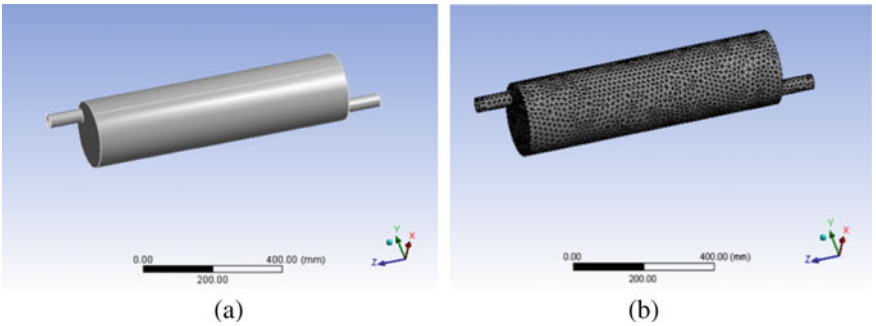

Fig. 2 **a** Imported from the ANSYS **b** Tetra meshing body

Table 1 Quality of meshing for the muffler

Mesh metric	Element quality	Aspect ratio	Skewness	Orthogonal quality
Min	0.20678	1.1402	4.1268e−5	0.1626
Max	0.9998	8.6137	0.8374	0.99975
Avg	0.83525	1.8544	0.22324	0.77774
Standard deviation	9.764e−2	0.46881	0.11885	0.11956

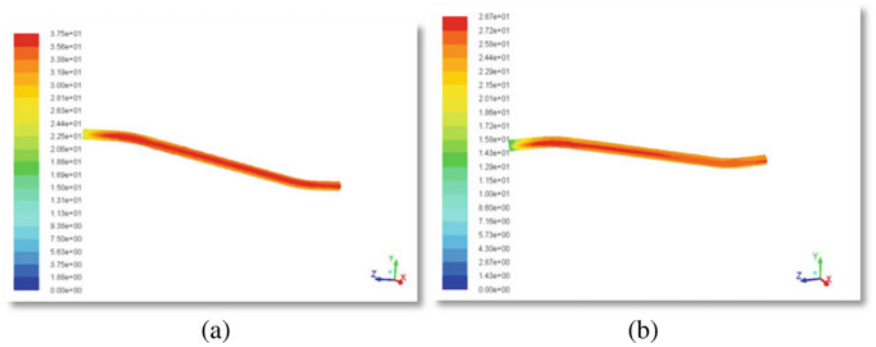

Fig. 3 Acoustic power level (dB) **a** Original model **b** Modified model

carbon fiber material and minimum for the rockwool. By comparing Figs. 4, 5, 6, and 7, the minimum energy levels are obtained for the material rockwool because it is having the capacity to observe the more energy.

Acoustic power level is compared with two different models and materials in Fig. 8. In this, the modified model having holes is observing more sound compared to original and also while compared with materials, the rockwool is the material having excellent acoustics and sound absorption properties, so it is getting less dB level compared to carbon fiber because of its properties.

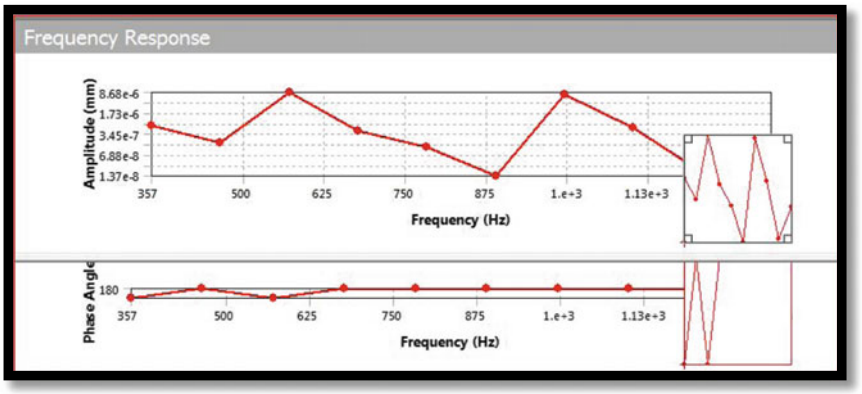

Fig. 4 Frequency response—carbon fiber—the original model

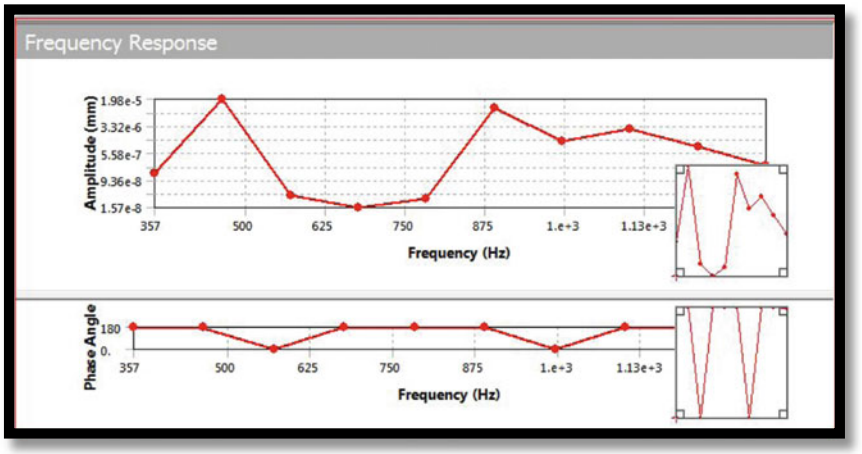

Fig. 5 Frequency response—Rockwool—Original model

Frequency is compared with two different materials in Fig. 9. In this, the rockwool is the material is getting less frequency compared to carbon fiber in all modes. Frequency (Hz) is compared with two different materials for the modified model in Fig. 10. In this, the rockwool is the material which is getting less frequency compared to carbon fiber in all modes, and if we compare to the original model, the frequency is less for the modified muffler.

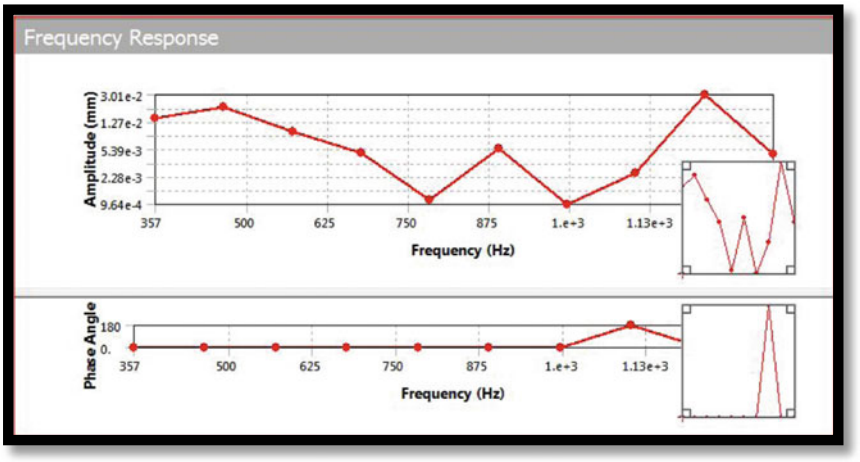

Fig. 6 Frequency response—carbon fiber—modified model

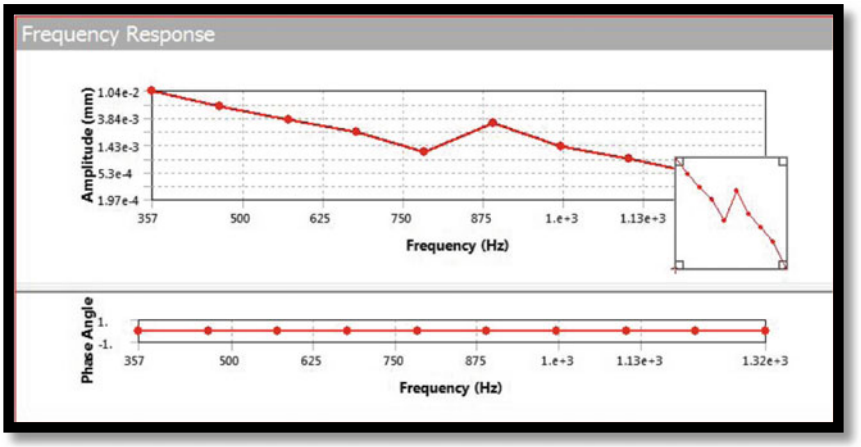

Fig. 7 Frequency response—rockwool—modified model

5 Conclusion

The following conclusions can be made from the analyses results:

- The acoustic power level is decreasing for the modified model than original model. So the sound level from the engine is less when modified model is used. When the material Rockwool is used, the sound level is lesser.
- The frequencies are decreasing for modified model than original model. Due to higher frequencies, vibrations will increase. Rockwool has lesser frequencies.

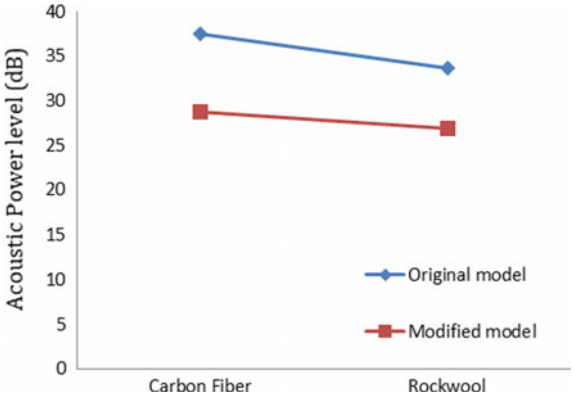

Fig. 8 Comparision of acoustic power level (dB) with different materials and models

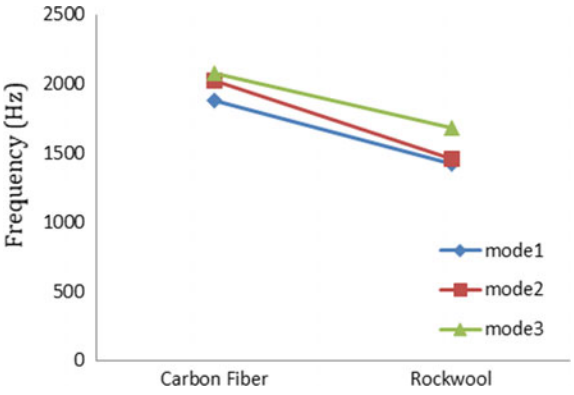

Fig. 9 Comparison of the frequency with different materials and models—original model

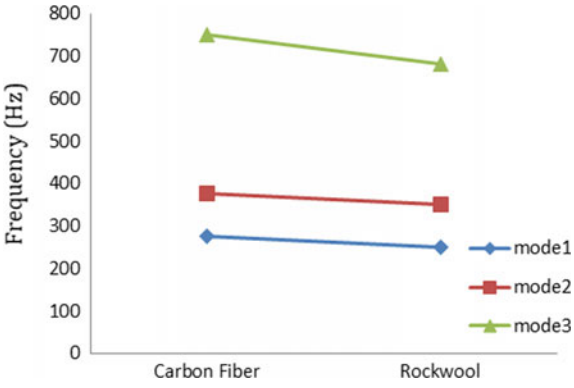

Fig. 10 Comparison of frequency (Hz) with different materials and models—modified model

- By comparing the Figs. 4 to 7, the minimum energy levels are obtained for the material Rockwool because it has the capacity to observe the more energy.

References

1. A Practical Approach towards Muffler Design, Development and Prototype Validation. Article in SAE Int J Eng September 2010, https://doi.org/10.4271/2010-32-0021
2. Chen H-J, Zhu G-Y (2013) Noise reduction of single cylinder diesel engine based on virtual prototype. Adv Mater Res 718–720:1499–1503. Trans Tech Publications, Switzerland https://doi.org/10.4028/www.scientific.net/AMR.718-720.1499
3. Uddin MN, Rahman MA, Rashid MM, Nithe NA, Rony JI Reduce generators noise with better performance of a diesel generator set using modified absorption silencer. Global J Res Eng
4. Prasad A (2019) Acoustic performance design of automotive muffler. Technologies, Atoa
5. Crocker M, Hamilton J (1979) Modeling of diesel engine noise using coherence, SAE technical paper. Feb 1, 1979, 790362
6. Meiling L (2013) Acoustic characteristic simulation and study of exhaust muffler based on CFD. Shandong University, Jinan. China
7. Gen L, Jiangbo X, Haihau X (212) The research and trend at home and abroad of acoustic performance on exhaust muffler Mod Manuteng 12:127–132 (in Chinese)
8. Vijayaraj VT, Vijay S, Vignesh S, Nandha Kumar M, Naveen Kumar M (2016) A study on modern diesel engine combustion noise. In: International conference on systems, science, control, communication, engineering and technology pp 894–900

Review of Polydimethylsiloxane (PDMS) as a Material for Additive Manufacturing

Qusai Alkhalaf, Sarang Pande, and Ritesh Ramesh Palkar

Abstract In manufacturing and product development, tremendous changes have been observed over a decade. The process of developments ensures the transformations to human life as and when required. The additive manufacturing is one of the processes involved in it, which emerged very fast in recent technical improvements/revolution. The additive manufacturing facilitates the development of the new range of materials along with improvements in the properties of existing materials. In this review article, the emphasis is on Polydimethylsiloxane in the additive manufacturing process. This article also discusses the primary considerations and the properties to be considered for the manufacturing of Polydimethylsiloxane to make it suitable for additive manufacturing. The review suggests the various parameters of the PDMS which made it a suitable option for additive manufacturing. Authors also tried to highlight the desired steps involved to enhance the additive manufacturing process with the help of emerging hybrid additive manufacturing processes.

Keywords Additive manufacturing · Polydimethylsiloxane · Photopolymerization · Direct ink writing · Digital light projector

Q. Alkhalaf (✉) · S. Pande
Mechanical Engineering Department, Faculty of Technology, Marwadi University, Rajkot, Gujarat, India
e-mail: qusai.khalaf106134@marwadiuniversity.ac.in

S. Pande
e-mail: sarang.pande@marwadieducation.edu.in

R. R. Palkar
Chemical Engineering Department, Faculty of Technology, Marwadi University, Rajkot, Gujarat, India
e-mail: ritesh.palkar@marwadieducation.edu.in

N. Gascoin and E. Balasubramanian (eds.), *Innovative Design, Analysis and Development Practices in Aerospace and Automotive Engineering*, Lecture Notes in Mechanical Engineering, https://doi.org/10.1007/978-981-15-6619-6_28

1 Introduction

In the global market, new products are introduced very rapidly due to varying customer's choices. İn order to meet customer preferences, different materials are essential. It is, therefore, necessary to introduce new materials. In such a scenario, the selection of the material depends on the application. The desired criteria which are satisfied by the material in the developing phase are viz. functionality, ability to retain its properties. The metals, polymers and ceramic are main components that are mostly used in the engineering products to meet the customer requirements. The products are manufactured conventionally with the help of a series of operations. The sequence follows primary processes such as casting, forging followed by the secondary processes like machining, involving roughing and finishing operations and then finally by the tertiary processes or the material joining processes, for example, fastening, welding, adhesive bonding.

PDMS, a soft rubber, which is used in many fields such as the medical to make prostheses and microfluidic as well as electrical devices. There is a big challenge in achieving curing and printing the PDMS owing to several reasons, such as it has lower yield stress, lower glass transition temperatures. The curing agents used lately were very much time-consuming; it used to take about 72 h for the curing. Therefore, the parts printed with PDMS generally have support material such as gel and PVA. The curing and hardening agents such as platinum catalysts, TOP-L and ITX are being used to achieve printing without support material along with improved mechanical and electrical properties (Table 1).

Table 1 Different materials used in applications similar to biomedical

Application	Materials	Process for additive manufacturing
Microfluidic	Polyethylene Glycol Diacrylate [1]	–
	PDMS [2–5]	SLA, FDM
	poly(ethylene glycol) diacrylate (PEGDA) [5]	SLA
Biomedical	Stainless steels, (Co–Cr–Mo) and Ti, (especially Ti–6Al–4V) [6]	electron-beam melted (EBM)
	Calcium Polyphosphate (CPP) with Polyvinyl alcohol (PVA) [7]	Solid freeform fabrication (SFF)
	Poly(ethylene glycol)- terephthalate poly (butylene terephthalate) (PEGT/PBT) [8]	FDM
Pharmaceutical	Hydroxypropyl methylcellulose, polyacrylic acid (PAA) [9]	FDM
	Polyethylene oxide, polyvinyl alcohol [10]	FDM

Additive manufacturing (AM) is the latest way to make products layer by layer. Using these processes, one can create a product with complex geometries. The developments in processes of AM have quickly occurred in the last few years. Based on the type of material, i.e. liquid, solid, powder, the processes are classified. In stereolithography (SLA) liquid polymer is used, and in selective laser sintering (SLS) powdered material is used, whereas a solid filament or solid wire is used in fused deposition modelling (FDM). The above-listed processes have a unique method of converting the raw material into the solid part and the different characteristics that help to distinguish each of the processes. In addition to this, all processes have similarities in the layer by layer manufacturing concept to make the solid model. In SLA, the liquid resin is available as a monomer, which is exposed to the UV light in a controlled manner. In this process of polymerization due to the incident light on the liquid resin surface, the spot gets polymerized. The solidification of the resin typically shows the polymerization. Although the resin is solidified, it is not having sufficient strength. Therefore, after the photo-polymerization, the solid part is kept in a UV chamber where the crosslinking of the polymeric chains occurs resulting in the strength of the solid. Usually, in the SLA process, the polymer used is of thermosetting type.

In contrast, FDM converts a thermoplastic polymer filament to make a solid part. A Polymer wire passes through a heated nozzle converting it into a sticky solid of reduced cross-section. The semisolid wire coming out of the extruder is deposited on a horizontal surface with the help of Computerized Numerical Contro (CNC) control. Within a few seconds, the wire gets converted back to solid. The sticky polymer gets adhered to the already laid wire. In SLS, the conversion to the solid part happens under laser incident on the powder spread on a horizontal surface. Wherever the laser spot incident, powder grain gets converted to the semisolid state. In that state, it fuses with the adjacent powder grain. As soon as the laser spot moves ahead, the fused powder grains get converted to solid. In this process, the manufacturing of the solid part results from the controlled incidence of the laser. With the help of the controlled incidence of laser, the solid part is manufactured.

The challenges faced in application and use of PDMS in AM are classified into two categories; the first includes the process of printing and the second is about enhancing the properties of PDMS.

Prior involves process, SLA with which, printing PDMS having high viscosity isn't possible. İn FDM printing the challenge is printing PDMS without support materials and with more resolution. İn addition, there is always problem clogging nozzle. İt is possible to print PDMS by increasing its yield stress. The later uses PDMS having low Young's modulus. İt should be able to increase Young's Modulus more than 2 MPa.

Even at levels significantly higher than those seen in the field sampling, experiments with both aquatical and terrestrial species demonstrated no adverse effects. Therefore, the environmental risk of PDMS is not expected [11].

2 PDMS Applied in Additive Manufacturing

The selection of material for AM is mostly dependent on the application. There is a large number of materials available for making a part. However, a limited number of materials support the AM. The choice of material is based on several considerations. The necessary points to be evaluated while selecting the material are functional requirements, mechanical properties, geometric criticalities, aesthetical and cost [12]. Over the last four decades, AM has significant applications in almost all fields. It includes engineering aerospace, automotive parts, a medical field such as prosthesis, tissue engineering and art, architectural [13].

Polydimethylsiloxane (PDMS) is a very versatile material that can be used in medical applications like to make prosthetics [14]. PDMS also serves as a promising material to create artificial human body parts like the brain and the heart since PDMS being biocompatible and non-toxic [4, 5]. PDMS is a thermosetting elastomer that finds application in electrical insulations [15]. Nowadays, a lot of research work is being carried out to use PDMS as additive manufacturing material in FDM and SLA processes owing to its versatile applications. In the pharmaceutical field, tablets or medicines are manufactured by embedding PDMS with the drugs [16]. The cost-effective material has prepared using [17].

The PDMS was also used to print in 3-D with digital light and phenyl phosphinate (TPO-L) as a photoinitiator. The parts manufactured using this process showed increased Young's modulus up to 1.44 MPa with lower permeability 15% as compared with a part manufactured with conventional processes [18]. Another way to is The Freeform Reversible Embedding (FRE) is also one of the effective methods to print parts using PDMS. As PDMS has less yield stress, the FRE printing is carried out with the help of support material and carbopol gel. The FRE complex objects can be made usually by adding PDMS with an agent for 72 h [19]. The Hydrostatic 3D printing (H3P) with low one-photon polymerization (LOPP) is applied for printing soft silicone polymer in support material [20]. Besides, LOPP is also used to print PDMS with 2H2M (2-Hydroxy-2-Methylpropiophenone) as a photoinitiator [21]. The PDMS is printed in SLA process with two types viz, PDMS-S (Methacryloxypropyl of group link by side-chains along the PDMS-chain) and PDMS-E (Methacryloxypropyl in the end terminal groups). In this process, with TPO-L photoinitiator it shows an effect on Young's module results in elongation and breaks. It is found that the elongation at a breakpoint for PDMS(E-S) is between 143 and 150%, and it is better than Sylgard 184 [22]. PDMS-DMAA printed with Irgacure 819, which lowers breakdown elongation to 51% and the maximum stress to $\sigma_{\max} = 0.58 \mp 0.09$MPa [23]. The Embedded 3D printing with two types of PDMS Sylgard-184 and SE-1700 with particles of the silica and Curing agent. It is also observed that, the silica gives the thixotropic behaviour, and the elastic module G'_{maximum} value is observed to be around 515.3 Pa and maximum shear stress is 127.3 Pa [24]. The soft silicone can be printed in fused deposition moulding using print with poly-vinyl alcohol (PVA). The quality of printing is affected by the adhesion between the silicon and PVA and angle overhanging [25]. The human body parts like, hand and nose, blood vessels, were printed

by PDMS with the help of liquid deposition modelling (LDM). It can be facilitated by mixing two types of PDMS, i.e. SE 1700 and Sylgard 184, with different sizes of the nozzle. In this work, the ultimate strength of 5.036 MPa and Young's modulus 1.672 MPa was observed [26]. The human heart for the training and surgery purpose was made and presented by using silicon PDMS which was printed in FDM. In this work, a group of researchers used the PDMS as pellets with Na-CMC. The modulus for the filament of PDMS/Na-CMC was observed to be 8.515 kPa when extruded at 205 °C, and the viscosity of 1958.45 Pa.s [27]. Scaffolds of size 40 × 300 μm were created by printing (Sylgard 184), PDMS agent and PVA. In the heating stage, the resolution of 500 μm, the nozzle of size 250 μm was used to achieve the thermal stability and [28].

The Direct Ink Writing (DIW) achieves a better modulus G'of 11,360 Pa by mixing PDMS (SE-1700) with Dragonskin 30. In this process of DIW, the different sizes of the nozzles were used with a specific pressure of 200 kPa [28]. The mixture of PDMS-co-PDPS (Polydimethylsiloxane-co-Diphenylsiloxane) with silica HMDZ (hexamethyldisilazane-treated) reveals the value of the coefficient, i.e. $G'/G'' =$ 410 Pa. The advantage of HMDZ-treated silica is, it helps to increase the yield stress and also allows to cure the PDMS when it is added with a platinum catalyst [29]. The low yield stress is one of the disadvantages of the LDM for printed LSR (PDMS with silica) solution the problem of low yield stress Polyethylene Glycol (PEG) can achieve the yield stress about 1000 Pa, which is suitable for printing [30]. The excellent elastic strength with 18 μm lateral resolution was achieved by the Laser Direct Writing (LDW) [31]. Apart from all these practices, a Full Reactive Inkjet Printing (FRIJP) accomplishes the printing PDMS by two different types with platinum catalysts as complex shapes [32].

3 Process of Making Solid Objects Using PDMS

3.1 Photoinitiators and Agents Used with PDMS

Polydimethylsiloxane is known as thermosetting material that has a challenge for printing, and it also serves as the potentials to apply in additive manufacturing. Therefore, it has acquired the attention of researchers. The researchers have been trying to experiment in printing this polymer. It is well known that this polymer is applied in several processes. In additive manufacturing, there are many ways for printing PDMS, but almost all of the printing processes of PDMS need an agent or a support material. These agents differ in many parameters as they are used to cure PDMS. The well-known agent applied is the Curing agent (Dow Corning) that can convert the PDMS from liquid to solid during several periods; it depends on the process, such as FRE. This FRE process takes around 72 h to cure the PDMS. The

FRE process helps to achieve an intricate part. The disadvantage of using Curing agent (Dow Corning) is time taken hours. To overcome this issue ultraviolet (UV) light is used so it can be achieved in less time as compared to the conventional process.

Most of the researchers have been using Sylgard-184 and SE 1700 because they have the ability to synthesis by UV light. With developments in processes of synthesis, the PDMS was applied in DLP with Phenyl Phosphinate (TPO-L) photoinitiator. The TPO-L helps to solidify the PDMS when it exposes to the light. The DLP with TPO-L showed an increase in Young's modulus up to 1.44 MPa. In the DLP and SLA process, the resolution of PDMS is based on the absorption of the light. The TPO-L improves the resolution, but the limiting parameter is the amount of TOP-L, it should be less than 2 wt% to achieve better curing. The Orasol Orange is added in this process, to increase the resolution. Though photoinitiation plays a vital role in PDMS, several types of PDMS are insensitive to photoactivity. However, the photoinitiators should have two basic characterizes, which are to be suitable in the synthesis of PDMS: first, the ability to be soluble with PDMS; second, the ability to absorb the light. These two things are more critical for any curing process based on UV light.

Irgacure 819 is another photoinitiator applied to cure PDMS. This photoinitiator is advantageous over other available photoinitiators as it is cheaper, having less toxicity, the ability to absorb the light. The percentage of Irgacure 819 in PDMS is 0.25 wt%. The 2-Hydroxy-2-Methylpropiophenone (2H2M) photoinitiator achieves the absorption of the light and can add N-vinylpyrrolidone (NVP) to achieve proper curing. The Polyethylene Glycol (PEG) can be applied in Liquid Deposition Modelling (LDM). Almost all the agents change the properties of PDMS, but PEG does not change the final properties. The LDM achieves the complex object, under the application of any yield stress. The Young modulus increase with PEG percentage. The printing of PDMS with silica isn't possible without adding PEG because the yield stress of PDMS is low. One of the drawbacks is the poor quality achieved in part with this agent is poor. Figure 1 shows the details of various agents used in the additive manufacturing process. A detailed study of the advantages and disadvantages has also listed in Table 2.

4 The Support Materials Applied with PDMS

The PDMS isn't only with agent or photoinitiator can print. The PDMS has low yield stress; for that purpose, it is challenging to print alone, especially in LDM, for that it can print with other material as support such as PVA water-soluble. The success of the process is based on the adhesive between the PVA and the silicone. It achieves maximum Elastic modulus $G'_{maximum}$ value around 515.3 Pa and maximum shear stress τ_{max} is 127.3 Pa. Direct Ink Writing (DIW) prints the PDMS with Dragonskin 30 to accomplishes a better modulus of elasticity $G' = 11{,}360$ Pa. Besides, it can print the PDMS with two types PDMS SE1700 and Sylgard 184. This process achieves an

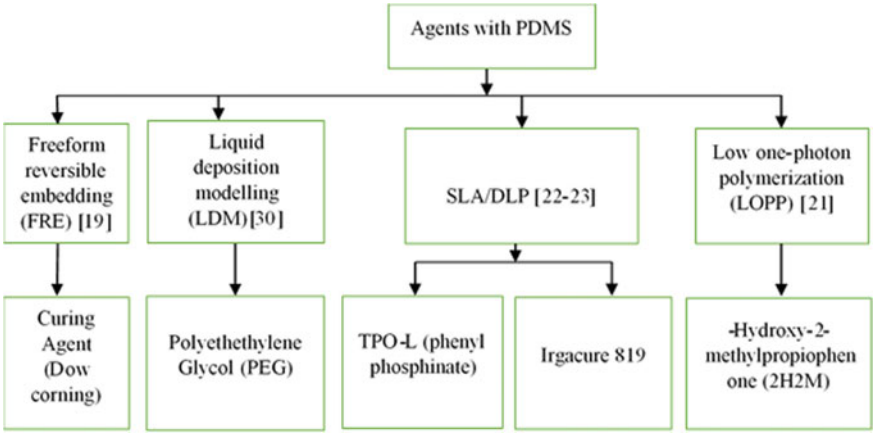

Fig. 1 Details of agents used in additive manufacturing

ultimate strength 3.432 ± 1.216 MPa comparing with casting 2.990 ± 0.414 MPa; if the filament direction is changed, it was 5.036 ± 0.657 MPa.

Figure 2 shows a detailed analysis of the additive manufacturing process, addressing the different aspects of product development.

5 Conclusion

The printing of PDMS has several processes, and all these processes were born early with PDMS. Therefore, it has many drawbacks and challenges to accomplish better properties and characteristics. In addition to conventional practice in product development, there are several hybrid techniques available to meet the needs of the industry. In line with this, we can see the better way to printing PDMS is LDM, as it doesn't lose the properties of PDMS and helps to improve the available properties. Apart from this, it helps to achieve complex shapes such as the human body part. SLA and LOPP processes have many challenges. Those can overcome in near future with detailed study and modifications. The photonics plays a vital role in all this process. The idea to photoinitiate the process to deviate its ability to offer required changes always turned to be as essential criteria for the product development. In addition to this, there are several fronts on which material scientists are taking an effort to produce and deliver the required material.

In this review article, the authors tried to focus on the use of PDMS as a single and mixed material along with necessary agents and conditions. The first study is concerned with the combination of different agents with available methods. In this article, the authors also highlight the use of PDMS as one of the efficient materials with appropriate agents.

Table 2 Summary of agents used in material processing

The agents or photoinitiators	Advantage	Disadvantage
Platinum catalysts	• It is using for crosslinking the PDMS	• It's costly
Curing agent (Dow corning) [11]	• It applied to cured specific type of PDMS such as Sylgard	• It takes a lot of time to cure PDMS
TPO-L [9, 14]	• Improving absorption and optical transparency • Improving the resolution, the penetration depth will be increased • Add the Orasol Orange with TPO-L in PDMS to increase the resolution • The higher amount of TPO-L gives fast curing • The wavelength for the light it can absorbance is 385-400 nm	• When increasing the TPO-L above 0.6, the optical transparency decreases • The solubility in PDMS is limited
Hydroxy-2-methylpropiophenone (2H2M) [13]	• Increase the absorption for PDMS • Applied in LOPP system	It's not sufficiency to cure PDMS; it should add N-vinyl-pyrrolidone (NVP) to advance the curing
Irgacure 819 [15]	• Absorption of the light happens in the visible light area • It can be applied with resin, which has a higher reactive • It's cheap • No-toxicity	• The amount of Irgcure 819 effect on the maximum strain and tensile strength • Irgcure 819 isn't sufficiency for curing the PDMS it should add other materials for examples: SilOHflex
Polyethylene Glycol (PEG) [22]	• Increase Yield stress for PDMS • It can get high quality when controlling the amount of PEG • Achieving a right ratio mass without failing the layers	The need for adding silica particles for achieving perfect printing

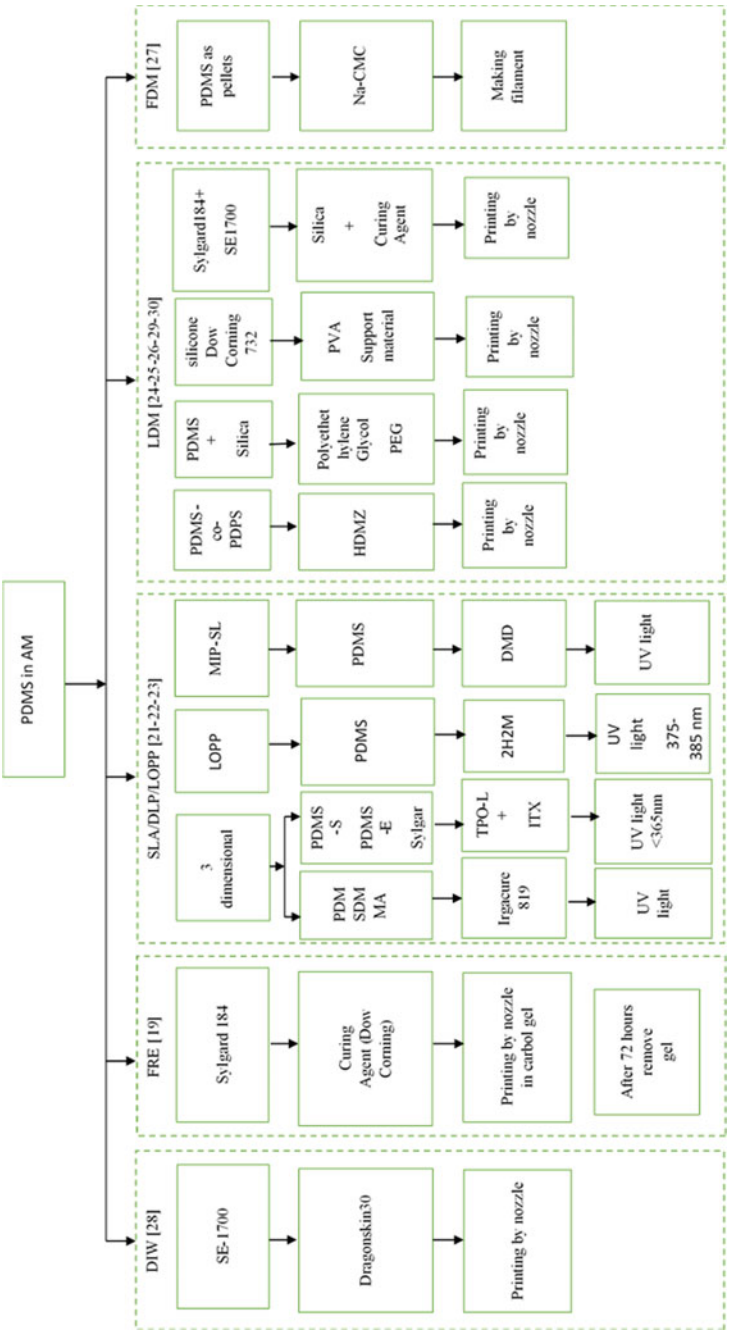

Fig. 2 Distinctive features of additive manufacturing

References

1. Rogers CI, Pagaduan JV, Nordin GP, Woolley AT (2011) Single-monomer formulation of polymerized polyethylene glycol. Anal Chem 83:6418–6425
2. Au AK, Lee W, Folch A (2014) Mail-order microfluidics: evaluation of stereolithography for the production of microfluidic devices. Lab Chip 14(7):1294–1301. https://doi.org/10.1039/c3lc51360b
3. Kanai T, Tsuchiya M (2016) Microfluidic devices fabricated using stereolithography for preparation of monodisperse double emulsions. Chem Eng J 290:400–404. https://doi.org/10.1016/j.cej.2016.01.064
4. Gaal G et al (2017) Simplified fabrication of integrated microfluidic devices using fused deposition modeling 3D printing. Sens Actuators, B Chem 242:35–40. https://doi.org/10.1016/j.snb.2016.10.110
5. Miri AK et al (2018) Microfluidics-enabled multimaterial maskless stereolithographic bioprinting. Adv Mater 30(27):1–9. https://doi.org/10.1002/adma.201800242
6. Murr LE et al (2009) Microstructures and mechanical properties of electron beam-rapid manufactured Ti-6Al-4 V biomedical prototypes compared to wrought Ti-6Al-4 V. Mater Charact 60(2):96–105. https://doi.org/10.1016/j.matchar.2008.07.006
7. Shanjani Y, Amritha De Croos JN, Pilliar RM, Kandel RA, Toyserkani E (2010) Solid freeform fabrication and characterization of porous calcium polyphosphate structures for tissue engineering purposes. J Biomed Mater Res - Part B Appl Bio 93(2):510–519. https://doi.org/10.1002/jbm.b.31610
8. Woodfield TBF, Malda J, De Wijn J, Péters F, Riesle J, Van Blitterswijk CA (2004) Design of porous scaffolds for cartilage tissue engineering using a three-dimensional fiber-deposition technique. Biomaterials 25(18):4149–4161. https://doi.org/10.1016/j.biomaterials.2003.10.056
9. Khaled SA, Burley JC, Alexander MR, Roberts CJ (2014) Desktop 3D printing of controlled release pharmaceutical bilayer tablets. Int J Pharm 461(1–2):105–111. https://doi.org/10.1016/j.ijpharm.2013.11.021
10. Melocchi A, Parietti F, Maroni A, Foppoli A, Gazzaniga A, Zema L (2016) Hot-melt extruded filaments based on pharmaceutical grade polymers for 3D printing by fused deposition modeling. Int J Pharm 509(1–2):255–263. https://doi.org/10.1016/j.ijpharm.2016.05.036
11. Carmichael N (ed) (2011) Linear polydimethylsiloxanes: CAS No. 63148-62-9. ECETOC
12. Tiwari SK, Pande S (2013) Material properties and selection for selective laser sintering process. Int J Manuf Technol Manag 27(4–6):198–217. https://doi.org/10.1504/IJMTM.2013.058904
13. Tiwari SK, Pande S, Agrawal S, Bobade SM (2015) Selection of selective laser sintering materials for different applications. Rapid Prototyp J 21(6):630–648. https://doi.org/10.1108/RPJ-03-2013-0027
14. Gerratt AP, Michaud HO, Lacour SP (2015) Elastomeric electronic skin for prosthetic tactile sensation. Adv Funct Mater 25(15):2287–2295. https://doi.org/10.1002/adfm.201404365
15. Nam Y, Musick K, Wheeler BC (2006) Application of a PDMS microstencil as a replaceable insulator toward a single-use planar microelectrode array. Biomed Microdevices 8(4):375–381. https://doi.org/10.1007/s10544-006-9145-9
16. Holländer J, Hakala R, Suominen J, Moritz N, Yliruusi J, Sandler N (2018) 3D printed UV light cured polydimethylsiloxane devices for drug delivery. Int J Pharm 544(2):433–442. https://doi.org/10.1016/j.ijpharm.2017.11.016
17. Zhou C, Chen Y, Yang Z, Khoshnevis B (2013) Digital material fabrication using stereolithography. Rapid Prototyp J 3(November 2011):153–165. https://doi.org/10.1108/13552541311312148
18. Femmer T, Kuehne AJC, Wessling M (2014) Print your own membrane: direct rapid prototyping of polydimethylsiloxane. Lab Chip 14(15):2610–2613. https://doi.org/10.1039/c4lc00320a
19. Hinton TJ, Hudson A, Pusch K, Lee A, Feinberg AW (2016) 3D Printing PDMS elastomer in a hydrophilic support bath via freeform reversible embedding. ACS Biomater Sci Eng 2(10):1781–1786. https://doi.org/10.1021/acsbiomaterials.6b00170

20. Sung D, Kim D, Kao Y, Tai BL (2016) Science direct hydrostatic 3D-printing for soft material structures using low one-photon polymerization. Manuf Lett 10:6–9. https://doi.org/10.1016/j.mfglet.2016.08.002
21. (Danny) Kim DS, Suriboot J, Grunlan MA, Tai BL (2019) Feasibility study of silicone stereolithography with an optically created dead zone. Addit Manuf 29:100793. https://doi.org/10.1016/j.addma.2019.100793
22. Bhattacharjee N, Parra-Cabrera C, Kim YT, Kuo AP, Folch A (2018) Desktop-stereolithography 3D-printing of a poly(dimethylsiloxane)-based material with sylgard-184 properties. Adv Mater 30(22):1–7. https://doi.org/10.1002/adma.201800001
23. Thrasher CJ, Schwartz JJ, Boydston AJ (2017) Modular elastomer photoresins for digital light processing additive manufacturing. ACS Appl Mater Interfaces 9(45):39708–39716. https://doi.org/10.1021/acsami.7b13909
24. Grosskopf AK, Truby RL, Kim H, Perazzo A, Lewis JA, Stone HA (2018) Viscoplastic matrix materials for embedded 3D printing. ACS Appl Mater Interfaces 10(27):23353–23361. https://doi.org/10.1021/acsami.7b19818
25. Muthusamy M, Safaee S, Chen R (2018) Additive manufacturing of overhang structures using moisture-cured silicone with support material. J Manuf Mater Process 2(2):24. https://doi.org/10.3390/jmmp2020024
26. Ozbolat V, Dey M, Ayan B, Povilianskas A, Demirel MC, Ozbolat IT (2018) 3D printing of PDMS improves its mechanical and cell adhesion properties. ACS Biomater Sci Eng 4(2):682–693. https://doi.org/10.1021/acsbiomaterials.7b00646
27. Calcagnile P, Cacciatore G, Demitri C, Montagna F, Corcione CE (2018) A feasibility study of processing polydimethylsiloxane-sodium carboxymethylcellulose composites by a low-cost fused deposition modeling 3D printer. Mater (Basel) 11(9):1–14. https://doi.org/10.3390/ma11091578
28. Dahlberg T, Stangner T, Zhang H, Wiklund K, Lundberg P (2018) 3D printed water-soluble scaffolds for rapid production of PDMS micro-fluidic flow chambers. Sci Rep September 2017:1–10. https://doi.org/10.1038/s41598-018-21638-w
29. Durban MM et al (2018) Custom 3D printable silicones with tunable stiffness. Macromol Rapid Commun 39(4):6–11. https://doi.org/10.1002/marc.201700563
30. Courtial EJ et al (2019) Silicone rheological behavior modification for 3D printing: Evaluation of yield stress impact on printed object properties. Addit Manuf 28:50–57. https://doi.org/10.1016/j.addma.2019.04.006
31. Obata K et al (2017) UV laser direct writing of 2D/3D structures using photo-curable polydimethylsiloxane (PDMS). Appl Phys A Mater Sci Process 123(7):2–6. https://doi.org/10.1007/s00339-017-1104-1
32. Sturgess C, Tuck CJ, Ashcroft IA, Wildman RD (2017) 3D reactive inkjet printing of polydimethylsiloxane. J Mater Chem C 5(37):9733–9745. https://doi.org/10.1039/c7tc02412f

A State-of-the-Art Review on 3D Printed Orthotic Devices for Flat Feet Condition

S. Koteswari and Yeole Shivraj Narayan

Abstract Flat feet are one of the most commonly occurring ailments among humans all over the world. About 20–30% of the global population is suffering from this condition. Not only elder people but middle-aged people between 40 and 60 years and even younger age people between 18 and 21 years are also suffering from this ailment. Based on the National Foot Health Assessment conducted in the USA, about 18 million people, aged 21 years or older have this condition along with another 8 million adults suffering from fallen arches. This is mainly attributed to the change in lifestyle of the people. Lack of physical activities, overrunning, sitting or standing for long time, obesity pregnancy, rheumatoid arthritis diabetes, etc. are the primary reasons for this condition to develop in a normal person. A flat foot generally affects skeletal alignment leading to pain in the ankles, knees and hips. In order to overcome this, orthopedists are recommending the usage of orthotic devices for providing relaxation and comfort to the foot. Conventionally, orthotic devices made from custom silicon using an injection molding methods are used but their performance in terms of providing comfort is not up to the satisfied state. Researchers are trying to find an alternative to the conventional ones by finding better comfort providing optimized designs like 3D printed orthotic devices. This paper presents an extensive review of the state of research being carried out in the field of leg prosthetics especially orthotic devices including 3D printed orthotic devices.

Keywords Flat feet · 3D printing · Orthotic devices · Fallen arch

1 Introduction to Human Foot

In humans, foot plays a major role to perform activities like standing, walking, running, etc. The foot contains 26 bones, 33 joints, 19 muscles, 107 ligaments and over 100 tendons. This constitutes 25% of bones in the human body [1].

S. Koteswari · Y. Shivraj Narayan (✉)
VNR Vignana Jyothi Institute of Engineering and Technology, Hyderabad, TS 500090, India
e-mail: shivrajyeole@vnrvjiet.in

N. Gascoin and E. Balasubramanian (eds.), *Innovative Design, Analysis and Development Practices in Aerospace and Automotive Engineering*, Lecture Notes in Mechanical Engineering, https://doi.org/10.1007/978-981-15-6619-6_29

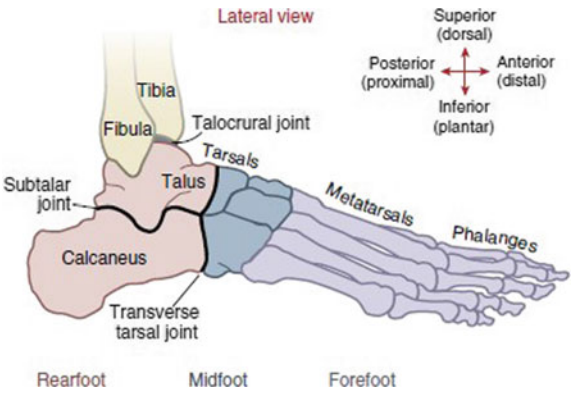

Fig. 1 Foot anatomy (*Source* EKPTA https://doi.org/10.1016/b978-0-323-54498-6.00011-4311–350)

1.1 Foot Anatomy [2, 3]

The foot is a flexible structure of bones, joints, muscles and soft tissues that help to stand upright and perform activities like walking, running, and jumping. The foot is divided into three sections as shown in Fig. 1.

- Forefoot contains phalanges and is connected to metatarsals.
- Midfoot is a pyramid-like collection of bones that form the arches of the foot.
- Hindfoot or tarsals forms the heel and ankle.

Postural alignments, lower limb mechanisms and disorders mostly depend on the height/type of arch [4].

1.2 Types of Foot Arches [2, 5, 6]

Low arch/flat foot/pes planus is foot with high shock-absorbing capabilities. It is classified as; flexible flat foot and rigid flat foot. Medium arch foot is biomechanically efficient, moderately flexible. High arch/pes cavus is very rigid, low shock-absorbing capabilities. All the 3 types of arches are as shown in Fig. 2.

Among the types of foot arches, the prevalence of flat foot is 10–25% [7]. There are different ways to identify flat foot during weight-bearing condition (Fig. 3).

1.3 Determination of Flat Foot on Weight Bearing Condition

Subtalar Joint Angle: For evaluation rear view of tibia is referred [8].

Calcaneal Pitch Angle: If the angle between metatarsal, calcaneus and navicular tuberosity is less than 17° to 18° it represents flat foot as shown in Fig. 4 [3].

Colour code: Arch height index range measurements are performed accordingly as shown in Fig. 5. A standard of arch height index in normal foot is between 0.2 and 0.26, high arch foot is below 0.2 and flat foot is beyond 0.26 [5].

$$\text{Arch Height Index } (I) = B/(A + B + C) \quad (5)$$

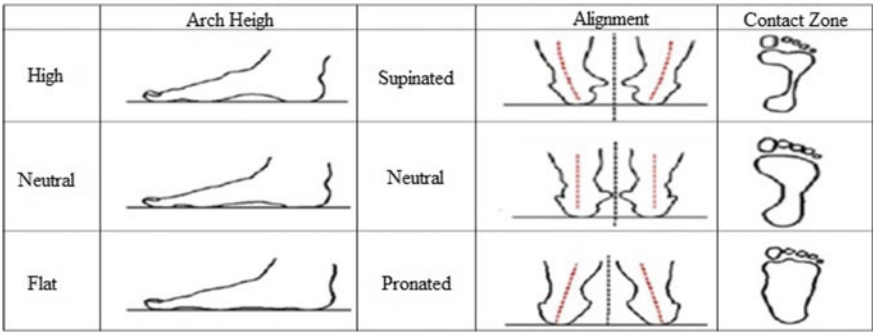

Fig. 2 Types of Foot (*Source* Int. J. Eng. Sci. Invent. 5:11–15)

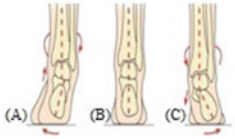

Axis	Supination	Normal foot	Pronation
Calcaneus central	Less than 180°	Equal to 180°	Greater than 180°
Fig. 3	(A)	(B)	(C)

Fig. 3 Weight Bearing Motion of Subtalar Joint (*Source* MSI 133–142)

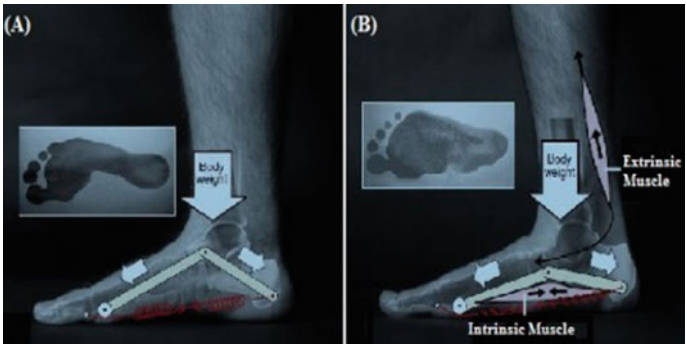

Fig. 4 **a** Arch with Slight Stretch of Plantar Fascia. **b** Arch with Over Stretch of Plantar Fascia (*Source* EKPTA https://doi.org/10.1016/b978-0-323-54498-6.00011-4311-350)

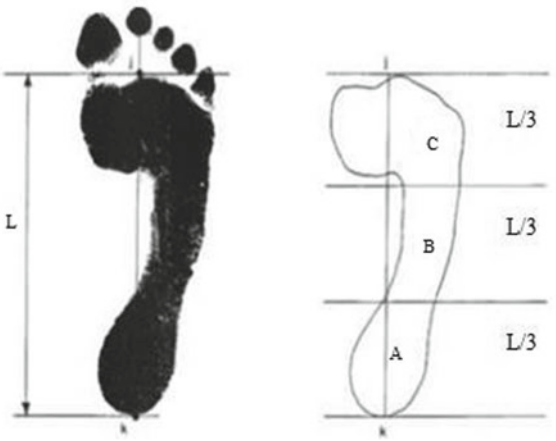

Fig. 5 Foot Print Area Division (*Source* BMEiCON pp. 1–4)

1.4 Technical Methods to Identify Foot Arch and Plantar Pressure

Effect of muscle and ligament stretch varies during weight and non-weight-bearing conditions. Radiology examinations like computer tomography (CT) scan, magnetic resonance imaging (MRI) and ultrasound are preferred [10]. Foot pressure measurements are generally considered to design a required insole. Foot scan plate generates accurate results based on the number of sensors arranged [9, 12]. Flatbed 3D scanner detects by reconstructing a 3D surface [11]. Acu gait force plate uses Hall Effect sensors to measure ground reaction forces [13]. Pedograph footprint measures Clarkes angle, Chippaux smirak index and Staheli index [14]. Standard flatbed scanners are recommended during static and in-shoe system during dynamic conditions [12]. Podata foot bar is sandwich arranged insoles with pressure sensors in between [15]. Force sensing resistor, piezoelectric sensors, capacitive sensors, textile sensors, optical sensors, hydro cell sensors, miniature load cells, Micro Electro Mechanical Systems (MEMS) sensors [16]. Camera-based motion analysis system. Few more devices are used for dynamic conditions like Pedar Novel, Parotec, F-Scan, Moticon, iShoe, 3-axis force sensor, smart insole, Flexible insole, textile, i-Smart shoe II [17].

1.5 Morphology of Foot [12]

During the dynamic study of feet, two phases are identified—stance phase and swing phase, which accommodates 60% of gait during stance and 40% of gait during swing phase as shown in Fig. 6.

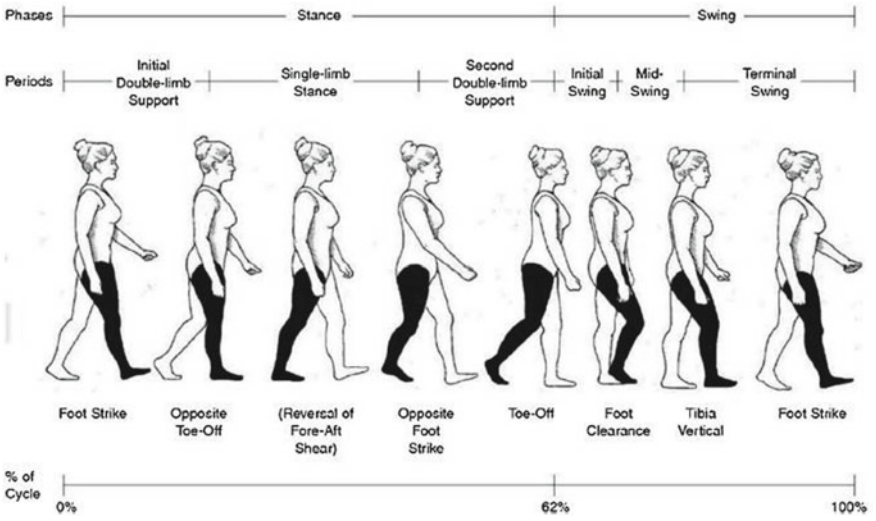

Fig. 6 Human Gait Cycle—Stance and Swing Phase (*Source* Foot and ankle surgery. 12)

2 Purpose of Using Insoles

As per the global assessment of adult people, flat foot is 3–25% [18]. Using foot orthosis, 14–35% of strain gets reduced [19]. Foot Health Status Questionnaire (FHSQ), Foot Function Index (FFI), Quality of Life (SF36) states the life of a person with flat foot [20]. Insoles can be preferred due to any of these reasons like over standing, running, pronation, supination, plantar fasciitis, arch pain, motion neuroma, hallux rigidus, hallux limitus, morton's toe, diabetes, arthritis, heel spurs, heel pain, shin splints, metatarsalgia, ball of foot pain, children, obesity, athletic and sports [17]. To reduce the archilis tendon, insoles are designed with rocker curve, for flat foot which reduces the dorsiflexion angles [21].

3 3D Printed Insoles

In 3D printed insole volume, weight, internal structures, density at selected regions can be defined [18]. Structures like Kelvin cell, honeycomb, octahedral porous, orthogonal cubic structures are more preferred for infill [22]. 3D printed insoles can be improved by varying the size of studs [23]. Possess high portability, low cost and high degree of customization [13]. Zone control in 3D design is preferred to increase cushioning capacity [18]. Contact stress can be reduced by proper design of insole [17]. Contact area is increased with a range of 60–70 cm^2 compared to flat insole [24]. 3D printed insoles along with shoes have an advantage in defining the continuity of the materials [26]. Being an important part of personal protective

equipment (PPE), the insoles should possess thermal insulation [27]. 3D printed arch can be placed at a targeted position on pre-fabricated insole [9]. Latest trend is with continuous core reinforced filament deposited with a matrix material [28]. Hydrophilic membrane can be laminated to avoid bromhidrosis [15]. Apart from the manufacturing time 3D printing has advantages like cost of equipment, geometric complexity, materials, material waste and labour time [6, 18]. To reduce printing time turnkey process is preferred [30]. The most preferred printer is Fused Filament Fabrication [13]. Selective laser melting 3D printing is preferred to reduce effective modulus by 75–80% [22]. Digital Light Projector 3D printing technique hardens layers by projecting light [28]. MEX 3D printer used for printing TPU and TPE materials [17]. Dual extrusion 3D printer is used with Poly Vinyl Alcohol as support material [25]. Selective Laser Sintering, Stereo Lithography Apparatus, Selective Laser Melting are preferred to print entire shoe [13, 27].

3.1 Materials Preferred for 3D Printing Insole

Depending on the methodology preferred, an insole can be printed with elastic material and support sole with hard material. Fila Flex, ninja flex, soft flexible PLA are preferred materials [29]. Few insoles use electrically conductive materials like velostat [25]. For insoles with different densities and porosity polyethylene material is used. Flexible polyurethane material is preferred for good abrasion, fatigue resistance, good impact and more friction [9, 27]. Monolithic induced matrix materials act as composites [28]. Polylactic acid (PLA), acrylonytrile butadiene styrene (ABS) preferred to develop base of insole [13, 15]. For high durability, strength and medium flexibility, polyethylene terephthalate glycol (PETG) is used [11]. For non-slip and smooth surface types of insoles tango plus material is used. For transparent insoles veloclear material is used [24]. Materials like liquid polymer, polyester is also preferred for 3D printed insoles [15].

4 Conclusions

Improper foot alignment is one of the major problems which tend to excess plantar pressure for flat foot patients. Neglecting this would increase severe pain at some portions of lower limb furthering to misalignment of body. Dysfunctions of the hip, knee, or even the back therefore may be associated with problems originating at the ankle or foot. Use of insoles reduces lower limb alignment problems. In teenagers, flat foot is due to over-weight. Effect of insole on sagittal plane is more compared to other planes. 3D printed insoles weight is reduced to 25% than traditional methods. Achilles tendon load is reduced by using rocker shoe hence more preferred for midfoot strikers. Advanced 3D printing prefers splitting zones technique. Turnkey

method is used to reduce printing time. According to estimation by 2020, the world market for orthotic devices would reach 3.5 billion euros.

References

1. Vijayaragavan E, Gopal TV (2016) Biomechanical modeling of human foot using finite element methods. J Indian J Sci Tech 9(1):5
2. Kumar VA, Sweta SV (2015) Basic study of the human foot. J Bio Pharm 8:435–444
3. Mansfield PJ, Neumann DA (2016) Structure and function of the ankle and foot. Ess Kins Phys Asst 3:311–350
4. López-López D, Vilar-Fernández J, Barros-García G, Losa-Iglesias M, Palomo-López P, Becerro-de-Bengoa-Vallejo R, Calvo-Lobo C (2018) Foot arch height and quality of life in adults: a strobe observational study. Int J Env Res Pub He 15(7):1555
5. Keatsamarn T, Pintavirooj C (2016) Foot plantar pressure measurement system using optical sensor. In: 9th IEEE Biomed Eng Int Conf 1.978.1-4
6. Surmen K, Ortes F, Arslan YZ (2016) Design and production of subject specific insole using reverse engineering and 3D printing technology. Int J Eng Sci Invent 5(11):5
7. Periya SN, Alagesan J (2017) Prevalence and incidence of flat foot among Middle East and Asian Population: an overview. Int J Pharm Sci He 4(7):1–4
8. Norris CM (2011) Lower limb motion during walking, running and jumping. Managing Sports Injuries 133–142
9. Braun B, Baritz M (2017) FEM modelling of shoes insoles components for standing and walking simulation. MATEC Web Conf EDP Sci 94:01002
10. De Cesar, Netto C, Roberts L, Saito G, Roney A, Sturnick D, Sofka C, Greditzer H, Deland J, Ellis S (2018) Weight bearing CT and MRI findings of stage II flatfoot deformity: can we predict patients at high risk for foot collapse? Foot Ankle Orthop. 3, p. 2473011418S00206
11. Golovin MA, Marusin NV, Golubeva YB (2018) Use of 3D printing in the orthopedic prosthetics industry. J Bio 52(2):22–27
12. Zulkifli SS, Ping LW (2018) A state-of-the-art review of foot pressure. Foot Ankle Surg
13. Leal-Junior AG, Díaz CR, Marques C, Pontes MJ, Frizera A (2019) 3D-printed POF insole: development and applications of a low-cost, highly customizable device for plantar pressure and ground reaction forces monitoring. Optics Laser Technol 116:256–267
14. Punniakotti M, Purushothaman S, Sharma V (2019) Correlation of Staheli's foot index and central distance measurement for classifying normal and flat-arched foot posture. Drug Invention Today 12(116):256–264
15. Peixoto J, Flores P, Souto AP (2017) A new approach to implement a customized anatomic insole in orthopaedic footwear of lower limb orthosis. IOP Conf Series: Mat Sci Eng 254(23):232006
16. Campo E, Charlon Y, Brulin D (2015) Instrumented insole for weight measurement of frail people. Int Conf Per Tech Assist Environ 60
17. Ma Z, Lin J, Xu X, Ma Z, Tang L, Sun C, Li D, Liu C, Zhong Y, Wang L (2019) Design and 3D printing of adjustable modulus porous structures for customized diabetic foot insoles. Int J J Lightweight Mater Manuf 2(1):57–63
18. Davia-Aracil M, Hinojo-Pérez JJ, Jimeno-Morenilla A, Mora-Mora H (2018) 3D printing of functional anatomical insoles. Comput Industry 95:38–53
19. Mo S, Leung SH, Chan ZY, Sze LK, Mok KM, Yung PS, Ferber R, Cheung RT (2019) The biomechanical difference between running with traditional and 3D printed orthoses. J J Spor Sci 1–7
20. Pita-Fernandez S, Gonzalez-Martin C, Alonso-Tajes F, Seoane-Pillado T, Pertega-Diaz S, Perez-Garcia S, Seijo-Bestilleiro R, Balboa-Barreiro V (2017) Flat foot in a random population and its impact on quality of life and functionality. J Clin Diag Res 11(4):C22

21. Sobhani S, Zwerver J, van den Heuvel E, Postema K, Dekker R, Hijmans JM (2015) Rocker shoes reduce achilles tendon load in running and walking in patients with chronic achilles tendinopathy. J J Sci Med Spor 18:133–138
22. Wang L, Kang J, Sun C, Li D, Cao Y, Jin Z (2017) Mapping porous microstructures to yield desired mechanical properties for application in 3D printed bone scaffolds and orthopaedic implants. Mater Des 133:62–68
23. Mason M, Bellot A (2016)Iinventors; TechnoGel, GmbH, assignee.: insole and shoe comprising a removable insole. US Patent 15/157,494, 8 Dec 2016
24. Ganesan S, Ranganathan R (2018) Design and development of customised split insole using additive manufacturing technique. Int J Rap Manuf 7(4):295–309
25. Majewski C, Perkins A, Faltz D, Zhang F, Zhao H, Xiao W (2017) Design of a 3D printed insole with embedded plantar pressure sensor arrays. In Proceedings of the ACM international joint conference on pervasive and ubiquitous computing and Proceedings of the ACM international symposium on wearable computers, pp 261–264
26. Jones DP, Larson RR (2015) inventors, Nike Inc, assignee.: direct printing to fabric. US Patent 8,993,061, 31 Mar 2015
27. García-Hernández C, Sánchez-Álvarez EJ, Huertas-Talón JL (2016) Foot model for tracking temperature of safety boot insoles: application to different insole materials in firefighter boots. J Int J Occup Erg 22(1):12–19
28. Mark GT (2019) Inventor; Markforged, Inc., assignee.: footwear fabrication by composite filament 3D printing. US Patent 10,226,103, 12 Mar 2019
29. Yarwindran M, Sa'aban NA, Ibrahim M, Periyasamy R (2016) Thermoplastic elastomer infill pattern impact on mechanical properties 3D printed customized orthotic insole. ARPN J Eng App Sci 11(10):6519–6524
30. Wang JC, Dommati H, Cheng J (2019) A Turnkey manufacturing solution for customized insoles using material extrusion process. In: 3D printing and additive manufacturing technologies. Springer, Singapore, pp 203–216

Synthesis and Characterization of 17 Cr Ferritic ODS Steel Developed Through Vacuum Hot Pressing

G. Dharmalingam, Sellamuthu Prabhukumar, and M. Arun Prasad

Abstract In the present investigation, on 17 Cr ferritic oxide dispersion strengthened (ODS) steel composition of ($430L + 0.3Y_2O_3 + 0.5ZrO_2 + 0.1Ti$) wt% (alloy A) and ($430L + 0.3Y_2O_3 + 0.5ZrO_2 + 0.1Ti + 4Al$) wt% (alloy B) were developed through mechanical alloying (MA) using VHP (vacuum hot pressing). The mechanically alloyed powders were taken at different milling time intervals for confirming the nanocrystalline size using X-Ray Diffraction (XRD). Finally, 20 h of milled powders were consolidated through vacuum hot pressing (VHP) at 1180 °C in the pressure levels of 60 MPa, and the cooling rate of 50°C/min. Throughout the experiments, the vacuum level was maintained by 10^{-3} Torr. Hot-pressed samples were subjected to densification studies; microstructural examination and hardness were analyzed in the current study. The nanocrystalline size of 3.6 nm (alloy A) and 6 nm (alloy B) were obtained at 20 h of milling time. The highest hot-pressed density of 7.60 g/cc (99% theoretical density) was acquired for aluminium-free ferritic ODS steel (alloy A) pressure at 60 MPa, whereas aluminium-contained alloy B lesser hot-pressed density of 7.34 g/cc was obtained. The microstructures of alloy A and alloy B containing ferrite along with complex oxides such as (Y–Zr–Ti–O) and (Y–Zr–Ti–Al–O), which is evident from TEM-EDS analysis. Alloy A has a higher hardness (870 VHN) due to the fine grains structure of material compared with alloy B (764 VHN).

Keywords Ferritic ODS steel · Mechanical alloying (MA) · Vacuum hot pressing (VHP) · TEM-EDS · X-Ray diffraction (XRD)

1 Introduction

For advanced fission and fusion reactions, a promising material is oxide dispersion strengthened (ODS) ferritic stainless steel (FSS). The presence of highly dense

G. Dharmalingam (✉) · S. Prabhukumar · M. Arun Prasad
Department of Mechanical Engineering, Vel Tech Rangarajan Dr Sagunthala R&D Institute of Science and Technology, Avadi, Chennai, Tamil Nadu 600062, India
e-mail: dharma21sona@gmail.com

N. Gascoin and E. Balasubramanian (eds.), *Innovative Design, Analysis and Development Practices in Aerospace and Automotive Engineering*, Lecture Notes in Mechanical Engineering, https://doi.org/10.1007/978-981-15-6619-6_30

nano-sized oxide particles in ferritic ODS steels has better resistance to neutron irradiation which acts as a barrier for dislocation and further resisting embrittlement and void swelling when compared with conventional ferritic steels. For heat resistance, structural applications like fast breeder reactors and thermal power plant high chromium FSS are widely used. Schroeder and Klueh et al. [1, 2] reported that for high-temperature applications the BCC (body-centred cubic crystal) FSS will have good swelling resistance, high tensile/compressive strength, good oxidation resistance, low coefficient of thermal expansion, high thermal conductivity, and creep resistance. But Kim et al. [3] reported that above 550°C FSS have restriction in creep strength and swilling. To overcome these deficiencies the FSS metal matrix is strengthened with nano oxide which is homogeneously dispersed which improves strength and prevents grain boundary slipping both at room and high temperatures. When compared to ASS, FSS has better mechanical properties and swelling resistance at high temperatures as reported by Henry et al. [4] ferritic ODS steel one of the majority hopeful structural materials for advanced nuclear applications, oxide particles which contain the immense number of density. McClintock et al. [5] reported that ferritic ODS steels confirm admirable high-temperature creep resistance, promising irradiation resistance and tensile properties due to the presence of its unique microstructure.

Recent literature reported that the addition of nano-sized, highly dispersed ZrO_2 particles in the ferritic ODS alloy attributed thermal stability by Zener pinning of grain boundaries. The addition of optimum chromium content of (< 18 wt% Cr > 13 wt%) in the ferritic ODS steel enhances corrosion resistance and tensile strength. These nano-sized oxides produced by mechanical alloying further strengthened by solution hardening with the addition of aluminium. With the addition of zirconium into ODS steel, appropriate to sustain a superior strength and resistance to corrosion. Finally, the zirconium (Zr) addition into aluminium, Yttrium ODS steels, which leads to an enhancement in the resistance to the irradiation harm with oxides exhibiting thermal stability and superior irradiation acceptance reported by Karak et al. [6].

With different weight percentages of chromium Li et al. [7] studied the oxidation behaviour of ferritic ODS alloys. It was suggested that due to the effects of Y_2O_3 addition in 12-Cr wt% ferritic ODS alloys have greater high-temperature oxidation resistance when compared to 9-Cr wt% ferritic ODS steel. It was also mentioned that the 13-Cr wt% ferritic ODS alloys have a very good oxidation rate at a temperature level of 1000°C superior to the 21-Cr wt% ferritic ODS alloys, due to development of a defensive chromium oxide layer.

Macia et al. [8] stated that grain growth for the duration of the sintering process is one of the key issues for Powder Metallurgy. It is possible to homogeneously distribute fine dispersoids such as ultrafine Y_2O_3, TiO_2, and ZrO_2 oxide particles to prevent grain growth at high temperature through a mechanical alloying process. The nano oxide particles especially Yttrium with titanium (Ti) added ODS alloys to refine the oxide particle size at their forming temperature of 1000–1150 °C. These non-stoichiometric enriched complex oxides (Y–Ti–O) found additional efficiency in attractive creep resistance and irradiation resistance due to their smaller sizes.

The present investigation aims towards the development of 17 Cr–0.3Y_2O_3 with Zirconium oxide (0.5 wt%), titanium (0.1wt%), and aluminium (4wt%) will be milled in a high energy ball milling to obtain the nano crystallite structure and the milled powder will be consolidated by vacuum hot pressing.

2 Materials and Processes

2.1 Processing of Ferritic ODS Steel Powder

Mechanical Alloying (MA) route was performed using the high energy planetary ball milling equipment (Fritsch Pulversitte PM400) under a closed environment, constant flow with help of a stainless steel vial and balls of 10 mm diameter. The ball milling process parameters were used of 300 rpm with the ball to powder ratio of 10:1, milled at 20 h. During MA to avoid combustion, control reagent of toluene was used. The presence of the toluene medium resists the formation of agglomeration of particles during the repeated collision and reduces the size of the particle.

Mechanical ball milling was conducted at different milling times (0 h, 5 h, 10 h, 15 h, 20 h) intervals. Finally, the different stages of milled powders were taken for phase transformation using X-Ray Diffraction (XRD), with the condition of Cu Kα ($\lambda = 1.542$ Å). Mechanically milled powders using Debye's–Scherrer method the crystallite size and lattice strain were calculated. The rule of mixtures was used to calculate the theoretical density of the compositions of the alloys as shown in Table 1.

The consolidated 20 h of milled powders were sintered using vacuum hot pressing in uni-directionally at a temperature and pressure level of 1180 °C, 60 MPa with the dwell time of 90 min and vacuum level of 10^{-3} Torr. Hot pressing was done at 10 °C per min during heating and 50 °C/min during cooling for the sintering cycle. With the help of appropriate graphite dies and punch assembly, hot-pressed billets were developed of 30 mm diameter and 10 mm height, as shown in Fig. 1. Sintered samples densities were measured using mass and physical dimensions method with an electronic balance in the precision of 0.1 mg. To identify the uniform distribution of oxide particles the TEM studies were carried out for the alloys. Sample preparation for TEM studies through Gatan model 656 (Dimple grinding) and Gatan model 691 (Ion milling) Process. Hot-pressed alloys hardness was measured using Vicker's hardness tester with a functional load of 5 kg and dwell time of 10 s.

Table 1 430L pre-alloyed powders and its chemical composition of alloys

Powder Grade	Cr wt%	Mn wt%	Si wt%	C nwt%	P wt%	S wt%	Fe wt%	Theoretical density (g/cc)
430L	17	0.89	0.89	0.02	0.01	0.01	Bal	7.70
Alloy A	(430L + 0.3Y_2O_3 + 0.5ZrO_2 + 0.1Ti) wt%							7.67
Alloy B	(430L + 0.3Y_2O_3 + 0.5ZrO_2 + 0.1Ti + 4Al) wt%							7.47

Fig. 1 Vacuum hot pressing machine

3 Results and Discussion

3.1 Powder Discriminating of XRD Pattern with Different Milling Time Intervals

XRD patterns of the aluminium-free (alloy A) and aluminium-containing ferritic ODS steels (alloy B) are shown in Figs. 2 and 3 respectively. XRD pattern of alloy A and B has the complete ferrite peaks for un-milled powders (0 h milled powder) sharp peaks were observed. XRD patterns clearly revealed that milling time influences the peak broadening with irrespective of compositions of both alloy A, alloy B longer milling time (20 h) has driven more broadening of peaks, which indicates that nano crystallite size of the composition was attained and broadening of α-Fe peak is shown more clearly in 20 h of milling.

Intensity peak was decreased with increases milling time, at 20 h of milled powder showed almost a flat peak was observed. A solid solution (alloying) formation was follows Hume-Rothery rules which point out the parameters like atomic size, valance, and electronegativity of elements on alloying. The electronic interactions of the solute

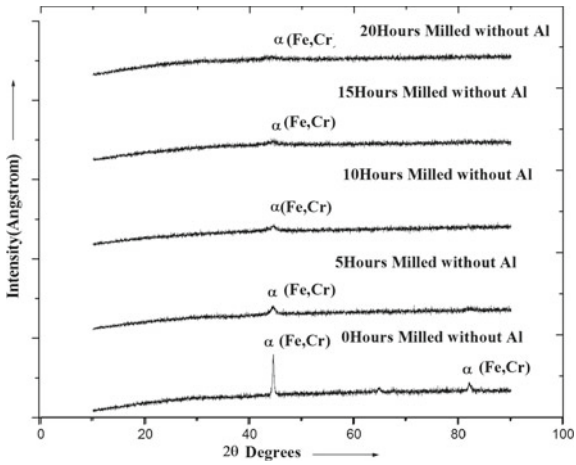

Fig. 2 XRD analysis of milled powder alloy A

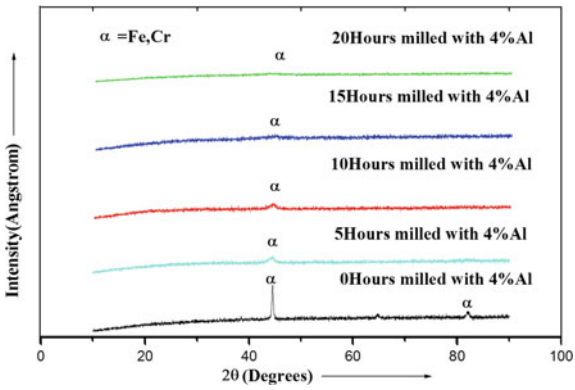

Fig. 3 XRD analysis of milled powder alloy B

and solvent atom in a matrix influence the lattice. The physical properties of the solute (Cr and Ti) and solvent (Fe) of this system were shown in Fig. 2. From the XRD pattern at different stages (0 h, 5 h, 10 h, 15 h, 20 h) the alloy formation during MA can be determined by fading of solute peaks and a peak shift in both solvent and solute peaks towards the alloy.

During the MA process, the particles have subjected to different stages in cold welding, fracture, and structure of a single-phase solid solution. On the other hand, the inclusion of titanium, zirconium, tungsten, aluminium and Yttrium peaks were not experiential in the XRD pattern due to lesser contented. During mechanical alloying of alloy A, alloy B have similar trends of phase transformation and structures, which is evident from the XRD patterns of alloys A, B (Figs. 2 and 3). Crystallite size of the milled powders (20 h) was calculated by means of Debye's Scherrer method and it was found that 3.6 nm, 6 nm for alloy A, and B, respectively. Lower reduction of crystallite size was due to the inclusion of aluminium in ferritic stainless steel in the alloy B. All solute atoms in the present study are reduced to a single-phase solid solution because of Gibbs–Thompson result (Karak et al. 2013).

3.2 Density Analysis on Vacuum Hot-Pressed Alloys

From the densification studies as shown in Fig. 4, it is observed that aluminium-containing ferritic ODS steels (alloy B) have lesser sintered density than the aluminium-free ferritic ODS steel (alloy A) irrespective of compositions. During hot pressing, the formation of grains coarsened the structure of complex oxides (Y–Zr–Ti–Al–O) in the alloy B has made volume expansion, which slightly reduced the hot-pressed density. But the aluminium-free alloy A has very fine grains structure complex oxides(Y–Ti–Zr–O) of Y_2O_3, Ti and ZrO_2 which led to higher hot-pressed density than the aluminium-containing ferritic ODS steels. A similar trend was observed by Andrea Garcia et al. (2015) for the 14 Cr ferritic steel with and without the addition of aluminium. Influence of hot pressure also additional effect on improving

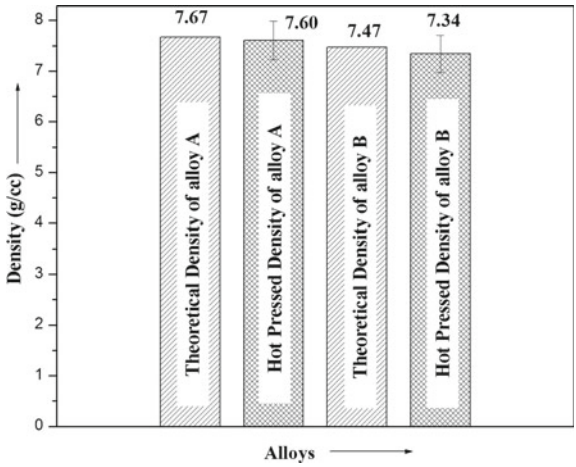

Fig. 4 Density analysis of hot-pressed alloys A, B

density after hot pressing. The higher sintering pressure (60 MPa) and temperature (1180°C) has enhanced the density with irrespective of its composition. For the duration of vacuum hot pressing, a higher driving force activates the enhancement in density of the alloys this effect due to the viscous flow of higher material transport mechanisms and a combination of plastic flow. Similar kind of effects was observed by Munir et al. Alloy A (aluminium-free) Yttrium–Zirconium–Titanium oxides have higher binding energy in an iron matrix and being of Yttrium–Zirconium–Titanium oxides easier to precipitate and more stable than the aluminium-containing of alloy B. The structure of fine grains zirconium–Yttrium–Titanium nano-oxides, which have oxide configuration energies lower, than aluminium-contained alloy B (Yttrium–Zirconium–aluminium oxide particles) due to higher density, were observed for alloy A (7.60 g/cc). Whereas aluminium-containing alloy B the coarse grains (Yttrium–Zirconium -Aluminium nano-oxides) were observed due to the lower density of an alloy B (7.34 g/cc) were obtained.

3.3 TEM-EDS Analysis of Hot-Pressed Alloys

To study the microstructure and uniform distribution of oxide particles were used transmission electron microscope (TEM) analysis for consolidated through vacuum hot pressing of alloy A, alloy B. The TEM analysis as shown in Fig. 5a of alloy A reveal that sphere-shaped particles which are Y–Zr–Ti–O complex oxides confirmed through EDS analysis shown in Fig. 5c, uniformly dispersed in the alloy matrix with dispersal in the range of 8 to 10 nm. From Fig. 5a, there are few oxides particles Y_2O_3 and ZrO_2 also revealed that uniformly distributed in the alloy matrix, average oxides particle size was observed 18–20 nm. Chemical compositions of alloys qualitative analysis were taken at different locations using EDS analysis. With the inclusion

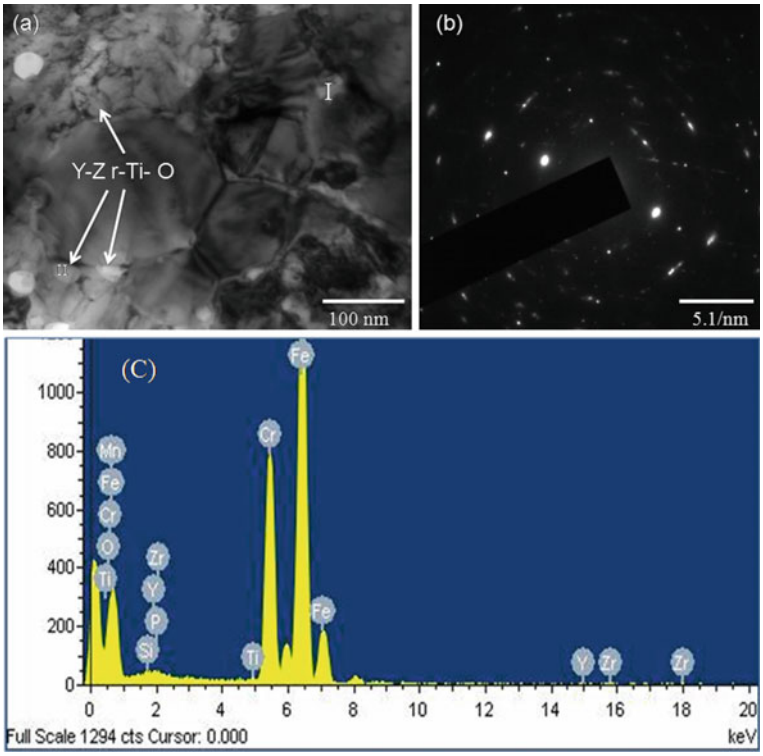

Fig. 5 Hot-pressed alloy A TEM with EDS analysis-I (**a** and **c**) (**b**) SAD patterns of complex oxides particles-II

of titanium could refine process the oxides particles reported as several researchers. The TEM microstructure of alloy B was shown in Fig. 6a. It can be observed that the sphere-shaped complex oxides particles were uniformly dispersed in the matrix with dispersal in the span of 15–25 nm more than the alloy A. Complex oxide particles Y–Zr–Ti–Al–O conformed through TEM-Energy dispersive spectroscopy (EDS) analysis as shown in Fig. 6c, indicated that Yttrium oxide, Zirconium oxide can easily react with titanium and aluminium. The size of the complex oxides (Y–Zr–Ti–Al–O) particles is 15–25 nm, moreover, larger than the alloy A complex oxides particles, which conforms to the coarsening result of aluminium inclusion on oxide particles. From Fig. 6c shows the EDS analysis elements distribution of alloy B. The basic principles behind that the binding energy of the alloy A complex oxides (Y–Zr–Ti–O) group is much higher than alloy B complex oxides (Y–Zr–Ti–Al–O) group in Fe matrix, which could be denoted as Y–Zr–Ti–O phase is easier to form more than the Y–Zr–Ti–Al–O phase. To associate the phases in the hot-pressed alloys, the SAD (selected area diffraction) was directed. In order to verify the complex nano oxide particles, the SAD pattern was taken which shows the ring pattern of SAD completely in the nanocrystalline regime analyzed for alloys A, B as shown

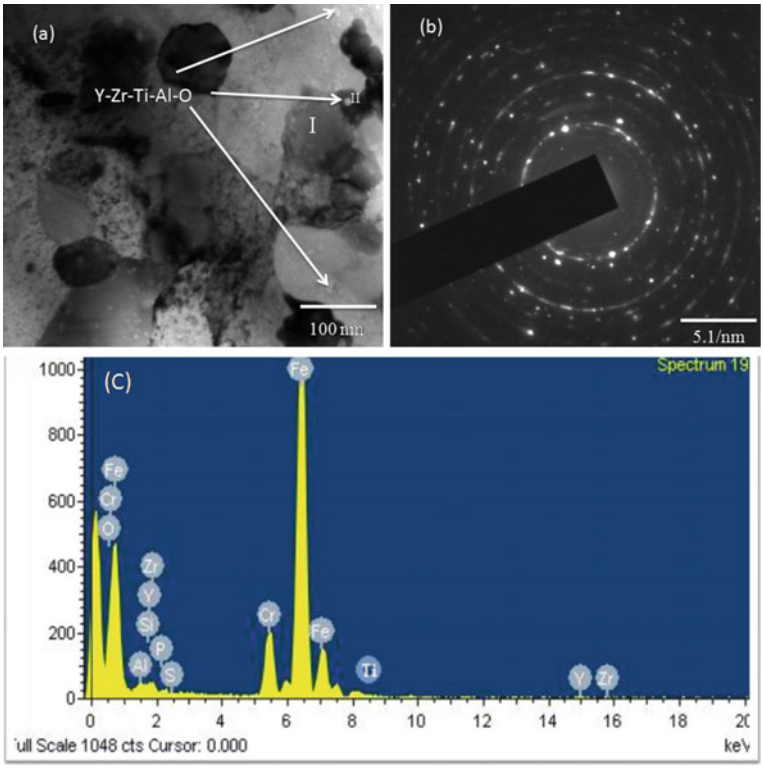

Fig. 6 Hot pressed alloy B TEM with EDS analysis-I (**a** and **c**) (**b**) SAD patterns of complex oxides particles-II

in Figs. 5b and 6b. The above-said results observed that the addition of aluminium content causes increases in the size of oxide particles and a decrease in the density which leads to the diminution of the strength of ferritic ODS steel alloys. Lee et al. [9] similar kinds of results were observed.

3.4 Hardness of the Hot-Pressed Alloys

Chemical composition has also influenced the hardness of the hot-pressed steels. Alloy A has a higher hardness of 870 VHN_5 than the alloy B 764 (VHN_5) which is shown in Fig. 7. Fine Y–Zr–Ti–O complex oxide in the aluminium-free ferritic steel (alloy A) enhanced hardness and strength by the dispersion strengthening effect, which was reported by several researchers (García-Junceda et al. 2016). Aluminium-free (Alloy A) 17 Cr ferritic steel has 12% higher hardness than the aluminium-contained (alloy B) ferritic steel at the pressure level of 60 MPa were observed.

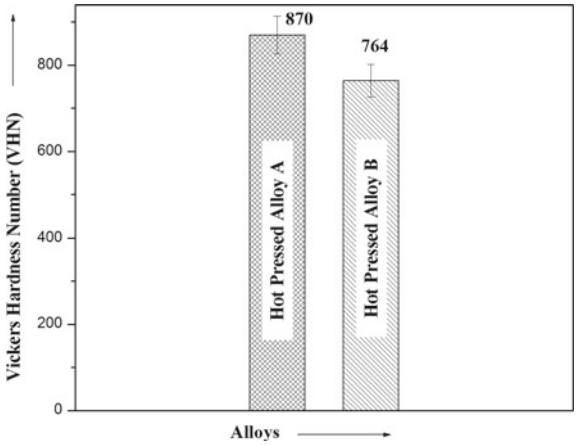

Fig. 7 The hardness of Hot pressed alloy A and alloy B

4 Conclusions

Two different ferritic ODS steel such as alloy A (430L + $0.3Y_2O_3$ + $0.5ZrO_2$ + 0.1Ti) wt%, alloy B (430L + $0.3Y_2O_3$ + $0.5ZrO_2$ + 0.1Ti + 4Al) wt% were fabricated through the MA using vacuum hot pressing. The summarized results are the following:

1. From the XRD analysis nanocrystalline size of 3.6 nm, and 6 nm were obtained at 20 h of milling for alloy A, B, respectively.
2. The highest hot-pressed density of 7.60 g/cc (99% theoretical density) alloy A (aluminium-free) ferritic ODS steel higher density were obtained than the alloy B 7.34 g/cc pressure at 60 MPa.
3. Microstructures of alloy A, alloy B containing ferrite along with complex oxides such as (Y–Zr–Ti–O), (Y–Zr–Ti–Al–O) which is evident from TEM-EDS analysis.
4. Alloy A has a higher hardness of 870 VHN were obtained than the alloy B (764 VHN), alloy A higher hardness was observed due to ultrafine grains, whereas alloy B reduction in hardness with the addition of aluminium coarse grains was observed.

References

1. Schroeder H, Ullmaier H (1991) Helium and hydrogen effects on the embrittlement of iron-and nickel-based alloys. J Nuclear Mater 179:118–124
2. Klueh RL, Ehrlich K, Abe F (1992) Ferritic/martensitic steels: promises and problems. J Nuclear Mater 191:116–124
3. Kim HY, Kwon OY, Jang J, Hong SH (2006) Modification of anisotropic mechanical properties in recrystallized oxide dispersion strengthened ferritic alloy. Scripta Mater 54(9):1703–1707

4. Henry J, Averty X, Dai Y, Pizzanelli JP, Espinas JJ (2009) Tensile properties of ODS-14% Cr ferritic alloy irradiated in a spallation environment. J Nuclear Mater 386:345–348
5. McClintock DA, Sokolov MA, Hoelzer DT, Nanstad RK (2009) Mechanical properties of irradiated ODS-EUROFER and nanocluster strengthened 14YWT. J Nuclear Mater 392(2):353–359
6. Li M, Zhou Z, He P, Liao L, Xu Y, Ge C (2010) Microstructure and mechanical property of 12Cr oxide dispersion strengthened ferritic steel for fusion application. Fusion Eng Des 85(7–9):1573–1576
7. Macía E, García-Junceda A, Serrano M, Hernández-Mayoral M, Diaz LA, Campos M (2019) Effect of the heating rate on the microstructure of a ferritic ODS steel with four oxide formers (Y-Ti-Al-Zr) consolidated by spark plasma sintering (SPS). J Nuclear Mater 518:190–201
8. Karak SK, Chudoba T, Witczak Z, Lojkowski W, Manna I (2011) Development of ultra high strength nano-Y_2O_3 dispersed ferritic steel by mechanical alloying and hot isostatic pressing. Mater Sci Eng, A 528(25–26):7475–7483
9. Lee JH (2012) Mechanical and microstructural properties of Al-added ODS ferritic steel. Adv Mater Res 567:49–53

Investigation on Mechanical Properties of AA6082-AA7075 Friction Stir Welded Dissimilar Aluminum Alloys

K. Giridharan, G. Chakravarthi, S. Karthick, S. MuthuKumaran, S. Padmanaban, and M. Kabeerr

Abstract In this present investigation, an effort has been made to evaluate the mechanical properties of AA6082 and AA7075 dissimilar aluminum alloys were joints fabricated by the Friction stir welding process (FSW). The effects of FSW process parameters such as tool revolving speed, welding speed, tool pin profiles, and axial load also investigated. Three different FSW tool pin profiles are used in this investigation like straight cylindrical, tapered, and taper threaded. The different tool speeds are 1000 rpm, 1300 rpm, and 1500 rpm. The welding speeds are utilized for this investigation is 20 mm/min, 40 mm/min, and 60 mm/min. The unvarying axial load 2kN is used in this work. The Friction stir welding process is a solid-state joining process. This method was most suitable for combined two dissimilar alloys of AA6082-AA7075. This experimental investigation was successfully done with the help of FSW process parameters. The mechanical properties and quality of the weld joints were observed after one by material testings. The material testing like as tensile and hardness test. It is used to determine the process parameters and their performance measure with the minimum variation. The optimization process was done with the help of FSW process parameters. In this context, the L9 Orthogonal array was used in the optimization process. After the end of the experimental investigation, the results indicate the massive tensile strength value is gained by a straight cylindrical pin profiled tool at a rotational speed of 1300 rpm and the welding speed is 60 mm/min. The hardness of the weld specimen is increased with the decreasing of tool revolving speed is 1000 rpm, as well as the traveling speed, which is 20 mm/min which obtained by a tapered pin profile tool. The results indicate tool pin profile plays a vital role in getting the quality of the weld joints.

K. Giridharan (✉) · G. Chakravarthi · S. Karthick · S. MuthuKumaran · M. Kabeerr
Department of Mechanical Engineering, Easwari Engineering College, Chennai 600089, India
e-mail: girimech4305@gmail.com

S. Padmanaban
Department of Automobile Engineering, VelTech Rangarajan Dr. Sangunthala R&D Institute of Science and Technology, Avadi, Chennai 600062, India

N. Gascoin and E. Balasubramanian (eds.), *Innovative Design, Analysis and Development Practices in Aerospace and Automotive Engineering*, Lecture Notes in Mechanical Engineering, https://doi.org/10.1007/978-981-15-6619-6_31

Keywords Friction stir welding (FSW) · AA6082-AA7075 alloys · Process parameters · Tool pin profiles · Mechanical properties

1 Introduction

The innovative solid-state joining process likely named as Friction stir welding process (FSW). This material joining technique also called an environment-friendly process.

It was invented by the welding institute (TWI) of the United Kingdom in1991 [1]. Initially, the legend Wayne Thomas and his team members carried by similar material joining process for this technique [1, 2]. At later in this technique was preferred to join two similar and dissimilar alloys in different combinations. In FSW, a non-consumable revolving tool used to fabricate weld joints with different tool configurations such as tool shoulder diameter, pin profile, and pin diameter. The specially designed FSW tool was inserted two metal plates and traveled along with the weld direction at various speeds. The tool shoulder surface contact with the top surface workpiece [3]. The FSW tool plunged into two plates at high speed and heat generate frictional heat between the two surfaces. Simultaneously the tool moves the specified conditions to the weld direction which results to get the weld joint. Compared to other fusion technology, the FSW process is the most attractive eco-friendly joining technology to receive fine microstructure, absence of the weld defects such as porosity, weld cracks, and minimum residual stresses produced in weld joints during the material combined process. In this method, there is no use for additional filler material and shielding process [2–4]. The tool turning speed, traveling speed, pin profiles, and downward force is the primary process parameters are used while joining the two alloys plate or sheets. The process parameters are involved in a major role in the microstructural behavior of the welded materials [5].

The FSW process has specified different zones named Nugget or weld zone (NZ), Heat Affected Zone (HFA), Thermo Mechanically Heat Affected Zone (TMAZ) and Unaffected Parent Material Zone (UAPZ) [5]. The internal defects and stresses are an important issue for all the types of material joining processes. But it could be seen the minimum amount of material defects induced in the FSW joining process because of its excellent combined characteristics [6]. The experimental arrangement of the Friction stir welding process has illustrated in Fig. 1.

Aluminum alloys are mostly used in different applications. Because of these aluminum alloys have good mechanical, material properties and it is future based applications. In day by day, aluminum alloys have become progressively more utilized in different engineering fields of applications [3–6]. The fields are automotive industry, shipbuilding, aerospace equipment manufacturing, construction, and building, marine engineering, food packaging, production of defense-related products and several structural applications, etc. [6]. Aluminum alloys have good unique mechanical properties named as corrosion resistance, good formability, fracture toughness, low density, thermal and electrical conductivity. Generally, the aluminum

Fig. 1 Schematic diagram of FSW joint making process

alloys are applicable both fusion and solid-state joining processes such as brazing, riveting, bolting, and soldering [7].

Since many of the investigators have done an experimental examination of dissimilar aluminum alloys that deal with microstructural behavior and mechanical properties is involved the materials joining process subjected to the FSW process with correlating the final values [6, 7]. Hence, in this present work, there is a detailed examination of the material joining process and parameters depended on the FSW joining process, because of the way of choosing the optimum process parameter range for the strength of the weld joint. The various FSW process variables used in this investigation were selected based on the previous experimental studies and Literature Survey that has been done so far [7]. Finally, the present work the select process parameters were used to Taguchi method for identified the optimal range involved in the material joining technique, and the final results are compared with the experimental data for getting successive weld joints.

2 Material and Experimental Setup

The size of 100mmx50mmx5mm rolled aluminum alloy plates (AA6082-AA7075) is used for this experimental investigation. Initially, 6 mm aluminum plates are resized in the required FSW process with help of milling machine and power hacksaw cutting machine. A vertical milling machine arrangement was used to fabricate FSW weld joints at SA Engineering College, Chennai. The manual top clamps are used to hold workpieces on the top surface of the work table. A non-consumable rotating High-speed steel tool material was selected to make weld joints with different pin shapes. The dimension for the FSW tool specified like shoulder diameter, pin diameter, and length of the tool pin.

The weld joints of AA6082-AA 7075 before and after conditions, different FSW tools are illustrated in Fig. 2. The mechanical values of the parent material are listed in Table 1.

The material chemical composition and mechanical properties of AA6082-AA7075 alloys are entirely different. The FSW rotational tool creates frictional heat

Fig. 2 Arrangement of before and after FSW joints

Table 1 Mechanical properties of base metal AA6082 and AA 7075 Alloy

Material	Tensile strength (Mpa)	Yield strength (Mpa)	Vickers hardness (HV100gm)	% of elongation
AA 6082	531	498	164	9
AA 7075	572	486	95	11

between the tool and the workpiece top surface. During the material joining process the material gets resulting in local plastic deformation of the parent material. Thus, the processing conditions selecting process is an important one because to establish the quality and strength of the welded material. The improper process conditions to lead with poor material flow, low amount of heat generation while the joint fabrication process. In addition to lead to kiss joints, tunnel defects, welding flash, and generate onion rings while making the joints. In this work, the unvarying axial load of 2kN, three different spindle speeds (1000 rpm, 1300 rpm & 1500 rpm), and three different pin profiles such as straight cylindrical, taper cylindrical and taper threaded pins are used in material joining process. The FSW joint making process parameters are given in Table 2.

Table 2 FSW process parameters

Sample	Pin profile	Rotational speed (rpm)	Welding speed (mm/min)	Axial load (kN)
1	Tapered	1000	20	2
2	Tapered	1300	40	2
3	Tapered	1500	60	2
4	Straight cylindrical	1500	40	2
5	Straight cylindrical	1300	60	2
6	Straight cylindrical	1000	20	2
7	Taper-Threaded	1000	60	2
8	Taper-Threaded	1300	20	2
9	Taper-Threaded	1500	40	2

3 Result and Discussion

Two various AA6082-AA7075 aluminum alloys were successfully combined by using FSW. In advance to examine the mechanical properties of the welded specimens using different mechanical tests were conducted.

3.1 Tensile Test

Once complete the material joining process to analyze the tensile strength of welded specimens to decided joint strength. The test specimens were prepared as per the ASTM standards along with the tool traverse of the weld direction. The maximum tensile strength of the weld joint is achieved at 1300 rpm and the welding speed is 60 mm/min from the straight cylindrical tool, since the welding speed is controlled by medium operating condition meanwhile the tool travel speed is in maximum.

The before and after tensile specimens and dimensions as shown in Fig. 3 and Table 3. The UTM was used to check a tensile test for the weld specimens. The tensile test values are listed in Table 4 and the graphical representation of the tensile test as illustrated in Fig. 4.

Fig. 3 Sample specimen diagram for before & after tensile test

Table 3 Dimensions of tensile test specimen

Parameter	Dimension (mm)
Overall Length	100
Gauge Span	25
Grip Distance	35
Grip Width	10 and 6
Fillet Radius	2

Table 4 Mechanical properties of the welded samples

Sample No	Rotational speed (rpm)	Welding speed (mm/min)	Axial load (kN)	Yield strength (Mpa)	Ultimate tensile strength (Mpa)	Hardness
1	1000	20	2	130	148	114
2	1300	40	2	52	69	112.67
3	1000	60	2	56	67	120.33
4	1500	40	2	43	159	111.67
5	1300	60	2	163	181	131.67
6	1000	20	2	115	131	141.67
7	1500	60	2	82	87	100.67
8	1300	20	2	60	68	112.33
9	1500	40	2	52	61	112.67

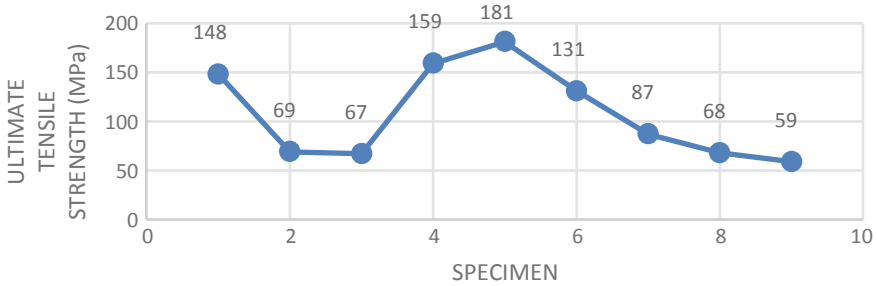

Fig. 4 Graphical representation of the tensile test in each weld joints

3.2 Hardness Test

The hardness is tested by using Vickers hardness tester under an Hv100gm loading condition and the rest period is 10 s. The hardness value of each weld samples is listed in Table 4. The extreme hardness value 141.67 is obtained at the weld zone from the straight cylindrical tool in the process parameters are 1000 rpm and the feed is 20 mm/min since both the welding speed and tool travel speed is in minimum operating conditions. The graphical representation of the hardness survey in each weld samples as shown in Fig. 5.

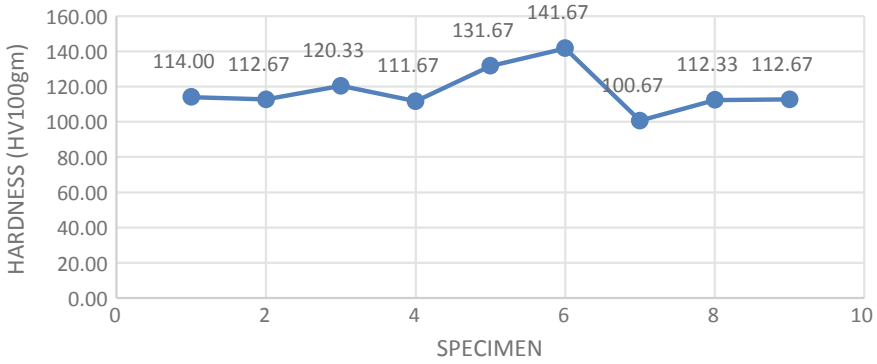

Fig. 5 Graphical representation of hardness survey in each weld samples

4 Conclusion

After done by the detailed investigation, the mechanical properties and the effect of friction stir welding parameters of two different aluminum alloys on AA 6082–AA7075 were successfully evaluated. Hence, we accomplished the following conclusions,

- The tool rotational speed and tool pin profiles play a vital role in getting the quality of the weld joint.
- The grain size and density of the weld specimen are to decide the joint strength and efficiency.
- The cylindrical tool pin profile produced successfully defectless weld joints with a low amount of flash during the joining process.
- The ordinary cylindrical pin profile (Straight cylindrical) gives the greatest tensile strength value of the weld joint in the tool revolving speed of 1300 rpm and the tool traveling speed is 60 mm/min.
- The amongst hardness value of the weld joint is obtained by the straight cylindrical pin-shaped tool at revolving speed is 1000 rpm and the tool traveling speed is 20 mm/min.
- Further, the particle size (grain) of the nugget zone is much better while comparing with parent material which strengthens the weld pool area.

References

1. Godhani PS, Patel VV, Vora JJ, Choudhary ND, Banka R (2019) Effect friction stir welding of aluminum alloys AA 6061/AA7075: temperature measurement, mıcrostructure, and mechanical properties. In: Innovations in infrastructure, advances in Intelligent systems and computing, vol 1966. Springer Nature, Singapore, p 981. https://doi.org/10.1007/978-981

2. Anil Kumar HM, Venkata Ramana V, Pawar M (2018) Experimental study on dissimilar friction stir welding of aluminum alloys (5083-H111 and 6082-T6) to investigate the mechanical properties: ICRAMMCE. In: IOP conference series, materials science, and engineering. IOP Publishing Ltd, p 330
3. Shahabuddin, Dwivedi VK (2018) Effect of tool geometry of friction stir welding on mechanical properties of AA 7075 Aluminum alloy. Int J Mech Eng Technol 9:625–633 (IAEME Publication)
4. Prasanna P, Penchalayya Ch, AnandamohanaRao D (2013) Effect of tool pin profiles and heat treatment process in the friction stir welding of AA6061 aluminum alloy. Am J Eng Res 02:7–15
5. Varun Kumar A, Bala Srinivasan M, Dulkiflee M (2016) Grey relational analysis and Taguchi method for the parametric optimization of single pass friction welded aluminum alloy 7075-T6 joints. Appl Mech Mater 852:331–336 (Trans Tech Publications)
6. Kumar K, Kailas SV (2008) On the role of axial load and the effect of ınterface position on the tensile strength of a friction stir welded aluminum alloy. Mater Des 29:791–797
7. Karthikeyan L, Senthilkumar VS (2011) Relationship between process parameters and mechanical properties of friction stir processed AA 6063-T6 aluminum alloy. Mater Des 3085–3091

Quieter Cabin Through Reduction in Uncontrolled Vehicle Air Leakage and Controlling Actions at Various Levels

Kedar Kulkarni, Pramod Patil, and Samar Deshpande

Abstract Quieter cabin and environment inside are important areas of success for any automobile as both are vital aspects of passenger comfort. On the contrary cabin air leakage can adversely affect these two areas to a greater extent. Air from the passenger cabin finds its way to the outer environment through the gaps formed in assembly interfaces and BIW, which is unintended and unrestricted air-leakage referred to as cabin air leakage. Same way may be followed by outer smell and noise, which directly affects the environment of cabin. Unintended air leakage is having some indirect effects such as reduction in the efficiency of HVAC cooling-heating causes excessive compressor engagement thus dropping fuel efficiency of the vehicle. Identifying accurate leakage paths and deploying suitable counteraction results in tangible benefits such as silent cabin, improved passenger environment and also adds up intangible benefit as higher fuel efficiency. In this paper, we used "Elimination methodology" to carry out the air leakage study on passenger vehicles, in which at static condition vehicle cabin is pressurized with air with the help of BLT (body leak test) machine and leakages were identified with help of stethoscope and soap water. Smoke machines can also be used for initial cabin leakage analysis. Later leakages and gaps were eliminated one by one by applying silicon sealant or putty thus getting the individual leakage contribution as well as final improvement value which can be achieved. The improvement in air leakage by 29% (254 CFM to avg. 180 CFM) is achieved through design modification of seals, BIW, application of expandable strips, plugs, closed-cell foam, stickers at various levels of manufacturing.

Keywords Body leak testing · BIW body in white · HVAC heating · Ventilation and air conditioning · Air leakage

K. Kulkarni (✉) · P. Patil · S. Deshpande
Automotive Division, Mahindra & Mahindra Ltd., Chennai, India
e-mail: kulkarni.kedar2@mahindra.com

P. Patil
e-mail: patil.pramod3@mahindra.com

S. Deshpande
e-mail: deshpande.samar@mahindra.com

N. Gascoin and E. Balasubramanian (eds.), *Innovative Design, Analysis and Development Practices in Aerospace and Automotive Engineering*, Lecture Notes in Mechanical Engineering, https://doi.org/10.1007/978-981-15-6619-6_32

1 Introduction

Passenger cabin of vehicle which is running on the road is subjected to various types of noise interventions, out of that prominent are road noise, wind noise and engine noise. Though technology has taken a leap ahead and we have managed to reduce engine and transmission noise to a great extent other parameters are majorly influenced by environmental conditions and are uncontrolled [1].

Cabin acoustic is directly proportional to cabin air leakage. Higher the rate more the noise inside the cabin. Uncontrolled and unintended cabin leakage happens mainly because of gaps formed due to parts assembly interface, gaps between body panels, misfit grommets used for electrical wiring harness and to cover PLP holes, steering column cup assembly gap in floor or firewall, suspended pedal assembly mountings, gaps between seals for doors and glasses. Even after pushing significant efforts during the early stage of design to minimize the mentioned unintended gaps, it may exist due to assembly failure, design failure, or manufacturing failure.

Considering all the above parameters it is important to identify the leakage sources, review the design in the respective area and find appropriate solutions to stop or minimize the air leakages.

2 Testing Methodology, Experimental Setup and Testing Procedure

2.1 Air Leakage Testing Methodology

In the overall process of evaluation of air leakage below are the main stages:

1. Current vehicle air leakage evaluation: Baseline value
2. Identify the leakage areas
3. Close or minimizes the leakages
4. Regularize the solutions.

The process is elaborated in Fig. 1.

2.2 Experimental Setup

Cabin air leakage of the vehicles is tested using body (cabin) leak tester also known as BLT machine. Figure 2 shows the block diagram of body leak test rig available at test laboratory. The vehicle is tested with constant cabin pressure methodology by maintaining 150 kPa in the cabin. Before connecting vehicle to the machine its standard practice to ensure that vehicle is in ignition off condition, AC is in recirculation mode, air extractors are closed (sealed with tape) and all window glasses

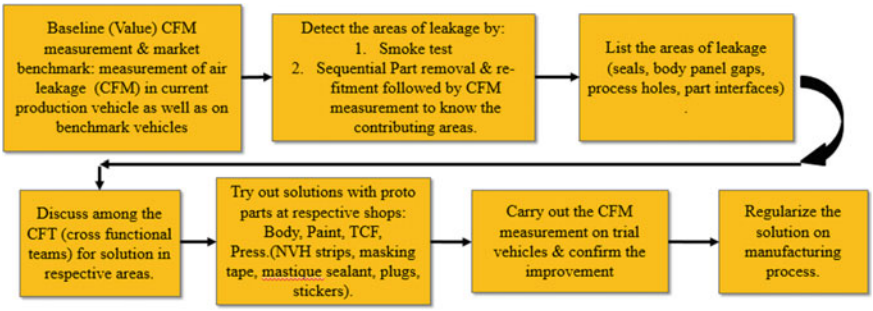

Fig. 1 Air leakage testing methodology

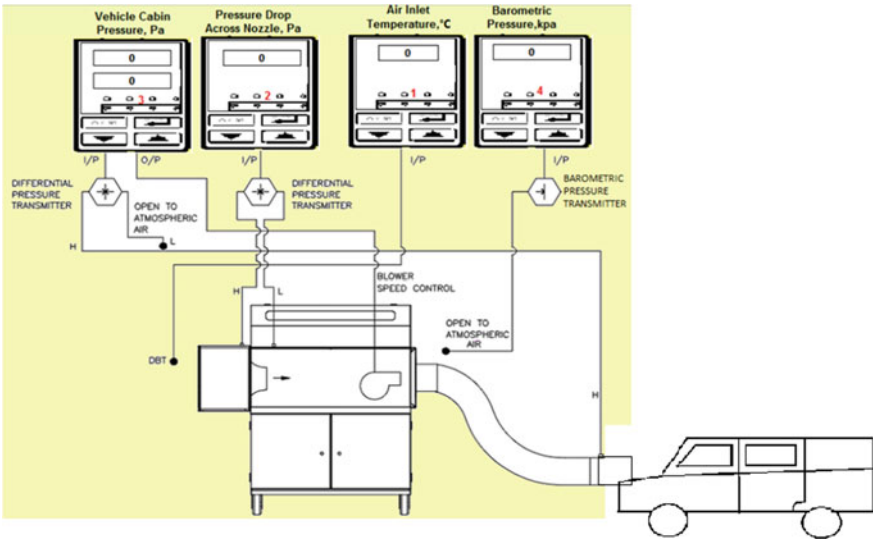

Fig. 2 Vehicle BLT set up and testing machine overview (Constant pressure methodology) [2]

are up except one where we are putting machine duct to pressurize the cabin. Machine is connected to the vehicle with the help of duct adapter to rear door window of vehicle with proper sealing. Once the test started, air is blown to cabin to achieve constant pressure of 150 kPa. Once the set pressure achieved machine evaluates leakage rate in terms of CFM (cubic feet per minute) and EBHS (equivalent body hole size). Figure 3 shows the mid-segment car is undergoing air leakage testing.

Fig. 3 Mid segment car undergoing air leakage testing

2.3 Testing Procedure

Vehicle preparation. To identify the unintended leakage areas and flow rate, one needs to seal the intended openings. So the first step is to seal the air extractor which is the only opening that affects the tests and needs to be closed. For closing the air extractor in most of the vehicles we may need to remove the rear bumper for test sake.

Before starting the test we need to ensure that vehicle ignition is in off condition. Air conditioning is in recirculation mode as fresh air entry mode opens to external environment and lead to leakage of cabin air. All doors and glasses are in closed condition. If the required vehicle can be mounted on two posters so that it will be easy to do inspection and detection of leakages in underbody along with other areas.

Body leak tester machine connections and setup. In set up air supply cum pressurizing hose is connected to vehicle through a window by taking glass down and with the help of customized adapter (Ref. Figure 3). According to vehicle model program is selected to run the test.

Testing and final reading. Once set up is done, after starting the test, machine (blower) pressurizes the vehicle cabin to the required pressure and maintains the constant pressure in cabin. At the same time, flow rate (cubic feet per minute) is calculated by machine and it will be displayed on a monitor connected to machine after completion of a cycle. In total three cycles needs to be conducted and final reading is average of these three readings.

Based on the final reading and market competitor benchmark from the same segment airlekage improvement target is set. Accordingly, analysis is done and action plan is deployed.

Table 1 Air leakage test values and in cabin noise level for different segment vehicles without air leakage improvement actions

Before implementation of improvement actions				
Vehicle	Test cabin pressure (kPa)	Leak rate		In cabin noise level (db)
		EBHS (cm^2)	Flow rate (CFM)	
Car (mid segment)	150	70	254	71
SUV (monocoque)	150	119	430	69
SUV (body on chassis)	150	91	330	72

3 Results and Discussions

3.1 Cabin Air Leakage

Table 1 shows the BLT readings for different segments of the vehicles in India. The tests were carried out with constant pressure method and following all standard practices mentioned in the test methodology and experimental Setup paragraph. Vehicle tested includes Car (mid-segment), SUV (monocoque), and SUV (Body on Chassis).

3.2 Improvement Actions

After getting the leakage (airflow) rate from BLT machine next task is to detect the leakages and take countermeasures. To know the exact root cause, during or after BLT, leakages are identified with touch and feel, using smoke machine, stethoscope and soap solutions wherever applicable. One, two or multiple methods from the above list can be applied as per the requirement to detect the leakages. Once leakage areas identified following solutions are to be considered which may prove as effective solutions at different levels of manufacturing (shops) and according to nature of gap or leakage.

Body shop actions: Application of expandable strips, butyl stickers, expansion baffles, mastic or spot weldable sealers, etc. Figure 4 shows the snaps of some of the solutions.

Paint shop actions: Application of paint sealers, paintable stickers, melt plugs, paintable (tesa) tapes, etc. Figure 5 shows the snap of paintable sticker.

TCF (trim, chassis, and final)/Assembly shop actions: Rubber grommets, clips with foams, closed-cell foams, acoustic plugs, stickers, gaskets, etc. Figure 6 shows the snaps of application of closed-cell foam.

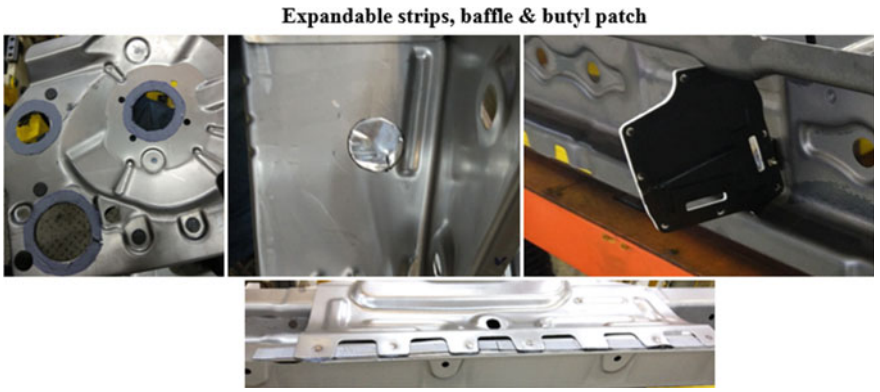

Fig. 4 Body shop actions to stop or reduce body level air leakage

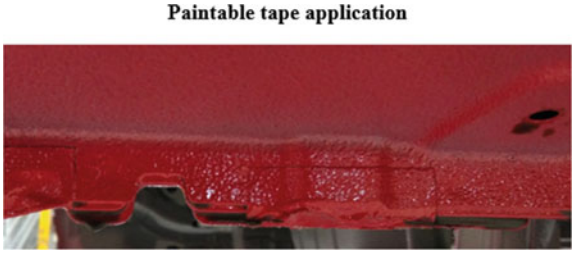

Fig. 5 Paint shop actions to stop or reduce body level air leakage

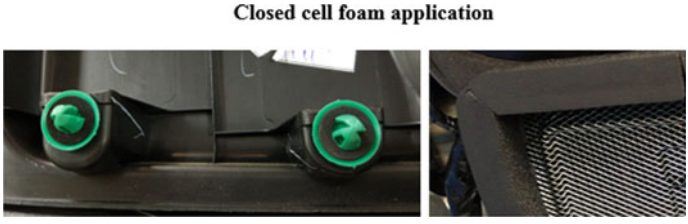

Fig. 6 Assembly shop actions to stop or reduce vehicle level air leakage

After the implementation of valid solutions improvement observed in leakage rate, the same is mentioned in Table 2.

Table 2 Air leakage test values and in cabin noise level for different segment vehicles with air leakage improvement actions

After implementation of improvement actions				
Vehicle	Test cabin pressure (kPa)	Leak rate		In cabin noise level (db)
		EBHS (cm^2)	Flow rate (CFM)	
Car (mid segment)	150	50	180	65
SUV (monocoque)	150	42	150	64
SUV (body on chassis)	150	44	160	66

3.3 Cabin Acoustic Measurement

To capture the acoustic improvement, in cabin noise measurement has been carried out in both conditions that is pre improvement and post improvement vehicles. Measurements are carried out with controlled parameters such as maximum speed of vehicle was 60 kmph, position of dB meter kept same in all segment of vehicle that is near co-drivers right shoulder, AC was in off condition, recirculation mode was ON, all window glasses were up, all vehicles tested on the same track with same surrounding condition.

4 Conclusion

Air leakage is one of the key parameters contributing to higher in cabin noise levels. The correlation can be established between air leakage rate and in cabin noise level. In cabin noise level is directly proportional to air leakage rate, higher the leakage more the in cabin dB level. Individual vehicle noise level improvement can be seen with the help of values mentioned in Tables 1 and 2. It shows that in cabin noise level reduced to on an around 65 dB which is rational value for vehicle cabin noise. Figure 7 is the combo chart which depicts all three segments with pre and post values of leakage rate and dB level.

Next level of study is planned with in cabin AI (Articulation Index) measurement to figure out direct benefit to passengers and improvement in cabin comfort.

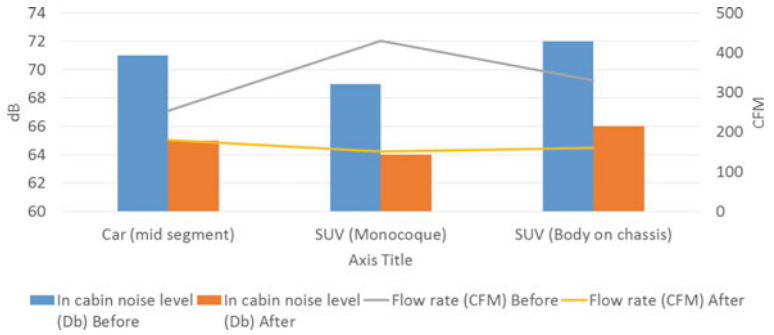

Fig. 7 Pre and post values for all three segment vehicles

Acknowledgements The author would like to thank assembly shop, body shop and paint shop along with NVH, GSM, and BIW teams of Mahindra & Mahindra for their support and collaboration in the process of improving the acoustic quality and cabin comfort of the vehicle.

References

1. Sottek R, Philippen B (2010) Separation of airborne and structure-borne tire-road noise based on vehicle ınterior noise measurements. SAE Technical Paper 2010-01-1430. https://doi.org/10.4271/2010-01-1430
2. Operation & Instruction Manual. Cabin Leakage Tester 40 CFM to 590 CFM. www.shreeref.com. Accessed Mar 2019

Aerodynamic Analysis of Manta Ray-Inspired Micro-air Vehicle Wing Planforms

Deepak Subramanian, Jerome Alex Revanth, Gangadhar Arasu Vasagan, Pankaj Soorya Ramnarendran, Rajesh Senthil Kumar Thangeswaran, and Balajee Ramakrishnananda

Abstract This study examines the performance of a bio-inspired micro-air vehicle's wing planforms at a low Reynolds number. The shape of the manta ray's wing was extracted from the real image of a manta ray and a B-spline curve was generated. The Zimmerman planform was taken as the base for the model. Using Bezier curve, the planform was extended on the sides to create two models with differing curvatures which were named Manta A and Manta B. Numerical simulations were conducted using ANSYS FLUENT 15.0 at a Reynolds number of 1×10^5, and the aerodynamic characteristics of the planforms were studied. It was clear from the results that the manta ray-inspired planforms provided better lift characteristics at all angles of attack between 0° and 20° when compared to the base Zimmerman planform. It can also be observed that both the manta planforms provide better C_L/C_D ratios by around 11–23% between angles of attack 10° and 20°.

Keywords Manta ray · Micro-aerial vehicle · Bio-inspired wing planform · Aerodynamic efficiency

1 Introduction

A lot of interest has been shown in design and development of micro-air vehicles lately. MAVs are the class of unmanned aerial vehicles which are miniature in size, generally less than 500 mm [1], and are widely used for surveillance and reconnaissance purposes. MAVs may be autonomous or semi-autonomous in nature and need to be extremely versatile in their performance. MAVs have been classified into fixed wing, vertical take-off and landing (VTOL), flapping wing and rotary wing types [2]. And of the four types, fixed wing has the longest endurance, range and highest

D. Subramanian · J. A. Revanth · G. A. Vasagan · P. S. Ramnarendran · R. S. K. Thangeswaran (✉) · B. Ramakrishnananda
Department of Aerospace Engineering, Amrita School of Engineering, Amrita Vishwa Vidyapeetham, Coimbatore, India
e-mail: t_rajesh@cb.amrita.edu

N. Gascoin and E. Balasubramanian (eds.), *Innovative Design, Analysis and Development Practices in Aerospace and Automotive Engineering*, Lecture Notes in Mechanical Engineering, https://doi.org/10.1007/978-981-15-6619-6_33

altitudes and flight speeds and is usually hand-launched. The design of MAVs is difficult due to a lack of exhaustive understanding of the aerodynamics pertaining to small vehicles. Also, due to the low endurance, which is often of the order of few minutes, design modifications are required in order to achieve high aerodynamic efficiencies. Mueller et al. [2] had conducted a thorough study on the lift, drag and pitching moment characteristics of low aspect ratio wings in low Reynolds number flows. They focused on the effects of aspect ratio and wing planform on moments and forces in low Reynolds number flows and they provide the experimental data of lift, drag and moment for Zimmerman planforms of various aspect ratios. Moreover, the Zimmerman planform is one among many MAV planforms which was proposed for real-time flight [2].

The manta ray (Manta birostis) is a giant ray found in temperate, subtropical and tropical waters and have been found to weigh as much as 3 tonnes [3]. Mantas propel through water by moving their pectoral fins in a wing-like fashion, which drives water backwards. The oscillatory swimming strokes of the manta ray have been studied by Fish et al. [4]. Wang et al. [5] studied the hydrodynamic performance of a manta ray-inspired underwater glider which displayed significant improvements in lift-to-drag ratios compared to a conventional underwater glider. However, manta ray-inspired designs have seldom been researched for applications in MAVs.

The current effort is focused on improving the aerodynamic characteristics of the base Zimmerman planform by providing bio-inspired modifications, thereby allowing it to be used for a wider range of applications.

2 Geometric Modelling

The baseline wing planform was decided to be the Zimmerman planform model with an aspect ratio of 1 as it was suitable for low aspect ratio MAVs. A Zimmerman planform is a combination of two ellipses that have a common axis length in which the upper ellipse's major axis coincides with the lower ellipse's minor axis as shown in Fig. 1a. The Zimmerman planform was chosen as it has been experimentally shown to have high C_{Lmax} and displays favourable post-stall behaviour which allows them operate at a wider range of angles of attack [6]. Drawing inspiration from manta rays and extensions were superimposed on the planform by taking reference from the curved pattern of the manta ray. The Manta A and Manta B planforms were created by providing extensions to the existing Zimmerman planform using Bezier curve as shown in Fig. 1b.

3 Computational Domain and Validation

A half-wing model enclosed in a half cylinder is used as the computational domain as shown in Fig. 2a, which minimize the mesh and the computation time. The length and

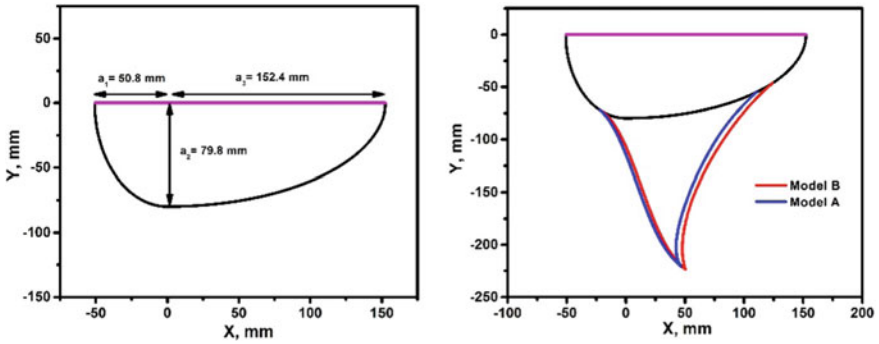

(a) Zimmerman model (b) Manta A and Manta B

Fig. 1 Wing planforms

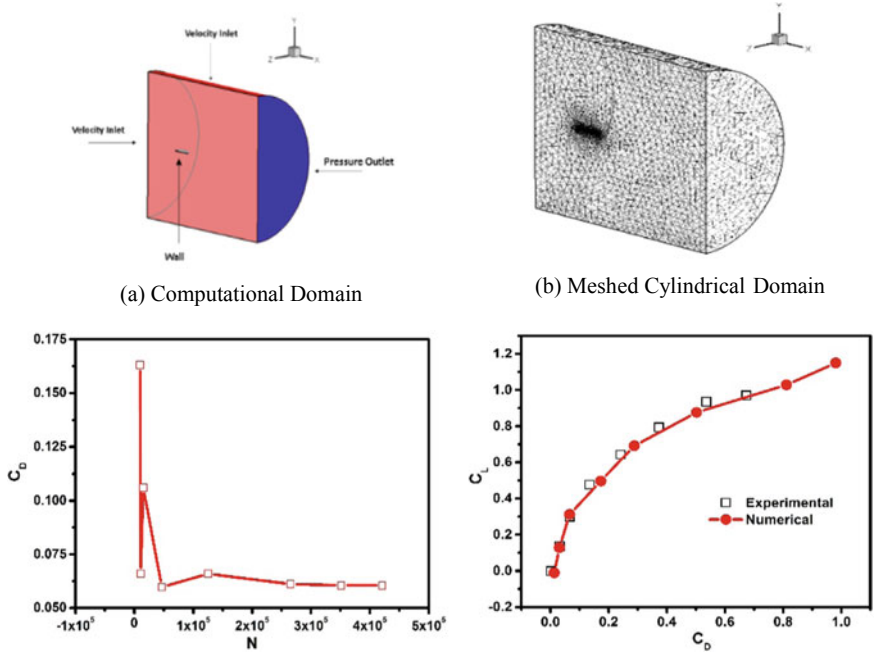

(a) Computational Domain (b) Meshed Cylindrical Domain

(c) Number of Nodes(N) vs C_D (d) C_L vs C_D

Fig. 2 Computational domain, meshing, grid convergence study and validation

diameter of the domain were about 10 times and 5 times of the root chord, respectively. Unstructured grid was generated in the domain along with 10 prism layers near the body as noted in Fig. 2b and the first layer height is 3×10^5 m to maintain wall y+ less than 1. Velocity inlet, pressure outlet, symmetry and wall boundary conditions were applied at the various domain boundaries. The CFD analysis was conducted at

a Reynolds number of 10^5 with the k-ω SST turbulence model. First-order upwind discretization scheme was used, and Green-Gauss cell-based method was used to compute the gradient. A grid convergence study was conducted to find the number of elements required, as shown in Fig. 2c. The solutions obtained from the CFD analysis were validated using the experimental data of Mueller et al. [2]. The CFD results closely match with the experimental results as evident from Fig. 2d.

4 Results and Discussion

In this section, the effectiveness of the manta planforms is estimated by comparing their aerodynamic performance to that of the base Zimmerman planform. First, the lift coefficients are compared, as they are important for take-off and gliding performance and hence directly affecting the endurance of the MAV. Figure 3a represents a plot between lift coefficient and angle of attack and from the plot, lift curve slope for the base Zimmerman planform is calculated as 0.582π. In comparison, the Manta A wing planform has a lift curve slope of 0.984π and the Manta B has a lift curve slope of

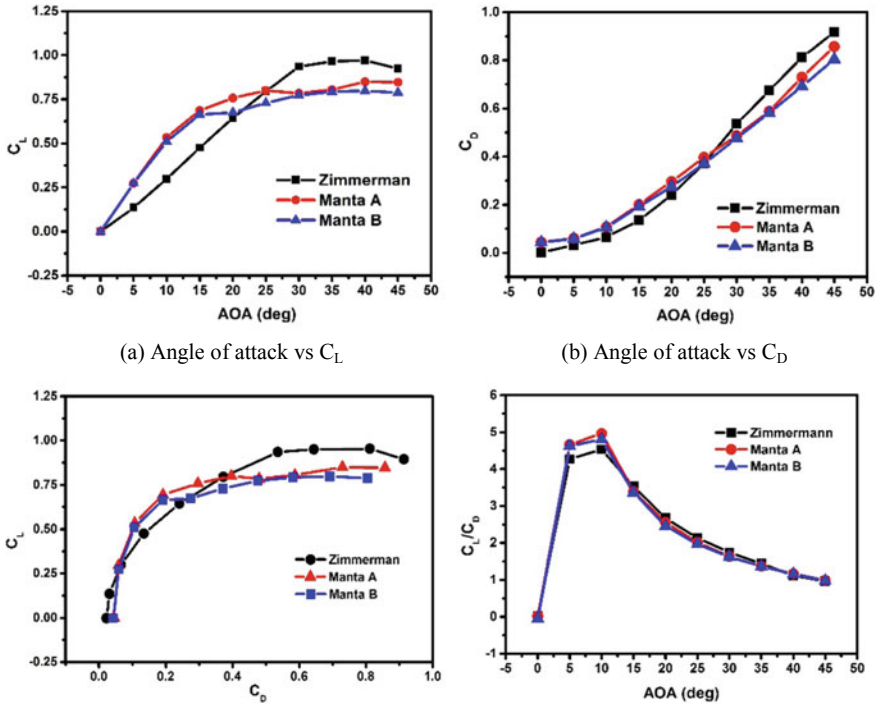

(a) Angle of attack vs C_L

(b) Angle of attack vs C_D

(c) C_D vs C_L

(d) Angle of attack vs C_L/C_D

Fig. 3 Comparison of aerodynamic performances of Zimmerman, Manta A and Manta B planforms

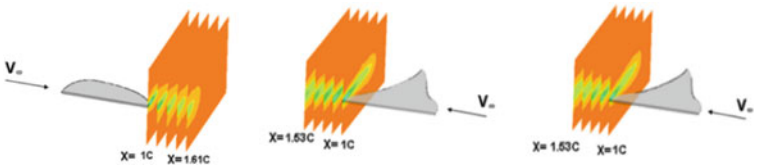

(a) Zimmerman (b) Manta A (c) Manta B

Fig. 4 Wake visualization

0.938π as seen from Fig. 3a. Hence, the lift curve slope of both the manta planforms proves to be more effective, outperforming the Zimmerman planform by 60% due to higher aspect ratio. The lift curve of the manta planforms reaches a maximum value of C_L at 25°, at which point its value exceeds that of the Zimmerman by 17%, as seen from Fig. 3a. The difference between the lift curves is truly incontrovertible at 15°, where the difference reaches a maximum value of 45% of that of base planform.

Second, the drag characteristics of the planforms were compared as the coefficient of drag is important for determining the power consumption of the MAV. The total surface area of the Manta A and Manta B planforms are 50.9% and 46% more than the Zimmerman planform, respectively, and this might have implications in the drag performance. From the drag polar graph in Fig. 3c, it is evident that the zero-lift drag is lower for the base planform in comparison to both the manta planforms which can be attributed to the smaller area of the base planform.

Third, the C_L/C_D ratios were compared as they are important in determining the operational range of the MAV. From the C_L/C_D vs angle of attack graph, Fig. 3d, it is evident that the manta ray-inspired planforms have higher efficiency at angles between 10 and 20 with the peak value being 5.59% higher than Zimmerman planform which occurs at angle of attack 10°.

It is important to study the wake of the planform in order to understand the effect of drag on the geometry. As seen from Fig. 4, the intensity of wake is more for the modified planforms which explains the higher zero-lift drag observed in Fig. 3c. The width of the wake is higher for the manta planforms due to their larger span. Also, the wake diminishes more rapidly for the Zimmerman planform which can be attributed to the larger area and span of the manta planforms.

5 Conclusion

From the study, it is evident that there is a change in the aerodynamic performance of the modified planforms. Both the manta planforms differ from the Zimmerman planforms in the following areas:

- The lift curve slope of both the manta planforms is 60% higher than the base Zimmerman planform, as evident from Fig. 4a. The lift characteristics of both the

manta planforms can be attributed to their aspect ratios. Manta A has an aspect ratio of 5.05, and Manta B has an aspect ratio of 5.3.

- The drag characteristic is of paramount importance for MAVs, since they have limitations in terms of on-board power storage. The zero-lift drag is higher for the manta planforms which is evident from the wake diagrams; this is mainly due to the larger span of the manta planforms. However, from Fig. 4b, it is evident that the manta planforms have better drag characteristics between 10° and 20°.
- The C_L/C_D ratio of the manta planforms is higher than the base planform between angle of attack 10° and 20° reaching a maximum difference of 5.59% at 10° as shown in Fig. 3d.
- Although the Zimmerman planform has a higher maximum lift coefficient, the take-off will not be efficient because the corresponding lift-to-drag ratio is low. In contrast, the stall angle and angle of attack for maximum aerodynamic efficiency are closer for the manta ray planforms than for Zimmerman, suggesting a more efficient take-off whose fuel savings can be used profitably elsewhere. However, more research is needed to confirm this.

This increases the scope and applications of these designs, having the ability to take-off and land from remote locations more efficiently. Further, research can be conducted to decrease the drag of the manta planforms, one method would be to curl the wingtips within the boundary of the Zimmerman planforms and reduce the overall area of the modified planform.

References

1. Hassanalian M, Abdelkefi A (2016) Design and manufacture of a fixed wing MAV with Zimmerman planform. In: 54th AIAA aerospace sciences meeting
2. Mueller TJ, Torres GE (2001) Aerodynamics of low aspect ratio wings at low Reynolds numbers with applications to micro air vehicle design and optimization. Final Report, University of Notre Dame, United states
3. Last PR, Stevens JD (2009) Sharks and rays of Australia. Harvard Univ Press, Cambridge
4. Fish FE, Schreiber CM, Moored KW, Liu G, Dong H, Bart-Smith H (2016) Hydrodynamic performance of aquatic flapping: efficiency of underwater flight in the manta. Aerospace 3
5. Wang Z, Yu J, Zhang A (2016) Hydrodynamic performance analysis of a biomimetic manta ray underwater glider. In: 2016 IEEE international conference on robotics and biomimetics, ROBIO 2016
6. Marek PLCNG (2008) Design, optimization and flight testing of a micro air vehicle

A Route Planning Strategy for Commercial Deliveries Using Drones

Soumen Manna and Anand Narasimhamurthy

Abstract In this work, we address the problem of route planning in the scenario of using drones for commercial deliveries. One main difference in such a scenario as compared to traditional truck-based deliveries is due to the limited weight capacity of the delivery vehicles, i.e. the drones. This necessitates solving the routing and scheduling together unlike many vehicle routing problems studied in the literature. Also, a practical solution must be scalable and must take into account the complexities of the real-world scenario (e.g. orders get updated dynamically and frequently). Accordingly, we propose a heuristics-based greedy approach which entails low computation overhead and is easily scalable. We show simulation results demonstrating the efficacy of the approach.

Keywords Drone scheduling · Vehicle routing problems · Greedy approach · Heuristic algorithm · Route planning

1 Introduction

Vehicle Routing Problems (VRPs) have a long history dating back to at least Dantzig et al. [1], several variants have been studied in the literature (e.g. [2, 8]). With the advancement of online shopping, we can anticipate significant usage of drones for commercial deliveries, once regulatory challenges are overcome. According to an ARK Investment report [10] the cost to deliver a package within 30 min using Amazon PrimeAir (a service proposed by Amazon in 2014, with the intended aim of delivering packages up to five pounds in 30 min or less using small drones) would work out

S. Manna · A. Narasimhamurthy (✉)
International School of Engineering, Bengaluru, India
e-mail: anand.narasimhamurthy@insofe.edu.in

S. Manna
e-mail: manna.soumen@gmail.com

N. Gascoin and E. Balasubramanian (eds.), *Innovative Design, Analysis and Development Practices in Aerospace and Automotive Engineering*, Lecture Notes in Mechanical Engineering, https://doi.org/10.1007/978-981-15-6619-6_34

to $1 in contrast with $12.92 by UPS ground next-day service. Existing delivery services that use drones include DHL's parcel service to the island of Juist in the North Sea and Zipline's service using fixed-wing drones started in Rwanda in 2016 [9].

Many innovative solutions for deliveries using drones have been proposed [3–7] Many proposed route planning approaches formulate an optimization problem, often making restrictive assumptions, in most cases these optimization problems are NP-hard or require significant computation. A solution that is intended to be deployed online should be lightweight and must be able to easily deal with dynamic updates of orders. In this work, we mostly focus on the scenario of a single warehouse and one drone servicing orders of multiple customers. This would be directly applicable in scenarios such as where a drone is used along with trucks (e.g. [3]), also this can be considered as a sub-routine when solving the more general cases.

2 Description and Notation

The general problem being addressed may be stated as follows:

Given a list of warehouses (locations and inventory of items), a set of customer orders (locations, product ID and quantity of each item ordered), and the initial locations of a set of drones, determine a delivery schedule so as to service all orders and minimize the total distance covered.

We introduce some notation that will be used in the rest of the paper. We assume there is a warehouse H with a sufficient quantity of each product to fulfill all orders and that the weight of a single unit of each product is less than the capacity M of the drone. All locations are specified using a 2D coordinate system, with the warehouse located at the origin (0,0). All customer locations are assumed to be under the drone flying area.

A trip starts from the warehouse H, visits certain customers and ends at the warehouse H (e.g. $H \rightarrow c_i \rightarrow c_j \rightarrow H$). We define a schedule to be a sequence of such trips such that all orders that could be serviced are fulfilled.

Let d_{HC} be the list of customers sorted according to increasing distance from the warehouse (refer example in Table 3(a)).

Additionally, the following supporting data structures are computed in the beginning and updated repeatedly.

- A list D, where the i th element of D is the list of other customers sorted according to distance from c_i (refer example in Table 3(b)).
- A list/array R, which stores status of each order (Order Serviced: True/False).

3 Drone Scheduling Algorithms

We propose mainly two models for drone delivery scheduling system, we refer to these as 1) **Not Allowing Partial Delivery (NAPD)** Model and 2) **Allowing Partial Delivery (APD) Model**. No partial delivery is allowed in the NAPD scheme, only those orders whose total weight is within the capacity of the drone (**M**) are serviced. The APD scheme allows the option of splitting orders, this allows servicing even those orders whose weight exceeds the drone capacity as long as the order can be split item wise such that each the total weight of each suborder is within the drone's capacity. However, there may be multiple trips made to a customer location.

3.1 NAPD Model

Initially, the status of each order is set to FALSE. A new trip is always assumed to start from the warehouse H. Scan the list d_{HC} and identify the customer closest to H whose order has not been fulfilled yet, let this customer be c_i. Add c_i to the current trip, calculate weight of current order (CW) and update the remaining capacity of drone (RW). Update start location of the next leg to c_i. Scan the relevant list in D to identify the nearest customer to c_i, whose order is not yet fulfilled and order weight is within remaining capacity. Repeat until no more orders can be included in current trip. The algorithm details are given in Table 1, the sub-routine new-route is called repeatedly on remaining customers until all orders are fulfilled.

Table 1 NAPD algorithm (sub-routine to compute a new trip)

new-route

step 1: Identify customer c_i *located closest to the warehouse and whose order is not yet fulfilled.*
route: $H \rightarrow c_i$; CW = w_i, RW= $M - CW$.
update status of c_i to TRUE in R list.

step 2: $C_{i+} = \{c_{i_1}, c_{i_2}, \ldots, c_{i_u}\}$ *are the unfulfilled customers from* c_i*-th row of* D *and* $W_{i+} = \{w_{i_1}, w_{i_2}, \ldots, w_{i_u}\}$ is the weight vector corresponding to C_{i+}.

step 3: for $j = \{1, 2, \ldots, u\}$, *do*
if $w_{i_j} \leq$ RW
update:
route: route $\rightarrow c_{i_j}$
CW: CW + w_{i_j}
RW: M - CW
update status of c_{i_j} to TRUE in R list.
end
end

step 4: route: route $\rightarrow H$.

Table 2 APD algorithm

APD-route
step 0: Let d^* is the total scheduling distance under NAPD algorithm.
step 1: route 1 = call new-route algorithm; let c_t last customer in route 1 and $RW = M - CW$.
step 2: Let $L = \{c_1^*, c_2^*, \ldots, c_m^*\}$, be the set of all customers whose total weight can be divided into two parts such that one part is less than RW.
step 3: For each customer c_i^* in L, consider them as two different customers with divided weights and call NAPD algorithm. Let d_i^* is the total scheduling distance when c_i^* is partial delivered.
step 4: Let d_j^* is the minimum total scheduling distance among all partial deliveries from the customer list L. If $d_j^* < d^*$, complete route 1 with partial delivery to c_j^* and set $d^* = d_j^*$, otherwise complete route 1 with c_t as the last customer of route 1.
step 5: Run the algorithm again for rest of the unfulfilled customers.

3.2 APD Model

In the APD model, we allow partial delivery to the customers. The first trip is selected in exactly the same manner as in the NAPD approach. Next, we consider splitting order of each customer whose order is not fulfilled as follows. For a candidate customer, sort the items in ascending order of total weight. Select the first item if its weight (= product unit weight x number of items) can be included within the drone's remaining capacity, continue including more items from same customer till no more items can be included. This greedy approach which splits itemwise ensures a unique split (if any) for each candidate customer. Run the NAPD approach on this modified set of orders and compute the schedule. This is repeated for each candidate customer. Of all possible candidate splits, suppose splitting order of customer c_j yields the lowest overall distance. If this is lower than the solution from NAPD, only then c_j's order is split as above (since it yields a solution better than not splitting any customer's order). Table 2 provides the APD algorithm in detail.

4 Results

We illustrate the details of the two proposed schemes, first by toy examples, these results are summarized in Table 4. We have run our experiments on larger problem sizes in order to assess the running time of the approach, these results are summarized in Table 5. In all our simulation experiments, we used a simple, basic approach as the baseline for comparison.The baseline approach used for comparison is just servicing one order fully in one trip, flying back to the warehouse, and so on till all orders are fully serviced. For illustration we have used integer coordinates and weights in the examples, we have dropped the unit for convenience, however, any suitable unit (e.g. grams for weight and metres for distance) can be used for the real-world scenario.

Example 1 *Toy example (the numbers are for illustration only:)*
Product catalogue: 4 products P1,P2,P3,P4 each unit weight = 50 gms
Warehouse location = (0,0)
Initial location of drone = (0,0), Weight carrying capacity of drone = 1000 gms
Customer locations: C_1: (10; 10);C_2: (15; 10);C_3: (15; 18);C_4: (17; 10)

Consider a set of four customers and a product catalogue of four items as in Example 1. The supporting data structures used repeatedly by the algorithms are shown in Table 3. For the same warehouse and customer locations, we consider two order sets as shown in Table 4a, b. In Order set 1, more than one order can be accommodated within the drone's capacity, whereas in Order set 2 no two orders can be combined without exceeding the drone's capacity. Table 4c, and d show the schedule computed by the NAPD approach for the two order sets in the toy example. As can be readily seen, the NAPD scheme tries to combine as many orders as possible into a single trip. However, in order set 2, since no two orders can be combined without exceeding the drone's capacity, the NAPD schedule is the same as the baseline approach. In the APD approach, the first trip is fixed as H $\rightarrow$ C_1. Next, the APD algorithm considers other customers as candidates whose orders can be split and accommodated on the same trip. The modified order set obtained by splitting order of customer C_2 is shown in Table 4e (split orders are assigned customer ids as $C_{2:1}$ and $C_{2:2}$). For this example, the total distance covered in best split in APD approach = 123.78, an improvement over the NAPD approach (distance = 150.65).

In the next set of experiments, multiple order sets each containing a fixed number of orders (say K) were randomly generated. Our proposed approach was run on each such order set and the percent improvement over the baseline approach was computed as $\%improvement = \frac{d_{baseline} - d_{alg}}{d_{baseline}} \times 100$

Table 3 Supporting data structures for toy example **a** Customers sorted in ascending order of distance from warehouse, e.g. since warehouse is located at (0,0) and C_1 at (10,10) the Euclidean distance is $\sqrt{200} = 14.14$ **b** For each customer, list of other customers arranged in increasing order of distance (D). For example, C_2, C_4 and C_3 are located at distances of 5,7 and 9.43 from C_1

(a)

Customers arranged according to distance from warehouse
$H : [C_1, 14.14], [C_2, 18.03], [C_4, 19.72], [C_3, 23.41]$

(b)

C_1	$[C_2, 5]$	$[C_4, 7]$	$[C_3, 9.43]$
C_2	$[C_4, 2]$	$[C_1, 5]$	$[C_3, 8]$
C_3	$[C_2, 8]$	$[C_4, 8.24]$	$[C_1, 7]$
C_4	$[C_2, 2]$	$[C_1, 7]$	$[C_3, 8.24]$

Table 4 **a** and **b** Order Sets 1 & 2. The Order details column specifies the items ordered by that customer as a set of (ProductID, Quantity) tuples. Eg. (P1,4),(P2,7) specifies that the order contains 4 units of product P1 and 7 units of product P2. **c** and **d**: Schedule computed by NAPD approach for order set 1 (possible to combine more than one whole order) and order set 2 (not possible to combine any two orders without exceeding drone capacity). The numbers indicate the distance for that particular leg of the tour. **e** Order split which yielded the lowest overall distance and **f** Schedule computed by the APD approach

(a) Order set 1 details

Customer	Location	Order Details	Weight (gm)
C_1	(10,10)	(P1,10)	500
C_2	(15,10)	(P2,10)	500
C_3	(15,18)	(P3,10)	500
C_4	(17,10)	(P4,10)	500

(b) Order set 2 details

Customer	Location	Order Details	Weight (gm)
C_1	(10,10)	(P1,4),(P2,7)	550
C_2	(15,10)	(P1,4),(P4,6)	500
C_3	(15,18)	(P3,7),(P4,5)	600
C_4	(17,10)	(P3,8),(P4,3)	550

NAPD results

(c) Computed NAPD schedule for order set 1

Tour 1	$H \rightarrow C_1 \rightarrow C_2 \rightarrow H$ 14.14 + 5 + 18.03
Tour 2	$H \rightarrow C_4 \rightarrow C_3 \rightarrow H$ 19.72 + 8.24 + 23.41
Total distance	88.57 m

(d) Computed NAPD schedule for order set 2

Tour 1	$H \rightarrow C_1 \rightarrow H(2 \times 14.14)$
Tour 2	$H \rightarrow C_2 \rightarrow H(2 \times 18.03)$
Tour 3	$H \rightarrow C_4 \rightarrow H(2 \times 19.72)$
Tour 4	$H \rightarrow C_3 \rightarrow H(2 \times 23.41)$
Total distance	150.65 m

APD results

CustomerId	Location	Order details	Weight (gm)
C_1	(10,10)	(P1,4),(P2,7)	550
$C_{2.1}$	(15,10)	(P1,4)	200
$C_{2.2}$	(15,10)	(P4,6)	300
C_3	(15,18)	[(P3,7),(P4,5)]	600
C_4	(17,10)	[(P3,8),(P4,3)]	550

(e) Best order split (APD) for order set 2

Tour 1	$H \rightarrow C_1 \rightarrow C_{2.1} \rightarrow H$ 14.14 + 5 + 18.03
Tour 2	$H \rightarrow C_{2.2} \rightarrow C_4 \rightarrow H$ 18.03 + 2 + 19.72
Tour 3	$H \rightarrow C_3 \rightarrow H$ 23.43 + 23.43
Total distance	123.78 m

(f) APD schedule computed for order set 2

where d_{alg} and $d_{baseline}$ are the total distances covered by the schedules computed by the algorithm and baseline approach, respectively. The minimum, average and maximum percentage improvement across multiple order sets and for different K are shown in Table 5. Although the improvement depends on the actual order details and locations of customers relative to the warehouse, we observed that the proposed approach was significantly better than the baseline in every case. The minimum improvement observed was > 45%. As number of orders increases, the algorithm would tend to yield significant improvement since there is more scope for combining multiple orders in every step.

5 Conclusions

In this work, a heuristics based greedy heuristics approach is proposed for scheduling drone deliveries. Although different types of approaches have been proposed in the literature for various scheduling and routing problems, many entail a significant

Table 5 **a** Details of simulation experiments **b** Summary of selected results across multiple simulations for different numbers of orders (K)

(a)

Inputs : Grid (2D) dimensions, Number of orders (K) max number of items in any single order ($nmax_{items}$) and max quantity of any item ($nmax_{units}$)
The same grid was used for all experiments, customer coordinates randomly generated for each run
For each fixed K, multiple order sets randomly generated such that in any customer order
number of unique items $\leq nmax_{items} = 7$ quantity of any item $\leq nmax_{units} = 4$

(b)

# orders (K)	% improvement over baseline approach		
	min	mean	max
50	45.40	48.35	49.82
100	48.44	49.35	50.19
200	49.92	50.50	51.15
500	52.25	52.84	53.71
1000	52.65	53.42	54.21

computation overhead and hence may not be suitable for a dynamic scenario where orders are frequently updated. The main advantage of our proposed approach is its simplicity which allows scalability to practical scenarios. We are currently working on extending it to the scenario of multiple drones and multiple warehouses.

References

1. Dantzig GB, Ramser JH (1959) The truck dispatching problem. Manage Sci 6:8091
2. Crevier B, Cordeau J-F, Laporte G (2007) The multi-depot vehicle routing problemwith inter-depot routes. Eur J Oper Res 176(2):756773
3. Murray CC, Chu AG (2015) The flying sidekick traveling salesman problem: optimization of drone-assisted parcel delivery. Transp Res Part C 54:86–109
4. Ha, Minh, Deville, Yves, Pham, Dung, Ha, Minh (2018) On the min-cost traveling salesman problem with drone. Transp Res Part C: EmergingTechnol 86:597–621
5. Dorling K, Heinrichs J, Messier GG, Magierowski S (2017) Vehicle routing problems for drone delivery. IEEE Trans SMC 47(1):70–85
6. Wang X, Poikonen S, Golden B (2017) The vehicle routing problem with drones:several worst-case results. Optim Lett 11:679697
7. Chang Y, Lee HJ (2018) Optimal delivery routing with wider drone-deliveryareas along a shorter truck-route. Expert Syst Appl 104:307–317
8. Caric T, Gold H (eds) (2008) Vehicle routing problem. In-Tech

9. Zipline homepage. https://www.flyzipline.com
10. How Can Amazon Charge $1 for Drone Delivery? Tasha Keeney, May 2015. https://ark-invest.com/research/drone-delivery-amazon

Assessment of Local Pressure Coefficient Over Conventional and Unconventional Tall Buildings

K. B. Rajasekarababu and G. Vinayagamurthy

Abstract This article provides an overview of local pressure coefficients (*Cp*) on conventional and unconventional tall buildings with the application of CFD. Various modifications in architectural shapes on tall buildings eventually lead to a reduction in the wind load on building surfaces. The surface pressure on conventional (Square and rectangular) buildings is relatively different in comparison to unconventional tall buildings. This study is to assess the surface pressure coefficient over rectangular, taper and setback buildings. The assessed results show that the taper building has 7% *Cp* rise at ground level ($y/H = 0.225$) in the windward face, and 34% *Cp* fall at the middle level ($y/H = 0.475$) in the side face when compared with the rectangular building. Whereas for the setback building, *Cp* at ground level near setback ($y/H = 0.225$) has reduced to about 25% and about 6% at the middle level ($y/H = 0.475$) in windward than that in the rectangle building. Also, the side faces of the setback showed a 15% drop in Cp than other buildings. In leeward face, *Cp* is reduced to 56% near setback at the top of the building ($y/H = 0.725$). This assessment of the *Cp* on these buildings shows that the effect of setbacks on building reduces the pressure variation on all faces and the downstream wake vortices.

Keywords Setback · Taper building · Rectangular building · Local pressure coefficients · Tall buildings · CFD · IDDES · Iso-surface

K. B. Rajasekarababu · G. Vinayagamurthy (✉)
Aerodynamics Laboratory, School of Mechanical Engineering, Vellore Institute of Technology (Chennai Campus), Chennai 600127, India
e-mail: vinayagamurthy.g@vit.ac.in

K. B. Rajasekarababu
e-mail: kb.rajasekarababu2014@vit.ac.in

N. Gascoin and E. Balasubramanian (eds.), *Innovative Design, Analysis and Development Practices in Aerospace and Automotive Engineering*, Lecture Notes in Mechanical Engineering, https://doi.org/10.1007/978-981-15-6619-6_35

1 Introduction

In developed countries, there is an extensive emergence of tall structures. They are highly sensitive to the action of wind force which is a challenging task for the structural engineers and architects terms of habitability, serviceability, and survivability. And the assurance of essential structural performance also becomes difficult to vindicate. The influence of the intensity of the strong wind excitation on tall buildings is effectively felt on adjacent buildings and wind environments outdoor. It inevitably affects wind acceleration at the ground level, wind noise, vegetation and the comfort of the pedestrian. Wind tunnel testing and field investigations are the two notable methods used to investigate and study the wind flow around the buildings. Both assessments are costly and time-consuming (Table 1).

An alternative as well as redundant tool to study and investigate wind loads on buildings in recent times is CFD (Computational Fluid Dynamics). CFD can be referred to as a virtual wind tunnel in wind engineering. It has capabilities to generate environmental flows that can be generated by means of CFD to predict the flow of physics around the building. The procedure of CFD in wind engineering studies has acknowledged a plethora of importance from several international engineering communities and has motivated the establishment of CFD practice guidelines by Franke et al. [1, 2], Tominaga [3] and Blocken et al. [4]. 3D RANS model approach was used by various researchers in the past to study wind flow around buildings [5–9]. Tanaka et al. [10] presented the flow features like pressure coefficients, overturning moment coefficients and PSD (Power Spectral Density) on and around aerodynamically modified tall buildings using numerical and experimental results. From the experimental analysis of suburban and open terrain wind flow, Kim and Kanda [11] concluded that the set-backed models are more practical to reduce the fluctuating lift force than the tapered or square models. Later, time-domain and frequency-domain analysis were performed by Kim [12] on a square, tapered and set-back models with the side ratio of 1:1. A lot of unconventional building studies are being carried out. Kim et al. [13] examined the wind-induced coupled motion on plan varying tall buildings and found that the along-wind and torsional accelerations are smaller than those

Table 1 Inflow boundary conditions

Inflow conditions	
Inflow boundary (Inlet)	$(Uy) = \frac{uABL^*}{\kappa} \ln\left(\frac{y+yo}{yo}\right); \varepsilon(y) = \frac{u^{*3}}{\kappa(y+y0)}; \omega(y) = \frac{\varepsilon(y)}{C\mu k(y)}$
Outlet	$\frac{\partial}{\partial x}(U, V, W, k, \omega) = 0$(Pressure − outlet)
Sky (top)	$U = U_{ABL}, k = k_{ABL,}\omega = \omega_{ABL},$ $W = 0, \frac{\partial}{\partial x}(U, V, W, k, \omega) = 0$
Wall (sidewall)	$V = 0, \frac{\partial}{\partial x}(U, V, W, k, \omega) = 0$
Ground wall	$KS = \frac{9.793y*0}{CS}$

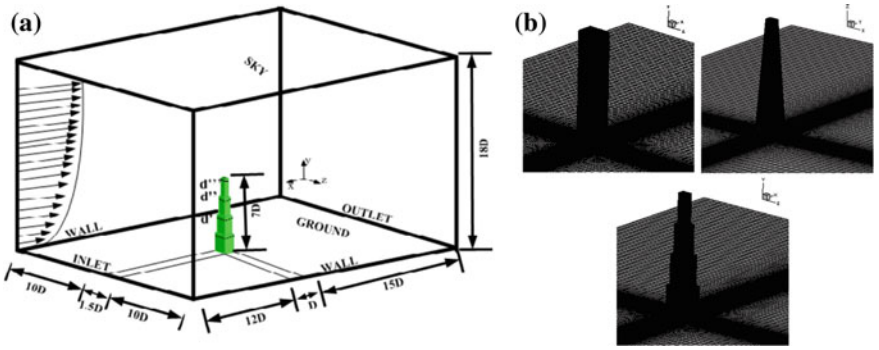

Fig. 1 Perspective views on **a** computational domain and building **b** Grid distribution (Fine)

of the square model. Using DDES (Delayed Detached Eddy Simulation) and IDDES (Improved Delayed Detached Eddy Simulation) turbulence models, Rajasekarababu et al. [14] explored the velocity profiles, upstream stagnation, and surface pressure distribution around a setback building. They concluded that DDES under predicted the downstream recirculation compared with IDDES turbulence model. Concerning recent literature studies, complex time-varying 3D wind flow field on and around the buildings have been estimated accurately with the support of IDDES turbulence model in CFD techniques.

The following section generally outlines several computational parameters that may affect both the accuracy and efficiency of computational simulation, such as the computational domain and its setting parameters. Meanwhile, pressure coefficients assessed in four different heights ($y/H = 0.225, 0.475, 0.725$ and 0.975 respectively) are shown in Fig. 1. ANSYS Fluent 18.1 is used to perform the CFD simulation, and IDDES turbulence model is used to assure the validity and reliability of this assessment. Section 3 comprehensively compared wind pressure coefficients on and around tall buildings throughout their perimeter. Overall, the outcome of this assessment is to enlighten the engineers and architects with a basic understanding of tall buildings. It helps to study natural ventilation in both indoor and outdoor environments.

2 Methodology

2.1 Model Description and Computational Parameter Settings

This work considered a setback building with side ratio 1:1.5 and roof–floor to base-floor area ratio 1:6.25 with a roof and three setbacks. The full-scale height of the building is 210 m. The geometric scale chosen is 1/300 for the open terrain environmental wind flow in the wind tunnel experiment. The longer building face

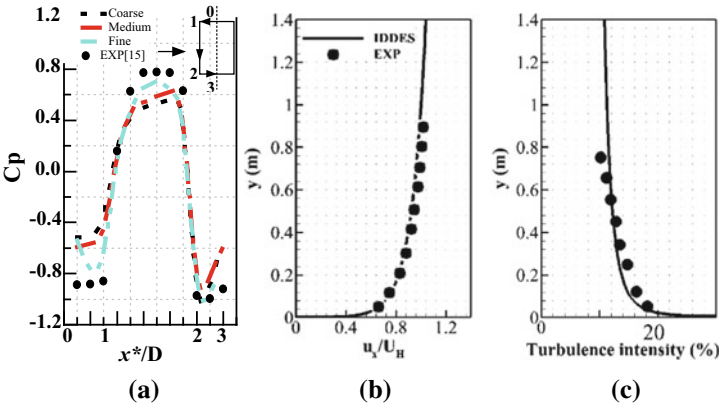

Fig. 2 **a** Grid independence comparison **b** Inlet velocity and **c** Turbulence intensity profiles

is 0. 015 m, and the shorter face is 0.01 m (D). H is the total height of the model, which is taken as 7D (H is same for all buildings); base floor area is 0.15 m × 0.1 m and subsequent setbacks in higher floors are d′ = D/1.25, d″ = D/1.66 and d‴ = D/2.5. For the rectangular building, roof dimension is the same as that of base floor dimension and for taper building roof dimension, d = D/2.5, and is as shown in Fig. 1a (For all building the base floor dimensions are the same (0.15 m × 0.1 m)). The grid distribution was done in ANSYS ICEM CFD for the 3 buildings is shown in Fig. 1b. A grid independence test was done, which includes a comparison of results from grids of various factors like, first wall distance, stretching ratio and density. The refined grid for rect, taper and setback buildings is 8.9, 8.2, 8.7 million cells, respectively. Further, the solver settings are taken from Rajasekarababu et al. [15].

The grid independence results are shown in Fig. 2a using the simulated and measured *Cp* values along half the perimeter of the setback building (x^*/D) at y/H = 0.625. The fine grid shows good results compared to the other two grids. In the grid independence test, it was challenging to accurately reproduce the negative pressure zone on building side face due to the viscous stress and high velocity of the bulk flow in the separation zone. The open terrain ABL profiles are simulated at a mean wind speed (U_{mean}) of 13.6 m/s and turbulent intensity of 11%. The wind profiles are shown in Fig. 2b, c.

3 Results and Discussion

*3.1 The Pressure Coefficient (*Cp*) on the Tall Building*

The below-given equation is used to calculate the pressure coefficient (*Cp*).

$$C_p = \frac{p - p_0}{\frac{1}{2}\rho U_H^2} \tag{1}$$

where p denotes is the extracted pressure from the required height. p_0 is the static pressure at the reference height, ρ indicates the density of air (1.225 kg/m^3), U_H^2 is the mean wind velocity at the building's reference height. The pressure coefficients are measured below 10% of each setback height (see d, d', d'' in Fig. 1). The pressure coefficient extracted at three different heights on the building are compared and are shown in Fig. 3. The assessed pressure coefficient on taper and setback building is compared with the rectangular (rect) building. In the windward face, taper building experienced high pressure compared with rect building and increased 3% at y/H = 0.225. In contrast, setback Cp fell 21% at the same height. In the windward face, at y/H = 0.475, both tapered and rect building showed the same positive pressure whereas at y/H =0.725 taper building showed a 7% increase concerning rect building.

Similarly, setback windward face at the corresponding heights mentioned before falls by 4% and 17%, respectively. The Cp for windward face is positive, and the windward edges experienced negative Cp due to wind shear. The side face of the building experienced fluctuating pressure due to strong shear wind force on its leading edges. The pressure in the right side face reduced by 11%, at the same time, there was a sudden pressure fall of 32% in the leeward side when compared with rect building at y/H = 0.225 for both taper and setback. The Cp in the right side face of taper and

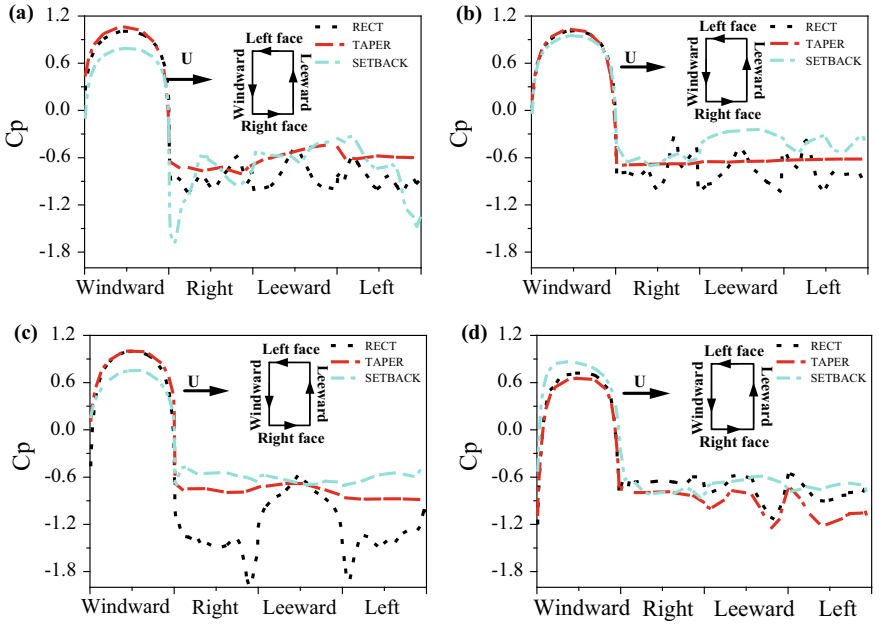

Fig. 3 Pressure coefficients on buildings at 4 different heights **a** y/H = 0.225, **b** 0.475, **c** 0.725 and **d** 0.975

the setback building were seen reduced by 5% and 12%, respectively at $y/H = 0.475$. At the same instance, there is a dramatic reduction of 51% in the leeward face for setback and just 16% for taper. Left side face of the taper and setback was observed to be reduced by 12% and 32%, respectively. The wind profile exponentially showed changing along with height; the increase of wind velocity influences the wind flow around the building. The pressure coefficients on the edges of the rect building at $y/H = 0.725$ observed a considerable drop as shown in Fig. 3c. Shows that a huge suction is created on the side faces. Similarly, a large fluctuation was noticed in the leeward face, which indicates the vortex formation. Furthermore, at $y/H = 0.725$ on the right side face of the taper and setback building, *Cp* decreased by 70% and 90%, respectively. Moreover, there is also a 54% and 82% reduction of *Cp* on the left side faces of the taper and setback buildings, respectively. At $y/H = 0.975$, taper and rect buildings evidenced vortex shedding and wake formation in downstream as a result, the pressure drops on leeward face as shown in Fig. 3d.

3.2 *Instantaneous Vortex Structure Formation Around Buildings*

The vortex formations on buildings are visualized in CFD to compare the vortex structures behind them; a Q-criterion was used to identify the wake vortices using Eq. 2.

$$Q = \frac{1}{2}\left(r_{ij}r_{ij} - s_{ij}s_{ij}\right)$$

Isosurface *Q*-criterion with non-dimensional velocity contour is used in this study to obtain the preferred large eddy flow structure (excluding small-scale vortices of no interest). The instantaneous vortex structures identified by $Q = 750$ behind the building with IDDES turbulence model using fine mesh are shown in Fig. 4. It represents the capability of the simulation to solve turbulence by providing shielding function for the SST-based IDDES model to achieve highly chaotic large and small scale vortices. The IDDES captures the massively separated flow of 3D streamwise

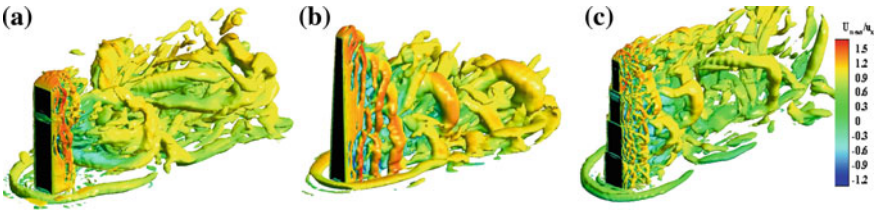

Fig. 4 Instantaneous vortex structure around buildings (Isosurface of velocity (Q = 750 ms^{-1})) **a** Rectangle, **b** Taper and **c** Setback

and transverse vertical structures. This flow structure reveals the streams behind the unconventional building physics, especially on the sides of the separation and wake regions. The visualization of vortices indicates the intensity of the turbulence downstream for the buildings. The upstream horseshoe (HS) vortex in windward face of the rect building has been compared with the other two buildings. At the same time, the trailing vortex structure in rect building has an un-symmetrical wake region which shows the presence of a wake oscillation with lower frequency. This phenomenon opposes the higher frequency vortex shedding with higher energy turbulence which is shown in Fig. 4a. In taper building, the area of the wake region reduces along the height (like a wake funnel as in Fig. 4b). The trailing wake regions in the setback building differ from the other two buildings as the setbacks on building break the vortices into small parts which eventually slows down the downstream driving parts. Moreover, it reduces the vortex stretching downstream, see Fig. 4c. Simultaneously, the permanently attached upstream edge vortices in windward face and roof of the setbacks are relatively smaller compared to the rest of the buildings.

3.3 *Comparison of Turbulence Intensity Around the Buildings*

Turbulence Intensity (TI) contour for three buildings is presented in Fig. 5. The TI changes along with the height in the wake zone. In regard to the intensity of the turbulence on rect building, the maximum intensity is located in the recirculation region due to viscous shear separated from the leading edge. In taper, the roof leading edge shear stress influences intensely in downstream wake zone (Fig. 5b), and the TI core extended up to 5D. The presence of setbacks design on building breaks the core intensity of the turbulence substantially and dissipates into small eddies downstream (Fig. 5c).

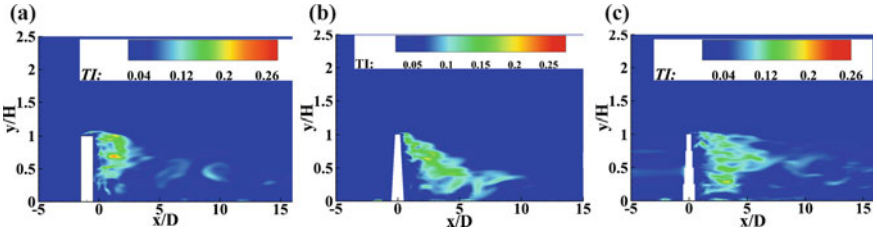

Fig. 5 Turbulence intensity around buildings **a** Rectangle, **b** Taper and **c** Setback

4 Conclusion

The purpose of this study is to assess and compare the wind flow features around conventional (rectangle) tall building over un-conventional (taper and setback) buildings using IDDES turbulence model. The substantial recommendations of this study derive the following conclusions.

- At $y/H = 0.475$, presence of setback on the building along with height shows 51% *Cp* reduction and just 16% for taper in comparison with rect building for the leeward face. This is because the setbacks slow down the downstream.
- Dimensional changes along the height of the building showed a reduction of 70 and 90 percentage in *Cp* on the right side face of the taper and setback buildings at $y/H = 0.725$. Moreover, there is a 54% and 82% reduction in *Cp* on the left side faces of both the buildings, respectively.
- Instantaneous vortex structure indicates the formation of hairpin vortices with high energy at downstream due to the driving and lagging vortices. Due to largely expanded wakes, wake regions in the taper building was observed falling along with the height.
- The features of trailing vortices of setback building differ from other buildings due to downstream vortex breaks down, stretching of vortices reduced by the setbacks and the intensity of the turbulence also reduces along with the height.

Overall, from this assessment, setbacks on building reduce the wind load and ensure comfort compared with conventional tall buildings. Also, IDDES turbulence model is possible to quantify the complex flow features in detail with limited grid spacing.

References

1. Franke J (ed) (2007) Best practice guideline for the CFD simulation of flows in the urban environment. Meteorological Inst
2. Franke J et al (2011) The COST 732 best practice guideline for CFD simulation of flows in the urban environment: a summary. Int J Environ Pollut 44(1–4):419–427
3. Tominaga Y, Stathopoulos T (2010) Numerical simulation of dispersion around an isolated cubic building: model evaluation of RANS and LES. Build Environ 45(10):2231–2239
4. Blocken B, Stathopoulos T, Carmeliet J (2007) CFD simulation of the atmospheric boundary layer: wall function problems. Atmos Environ 41(2):238–252
5. Hang J et al (2012) The influence of building height variability on pollutant dispersion and pedestrian ventilation in idealised high-rise urban areas. Build Environ 56:346–360
6. Janssen WD, Blocken B, van Hooff T (2014) Computational evaluation of pedestrian wind comfort and wind safety around a high-rise building in an urban area
7. Liu J, Niu J (2016) CFD simulation of the wind environment around an isolated high-rise building: an evaluation of SRANS, LES and DES models. Build Environ 96:91–106
8. Blocken B, Stathopoulos T, Van Beeck JPAJ (2016) Pedestrian-level wind conditions around buildings: review of wind-tunnel and CFD techniques and their accuracy for wind comfort assessment. Build Environ 100:50–81

9. Tse K-T et al (2017) Pedestrian-level wind environment around isolated buildings under the influence of twisted wind flows. J Wind Eng Industrial Aerodyn 162:12–23
10. Tanaka H et al (2012) Experimental investigation of aerodynamic forces and wind pressures acting on tall buildings with various unconventional configurations. J Wind Eng Industrial Aerodyn 107:179–191
11. Kim YC, Kanda J (2010) Characteristics of aerodynamic forces and pressures on square plan buildings with height variations. J Wind Eng Industrial Aerodyn 98(8–9):449–465
12. Kim YC, Kanda J, Tamura Y (2011) Wind-induced coupled motion of tall buildings with varying square plan with height. J Wind Eng Industrial Aerodyn 99(5):638–650
13. Kim YC, Kanda J (2013) Wind pressures on tapered and set-back tall buildings. J Fluids Struct 39:306–321
14. Rajasekarababu KB, Vinayagamurthy G (2019) Experimental and computational simulation of an open terrain wind flow around a setback building using hybrid turbulence models. J Appl Fluid Mech 12(1)
15. Rajasekarababu KB, Vinayagamurthy G, Selvi Rajan S (2019) Experimental and computational investigation of outdoor wind flow around a setback building. Build Simulation 12(5) (Tsinghua University Press)

IoT-Based Protection of Ventilation and Air Conditioning Units in Chemical Industry

M. Vigneshwaran, P. Lakshmanan, and Muniyandy Elangovan

Abstract In this industrial world, the dependence on the chemicals for the growth of the nation has become evident from the looming of more chemical industries. As a result, there has been more and more case of chemical disasters both in developed and developing countries. The disaster is due to the failure of the conventional secure system, which is based on Wi-Fi, and many times, it becomes unreliable during the unfortunate event of disaster. This project aims to provide a safe environment during emergency situations by an automated response and a means to communicate the information of the disaster immediately so that the impacts of it can be reduced. Present technological advancements such as Global System for Mobile communication (GSM), General Radio Pocket Service (GPRS) have been utilized in the communication of the disaster informations through Internet of Things (IoT). Also, the primary focus of the project is to make a building-independent monitoring system so that the loss of connectivity does not occur due to the damage in the building. Further, the real-time sensor data will be transferred to the IoT server via GPRS connectivity. The real-time values are sent to IoT through API by using the GPRS connection on the GSM module. The data logging can be separated channel wise and more actions can be programmed on the IoT platform through MATLAB. The system deals with monitoring and controlling the working environmental conditions like carbon monoxide, methane, hydrogen, LPG and flammable gases with sensors and using Arduino to make a decision as per preprogrammed also send this data to the cloud server and draw the sensor data as pictorial statistics. The data upgraded from the enforced system is accessible within the Web from anywhere within the world. The automatic venting off the toxic gases from the working premises immediately

M. Vigneshwaran · P. Lakshmanan · M. Elangovan (✉)
Vel Tech Rangarajan Dr. Sagunthala R&D Institute of Science and Technology, Outer Ring Round, Avadi, Chennai, Tamil Nadu 600062, India
e-mail: drmelangovan@veltech.edu.in

M. Vigneshwaran
e-mail: vgnshwrn871@gmail.com

P. Lakshmanan
e-mail: drplakshmanan@veltech.edu.in

N. Gascoin and E. Balasubramanian (eds.), *Innovative Design, Analysis and Development Practices in Aerospace and Automotive Engineering*, Lecture Notes in Mechanical Engineering, https://doi.org/10.1007/978-981-15-6619-6_36

after the detection and without waiting for the communication from higher position, which makes the lesser impact on worker's life that is unaware of consequences of the accident.

Keywords IoT · Arduino · GSM · GPRS · Safety · Chemical · Hazard

1 Introduction

World nations have been experienced to most pessimistic scenario substance calamities in the previous history and draw exercises gained from them. An expansion in the quantity of mishaps in the process businesses and the attending harm potential is a reason for worry in numerous nations. So as to control the disturbing danger presented by these businesses, the US government has requested that each assembling office complete a most pessimistic scenario debacle study and to creates choices to control the high risk. The Bhopal fiasco coming about because of a blend of characteristically dangerous structures and inadequately oversaw activities is an outstanding contextual analysis [1].

Handling great amount of venturous chemicals at installations, isolated storages and through transportation pose a grave risk of sharp unharness of a lot of quantities of toxicants in a surroundings. There are 1865 major accident hazard units in India. Large number of chemical as raw materials used are corrosive inflammable and toxic chemicals, which have an adverse impact on environment and community at the workplace. Lack of awareness and inappropriate construction enhances the vulnerability of the community exposed [2]. The potential heavy losses and undesirable consequences on both environment and community call for further improvement of safety procedure and adoption of appropriate methods in handling hazardous chemicals and quick action on standard operating procedure in case of release of hazardous chemical detected. Bhopal disaster is the major incident which brought into focus the unprecedented potential of hazard chemicals like methyl isocyanate in terms of loss of life health and property and long-term impacts. Chemical disaster occurs due to deviation in process concerning pressure, temperature and other identified parameters about the state of substances proximity to hazardous substances and probability of intermixing of two dissimilar hazardous chemicals [3].

Moreover, failure of hardware resulting of large-scale spills of toxic substances or an explosion. Boiling liquid expanding vapour explosion (BLEVE) happens due to friction and sparks while transportation of toxic chemicals. The effects further compounded by micrometrology of area, wind speed, direction of air, the amount of chemicals released, reach of population while release and other industrial activities performed in the vicinity. It is very important to know the state of chemical substance (solid, liquid, gas) contributes to the gravity of accident and influences the control measures. Devastating effects will be experienced if chemicals in the solid form change property suddenly (e.g. sublimation). Large spills of liquid or compressed gases like liquefied petroleum gas or chlorine due to any human or mechanical failure

cause BLEVE and directly affect the human life's nearby and working communities [4]. The release of compressed gases gives rise to be cryogenic stresses and thermal stresses, which can also impact the surrounding structure and damage to property, compounding the damage.

Chemical units incorporate a wide scope of risks emerging from the procedure itself, properties of the synthetic concoctions and their taking care of, for example, fire, blast and presentation to poisonous substances. Be that as it may, there is a still genuine capability of major modern mishap with disastrous impact26. In expansion to the death toll, the significant outcomes of concoction catastrophes remember to sway for domesticated animals, greenery/fauna, nature (air, soil, and water) and misfortunes to industry27. A little mishap happening at the nearby level might be an earlier cautioning sign for looming and the catastrophe. Compound catastrophe, through low in recurrence, can possibly cause noteworthy prompt or long haul damage9. Frequency and seriousness of synthetic calamities have expanded in the most-recent couple of years [5].

In addition to loss of human life and property during chemical disaster, the dire consequences include the impact on livestock, flora fauna, environment (air, water, land) Chemical accidents depending upon the number of casualties injuries damage to property, and environment can be categorized as a major accident or a disaster. A major accident is defined in environment protection act 1986, and disaster is defined in disaster management act 2005.

2 Resourced Used

2.1 Gas Sensor

Semiconductor-based gas sensor helps in detection of presence of gas in environment. The MQ-6 sensor primarily used in detection of gases in industries as well as it has home applications. SnO_2 metal oxide coated gas sensor is used for its sensitivity. When Sno_2 gas sensor is heated at a threshold value, the oxygen on a crystal surface gets absorbed with a negative charge. Sensor resistance to electric flow recognized by the potential barrier in gas deoxidising atmosphere. There is a direct relationship with the sensor resistance and barrier height.

2.2 LCD Screen

A 16 × 2 LCD display with green LED backlight. Each panel displays symbol in a 5 × 7 pixel matrix. A 16 × 2 means it can display 16 symbols in a line and with 2 displays lines. It has a two registers, namely data register and command register. Command register helps/register commands such as clear screen, shift line whereas

the other register aid in character values. It is commonly used module and mostly preferred because of its easy programmable, economic and display many special characters. Arduino is an extraordinary stage for prototyping to interface sensors, LCD, etc.

2.3 Temperature Sensor

A DTH 11 Sensor use in detecting the flame around the region. The heat waves which are generated due to the abnormal temperature got sensed. DHT11 temperature sensor consists of four pins: VCC, Data Out, Not Connected (NC) and GND. The range of voltage for VCC pin is 3.5–5. 5 V. A 5 V supply would do fines. A single wire communication can be instituted between any microcontroller like Arduino and the DHT11 Sensor.

2.4 Power Supply

To turn on the board power supply in the range of 6–20 V is to be supplied. On the chances of supplying more than 12 V, the voltage controller unit may get overheated and may harm the board. Hence, the range prescribed will be 7–12 V. In this case using the step-down transformer, the voltage will be stepped down. Furthermore, the components such as sensors, display need various volts. Bridge rectifier is used to split the supplied volt into required volt. In this case, we splitted as 5 V and 12 V for sensors, alarm and exhauster, respectively. ARDUINO is controlled by USB link originating from the PC.

2.5 Arduino UNO Board

Arduino is an open-source platform intended for building electronics projects. Arduino comprises of both a physical programmable circuit board (often referred to as a microcontroller) and a piece of software, or Integrated Development Environment (IDE) that runs on your computer, used to write and upload computer code to the physical board.

- In the picture above, the USB connection is labelled (1) and the barrel jack is labelled (2).
- NOTE: Do not use a power supply greater than 20 V as you will overpower (and thereby destroy) your Arduino. The recommended voltage for most Arduino models is between 6 and 12 V.

- GND (3): Short for 'ground'. There are several GND pins on the Arduino, any of which can be used to ground your circuit.
- 5 V (4) and 12 V (5): As you might guess, the 5 V pin supplies 5 V of power, and the 12 V pin supplies 12 V of power. Most of the simple components used with the Arduino run happily off 5 or 12 V.
- Analog (6): The area of pins under the 'Analog In' labels (A0 through A5 on the UNO) is Analog In pins. These pins can read the signal from an analog sensor (like a temperature sensor) and convert it into a digital value that we can read.
- Digital (7): Across from the analog pins are the digital pins (0 through 13 on the UNO). These pins can be used for both digital input (like telling if a button is pushed) and digital output (like powering an LED).

2.6 GSM Module

GSM module used to send SMS to the corresponding person mobile number. Module has a unique identity number similar like mobile IMEI. It can use the range of 900/1800 MHz bands for the purpose of communication. The inbuilt interface allows serial communication from a microcontroller like Arduino.

2.7 Arduino

Arduino software is the best re-enactment and most prominent in view of accessibility of all microcontrollers within it. So, it is easily programmable and can be understood the programme very simply. And, modification to the programme done at an ease. Here is the important setup in software.

3 Working

The whole mechanism will be activated/triggered with the support of high gas concentration or flame detection or abnormal temperature rises above the threshold. With the aid from analog/digital gas sensors coated with the most sensitive layer SnO_2, the gas above the threshold level is detected. The sensor MQ-6 is well suited for detection of gases like iso butane, liquefied petroleum gas (LPG) as well as some important hydrocarbons. The sensor with the heater activates the layer of Sno_2 for detection. It then gives analog voltage as output to the Arduino and which with the help of ADC of microcontroller reads the signal. And then the analog output converted to digital output, which used as an external stimulus to initialise or activate the whole system. The concentration of the gas/smoke will be detected by analog digital converter of the Arduino. Microcontroller Arduino reads the values of the gas/smoke concentration

and compared the values with the threshold value which vary according to chemicals. If the gas concentration values overdo the threshold value, an emergency alert will be generated and information as well as data about the information is sent to the responsible authority. To make immediate action and reduce the impact of the leakage of the gas on both workers and the environment, GSM module connected using the universal asynchronous receiver transmitter of the Arduino which makes transmission of data via wires RX and TX. Serial AT the command used for communicating between the Arduino and gsm module. After realization of gas/smoke, Arduino directs the GSM module using AT commands. An SMS sends to the registered mobile number which was predefined in the system for emergency.

4 Result and Discussion

The gas sensor gives the distinguished (ADC) values 600–700 for high gas focuses and 300–450 for smoke location. Along these lines, them two are effectively discernable. The ongoing qualities are sent to IoT through API by utilizing the GPRS association on the GSM Module. The information logging can be isolated channel savvy and more activities can be customized on the IoT stage through MATLAB. Gas spillages in family units and ventures to cause the hazard to life and property. An enormous misfortune must be brought about for the mishap happened by such as spillages. An answer for such an issue is to set up a checking framework which continues observing the spillage of any sort of combustible gases and shields the purchaser from such mishaps. The present paper gives an answer for avoid such mishaps by checking the framework yet in addition discussing the equivalent with IoT system to turn off the gas supplies and the principal control if there should arise from an occurrence of a spillage. What's more, it enacts an alert just as makes an impression on the specialists. A further headway can be as an avoiding shading sensor which will have the option to detect the area dependent on shading coding.

5 Conclusion

This paper propounded the model and development of IoT-based harmful condition overseeing the structure. The proposed framework is proficient to checking lethal gases for individual's security applications in unsafe spots. The different parameters like hydrogen, carbon monoxide, methane and combustible gases were checked utilizing IoT. The noxious gases were checked in chimneys. Substance ventures and trashes places. Every single gas esteem was observed utilizing sensors, and these qualities are transmitted to cloud server through a Web. The consequences of sensors and framework viability demonstrated that Arduino-based sensors can successfully

be utilized to screen dangerous gases. This IoT framework gives continuous applications and makes the measurements perceptible wherever on the planet. In future work, the proposed framework can be reached out to a mine security man-made consciousness-based stage for individuals well-being applications.

References

1. Alexander D (2015) Disaster and emergency planning for preparedness, response, and recovery. In: Recovery, risk management, response, preparedness. Online Publication
2. Masellis M, Thermal agent disaster and fire disaster: definition, damage, assessment and relief operations. Springer Books
3. Arpitha, Kiran D, Sitaram Gupta VSN, Duraiswamy P, FPGA-GSM based gas leakage detection system 5(6)
4. National chemical disaster management—NDMA. Ministry of home affairs
5. Rajalakshmi, Vidhya J (2018) A survey on toxic environment monitoring using sensors. Int J Sci Dev Res

Numerical Study on Supersonic Co-flowing Jet with Varying Lip Thickness

R. Naren Shankar, K. Sathish Kumar, N. Dilip Raja, Kamal Raj Chandra Shekar, Nishant Kumar Raj, and Dipranjan Gupta

Abstract The study on jet mixing characteristics by varying the lip thickness has been done by the many researchers in low subsonic, high subsonic, and sonic Mach numbers (0–1.0). Additionally, researchers have performed supersonic primary jet surrounded by subsonic and sonic secondary jet. The jet mixing characteristics of a supersonic primary jet surrounded by a supersonic co-flowing jet with varying lip thickness have not been performed yet. The present study probes into this numerically. Numerical results were validated with existing experimental results in the open literature. Centerline pitot pressure is calculated using the Rayleigh pitot tube formula. Results show that increasing lip thickness enhances mixing and vice versa. The numerical shadowgraph shows the shock wave propagation and its interaction. Supersonic jet phenomenon such as supersonic core, Mach disk, oblique shock waves, shock crossover, expansion waves, subsonic flow pockets behind Mach disk, recirculation zone, near-field turbulence, subatmospheric region (wake), shear layer, characteristic decay region, fully developed region, and jet interaction was studied.

Keywords Supersonic co-flow · Lip thickness · Mach disk

R. Naren Shankar (✉) · N. Dilip Raja · K. R. C. Shekar · N. K. Raj · D. Gupta
Vel Tech Rangarajan Dr. Sagunthala R&D Institute of Science and Technology, Outer Ring Road, Avadi, Chennai, Tamil Nadu 600062, India
e-mail: narensankar@veltech.edu.in

N. K. Raj
e-mail: vtu8056@veltechuniv.edu.in

K. Sathish Kumar
P.B. College of Engineering, Irungattukottai, Chennai, Tamil Nadu 602117, India

N. Gascoin and E. Balasubramanian (eds.), *Innovative Design, Analysis and Development Practices in Aerospace and Automotive Engineering*, Lecture Notes in Mechanical Engineering, https://doi.org/10.1007/978-981-15-6619-6_37

1 Introduction

Supersonic jet finds application in rockets, missiles, fuel injectors, commercial, and fighter jet exhausts [1]. Supersonic co-flowing jet (CFJ) is beneficial in mixing enhancement and in jet noise reduction. It overtakes the usage of tab and chevron because there is no blockage and reduces manufacturing complexity respectively.

Subsonic secondary jet eliminates Mach wave of supersonic primary jet [2]. Surrounding jet elongates central jet potential core length by 68% when compared to single free jet [3]. Sukumar et al. [4] studied under-expanded and Sharma et al. [5] studied over-expanded central jet with surrounding subsonic and sonic flow. Both reported co-flow inhibits mixing because the lip thickness (LT) value ranges from 0.7 to 3 mm. Satyajit et al. [6] studied mixing characteristics supersonic CFJ with constant finite LT 7.75 mm at nozzle pressure ratios (NPR) ranging from 3 to 8 in steps of one. The effect of lip thickness has not been addressed. Subsonic and correctly expanded sonic CFJ were studied with varying lip thickness by Naren et al. [7–11]. But they have not analyzed supersonic flow. The present study is the first effort to study supersonic CFJ with varying lip thickness numerically.

2 Numerical Details

The supersonic co-flowing nozzle (Fig. 1) used in the current study is acquired from Satyajit et al. [6]. The primary nozzle has inlet diameter 10 mm, throat 5 mm, and exit 6.5 mm. The secondary nozzle has inlet width (outer diameter minus inner diameter) of 6 mm, throat width of 1 mm, and exit width of 1.65 mm. The geometry was created in CATIA, ICEM CFD is used for meshing and ANSYS CFX solver is used for numerical analysis. The fluid is set to ideal gas. Compared to other models, the SST turbulence model is better in capturing the shear layers. The total temperature of 298 K is taken to match with the experimental conditions. At inlet, corresponding pressure value of NPR 3 and NPR 5 is set. No-slip adiabatic wall function is chosen for the nozzle wall. The average static pressure is 1 atm at outlet, and the equations are converged to a minimum error of 10^{-4} [12, 13].

A coarse grid with 0.55 million nodes, medium grid with 1.1 million nodes, and a fine grid with 2.2 million nodes were created for grid independence study. Figure 2 shows the validation plot for the nozzle pressure ratio (NPR) 5. The results show that numerical simulation has good agreement with experimental curve.

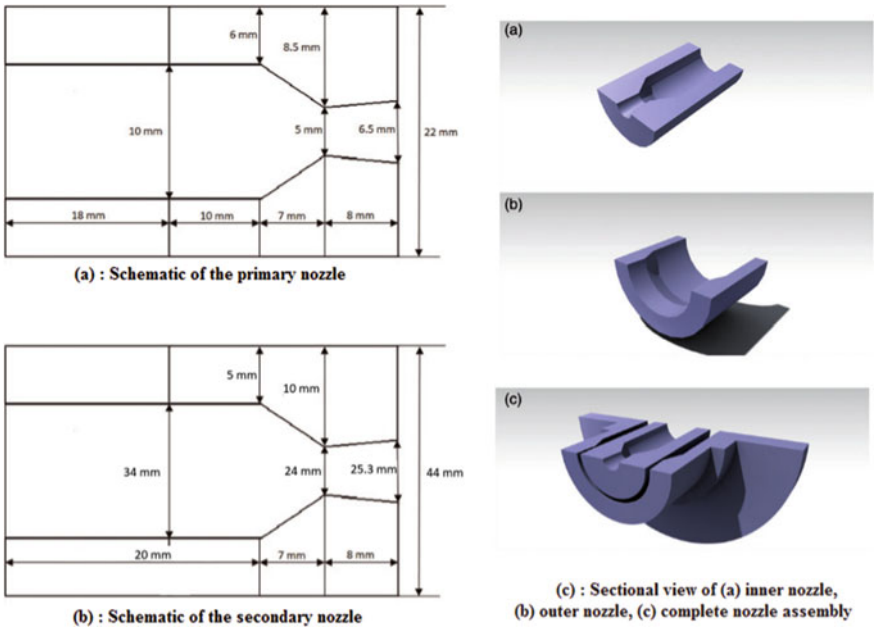

Fig. 1 Schematic and sectional views of supersonic CFJ nozzle (Satyajit et al. [6])

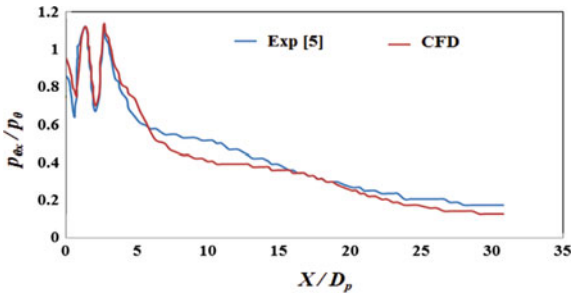

Fig. 2 CFD validation with the experimental result of Satyajit et al. [6], for NPR 5

3 Results and Discussions

3.1 Centerline Total Pressure Decay

Primary jet centerline total pressure decay (CTPD) is a good measure to find the zones of a CFJ. Three zones exist. They are potential core length, characteristic decay region, and fully developed region. At the exit of the nozzle, weak shock waves prevail which crossover resulting in reflected shock. The reflected shock again hits the core boundary that gives rise to expansion waves. Expansion waves again

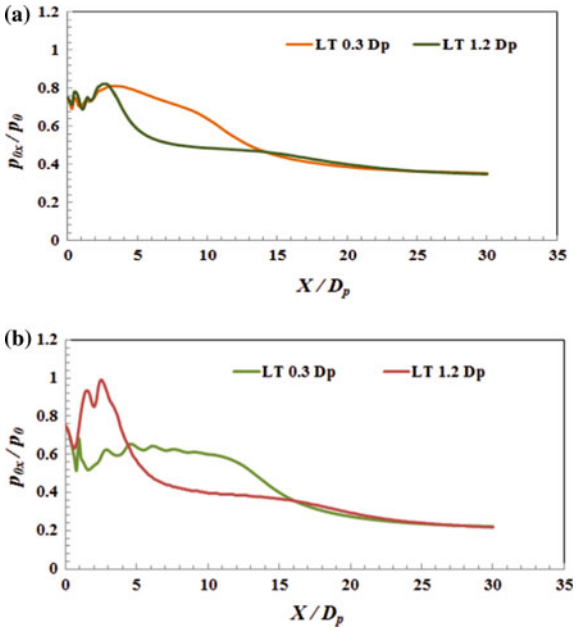

Fig. 3 **a** CTPD of lip 2 mm and 7.75 mm for NPR 3. **b** CTPD of lip 2 mm and 7.75 mm for NPR 5

reflect to form shock waves. This process continues till the supersonic flow becomes subsonic. This region is called potential core length. Entrainment is the process of momentum transfer between surrounding still air and the jet. Because of entrainment, characteristic decay occurs, i.e. jet loses its strength. Finally, fully developed region is the one where there is minimum variation with jet and surrounding air.

For the comparative purpose, NPR 3 and 5 are chosen for the study. Figure 3a, b shows the CTPD results for NPR 3 and NPR 5, respectively. From Fig. 3a, the supersonic core length has extended up to $X/D_p = 3.4$ for lip thickness LT 2 mm (LT 0.3 D_p) whereas it is $X/D_p = 2.78$ for lip thickness 7.75 mm (LT 1.2 D_p) which is 18% reduction in potential core length. But in characteristic decay region (CDR), LT 1.2 D_p has decayed faster than LT 0.3 D_p. For example, at $X/D_p = 6$, LT 7.75 mm has decayed 47% whereas LT 2 mm has decayed only 25%. Hence, the effect of lip thickness is well pronounced in the CDR.

From Fig. 3b, the LT 2 mm has extended core of $X/D_p = 7.73$ compared to LT 7.75 mm of $X/D = 2.47$ which is 65% reduction in potential core. The primary core has been greatly reduced because of the interaction because of the interaction between primary and secondary jets. The primary and secondary jets interact vigorously with in a shorter axial distance due to the wave dominance. Mach disk is dominant with CFJ with LT 7.75 mm and there is no Mach disk formed for CFJ with LT 2 mm.

Wake region appears but its dominance is less felt. Surrounding and central jets merge at a near exit region. The outer jet shields inner jet to elongate supersonic core as shown in Fig. 4a. Because of the shock crossover, subsonic pockets appear and due to expansion wave crossover, supersonic pockets appear as observed from Fig. 4b. Shear layer found dominant between jets and found less dominant between outer jet and ambient atmosphere (Fig. 4c). Shock crossover appears in the numerical shadowgraph (density gradient, Fig. 4d).

Comparing to CFJ with LT 2 mm, LT 7.75 mm has dominant wake region (Fig. 5a). The wake region is clearly visible between jets, with a least value of 0.4 bar, i.e., subatmospheric region. Due to the wake region, the secondary jet merges with the primary jet at an axial distance, and this happens because of mixing core length that has been shortened. We can see here that the pressure is dropping because of reverse shock crossover. Because of this, recirculation zone appears in Mach number

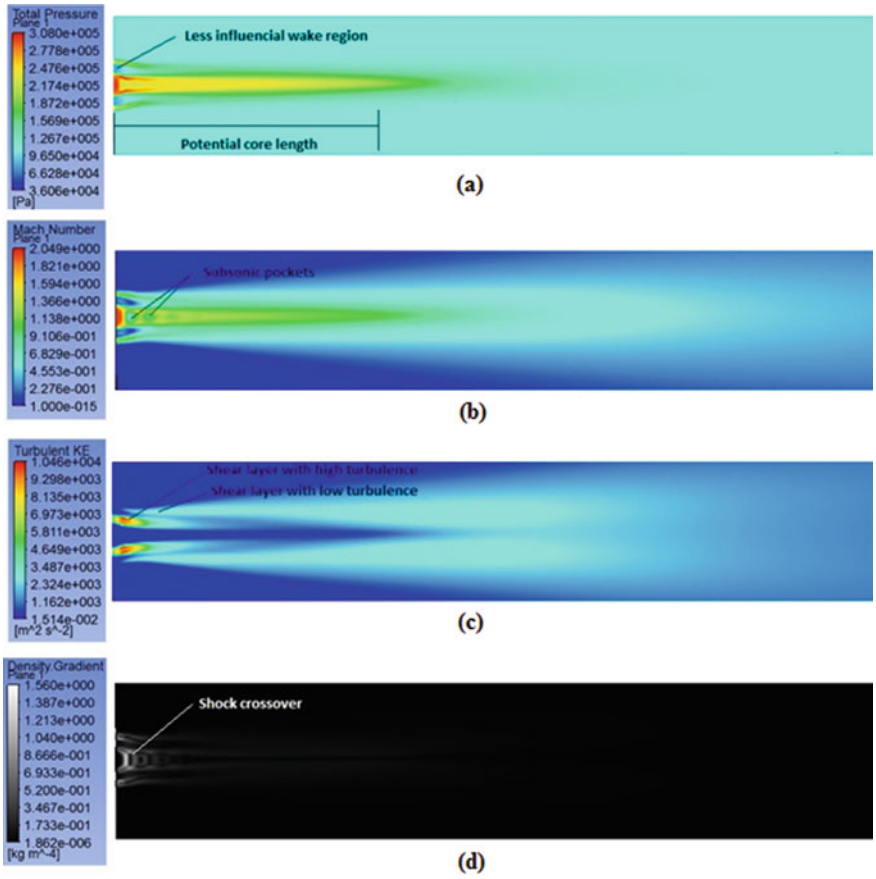

Fig. 4 Contours of LT 2 mm for NPR 3: **a** total pressure, **b** Mach number, **c** turbulent kinetic energy, and **d** density gradient

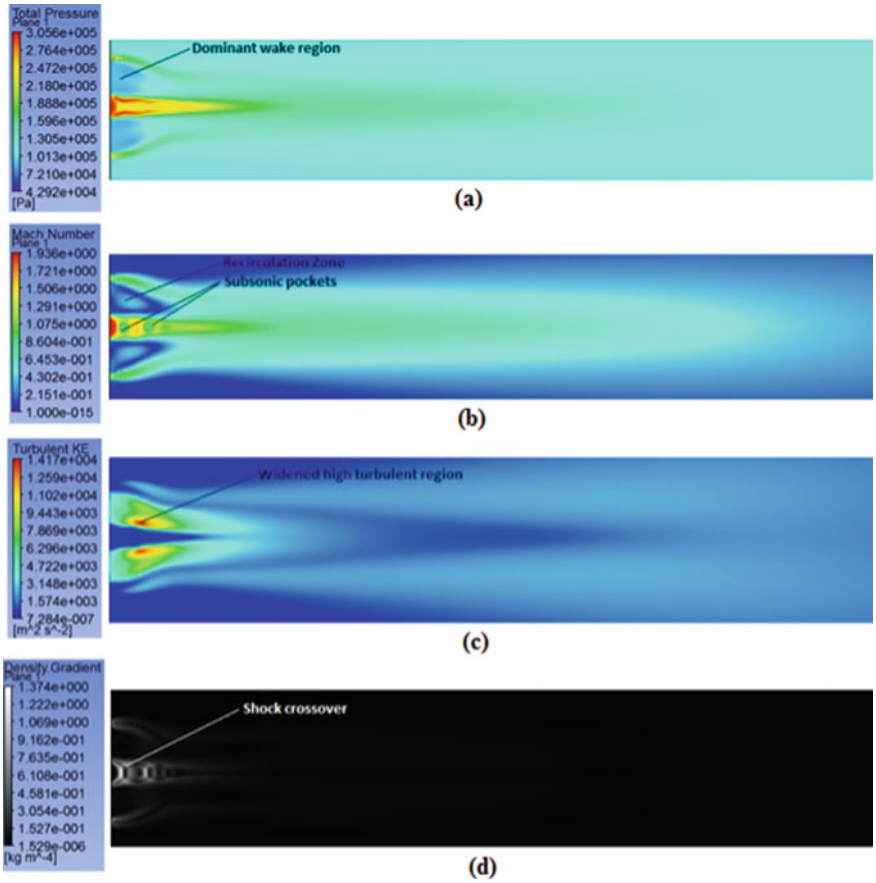

Fig. 5 Contours of LT 7.75 mm for NPR 3: **a** total pressure, **b** Mach number, **c** turbulent kinetic energy, and **d** density gradient

contour (Fig. 5b). Visible recirculation zone appears between jets at subatmospheric region. The secondary jets core orients toward jet centerline. The region between jets shows a recirculation zone. In CFD analysis, we can capture supersonic nozzle characteristics but we cannot see subsonic pockets in the co-flow as the mass flow is less. The turbulent kinetic energy between jets becomes widened and magnitude increased (10460–14170 m^2/s^2). The shock crossover looks similar between both jets (which was also confirmed with CTPD) but there is a significant mixing in the characteristic decay region (Fig. 5c).

The region of high turbulence widens because of wake dominance. Increased turbulence is observed in the recirculation zone and least turbulence is inside the potential cones. The turbulence contour shows the progressive nature of jet along its axis and the shear layer shows the momentum transport. Shear layer is small at starting and then gets widened. The numerical shadowgraph (density gradient)

(Fig. 5d) shows that weak oblique shocks that emerge out crossover as Mach disk and then reflects as expansion wave again reflects as shock wave and the process continuous till the supersonic jets becomes subsonic. The secondary jet has weak shocks (weaker than primary jet), and the shock crossover turns toward the jet axis. Thus by increasing the LT, the core of the supersonic jet is reduced. This reduction in the supersonic core signifies the mixing enhancement between primary and secondary jet.

4 Conclusion

The jet mixing characteristics of supersonic jet surrounded by a supersonic co-flowing jet with lip thickness of 2 mm and 7.75 mm are studied for the NPR 3 and 5 using ANSYS CFX. Increase in LT and NPR results in reduction in the supersonic core length. From the centerline pitot pressure plot, supersonic core length reduces by 18% for NPR 3, when LT increases from 2 mm to 7.75 mm, whereas the supersonic core length reduces up to 65% for NPR 5. Pressure drop has been observed in the total pressure contour because of the shock crossover. Subsonic pockets are visible in Mach number contour. In turbulence contour, the core has reduced turbulence.

References

1. Sathish Kumar K, Chidambaram S (2019) Supersonic jet flow control using semi-circular corrugated tabs. Aircraft Engineering and Aerospace Technology
2. Debiasi M, Papamoschou D (2001) Noise from imperfectly expanded supersonic coaxial jets. AIAA 39:388–395
3. Murakami E, Papamoschou D (1986) Mixing layer characteristics of coaxial supersonic jets. AIAA Paper, 86–0162
4. Sukumar VN, Sundaravadivelu T, Lovaraju P et al (2007) Effect of co-flow on near field shock structure of under expanded central jet. In: Ninth Asian symposium on visualization. ASV0031-001, Hong Kong, 4–9 June 2007
5. Sharma H, Vashishtha A, Rathakrishnan E et al (2008) Experimental study of overexpanded co-flowing jets. Aeronaut J 112:537–546
6. De Satyajit, Rathakrishnan E et al (2018) Experimental study of supersonic co-flowing jet. IMechE 2018
7. Naren Shankar R, Thanigaiarasu S, Rathakrishnan E (2016) Numerical characterization of lip thickness on subsonic and correctly expanded sonic co-flowing jets. Trans Japan Soc Aeronaut Space Sci 59(3):134–141. https://doi.org/10.2322/tjsass.59.134
8. Naren Shankar R (2017) Effect of lip thickness and bypass co-flowing jets. Ph. D. thesis, Anna University
9. Naren Shankar R et al (2018) Co-flowing jet control using lip thickness variation. Int J Turbo Jet Engines. https://doi.org/10.1515/tjj-2018-0024
10. Thanigaiarasu S, Naren Shankar R, Rathakrishnan E (2018) Influence of bypass ratio on subsonic and correctly expanded sonic co-flowing jets with finite lip thickness. Proc Institut Mech Eng Part G J Aerospace Eng 233(7):2536–2548. https://doi.org/10.1177/0954410018782511

11. Naren Shankar R, Kevin Bennet S, Dilip Raja N, Sathish Kumar K (2019) Characteristics of a co-flowing jet with varying lip thickness and constant velocity ratio. Aircraft Engineering and Aerospace Technology, Manuscript under review
12. Sathish Kumar K, Chidambaram S (2018) Jet flow control using semi -circular corrugated tabs. J Turbo Jet Engines
13. Naren Shankar R, Dilip Raja N (2020) Novel characteristics of subsonic co-flowing jets with varying lip thickness. J Aerospace Technol Manage (accepted for publication)

Design of Automatic Deluge Fire Protection System for Explosive Processing Building

G. Vishnu Teja and M. Meikandan

Abstract Safe handling of raw materials is one of the greatest challenges in the processing of solid propellants. The major raw materials of the solid propellants are metallic fuel, inorganic oxidizer, polymeric binder, plasticizer, cross linking agent, anti-oxidant, curator, and burn rate modifier are processed in various stages. Most of the raw materials are susceptible to cause fire, explosion, or toxicity hazards due to their inherent sensitivity to shock, impact, or spillage. Each processing stage has its variation in degree of risks. If any fire initiation occurs in the processing stage, it leads to fire accident or severe explosion. It affects the personnel, equipment inside facility, and extends to the surrounding facilities. To reduce the effects of fire accident or severe explosion and prevent consequences (damages), an effective fire protection system is to be installed in the facility. The fire protection system includes sprinkler system, deluge system, fire hydrants, and water monitors. The selection, design, water demand, and pump selection depend on the degree of risk and explosive handling class. Comparing with other fire protection system, UN hazardous class HD 1.3 explosives handling facility, it requires deluge system with fire hydrants and water monitors. In this work, we have designed an effective deluge system that considers the floor area, water demand of the facility, number of nozzles inside the facility.

Keywords Solid propellants · Explosion · Fire protection · Deluge system

G. Vishnu Teja · M. Meikandan (✉)
Department of Mechanical, Vel Tech Rangarajan Dr. Sagunthala R&D Institute of Science and Technology, Outer Ring Road, Avadi, Chennai, Tamilnadu 600062, India
e-mail: mmeikandan@veltech.edu.in

N. Gascoin and E. Balasubramanian (eds.), *Innovative Design, Analysis and Development Practices in Aerospace and Automotive Engineering*, Lecture Notes in Mechanical Engineering, https://doi.org/10.1007/978-981-15-6619-6_38

1 Introduction

Hazardous materials are used in chemical or explosive processing plants. Each material used in the explosives plant is highly reactive which will affect the personnel in the plant when exposed to it. While processing the materials or chemicals, it changes its nature and becomes more reactive. Those reactive nature is an explosive material which must be handled with precautions and standards. It also requires installation of fire protection systems which reduce the effect in case of any accidents occur.

Hazardous materials are divided depending on rate it expands. Hazardous materials that detonate (rate of the chemical reaction is faster with the material then the speed of sound) are said to be "hazardous explosives" and materials which deflagrate are known to be "low explosives". Explosives also divided by their sensitive nature. Sensitive substances that can be ignited by a small amount of heat or pressure are primary hazardous explosives and substances that is insensitive are secondary or tertiary explosives.

An explosion is a rapid release of gases results in a rapid moving shock or pressure wave. The expansions will be mechanical (Sudden rupture due to pressurized vessel) or it will be the rapid chemical reaction as a result pressure or shock wave leads to damage.

James [1] explained the different stages of realizing a solid propellant grain are raw material preparation and characterization; propellant mixing, casting and curing; extraction of mandrel and other casting fixtures; propellant trimming and end inhibition; handling and transportation operations; non-destructive testing and storage. In each of these stages, the hazards exist and could be triggered to cause undesirable situations due to impact, friction, heat, static electricity and shock. Such situations have to be accounted for during the design stage of process equipment's and maximum care has to be exercised during processing.

The raw materials used in the propellant are highly energetic as well as toxic. Their preparation involves mechanical operations such as sieving, grinding, and careful handling. If these materials are subjected to impact, friction, heat, and static electricity beyond certain levels, they can undergo either mass fire or mild explosion or dust explosion.

CPIA [2] concluded that, there are hazards involved in stage processing. The propellant should have an acceptable sensitivity to impact. Laboratory impact tests of the propellant ingredients should be tested in a well-standardized impact tester to establish the 50% fire level and 100% fire level.

Impact hazard—A propellant that gives a zero fire at the maximum height of this tester may be considered safe to handle by unprotected personnel. Propellants in the range of 10 kg cm or below should be treated with caution. Propellants in the 5 kg cm range should be viewed as hazardous to process and handle.

Friction hazard—The uncured propellant should have friction sensitivity low enough that shear stresses in the mixer will not ignite the propellant, and the cured propellant should have a friction sensitivity low enough that normal handling operations are not likely to ignite the propellant. Composite propellants used worldwide today have substantial amount of metal powder as an ingredient. This increases the friction hazard of composite propellants. Of the techniques available for characterization, a form of the pendulum-and-slide friction tester is preferred. If the friction force is less than 5 kg m, it is considered as very sensitive and if the friction force is between 5 and 17.5 kg m, it is considered as moderately sensitive.

Spark hazard—The propellant should have spark sensitivity low enough that the normal static charge of a human body discharge will not ignite the propellant. The propellant in both the cured and uncured states should be characterized for spark sensitivity. The spark apparatus should be calibrated against materials of known spark sensitivity. A sufficiently large number of samples should be run in order to get a statistically significant set of data. The propellant should not have a spark sensitivity less than 0.015 J.

Auto ignition hazard—The propellant should have an autoignition point so high that its probability of autoignition is low under the thermal environment to which it will be exposed. Also, the propellant should not develop so high internal temperature during cure or from degradation chemical reactions that there is danger of autoignition. Composite propellants autoignition temperature lies in the range 280–310 °C. The curing temperature of these temperatures should be half or less than half of the autoignition temperature.

The consequences of fire in processing facility are deflagration, detonation, confined explosion, unconfined explosion, boiling liquid expanding vapor explosion, and dust explosion.

2 Methodology

To design fire protection system, inputs are required based on the nature of chemical and reactivity of chemicals used in the building. The parameters are class of chemicals to decide the hazardous nature. Once hazardous nature is known, it is easy to design firefighting systems in the facility. If building is low hazardous, it can be planned with hydrants and water monitors. If building is medium hazardous, it can be planned with sprinkler alarm valve. If building is high hazardous, then it has to be planned with deluge system which is automated.

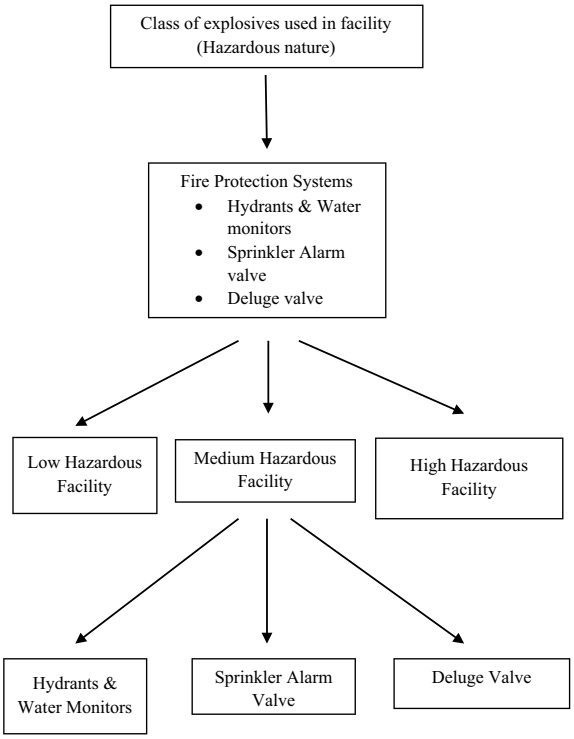

As shown in Fig. 1, deluge valve assembly functions on differential pressure operation allowing quick opening of the valve and thereby rush of water to the protection system. The valve consists of top valve, bottom valve, and pilot chamber. Inlet and outlet chambers are separate in deluge valve from set chamber at the valve chamber and a diaphragm. In setting, pressure is applied to the chamber through a small pipeline. Pressure is set into set chamber and clapper will hold on to the seat due to differential design. In the "Setting" position, the clapper divides the inlet from the outlet by keeping the system piping as dry. If the pressure is release from priming chamber, the clapper moves and starts the supply water inlet to flow through the discharge outlet and to spray nozzles.

The deluge valve shall be a control valve assembly which will operate on pressure difference in the deluge valve assembly due to QBD actuation and also by operating MCP switch at annunciation panel/control panel in control room.

The deluge valve assembly will consist mainly of the following:

1. Isolation valves
2. Inline strainer
3. Deluge valve assembly
4. Actuator/pilot assembly
5. Water motor gong
6. Drain valve

7. Pressure gauges
8. Solenoid valve
9. Pressure switches
10. Pressure transmitters.

3 Design of Deluge System and Calculation

For hazardous chemical processing building of class 1.3 explosives, designing a deluge valve (as shown in Fig. 2) requires parameters as per TAC norms. Those parameters are

- Design density: 10.2 LPM/m^2
- Minimum pressure at remotest nozzle, $P = 1.4$ kg/$cm^2 = 1.37 \times 10^5$ pa
- Velocity in feed lines: 5 m/s
- Space between nozzles: 2–3 m
- Each nozzle covers an area: 6 m^2.

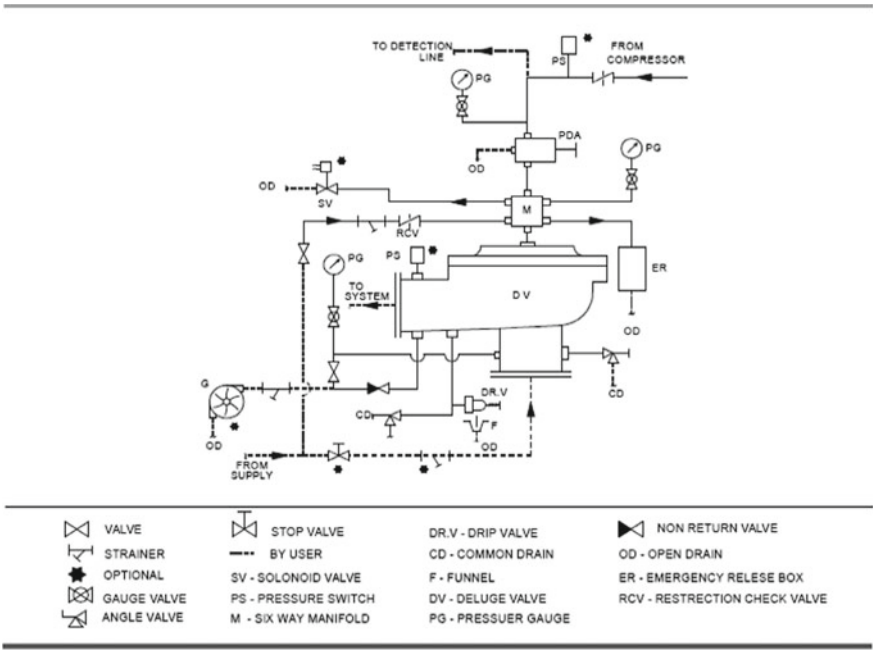

Fig. 1 Deluge valve assembly. *Source* HD fire catalogue

Fig. 2 Deluge valve. *Source* https://www.hdfire.com/images/product-detail/deluge-valves/img1-big.jpg

3.1 Design Calculation for Deluge Valve

- Dimensions of the building = 41.5 m (Length) × 20 m (Breadth)
- Area of the building = 830 m^2
- Water flow inside the building = area × design density
  = 830 × 10.2 LPM
  = 8466 LPM
- Nozzles inside the building = Area/area coverage by a nozzle
  = 830/6
  = 138.3 nos
- Each nozzle flow = 8466/138.3
  = 61.2 LPM
- K-factor for nozzle, $Q = K\sqrt{P}$
  $61.2 = K \times \sqrt{1.4}$
  $K = 51.7$

  * Actual K factor is 64 as per standard sizes
- Actual Nozzle flow, $Q = 64 \times \sqrt{1.4}$
  = 75.724 LPM

Considering 140 nozzles,

- Actual water demand inside the facility = no. of nozzles × nozzle flow
  = 140 × 75.724
  = 10601 LPM
  = 636 m^3/hr

*Consider the facility into 2 zones, each zone requires 318 m^3/hr

- For 318 m^3/hr water demand, 150 mm size of deluge valve shall be installed.

(Recommended flow for 150 mm deluge valve size is 170 to 650 m^3/hr as per make)

Deluge valve = 150 mm

4 Conclusion

The deluge system (Automatic fire protection system) is an emergency equipment to be used in an untoward situation to control the consequences. The effective design of such emergency equipments will ensure the containment of effects in case of fire. It will prevent the extent of damage that the equipments in buildings undergo. Water demand to suppress the fire in the facility is found by dimensions of the facility and the design density of fire protection system.

References

1. James RW (1974) Propellants and explosives. Noyes Data Corporation
2. CPIA (1972) Hazards of chemical rockets and propellants handbook—vols I and 11

Numerical Study on Sonic Underexpanded Co-flowing Jet with Varying Separation Distance

R. Naren Shankar, K. Sathish Kumar, N. Dilip Raja, J. Sumendran, Nishant Kumar Raj, Purushottam Kumar Yadav, S. Smruthi, and Krishna Kumar Gosain

Abstract Mixing characteristics of sonic under expanded co-flowing jets are analysed with varying separation distance. The separation distance is defined as the distance separating the primary and secondary nozzles. The varying separation distance is understood as a passive way to control a jet. Reduced separation distance value of 3 mm and a dominant separation distance value of 15 mm is used in the current study. The nozzle pressure ratio chosen for the study is 5. The centreline total pressure decay, contours of total pressure, Mach number, density gradient, and turbulent kinetic energy were studied. The present study has been validated with experimental results available in the open literature. Results show that the secondary jet elongates the primary jet potential core length for the reduced lip 3 mm because the surrounding jet shields the central jet. The potential core length for the dominant lip 15 mm is reduced because the surrounding jet vigorously interacts with the central jet due to increased lip thickness. The contours show the jet mixing phenomena such as the wake region, sub-atmospheric region, recirculation zone and shock crossover, Mach disc, Shear layer amidst jets, shear layer between surrounding jet and atmosphere. The characteristics like potential core region, jet spread, Primary and secondary jet interaction and sub-atmospheric region are studied.

Keywords Sonic under expanded · Co-flowing jet · Separation distance

R. Naren Shankar (✉) · N. Dilip Raja · J. Sumendran · N. K. Raj · P. K. Yadav · S. Smruthi · K. K. Gosain
Vel Tech Rangarajan Dr. Sagunthala R&D Institute of Science and Technology, Outer Ring Road, Avadi, Chennai, Tamil Nadu 600062, India
e-mail: narensankar@veltech.edu.in

N. K. Raj
e-mail: vtu8056@veltechuniv.edu.in

S. Smruthi
e-mail: vtu10147@veltechuniv.edu.in

K. Sathish Kumar
P.B. College of Engineering, Irungattukottai, Chennai, Tamil Nadu 602117, India

N. Gascoin and E. Balasubramanian (eds.), *Innovative Design, Analysis and Development Practices in Aerospace and Automotive Engineering*, Lecture Notes in Mechanical Engineering, https://doi.org/10.1007/978-981-15-6619-6_39

1 Introduction

Co-flowing jets (CFJ) finds application in various engineering devices. It is used in fire fighting hoses to spray water to a greater distance, it is also used in exhaust chimneys to transport polluted air to a greater height in welding torch to increase the length of the jet torch and so on. In all these applications the surrounding jet elongates the potential core of the inner jet. Co-flow jets are also used in aerospace applications like injectors and exhaust nozzles. Co-flow is considered as a passive control of the primary jet because jet can be controlled without any external power source for example in high bypass turbofan engines the bypass jet (Secondary jet) suppresses primary jet noise. In this case, chevrons are used to suppress the noise which has its own drawbacks like manufacturing complexity. Tabs are also used to control jets which creates a blockage in the flow that results in thrust loss [1], hence co-flow by varying separation distance can be suggested as a vital alternative compared to chevrons and tyres as passive controls.

Separation distance variation at low subsonic Mach numbers has been reported in plenty in open literature as listed in Naren et al. [2]. Separation distance variation at subsonic and sonic correctly expanded regimes have also been reported [2–7]. But very few researches have performed sonic under expanded CFJ [8, 9]. Even in these studies, the central jet is sonic under expanded and the surrounding jet is subsonic. The characteristics of overexpanded co-flowing jet were studied by Sharma et al. [10] and reported the increase in core length up to 104% when the jet is surrounded by another jet. The jet exit characteristics of Mach 2 jet surrounded by a Mach 1.6 co-flowing jet are studied by De Satyajit and Rathakrishnan [11]. The present study is the effort to analyse sonic under expanded CFJ in both primary and secondary jets with varying separation distance which has not been reported in studied ever before.

2 Numerical Detail

The CFJ nozzle used in the current study has a primary convergent nozzle with inlet diameter 20 mm and exit diameter 10 mm with a length of 35 mm. The secondary duct is maintained with a constant width of 5 mm. The geometry is created in CATIA V5 R18, meshed with ICEMCFD, and analysed in ANSYS CFX 16. A course grid with 5.5 lakh nodes, medium grid with 11 lakh nodes and fine grid with 22 lakh nodes were created for mesh independence study.

Based on the mesh independence study, medium mesh with 11 lakh nodes is selected for the study. The simulation has been validated with the experiment and has good agreement with experimental results [8] as shown in Fig. 1. A primary nozzle of length 60 mm, 20 mm inner diameter and 10 mm outer diameter is used. Secondary duct with a uniform width of 5 mm throughout the length is used. Separation distance is maintained as 3 and 15 mm between the nozzle and the duct [2]. Mesh has been imported to CFX and 0 atm. pressure has been given to ideal gas in fluid section. SST

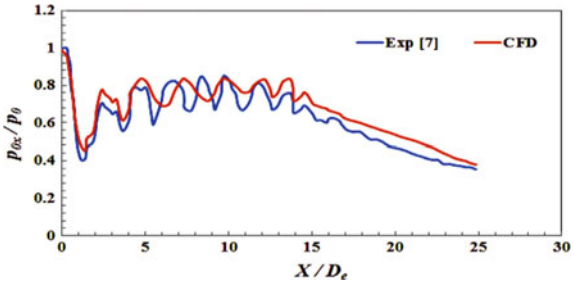

Fig. 1 Comparison between experimental result [8] and current simulation for NPR 5 for the separation distance 2.65 mm

K-epsilon model has been selected for simulation. 298 K has been given as inlet total temperature and 1 atm pressure has been given to pressure outlet. High-resolution turbulence numeric and high-resolution advection scheme has been given in solver control. For better accuracy residual target has been set to 10-4 [12, 13].

3 Results and Discussions

Sonic under expanded jet exceeds from a convergent nozzle undergoes expansion that gives rise to an expansion wave at the nozzle exit. This expansion waves cross over at the jet centreline and gets reflected back from the potential core boundary as a shock wave. Then the shock wave crosses over and gets reflected back to the potential core boundary. From the core boundary, it gets reflected back as expansion waves. This process repeats itself till the local supersonic region becomes subsonic or the jet becomes fully subsonic. Figure 2 shows the centerline total pressure plotted along the primary jet axis. The total pressure measured along the jet axis (p_{0x}) is made dimensionless with the inlet total pressure (p_0= 5 bar) and is plotted against the dimensionless axial distance (X/D_e).

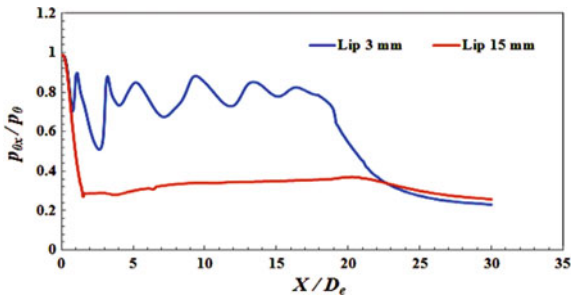

Fig. 2 Centerline total pressure comparison along primary jet axis for 3 mm and 15 mm separation distance for NPR 5

From the figure, we can observe a sinusoidal wave pattern. From pressure value of 1, initially, it drops because of the expansion waves. Velocity of the flow is increasing here because of decrement of pressure.

The expansion wave is reflected and converted into shock waves which leads to increment of pressure. Again the shock waves are reflected back and are converted into expansion wave leading to decrement of pressure. Because of this reflection of expansion and shock waves the pressure value is oscillating sinusoidally. This sinusoidal oscillation is termed as jet core that extends up to $X/D_p = 17.85$. After $X/D_p = 17.85$ there is no oscillation in pressure which is referred to as characteristic decay region. NPR 5 is a moderate under expanded level where the formation of Mach disc is expected. But Mach disc is deteriorated to shock crossover by secondary jet as can be observed in Fig. 3c. For separation distance 15 mm co-flowing jet (CFJ), there are no oscillations whereas one single fall occurs. This is due to the formation of Mach disc since it is not deteriorated by secondary jet because of finite separation

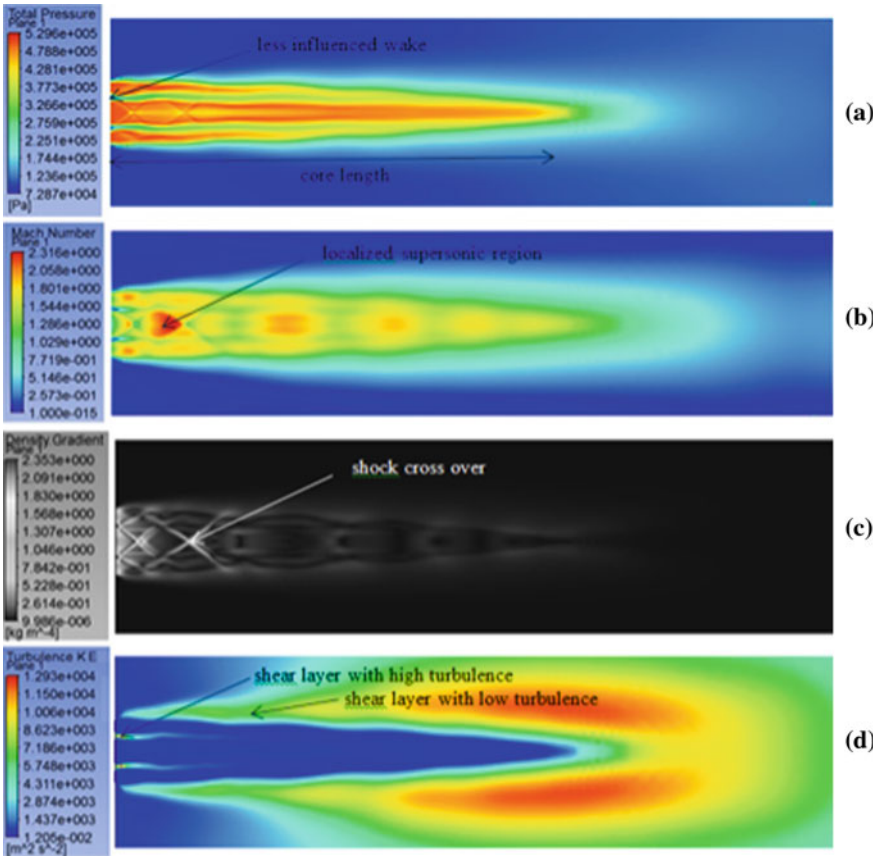

Fig. 3 Contrours for the 3 mm separation distance: **a** Total pressure contour, **b** Mach number contour, **c** Numerical shadowgraph, **d** Turbulence KE

distance. Total pressure contour, Mach number contour, Numerical shadowgraph, and turbulence contour for 3 mm separation distance is shown in Fig. 3.

From the pressure contour, we can see that less influenced wake region is occurring because of less value of the separation distance. Potential core has been elongated because of the presence of the surrounding flow. Surrounding jet prevents the central jet to interact with the atmosphere reducing mixing. From the Mach contour, localised supersonic reason is visible. The localised supersonic reason demises in magnitude. Even though the flow is sonic under expanded the inlet pressure gives raise to localised supersonic regions that occur along the X-axis. There are six supersonic regions visible. Numerical shadowgraph shows the occurrence of expansion waves and shock waves reflection. The shocks from primary and secondary jets interact together in the near field. Weak potential core is found as shock waves are crossing the potential core of the inner jet. Shear layer between the jets is very insignificant, i.e. not dominant. Whereas the outer shear layer becomes dominant. Figure 4, shows the contours for the 15 mm separation distance. Potential core length has been reduced because of the interaction between secondary jet and primary jet. In the Mach number contour localised supersonic region is visible. In density gradient contour we can see that for 15 mm separation distance potential core has been reduced. Because of the reduced potential core less number of Mach discs has been formed in that. We can also see shear layer with high turbulence in wake region. Figure 5 shows the total pressure contours at various X/D_p locations for the 3 and 15 mm lip thickness. From the figure, it is clearly evident that the wake region is very high for increased lip thickness. Because of this, the core length of the 15 mm lip configuration is reduced compared to the reduced lip of 3 mm configuration. Thus, it is concluded that wake dominance plays a vital role in reducing the core.

4 Conclusion

Numerical simulation was carried out to study the effect of separation distance in co-flowing jet. From the results of the total pressure plot, the core length of 15 mm lip configuration is reduced very much because of wake dominance due to the separation distance. The total pressure is increasing and decreasing because of expansion and shock waves for 3 mm separation distance and for the 15 mm separation distance only pressure drop is seen. From the contours of Mach number and density gradient it is observed that for the 15 mm separation distance Mach discs are seen and for the 3 mm separation distance, shock crossover is observed. The results of the numerical simulation are also validated with the experimental results. The interaction of shock waves in primary and secondary jets was observed in the numerical shadowgraph. Hence it is concluded that the separation distance plays a vital role in reducing the core.

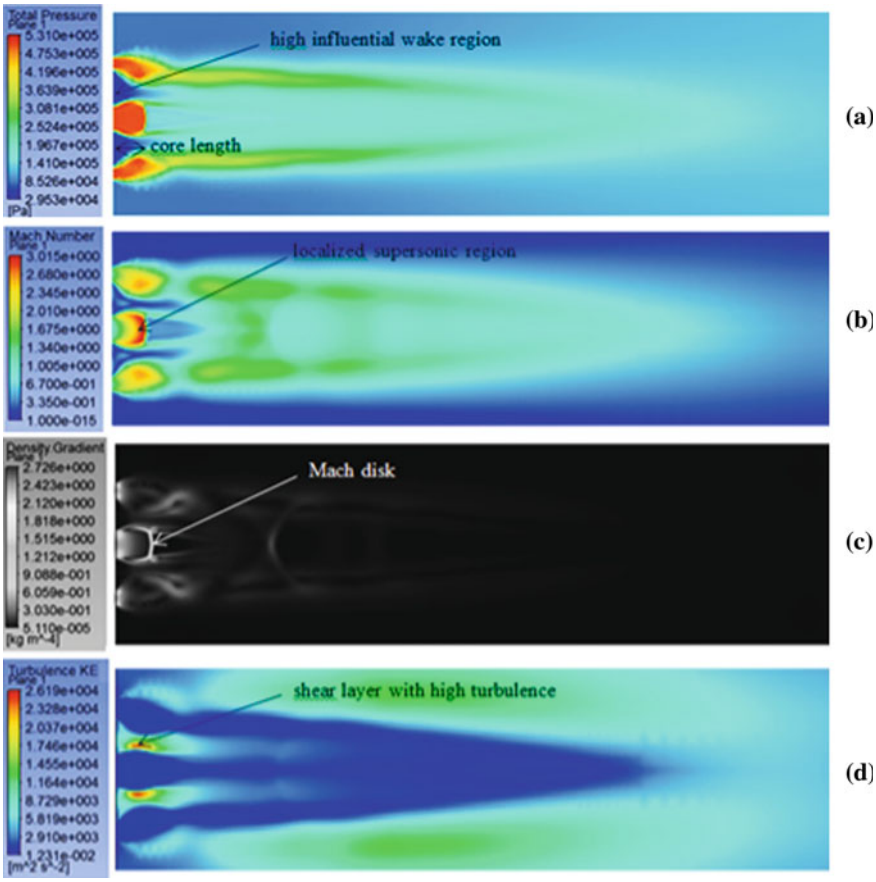

Fig. 4 Contrours for the 15 mm separation distance: **a** Total pressure contour, **b** Mach number contour, **c** Numerical shadowgraph, **d** Turbulence KE

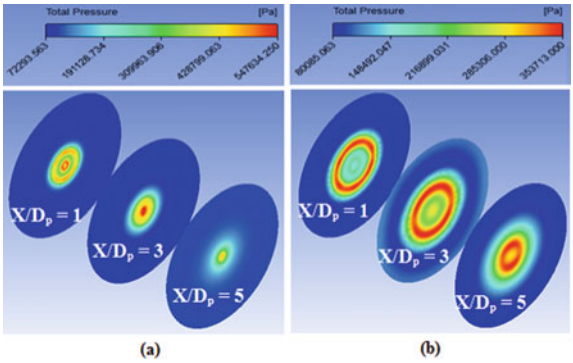

Fig. 5 **a** Total pressure contour at various X/D_p locations for 3 mm lip thickness, **b** Total pressure contour at various X/D_p locations for 15 mm lip thickness

References

1. Sathish Kumar K, Chidambaram S (2019) Supersonic jet flow control using semi-circular corrugated tabs. Aircraft Eng Aerospace Technol
2. Naren Shankar R, Thanigaiarasu S, Rathakrishnan E (2016) Numerical characterization of lip thickness on subsonic and correctly expanded sonic co-flowing jets. Trans Japan Soc Aeronaut Space Sci 59(3):134–141. https://doi.org/10.2322/tjsass.59.134
3. Naren Shankar R, Kevin Bennet S (2019) Characteristics of a co-flowing jet with varying lip thickness and constant bypass ratio. Aircraft Eng Aerospace Technol. https://doi.org/10.1108/AEAT-01-2019-0007
4. Naren Shankar R (2017) Effect of lip thickness and bypass co-flowing jets. Ph. D. thesis, Anna University
5. Naren Shankar R et al (2018) Co-flowing jet control using lip thickness variation. Int J Turbo Jet Engines. https://doi.org/10.1515/tjj-2018-0024
6. Thanigaiarasu S, Naren Shankar R, Rathakrishnan E (2018) Influence of bypass ratio on subsonic and correctly expanded sonic co-flowing jets with finite lip thickness. Proc Institut Mech Eng Part G J Aerospace Eng 233(7):2536–2548. https://doi.org/10.1177/0954410018782511
7. Naren Shankar R, Kevin Bennet SN, Raja D, Sathish Kumar K (2019) Characteristics of a co-flowing jet with varying lip thickness and constant velocity ratio. Aircraft Eng Aerospace Technol, Manuscript under review
8. Lovaraju P, Rathakrishnan E (2011) Experimental studies on co-flowing subsonic and sonic jets. Flow Turbul Combust 87(1):115–132. https://doi.org/10.1007/s10494-011-9332-5
9. Srinivasarao T et al (2017) Effect of inner nozzle lip thickness on co-flow jet characteristics. Int J Turbo Jet Engines 34(3):287–293. https://doi.org/10.1515/tjj-2016-0004
10. Sharma H, Vashishtha A, Rathakrishnan E et al (2008) Experimental study of overexpanded co-flowing jets. Aeronaut J 112:537–546
11. De Satyajit, Rathakrishnan E (2017) Experimental study of supersonic co-flowing jet. Proc Institut Mech Eng Part G J Aerospace Eng
12. Sathish Kumar K, Chidambaram S (2018) Jet flow control using semi -circular corrugated tabs. J Turbo Jet Engines
13. Naren Shankar R, Dilip Raja N (2020) Novel characteristics of subsonic co-flowing jets with varying lip thickness. J Aerospace Technol Manag (accepted for publication)

Study of Gas-Centered Coaxial Injector Using Jet in a Cross-Flow Mechanism

K. R. Arun

Abstract For the design of liquid propellant rocket engine, the finalization of the main injection scheme/pattern is an important factor. For controlling combustion and engine performance the design of injector geometry is most important. In air-breathing engines and liquid rocket engines, proper atomization and mixing of fuel are required for fuel prior to burning. An injector having configuration conforming to liquid jet in cross-flow (JICF) can be used in air-breathing engines using liquid fuels. In this work, atomization studies using Malvern Particle Analyzer conducted for gas-centered coaxial injectors using jet in cross-flow scheme. Water and gaseous nitrogen (GN2) were used as simulant fluids. Sauter Mean Diameter (SMD) and drop size distribution were measured for various momentum flux ratio (MFR) and at different downstream positions.

Keywords Gas-centered coaxial injector · Momentum flux ratio · Sauter mean diameter

Nomenclature

MFR	Momentum Flux Ratio (ρ_j V_J ^{2}/ρ_g Vg $^{2)}$
d_g	Center post diameter
L_{in}	Total Injector length
ρ_j	Density of liquid jet
ρ_g	Density of gas
V_j	Velocity of liquid jet
V_g	Velocity of gas
l	Liquid orifice length
j	Liquid jet

K. R. Arun (✉)
Viswajyothi College of Engineering and Technology, Vazhakulam, Ernakulam, India
e-mail: arunkr@vjcet.org

N. Gascoin and E. Balasubramanian (eds.), *Innovative Design, Analysis and Development Practices in Aerospace and Automotive Engineering*, Lecture Notes in Mechanical Engineering, https://doi.org/10.1007/978-981-15-6619-6_40

g	Gas
In	Injector
Row	Liquid injection rows
Exit	Exit of the injector
D	Distance

1 Introduction

The performance of atomization is the disintegration of the liquid jet by the momentum change of liquid itself, or by the influence of high-velocity gas or air, or apply a mechanical force by using vibrating and rotating equipment [1]. Spray pattern depends on the number of parameters like atomizer characteristics, properties of the liquid used, type of application, etc. Atomization process is characterized mainly by distribution of different sizes of drop, mean size of the droop, spray pattern, cone angle of spray, etc. Atomization strongly affects the combustion and pollutant emissions of internal combustion engines and gas turbines.

Previous studies about liquid jet in a cross-flow explained primary and secondary atomization of liquid sheet in a gaseous flow. Masheyek et al. [2] observe that the liquid jet disintegrated into drops depending upon the momentum flux ratio of liquid to gas, Webber number, and Reynolds number. The atomization of liquid jet depends on the velocity of the jet and cross-flow velocity. An experimental investigation of round jet in a gaseous cross-flow was conducted by Crab et al. [3]. They measured the velocity characteristic of flow using Laser Droplet Anemometry and hot wire anemometry in the upstream region and downstream region, respectively.

The penetration height of the liquid jet is an important parameter that indicates how well the injected liquid mixes with the free stream air. Single and double liquid column penetration in gaseous cross-flow was experimentally studied [4]. They found the correlation for penetration height for single and double injection orifices separately and concluded that when the orifice spacing increases the penetration height also increases. In the field of disintegration of liquid stream, the Weber number is an important parameter. Pai et al. [5] studied the role of Weber number in primary atomization of turbulent liquid stream in gas cross-flow. They recommended that the characteristic thickness of the liquid structures is regulated by cross-flow Weber number, while the structure of the liquid structures is controlled by the liquid Weber number [6].

The disintegration of the liquid ligament depends on whether the liquid flow is turbulent or laminar. For understanding the flow and turbulence characteristics at different velocity ratio, Andreopoulos and Rodi [7] conducted the experimental investigation. At less ratios of jet velocity to cross-flow velocity, the jet bent over abruptly by the cross-flow and at higher ratio, the jet penetrates further into the cross-stream, and bending over takes place more gradually. In accordance with detailed studies of Wu et al. [8] suggested that the axial point of liquid sheet breakup is

8.06 times of its injection diameter for non-turbulent jet and for turbulent jet it is five times of injection diameter of jet. In primary atomization, the location of liquid jet breakup is an important factor. Wu et al. [8] studied the transverse height (Y/d) and the axial distance of jet breakup (X/d) and proposed correlations for transverse breakup point (Y/d) and axial breakup point (X/d). For the safe disintegration of liquid jet, the transverse and axial breakup point will be within the center post of the injector element. The center post diameter of the injector is designed on the basis of the transverse breakup point. The distance of the injection orifice from the exit of the orifice depends on the axial breakup length.

Nozzle geometry design is mandatory that control the characteristic of the liquid jet. The importance of nozzle parameters on breakup and trajectory of liquid jet was investigated by Birouk et al. [9]. When the momentum flux ratio increases the effect of nozzle geometry on the jet's breakup length becomes more important because the water jet starts to experience cavitation or hydraulic flip at high values of momentum flux ratio. It was also observed that when the nozzle's L/d ratio or the contraction angle increases then the water jet's trajectory increases slightly. Song et al. [10] studied the effect of orifice internal flow of perpendicular to subsonic gas flow and spray plume characteristic of liquid jet in subsonic cross-flow. The shape of the orifice entry affected the column trajectory and breakup point [11, 12]. They also studied how the cavitation and hydraulic flip affected the spray plume characteristic [13–16]. The liquid column diameter is less than that of the orifice due to an air envelope in the area of hydraulic flip flow inside the orifice. If the orifice length to diameter ratio is greater than 10 or less than 4 the hydraulic flip does not occur [17–20].

Objective of this work is to design gas-centered coaxial injector elements using jet in cross-flow mechanism for breakup and study their spray and atomization characteristics under cold flow ambient condition. Malvern Particle Analyzer, a laser-based equipment is chosen for cold flow atomization studies. Study the atomization and spray characteristics of injectors at different liquid momentum flux ratio (MFR) and at different downstream positions using Malvern Particle Analyzer.

2 Experimental Setup

2.1 Details of Injector Hard Ware

Gas-centered coaxial injectors fabricated for the study. The line diagram and specifications of injector are shown in Fig. 1 and Table 1, respectively. In this injector, the gas (GN_2) supplied through the center post pipe (Gas orifice) and liquid (water) injected through six holes drilled in the center post by two rows. The distance from last row of liquid injection to injector exit (L_{exit}), total injector length (L_{inj}), and center post diameter (d_g) will change with respect to the MFR. The center post diameter is depending on the transverse breakup point and L_{exit} depends on the axial breakup point. At maximum MFR the breakup of liquid jet is mainly due to its momentum

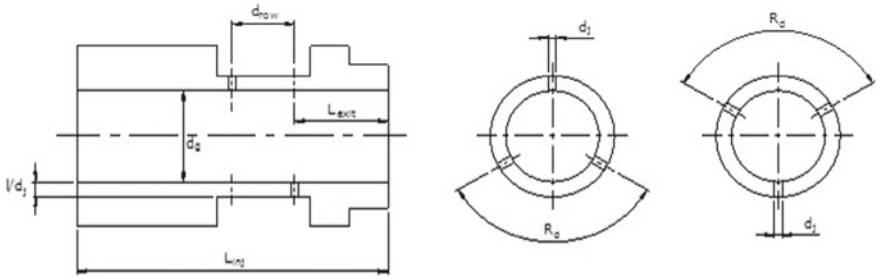

Fig. 1 Line diagram of injector

Table 1 Geometric specification of gas-centered coaxial injector

S. No.	Parameter		Value
1	Liquid injection orifice diameter	d_j	1 mm
2	Number of liquid injection orifices		6
3	Number of row of orifices		2
4	Radial angular distance between the two injectors in single row	R_d	120°
5	Axial distance between the two row	d_{row}	8.06 mm
6	Ratio of Length of liquid orifice to diameter of orifice	l/d_j	2 mm
7	Distance from last row to the exit of injector	L_{exit}	Varying depend upon the MFR

change because when MFR increases then the velocity of cross-flow decreases and the transverse breakup of liquid jet gradually increases. Therefore, the center post diameter ($d_{g)}$ designed on the basis of maximum MFR. When the MFR Z point of liquid jet increases. Therefore, the distance from the last row of liquid injection to injector exit (L_{exit}) designed on the basis of minimum MFR. At low, MFR L_{exit} will be maximum value. From this designed value, ensure that the primary breakup of liquid jet within the injector. The distance between the two rows of liquid injection orifice is fixed as 8.06 mm for all hardware because the axial breakup length for single jet is equal to 8.06 times of liquid jet diameter [4]. In order to avoid the hydraulic flip and cavitation, the ratio of length of liquid injection orifice to diameter of orifice is fixed as 2 [10]. Six number of liquid injection orifices are arranged in two rows. The radial angular distance between two orifices in single row is 120°. In the next rows, three orifices are drilled 60° offset at angular distance 120°. Thus two rows of the orifices are arranged in zigzag manner to avoid the striking of the liquid jets when it emerges out.

2.2 Experimental Setup

Cold flow atomization study of gas-centered coaxial injectors are planned using water and GN2 as the simulating fluids. The experimental setup consists of a water feed system; GN2 feed upstream/downstream of the pressure regulator. A filter system and Instrumentation system. A water tank is used which can be pressurized using gaseous nitrogen from a 50 L GN2 cylinder through a spring-loaded pressure regulator capable of regulating from 140 bar to 30 bar. Pressure gauges are mounted on the water tank as well as installed in the water line to avoid any particulates getting into the injector. A needle valve is installed in the water line to regulate the flow. For finding the pressure of water injection, there are two measurements are incorporated (one pressure gauge and a strain gauge type pressure transducer). Setup bank of four cylinders connected to a common header to supply the gaseous nitrogen. The pressure is regulated by an inline pressure regulator with pressure measurement provisions upstream and downstream. A needle valve installed in the gas line for controlling the flow rate. Instrumentation system consists of measurement systems and data acquisition systems. Measurement system is required for measuring and monitoring parameters like pressure and flow. Data acquisition system acquires and records the test parameters during the test which is used for analysis. Though many non-intrusive procedure have been applied for measuring drop size patterns, Malvern Particle Analyzer is most widely used. It is used to measure the SMD, process and record the drop size data. It works based on Fraunhofer diffraction theory of a collimated laser beam scattered by moving droplets.

3 Test Conditions

Experiments were carried out for injector element by varying Momentum Flux Ratio of Liquid to Gas at different downstream positions. Momentum flux ratio of liquid to gas is varied from 0.5 to 11 keeping into design considerations. In all case of momentum flux ratio, mass flow rate of water was kept constant and GN2 mass flow rate was varied. The GN2 mass flow rate was regulated through a needle valve positioned in the GN2 feed line. Injectors hardware tested at different momentum flux ratio at a particular position to find the spray and atomization characteristics. Malvern Particle Analyzer was used to study the atomization characteristics. Experiments at each MFR were repeated at different downstream positions. The downstream positions were fixed by changing the distance from the injector exit to the Malvern Particle Analyzer (Fig. 2).

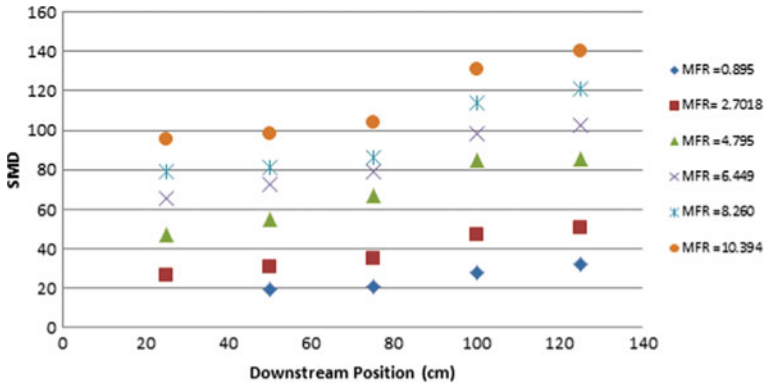

Fig. 2 Variation of SMD with different downstream positions

4 Result and Discussion

Figure 3 shows the variation of SMD with respect to MFR at different downstream positions. From this plot, it is clear that in each injector configuration at all downstream positions, Sauter Mean Diameter (SMD, D32) increases as momentum flux ratio (MFR) increases. When MFR increases, the velocity of the gas flow decreases and when MFR decreases, velocity of gas flow increases. In the range of MFR the mass flow rate of the liquid and hence the velocity of liquid jet is fixed and GN2 is varied and hence the gas velocity changes according to change in mass flow rate of GN2. Atomization characteristics of the injector will mainly depend on the gas flow velocity. At low MFR, the aerodynamic force acting on the liquid jet is more and hence the liquid jet tends to disintegrate into finer drops with large penetration. At high MFR, the aerodynamic force acting on the liquid jet is less and hence the

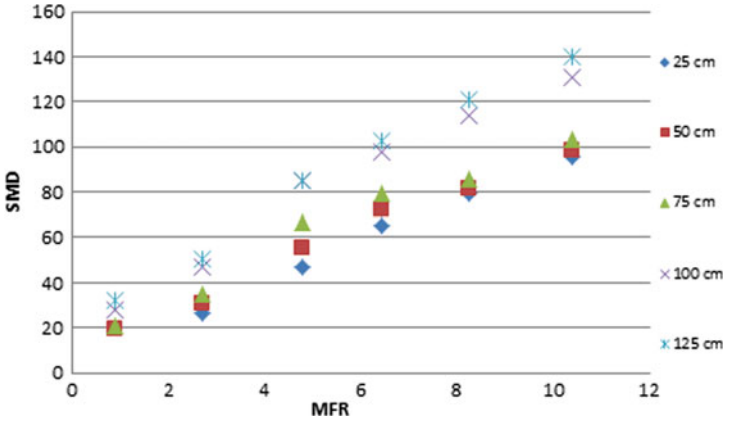

Fig. 3 Variation of SMD with different MFR

liquid jet tends to disintegrate into larger drops with lesser penetration. From Fig. 3 it is also evident that as MFR increases, variation in the drop sizes at downstream locations increases. At low MFR, the differences between the drop sizes (SMD) at downstream positions are less. At higher MFR, the difference between the drop sizes increases. At low MFR, due to high gas velocity, atomization is very fine and the spray coming out from the injector is very dense. This is why no major difference in SMD was observed at different downstream positions. But at higher MFR, the velocity of the gas is comparatively less and the disintegration of jet is basically due to the momentum of the jet itself. Hence, in this case, differences in the value of SMD were observed at different downstream positions.

The distances from the exit of the injector to the laser beam of the Malvern Particle Analyzer were kept at 25, 50, 75, 100 and 125 cm. From Fig. 3, it is clear that at all MFR as the downstream position increases, the drop size (SMD) also increases. At nearer downstream positions, the velocity of the spray is high and at further downstream positions, the velocity is less due to resistance of the air. Figure 3 shows that there is no major difference in SMD at initial three positions (25, 50 and 75 cm). But the SMD is high at other two further positions (100 and 125 cm), which means after a certain point of downstream positions the drop size increases due to the effect of coalescence. Increase in drop size after reaching a minimum value may be due to the adhesion of decelerated particle which experienced momentum loss due to the drag effect and momentum exchange with gas streams.

Figure 4 Show the variation of SMD with Weber number of gas flow. From this graph we see that as Weber number increases, drop size decreases at all downstream positions. At high Weber number, the velocity of the gas and the relative velocity were high. Figure 5 shows the variations of SMD with relative velocity between gas flow and liquid jet. In case of higher relative velocity the disintegration of liquid jet is perfect atomization is fine. Therefore, at higher Webber Number atomization is better and drop size is lower. Increase in Weber number means the disruptive force increases and the liquid jet disintegrates into drops easily. As seen in Fig. 6a–f as

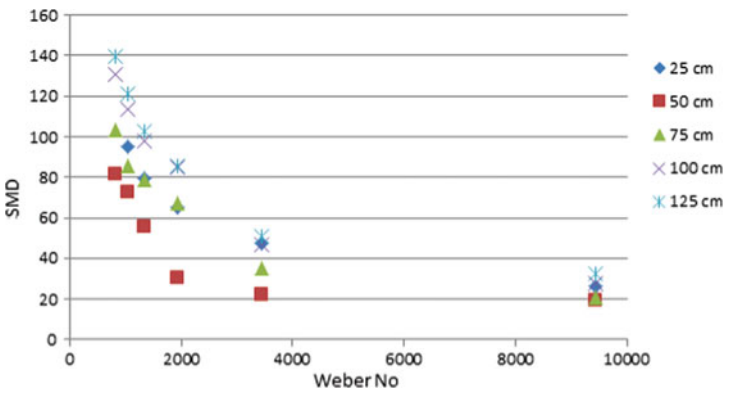

Fig. 4 Variation of SMD with different Weber No

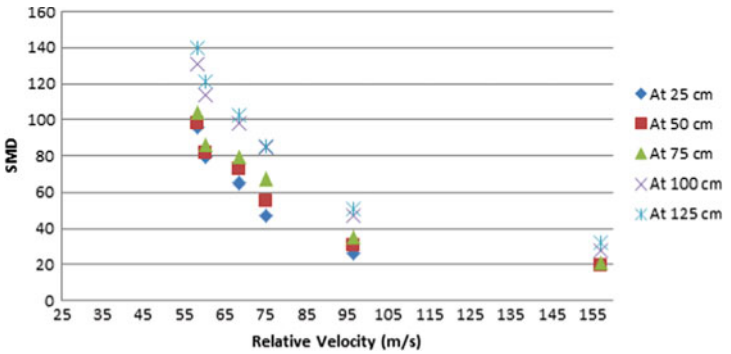

Fig. 5 Variation of SMD with relative velocity

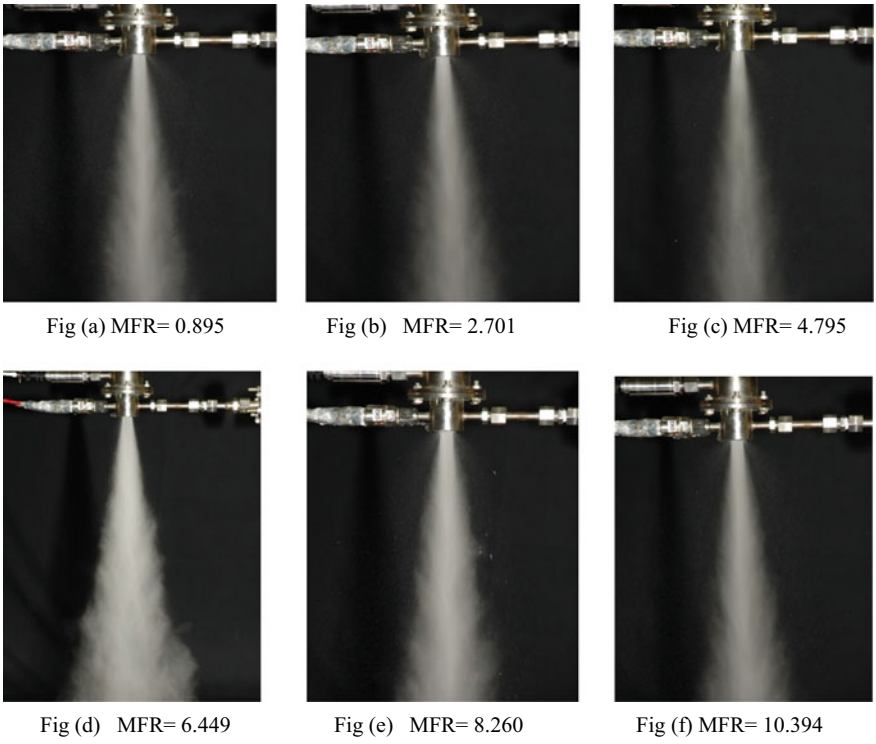

Fig (a) MFR= 0.895 Fig (b) MFR= 2.701 Fig (c) MFR= 4.795

Fig (d) MFR= 6.449 Fig (e) MFR= 8.260 Fig (f) MFR= 10.394

Fig. 6 Spray pattern at different MFR

MFR increases the density of the spray decreases and drop size increases. At low MFR, the mass flow rate of the GN2 is high and the velocity of the gas flow also high compared to large MFR. Due to that high mass flow rate, the spray structure becomes high dense. When the MFR increases, mass flow rate and velocity of GN2 decreases,

due to which spray becomes less dense and drop size increases. From Fig. 6a–f, as MFR increases cone angle decreases slightly. This is mainly due to the reduction of flow rate of GN2.

5 Conclusion

The major findings achieved through the experimental cold flow atomization study of coaxial injectors are, in the mixing of propellants the Momentum flux ratio is a key parameter. When the MFR (liquid to gas) increases, the drop size increases and degree of atomization decreases. In all injectors, increasing trend of drop size is observed, when the downstream position increases. Up to the initial three points, drop size are nearly identical and last two points show the wide variation due to the reduction of velocity of gas and the effect of coalescence. As MFR increases spray cone angle decreases and vice versa. The spray cone angle is higher at low MFR due to the presence of high mass flow rate of GN2. Weber number increases, drop size decreases at all downstream positions. At high Weber number, the velocity of the gas and the relative velocity were high. Therefore, atomization is better and drop size is lower. Increase in Weber number means the disruptive force increases and the liquid jet disintegrates into drops easily.

References

1. Lefebrve AH (1989) A text book of atomization and sprays. Taylor & Francis Publication
2. Mashayek A, Ashgriz N (1985) A text book of atomization and sprays. Springer Publication
3. Crabb D et al (1981) A round jet in a cross flow. The American Society of Mechanical Engineering 142/103
4. Yoon HJ et al (2011) Correlations for penetration height of single and double liquid jets in cross flow under high-temperature conditions. Atom Sprays 21(8): 673–686
5. Im J-H et al (2010) Comparative study of spray characteristics of gas centered and liquid centered swirl co axial injectors. J Propul Power 26(6)
6. Zheng Y, Marshall A (2011) Characterization of the initial spray from low webber number jet in cross flow. Atom Sprays 21(7):575–589
7. Andreopoulos J, Rodi W (1984) Experimental investigation of jet in a cross flow. J Fluid Mech 133:93–127
8. Wu P-K et al (1997) Breakup process of liquid jet in subsonic cross flows. Journal of propulsion and power 13(1)
9. Birouk M et al (2011) Effect of nozzle geometry on break up length and trajectory of liquid jet in subsonic cross flow. Atom Sprays 21(10):847–865
10. Song J et al (2011) Effect of orifice internal flow on liquid jet in subsonic cross flow. J Propul Power 27(3)
11. Pai MG et al (2009) Role of webber number in primary break up of turbulent liquid jet in cross flow. Annual research briefs of center for turbulent research
12. Kim JG et al (2013) Study on spray patterns of gas entered swirl coaxial injector in high pressure conditions. Aerospace Sci Technol 27:171–178

13. Lynch Amy et al (2011) Spray characteristics of a pressure-swirl fuel injector subjected to a cross flow and co flow. Atom Sprays 21(8):625–643
14. Bellofiore A (2006) Experimental and numerical study of liquid jets injected in high density air cross flow. Ph.D. thesis work at University of studies of Naples Ferderico II
15. Bellofior A et al (2010) Placement and acceleration of liquid jets in pressurized cross flows. Atom Sprays 20(9):775–789
16. Wang Q et al (2011) Characterization of trajectory, break point and break point dynamics of a plan liquid jet in across flow. Atom Sprays 21(3):203–219
17. Wu P-K et al (1998) Spray structures of liquid jets atomized in subsonic cross flows. J Propul Power 14(2)
18. Choi SM et al (2012) Spray in cross flow of rotary atomizer. Atom Sprays 22(2):143–161
19. Choi SM et al (2012) Spatial drop behavior of a rotary atomizer in a cross flow. Atom Sprays 22(12):1077–1095
20. Fuller RP et al (2000) Effect of angle on atomization of liquid jets in transverse air flow. AIAA J 38(1)

Fatigue Analysis of Helical Spring Subjected to Multi-axial Load

Tarek Al Musalli, Tesfaye Kebede Ali, and Balasubramanian Esakki

Abstract Helical spring is being widely used in diverse industrial applications such as automobiles, airplanes, mechanical watches, lock mechanisms, airsoft gun and even in writing pens. It is a long-term investment product, which subjected to time-varying loads. Prediction of fatigue life characteristics of helical springs is a major concern. The main challenge is to find the appropriate mechanical criteria that can predict the number of life cycles. Helical springs are subjected to multi-axial load and it causes shear effect on the coil wire. In order to predict the fatigue life characteristics of under this loading condition, non-proportional multi-axis approach is preferred due to handling of varying loads. The present study focuses on performing finite element analysis (FEA) to investigate the fatigue behavior of helical spring with stress-life and strain-life approaches. FEA results are compared with the stress and strain life theoretical calculations to predict the fatigue life and numerical simulations are also carried out to determine the maximum shear stress. It is observed that strain-life approach is able to predict the fatigue life accurately than stress-life methodology.

Keywords Helical spring · Fatigue analysis · Stress life · Strain life

1 Introduction

A helical spring is a flexible object that distorts its function when subjected to a load and restores its original shape when the load is released [1]. This element is included in many machine industrial applications. For example, the automotive industry uses helical spring in the suspension, brakes, and transmission components to absorb shock or vibration. Helical springs are always exposed to alternating loads and require millions of operating cycles to be maintained without failure, so it must be designed for infinite fatigue life. There are few previous studies have dealt with

T. A. Musalli · T. K. Ali · B. Esakki (✉)
Department of Mechanical Engineering, Vel Tech Rangarajan Dr. Sagunthala R&D Institute of Science and Technology, Avadi, Chennai, Tamil Nadu 600062, India
e-mail: balasubramaniane@veltech.edu.in

N. Gascoin and E. Balasubramanian (eds.), *Innovative Design, Analysis and Development Practices in Aerospace and Automotive Engineering*, Lecture Notes in Mechanical Engineering, https://doi.org/10.1007/978-981-15-6619-6_41

helical spring fatigue analysis. Del Llano-Vizcaya et al. [2] have compared experimental fatigue life with multiaxial fatigue criteria prediction method based on shear deformation. The finite element code ANSYS was used for stress analysis, and a multi-axis fatigue study was carried out using the fatigue software nCode. The results emphasize that the fatigue life of the helical spring component could be adequately predicted by the Fatemi-Socié critical surface method. Based on the strain life finite element method, Kamal and Rahman [3] were investigated the fatigue behavior of shock absorber springs used in automotive suspension systems made of SAE 9254 material. Mulla et al. [4] were conducted a fatigue analysis on the helical compression springs used in three wheeler's auto-rickshaw. The FEA results emphasize that classical models were less accurate when compared with these spring geometries. When compared to the value calculated using a simple analytical model, the maximum shear stress error obtained was limited to 1.5–4%. In this work, the applicability of a multi-axial non-proportional approach on the compression spring analysis was investigated. Stress and strain life analyses were tested to determine equivalent Von-Mises and maximum shear stresses. The estimated lifetime was compared with theoretical calculations to evaluate the various numerical analysis criteria. The multi-axial non-proportional fatigue analysis is yielded minimal error between the numerical and theoretical analysis.

2 Spring Geometry, Loading Condition and Material

2.1 Spring Geometry and Applied Loads

In this study, a standard helical compression spring DIN 2098-1 [5] without heat treatment was considered. It is made of chrome-silicon AISI 9254 [6] with both ends squared and ground. This spring is to be assembled with a preload of a minimum of $F_{\min} = 60$ N and will operate with a maximum load of $F_{\max} = 500$ N during use. The nomenclature of the spring is listed in Table 1 and the spring geometry is shown in Fig. 1.

2.2 Material Properties

AISI 9254 chrome-silicon is an alloy to withstand high-loading of springs, which are subjected to shock loads and require a long service life. It has a great hardness and is able to use it in a high-temperature condition up to 250 °C [6]. Its fatigue Stress-life and Strain-life characteristics were obtained from the nCode (FEA) software material library [7]. The mechanical property of the considered materials is given in Table 2.

In order to perform strain-life fatigue analysis approach, various parameters have to be considered for Chrome-silicon AISI 9254 which are given in Table 3.

Table 1 Standard spring DIN 2098 specification

Parameter	Symbol and unit	Value
Free length	L_f[mm]	110
Maximum displacement	$s_{\max}$[mm]	52.5
Wire size	d[mm]	5
Mean coil diameter	D_m[mm]	32
Internal coil diameter	D_i[mm]	27
External coil diameter	D_o[mm]	27
Maximum spring force	$F_{S.\max}$[N]	1226
Spring rate	R[N/mm]	22.9
Active number of coil	i_s	8.5
Total number of coil	i_t	10.5

Fig. 1 Spring geometry

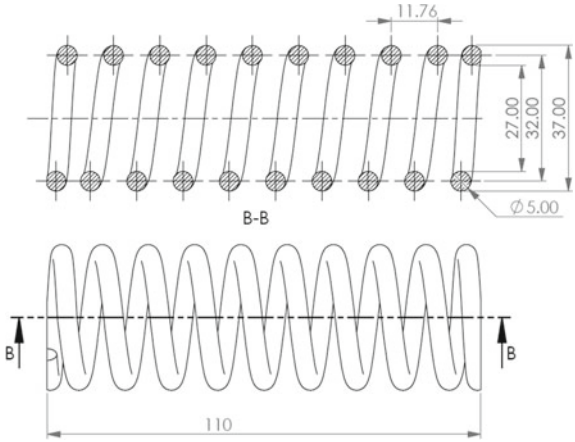

Table 2 Chrome-silicon mechanical property

Parameter	Symbol and unit	Value
Ultimate tensile strength	S_u[MPa]	2950
Yield stress	σ_y[MPa]	2270
Elastic modulus	E[GPa]	205
Poisson's ratio	v	0.3

Table 3 Chrome-silicon strain-life property

Parameter	Symbol and unit	Value
Fatigue strength coefficient	$\sigma_f^{'}$[MPa]	5943.6
Fatigue strength exponent	b	−0.1463
Fatigue ductility coefficient	$\varepsilon_f^{'}$	0.5828
Fatigue ductility exponent	c	−1.0777
Cyclic strength coefficient	K'[MPa]	4086.2
Cyclic Strain exponent	n'	0.1251

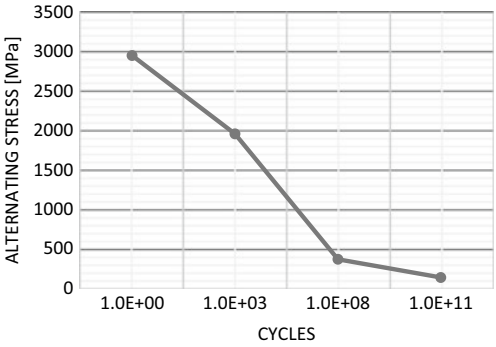

Fig. 2 Chrome-silicon AISI 9254 stress-life curve

For the stress-life fatigue analysis approach, the relation between alternative stress and the number of cycles [7] considered for the present analysis is shown in Fig. 2.

3 Theoretical Calculation

3.1 Stress in Helical Spring

In order to calculate stress in the spring, consider an axial load F which is applied at the central axis of helical spring. The spring maintains equilibrium by generating an internal shear force F and torque T, which is shown Fig. 3.

The maximum shear stress is determined by,

$$\tau_{\max} = \pm\frac{Tr}{J} + \frac{F}{A} \tag{1}$$

where J is polar moment of inertia, A is cross-section area, r is wire radius and d is diameter.

In general, the following relationship holds for calculating the shear stress [6]

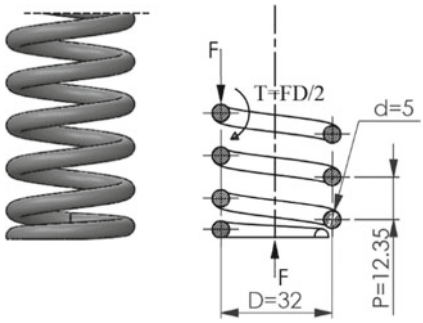

Fig. 3 Force and torque acting on the helical spring

$$\tau = \frac{8FD}{\pi d^3} + \frac{4F}{\pi d^2} = K\frac{8FD}{\pi d^3} \tag{2}$$

where D denotes mean coil diameter and C is the spring index. Shear stress-correction factor k is calculated by using the following relation,

$$K = 1 + \frac{0.5}{C};\ C = \frac{D}{d} \tag{3}$$

The mean stress τ_m and the amplitude stress τ_a are given by [6]

$$\tau_m = K_b\frac{8F_mD}{\pi d^3};\ \tau_a = K_b\frac{8F_aD}{\pi d^3} \tag{4}$$

K_b is "*Bergsträsser factor*", which is used as a correction factor due to curvature of the spring, it can be found by using the Eq. (5).

$$K_b = \frac{4C+2}{4C-3} \tag{5}$$

3.2 Fatigue Life Calculation

In case of stress life approach [6], the maximum number of cycle is calculated by using the following relation,

$$S_f = aN^b;\ N = \left(\frac{S_f}{a}\right)^{\frac{1}{b}} \tag{6}$$

Where

$$b = -\frac{1}{3}\log\left(\frac{f.S_{ut}}{S_e}\right); a = \left(\frac{f.S_{ut}}{S_e}\right)^2 \tag{7}$$

where S_f is fatigue stress for N number of cycles, a and b are fatigue constant found from Eq. (7), f is fatigue strength fraction and S_e is the endurance limit for specific material [6].

$$S_{ut} = \frac{A}{d^m} \tag{8}$$

A is intercept coefficient equal to 2911 MPa.mm$^{\text{m}}$ for wire diameter between (5 to 10) mm, m is slope coefficient equal to 0.478 [6, p 525] for chrome-silicon material. Then, we can find $f = 0.9$ [6, p 285] by approximation from fatigue

strength fraction curvature for the corresponding value of S_{ut}

$$S_e = K_a.K_b.K_c.K_d.K_e.K_f.S_e^{'} \tag{9}$$

where K_a, K_b, K_c, K_d, K_e, K_f and $S_e^{'}$ are surface factor, size factor, load factor, Temperature factor, reliability factor, miscellaneous factor, rotary-beam test specimen endurance limit, respectively. The values of K_d, K_e, $K_f = 1$; $K_a = 0.84$ $K_b = 1.4$ [6, p 282] $K_c = 0.59$ [1, p 290] and $S_e^{'}$ is the rotary-beam test specimen endurance limit which equal to $S_e^{'} = 700$ MPa for $S_{ut} > 1400$ MPa. Using the modified Goodman criterion to find the fatigue load S_f [6]

$$\frac{\tau_a}{S_f} + \frac{\tau_m}{S_u} = 1; \; S_f = \frac{\tau_a}{1 - \frac{\tau_m}{S_u}} \tag{10}$$

where

$$\tau_m = K_b \frac{8F_m D}{\pi d^3}; \; \tau_a = K_b \frac{8F_a D}{\pi d^3} \tag{11}$$

$$F_m = \frac{F_{\max} + F_{\min}}{2}; \; F_a = \frac{F_{\max} - F_{\min}}{2} \tag{12}$$

4 Numerical Simulation

The spring geometry was modeled using Solid Work platform as per the nomenclature given in Table 1. The ANSYS commercial program was employed in helical spring fatigue analysis to predict the number of cycles [8]. The two compounds of forces viz. amplitude force F_a and the midrange force F_m have been applied. Instead of using fatigue rates to describe the relationship between stresses, a non-proportional loading procedure was employed that required the use of two loading environments for the calculation [9] and stress-life and strain-life approaches were considered for the fatigue life evaluation. The FE mesh with 68,000 elements was generated using quadratic tetrahedral [2]. The mesh quality of the average elements is 84.1% (Fig. 4).

4.1 Stress-Life Approach

Unlike the stress-life approach, the strain-life approach considers the effect of plasticity and elasticity. The equation relating total strain amplitude ε_n to the stress amplitude σ_a is given as [10],

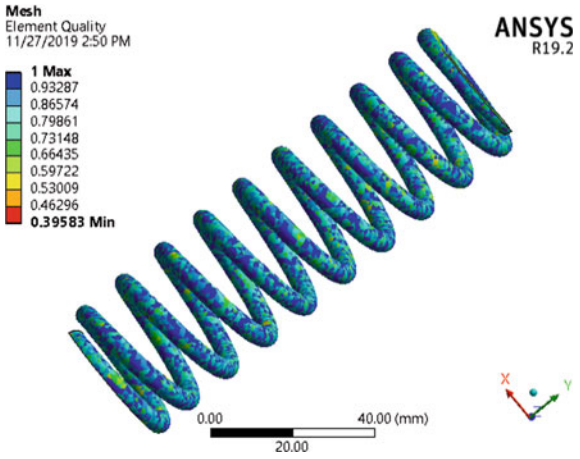

Fig. 4 Mesh quality

$$\varepsilon_n = \frac{\sigma_a}{E} + \left(\frac{\sigma_a}{K'}\right)^{\frac{1}{n'}} \tag{13}$$

The relation between strain and the total life cycle is given as

$$\varepsilon_n = \frac{\sigma_f'}{E}(2N_f)^b + \varepsilon_f'(2N_f)^c \tag{14}$$

4.2 Fatigue Analysis

The flow chart is shown in Fig. 5 describes [10–12] the procedure for estimating the fatigue life characteristics of helical spring.

5 Results and Discussion

The fatigue life of helical spring [13] obtained using theoretical calculation was 1.77E + 07 cycles, which will be compared with numerical simulation results. Table 4 shows the comparative evaluation of stress and strain life approaches. It is observed that Max shear stress in the stress-life approach [14] obtained less error than other approaches and hence it will be considered for evaluating the fatigue life of helical spring.

The cross-section C-C [15] as shown in Fig. 6 is considered for examining the strain and stress life of all the four types of numerical simulation approaches. It is

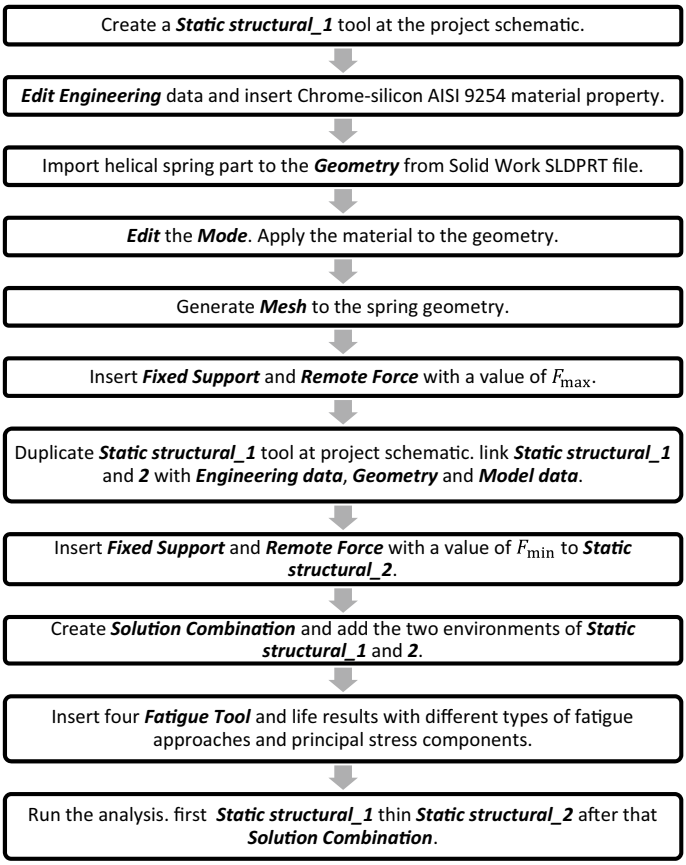

Fig. 5 Methodology of fatigue analysis

Table 4 Numerical simulation result

Approach	Principal stresses	Number of cycles	Error deviation [%]
Strain-life	Equivalent (Von Mises)	1.171E + 08	561.58
	Max shear	1.219E + 07	31.13
Stress-life	Equivalent (Von Mises)	6.769E + 07	282.43
	Max shear	2.158E + 07	21.92

observed from Figs. 7, 8, 9 and 10 that, in the middle of the coil has more strength in comparison to the outer periphery and fatigue life is reduced correspondingly.

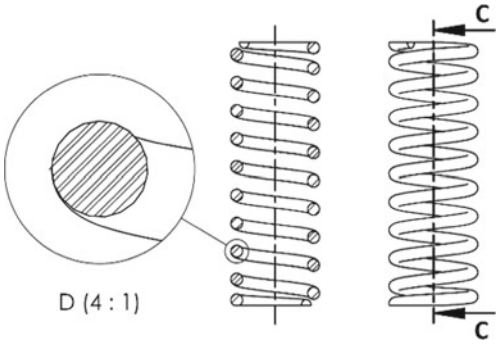

Fig. 6 Cross-section of spring

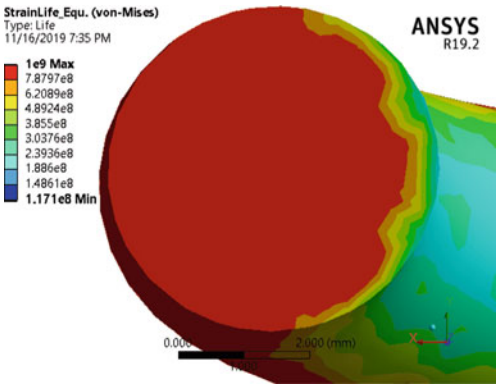

Fig. 7 Strain life_ equivalent (Von-Mises)

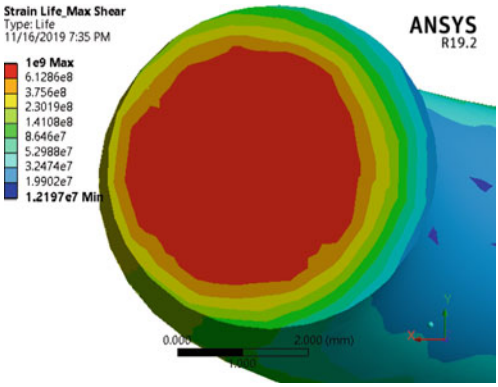

Fig. 8 Strain life_ max shear

6 Conclusion

Fatigue analysis of helical spring subjected to non-proportional multi-axial load is performed using FEA. Comparative evaluation of stress and strain life approaches

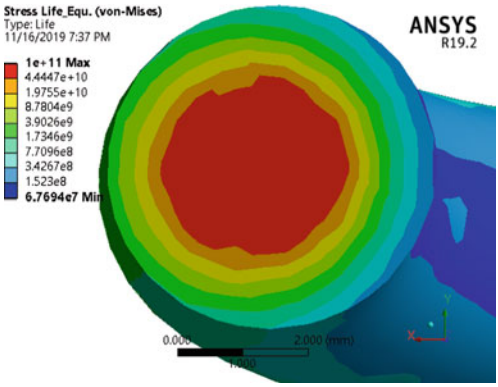

Fig. 9 Stress life_ equivalent (Von-Mises)

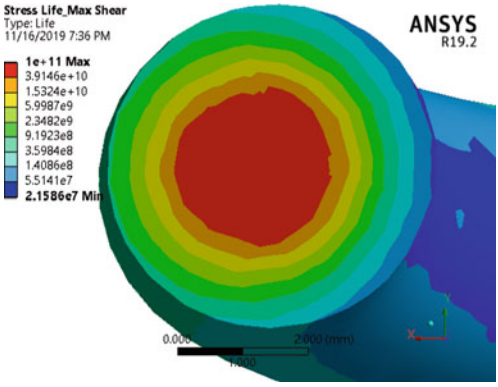

Fig. 10 Stress life_ max shear

on estimating the Von-Mises and maximum shear stress with theoretical calculations resulted that, stress-life approach obtained minimal error in comparison to other approaches. The multi-axial fatigue analysis predicted the endurance limit of 1.77E + 07 cycles to withstand the cyclic load of maximum as 500 N and minimum of 60 N. The results suggested that, the helical springs of multi-axial load can withstand more number of cycles and it can absorb heavy shock loads are generated from various machine elements.

References

1. Khurmi RS, Gupta JK (2005) A text book of machine design. Eurasia Publishing house (PVT.) Ltd. First multi-color edition, pp 576–586
2. Del Llano-Vizcaya L, Rubio-González C, Mesmacque G, Cervantes-Hernández T (2006) Multiaxial fatigue and failure analysis of helical compression springs. Eng Fail Anal 13(8):1303–1313

3. Kamal M, Rahman MM (2014) Finite element-based fatigue behaviour of springs in automobile suspension. Int J Automot Mech Eng 10
4. Mulla TM, Kadam SJ, Kengar VS (2012) Finite element analysis of helical coil compression spring for three wheeler automotive front suspension. Int J Mech Ind Eng 2(3):74–77
5. Fischer U, Heinzler M, Näher F, Paetzold H, Gomeringer R, Kilgus R, Stephan A (2010) Mechanical and metal trade's handbook. Europa Lehrmittel
6. Shigley JE (2011) Shigley's mechanical engineering design. Tata McGraw-Hill Education
7. Newbold P (2013) Design life theory guide
8. Chen X, Liu Y (2014) Finite element modeling and simulation with ANSYS Workbench. CRC Press
9. Lee YL, Barkey ME, Kang HT (2011) Metal fatigue analysis handbook: practical problem solving techniques for computer-aided engineering. Elsevier
10. Browell R, Hancq A (2006) Calculating and displaying fatigue results. ANSYS® on-line white papers
11. Gokhale NS (2008) Practical finite element analysis. Finite to infinite
12. Pharne MJ, Todkar RG, Sangle ND, Design, analysis and experimental validation for fatigue behavior of a helical compression spring used for a two wheeler horn. IOSR J Mech Civ Eng (Iosr-Jmce) E-Issn, 2278–1684
13. Liao D, Zhu SP (2019) Energy field intensity approach for notch fatigue analysis. Int J Fatigue
14. Batra RC (1978) Saint-Venant's principle for a helical spring
15. Wu MH, Ho JY, Hsu W (1997) General equations of a helical spring with a cup damper and static verification

Wear Properties on AA2014/Al_2O_3/TiB_2 Hybrid Metal Matrix Composites

Jayavelu Sundaram, J. Udaya Prakash, and Harivind Kagitha

Abstract Wear properties of aluminium hybrid metal matrix composites have been analyzed in this study. The driving force behind this study is too broad a knowledge base on aluminium powder metallurgy to provide ideas for making aluminium powder components economical and wear-resistant. In this study, AA2014, AA2014 + Al_2O_3 + TiB_2 wear analysis was concentrated using pin-on disc tribotester. The samples tested for wear were prepared using the powder metallurgy method. Wear tests were carried out with loading conditions of 20 N under normal atmosphere at a sliding velocity of 1.5 m/s. Coefficient of friction, specific wear rate and wear rate have been calculated. AA2014 + 5 wt%–Al_2O_3 + 5 wt%–TiB_2 has a lower rate of wear due to the presence of wear resistance materials when compared with the AA2014 alloy.

Keywords Hybrid metal matrix composites · Titanium diboride · Alumina · Wear

1 Introduction

Today, the biggest problem of worn-out rotating and frictional parts due to wear is faced by major industries. Wear is causing energy and natural resource shortages. Because of traditional production methods and materials, there are a number of significant amounts of wear-based research and development that have shown a lack of significant improvements in wear resistance [1].

Powder metallurgy (P/M) has become a significant method for the processing of metal parts, such as high efficiency in the production of net or near-net types of medium to high size. P/M also has uniform characteristics: structures of fine grain and chemical homogeneity. Current consumer goods have a growing number

J. Sundaram (✉) · J. Udaya Prakash · H. Kagitha
Department of Mechanical Engineering, Vel Tech Rangarajan Dr. Sagunthala R&D Institute of Science and Technology, Chennai, India
e-mail: jayavelu.sundaram@gmail.com

N. Gascoin and E. Balasubramanian (eds.), *Innovative Design, Analysis and Development Practices in Aerospace and Automotive Engineering*, Lecture Notes in Mechanical Engineering, https://doi.org/10.1007/978-981-15-6619-6_42

of P/M components and are used in automotive, aerospace and non-vehicle applications. In automotive applications, ferrous P/M components predominate over all other available P/M products [2].

High-resistance aluminium-based materials manufactured by P/M over the past two decades have been engineered for use in high-temperature applications such as struts and other structural components in aerospace. P/M aluminium materials have gained popularity in critical applications of reduced weight and relatively high resistance.

Two distinct examples of P/M materials enhanced by aluminium. One is a standardized mix of aluminium powder and "extrinsic" dispersoids such as silicon carbide or particulates of aluminium. The other is a rapidly solidified aluminium powder with "intrinsic" dispersoids that contain metastable phases like AlfiFe contained in Al–Fe–X alloys, where X is another element or rare earth metal transition. The strength of these two types of reinforced aluminium powder materials is due in the integrated microstructure to the distribution and thermal stability of each phase [3].

Baradeswaran et al. find that Al7075 is reinforced with 5–20 wt% of B_4C, increased wear resistance due to the presence of hard B_4C particle load-bearing and preventing micro-cutting pin removal on composite surfaces. [4].

Jayavelu et al. studied the wear resistance of two composites and aluminium alloy with dry sliding wear by powder metallurgy method. Of these, aluminium alloy with titanium diboride provides increased wear resistance and low friction coefficient [5].

Baskaran et al. stated by Taguchi method in the dry sliding wear study of Al7075 insitu casting with TiC. In this high-temperature pin, plastic deformation occurs due to the formation of an oxide layer called a mechanically mixed layer (MML), which is the reason for the gentle sliding of wear parts, providing excellent wear resistance [6].

Wear is an important parameter to be considered in engineering field due to the replacement of parts, component and assemblies especially in the automobile filed. Hence, wear resistance calculation will give an idea how to improve the efficiency by reducing the materials replacing rate [7].

In this study, wear test was conducted for the AA2014 and AHMMCs at 20 N loading conditions, sliding velocity of 1.5 m/s, distance of 1000 m and under normal atmosphere. The results were compared.

2 Experimental Procedure

AMMC is formed using the technique of powder metallurgy. The composite hybrid comprises aluminium AA2014 alloy, alumina (Al_2O_3) of 40 nm particle size and titanium diboride (TiB_2) of 20 nm particle size elements.

Initially, for the production of hybrid aluminium composite, the elemental powder mixture of aluminium alloy AA2014, alumina and TiB_2 powder was milled for 8 h. In this process, two specimen combinations were developed as AA2014 and Aluminium

AA2014 alloy/5% Al_2O_3/5% TiB_2. Uniaxial pressure was used to process the green compacts at room temperature and 350 MPa of compaction pressure.

Sintering conducted in the vacuum hot press at 620 °C for 2 h. Sample will continue to be cooled for 24 h in nitrogen. The diameter and height of the specimen is 20/20 mm.

Green compacts of composites were sintered under the nitrogen atmosphere at 620 °C for 2 h. Sample-I and sample-II sintered and green densities were estimated by weight and physical dimensions. Theoretical densities of the composition were calculated by rule of mixture.

The ASTM G99-05-based pin-on-disc (EN31) discs analyze specimen's dry sliding wear property. Tests conducted of 20 N applied load, at 1000 m sliding distance and 1.5 m/s sliding speed. Before and after testing, the specimen was weighed, and subsequently, SEM images of worn-out surfaces are analyzed.

3 Results and Discussion

3.1 Studies on Microstructure

A prefilled in the scanning electron microscopy, the polished sample images are captured. Figure 1 displays 25-μm-scale microstructure of AA2014. The image shows aluminium, copper, chromium and manganese evenly distributed in layer of aluminium.

Figure 2 displays the 25-μm-scale microstructure of hybrid metal matrix composite. The image shows a uniform distribution of aluminium, copper, titanium, boron, chromium and manganese in the hybrid metal matrix composite.

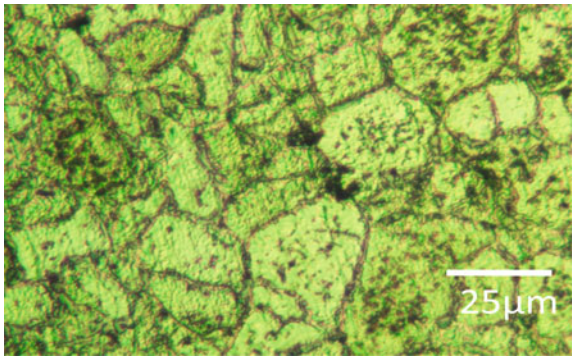

Fig. 1 Microstructure of AA2014 alloy

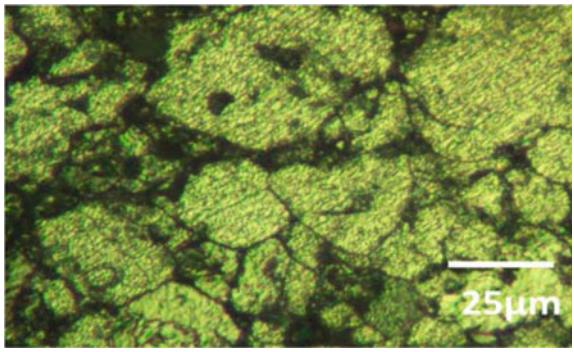

Fig. 2 Microstructure of AA2014/TiB_2/Al_2O_3

Table 1 Various densities of sample-I and II

Sample	Green density g/cc	Sintered density g/cc	Theoretical density g/cc	Theoretical density %	Porosity %
Sample-I	2.731	2.774	2.816	98.5	1.4
Sample-II	2.722	2.735	2.907	94.1	5.9

3.2 Studies on Density

Table 1 reveals the sample-I has a 98.5% higher sintered density compared to the potential density. Effect of pressure, powder particles are forced together, resulting in surface defects interlocking and cold welding between the layers [8]. Sample-II showed a theoretical density of 94.1% sintered relative to sample-I. During sintering, due to the gas trap, porosity may occur in aluminium alloys. The percentage of porosity indicates that ceramics with aluminium alloys are properly wetted in both samples. From the table, sample-I displays 50% porosity of the average porosity; it is also compliant with the lower volume fraction of the reinforcements having less porosity than the sample-II.

3.3 Studies on Wear Analysis

Pin-on-disc of load 20 N, sliding distance 1000 m and sliding speed 1.5 m/s analyzed wear and coefficient of friction properties. It has been inferred from previous research that the wear rate increases at the sliding distance [9].

The wear rate depends upon the different factors like size of pin particle, applied load, sliding velocity, sliding distance, surface hardness and fracture of toughness of testing samples [6].

Canakci et al. reported using hard ceramic materials as reinforcement in metallic matrix influence wear characteristics. Wear rate depreciated due to increase in volume of hard phase and particle size. This is due to abrasive particles first protrude inside the surface of specimen and slow move towards the surface which results continuous grooves [10].

To calculate the wear loss, the pin-on-disc equipment was operated at a constant sliding speed of 1.5 m/s and a constant sliding distance of 1000 m. Wear loss and friction coefficient for AA2014, AA2014 + 5% Al_2O_3 + 5% TiB_2 were calculated for load of 20 N listed in Table 2.

Grooves, created by the steel disc surface touch, tend to cross the surface of the composite specimen. Due to abrasion, the grooves are created by removing particles from the surface of the AA2014 aluminium alloy is shown in Fig. 3. The aluminium matrix tends to plastic deformation, creating an oxide surface at high temperature, allowing smooth sliding on the surface of the disc, and reducing wear loss at higher speeds.

Figure 4 wear rates show a downward trend that indicates less material removal from the surface. The SEM micrograph demonstrates the delamination of the removal

Table 2 Specific wear rate and coefficient of friction of sample-I and sample-II

Composition	Specific wear rate = (volume loss)/(sliding distance * load) mm^3/Nm	Coefficient of friction (μ)
Sample-I	0.001320	0.517
Sample-II	0.000963	0.488

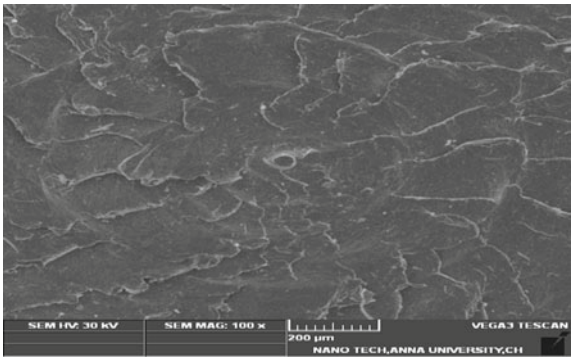

Fig. 3 SEM images of aluminium AA2014 alloy

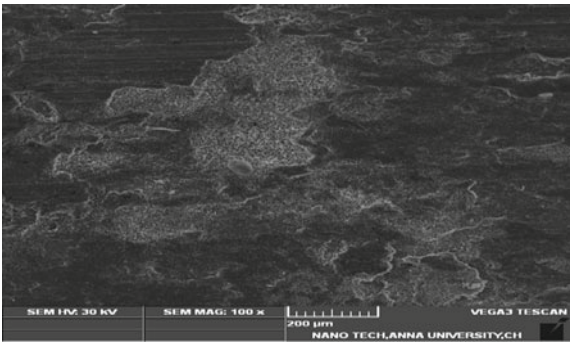

Fig. 4 SEM images of AA2014/5% Al_2O_3/5% TiB_2

of material. Besides this, cracks are created on the surface along with particles pulling out.

4 Conclusions

The following facts can be found on the basis of this study:

- Sample-I show less than 50% of the composition's average porosity and 98.5% of its theoretical density.
- Sample-II indicates a lower friction coefficient and higher wear resistance that will be ideal for the manufacture of automotive components such as automobile components and cylinder pistons.
- As the friction coefficient decreases, it reduces the friction force (caused by wear and tear of moving parts), thus increasing the engine's mechanical efficiency, decreasing fuel consumption and lubricating costs.

Acknowledgements The authors would like to thank the Chairman, Vel Tech Rangarajan Dr. Sagunthala R&D Institute of Science and Technology, India, for supporting the use of the Metallurgical and Materials Laboratory at Research Park, Chennai.

References

1. Mishra AK, Sheokand R, Srivastava RK (2012) Tribological behaviour of Al 6061/SiC metal matrix composite by Taguchi's techniques. Int J Sci Res Pub 2:1–8
2. Vencl A, Rac A, Bobic I (2004) Tribological behaviour of Al-based MMCs and their application in automotive industry. Tribol Indus 26:31–38
3. Surappa MK (2003) Aluminium matrix composites: challenges and opportunities. Sadhana 28:319–334
4. Baradeswaran A, Perumal AE (2014) Study on mechanical and wear properties of Al 7075/Al2O3/graphite hybrid composites. Compos B Eng 56:464–471

5. Jayavelu S, Mariappan R, Rajkumar C (2018) Wear characteristics of sintered AA2014 with alumina and titanium di-Boride metal matrix composites. Int J Ambient Energy 17:1–6
6. Baskaran S, Anandakrishnan V, Duraiselvam M (2014) Investigations on dry sliding wear behavior of in situ casted AA7075–TiC metal matrix composites by using Taguchi technique. Mater Des 60:184–192
7. Ravindran P, Manisekar K, Rathika P, Narayanasamy P (2013) Tribological properties of powder metallurgy–Processed aluminium self lubricating hybrid composites with SiC additions. Mater Des 45:561–570
8. Vani VV, Chak SK (2018) The effect of process parameters in aluminum metal matrix composites with powder metallurgy. Manufact Rev 5:7–20
9. Sardar S, Karmakar SK, Das D (2018) Tribological properties of Al 7075 Alloy and 7075/Al2O3 composite under two-body abrasion: a statistical approach. J Tribol 140:051602
10. Canakci A, Ozsahin S, Varol T (2014) Prediction of effect of reinforcement size and volume fraction on the abrasive wear behavior of AA2014/B4Cp MMC s using artificial neural network. Arab J Sci Eng 39(8):6351–6361

NiP Composite Coating of Piston Ring by Plate and Bumper Method

M. Malathi, J. Herbert Mabel, and R. Rajendran

Abstract In automotive engines, piston rings are one of the critical components operating inside the engine keeping the vehicle mileage. The function of piston rings is for better sealing of combustion gases and oil scrapping. With the usage and time, the piston rings wear out. This introduces the need for ring coating of high quality which can operate under high temperature without damaging or peeling off and is also corrosion resistant. The NiP composite coating gives preferable high hardness and improves wear and friction resistance. The good property enhancement of the composite material is also an important factor to be considered. Property of a composite depends on the volume fraction of dispersed phase. In order to achieve good property enhancement, the volume fraction has to be increased. One such technique of achieving this is the plate and bumper method which involves the usage of fixture and is to be moved up and down. The volume fraction achieved in this method is around 8–10%. This method helps in incorporating the particles and achieving a high volume fraction with a slow plating rate. Results shows that considerably the plate and bumper helps in improving the incorporation of composite and contributes more to the mechanical property enhancement of the piston rings.

Keywords Composite plating · Piston rings · Plate and bumper method

1 Introduction

In IC engines, piston rings are subjected to very high mechanical and thermal stresses, and the durability of the part has to be ensured for maintaining the performance parameters throughout the vehicles's life time [1–3]. To achieve the durability with various fuels like gasoline, diesel, CNG, LPG and alcohol fuels, the parts are

M. Malathi (✉) · J. Herbert Mabel
B. S Abdur Rahman Crescent Institute of Science & Technology, Chennai, India
e-mail: malathi@iprings.com

R. Rajendran
SRM Institute of Science and Technology, Chennai, India

N. Gascoin and E. Balasubramanian (eds.), *Innovative Design, Analysis and Development Practices in Aerospace and Automotive Engineering*, Lecture Notes in Mechanical Engineering, https://doi.org/10.1007/978-981-15-6619-6_43

subjected to the various types of coatings like GN, plating, thermal spray, PVD and so on. Electroplating process of NiP and NiP composite is attempted to improve the wear and corrosion resistance property. The ultrafine SiC is used for co-deposition of ceramic particles in the NiP bath. The homogeneity of the electroplating bath is improved by keeping the cathode and anode in dunking mode. The incorporation of composite material depends on the concentration of SiC and dunking cycles per minute [4–6].

2 Experimental Procedure

Several grades of martensitic stainless steel and hardened & tempered steel grades are used for piston ring application. The SAE9254 is one such grade popularly used for plating application [7, 8]. The material composition is as given Table 1.

The electroplating bath composition [1] is as given Table 2.

The electroplating of NiP and NiP + SiC is dependent on parameters like temperature, time and current density. The concentration of phosphorus content selected as medium phosphorus and SiC ceramic particle used is to improve the wear properties of the piston ring. The rings are assembled in the form of mandrel as shown in Fig. 1. The pretreatment processes are alkaline degreasing, buffing, vapour blasting, reverse etching to improve the adhesion. The mandrel is then assembled in the specially made fixture as given in Fig. 2a, b and plated.

To improve the incorporation of SiC, special fixture was made and placed in the tank for electroplating as given in Fig. 2a, b.

Trial conducted is varying the current densities 10A, 5A, 3A and 1A keeping the other parameters constant, temperature 70 ± 1 °C, time −1 h and dunking speed −50

Table 1 Material composition of SAE 9254

Elements	Weight in %
Carbon	0.50–0.60
Silicon	1.20–1.60
Manganese	0.50–0.80
Phosphorus	0.03 max.
Sulphur	0.03 max.
Chromium	0.50–0.80

Table 2 Electroplating bath composition

Chemical name	Weight in gms/lt
Nickel sulphate	150.00
Nickel chloride	45.00
Sodium lauryl sulphate	0.25
Orthophosphoric acid	40.00
Phosphorus acid	6.00
Silicon carbide (composite material)	(5, 50, 100)

Fig. 1 Assembled mandrel

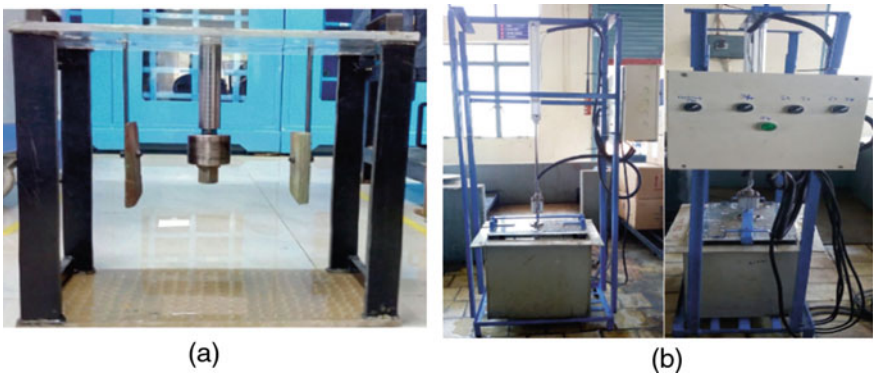

Fig. 2 **a** Front view of the special fixture, **b** plating set up for composite coating

cycles per second. The current density optimized is 3 amps/dm^2 to achieve uniform plating (Fig. 3).

The composite plating was carried out similar to that of conventional NiP plating by varying concentration of SiC and dunking speed and is given in Fig. 4a–d.

Fig. 3 NiP composite-coated piston ring

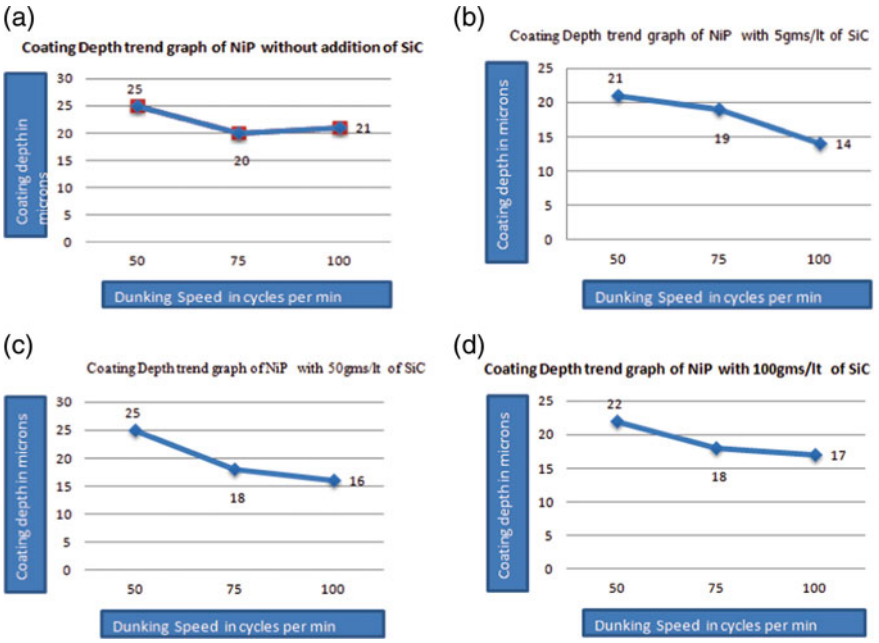

Fig. 4 **a** Coating depth trend without SiC, **b** coating depth trend with 5 g/lt of SiC, **c** coating depth trend with 50 g/lt of SiC, **d** coating depth trend with 100gms/lt of SiC

The piston rings composite plated with SiC ceramic particle at current density 3 amps/dm^2 for 60 min plating time (with various concentrations of SiC) were subjected to heat treatment at 300 °C for 2 h. The coating characterization for hardness, microstructure, XRD, wear and corrosion.

3 Results and Discussion

3.1 Micro-Vickers Hardness

The micro-Vickers hardness of both the rings (with and without heat treatment) measured in Matsuzawa hardness tester using 50 gm load is given below. Table 3 gives the hardness readings of the rings with various dunking cycles and SiC concentration.

The hardness on the electroplated composite coating has increased with an increase in concentration of ceramic particle (SiC) and dunking speed. The increase in hardness after heat treatment is due to precipitation of nickel phosphide intermetallics like Ni3P [2].

Table 3 (a) Micro-Vickers hardness in HV 0.05 of NiP without addition of SiC, (b) micro-Vickers hardness HV 0.05 of NiP with addition of SiC 5 g/lt, (c) micro-Vickers hardness in HV 0.05 of NiP with addition of SiC 50 g/lt and (d) micro-Vickers hardness in HV 0.05 of NiP with addition of SiC 100 g/lt

(a)

Dunking speed of special fixture	As plated	Heat treated
50 cycles per minute	322	541
75 cycles per minute	325	555
100 cycles per minute	350	560

(b)

Dunking speed of special fixture	As plated	Heat treated
50 cycles per minute	418	680
75 cycles per minute	420	700
100 cycles per minute	460	720

(c)

Dunking speed of special fixture	As plated	Heat treated
50 cycles per minute	518	780
75 cycles per minute	555	825
100 cycles per minute	580	885

(d)

Dunking speed of special fixture	As plated	Heat treated
50 cycles per minute	708	920
75 cycles per minute	751	965
100 cycles per minute	828	1015

3.2 Micro-structure

The photograph of micro-structure of the cross section of the piston ring was taken in Zeiss optical microscope at 500× to study the incorporation of composite material SiC as shown in Fig. 5a–c.

3.3 SEM/EDAX Analysis

The piston ring periphery was analysed in FESEM Zeiss make to study the incorporation of SiC [2] of sample A (SiC 5 gms/lt at dunking speed 150 cycles per minute) and sample B (SiC 100gms/lt at dunking speed 150 cycles per minute) at 500×. The given below are the results of SEM images and EDAX results as shown in Fig. 6a, b.

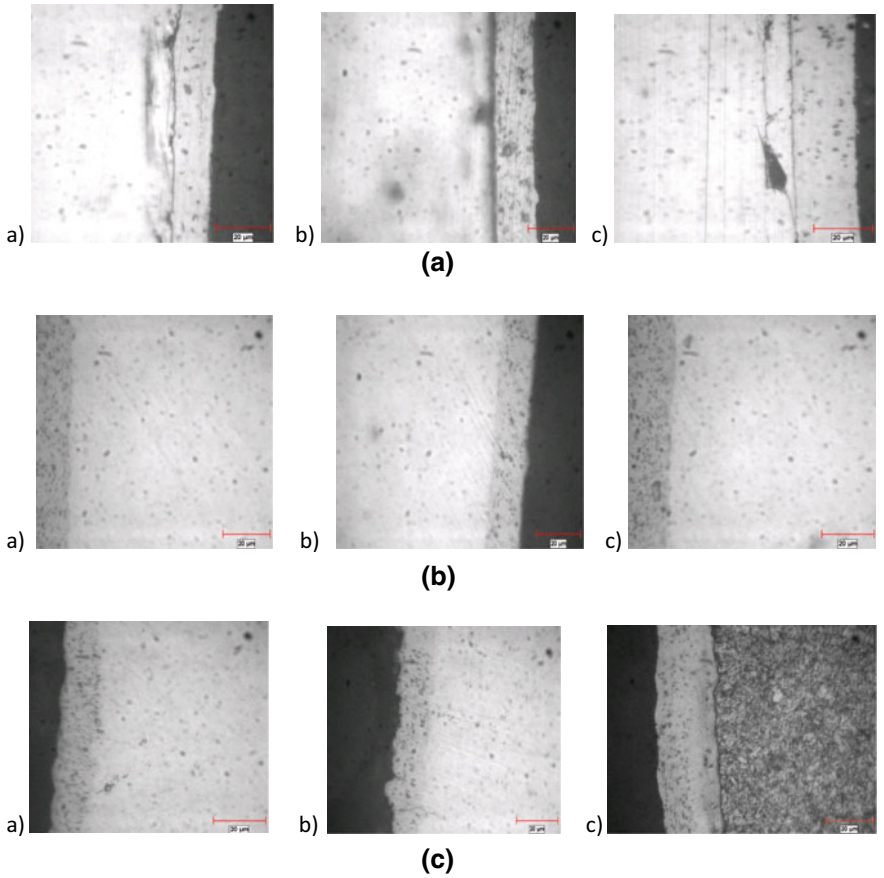

Fig. 5 (a) Photograph of NiP 5 g/lt SiC at 50 cycles per minute, (b) 100 cycles per minute and (c) 150 cycles per minute. (b) Photograph of NiP 50 g/lt SiC at (**a**) 50 cycles per minute, (**b**) 100 cycles per minute and (**c**) 150 cycles per minute. (c) Photograph of NiP 100 g/lt SiC at (**a**) 50 cycles per minute, (**b**) 100 cycles per minute and (**c**) 150 cycles per minute

SEM/EDAX analysis shows that the incorporation of SiC is better with an increase in concentration of SiC and dunking speed. However, agglomeration is observed, and this may be improved by additional air agitation in the electroplating bath.

3.4 X-Ray Diffraction

The precipitation of nickel phosphide (Ni3P) and composite SiC material is confirmed by subjecting the heat treated piston ring at 300 °C for two hours to XRD analysis as given in Fig. 7.

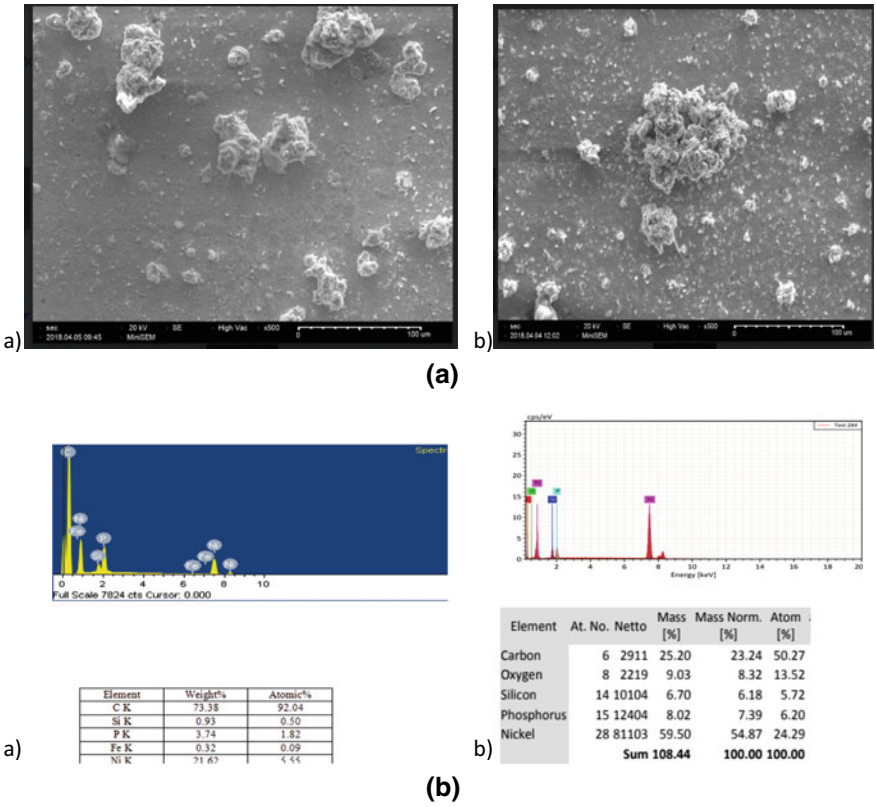

Fig. 6 **a** SEM image of piston ring at dunking speed (**a**) 5 g/lt of SiC, (**b**) 100 g/lt of SiC. **b** EDAX analysis of piston ring at dunking speed (**a**) 5 g/lt of SiC (**b**) 100 g/lt of SiC

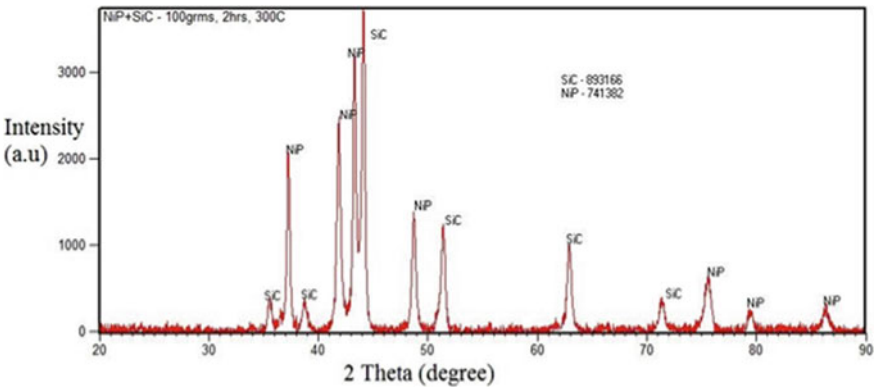

Fig. 7 XRD of NiP + SiC after HT

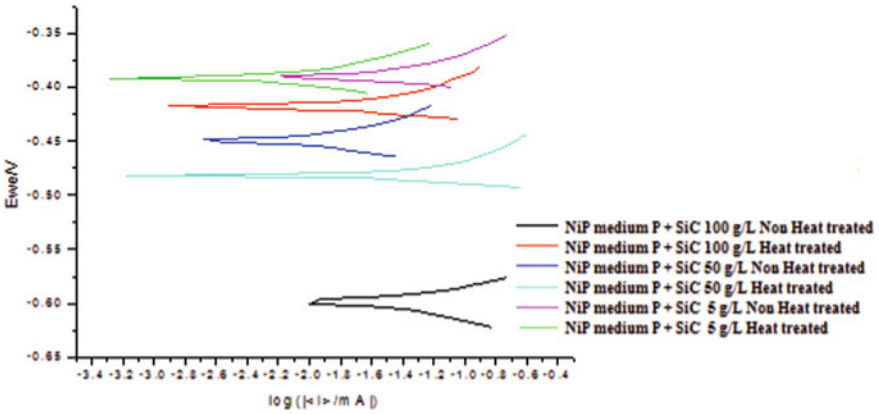

Fig. 8 Tafel plots of NiP composite-coated piston rings obtained for non-heat treated and heat-treated conditions

3.5 Potentiodynamic Measurements

The polarization curves of Ni-medium P with SiC (5, 50 and 100 gms/lt) in the heat treated and non-heat treated condition were measured on exposing the samples in 0.5 M Na_2SO_4 solution is shown in Fig. 8. The corrosion data was compared with conventional chrome-coated piston ring [1]. The corrosion potentials—Ecorr EC, corrosion current densities—icorr CC and the Tafel line inclinations βa & βc and corrosion rate mmpy are shown in Table 4.

From Table 4, the corrosion rate mm per year of heat-treated NiP composite plated of concentration 5 g/lt is comparable with that of chrome-plated.

3.6 Wear Study

The wear study was conducted as shown in pin on disc TR10LE wear tester. The weight loss is studied as a function heat-treated and non-heat-treated NiP composite-coated piston rings for SiC concentrations 5, 50 and 100 gm/lt. The wear testing parameters are at an applied load of 50 N at 900 rpm for 15 min duration (Fig. 9).

The weight loss achieved for NiP med Phos + SiC 5g/lt is comparable with that of chrome plating as shown in Table 5.

Table 4 Potentiostat measurement of NiP/SiC (5, 50, 100 gm/lt) in 0.5 M solution of Na_2SO_4 of heat-treated and non-heat-treated piston rings

Description of the piston rings	*E* Corr (mv)	*I* Corr (μ A)	Beta (A) (mv)	Beta (C) (mv)	Corrosion rate (mmpy)
Chrome plated	−636.451	0.073	60.3	82.3	0.8595
NiP medium P (100 g/lt SiC) without HT	−600.650	33.850	33.4	33.1	1.32693
NiP medium P (100 g/lt SiC) after HT	−423.562	25.068	58.6	10.1	0.98267
NiP medium P (50 g/lt SiC) without HT	−454.499	11.915	51.5	20.2	0.46707
NiP medium P (50 g/lt SiC) after HT	−487.573	59.783	68.7	8.7	2.3435
NiP medium P (5 g/lt SiC) without HT	−395.556	37.997	62.6	10.9	1.48949
NiP medium P (5 g/lt SiC) after HT	−396.496	8.512	44.6	20.7	0.333672

Fig. 9 TR10 LE model pin on disc wear testera

Table 5 Weight loss comparison of NiP medium P + SiC non-heat treated & heat treated with that of chrome-plated piston rings

S. No.	Specimen name	Initial weight (gm)	Final weight (gm)	Weight loss (mg)
1.	NiP medium P + SiC 100 g/lt non-heat treated	0.34030	0.33809	2.21
2.	NiP medium P + SiC 100 g/lt heat treated	0.316089	0.31320	2.88
3.	NiP medium P + SiC 50 g/lt non-heat treated	0.31282	0.31053	2.29
4.	NiP medium P + SiC 50 g/lt heat treated	0.31192	0.30969	2.23
5.	NiP medium P + SiC 5 g/lt non-heat treated	0.34494	0.34196	2.98
6.	NiP medium P + SiC 5 g/lt heat treated	0.34593	0.34369	1.45
7.	Base material without any coating	0.39764	0.39399	3.65
8.	Chrome-plated piston ring	0.3165	0.315	1.5

4 Conclusions

In this study, a novel method plate and bumper method was attempt for co-deposit ultrafine composite SiC dispersed in electrolytic bath onto the piston rings. From the detailed investigations, the following conclusions can be drawn.

(i) Micro-structure and XRD measurement show co-deposition of ultrafine SiC particles size was homogenously co-deposited with nickel phosphorus onto the piston ring.
(ii) Hardness of the composite-coated piston ring is observed to be max with increase in concentrations of SiC and dunking speed. Hardness of the NiP-SiC composite coated is in the range of 700–1015 HV0.05 g which is comparable to chrome-plated hardness (800 HV0.1). Chrome plating is a regular plating process in vogue for innumerable engine piston ring applications today.
(iii) The wear and corrosion results of the NiP composite-coated piston ring is comparable with that of existing chrome plating process which is in current application.

References

1. Pillai AM, Rajendra A, Sharma AK (2014) Electrodeposited nickel-phosphorous (Ni-P) alloy coating: an in-depth study of its preparation, properties, and structural transitions. J Coat Technol Res 9(6). ISSN 1547-0091
2. Wang L, Gao L, Xu T, Xue Q (2005) Corrosion resistance and lubricated sliding wear behaviour of novel Ni–P graded alloys as an alternative to hard Cr deposits
3. Ramachandran S, Anderson A, Abbas Mohaideen J (2007) Corrosion behaviour of Ni PTFE and Ni Al_2O_3 coating. India J Des Manuf Technol 1(1)
4. Szczygieł B, Kołodziej M (2005) Composite Ni/Al_2O_3 coatings and their corrosion resistance
5. Shao W, Nabb D, Renevier N, Sherrington I, Fu Y, Luoa J (2012) Mechanical and anti-corrosion properties of TiO_2 nanoparticle reinforced Ni coating by electrodeposition. J Electrochem Soc
6. Gérard B (2006) Application of thermal spraying in the automobile industry
7. Bratu F, Benea L, Celis J-P (2007) Tribocorrosion behaviour of Ni-SiC composite coatings under lubricated conditions
8. Lekka M, Lanzutti A, Casagrande A, de Leitenburg C, Bonora PL, Fedrizzi L (2012) Room and high temperature wear behaviour of Ni matrix micro- and nano-SiC composite electrodeposits. Surf Coat Technol

Microstructural and Mechanical Characterization of Sintered and Hot Pressed Hybrid Metal Matrix Composites

Jayavelu Sundaram, J. Udaya Prakash, and Mariappan Ramajayam

Abstract This work analyzed the microstructural and mechanical properties of sintered and hot pressed aluminum alloy AA2014, an aluminum metal matrix composite and an aluminum hybrid metal matrix composite. Sample-1 (AA2014), sample-2 (AA2014 + 5wt% TiB_2) and sample-3 (AA2014 + 5 wt% TiB_2 + 5 wt% Al_2O_3) were developed by powder metallurgy. It involves elemental powder mixing and uniaxial green compaction in a 350 MPa universal testing machine followed by sintering in a 550 °C electric muffle furnace for 2 h and hot pressing in a vacuum hot press at nitrogen atmosphere for 2 h at 620 °C. Density assessment, study of microstructure and mechanical characterization were subjected to three samples. For both sintering and hot pressed condition, mechanical and physical properties were analyzed. Samples-1, 2, and 3 display a marginal increase of 1, 1.4 and 1.4% of sintered densities after hot pressing. Sample-1, 2, and 3 porosity were decreased by 15.94, 25 and 22.2% after hot pressing. Improved mechanical properties due to the transfer of load from the matrix to the two reinforcements TiB_2 and Al_2O_3 after hot pressing.

Keywords Sintering · Tensile test · Hot press · Aluminum hybrid metal matrix composites

1 Introduction

In aircraft fuselages and wings, ground transportation, electrical and heat exchange applications, aluminum metal matrix composites (AMMCs) are used. Due to its excellent properties, such as light weight to strength ratio, slender density, increased rigidity, higher thermal stability, tremendous thermal and electrical conductivity [1].

J. Sundaram (✉) · J. Udaya Prakash · M. Ramajayam
Department of Mechanical Engineering, Vel Tech Rangarajan Dr. Sagunthala R&D Institute of Science and Technology, Chennai, India
e-mail: jayavelu.sundaram@gmail.com

N. Gascoin and E. Balasubramanian (eds.), *Innovative Design, Analysis and Development Practices in Aerospace and Automotive Engineering*, Lecture Notes in Mechanical Engineering, https://doi.org/10.1007/978-981-15-6619-6_44

Hybrid metal matrix composites (HMMCs) are the composites of the second generation that are much needed to meet the need for advanced engineering. Among these, aluminum hybrid metal matrix composite (AHMC) is one of the HMMCs in which we can produce suitable materials [2].

AHMCs are produced using the powder metallurgy (P/M), mechanical alloying, casting methods such as stir, compo and squeeze casting and spray deposition method [3]. Among these, P/M has a low processing temperature compared to casting phase, which prevents undesirable reactions between reinforcements and matrix, as well as near-net-shaped parts. P/M has control over pore size, number of pores and phase distribution due to compaction of powders and sintering conditions [4, 5].

Anandpratheepan et al. investigated that TiB_2 particles will not be subjected to any reaction with the aluminum matrix, thereby preventing the development of brittle existence in the composite Al metal matrix. TiB_2 has good thermal conductivity and stability, high youth modulus and electrical conductivity, low specific gravity and superior wear characteristics that make the TiB_2 suitable for hybrid reinforcement [6]. Gajakosh et al. also reported that the Al7075-based composite microstructure reinforced with TiB_2 showed a homogeneous distribution of reinforcements with superior matrix Al 7075 [7].

Penchalreddy et al. studied when Al–Cu–Li particle reinforced composite fabricated through P/M route involving microwave sintering and hot extrusion (HET). In their investigation, they found that ductility, yield strength, ultimate tensile and compression strength, Young's modulus and microhardness are increased due to uniformly distribution of hard and brittle particle of alumina reinforcement phase in ductile Al matrix [8]. Sajjad sattari et al. investigated in a micron-sized Al matrix was reinforced with nano-sized SiC particles through P/M and HET. They inferred that 550 °C temperature is an apt temperature for HET at which yield strength enhanced by 75% and hardness by 40% due to presence of nano-SiC reinforcements [9].

Senthilkumar et al. manufactured various composite by using aluminum alloy AA2014 with micro and nano-sized Al_2O_3 particle ranging from 1 to 10 wt% through powder metallurgy method and hot extrusion method at 550 °C temperature. They revealed that composites have combination of 8 wt% of micron Al_2O_3 and 2 wt% of nano-Al_2O_3 having better hardness than the other combinations [10]. C. E. da costa et al. reported that when aluminum alloy (AA2014) reinforced with the nickel aluminide through powder metallurgy route increases wear resistance two to three times than base alloy [11].

Chandrasekar et al. analyzed microstructure, hardness, tensile properties and corrosion properties of stir casted AlMg4.5 with various proportions of ceramic alumina particles. Reinforced nano-alumina particles of 6 wt% improved their corrosion properties due to exposure of NaCl solution. The tensile strength has also improved with same reinforced due to the stress transformation [12]. Shrivanimoghaddam et al. revealed when Al reinforced with B_4C, TiB_2, $ZrSiO_4$ in which ceramic/aluminum composite can withstand load due to interfacial bonding between them. An effective interfacial bond shifts the load from matrix to reinforcements without any failures which determine physical and mechanical properties of composites [13].

Baradeswaran et al. find that Al7075 is reinforced with B_4C; hardness value increases considerably due to increases in strain energy because of particle dispersion at peripheral region of the composite [14]. Jayavelu et al. investigated wear resistance of two composites and aluminum alloy fabricated through powder metallurgy using dry sliding wear. Of these, aluminum alloy with titanium diboride provides higher wear resistance and low coefficient of friction [15]. Basakaran et al. reported in dry sliding wear analysis of insitu casting fabricated Al7075 with TiC through Taguchi method that elevated temperature pin undergo plastic deformation due to formation of oxide layer which is reason for gentle sliding of wear parts which provides excellent wear resistance [16].

With these studies, an attempt has been made to synthesis an aluminum AA2014 alloy from elemental powders, a composite of AA2014 with 5 wt%—TiB_2 and a HMMC AA2014 with 5%—TiB_2 and 5%—Al_2O_3 through powder metallurgy route. Green, sintered and theoretical densities of samples-I, II and III were calculated and compared. Samples-I, II, III were undergone vacuum hot press condition in order improve the existing mechanical properties. The results are compared with all three samples.

2 Materials and Methods

Materials used in the present study were elemental powders of aluminum alloy AA2014, TiB_2 and Al_2O_3, and their compositions were tabulated in Tables 1, 2, and 3.

Aluminum (67 μm) from M/s Metal Powder Company, Thirumangalam, copper (45 μm) from M/s Innomet powders, Hyderabad, magnesium (μm) from M/s Jagada Industries, Virudhunagar, chromium (45 μm), and manganese (37 μm) from M/s

Table 1 Constituent of AA2014 [17]

Element	Cu	Si	Mg	Mn	Fe	Al
Weight %	4.0	0.8	0.5	0.8	0.7	Balance

Table 2 Constituent of TiB_2 powders [18]

Element	Ti	B	O	C	Fe	N
Weight %	67.60	31.04	0.45	0.25	0.09	0.26

Table 3 Constituent of Al_2O_3 particles [19]

Element	Alumina	Fe_2O_3	TiO_2	CaO	Other magnetic materials
Weight %	93.0	0.80	1.80	1.10	0.20

Royal Scientific suppliers, India, alumina (40 nm) from M/s US research nanomaterials corporation and titanium diboride (20 nm) from M/s Guangzhou Hongu Material Technology Company were procured.

Elemental powders of the aluminum AA2014 alloy, TiB_2 and Al_2O_3 were measured in 50 g of weight percentage through electronic weighing machine (Make: SHIMADZU, Model AUY220) with precision of 0.001 g. Measured powders were mixed in pot mill for 12 h. Powders were allowed to flow in a die of high carbon high speed steel of the 50 mm of diameter and 12.5 mm height. Die's inner surface, punch, and butt outer surface were pasted with mixture of acetone and zinc stearate punch for removal of samples without damages [20]. Lauric acid is used as lubricator in the die wall for easy removal and avoiding damages of samples from the die [21].

Green compaction was done in hydraulically operated universal testing machine at pressure of 350 MPa. In the UTM (Make: Fine Spavy Associates & Engineers Pvt Ltd, Model TUN 400), when compaction pressure increases gradually, particles movement is stopped; as pressure gradually increases, it is used for powder compaction which involves process fragmentation and plastic deformation of powders [22]. After removal of billets from the die, green densities were measured using electronic weighing machine. Samples were kept inside chamber of electrical muffle furnace (Make: Geniune Equipment Manufacturers, Model:MF01) for sintering at 550 °C for 2 h which involves densification and bond formation using furnace atmosphere. Sintered densities were measured after removal of samples from electrical muffle furnace. Samples were kept inside chamber of vacuum hot press (Make:VB CERAMICS) for hot pressing at 620 °C with 360 MPa in nitrogen atmosphere for 2 h.

Sintered density was determined by Archimedes's principle. Porosity of samples was derived by using the formula [23].

$$\text{Porosity} = (\rho\text{th} - \rho\text{exp})/(\rho\text{th} - \rho\text{air}) * 100.$$

where ρth—theoretical density in g/cm^3, ρexp—experimental density in g/cm^3, ρair—density of air (0.001225 g/cm^3).

Microstructural analysis was carried by Metscope–I supplied by Chennai Metco; tensile strength of samples was analyzed in Hounsfield Tensometer with ASTM standard E8. Hardness was measured in Rockwell hardness tester make Navin Engineering, Model RHS 150 of Capacity 150 kgf in B scale. Billets were made into mirrors like polishing with double disk polishing machine with emery grades sheets of size 800, 1000 and 1200 and velvet with diamond paste. Billets were etched with Keller's reagent (HNO_3 + HCl + HF) for micrographs examination [24]. Samples were arranged inside the chamber of vacuum hot press for hot pressing at 610 °C ± 10 °C under vacuum condition for 2 h in order to improve existing mechanical properties.

3 Result and Discussion

3.1 Microstructure Study

Microstructure of samples depends upon the amount of reinforcements and its size. Figure 1 shows aluminum AA2014 alloy (sample-1), AA2014 with addition of 5 wt% TiB_2 (sample-2), and AA2014 with 5 wt% TiB_2 and 5 wt% Al_2O_3 (sample-3). By deep etching on the surface with Keller's reagent, shape, size, and grain boundary of particles were exposed. Porosity of samples was shown as black spot which reduces mechanical properties. Porosity associated with grain boundary appears to be spherical shape later its change to oblate, these shape formed because of gas originated within materials [25].

In sample-1, aluminum particles were dispersed randomly in aluminum AA2014 alloy. It is also confirmed that microstructure contains smaller, coarse grain particles of aluminum, copper, chromium, silica and magnesium. From Fig. 1, sample-2 titanium diboride particles were dispersed uniformly in aluminum AA2014 matrix. TiB_2 particles are naturally hexagonal or typically spherical form clusters at grain boundaries which reveal that it will facilitate grain refinement and strengthening effect. Addition of TiB_2 particles in ductile matrix, which enhances diffusivity and

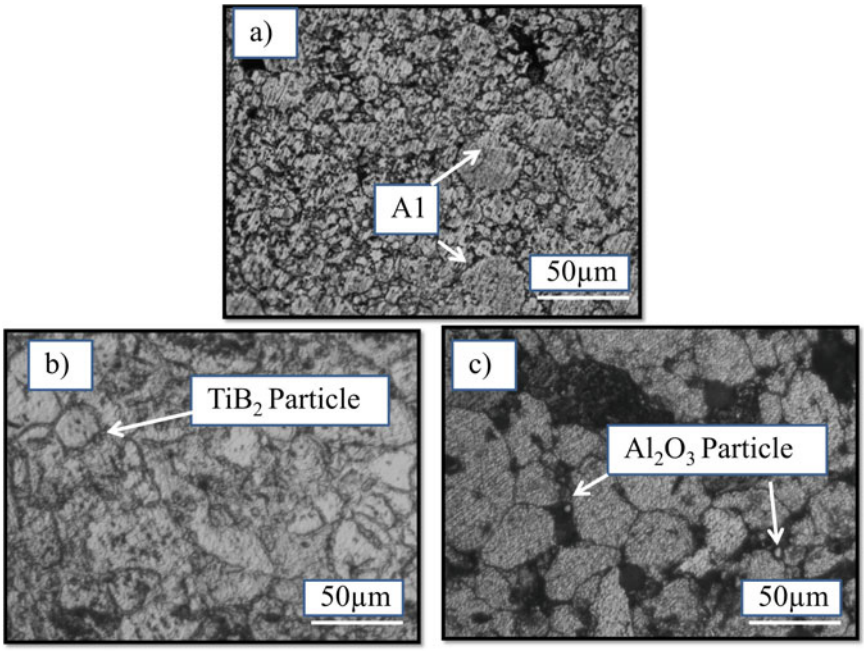

Fig. 1 Microstructure of **a** sample-1, **b** sample-2, **c** sample-3

subsequently, reduces agglomeration in the composite. Due to Zener effect, nano-sized particles of TiB_2 which located at boundary strengthened the grain boundary which improve mechanical properties of composites. Morphology of sample-3 from Fig. 1, we can infer that the nano-alumina was observed around the grain boundary which also hinders dislocation of grain [25–27]. During sintering process, particles of alumina will act as obstacle at the grain boundary which restricts dislocation this allows grain will move freely within grain boundary leads increase in size of grain. Rahimian et al. also reported the same that Al_2O_3 particles acts as obstacle in rearrangement, dislocation and dispersion of the alumina particles which leads to high porosity without considering sintering consideration [28].

3.2 *Density Analysis*

The theoretical density was measured with the rule of mixture [29]. Green and sintered densities were measured by Archimedean principle [30] (Fig. 2).

From Table 4, green densities of sample-1, 2, and 3 were 95.2, 92.1, and 91.6% when compared with theoretical density. Sintered densities of sample-1, 2 & 3 were

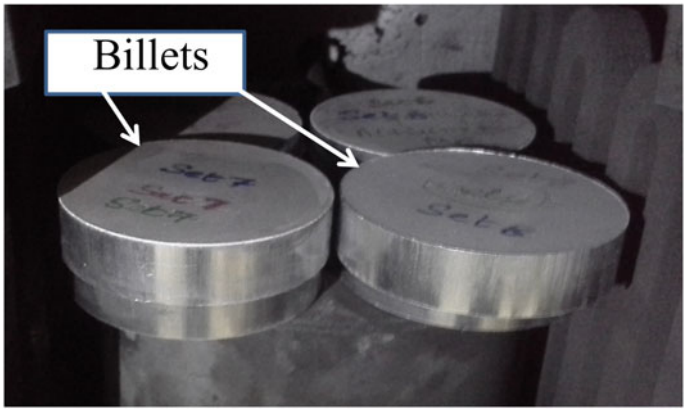

Fig. 2 Billets inside the electrical muffle furnace

Table 4 Comparison of green, sintered, hot pressed and theoretical density

Test	Green	Sintered	Hot pressed	Theoretical
Specimen	density	density	density	density
	g/cm^3	g/cm^3	g/cm^3	g/cm^3
Sample-1	2.58	2.63	2.66	2.71
Sample-2	2.59	2.65	2.69	2.81
Sample-3	2.63	2.69	2.73	2.87

Table 5 Comparison of porosity after sintering and hot press

Test specimen	Porosity after sintering	Porosity after hot press
	%	%
Sample-1	2.848	2.394
Sample-2	5.696	4.272
Sample-3	6.274	4.880

97.1, 94.3, and 93.7% of theoretical density. Addition of titanium diboride particles in sample-2 improves diffusivity of nano-particles which lowers agglomeration. Addition of reinforcement particles like $TiB_2$and Al_2O_3 particles in sample-3 has lower agglomeration which increases sintered density and also alumina can flow and fill up the pores in samples and Al powders rearrange themselves in contact areas. Then samples were undergone hot press in vacuum condition; then densities of the billets were measured for sample-1, 2, and 3; they were 98.1%, 95.7%, and 95.1%, respectively, which shows marginal enhancement in densities (Table 5).

Porosity of samples-1, 2, and 3 were reduced after hot press by 15.94, 25 and 22.2%.

3.3 Mechanical Properties

Table 6 provides summary of hardness, yield strength, tensile strength and elongation. Yield strength of sample-2 and sample-3 was increased by 15.7 and 33.3% than aluminum alloy. Tensile strength of samples-2,3 was increased by 21.38 and 30.6% than alloy. Wu et al. reported that reinforcement increases strength at cost of ductility which due to collective effect of solid solution, intermetallics and its constitution. In sample-1, mechanical property is influenced by θ' (Al_2Cu) precipitates which bypasses the dislocations in turn determines size and number of precipitates.

TiB_2 nano-particles in sample-2 which inhibit movement of particles at grain boundary due to Orowan's mechanism. These grain boundaries in turn prohibit dislocations due to this strength increase at cost of ductility [31]. It is evident from Table 6; base metal deformation is higher than composite due to reinforcement which results in load is transferred from matrix to reinforcement.

Table 6 Mechanical properties

Test specimen	Yield strength	Tensile strength	Hardness	Elongation
	MPa	MPa	HRB	%
Sample-1	159	173	144	22
Sample-2	184	210	190	12
Sample-3	212	226	204	6.25

Zhao et al. also reveal elongated grain of TiB_2 improved flexural strength and fracture toughness which is essential for higher temperature structural application such as wear parts, cutting tools and armor due to toughening and strengthening mechanisms of TiB_2 which includes grain refinement (grain fracture and grain pullout) and crack branching, crack bridging and crack deflection. They also concluded that fracture toughness enhanced due to mixed mode of transgranular and intergranular fracture [32].

Mechanical properties of HMMC are influenced by reinforcement of titanium diboride and alumina in sample-3. Hardness of sample-2 and 3 was increased by 31.94 and 41.6% than the base alloy.

4 Conclusion

- Microstructure reveals randomly distribution aluminum in aluminum AA2014 alloy of the sample-1, which as coarse particles. Addition of TiB_2 particles in ductile matrix, which enhances the diffusivity and subsequently, reduces agglomeration in the composite.
- Samples were undergone hot press in vacuum condition; then densities of the billets were measured for sample-1, 2, and 3; they were 98.1%, 95.7%, and 95.1%, respectively, which shows marginal enhancement in densities.
- Yield strength of sample-2 and sample-3 was increased by 15.7 and 33.3% than aluminum alloy. Tensile strength of sample-2 and 3 was increased by 21.38 and 30.6% than alloy.

References

1. Mahamani A, Jayasree A, Mounika K, Reddi Prasad K, Sakthivelan N (2015) Evaluation of mechanical properties of AA6061-TiB_2/ZrB_2 in-situ metal matrix composites fabricated by K2TiF6-KBF4-K2ZrF6 reaction system. Int J Microstruct Mater Prop 10:185–200
2. Rajmohan T, Palanikumar K, Arumugam S (2014) Synthesis and characterization of sintered hybrid aluminium matrix composites reinforced with nano copper oxide particles and microsilicon carbide particles. Compos B Eng 59:43–49
3. Khan MM, Dixit G (2017) Erosive wear response of SiCp reinforced aluminium based metal matrix composite: effects of test environments. J Mech Eng Sci 14:2401–2414
4. MariappanR, Kishore Kumar P, Jayavelu S, Dharmalingam G, Arun Prasad M, Stalin A (2015) Wear properties of P/M duplex stainless steels developed from 316L and 430L powders. Int J ChemTech Res 8(10):109–115
5. Rahimian M, Parvin N, Ehsani N (2011) The effect of production parameters on microstructure and wear resistance of powder metallurgy Al–Al_2O_3 composite. Mater Des 32:1031–1038
6. Partheeban CMA, Rajendran M, Vettivel SC, Suresh S, Moorthi NSV (2015) Mechanical behavior and failure analysis using online acoustic emission on nano-graphite reinforced Al6061–10TiB_2 hybrid composite using powder metallurgy. Mater Sci Eng: A 632:1–13

7. Gajakosh AK, Keshavamurthy R, Ugrasen G, Adarsh H (2018) Investigation on mechanical behavior of hot rolled Al7075-TiB_2 in-situ metal matrix composite. Mater Today: Proc 5:25605–25614
8. Reddy MP, Manakari V, Parande G, Shakoor RA, Mohamed AMA, Gupta M (2019) Structural, mechanical and thermal characteristics of Al–Cu–Li particle reinforced Al-matrix composites synthesized by microwave sintering and hot extrusion. Compos Part B: Eng 164:485–492
9. Sattari S, Jahani M (2017) An investigation of parameters involved and defects in the fabrication of Al–SiC nanocomposite using hot extrusion technique. Trans Indian Inst Metals 70:2361–2370
10. Senthilkumar R, Arunkumar N, Manzoor Hussian M (2015) A comparative study on low cycle fatigue behaviour of nano and micro Al_2O_3 reinforced AA2014 particulate hybrid composites. Results Phys 5:273–280
11. Da Costa CE, Zapata WC, Velasco F, Ruiz-Prieto JM, Torralba JM (1999) Wear behaviour of aluminum reinforced with nickel aluminide MMCs. J Mater Process Technol 92:66–70
12. Chandrashekar A, Ajaykumar BS, Reddappa HN (2018) Mechanical, structural and corrosion behaviour of AlMg 4.5/nano Al_2O_3 metal matrix composites. Mater Today: Proc 5:2811–2817
13. Shirvanimoghaddam K, Khayyam H, Abdizadeh H, Karbalaei Akbari M, Pakseresht AH, Abdi F, Abbasi A, Naebe M (2016) Effect of B_4C, TiB_2 and $ZrSiO_4$ ceramic particles on mechanical properties of aluminium matrix composites: experimental investigation and predictive modelling. Ceram Int 42:6206–6220
14. Baradeswaran A, ElayaPerumal A (2014) Study on mechanical and wear properties of Al7075/Al_2O_3/graphite hybrid composites. Compos Part B: Eng 56:464–471
15. Jayavelu S, Mariappan R, Rajkumar C (2018) Wear characteristics of sintered AA2014 with alumina and titanium di-Boride metal matrix composites. Int J Ambient Energy 1–6
16. Baskaran S, Anandakrishnan V, Duraiselvam M (2014) Investigations on dry sliding wear behavior of in situ casted AA7075–TiC metal matrix composites by using Taguchi technique. Mater Des 60:184–192
17. Wang Z-G, Li C-P , Wang H-Y, Zhu X, Wu M, Jiang Q-C (2016) Effect of nano-SiC content on mechanical properties of SiC/2014Al composites fabricated by powder metallurgy combined with hot extrusion. Pow Metall 59:236–241
18. Suresh S, ShenbagaVinayaga Moorthi N, Vettivel SC, Selvakumar N (2014) Mechanical behavior and wear prediction of stir cast Al–TiB_2 composites using response surface methodology. Mater Des 59:383–396
19. Kok M (2005) Production and mechanical properties of Al_2O_3 particle-reinforced 2024 aluminium alloy composites. J Mater Process Technol 161:381–387
20. Bodukuri AK, Eswaraiah K, Rajendar K, Sampath V (2016) Fabrication of Al–SiC–B_4C metal matrix composite by powder metallurgy technique and evaluating mechanical properties. Perspect Sci 8:428–431
21. Jayavelu S, Mariappan R, Rajkumar C, Surryaprakash D (2018) Study on microstructure, mechanical and wear characteristics of sintered AA2014 with alumina and titanium di-boride metal matrix composite. Int J Mech Prod Eng Res Dev 2018:125–130
22. Canakci A, Varol T(2014) Microstructure and properties of AA7075/Al–SiC composites fabricated using powder metallurgy and hot pressing. Pow Technol 268:72–79
23. Reddy MP, Ubaid F, Shakoor RA, Parande G, Manakari V, Mohamed AMA, Gupta M (2017) Effect of reinforcement concentration on the properties of hot extruded Al-Al_2O_3 composites synthesized through microwave sintering process. Mater Sci Eng: A 696:60–69
24. Alaneme KK, Sanusi KO (2015) Microstructural characteristics, mechanical and wear behaviour of aluminium matrix hybrid composites reinforced with alumina, rice husk ash and graphite. Eng Sci Technol, Int J 18:416–422
25. El-Kady O, Fathy A(2014) Effect of SiC particle size on the physical and mechanical properties of extruded Al matrix nano composites. Mater Des 54:348–353
26. Tan A, Teng J, Zeng X, Fu D, Zhang H (2017) Fabrication of aluminium matrix hybrid composites reinforced with SiC microparticles and TiB_2 nanoparticles by powder metallurgy. Pow Metall 60:66–72

27. Araz, ŞO, Çalın R, Pul M, Bican O, Okur O (2015) An investigation on the microstructure and wear properties of TiB_2 reinforced AA2014 aluminium alloy produced by vacuum infiltration. High Temp Mater Process 34:487–493
28. Rahimian M, Ehsani N, Parvin N, Baharvandi H (2009) The effect of particle size, sintering temperature and sintering time on the properties of Al–Al_2O_3 composites, made by powder metallurgy. J Mater Process Technol 209:5387–5393
29. Rahimian M, Parvin N, Ehsani N (2010) Investigation of particle size and amount of alumina on microstructure and mechanical properties of Al matrix composite made by powder metallurgy. Mater Sci Eng: A 527:1031–1038
30. Akhlaghi F, Zare-Bidaki A (2009) Influence of graphite content on the dry sliding and oil impregnated sliding wear behavior of Al 2024–graphite composites produced by in situ powder metallurgy method. Wear 266:37–45
31. Abdollahi A, Alizadeh A, Reza Baharvandi H (2014) Dry sliding tribological behavior and mechanical properties of Al2024–5 wt.% B_4C nanocomposite produced by mechanical milling and hot extrusion. Mater Des 55:471–481
32. Zhao G, Huang C, He N, Liu H (2017) Mechanical properties, strengthening and toughening mechanisms of reactive-hot-pressed TiB_2-SiC-Ni ceramic composites. J Ceram Sci Technol 8:233–242

A Novel Methodology of Enhancing Vehicle Safety Using a Safety Valve for Vehicle Wheels

T. Sundararajan, R. Muthuraj, P. Hariharan, and R. Srinivasan

Abstract The primary objective of this project is to use a supplementary valve for releasing the excess pressure in a tubeless wheel for commercial vehicles. The recommended cold inflation pressure for a wheel is 130–140 psi. During running conditions, the pressure increases as the temperature of the wheel increases. So, the PRV was designed in such a way that it must accept 20% of pressure rise in the tire due to heat produced during running conditions. The PRV was designed to open up at high tire pressure and to continue bleeding until it reaches a predetermined value. One of the supplementary issue which the PRV reduced is the wheel unbalance issue. The inflation valve adds up a mass in the wheel rim, which acts as an eccentric mass and requires a balance weight to solve the unbalance. Here, addition of PRV will reduce the amount of the external balance weight, since it adds up its own mass vertically opposite to the inflation valve.

Keywords Pressure relief valve · PRV · Blow down pressure · Spring stiffness

1 Introduction

In tubeless commercial vehicle wheels, over inflation of the tyre causes a lot of issues, like uneven tyre wear, lesser traction, flange bend, vibration issues, and including catastrophic failures like tyre bursts [1]. Prevention of over inflation is also an indirect

T. Sundararajan · R. Muthuraj · P. Hariharan (✉) · R. Srinivasan
Wheels India Limited R&D Center, Padi, Chennai, India
e-mail: hariharanofficialid@gmail.com

T. Sundararajan
e-mail: sundararajan_t@wheelsindia.com

R. Muthuraj
e-mail: muthuraj@wheelsindia.com

R. Srinivasan
e-mail: srinivasan_r@wheelsindia.com

N. Gascoin and E. Balasubramanian (eds.), *Innovative Design, Analysis and Development Practices in Aerospace and Automotive Engineering*, Lecture Notes in Mechanical Engineering, https://doi.org/10.1007/978-981-15-6619-6_45

method of preventing overload, thereby reducing the number of warranty issues for the company. So, in addition to the usual valve in the wheel which is used for inflation, an additional valve opposite to the inflation valve was employed, called the pressure relief valve (PRV) [1, 2].

This valve, which will be installed vertically opposite to the inflation valve, serves to enhance the safety of the vehicle by avoiding catastrophic failure like tyre bursts. Without overinflation, overloading becomes diffucult, and with a wheel having PRV, overinflation will be impossible. The PRV will be fixed to the wheel with a permanent seal to make sure that the warranty of the wheel and other auto components will become void if someone tried to tamper the same. The PRV was made in such a way that the design was simple, with low cost with little to no overall cost impact on the wheel.

2 Issues with Overinflation & PRV's Solution to the Same

Overinflation of wheels leads to uneven tire wear, with excessive wear at the center [3]. This creates a necessity to retread (or) to replace the tire more frequently than usual. The wheel–tire assembly serves as the primary suspension and shock absorbing system of the vehicle. With an overinflated tire, the said function of the component loses its complete potential, and steering vibrations happen. A properly inflated tire theoretically has line contact and practically has surface contact with the road. Overinflation theoretically has point contact and practically has very less surface contact with the road. This, besides leading to lesser traction, also reduces the braking effect on the vehicle. Also, at hazardously high pressure, the rim flange tends to bend, and catastrophic failures like tire bursts happen. PRV functions as a single-point solution to all the mentioned issues.

One of the supplementary issues which the PRV reduced was the wheel unbalance issue. The inflation valve acts as a point of higher mass compared to the other sectors of the wheel, which causes a static unbalance in the wheel. This unbalance will be usually corrected by an additional balance weight which will be clamped onto the front and/or rear flange. The fixage of PRV vertically opposite to the inflation valve reduced the unbalance, as the PRV partially balanced the additional mass of the inflation valve.

3 Mechanism of Working

The main advantage of the PRV is the simplicity of its design and working. The PRV fits in a hole of diameter which is equal to the diameter of the inflation valve [4]. The ultimate aim of the component is to release the excess pressure of the wheel, and so, the redundant parts were removed, and complete optimization was done. The PRV consists of a spring which is under compression and calibrated to the required value

of pressure at which the PRV should open. Initially, the blowdown pressure was too low, which was then corrected by tweaking the design of the PRV.

We know that the force exerted by the spring is given by the formula,

$$F_s = -kx \tag{1}$$

where 'k' is the spring stiffness and x is the displacement of the spring.

The required force necessary to overcome the force of the spring F_s is F_P, which must be greater than F_s.

However, the required force F_t must be given only by the tire pressure. Since pressure is given by the formula,

$$P = F_P/A \tag{2}$$

where A is the area of the hole in the valve which is exposed to the tire pressure. By tweaking the above parameters, the opening and closing of the valve can be determined.

4 Setup, Testing, and Validation

4.1 Setup

- An additional valve hole was made in the wheel, and the PRV was fixed in the wheel vertically opposite to the inflation valve.
- The wheel-tire assembly was caged inside an inflation chamber for safety.
- The wheel was inflated beyond the recommended inflation pressure to check the opening and closing pressure of PRV.

4.2 Testing for Pressure Release Start/Release Stop

Ten valves were tested with a simple device attached to the valve filled with soap solution. The opening and closing pressure was noted for five iterations for each valve (Fig. 1).

During running conditions, the heat which builds up in the wheel causes the pressure to increase. The recommended cold inflation pressure of the wheel is 130 psi, and the wheel has a marking which says, '140 PSI MAX (COLD).' Hence, the temperature rise during running conditions may bring the maximum allowance to 165 psi, so the PRV should be designed in such a way that even after the excessive release of air, the pressure should not drop below 165 psi so that when the wheel cools down, the pressure does not drop below 130–135 psi (recommended value).

Fig. 1 Measurement setup

This collectively infers that the PRV should not open below 180 psi and should not bleed below 155 psi.

However, the initial prototype testing had an opening PRV pressure of 180 psi and the PRV stopped only at 130 psi. Hence, measures to increase the blowdown pressure was taken to bring it up to 155 psi.

4.3 Testing for Unbalance

The dynamic unbalance of the wheel was checked before the installation of PRV and rechecked after mounting the PRV. The value of unbalance had a significant improvement in the wheel level inspection. This will reduce the amount of the additional balance weight which needs to be placed in a wheel-tire assembly while fitting in the vehicle.

5 Improvement Actions

5.1 Problem Statement

The blowdown pressure of the PRV is too low—130 psi, and it needs to be increased, such that the PRV does not release any pressure below 155 psi. This has to be done keeping in mind that this PRV is purely a mechanical device, and it operates entirely based on spring action, and it needs a tolerance range of 10 psi.

5.2 *Understanding the Existing Product*

5.2.1 Parts

A general PRV is composed of seven major parts, namely

(a) Body (which contains the core, spring, and 'O' ring)
(b) Nut (to tighten the valve)
(c) Core (which acts as the plunger)
(d) Spring
(e) Screw (to adjust the spring tension)
(f) Sealant ring
(g) 'O' ring.

5.2.2 Understanding the Functions of the Parts

(a) **Body (depicted as dark blue line in Fig. 2)**
The body of the PRV houses the core, the spring, the screw, the 'O' ring, and sealant ring. The sealant ring (movable) is attached to the core, and the 'O' ring is in the lower outer surface of the body to prevent air leaks from valve loosening (stationary). The body of the PRV has a diameter which is exactly same as the existing commonly used inflation valves V3-20-6 or V3-22-1. This measure was taken in order to make sure that no additional tool is required for piercing the valve hole in the rim during manufacturing of the wheel. The body of the PRV has external threads on it, to facilitate the nut. It has internal threads

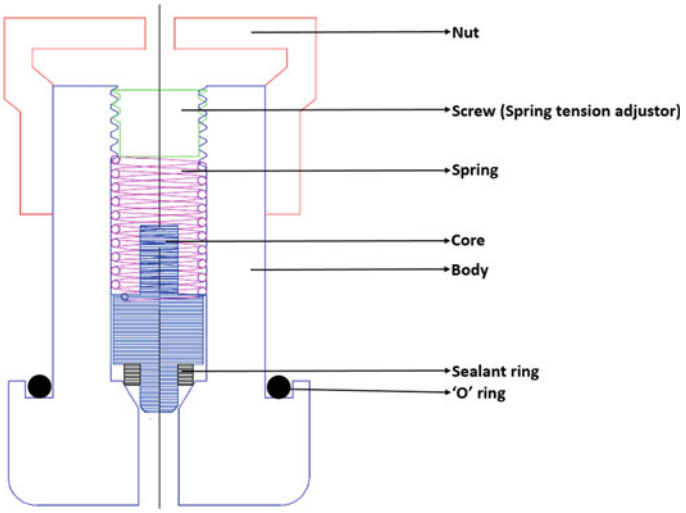

Fig. 2 Parts of a PRV

to house the screw, which is used to adjust the spring tension. It has an opening on one end which faces the pressurized tire.

(b) **Nut (depicted as red line in Fig. 2)**
The nut is used for tightening the PRV in the wheel rim, with a torque equal to 15–20 KN. The nut may be hexagonally indexed for easing spanner accessibility. The nut has a hole in the top to facilitate the exhaust of air through the same. The excess air pressure escapes through the hole in the body of the PRV and escapes though the hole in the nut toward the atmosphere.

(c) **Core (depicted as shaded gray-blue in Fig. 2)**
The core of the PRV is the only moving component of the valve. One end of the core has a plunger, in which sealant ring will be present. In this case, the sealant ring is made out of silicone to withstand high temperature. The plunger seals the valve on the inside, i.e., the valve end which is exposed to the tire pressure. The other end of the core contains the seating of the spring.

(d) **Spring (depicted as pink spiral lines in Fig. 2)**
The spring is located in-between the screw and the core. The spring provides the necessary tension to keep the core in position, and to push the core back after pressure drop. The spring in this PRV is made out of stainless steel, due to its excellent anti-corrosion properties.

(e) **Screw (depicted as green line in Fig. 2)**
The screw is located in the body of the PRV, in the topmost portion. The body of the PRV has internal threads in it, in which the screw rotates. The primary function of the screw is to adjust the spring tension, which determines the opening pressure of the PRV.

(f) **Sealant ring (depicted as shaded black in Fig. 2)**
The sealant ring made of silicone is located in the bottom side of the core. It firmly closes the opening of the PRV under spring tension during static conditions and when it re-establishes contact.

(g) **'O' ring (depicted as solid black in Fig. 2)**
The 'O' ring is used to prevent any air leak in fitment. This is similar to the function of an 'O' ring in any inflation valve.

5.3 Problem and Solution

5.3.1 Higher Area of Exposure in the Core Post Opening of PRV

Apparently, the core of the PRV exposes a higher area toward the tire after the PRV opens up. This is depicted in the picture and explanation below:

Figure 3 depicts a zoomed view of Fig. 2 in the opening region of the valve. The thick red line marks the total area exposed to the tire pressure prior to the opening of the valve. Let the area be A_1. When the tire pressure acts on this area, it produces a force F_{p1} on the core, which in turn causes a force F_{p1} to act on the spring. When

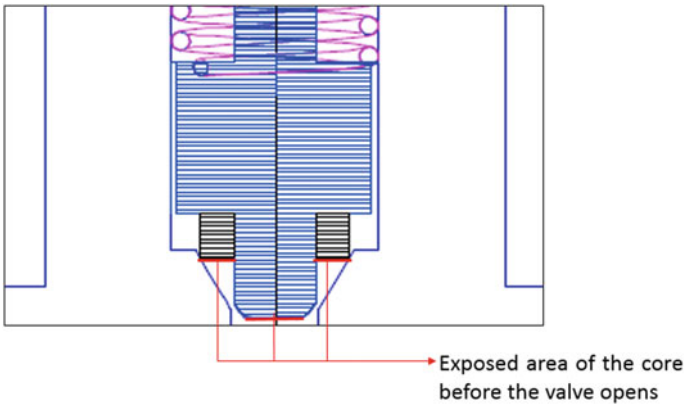

Fig. 3 Exposed area of PRV before the valve opens

the force F_{p1} is greater than the force produced by the spring tension F_s, the valve opens.

Once the valve opens, the core exposes a larger area of itself toward the tire pressure compared to the former (as depicted in Fig. 4). Let the area be A_2. Obviously, Since $A_2 > A_1$, the force acting on the core and spring F_{p2} will correspondingly be greater than F_{p1}. This means that a greater amount of force will now act on the core, and a higher spring force will be required to push it back to the original position. If this is not taken care of, the blowdown pressure will be too low, which is undesirable. Hence, reducing the area in which the pressure acts will bring down the blowdown pressure value.

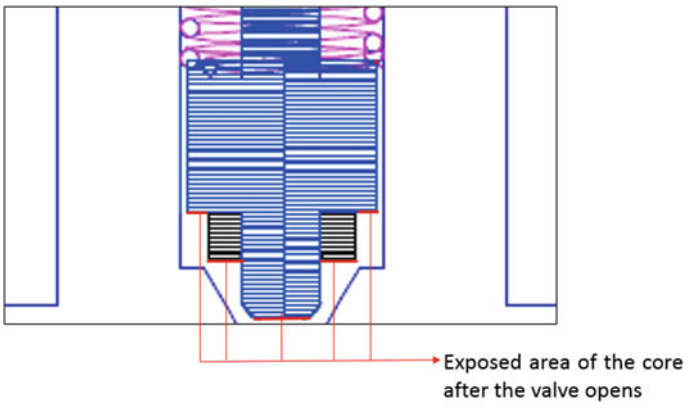

Fig. 4 Exposed area of PRV after the valve opens

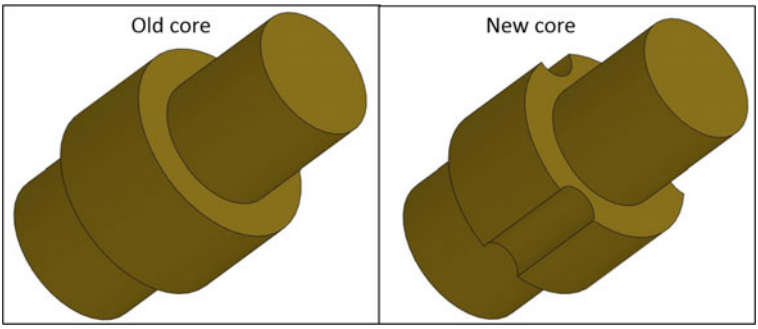

Fig. 5 Core of PRV—old versus new

5.3.2 Reducing the Area of Exposure in the Core

The new PRV's core had equiangular, semi-cylindrical grooving on it to reduce the area of exposure to the tire pressure even during the opening condition of PRV. Instead of this, an equiangular flat machining through indexing of the core can also be done to ensure the same result. The intention is to reduce the area of exposure, which can be done through multiple ways. The modified PRV was manufactured, and it gave the desired result by increasing the blowdown pressure to 155 psi. This also increased the flowrate of the air, resulting in a faster release of air compared to the former (Fig. 5).

6 Conclusion

The mentioned benefits of PRV not only enhances the safety of the vehicle, but also decreases the undue number of warranty issues for the company. The dynamic unbalance value of the wheel reduced, so the amount of additional balance weight also had a reduction in value. The effect on the area of the exposed core was also studied in detail. This valve, which is currently used in tubeless wheels, can be further extended to tubed commercial wheels.

References

1. CROSBY, Pressure Relief Valve Engineering Handbook, Practical Document No. TP V300
2. KLM Technology Group, Pressure Relief Valve Sizing and Selection (Engineering Guideline)
3. Selection and Sizing of Pressure Relief Valve, Randall W. Whitesides P.E
4. https://www.adamantvalves.com/the-mechanism-of-pressure-relief-valves.html

An Innovative Method of Preventing Bolt Hole Crack in Aluminium Wheels by Using Laser Peening Technique

T. Sundararajan, R. Muthuraj, R. Srinivas, and A. Hariprasad

Abstract The primary objective of this project is to increase the fatigue life of aluminium wheels and to prevent the fatigue failure of the wheel above the bolt hole region. In the testing and validation of wheels, the cornering fatigue test (CFT) plays an important role in deciding the stiffness of the wheel. In CFT testing, the wheel will be fixed in the bottom flange, and the bending moment will be applied, according to the load rating of the wheel multiplied by its corresponding test factor. CFT testing results of aluminium wheels showed crack above the bolt hole region in most of the cases. To prevent this mode of failure, and also to improve the fatigue life of the wheel further, it has been found that increasing the localized hardness above the bolt hole region will improve the fatigue life in CFT. Laser peening is a surface hardening technique by which the surface hardness of the material will be enhanced, along with which hardness and compressive residual stresses will be imparted on the surface in which the treatment is done. The depth of the high magnitude compressive stresses will greatly improve the material's resistance to fatigue failure. In aluminium wheels, laser peening was done circumferentially around the bolt hole region to induce localized compressive stress and increase the hardness in that area. The wheel in which laser peening was done was tested on CFT and showed a significant improvement in life.

Keywords Laser peening · Surface roughness · Hardness · Compressive residual stress · Cornering fatigue test (CFT)

T. Sundararajan · R. Muthuraj · R. Srinivas · A. Hariprasad (✉)
Wheels India Limited R&D Center, Padi, Chennai, India
e-mail: hariprasad_a@wheelsindia.com

T. Sundararajan
e-mail: sundararajan_t@wheelsindia.com

R. Muthuraj
e-mail: muthuraj@wheelsindia.com

R. Srinivas
e-mail: Srinivas_r@wheelsindia.com

N. Gascoin and E. Balasubramanian (eds.), *Innovative Design, Analysis and Development Practices in Aerospace and Automotive Engineering*, Lecture Notes in Mechanical Engineering, https://doi.org/10.1007/978-981-15-6619-6_46

1 Introduction

To induce compressive residual stress, there are various methods such as cold working, deep rolling, shot peening and so on. But one such recent and advance method is **Laser Peening (LP) or Laser shot peening**.

Laser peening is a surface engineering technique, which strengthens the component surface, where it is structurally vulnerable, without adding any material. Laser peening is a mechanical process that uses a high energy pulse laser beam to produce a plasma, that creates a shock wave where the surface that plastically deforms and improves the surface hardness. This process has a wide range of applications such as aerospace, defence, medical equipment, automobiles and so on.

1.1 Working Principle of Laser Peening

Before starting the process, surface should be applied with an opaque overlay (basically paint or a tape) and then a thin curtain of water should have flowed over the opaque overlay, where the water should be transparent to laser pulse. Then the required target should be hit by a high energy pulse laser beam. This beam passes through the water film and is absorbed by the opaque overlay and produces a plasma. In this condition, water will act as a tamping mechanism and magnifies the effect of plasma. Once the surface is blown, a shock wave will be produced on the surface, which gets plastically deformed which in turn increases the hardness and inducing compressive residual stress (Fig. 1).

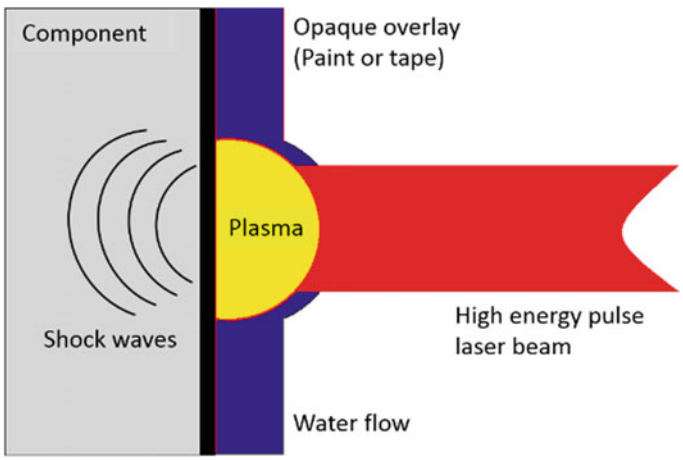

Fig. 1 Schematic diagram of the process

1.2 Problem Statement

In the validation of wheels, **Cornering Fatigue Test (CFT)** plays an important role in deciding the stiffness of the wheel. CFT will exactly simulate the loading effect on the wheel, during vehicle turning conditions. In CFT, the wheel (For this project forged single-piece aluminium wheel is used) will be fixed on the bottom flange and bending moment will be applied to the disc, according to the load rating of the wheel multiplied by its corresponding test factor (For test setup and loads ratings—SAE J267 international standard is referred). In CFT of Aluminium wheels, crack above the bolt hole region is the most common failure observed. To prevent this mode of failure and to improve the fatigue life of the wheel further, Laser Peening (LP) technique is used.

1.3 Wheel Used

Plenty of wheels are available with different sizes and materials in market. For this project forged aluminium single-piece wheel (AA6061-T6 material grade) of 8.25″ × 22.5″ size was employed. This type of wheels basically used in commercial vehicles such as trucks and buses (Fig. 2).

Fig. 2 Image of a forged aluminium wheel 8.25 × 22.5

Table 1 Chemical composition in wt% of material used

Si	Fe	Cu	Mn	Mg	Cr	Zn	Ti	Al
0.40–0.80	0.70 max	0.15–0.40	0.15 max	0.80–1.20	0.04–0.35	0.25 max	0.15 max	Rest

Table 2 Mechanical properties of the material used

YS (MPa)	UTS (MPa)	Elongation (%)	Density(g/cm^3)
255 min	290 Min	10% min	2.70

2 Materials and Methods

2.1 Materials

In aluminium, different types of grades according to its composition and heat treatment are available. For this project, **AA6061** grade and **T6** conditions were employed. This grade of the material was particularly chosen for its superior mechanical properties, better workability, excellent fusion characteristics and high resistance to corrosion. It also has a wide range of applications such as Aircraft, marines, electrical fittings, automobiles and so on.

The wheel is heat-treated (Solutionized + Quenched + aged) to achieve T6 condition. Below are the chemical and mechanical properties specification, which was achieved (Tables 1 and 2).

2.2 Methodology Employed

As discussed in Sect. 1.1, high energy pulse laser beam passes through the thin curtain of water and it is absorbed by an opaque overlay by producing a plasma. Once the surface is blown off, a shock wave will be produced on the surface, which will plastically deform the surface and in turn increase the hardness and inducing compressive residual stress. In our wheel, the surface above the bolt hole region was treated with LP to achieve surface hardness. Final Laser Peened (LP) treated surface is shown in Fig. 3.

3 Effect of Hardness at Laser Peened Region

To validate the process, surface hardness of the wheel is checked in two direction

1. On the surface of LP treated

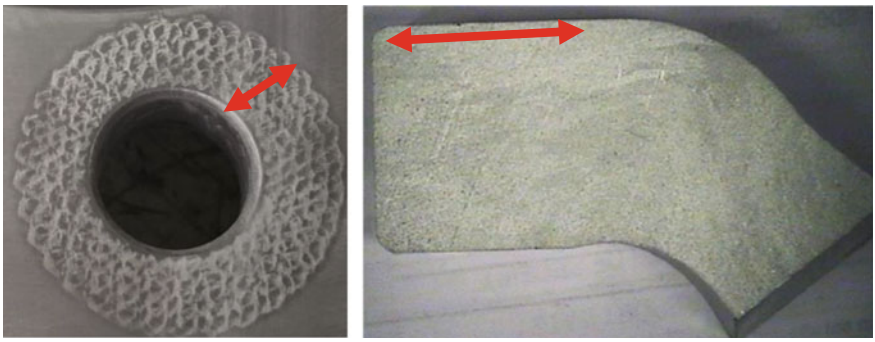

Fig. 3 Marked region is a laser peened surface

2. From LP treated surface to core (Fig. 4).

Below are the harness observed ●**along the laser peened surface (LP)** for a normal and laser peening treated wheel. For hardness checking Vickers hardness, HV at 1kgf was used.

Below are the hardness values observed from ✖**surface to core** for laser peening treated wheel. For hardness checking Vickers hardness, HV at 50 gm was used.

Figure 5 shows that the hardness above the bolt hole is higher for an LP surface.

Figure 6 shows that hardness value drops from LP surface to the core.

Microstructure of an LP surface reveals plastic deformation on the same. Figure 7 shows the comparison of microstructure between an LP surface and a normal surface of the same wheel.

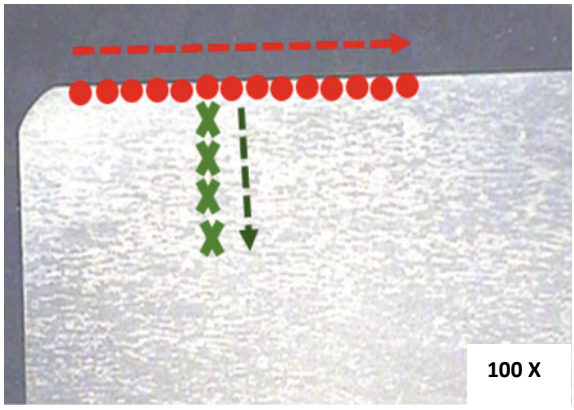

Fig. 4 Hardness inspection direction

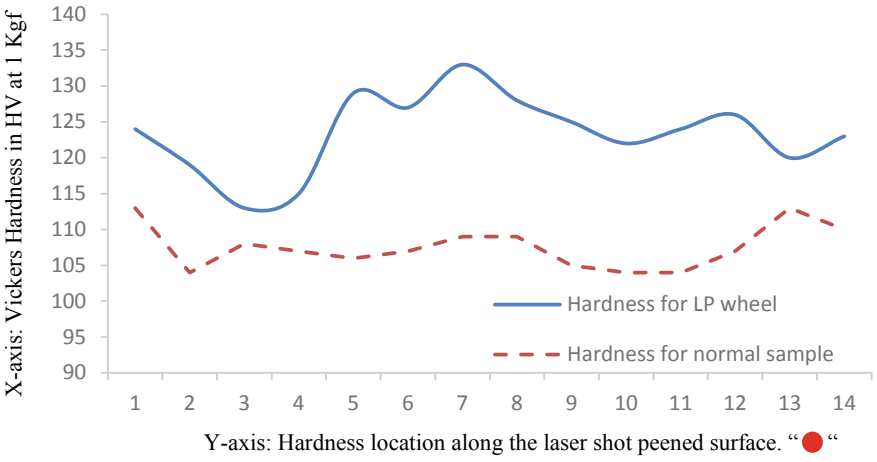

Fig. 5 Hardness comparison of normal surface and LP treated surface

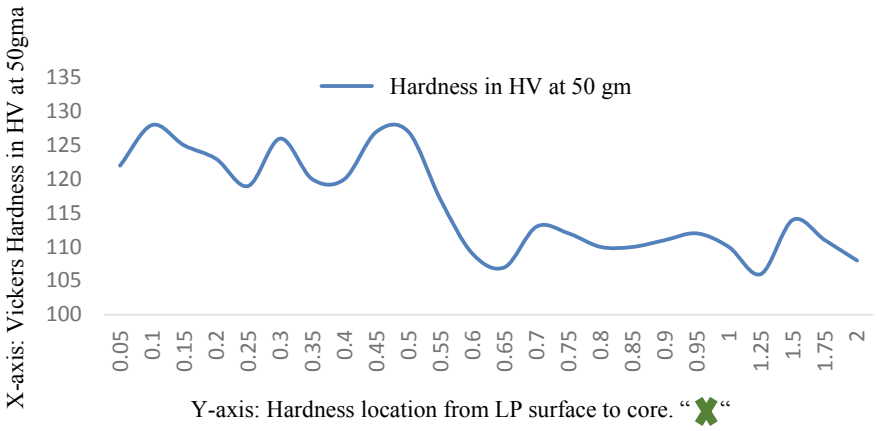

Fig. 6 Variation of hardness with depth at the laser peened (LP) surface

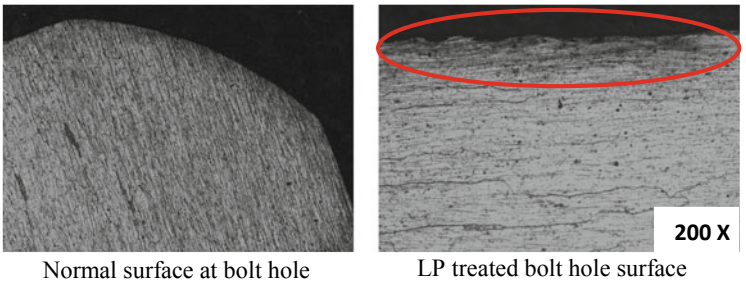

Fig. 7 Microstructure comparison of normal and LP treated bolt hole surface

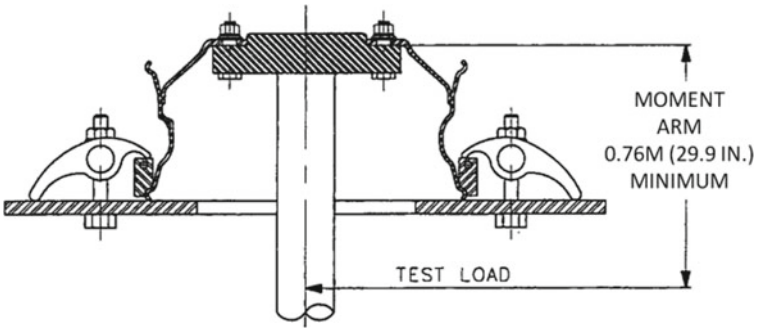

Fig. 8 Schematic representation of CFT test setup as per SAE J267 standard

4 Product Validation and Results Discussion

4.1 Cornering Fatigue Testing (CFT)

As discussed on Sect. 1.2, SAE J267 is used for test setup and bending moment calculation. The bottom flange of the wheel is held and a known mass attached eccentrically to the shaft, in its very bottom rotates with a given rpm, which will be equal to the calculated Bending Moment (BM) (Fig. 8).

4.2 Results of Cornering Fatigue Testing (CFT)

Bolt hole failure due to fretting is one of the common issues of forged aluminium wheels in the cornering fatigue test. But in laser peened product, even though fretting was observed, bolt hole crack was completely eliminated and fatigue life of the wheel significantly improved than the normal product, because of the hardness improvement above the bolt hole area.

5 Conclusion

The methodology described in this paper collectively gives an inference that Laser peening has prevented wheel crack above bolt hole. Laser peening has proved that, if high stresses are observed in highly localized areas, those areas can be treated with it, so as to achieve localized hardness. This method may also be extended to other areas of the high-stress location on the wheel rim to enhance surface hardness thereby improving the overall performance of the wheel.

References

1. Mostafa AM, Hameed MF, Obayya SS (2017) Effect of laser shock peening on the hardness of AL-7075 alloy. J King Saud Univ—Sci. http://dx.doi.org/10.1016/j.jksus.2017.07.012
2. Adu-Gyamfi S, Agyepong Boateng P, Asuako Larson E, Yamba P, Akayeti A (2018) Effects of laser shock peening on mechanical properties and surface morphology of AA2024 alloy. Am J Mech Mater Eng 2(2):15–20
3. Kulkarni A, Prabhakaran S, Chettri S, Kalainathan S (2018) Effect of Laser Shock Peening (LSP) Without Coating on the Surface Morphology and Mechanical Properties of Nickel Alloy. Int J Peen Sci Technol 1:87–98
4. Abdullahi K (2014) Gujba 1 and Mamoun Medraj: laser peening process and its impact on materials properties in comparison with shot peening and ultrasonic impact peening. Materials 7:7925–7974. https://doi.org/10.3390/ma7127925
5. Salimian A, Foroozmehr E, Badrossamay M (2015) Laser shock peening of Al 6061- T6 alloy, a theoretical and experimental study. Modares Mech Eng 15(7):73–79. (In Persian)
6. Troiani E, Zavatta N (2019) The E_ect of laser peening without coating on the Fatigue of a 6082-T6 Aluminum Alloy with a Curved Notch. MMetals 728
7. Ye C, Liao Y, Suslov S, Lin D, Cheng GJ (2014) Ultrahigh dense and gradient nano-precipitates generated by warm laser shock peening for combination of high strength and ductility. Mater Sci Eng A 609:195–203
8. Sathyajith S, Kalainathan S (2012) Effect of laser shot peening on precipitation hardened aluminum alloy 6061-T6 using low energy laser. Opt Lasers Eng 50(3):345–348
9. Amarchinta HK, Grandhi RV, Langer K, Stargel DS (2009) Material model validation for laser shock peening process simulation. Modell Simul Mater Sci Eng 17:015010–015016. [CrossRef]
10. Troiani E, Taddia S, Meneghin I, Molinari G (2014) Fatigue crack growth in laser shock peened thin metallic panels. Adv Mater Res 996:775–781. [CrossRef]

Lab VIEW and PID Action-Based Brake Lever Effect for Validation of Servo Vacuum Booster

A. Selwin Mich Priyadharson and S. Vinson Joshua

Abstract A servo vacuum, equally termed as power booster or power brake unit, utilizes vacuum to maximize the pedal action of the drivers and consequently to the master cylinder. In manufacturing of this equipment, companies have established several strategies. Such methods are designed to eliminate the potential defects, failure, or malfunction of the system. Therefore, an effective approach, Laboratory Virtual Instrumentation Engineers' Workbench (Lab VIEW) and Proportional Integral Derivative (PID) based real-time verification of servo vacuum booster is built to avoid failures in component testing in order to exclude components or parts that do not meet the required or defined requirements. The objective of this work is to test the servo booster using the already saved standard measures for an effective servo booster. A Lab VIEW simulation system to track servo vacuum booster output was developed. The pedaling motion is provided using the servo motor, operated by means of the control signal from PID controller, in real time to check the vacuum booster. The checked servo vacuum booster in the specified range is finally ready to mount in vehicles.

Keywords Lab VIEW · Power booster · PID action

1 Introduction

The evolution of braking systems began with brake heels, which are pressed against the wheel by a simple wooden block to slow down the vehicle's speed and its movement. The brake pedal feeling is exclusivity for the driver's trust and was discussed by Guan et al. [1]. It is mentioned that the performance of the vacuum booster occupies a unique place in study of the brake feeling. Because of its competence

A. Selwin Mich Priyadharson (✉) · S. Vinson Joshua
ECE Department, School of Electrical and Communication, Vel Tech Rangarajan Dr. Sagunthala R&D Institute of Science and Technology, Avadi, Tamil Nadu, India
e-mail: aselwinmich@veltech.edu.in

N. Gascoin and E. Balasubramanian (eds.), *Innovative Design, Analysis and Development Practices in Aerospace and Automotive Engineering*, Lecture Notes in Mechanical Engineering, https://doi.org/10.1007/978-981-15-6619-6_47

and conveniences than other braking methods, vacuum boosters brake systems were manufactured by several companies in series with mechanical drum brake.

It is mounted intermediate on the master cylinder & brake lever and minimizes driver's effort in braking. There twice spaces with movable rubber diaphragm built in a hollow frame.

To minimize the brake lever force, push rod servo vacuum booster with master cylinder is mechanically fabricated so as to increase the brake hydraulic pressure. Due to this high hydraulic pressure, less effort is enough in brake lever. The booster normally uses vacuum from the engine to increase the pressure on the accelerator. Braking is ineffective and difficult in conventional break systems during unexpected shut down of the automobile engine. While the booster open its air valve to move the master cylinder to the front automatically to manage dynamic stability in controlling the speed of the automobile.

A new electronic brake booster and precise pressure control method for technical engineering were discussed by Wua et al. [2] and the weaknesses in active braking for smart driving of existing braking systems is addressed. Those results illustrated the optimal performance of pressure, acceleration, and speed control. Mosayebi et al. [3] described the importance of designing and optimizing braking systems for various vehicles. The vacuum brake device, as with the air brake, is regulated or operated through a brake tube, as was described by Ugale et al. [4]. Muenchhof et al. [5] have designed a model that measures the vacuum chamber pressure and working chamber pressure of the vacuum brake booster. Anbalagan et al. [6] modified the vacuum braking system in light and heavy cars and the same has been tested for implementation. The brake pedal was designed by Mangukia et al. [7] to provide the necessary leverage and pressure to touch the four wheels.

A simulation model with Lab VIEW is developed for this work to monitor and validate the performance of the vacuum booster based on real-time PID speed control action. If the validated booster fulfills the required measurements which have been designed in the simulation model, it will be separated as effective without defects for further processing. In Lab VIEW software, the validated plot for the particular vacuum booster is obtained. Therefore, real effect of braking test based on PID action and validation by Lab VIEW simulation model for servo vacuum booster enables a healthy servo vacuum booster to be achieved.

2 Lab VIEW and PID Action in Vacuum Booster Verification

In order to get the real effect of braking, the brake lever action is simulated as that of PID action for controlling the speed. Since PID action is similar to that of braking action, it is well suited for this application of testing.

The PID speed control operation by the brake lever as actuator is denoted by the formula

$$U(s) = K_{\mathrm{p}}\left(1 + \frac{1}{T_{\mathrm{I}}s} + T_{\mathrm{D}}s\right)E(s) \tag{1}$$

where

$U(s)$ Control signal
K_{p} Proportional gain
T_{I} Integral time
T_{D} Derivative time and
$E(s)$ Error signal.

Parameters K_{p}, T_{I} and T_{D} were found in Ziegler Nichol's approach by means of tests in the built Lab VIEW-based simulation model for various speed conditions and is indicated in Table 1.

Lab VIEW is utilized to get inputs and also for the plot validation on Lab VIEW screens. The front and rear panels are available in Lab VIEW and in Fig. 1 servo performance which is in front panel is represented. It is with buttons such as sensor calibration, auto cycle, setting menu, and parameter entry is designed separately for enabling. These parameter is edited in the rear panel based on loops and clusters and plot is exposed as soon as "run" button is enabled in the front panel. Setting Menu, Sensor Calibration, Auto Cycle, Parameter Entry, Help, and Exit application are in front panel. Usual platform in the Lab VIEW front panel will be back by enabling

Table 1 PID parameters

Control loop	PID parameters		
	KP	KI	KD
Speed control	2	1.2	0.9

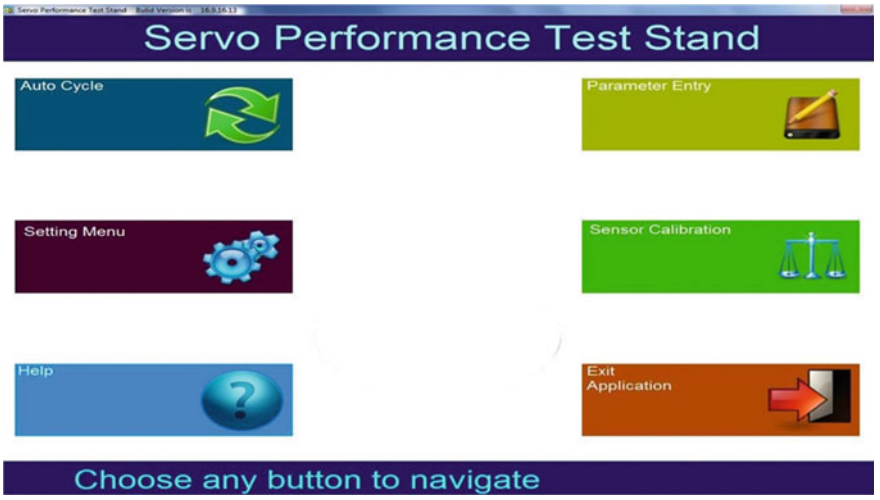

Fig. 1 Front panel—performance of the vacuum booster

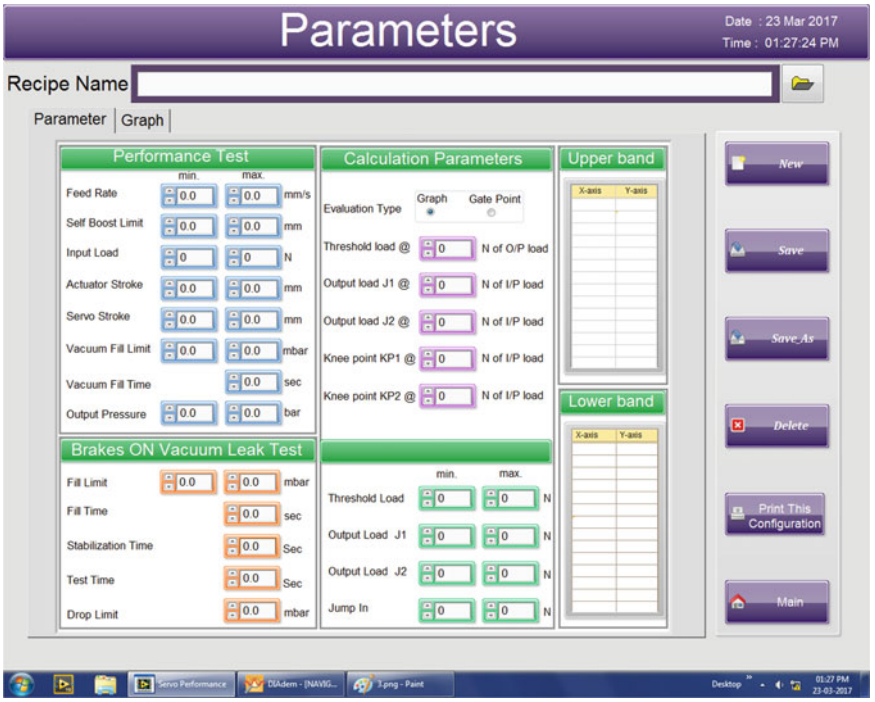

Fig. 2 Front panel of the vacuum booster—entering the parameters

auto cycle button. The Lab VIEW front panel is set for entering the parameters such as brakes ON vacuum leak verification, calculation parameters, and performance validation as shown in Fig. 2.

By setting menu application, the parameter can be edited. On the sensor calibration screen that appears in the front panel of the Lab VIEW, the measured pressure and torque values are displayed.

Values can be modified and saved by entering the parameter. Different companies will have different performance values, so that this parameter entry can modify them accordingly.

In this standardization, physical high, low quantities are established and actual value quantities will be indicated as in Fig. 3. Establishing physical max (high) & min (low) quantities and actual measured quantities for standardization is indicated. It displays the sensor type to be chosen. The pressure or torque is selectable by entering the Enum button and saving that one using a save button in Lab VIEW front panel. The max (high) as well as min (low) values of the physical quantity must be entered after selection as in Fig. 4. The final result is shown as a slope of the maximum and minimal quantities values.

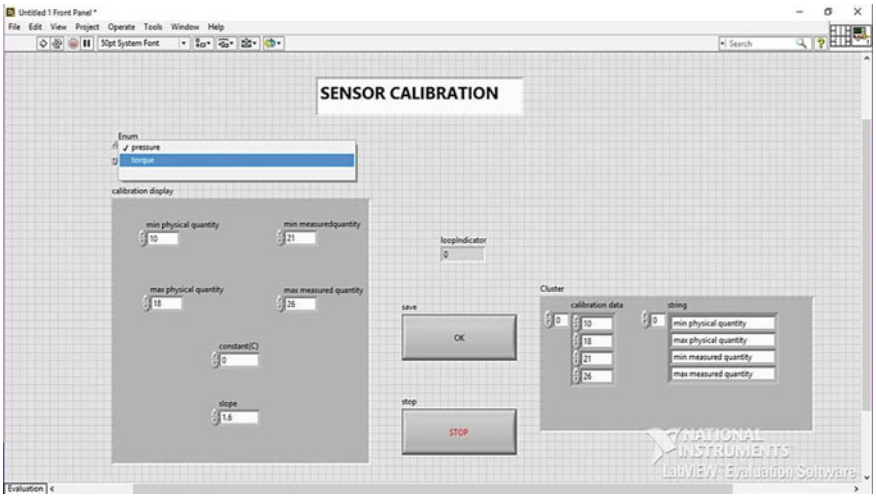

Fig. 3 Calibration of pressure sensor—Lab VIEW front panel

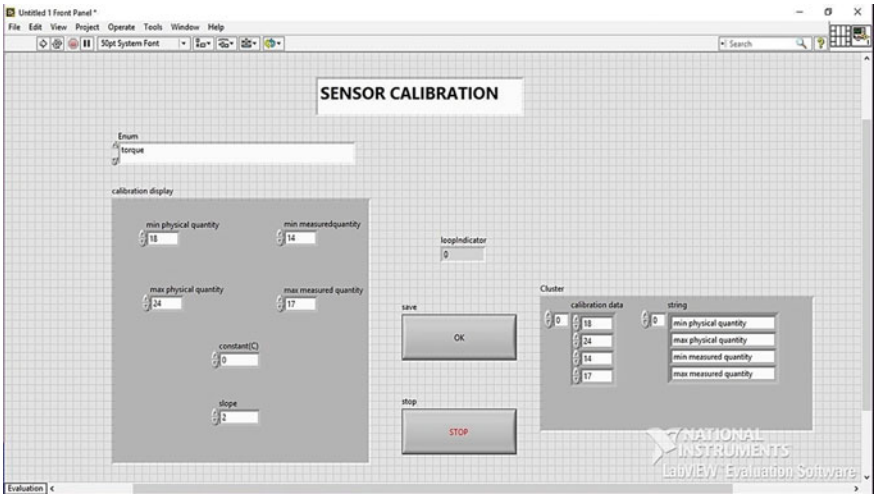

Fig. 4 Calibration of torque sensor—Lab VIEW front panel

The real effect of pedaling motion in brake lever is achieved by PID control action in the programmable logical control by using servo motor for the operation and testing of the vacuum booster.

Figure 5 is the block diagram of Timeout. A "case structure" and "while" loop are used in this block diagram. The time has provided 100 s for the event "case structure." It returns to its original position and runs continuously after 100 s, by using "while" condition. In addition to the "stop" button, numerical data are included in "case

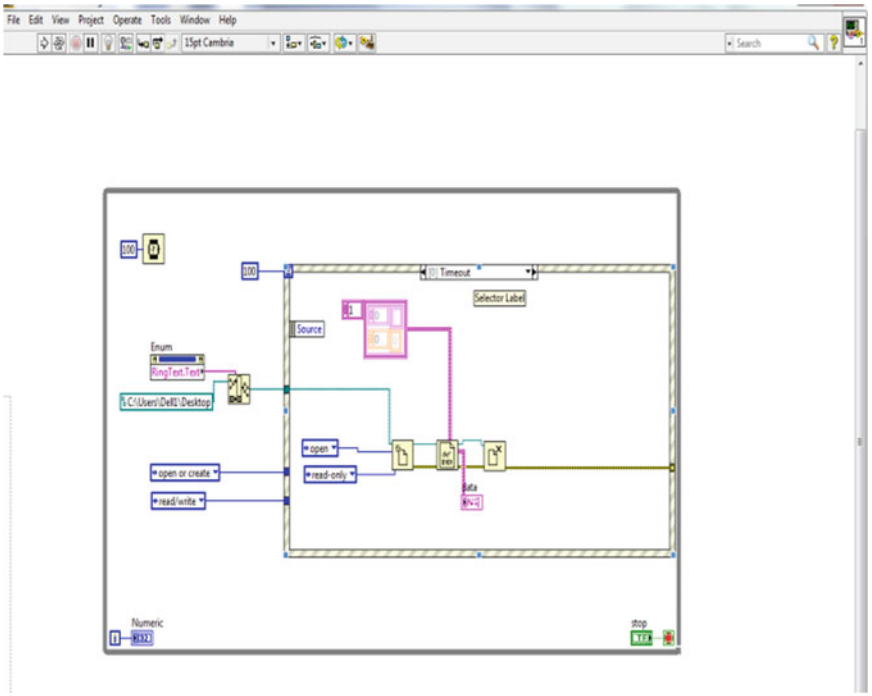

Fig. 5 Lab VIEW back panel representing "Time Out"

structure" below. Open and close data files are presented within the "case structure" event to open and close.

3 Outcome Assessment

The brake pedal action by means of PID action using servo motor is simulated and it is represented in Fig. 6.

The speed of the vehicle is simulated as getting down from 100 to 40 km/hr within 5 s because of braking effect by PID is utilized to test that particular vacuum booster. The performance is shown in Fig. 7 in the Lab VIEW window. To receive the plot input versus output, graph method is used.

A minimum and maximum sets of limits will be defined in the graph point system. A peak line is achieved after the run check. The output is justified in accordance with this line. If the graphically plotted line is in the middle of min (low) and max (high) values, then the booster is deemed as suitable and recommended to use; otherwise, it is excluded.

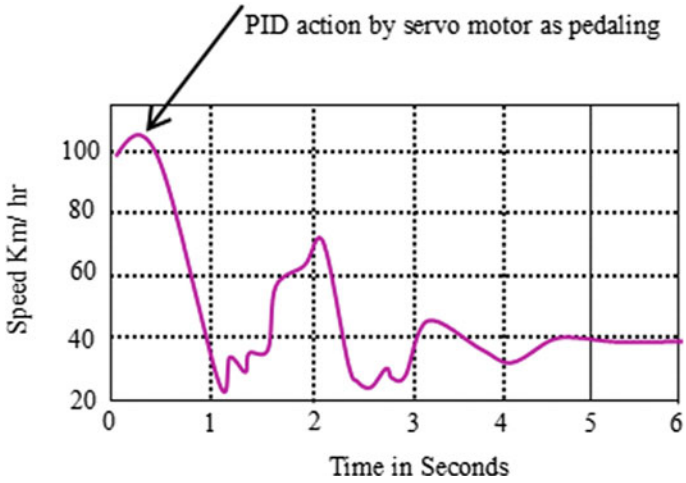

Fig. 6 Speed 100–40 km/hr

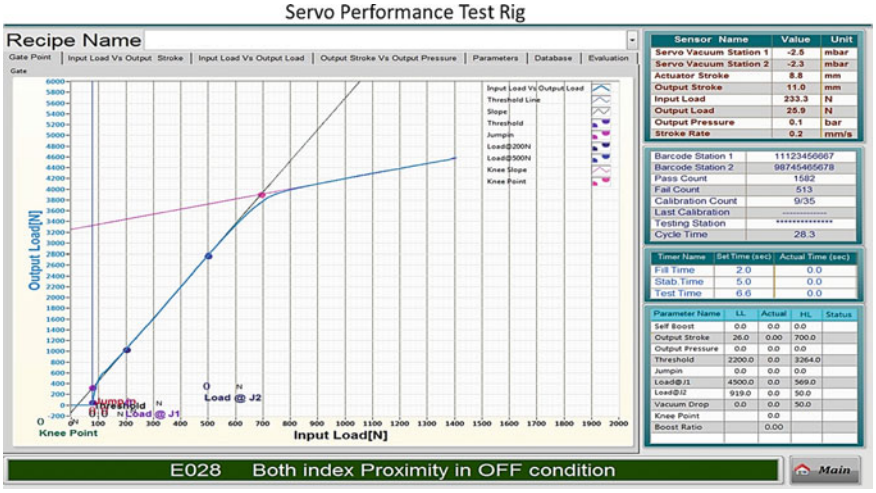

Fig. 7 Assessment of vacuum booster

4 Conclusion

The PID speed control action is simulated as that of the real effect of braking the lever. The lab VIEW simulation system, based on the performance test by means of PID speed control action in pedal, was developed for the efficient study and testing of the vacuum booster through several auto manufacturers. For programming, Lab VIEW technology is utilized. This Lab VIEW and PID action-based real effect

verification of servo vacuum booster will suggest manufacturers for ensuring efficient servo vacuum booster in dispose of flaws with which it can be mount in automobiles with more years of guarantee.

References

1. Guan H, Hao W, Zhan J (2013) A vacuum booster model for brake pedal feeling analysis. Adv Mater Res 622–623:1248-1252
2. Wua J, Chenb P, Zhaoa J, Heb R (2018) Active braking of an electronic brake booster facing intelligent automobile. Int J Perform Eng 14(8):1735–1744
3. Mosayebi J, Hooshmand A, AsadiGarmaroudi M (Iran) (2008) Simulation of hydraulic brake system components. 609(040):40–48
4. Ugale S, Rohmare B, Sadafal S, Dhat R (2018) Review of vacuum braking system. Int Res J Eng Technol (IRJET) 05(10):2854–2857
5. Muenchhof M, Straky H, Isermann R (2003) Model based supervision of a vacuum brake booster. IFAC Proc 36(5):429–434
6. Anbalagan R, Jancirani J, Venkateshwaran N(2013) Design and modification of vacuum braking system. Int J Eng Res Appl (IJERA) 3(3):907–916
7. Mangukia N, Mangukia N (2018) Design and fabrication of brake pedal for all terrain vehicle. Int J Eng Dev Res 6(2):562–568

Design and Development of a Cost-Effective Reloadable Motor for Sounding Rocket

Ravikiran, Mohd. Jawad Shariff, H. Kaushil, S. Likhitha, Nikhil Bhootpur, and Sreejith Mohan

Abstract A sounding rocket, also known as a research rocket, is an instrument-carrying rocket designed to take measurements and perform scientific experiments during its sub-orbital flight. This paper reports the design and fabrication of a reloadable motor with a reusable nozzle for an experimental sounding rocket. The motor can be retrieved after a flight using a parachute mechanism and hence the name reloadable. A mixture of sugar and Potassium Nitrate in a ratio of 7:13 was used as the solid propellant. The burning rate of the propellant was measured in open atmosphere and found to be 7.22 mm/s. The nozzle which is the functional part of the motor was robustly designed to yield the required thrust load for lifting the rocket. The throat diameter of the nozzle was estimated to be 8 mm corresponding to a thrust load of 688 N which could raise the rocket to an altitude of 1500 ft from the ground level. The time-dependent variation of thrust, pressure and propellant mass flow rate inside the combustion chamber was analyzed using the Meteor software. The pressure, temperature and velocity distribution within the nozzle were estimated through computational analysis using ANSYS fluent. The maximum velocity at the nozzle exit was found to be 2.86 M. Further, the cost-effective analysis of the proposed design was carried out in terms of the fuel and materials used for fabrication of the motor assembly.

Keywords Sounding rocket · Reloadable motor · Nozzle · Thrust load · Cost-effectiveness

Ravikiran (✉) · Mohd. J. Shariff · H. Kaushil · S. Likhitha · N. Bhootpur
The National Institute of Engineering, Mysuru, India
e-mail: nayak.ravikiran@gmail.com

S. Mohan
National Institute of Technology, Tiruchirappalli, India

N. Gascoin and E. Balasubramanian (eds.), *Innovative Design, Analysis and Development Practices in Aerospace and Automotive Engineering*, Lecture Notes in Mechanical Engineering, https://doi.org/10.1007/978-981-15-6619-6_48

1 Introduction

A sounding rocket is a small rocket capable of performing scientific and research experiments at altitudes well below the orbit [1, 2]. Model rockets are small prototypes of sounding rocket commonly made of wood, plastic and other lightweight materials. Regardless of the use of highly flammable substances and high travel speeds, the model rocketry still stands as a safe amusement and a great source of inspiration for infants and young scientists. Model rockets which combine different fields from aerodynamic design to pyrotechnics to the model building were difficult to be manufactured early [3]. Rapid technological advancements had outpaced this and presently these rockets are affordable as well as safe to fabricate. Model and high-power rockets are designed for safe recovery and repeated flight. To aid this, several methods are adopted, the most common of which is the use of parachute and streamer [4, 5]. A parachute recovery system is annexed to the nose of the rocket and is triggered by the ejection charge of the engine. This ensures the safe retrieval of the rocket motor [6]. This paper aims to understand the underlying principle of model rocketry. The primary objective of this work is to design and develop a cost-effective reloadable motor with a reusable nozzle for an experimental sounding rocket [7]. The nozzle which is a functional part of the rocket was carefully designed to generate the necessary thrust load for lift. The pressure, temperature and velocity distribution within the nozzle are evaluated through computational analysis using ANSYS fluent.

2 Materials and Methods

2.1 Solid Propellent

The solid propellant used in this study was a mixture of Potassium Nitrate (KNO_3) and sugar hereby referred to as KNSu taken in a ratio of 13:7. Prior to mixing, the powdered KNO_3 was baked in an oven for 20 min at a temperature of 250 °C in order to remove the moisture content. The method of dry compression was adopted for the preparation of propellent [5]. Initially, 35 g of fine sugar powder and 65 g of pre-heated finely ground Potassium Nitrate were carefully mixed by hand in a closed container to avoid self-ignition. The resultant white mix was then rammed into the aluminium motor with the help of a rubber mallet. Following this, a layer of bentonite clay was rammed to keep the fuel intact and a hole was drilled in it to allow for the expansion of fuel.

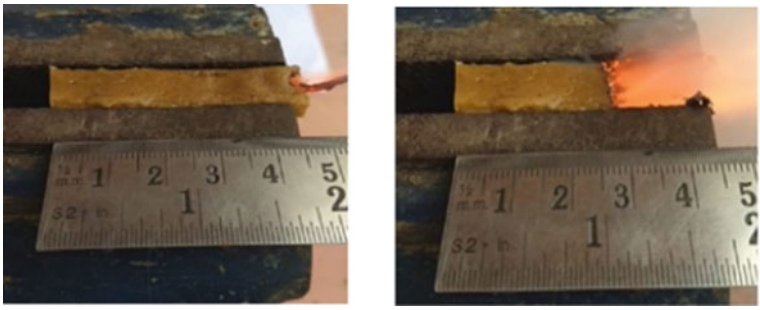

Fig. 1 Measurement of burning rate of propellent

2.2 Burning Rate Measurement

Figure 1 shows the process of measurement of burning rate. The samples of KNSu were prepared in the dimensions 50 mm × 12.5 mm × 5 mm using the dry heating method. İn dry heating method the white mix is heated with little water. When the mixture is heated the sugar melts and KNO_3 grain suspends. This mixture is heated until a paste is formed, which is then dried and a bar of the above dimensions is made. This was fixed in a vise and a graduated scale was placed adjacent to it to enable the measurement of the burning rate. All five faces of the sample were insulated using glue to ensure the unidirectional propagation of flame. The remaining face of the sample was covered with gun powder for rapid initiation of flame. For safety reasons, a fuse was used to ignite the powder. The burning rate of the propellant was estimated by measuring the time interval of flame travel between two arbitrary points. The burning rate was measured to be 7.22 mm/s.

2.3 Nozzle Design

The nozzle in the rocket does the process of transforming thermochemical energy into kinetic energy [8]. Suitable design of the nozzle is required to ensure optimum mass flow rate, exit velocity and exit pressure of the combustion gas. Selecting the combustion chamber radius (r_c) as 16 mm, the cross-sectional area of combustion chamber was obtained as 804.25 mm^2. Assuming the ratio of area of combustion chamber to the area of throat (A_c/A_t) as 16, the value of A_t was estimated as 50.26 mm^2. Hence, the radius of the throat (r_t) was calculated to be 8 mm. The ratio of cross-sectional area at the end of nozzle to area of cross-section at the throat section (A_e/A_t) was taken as 20. Considering this, the radius at the exit of the nozzle (r_e) was obtained as 17.89 mm. Assuming the divergent angle of the nozzle (θ) as 15° and the convergent angle (β) as 50°, the length of converging (L_{cn}) and diverging section

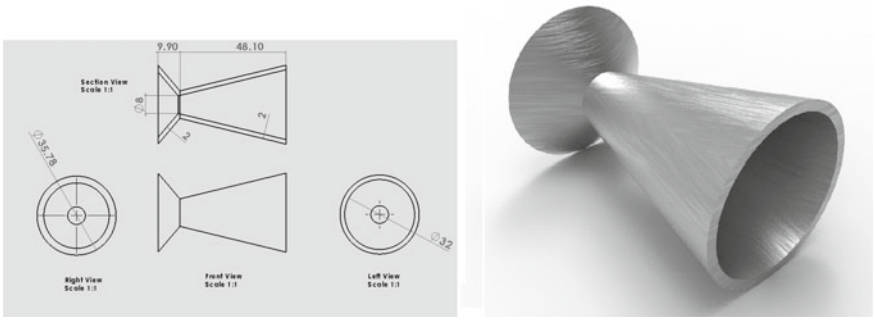

Fig. 2 Drawing and 3D model of the nozzle

(L_{dn}) of the nozzle were determined to be 9.9 mm and 48.1 mm, respectively. Figure 2 shows the drawing and the 3D model of the nozzle created using SOLIDWORKS.]

Inorder to analyze the pressure, temperature and velocity distribution within the nozzle, a 2D finite element model of the nozzle was created in ANSYS. The inlet gauge pressure was fixed at 6.3×10^5 Pa and the outlet gauge pressure was fixed at 0 Pa. Further to analysis, the nozzle was fabricated out of aluminium using the CNC machining process.

2.4 Evaluation of Motor Performance

Inorder to evaluate the motor performance and establish its specifications, the Meteor software was used. By specifying the type of propellant, nozzle dimensions and grain dimensions as input parameters, the time-varying thrust, mass flow rate, KN and chamber pressure curves were generated alongside the total thrust time. Figure 3 shows the results of the analysis.

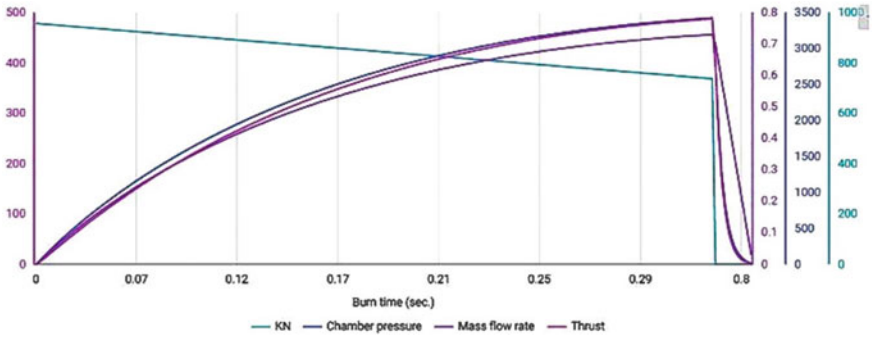

Fig. 3 Variation of KN (65 g), chamber pressure, mass flow rate and thrust with burn time

Table 1 Specification of motor

Parameter	Values
Motor class	G158
Thrust time, s	0.99
Total impulse, Ns	156.20
Specific impulse, s	141.92
Maximum thrust, N	688
Average chamber pressure, MPa	15.7
Launch mass, g	225
Empty mass, g	125
Length of the motor, mm	185
Diameter of the motor, mm	33.02

Based on the above variations, the specifications of the motor were selected as shown in Table 1.

2.5 Rocket Modelling and Flight Simulation

The components of the rocket were modelled and assembled in Open Rocket Simulator software. The rocket was modelled to have the least drag co-efficient and maximum stability (without making it overstable). To improve the stability, material was added at the nose and the fin areas without affecting the drag co-efficient much. The total drag co-efficient of the rocket was found to be 0.94 and its stability was 1.55 cal well within the acceptable range of is 1.5–2 cal. The component analysis for drag characteristic is as shown below (Fig. 4).

Fig. 4 3D model of the model rocket

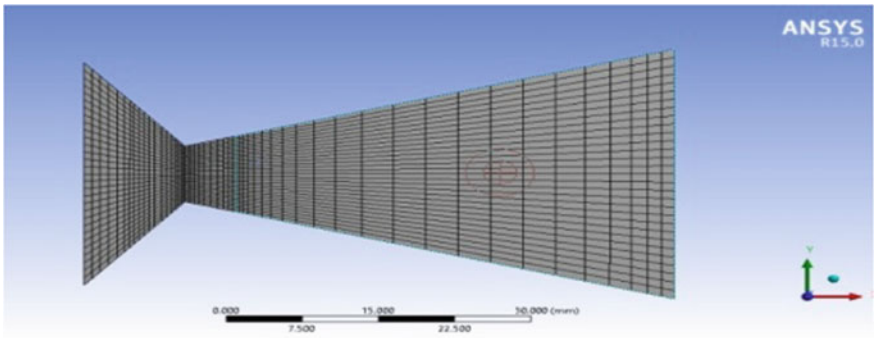

Fig. 5 Meshed geometry

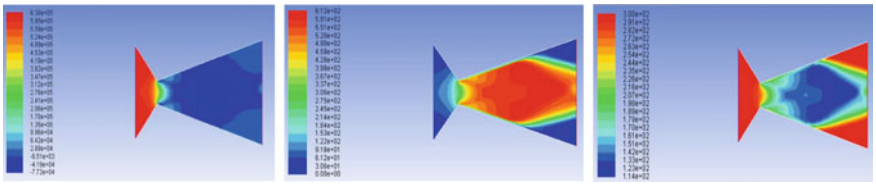

Fig. 6 Pressure, temperature and velocity contours inside nozzle

3 Results and Discussion

3.1 Nozzle Analysis

The nozzle model was created in ANSYS and analyzed for pressure, temperature and velocity variations as discussed in Sect. 2.3. Figure 5 shows the meshed view of the nozzle model. The results of post-processing are shown in Fig. 6.

As seen in Fig. 6 the pressure and temperature were maximum at the inlet of the nozzle and gradually decreased towards the outlet. On the contrary, the velocity was minimum at the inlet and increased towards the outlet. The velocity was found to be 1 M at the throat and 2.86 M at the outlet of the nozzle corresponding to the choked flow condition. The final fabricated model of the nozzle along with the motor casing weighed 225 g.

3.2 Thrust Force and Altitude

The thrust force of the motor was measured after mounting it inside a paint box and keeping it upside down in a weighing balance. The thrust force due to fuel ignition

Fig. 7 Rocket model and flight

was recorded to be 688 N. With this thrust force, the rocket reached an altitude of 1500 ft. The rocket model fabricated in this study and its testing is shown in Fig. 7.

3.3 Cost Analysis

A detailed cost-effective analysis of the developed rocket motor was carried out in order to enable its commercial production. The analysis showed that the total cost for preparing a considerable quantity of propellent mixture (KNSu) was as much as Rs. 1000/- which could fill at least eight motors. The total cost for a single unit of motor was found to be Rs. 500/- (approx.) which includes the cost of nozzle and barrel. Table 2 shows the cost incurred in reloading the motor after the first launch. As seen from the figure, the cost related to reloading of the motor is only Rs. 40/- (approx).

4 Conclusions

This paper was aimed at the design and development of a cost-effective reloadable motor for an experimental sounding rocket. The nozzle of the motor was carefully designed following finite element simulations. The thrust force developed from the motor was found to be 688 N and with this, it reached an altitude of 1500 ft above the ground level. Finally, a cost-effective analysis of the motor was carried out and it

Table 2 Cost to reload the motor after first launch

Sl. No.	Final product	Product used	Qty (g)	Cost (Rs)	Total (Rs)	Quantity produced (g)	Quantity utilized (g)	Actual cost (Rs)
1	White mix	KNO_3	65	32.5	33.9	75	75	33.9
		Sugar	35	1.4				
2	Delay mix	White mix	20	6.78	7.68	23	13	4.34
		Baking Soda	3	0.9				
3	Kitty Litter	Kitty Litter	25	1.5	1.5	25	25	1.5
4	Gun powder	Charcoal	75	0	11.2	100	2	1.0
		KNO_3	15	7.5				
		Sulphur	10	3.7				
5	Barrel and nozzle for motor							460
Intial cost per motor (Rs.)								500.63
Cost to reload the motor (Rs.)								40.74

was noted that the motor could be reloaded for every flight at a nominal cost of Rs. 40/-.

Acknowledgements The authors profusely thank the Head of the Department, Mechanical Engineering and the Principal of The National Institute of Engineering, Mysuru for providing the necessary support and facilities for the smooth execution of this work.

References

1. Laura NM, Krus P (2018) Sounding rockets: analysis, simulation and optimization of a solid propellant motor using Hopsan. Transp Res Procedia 29:255–267
2. Seibert G The history of sounding rockets and their contribution to European Space Research. ESA Publications Divisions
3. Tizón JM (2015) Motores Cohete. Apuntes y Trasparencias (Rocket engines. Notes and slides); Polytechnic University of Madrid Richard Nakka's Experimental Rocketry website; 2016; http://www.naka-rocketry.net
4. Eringen AC, Liebowitz H, Koh SL, Crowley JM Mechanics and chemistry of solid propellants. Ed. Pergamon Press
5. Singh DA Sugar based rocket propulsion system-making, analysis & limitations
6. Davenas A (1992) Solid rocket propulsion technology. Ed. Pergamon Press
7. Durojaye RO, Adefuye OA, Nurudeen A, Oyetunji EO Design analysis of mild steel combustion chamber for a sugar base propellant of a solid rocket motor
8. Washington (1969) Space Handbook: astronautics and its applications. United States Government Printing Office

Challenges in the Design of Safe Handling System for Explosive Dust

Nagababu Kurakula and Elangovan Muniyandy

Abstract Powders manufacturing industries have been growing significantly for the past few decades due to their economic benefits of producing net-shaped or near-net-shaped components compared with conventional metal-working methods. The incidents related to fires and explosions due to powders are unfortunately regular occurrences throughout the world with many injuries to severe injuries and fatalities every year. It is observed that 30% of the industrial accidents are occurred due to dust explosions and also happened in the dust collection systems. But there are no explicit studies carried out on the handling of explosive dust, which are potentially hazardous with their sensitivities viz., friction, heat, vibration, and impact and static. Since these are uncommon materials used in the industries; no reliable data has been established for the safe handling of explosive dust by different dust collectors. Aerospace and military industries are operating the explosive materials for different applications. Dust is generated during the manufacturing of various components of the rocket for space applications. Explosive machining is one of the critical operations in rocket production. Dust generated during explosive grain machining shall be properly collected and carefully handled to mitigate the associated potential risks. In order to meet this challenging task of collecting highly hazardous dust, a safe and healthy collection extraction system is inevitable. To address the above challenge, a suitable dust collection system is designed by considering various critical parameters. System worthiness for safe handling of dust is verified using risk control technique ETA. The designed system minimizes the manual cleaning and provides provision for easy maintenance. This paper deals with the challenges in designing a suitable collection system for explosive dust and verification its worthiness using ETA.

N. Kurakula (✉) · E. Muniyandy
Vel Tech Rangarajan Dr. Sagunthala R&D Institute of Science and Technology, Chennai, India
e-mail: Nag14577@gmail.com

E. Muniyandy
e-mail: drmelangovan@veltech.edu.in

N. Gascoin and E. Balasubramanian (eds.), *Innovative Design, Analysis and Development Practices in Aerospace and Automotive Engineering*, Lecture Notes in Mechanical Engineering, https://doi.org/10.1007/978-981-15-6619-6_49

Keywords Fire · Explosion · Accident · Explosive dust · Hazard · Dust collector · Design

1 Introduction

Explosive grain machining is one of the critical activities associated in the manufacturing of rocket components. Machining is carried out when the explosive is in its solid-state. Since the explosive materials are highly energetic and dangerous, special features and auxiliary equipment shall be adapted. Machining is associated with the generation of many kinds of chips and ribbons based on the material being machined, type of operation and cutting parameters therein selected. During the explosive machining also different kinds of machined out chips are anticipated. These shall be properly collected and carefully handled in order not to have any unforeseen, undesirable and unfortunate occurrence during the process of machining. For attempting this precise requirement of careful collection and appropriate handling of the machined out chips, it is essential to have a suitable dust extraction system in the close proximity of the machine. The dust collection system shall be composed of functionally a good combination among the available industrial dust-collecting devices. Gravitational settler, cyclone separator, scrubbing unit, electrostatic separator and bag housing type filters are commonly used dust-collecting devices used in various process industries to collect the produced dust therein.

2 Methodology

For attempting to design a dust handling system for the intended purpose, it is proposed to make a thorough study that paves the strong way to materialize a healthy system that can combat the associated hazards in a systematic manner and eliminate corresponding risks. The methodology of doing the current work is as follows (Fig. 1).

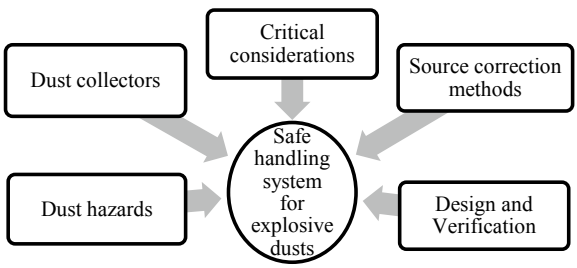

Fig. 1 Schematic structure of work plan

3 Design of Explosive Dust Extraction System

During the pre-design phase, various hazards associated with explosive dust are considered. All process industry accidents fall under three broad categories-fire, explosion, and toxic release. Out of these three, fire is the most common occurrence in the industries. Within this broad category there occur subcategories, each depicting a specific sub-type of fire/explosion/toxic release. A bewildering variety of accidents occur in various process industries during storage, manufacture and transportation of different hazardous and toxic chemicals [1]. These accidents range from minor innocuous leaks to catastrophic releases, barely noticed tiny sparks to all-consuming fires and plop of a bubble to earth-shattering explosions [1].

It is a mechanical system designed with the right combination of different dust-collecting devices to suit the particular material dust with the highest efficiency. The basic mechanisms of removing particulate matter from gas steams in dust collection systems are gravitational settling, centrifugal impaction, inertial impaction, direct interception, diffusion, electrostatic precipitation. Owing to the safety aspects and functional requirements in the explosive handling areas the combination of dust collectors is gravitational settling chamber, cyclonic chamber, scrubber and bag filter are chosen for the extraction system.

Though the concept for dust collection looks simple, things can go wrong if careful attention is not paid to the details. There are four key components in any dust collection system filter, piping, pick up hood and air mover [2]. Dust collection system components for various applications can be manufactured excellently that can do their "intended job" but the key to a dust collection system is to get the system components to work well together in a cohesive manner [2]. Dust that generates at a point source is pulled into pick up hood that is the start of dust extraction system. Air flow through the hood can be controlled either by blast gates or by pipe/duct sizing. The dust collector operates either by inertial or physical barrier, means, for example, a cloth "sock" or fabric or sintered metal, to retain the particles while the air leaves to the air mover. The heart of the dust collection system is the air mover and the filter combination [2, 3]. The symbiotic relationship between these two components is important; for instance, if the filter is clogged with dust, the fan (air mover) performance will likely be reduced and can cause major system problems [2]. Based on the expertise gained by the experts in the field of industrial dust collection systems design and operations, design of a proper dust collection system may be broken down to the following pivotal considerations.

- Adequate conveying velocity
- System balancing with the design
- Selection of correct air mover
- Prevent flow hindrances/plugging
- Selection of right component for collection
- Understanding on dust hazards.

During the design of an efficient dust collection system for any application either to control the air pollution or to prevent the dust posing accidents in the industries, it is wise to control or minimize their emission at the source itself. In case of industrial dust, this can often be achieved by investigating various approaches at an early stage of process design and development and selecting those methods which do not contribute to undesirable dust generation. These are known as source correction methods. Application of these methods to existing plants is difficult, but still some of these correction methods could be applied without severely upsetting economy of the operation. Control of the dust at the source can be accomplished in several ways of source correction methods as follows:

- Raw material changes
- Operational changes
- Modification/replacement of the existing process equipment
- More effective utilization of existing equipment.

Prioritzing all necessary key considerations required for safe handling of explosive dust a collection system is designed in analytical approach by assuming a suction air mover instead of a positive air mover. With the suction air mover, the tendency of accidents is very less during the handling of the hazardous dusts.

Event tree analysis (ETA) is quantitative risk control technique that is applied to the designed system and verified the safety adequacy of the system throughout and of entire operating conditions applicable for the explosive machining process [4, 5]. It is inferred that the designed system is adequate to cater to the safety requirement of dust collection system during explosive grain machining in aerospace as well as defence applications.

4 Basic System and Components

Explosive dust collection system is freezed to be a group of (i) Gravitational settling chamber, (ii) Cyclone separator, (iii) Wet scrubber and (iv) Bag hosing filter. In addition to that systems, diving system (Vacuum air mover), Computer numerical control to have automatic interface with the dust collection system with the machine tool in order to operate it in a non-local mode to comply with the safety requirement of potentially hazardous material machining.

5 System Life Cycle Verification

The system is verified for its safe performance under the appropriate conditions and recorded the benefits that manual intervention is avoided by adapting a mechanical tilting arrangement of gravitational settling chamber as it is the major quantity collecting chamber almost of 300 kg material as per the designed size. L/D ratio at

different heights are freezed to increase the performance of the cyclone unit. Different water levels in scrubber are suggested for machining different material that shows its versatility. In place of bag filter, with the use of cartridge type filter, mechanical simplicity and easy maintenance are achieved. By adapting vacuum driving force the probability of occurrence of incidents is minimized significantly. Using the ETA technique, the system is verified for all possible causes of hazards.

6 Conclusion

Machinng of explosives is an interesting and unique technical art as it needs concerted efforts from engineering and safety domains in order to achieve the intended objective. This paper attempted with primary concepts to execute the safe design of explosive dust extraction system and verifying the design with the ETA technique. There is a vast provision to make a further study for the researchers to exploit insights to reach greater ends in this particular field.

References

1. Abbasi T, Pasman HJ, Abbasi SA (2009) A scheme for the classification of explosions in the chemical process industry. J Hazard Mater
2. Maynard E, Jenike & Johanson (2018) Six key considerations for proper dust collection system design. A technical article from Powder and Bulk Engineering (PBE)
3. Krbec J, Stevenson B (2014) How to prevent dust explosion in your dust collector. A technical article from Powder and Bulk Engineering (PBE)
4. C Ericson (2005) Hazard analysis techniques for systems safety. Wiley
5. Kumamoto (1996) Probabilistic risk assessment and management for Engineers and Scientists

Risk Assessment on Storage and Handling of Highly Toxic Chemical in Rocket Industry

P. Srinivas and Muniyandy Elangovan

Abstract In solid propellant manufacturing of the rocket industry, many chemicals are used, but among all Toluene di-isocyanate (TDI) is highly toxic and also recently the threshold limit value (TLV) was amended from 0.005 to 0.001 ppm by American Conference of Government Industrial Hygienists (ACGIH). The exposure to TDI occurs mainly through inhalation of vapors at workplace and storages; hence, TDI is to be carefully handled due to its toxic nature which affects human health and environment; therefore, spillage of Toluene di-isocyanate causes adverse effects, so utmost care should be taken to avoid human exposure to the toxic vapors. Due to industry demand, in processing of solid propellant, large quantity of TDI was used as curator, which will be in the form of containers stored in bulk in designated storage rooms of the order 8–16 tons. Any major spillage/leakage in this store may affect the plant personnel as well as nearby residential area people in this paper; we evaluated the TDI evaporation rate and concentration level at residential area locations by ALOHA software and as per the Acute Exposure Guideline Level (AEGL) or Emergency Response Planing Guidelines (ERPG), and by this, we found that at 5000 m no significant concentration. At the same time, for the processing of solid propellant, various methods of TDI handling require the usage of different types of valves, hoses, and pipe fittings. Further, the failure modes of these handling components can lead to TDI spill/leakage and evaluated the exposure concentration level for that spills by using different hazard identification techniques. With the results, we conclude that the concentration is within the acceptable range by applying risk control measures.

Keywords Toluene di-isocyanate · Threshold limit value · Spill · Hazard · Toxic chemical

P. Srinivas · M. Elangovan (✉)
Mechanical Department, Vel Tech Rangarajan Dr. Sagunthala R&D Institute of Science and Technology, Chennai, India
e-mail: mmeikandan@veltech.edu.in

N. Gascoin and E. Balasubramanian (eds.), *Innovative Design, Analysis and Development Practices in Aerospace and Automotive Engineering*, Lecture Notes in Mechanical Engineering, https://doi.org/10.1007/978-981-15-6619-6_50

1 Introduction

In rocket industry for solid propellant manufacturing, various chemicals are used along with raw material ingredients in which Toluene di-isocyanate (TDI) is highly toxic chemical as exposure to Toluene di-isocyanate causes chronic respiratory problems, which may be development of asthma [1]. Asthma once induced and person become sensitized to a di-isocyanate, and even concentration much below the permissable exposure limits is sufficient to induce an asthmatic affect.

The storage and handling of TDI is very critical, spillage or any accidental release of TDI may affect the site-working people as well as near by residential colony people, and hence, suitable risk control system is to be adopted after hazard identification by ALOHA software for TDI storage area. Areal location of hazardous atmosphere (ALOHA) is a software designed to evaluate the toxic cloud dispersion from major chemical spillages and also ALOHA used to estimate radiation zone for fires and explosion zones. At TDI handling and process area, various components like different bins, valves, hoses, and pipe fittings will be used in this area. Failure-mode effect analysis (FMEA) is best method for hazard analysis, and by applying suitable risk control mechanism, we can prevent the toxic vapor release from process area.

2 Methodology

2.1 Storage Area

Risk assessment in storage area was evaluated by using Public Exposure Guidelines in ALOHA software, and Public Exposures Guideline are generally used to predict the effect on members of the general public, if they are exposed to a particular hazardous chemical in an emergency response situation.

2.1.1 Types of Public Exposures Guideline Are

- AEGLs—Acute Exposures Guidelines Level
- ERPGs—Emergency Responses Planing Guideline
- TEELs—Temporary Emergency Exposures Limit.

Above exposure guidelines has three tiers of exposure values for each chemical, and they are:

- Tier I—Momentary, minor effects
- Tier II—Unable to escape due to impairment and disabling effects
- Tier III—Life-threatening effects.

These three-tiered guidelines can be used as toxic level of concern (LOC), while modelling a toxic chemical release in ALOHA [2]. By using LOCs, ALOHA generates a threat zone estimation, and it indicates red, orange, and yellow zones in which the red zone indicates the most hazardous LOC.

2.1.2 Acute Exposure Guideline Levels (AEGLs)

Designed to help general public (responders) deal with emergencies involving chemical spills or other catastrophic events where members of the general public are exposed to a hazard airborne chemical.

2.1.3 Emergency Response Planning Guidelines (ERPGs)

Designed to anticipate health effects from exposure to certain airborne chemical concentrations.

2.1.4 Temporary Emergency Exposures Limit (TEELs)

During an emergency situation, TEEL is designed to estimate the action of members of the general public at different concentrations of a chemical.

2.2 Handling/Process Area

For hazard identification at risk assessment at TDI handling/process area, many techniques available in which following are commonly used hazard identification techniques:

- What-if checklist
- Preliminary hazard analysis (PHA)
- Hazard and operability studies (HAZOP)
- Failure modes effect analysis (FMEA)
- Failure mode effect and criticality analysis (FMECA)
- Fault tree analysis
- Even tree analysis
- Layers of protections analysis (LOPA)
- Humans reliabilities assessment (HRA).

Among above, here, we are considering that failure modes effect analysis (FMEA) is suitable hazard identification method for TDI storage as this process area contains equipment, and FMEA is king in equipment and machinery area for hazard analysis [3]. FMEA process flowchart is shown in Fig. 1.

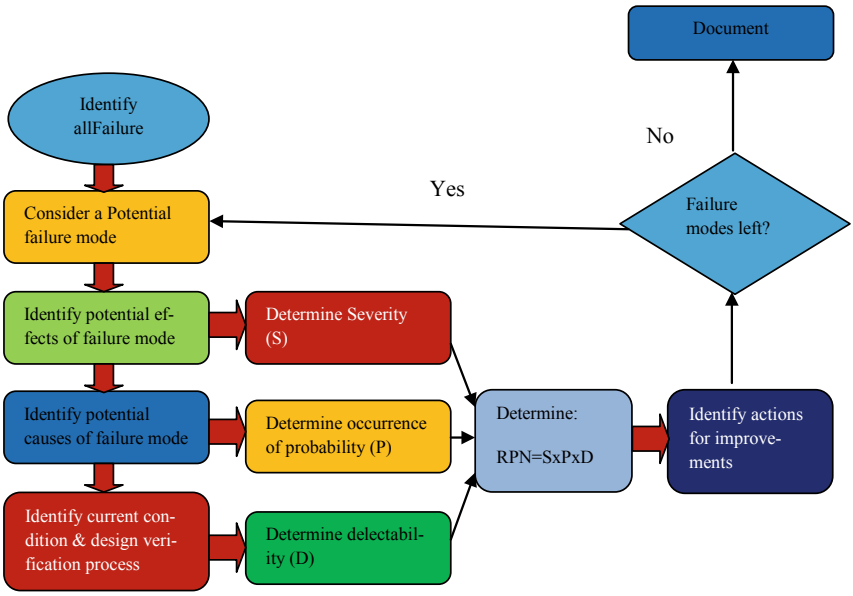

Fig. 1 FMEA flowchart

3 Result

3.1 Storage Area

Generally, TDI receiving in 200 kg barrels from supplier will be unloaded and stored at TDI storage. Due to increased production, the storage capacity made to 16 tons. Barrels unloading from truck will be carried out by barrel unloader with safety precautions but due to any accidental falling of 200 kg barrel may rupture and TDI spillage which may lead to emergency situation, and for this situation, suitable public exposure guidelines are adopted in ALOHA 5.4.7 software and evaluated the safe distance for residential colony.

Figure 2 showing the threat zone for TDI spillage using ALOHA software, and for developing this, we have taken following considerations:

- 200 kg of TDI spillage by barrel rupturing
- Release duration 1 min
- Wind velocity 2 m/s
- Air temperature 35 °C
- Relative humidity 75%
- Public exposures guideline—ERPGs-Emergency Response Planing Guideline.

By giving above inputs to ALOHA 5.4.7 software, we have found threat zone which indicated in red, orange, and yellow colors and distances found as follows:

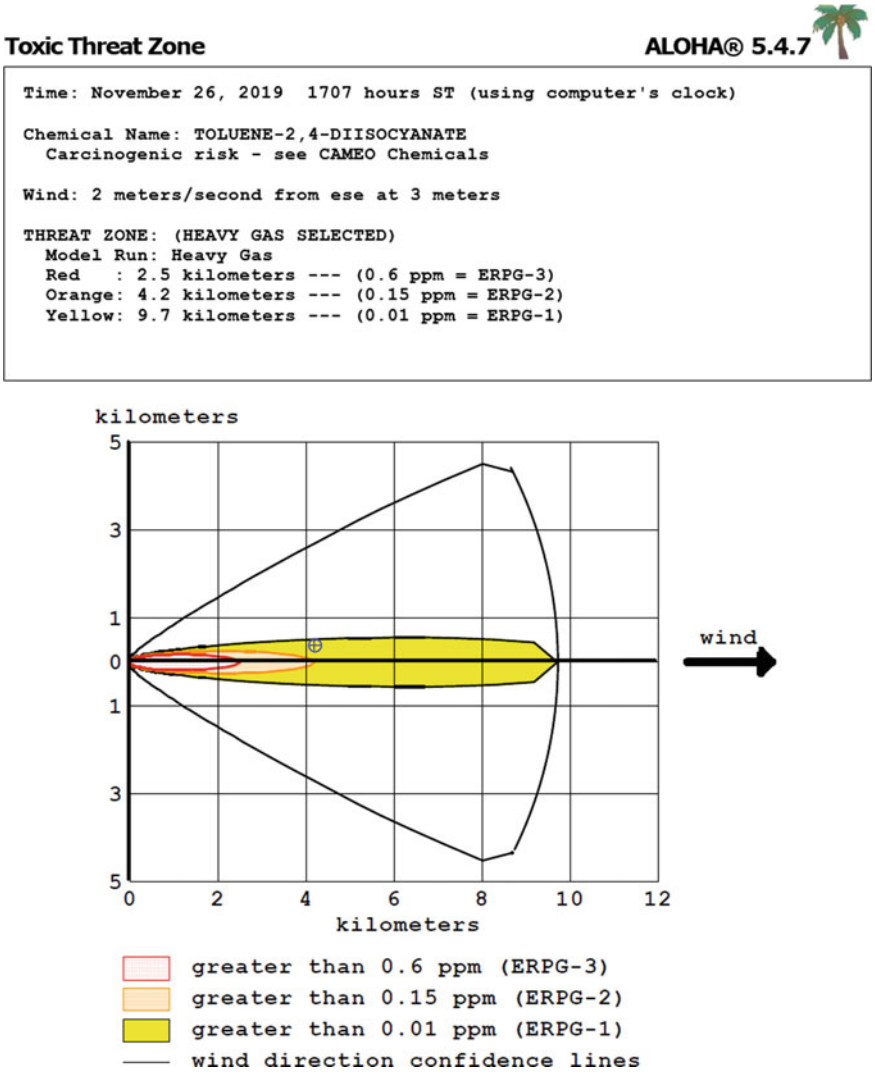

Fig. 2 Threat zone (ALOHA software screen shot)

Red 2.5 km (0.6 ppm = ERPG3)
Orange 4.2 km (0.15 ppm = ERPG2)
Yellow 9.7 km (0.01 ppm = ERPG1).

ERPG-3 is the maximum airborne concentration below which people could be exposed for up to 1 h without experiencing life-threatening health effects.

ERPG-2 is the maximum airborne concentration below which people could be exposed for up to 1 h without experiencing other serious health effects or symptoms which could impair an individuals ability to take protective action.

ERPG-1 is the maximum airborne concentration below which people could be exposed for up to 1 h without experiencing any adverse health effects.

From the above, it was observed that red (life-threatening zone) is up to 2.5 km, orange (health effects which impair an individuals ability) is up to 4.2 km, and yellow (without any adverse effects) is up to 9.7 km; hence, residential colony can be located outside the EPRG-2 (orange zone), so that people at residential colony will not have any adverse effects when TDI vapor release from spillage site.

Onsite emergency preparedness plan will be implemented for plant people who are at ERPG-3 (red zone), and this plan consists of emergency declaring procedure, incident controller, alarm system, assembly points, emergency vehicle, emergency lighting (DG Set), escape respirators, etc. By implementing a emergency preparedness plan, plant people will be protected from TDI vapor exposure.

3.2 Handling/Process Area

In rocket industry for solid propellant manufacturing TDI processed/handled which involves hoppers/bins, ball valves, hoses, and pipe fittings, any of these components failure may lead to TDI spillage, and people may effect due to toxic vapor exposure [4], and hence, risk assessment is carried out at TDI handling area by failure modes effect analysis (FMEA).

To identify the various ways in which components, systems, or processes can fail to fulfill their design intent, failure modes effect analysis (FMEA) is used. FMEA specifies the following:

- All probable modes of failure for the various parts of a system (which is observed to fail or to perform incorrectly)
- On system, these failures affect
- The failure mechanisms and
- How to avoid the failures and/or mitigate the effects of the failures on the system?

FMEA estimate the failure of each component in system by reviewing the components in the machinery and equipment. The failure modes of each components and their resulting effects are recorded in FMEA form. Probability of occurence (P), severity (S), and detection (D) is found out by this reviews from that risk priority number (RPN) evaluated by multiplying occurence, severity, and detection [5]. Risk priority number gives clear idea about which activity is most hazardous and where we need to more attention to reduce the failure rate.

$$\text{RPN} = \text{Occurence}(P) \times \text{Severity}(S) \times \text{Detection}(D)$$

3.2.1 Occurence

Occurence rating is given based on past performance and failure rate, and generally, it was scaled in 1–10 ranking, and this scale gives the probability of occurence in its lifetime.

3.2.2 Severity

Severity rating is given based on seriousness of risk which could cause an accident lead to permanent disablement or death. Generally, severity rated in scale 1–10, rank 1 indicates the high severity.

3.2.3 Detection

Detection rating is given based on how early detected before failure happens. If detection is possible early before major failure, we can reduce no of accidents, generally detection rated in scale 1–10, and here, rank 1 indicates easily detectable, whereas rank 10 indicates the almost not detectable (Table 1).

Table 1 FMEA format for TDI handling system components

Item no.	Component description	Failure mode	Effects	Safeguards	Actions
1	Ball valve	Plugged	Intended flow not occurs	Periodic maintenance and testing	Prepare checklist
		Struck open	TDI spillage due to receiving bin over flow	Periodic maintenance and testing	Prepare checklist
2	Bin/Vessel	Rupture	TDI spillage	Hydrotesting of vessel	Check due date of testing
3	Hoses	Rupture	TDI spillage	Replacement of hoses	Fix the replacement schedule
4	Flange joints	Gasket failure	TDI spillage	Replacement of gasket	Fix the replacement schedule
		Fasteners loose	TDI spillage	Periodic maintenance	Add checklist

4 Conclusion

Risk assessment made for TDI storage and handling area by using ALOHA software and FMEA technique, respectively, and we concluded that any accidental rupture of TDI barrel lead to spillage of TDI at storage area not a level of concern for residential colony located at 5000 m away from the plant site. At TDI handling area, risk assessment is carried out for each component through FMEA technique and concluded that by applying suitable safeguards, spillage of TDI can be avoided. If spillage occurs, engineering control like local exhaust ventilation can be adopted to control the TDI exposure levels to the below the permissable exposure level.

References

1. Chaturvedi S, Dave PN (2014) Solid propellants: AP/HTPB composite propellants. Arab J Chem
2. Occupational Safety and Health Administration (OSHA) (1998) Occupational safety and health standards, toxic and hazardous substances. Code of Federal Regulations, 29 CFR 1910.1000
3. Ben-Daya M (1992) Failure mode and effect analysis. Maintenance Management and Engineering, London
4. Guidelines for safe loading/unloading, transportation and storage of TDI and MDI in bulk. ISOPA Guidelines (2006)
5. Strojniski V (2010) Failure mode ad effect analysis application. J Mech Eng 21(2):14–22

Performance Evaluation of Linear Solar Collector Using Hybrid Nanofluid

Sreejith Mohan, Albin Joseph, Akash Poovathinkal, K. H. Akhilesh, Jerin Reji, Jithin Ninan Idicula, B. R. Vishnu, and S. P. Sivapirakasam

Abstract This paper reports an experimental investigation on the performance evaluation of a linear solar collector using a hybrid nanofluid of CuO and TiO_2. The scanning electron microscope was employed to study the morphology of the nanomaterials. A linear fresnel lens was used to concentrate solar energy on the required length of the glass tube. The nanofluid was made to flow through the glass tube and absorb the solar energy. Transmittance spectrum of samples indicated optimum properties for 0.20% volume concentration of CuO and 0.25% volume concentration of TiO_2 based on which the hybrid nanofluid was prepared. The results indicated superior thermal and optical properties for the hybrid nanofluid. The absorbance of the nanofluid was found to increase with the concentration of CuO nanoparticles. Temperature profile indicated that the hybrid nanofluid could absorb more heat then water and the base fluid even at lower concentrations. Further, the photo-thermal conversion rate of the samples was found to increase with the absorptivity of the nanofluid.

Keywords Nano-fluid · CuO · TiO_2 · Fresnel lens · Transmittance · Absorbance

S. Mohan (✉) · S. P. Sivapirakasam
National Institute of Technology, Tiruchirappalli, Tamil Nadu, India
e-mail: sreejith@nitt.edu

A. Joseph
National Institute of Technology, Calicut, India
e-mail: ojalbin92@gmail.com

A. Poovathinkal · K. H. Akhilesh · J. Reji · J. N. Idicula
Sree Buddha College of Engineering, Pattoor, India

B. R. Vishnu
Marian Engineering College, Trivandrum, India

N. Gascoin and E. Balasubramanian (eds.), *Innovative Design, Analysis and Development Practices in Aerospace and Automotive Engineering*, Lecture Notes in Mechanical Engineering, https://doi.org/10.1007/978-981-15-6619-6_51

1 Introduction

Renewable energy being a clean and economical energy resource has high demand in the society. Different types of renewable energy sources currently in use include solar, wind, tidal, and geothermal energy. Among these, solar energy is the most common on account of its abundant availability in the earth. Tapping of solar energy by means of photo-thermal conversion can meet most of the energy needs of the society [1]. A solar thermal power system employs both concentrating and non-concentrating type of energy tapping out of which the former is more effective [2]. In concentrating type, the light energy is focused onto a receiver which converts it into heat energy. Solar thermal conversion using direct absorption was known to be one of the modes through which thermal energy conversion could be achieved directly by the working fluid. This energy is transferred for various applications like water heating, drying, etc. Dispersing nanoparticles into the base fluid enhances its thermo-physical and optical properties and aids in better capture and transport of solar radiation [3, 4]. The investigations on nanofluids for energy conversion started in the early 1980s wherein prime focus was given to enhance the optical and thermal properties of the heat transfer fluid for thermal transport. However, most of the studies were conducted with nanofluid containing single nanoparticles which include but not limited to Al, Cu, Ag, Au, Ti, and its oxides [2]. In course of time, researchers developed binary (hybrid) nanofluid which exhibited superior properties than their counterpart containing single nanoparticles.

Nambiar et al. [5] suspended copper oxide nanoparticles in ethylene glycol in a weight ratio of 60:40 and noted an increase in thermal conductivity by as much as 40%. Allen Zennifer et al. [6] noted about 13% reduction in the viscosity and 11% enhancement in thermal conductivity of ethylene glycol when 26% (by volume) of CuO nanoparticles was added to it. Muraleedaran et al. [7] evaluated the thermo-optical properties of Al_2O_3-Therminol 55 nanoheat transfer fluid using a line concentrating Fresnel lens. The authors carried out the solar conduction tests in real-time environment and found that the addition of nanoparticles dramatically increased the thermal conductivity of the nanofluid at lower concentrations. Accordingly, there was an increase in the refractive index of the nanofluid. The authors further observed that higher the concentration of nanoparticles, higher the absorbance of the heat transfer fluid. Amiri et al. [8] found out the favorable effect of addition of SiO_2–Cu nanoparticles on the thermal conductivity of two base fluids, water, and ethylene glycol. Murshed et al. [9] prepared a nanofluid by dispersing spherical-shaped and rod-shaped TiO_2 nanoparticles in deionized water. The thermal conductivity of the nanofluid was found to increase with an increase in concentration of TiO_2 nanoparticles. Arulprakasajothi et al. [10] used TiO_2-water based nanofluids to enhance the performance of a heat exchanger. The thermal conductivity was increased with the concentration of nanoparticles. Zeiny et al. [11] concluded that the direct absorption nanofluid is an effective alternative in increasing the efficiency of solar-thermal energy conversion. The study experimented different categories of nanofluid under well-controlled conditions.

In the present study, a hybrid nanofluid was prepared by suspending CuO and TiO_2 nanoparticles in ethylene glycol with the primary objective of enhancing its solar thermal energy conversion. The volume concentration of CuO and TiO_2 nanoparticles yielding the optimum optical properties was selected for the preparation of the hybrid nanofluid.

2 Materials and Methods

2.1 Preparation of Binary Nano-fluid

Commercially available CuO and TiO_2 nanoparticles (Sigma Aldrich) were used to prepare the nanoheat transfer fluid. The particle morphology was examined in scanning electron microscope. The base fluid employed was ethylene glycol. The volumetric concentration (φ) of the nanoparticle was estimated from the following equation.

$$\varphi = \frac{w_{\mathrm{np}/\rho_{\mathrm{np}}}}{w_{\mathrm{np}/\rho_{\mathrm{np}}} + w_{\mathrm{bf}/\rho_{\mathrm{bf}}}} \tag{1}$$

where

w_{np} Mass of nanoparticles;
ρ_{np} Density of nanoparticles;
w_{bf} Mass of heat transfer fluid and
ρ_{bf} Density of heat transfer fluid.

Using the above equation, varying concentrations of CuO and TiO_2 nanofluids (0.020, 0.025, 0.075, 0.1, and 0.2% by volume) were prepared. These were then subjected to optical study to estimate its absorbance behavior, and the optimum concentration of each nanoparticles was selected for the performance evaluation on Fresnel lens solar collector.

The nanofluid was prepared as follows; the nanoparticles of CuO and TiO_2 at varying volume concentrations were mixed in ethylene glycol. The resultant solution was subjected to magnetic stirring for 45 min followed by sonication in an ultrasonicator for 90 min.

2.2 Measurement of Solar Thermal Energy Conversion of Nano Fluid

Figure 1 shows the experimental set-up used for measuring the solar thermal energy conversion.

Fig. 1 Experimental set-up

The concentrator comprised of two glass receiver tubes, each focused by two Fresnel lens placed vertically above them, and storage tank is insulated with glass wool. The Fresnel lens had linear grooves on the surface to concentrate the incoming solar radiation to the focus of glass tube. The receiver tube used was a concentric borosilicate glass tube with internal diameter 23 mm and external diameter 25 mm. The annular space was evacuated in order to decrease the heat loss to the surroundings through convection. Necessary piping arrangement was made to achieve the circulation of the working fluid. The working fluid from the reservoir is made to flow through the receiver tube where the photo-thermal conversion takes place. The fluid from the receiver is sent back to the receiver by employing a pump. A manual solar tracking was employed for the constant line focus. During experimentation, the heat transfer fluid was pumped at a constant flow rate into the Fresnel lens concentrator with the help of a submersible pump kept dipping in the storage tank. The experiments were carried out from 10:00 a.m. to 4:00 p.m., the temperature readings of the fluid at reservoir were noted by means of a *T* type thermocouple, and the values were compared with base fluid.

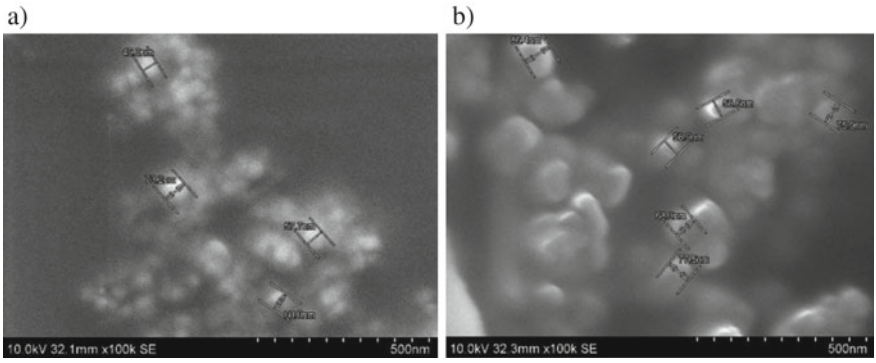

Fig. 2 SEM image of **a** TiO_2 nanoparticle and **b** CuO nanoparticle

3 Results and Discussion

3.1 Morphology of Nano Particles

Figure 2 shows the results of the morphological analysis. The TiO_2 and CuO nanoparticles exhibited a homogenous morphology, and the particle size was found to be 73.2 and 86.4 nm in that order. Stability of the nanofluid was quantified using the zeta potential analyzer and was found to be −28.54 mV. Moreover, as per the reports of Yu and Xuan [12] for the flow application, the stability is of less importance due to the flow stirring of the nanofluid.

3.2 Optical Study

Transmittance spectrum of the nano-CuO and -TiO_2 heat transfer fluid and ethylene glycol was taken to estimate the optical absorptivity. The results revealed that 0.02% volume concentration of CuO and 0.025% volume concentration of TiO_2 had maximum optical absorptivity, and the hybrid nanofluid was prepared according to these concentrations. Absorbance of the nanoheat transfer fluid increased with the concentration of CuO in it which was attributed to the direct absorption of radiation. The maximum absorbance was noted in the visible region of the spectrum, and it is increased with nanoparticle concentration. Figure 3 shows the transmittance spectra of 0.02% CuO, 0.025% TiO_2, and ethylene glycol.

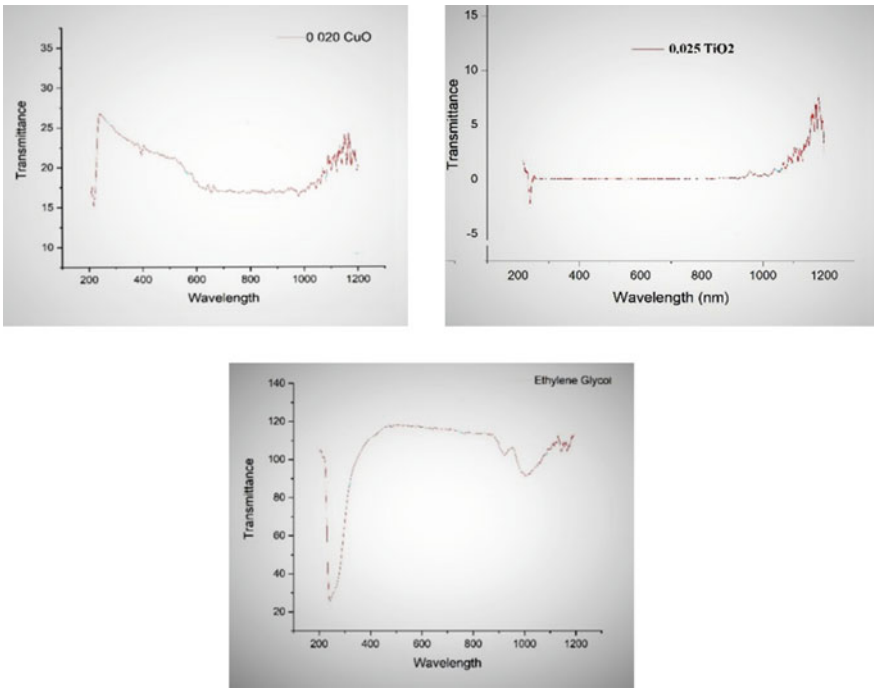

Fig. 3 Transmittance spectrum of 0.02% CuO, 0.025% TiO_2, and ethylene glycol

3.3 Temperature Profile

During the experimentation, it was found that on using water as the fluid medium, a temperature of 44 °C was achieved meanwhile, and in case of pure ethylene glycol, it was heated to a temperature of 53 °C. While in the case of hybrid nanofluid, a temperature of 70 °C was noted. This reading shows that the hybrid nanofluid is capable of absorbing more heat than base fluid. The amount of heat absorbed can be increased if the surface area of the experimental setup is increased, and as area increases, there will be more amount of heat absorption, which in turn enhances the performance. It was evident form the literature that the absorptivity is a direct function of photo-thermal conversion. Hence, photo-thermal conversion increases with the absorptivity of the nanofluid. Further, the energy absorbed by the nanofluid could be quantified using the following energy equation.

$$Q = mC_{\mathrm{p}}(T_{\mathrm{in}} - T_{\mathrm{out}}) \tag{2}$$

As per this equation, the photo-thermal conversion increases with the temperature. As the outlet temperature of hybrid nanofluid is higher than the base fluid, the photo-thermal conversion is high for the hybrid nanofluid.

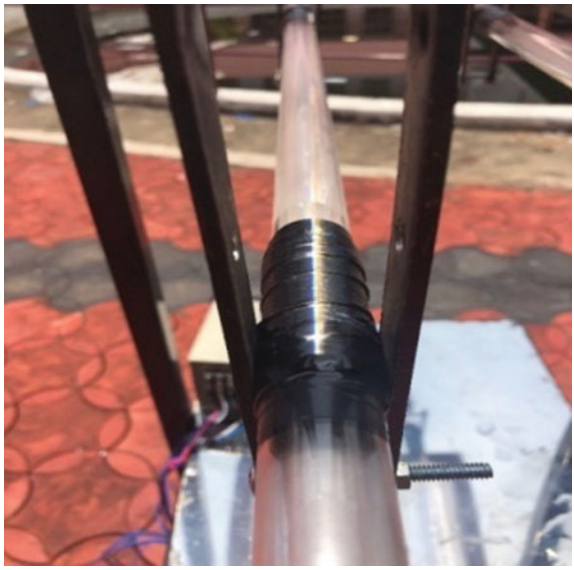

Fig. 4 Solar rays impinging on glass tube

Figure 4 shows the photograph of the solar rays impinging along a line on the glass tube.

4 Conclusions

Thermal properties of heat transfer fluid comprising of CuO–TiO_2 nanoparticles with ethylene glycol base fluid with a range of volumetric concentrations (0.020–0.2 vol%) have been studied experimentally. The solar radiation was concentrated along the length of the tube by means of a Fresnel lens. The result revealed that the temperature of the heat transfer fluid increased even at lower concentration of nanoparticles. The photo-thermal conversion rate was found to increase with the absorptivity of nanofluid.

References

1. Sreekumar S, Joseph A, Sujith Kumar CS, Thomas S (2019) Investigation on influence of antimony tin oxide/silver nanofluid on direct absorption parabolic solar collector. J Cleaner Prod. https://doi.org/10.1016/j.jclepro.2019.119378
2. Joseph A, Sreekumar S, Sujith Kumar CS, Thomas S (2019) Optimisation of thermo-optical properties of SiO_2/Ag–CuO nanofluid for direct absorption solar collectors. J Mol Liq. https://doi.org/10.1016/j.molliq.2019.111986

3. Ozerinc S, Kakoc S, Yazicioglu AG (2010) Enhanced thermal conductivity of nanofluids 145–170
4. Khullar V, Tyagi H, Phelan PE, Otanicar TP, Singh H, Taylor RA (2012) Solar energy harvesting using nanofluids—based concentrating solar collector 259–267
5. Nambiar PK, Kulkarni DP, Misra D (2007) Viscosity of copper oxide nanoparticles dispersed in ethylene glycol and water mixture 397–402
6. Allen Zennifer M, Manikandan S, Siganthi KS, Leela Vinodthan V, Rajan KS (2015) Development of CuO—ethylene glycol nano fluids for efficient energy management: assessment of potential for energy recovery 685–696
7. Muraleedaran M, Singh H, Suresh S, Udayakumar M (2016) Directly absorbing therminol—nano heat transfer fluid for linear solar concentrating collector 134–142
8. Amiri M, Movahedirad S, Manteghi F (2016) Thermal conductivity of water and ethylene glycol nanofluids containing new modified surface Si-Cu nanoparticles: experimental and modelling 45–53
9. Murshed SMS, Leong KC, Yang C (2016) Enhanced thermal conductivity of Ti-water based nanofluids 47–55
10. Arulprakasajothi M, Elangovan K, Hema Chandra Reddy K, Suresh S (2015) Heat transfer study of water-based nanofluids containing titanium oxide nanoparticles 3648–3655 (2015)
11. Zeiny A, Jin H, Bai L, Lin G, Wen D (2018) Comparative study of direct absorption nanofluids for solar thermal applications 74–82
12. Yu X, Xuan Y (2018) Investigation on thermo-optical properties of CuO/Ag plasmonic nanofluids. Sol Energy 160:200–207

Review of Experimental Approaches for the Analysis of Aerodynamic Performance of Vertical Axis Wind Turbines

Vishal Kaushik and R. Naren Shankar

Abstract World of today is facing the problem of power crisis, because most of the power generation units are running on the conventional resources which are depleting day by day. Therefore, the need of alternative resources is the prime necessity of the hour. Many experiments and studies have been conducted that highlights the benefits of VAWT and its better performance over HAWTs. This paper presents a review of various designs and performances delivered by different types of VAWTs. Major designs that are in question in the presented paper are Savonius-type and Darrieus-type vertical axis wind turbine. The paper aims at comparing various designs along with their merits and demerits and parameters of various experimented VAWT. The objective of this study is to derive an optimum design that can deliver the maximum efficiency and power output within the given set of parameters like blade angle, number of blades, aerofoil shapes, tip speed ratios, and wind velocity.

Keywords VAWT · Aerofoil · Optimization · Savonius · Darrieus · TSR (tip speed ratio)

1 Introduction

With conventional resources of energy going toward extinction, there is a dire need to move toward non-conventional energy resources. "Wind" energy is deemed to be prime source to harvest energy. And modernized wind turbines can empower us to do so. Optimizing the design parameters of wind turbines will lead us in achieving more

V. Kaushik (✉)
Research Scholar, Department of Aeronautical Engineering, Vel Tech Rangarajan Dr. Sagunthala R&D Institute of Science and Technology, Avadi, Chennai, Tamil Nadu, India
e-mail: vishalk.kaushik42@gmail.com

R. N. Shankar
Associate Professor, Department of Aeronautical Engineering, Vel Tech Rangarajan Dr. Sagunthala R&D Institute of Science and Technology, Avadi, Chennai, Tamil Nadu, India
e-mail: narensankar@veltech.edu.in

N. Gascoin and E. Balasubramanian (eds.), *Innovative Design, Analysis and Development Practices in Aerospace and Automotive Engineering*, Lecture Notes in Mechanical Engineering, https://doi.org/10.1007/978-981-15-6619-6_52

power. There are two kinds of wind turbines based on the placement of the blades: (a) horizontal axis wind turbine mainly deployed in large-scale use and (b) vertical axis wind turbine [1, 2]. VAWTs are better than HAWTs due to simple assembly and installation process, less maintenance cost, better self-starting capacity and less noisy, less wear and tear of mechanical components, and multidirectional trapping of air. For urban and household, the use of Savonius-type VAWT is best suited as they can be operated at very less wind speed of 4–10 m/s and have very less installation cost [3]. Figures 1 and 2 represent the share of top global markets in terms of Mega Watts and show the emerging trends in the field of VAWT to meet the desirable targets in green energy [4].

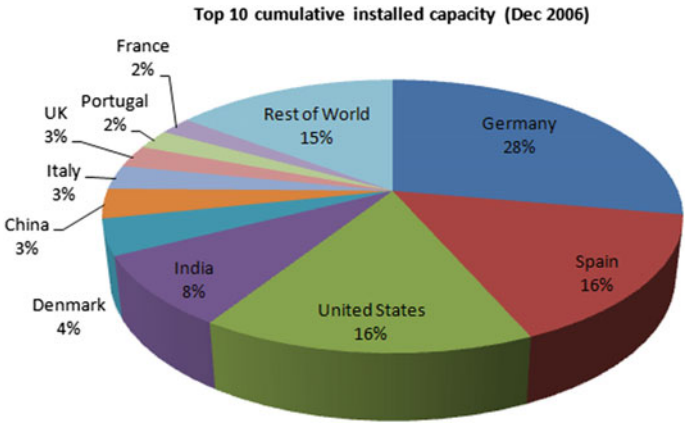

Fig. 1 Top ten cumulative installed capacity (Dec 2006) [4]

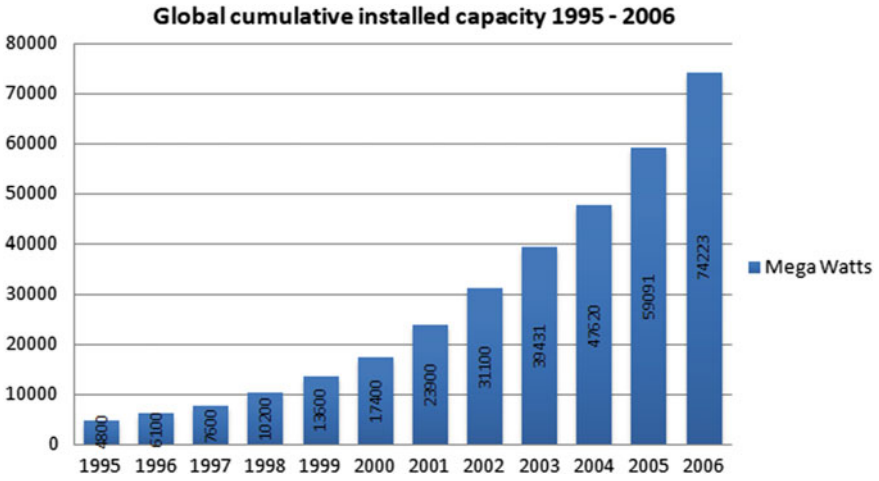

Fig. 2 Global cumulative installed capacity 1995–2006 [4]

Emerging economies like India and China are investigating in the aerodynamics of VAWT from numerical, computational, and experimental aspects [5]. Researches are ongoing to improvise the turbine in order to get maximum efficiency for various possibilities of wind speeds and TSR. India as well is embarking on this journey toward renewable energy. This paper includes results of various experiments and researches done on VAWT [6]. This paper includes various experiments done in both wind tunnel and field test setup, and the results are obtained in terms of optimization of parameters. Unlike various research works up till now, the prime objective of this study paper is the examination of various experimental approaches which were utilized for analyzing the efficiency based on the various aerodynamic performance parameters of the vertical axis wind turbines. These parameters are tip speed ratio (TSR), coefficient of power (C_p), coefficient of torque (C_T), wind speed (v), and RPM. This also gives a helping hand to all the researchers who are pursuing and would like to pursue their researches in this area.

2 Vertical Axis Wind Turbines (VAWT)

The vertical axis wind turbines can be mostly placed into the following kinds:

Darrieus or lift type wind turbine	The rotors consist of curved and straight blades placed axially on the framework to utilize the lifting force for the rotation
Savonius or drag type wind turbine	The rotors of turbines which utilizes the drag force difference along its sides due to the shape and use it for the rotation [1]

3 Experimental Techniques

The results obtained from the experimentations are done mainly by two methodologies wind tunnel experimentation in steady flow and uniform conditions and field test setup under natural wind conditions and dynamic flows. All the tests are done under the guidelines given by the IEC and AWEA standards [7].

3.1 Experimentation by Field Tests Methodology

Demerit	Dynamic condition test, wind speed, and direction not constant
Executed by	Sheldahl et al. [8]
Performed at	Field test of 2 m Darrieus turbine at the Sandia National Laboratory
Conditions	Turbine speed 460 rpm, three blade configuration, Re No. 1.5×10^5, rotational speed 100 rpm, wind speed (v) is linearly proportional to the C_p and directly proportional with the TSR
Output	Optimum power coefficient obtained 0.34 at TSR 5.15 [9]

3.2 Experimentation Using Wind Tunnel Setup

Wide variety of experimentations with wind tunnel setup under varied conditions has been performed by many researchers/authors. The objective of these experiments was:

- To determine aerodynamic parameters under conditions like different Reynolds number and different wind tunnels specifications
- To analyze performance of mono-, two-, and three-stage rotor at various aspect ratios and Reynolds number. Comparison of TSR (0.7–1.0) corresponding to maximum C_p is showed in Table 1, and a comparative result of all the experiments is presented in Table 2.

4 Conclusions

(1) This paper speaks about experiments done to assess parameters influencing aerodynamics of VAWT.

Table 1 Comparison of tip speed ratios (0.7–1.0) corresponding to maximum C_p [3]

Authors	Optimum TSR	Authors	Optimum TSR
Kamoji et al. [10]	0.64–0.69	Gupta et al. [4]	0.4950
Dobrev and Massouh [11]	0.8	El Beheiry and El-Askary [12]	0.7
Scungio et al. [13]	1.24	Yoon and Lim [14]	0.39
Bergeles and Athanassiadis [15]	0.7	Morshed et al. [16]	0.24
Fujisawa and Gotoh [17]	0.8–0.9	Malge and Pawar [18]	0.85
Morshed [19]	0.47	Vincenzo Dossena et al. [20]	2.5
Huda et al. [21]	0.68–0.71	Mishra et al. [22]	0.65
Sheldahl et al. [8]	0.7–1.0	Wenehenubun et al. [23]	0.555

Table 2 Comparative data of maximum power coefficient for various VAWT

Authors	Wind tunnel dimension (m × m)	Test section type	Dimension of rotor of VAWT ($H \times D$) (m × m)	Maximum C_p	TSR
Huda et al. [21]	0.5 (circular open jet)	Open type	0.185 × 0.32	0.17	0.71
				0.21 (deflector)	0.72
Kamoji et al. [10]	0.4 × 0.4	Open type	208 × 208	0.161 (1 stage)	0.78
			226 × 113	0.14 (2 stage)	0.83
			289.9 × 96.6	0.132 (3 stage)	0.77
Bowden and McAleese [24]	0.76 (open jet)	Open type	0.164 × 0.162	0.15	0.72
Alexander and Holownia [25]	2.4 × 1.2	Closed type	0.46 × 0.19	0.147	0.52
				0.243 (with shielding)	0.72
Ogawa and Yoshida [26]	0.8 × 0.6	Open type	0.175 × 0.3	0.17	0.86
				0.212 (with deflector)	0.7
Bergeles and Athanassiadis [15]	3.5 × 2.5	Closed type	0.7 × 1.4	0.128	0.7
Fujisawa and Gotoh [17]	(Open circuit)	Open type	0.32 × 0.32	0.17	0.9
Baird and Pender [27]	0.305 × 0.305	Closed type	0.076 × 0.06	0.185	0.78
Jeon et al. [28]	1 × 1.5	Open type	0.35 × 0.7	0.16	0.8
Hayashi et al. [29]	1.5 × 1.5	Open type	0.23 × 0.33	0.175 (1 stage)	0.75
			0.074 × 0.184	0.13 (3 stage)	
Dobrev and Massouh [11]	1.35 × 1.65	Closed type	0.2 × 0.22	0.18	0.8
Alexander and Holownia [25]	1.20 × 1.20	Closed type	0.19 m chord and 0.38 m length from 0.46 to 0.91 m	0.102	0.42
Kamoji et al. [10]	0.4 × 0.4	Open jet	Single stage 0.208 × 0.208	Single stage 16.1	0.78
			Two stage 0.226 × 0.226 0.131 × 0.262	Two stage 13.7	0.72

(continued)

Table 2 (continued)

Authors	Wind tunnel dimension (m × m)	Test section type	Dimension of rotor of VAWT ($H \times D$) (m × m)	Maximum C_p	TSR
			Three stage 0.225 × 0.225 0.96 × 0.289	Three stage 13.2	0.77
Sheldahl [30]	4.6 × 6.1	Open type	2 × 0.98	0.32	4.70
Gupta et al. [4]	0.3 × 0.3	Open ckt	1.2 × 0.08	0.3579	0.4950
Scungio et al. [13]	0.3 × 0.3	Closed ckt	0.15 × 0.2	0.161	1.24
Meana-Fernandez et al. [31]	4.45 × 2.80	Closed loop open jet	0.4 × 0.6	0.45	3.5
Wenehenubun et al. [23]	–	Open circuit	0.37 × 0.37	0.35	0.555

(2) Many field tests that have carried out by the researchers have been included in this paper to understand about the three-dimensional characteristics and performance under natural wind conditions.
(3) The aerodynamic design of the rotor has also evaluated by the wind tunnel experimentation to measure various parameters like tip speed ratio, power coefficients, torque coefficient, blockage effects, overlapping effects, effect of Re number, and effect of blade number on the performance of the rotors.

5 Future Scopes for Research

1. Development of the methods to evaluate the innovative configurations of VAWT which comprises of variable pitch blades and tip devices for the rotor which can automatically adjust itself as per the flow field, so as to enhance the aerodynamic performance.
2. Many researches have to be carried out on various configurations which include the confined or closed VAWT structure which is having a nozzle-like structure at the opening end of the rotor from where the air is directed toward the blades of the turbine.
3. Development of the techniques for the flow visualization and to determine the flow separation points during turbulent flow and methods to avoid the flow separation.

References

1. Tummala A, Kishore R, Kumar D, Indraja V, Krishna VH (2016) A review on small scale wind turbines. Renew Sustain Energy Rev 56:1351–1371
2. Saha UK, Thotla S, Maity D (2008) Optimum design configuration of Savonius rotor through wind tunnel experiments. J Wind Eng Ind Aerodyn 96(8–9):1359–1375
3. Roy S, Saha UK (2013) Review of experimental investigations into the design, performance and optimization of the Savonius rotor 227:528–542
4. Gupta RÃ, Biswas A, Sharma KK (2008) Comparative study of a three-bucket Savonius rotor with a combined three-bucket Savonius—three-bladed Darrieus rotor 33(2008):1974–1981
5. Brusca S, Lanzafame R, Messina M (2014) Design of a vertical-axis wind turbine: how the aspect ratio affects the turbine's performance. Int J Energy Environ Eng 129:1–8
6. Howell R, Qin N, Edwards J, Durrani N (2010) Wind tunnel and numerical study of a small vertical axis wind turbine. Renew Energy 35(2):412–422
7. Sivasegaram S (1981) Wind tunnel tests on slow running vertical axis wind rotors. Proc Indian Acad Sci (Eng Sci) 4(September):395–404
8. Sheldahl RE, Blackwellt BF, Feltzt LV (1978) Wind tunnel performance data for two- and three-bucket Savonius rotors 2(3):160–164
9. Bedon G, Castelli MR, Benini E (2013) Experimental tests of a vertical-axis wind turbine with twisted blades, June 2013, 2014
10. Kamoji MA, Kedare SB, Prabhu SV (2008) Experimental investigations on single stage, two stage and three stage conventional Savonius rotor 877–895
11. Dobrev I, Massouh F (2011) CFD and PIV investigation of unsteady flow through Savonius wind turbine 6:711–720
12. El Beheiry EM, El-Askary WA (2012) Analysis and experimentation of multi-S rotors for vertical wind turbine analysis and experimentation of multi-S rotors for vertical wind turbine applications, Dec 2012, 2015
13. Scungio M, Arpino F, Focanti V, Profili M, Rotondi M (2016) Wind tunnel testing of scaled models of a newly developed Darrieus-style vertical axis wind turbine with auxiliary straight blades. Energy Convers Manage 130:60–70
14. Yoon S, Lim H (2017) Study of several design parameters on multi-blade vertical axis wind turbine, Feb 2017
15. Bergeles G, Athanassiadis N (1982) On the flow field of the Savonius rotor. J Wind Eng 6(3):140–148
16. Morshed KN, Rahman M, Molina G, Ahmed M (2013) Wind tunnel testing and numerical simulation on aerodynamic performance of a three-bladed Savonius wind turbine 1–14
17. Fujisawa N, Gotoh F (1992) Pressure measurements and flow visualization study of a Savonius rotor. J Wind Eng Ind Aerodyn 39(1–3):51–60
18. Malge A, Pawar P (2015) Wind tunnel and numerical performance analysis of multi-storey vertical axis wind turbines 053121
19. Morshed KN (2010) Digital commons @ Georgia southern experimental and numerical investigations on aerodynamic characteristics of Savonius wind turbine with various overlap ratios
20. Dossena V, Persico G, Energia D, Battisti L, Anna SD, Brighenti A, Benini E (2015) An experimental study of the aerodynamics and performance of a vertical axis wind turbine in a confined and unconfined environment. 137
21. Huda MD, Selim MA, Sadrul Islam AKM (1992) The performance of an S-shaped Savonius rotor with deflecting plate. REPIC Int Energy J 14:25–32
22. Mishra N, Gupta AS, Dawar J, Kumar A, Mitra S (2018) Numerical and experimental study on performance enhancement of Darrieus vertical axis wind turbine with wingtip devices 140(December):1–7
23. Wenehenubun F, Saputra A, Sutanto H (2015) An experimental study on the performance of Savonius wind turbines related with the number of blades. Energy Procedia

24. Bowden GJ, McAleese SA (1984) The properties of isolated and coupled Savonius rotors. Wind Eng 8(4):271–288
25. Alexander AJ, Holownia BP (1978) Wind tunnel tests on a Savonius rotor. J Ind Aerodyn 3:343–351
26. Ogawa T, Yoshida H (1986) Effects of a deflecting plate and rotor end plates on performance of Savonius type wind turbine. Bull JSME 29(253):20–30
27. Baird JP, Pender SF (1980) Optimization of a VAWT for small scale applications. In: 7th Australasian hydraulics and fluid mechanics conference, Brisbane, pp 18–22
28. Jeon KS, Jeong JI, Pan JK, Ryu KW (2015) Effects of end plates with various shapes and sizes on helical Savonius turbines. Renew Energy 79:167–176
29. Hayashi T, Li Y, Hara Y, Suzuki K (1931) Wind tunnel tests on a three-stage out-phase Savonius rotor (5)
30. Sheldahl RE, Comparison of field and wind tunnel Darrieus wind turbine data
31. Meana-Fernández A, Oro JMF, Díaz KMA, Galdo-Vega M, Velarde-Suárez S (2018) Aerodynamic design of a small-scale model of a vertical axis wind turbine. Proceedings 2(23):1465

Analysis and Design of an Optical Biosensor Using Mathematical Modeling

G. Sowmya Padukone, H. Uma Devi, Shivaputra, and Meenakshi L. Rathod

Abstract Photonics is a branch of science which deals with creation, perception, and arrangement of light in a suitable form. The waves are electromagnetic waves (EM waves) where electric and magnetic waves are perpendicular to each other. These sensors are used to detect diseases like cancer, forensic analysis, pattern, parental recognition, pattern recognition, etc. But, photonic biosensors are first designed so as to get the optical-designed simulation pattern using MEEP and opti-FDTD algorithms. The patterns are nothing but light wave patterns. These patterns are analogous to electromagnetic waves. These waves are linked mathematically by using different laws and equations. The study of mathematical model for generation of images and simulation is done mainly in this paper. Mathematical modeling of any sensor is an excellent approach to design and model it.

Keywords Photonics · FDTD · Biosensors · Electromagnetic · Mathematical model

1 Introduction of Existing Methods in Optical Sensors

A sensor is an instrument which recognizes a small change in the input, and then, this will be given recognition at an output device. A sensor is a most important instrument in the field of electronics. A sensor has the most important property of sensitivity and selectivity. Sensors can be classified into so many categories based on the type of analyte as well as its properties. The other most important property of a sensor

G. Sowmya Padukone (✉)
Department of ECE, The Oxford College of Engineering, Bangalore, Affiliated to VTU, Belagavi, Karnataka, India
e-mail: sowmyapk121@gmail.com

H. Uma Devi · Shivaputra · M. L. Rathod
Department of ECE, Dr. Ambedkar Institute of Technology, Bangalore, Affiliated to VTU, Belagavi, Karnataka, India
e-mail: umadevi.h@dr-ait.org

N. Gascoin and E. Balasubramanian (eds.), *Innovative Design, Analysis and Development Practices in Aerospace and Automotive Engineering*, Lecture Notes in Mechanical Engineering, https://doi.org/10.1007/978-981-15-6619-6_53

[1] is its resolution. It means the least change in the output that could be detected for the minimum changes in the input applied.

The following are the some of the types of sensors:

(i) Thermal sensor, (ii) speed sensor, (iii) accoustic sensor, (iv) chemical sensor, (v) optical sensor, etc.

First let us see optical sensor. It is an instrument or a device which transforms light signals to electrical signals. The output of an optical sensor can be easily deciphered by a readable device. An optical sensor mainly consists of a transmitter and a receiver. Optical sensors are an integral part of most of the electronic devices like Xerox machines, scanning machines, printers, computers, etc.

Different types of optical sensors are: (i) photo-conductive devices, (ii) photo-voltaic cell, and (iii) photodiodes. All these devices take input as light energy and convert to other form of energy. The optical sensor based on hydrogen material is known to be as highly sensitive [2] optical fiber. It is having a fast time response with respect to input and output.

Optical sensors are also mainly used for biomedical applications. The following are some of the applications of optical sensors in the field of medicine (Fig. 1).

Optical heart rate sensor is the one which is placed on the wrist of a user. By measuring the variation of the movement of blood, the corresponding heart rate will be detected and given to the sensor in a readable form. Almost all optical biosensors have sensitivity of around parts per billion. The water level content present in the human body can also be measured by using optical sensor. Optical heart rate sensor uses the flow of blood to assess the heart beat rate.

Whenever the light passes through the tissue, where optical sensor is placed, then if there is more volume of blood in that region, it gives less-calibrated output at the output. If there is low volume of blood in that region where the sensor is placed, then it returns a high-calibrated [3] value to the corresponding detector. It uses a technique called as photoplethysmography (PPG) to calibrate the **heart rate**. The heart beat rate for a normal and healthy person is around 60–100 beats per minute.

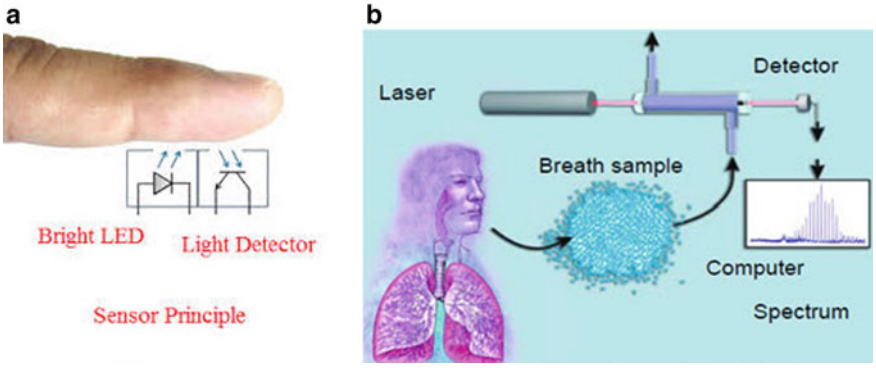

Fig. 1 **a** Optical heart rate sensor **b** tunable diode laser used for breath analysis

By analyzing one's breathing rate also, most of the body's nature can be detected. Standard human breath consists of water, carbon dioxide, nitrogen, and oxygen. Recent technologies are adopted to construct breathing sensor with high precise sensitivity. By doing breath analysis, different types of diseases could be detected. An high intensity wave could be achieved in a laser source [4] by using Raman spectroscopy method. Laser is used in applications like dental and medical treatment such as cancer treatment.

Nowadays, we are having medical sensor where by using blood as the sample, many outputs could be detected. This sensor uses current to frequency converter. Presently, we have optical fiber sensor so as to measure refractive index of a sample. In this case, a hybrid reconstruction algorithm is used. It also uses analog-to-digital converter. But whatever be the type of sensor is designed, it should have a good resolution, high precision, high selectivity, and so on. There may be so many layers which may be constructed by using photolithography technique. The layers have to be constructed, so that they should be less than 0.1 nm as much as possible. It is also used for checking drugs present in the materials of interest. Most of the sensors are based on surface plasmon resonance. It consists of a biosample, biorecognition element, transducer, and the detected blood.

Light is nothing but an electromagnetic wave [5]. It consists of varying electric and magnetic waves which vary perpendicular to each other. The electromagnetic waves travel with a speed of 3×10^8 m/optical fiber that uses light which ranges in infrared range which has wavelength of 700 nm to 1 mm.

Introduction to MEEP Tool It is an electromagnetic simulation tool. It has improved features of signal processing conditions. It has many adaptable features for many different types of environments. This tool mainly uses FDTD algorithm, time, and space with regularity, and it also mainly uses Maxwell's equations. The light source which is placed for an optical sensor is assumed as a continuous wave [2] source. It gives the output in time as well as space domain. Maxwell's equations that will be followed are (Fig. 2):

$$\partial B \, \partial t = -\nabla \times E - J_B \tag{1}$$

$$\partial D \, \partial t = +\nabla \times H - J \tag{2}$$

The waveguide stimulates the scattering electric fields which propagates through the waveguide. These fields move from left to right that is from source to detector. Inside the waveguide sample like blood, saliva, etc., will be placed. Since this MEEP is a simulation tool, refractive index value of normal blood and cancerous cell blood refractive index value will be given to the MEEP algorithm. When the MEEP program is run or simulated based on the number of steps required, the result will be quality factor (QF). Based on the value of quality factor which will be different for normal and cancerous cells [4–6], we can detect whether a person has cancer or any other type of disease or he is normal that is without any disease. Practically, when light is made to pass through the waveguide [3], the photons in light which has certain

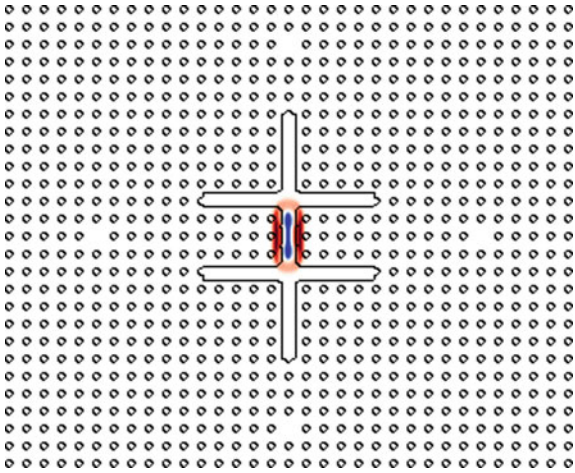

Fig. 2 Optical biosensor with light source and detector

refractive index interact with the biological material which has different refractive index [7, 8], and then, it produces simulation result in the form of effective refractive index as well as quality factor.

It follows master wave equation which is given as

$$\text{Gradient} \times (1/\varepsilon \,\text{Gradient} \times H) = (\omega/\text{c})^2 \tag{3}$$

Dielectric constant $(\text{`}\varepsilon\text{'})^{1/2} = n$ (refractive index). Further 'n' is reciprocal to ω which is equal to $2\pi f$. Thus, change in refractive index will also cause frequency shift or wavelength shift. These parameters determines the quality factor 'Q' which is given as

$$Q = \big[\text{Real part of } (\omega)\big]/\big[(-2)\,\text{Imaginary Part } (\omega)\big] \tag{4}$$

Opti-FDTD Algorithm This algorithm can be used for modeling a wide range of frequencies. This algorithm also follows Maxwell's equations. Optical signal or light signal is an electromagnetic wave. It consists of electric and magnetic fields which are located perpendicular to each other. FDTD algorithm also uses electric and magnetic fields. Therefore, FDTD algorithm could be applied for optical signals which are used for quality factor measurement in the case of optical sensors. This algorithm could be used in implementations where resonant frequencies are developed. Optical sensor [4] is made up of majorly of silicon material [9], and sometimes they are constructed by using gallium arsenide material (GaAs) which has properties like permittivity, conductivity, permeability, and so on.

Here, we have layout and profile design. After we simulate by giving the data in the form of refractive index, we will get the result in an analyzer window. After we get the result in the form of graph, we will do observation area analysis to get

the quality factor value. Based on the material and waveguide properties, we get the different structures, designs, and results.

2 Mathematical Modeling

The main aspect of this paper is mathematical modeling using sensitivity. This factor has to be considered both with respect to instrument as well as with respect refractive index of the sample being placed in an optical sensor. The sensitivity is nothing but a small change in an output to the input being considered or measured. Sensitivity [10] is very closely related to resolution [3]. It is always a good practice to design an instrument with high sensitivity and low specificity. Both sensitivity as well as specificity are applied so as to find whether a person has a disease or not by checking the factor true positive and false negative.

It is calculated as follows:

$$\text{Sensitivity} = (\text{TP})/(\text{TP} + \text{FN})$$
$$\text{Also Sensitivity} = (\text{TN})/(\text{TP} + \text{TN})$$

If specificity value becomes lesser, then it means a person may said to have a disease means he may be prone to disease. Positive predictive value (PPV) [8] shows that a person is said to have a disease. If negative predictive value occurs, then the person is not prone to have a disease. This means that we have to check a positive or a negative outcome [5] from the test being carried out.

In the same way, we can calculate specificity by using the following equation

$$\text{Specificity} = (\text{TN})/(\text{TN} + \text{FP})$$

From this even, we can predict positive predictive value (PPV) by using the following equation from Table 1.

$$\text{Positive Predictive Value} = (\text{TP})/(\text{TP} + \text{FP})$$

Negative predictive value (NPV) is calculated by using the equation given below:

$$\text{Negative Predictive Value} = (\text{TN})/(\text{TN} + \text{FN})$$

Table 1 Determination of sensitivity

	Disease	No disease
Test	True positive (TP)	False positive (FP)
Test	False negative (FN)	True negative (TN)

Table 2 RI value of normal and cancerous breast cell

Normal or healthy breast cell	True negative	1.7
Malignant breast cancerous cell	True positive	1.395

Sensitivity = (1.7)/(1.7 + 1.395) = 0.549 = 54.9%
This is approximated to around **55%**

Table 3 RI values of normal and cancerous hepatocellular carcinoma cells

	Hepatocellular carcinoma (primary stage)		
Non-cancerous	Wavelength range (1550 nm)	True negative	1.361
Cancerous		True positive	1.343

Sensitivity = (1.361)/(1.361 + 1.343) = 0.5033 = 50.33%
This is approximated to around **50%**

Table 4 RI values of normal and cancerous living cells

	Normal compared cancerous living cells	
Normal living cell	True negative	1.353
Cancerous living cells	True positive	1.370

Sensitivity = (1.353)/(1.353 + 1.370) = 0.4968
This is approximated to around 49.68%

Thus, we can calculate PPV from first row of Table 1 and NPV from the second row of Table 1.

3 Results Based on Mathematical Modeling

Based on the refractive index value of diseased cells and healthy cells, sensitivity is calculated (Tables 2, 3, and 4).

4 Results Based on Opti-mode Designer and Opti-analyzer Window

Let us see the results of 2D TE coupler (nonlinear mode). Here, a waveguide is constructed which works in 2D mode. Through the waveguide, light is transmitted, and we can find the observation area analysis as well as power spectrum analysis. Most of the time, light follows nonlinearity path, and thus, nonlinear waveguide is taken into consideration (Fig. 3).

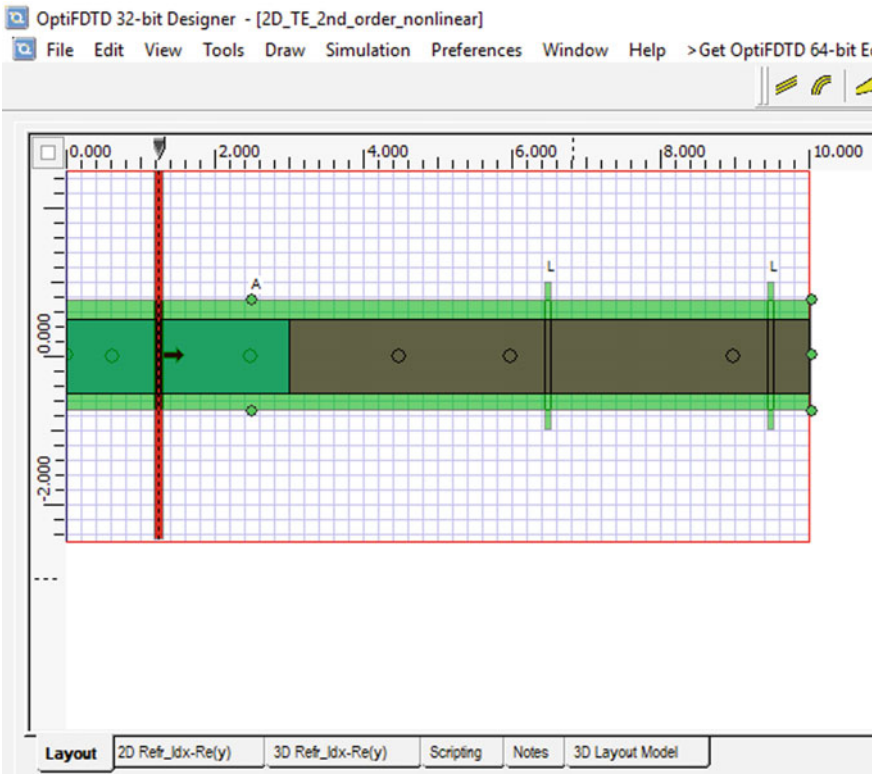

Fig. 3 Opti-designer window for two-dimensional TE coupler

When power analysis is done using simulation, the following power spectrum analysis is obtained. The type of material chosen will be silicon (Si) (Fig. 4).

By using this technique, many more results could be obtained which could also be proved mathematically to calculate many more parameters (Figs. 5 and 6; Tables 5 and 6).

5 Conclusion and Future Scope

In this paper, sensitivity value that could be obtained for different types of cells are illustrated. Using opti-mode designer, we can obtain different parameters like amplitude, dimensions, effective confinement area, mode number, polarization, grid size, etc. This will be helpful to design a good optical sensor for detection of diseases in the future. By using sensitivity and specificity like characteristics, we can suspect the type of the disease a human being is said to have. In future, most of the VLSI devices will be replaced by photonic devices.

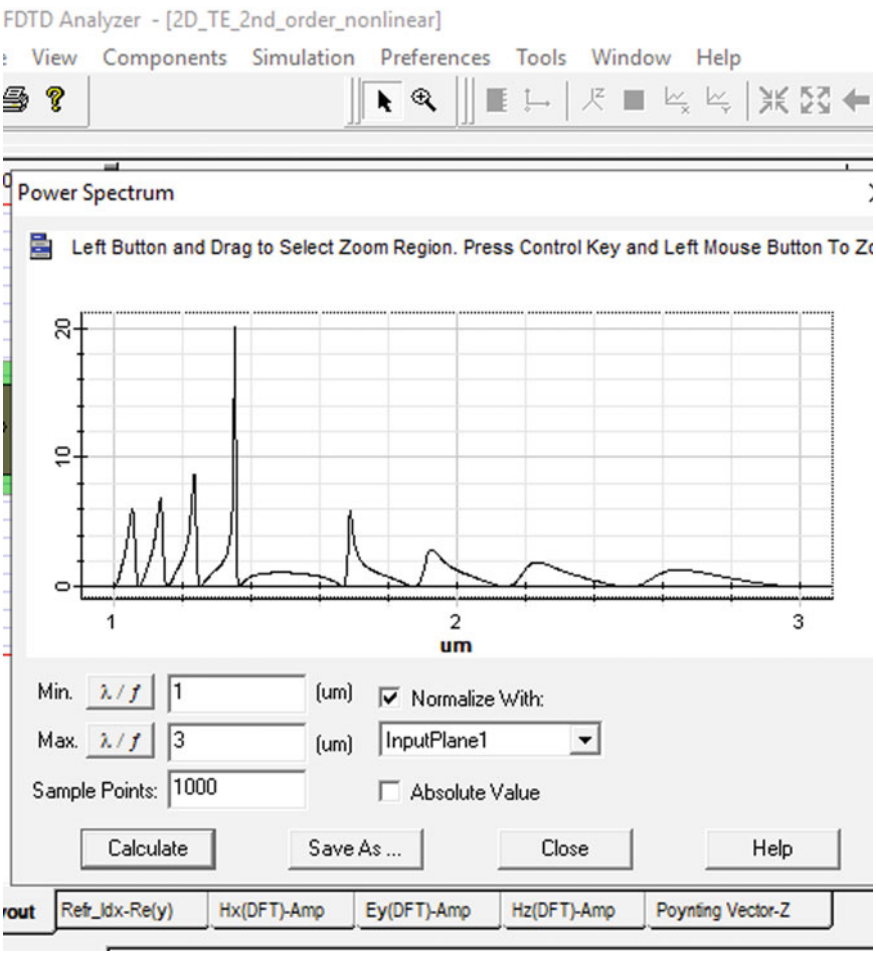

Fig. 4 Power spectrum analysis of 2D TE coupler which shows around 20 μW

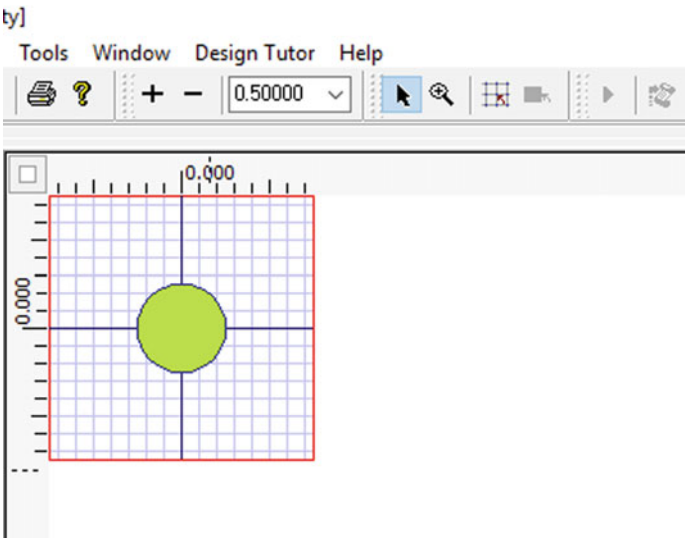

Fig. 5 Opti-designer window in a circular structure with RI = 1.353 of a normal living cell

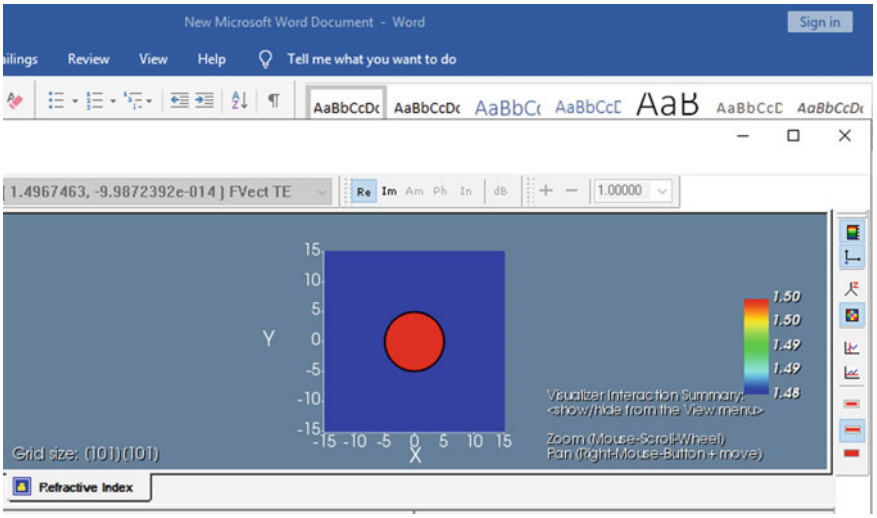

Fig. 6 Opti-analyzer window in a circular structure with RI = 1.353 of a normal living cell

Table 5 Parameters for a normal living cell

Parameter	Values
Amplitude	30
Grid size	101 × 101
Modal field	1.4967463, −9.9872392e−014
Mode number	1
Polarization	Field vector TE
Confinement	0.97042118
Effective mode area (μm^2)	55.27003546
FWHM in X direction (in μm)	5.7
WHM in Y direction (in μm)	6.0

Table 6 Parameters for a cancerous living cell

Parameter	Values
Amplitude	30
Grid size	101 × 101
Modal field	1.4967678, 0
Mode number	1
Polarization	Field vector HE
Confinement	0.97018807
Effective mode area (μm^2)	55.6364164055

References

1. Raman S, Barker SN, Rebeiz GM (1998) A w-band dielectric-lens-based integrated monopulse radar receiver. IEEE Trans Microw Theory Tech 46(12):2308–2316
2. Kanda K, & Maekawa T (2005) Development of a WO_3 thick-film-based sensor for the detection of VOC. Sens Actuators B Chem 1–2:97–101
3. Parsons MT, Sydoryk I, Lim A, McIntyre T, John TJ, Jäger W, McDonald K (2011) Appl Opt 50 A90[13]
4. Jyothi B, Latha YM, Reddy VSK (2010) Medical image retrieval using multiple features, vol 3. Research India Publications, pp 387–396. Available: searchdl.org/public/book_series/AETS/7/546.pdf
5. Singh V, Varsha, Misra AK (2015) Detection of unhealthy region of plant leaves using image processing and genetic algorithm. In: 2015 International conference on advances in computer engineering and applications (ICACEA), IMS Engineering College, Ghaziabad, India
6. Rani R, Kumari S (2016) An approach of detecting discontinuities in images. Int J Sci Res (IJSR) 5(7)
7. Mukherjee M, Pal T, Samanta D (2012) Damaged paddy leaf detection using image processing. J Global Res Comput Sci 3(10):7–10
8. Mazhir SN, Ali AH, Harb NH, Hadi FW (2017) The effect of dielectric barrier discharge plasma on smear of leukemia blood cells by texture analysis images. J Appl Sci Res (JASR) 13(3)
9. Niemeijer M, Abràmoff MD, Van Ginneken B (2005) Automatic detection of the presence of bright lesions in colour fundus photographs. In: Proceedings of IFMBE the 3rd European

medical and biological engineering conference, Nov 2005, vol 11 of 1, pp 1823–2839, Prague, Czech Republic
10. Yang Y, Wei L, Nishikawa RM (2007) Micro calcification classification assisted by content based image retrieval for breast cancer diagnosis. In: IEEE international conference on image processing, vol 5, pp 1–4

A Contemporary Review on Knee Injuries and Protective Pads

K. Anirudh and Shivraj Narayan Yeole

Abstract Osteoarthritis (OA) is a medical condition that affects the knee joint of humans primarily in the age group of 55–60 years. It specifically triggers cartilage breakdown due to aging. However, injury, obesity, inactivity, genetics, inflammation, diabetes, and other medical reasons may also lead to osteoarthritis in lesser age groups. Some of the symptoms used for detecting osteoarthritis are muscular pain, a decrease in range of motion at joint, difficulty in joint mobilization, and mild swelling around the joint. Orthopaedic practitioners analyze this condition using the Kellgren Lawrence grading system based on X-rays and magnetic resonance imaging. Diagnosis involves suggesting regular exercises for increasing muscle strength, losing weight, and putting less effort into the affected joint. Knee braces, knee caps, knee protective pads, and knee sleeves are recommended for use depending on the grade of cartilage wear. As a measure of precaution, many people in the aforementioned age group as well as sportspersons are moving towards using personal protective devices as prevention is better than treatment to the injury. Personal protective device is a patient-specific device used to decrease risk factors associated with the injury. One such device is a knee protective pad which safeguards the knee and provides comfort. This paper presents a critical review and detailed analysis of the latest trends in the development and use of conventional and unconventional knee protective pads.

Keywords Osteoarthritis · Knee protective pads · Protective devices

1 Introduction to Knee

Knee joint is responsible for body support and movement. It consists of bones, ligaments, tendons, and meniscus [1]. The femur, tibia, and patella structure are the bones present in knee. The knee bones are connected with ligaments. Tendon is soft

K. Anirudh · S. N. Yeole (✉)
VNR Vignana Jyothi Institute of Engineering and Technology, Hyderabad, Telangana 500090, India
e-mail: shivrajyeole@vnrvjiet.in

N. Gascoin and E. Balasubramanian (eds.), *Innovative Design, Analysis and Development Practices in Aerospace and Automotive Engineering*, Lecture Notes in Mechanical Engineering, https://doi.org/10.1007/978-981-15-6619-6_54

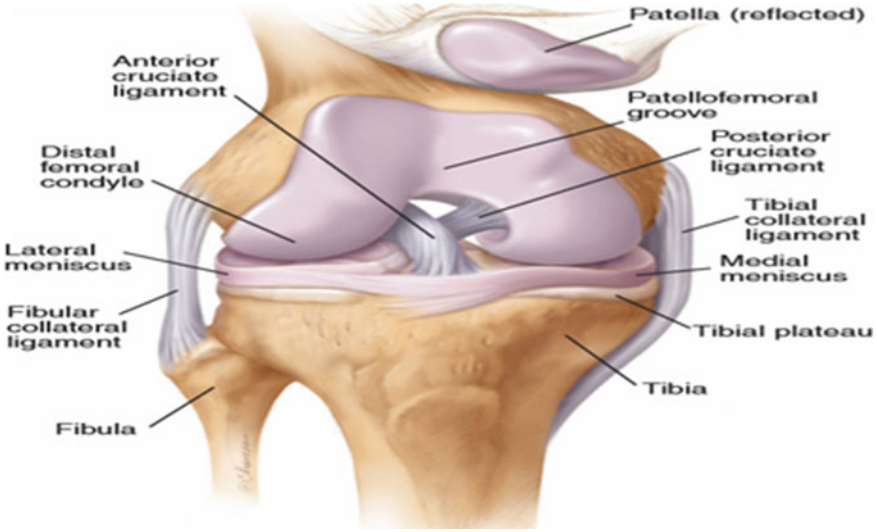

Fig. 1 Anatomy of knee. *Source* Adv Stud Med 4, p. 364

tissue, which provides stability to the joint and it is used to connect bone and muscle. Anatomy of knee is shown in Fig. 1.

Knee anatomy is used to study the knee joint and type of knee injury is identified while knee examination to diagnosis:

(a) **Palpation**—It uses radiography images like X-rays, magnetic resonance imaging (MRI), and computed tomography scan (CT) [2].
(b) **Motion**—It is the degree of knee joint allowed to rotate [3]

1. Assessment of effusion
2. Assessment of range of motion—0 to 10 degrees of flexion
3. Assessment of collater ligaments—25 degrees of flexion
4. Assessment of ACL—90 degrees of flexion
5. Assessment of PCL—90 degrees of flexion sag test
6. Assessment of meniscus—90 degrees of flexion from a prone position

The occurrence of injury can be reduced by using personal protective equipment (PPE). The National Operating Committee on Standard for Athletic Equipment (NOCSAE) has tested protective pads for different materials and conditions [4]. It has stated that protective pads should be designed based on individual orthopaedic history.

As per the study carried out in the sports category, 57% of the injuries occurred on head and 22% of injuries occurred to leg due to loss of balance and failed trick attempt [5]. The Major League Baseball health and injury tracking system has identified 19% of occurrence of knee injuries during 2011–2014 seasons. These injuries can be reduced using kneepad and also to provide stability support at the joint [6].

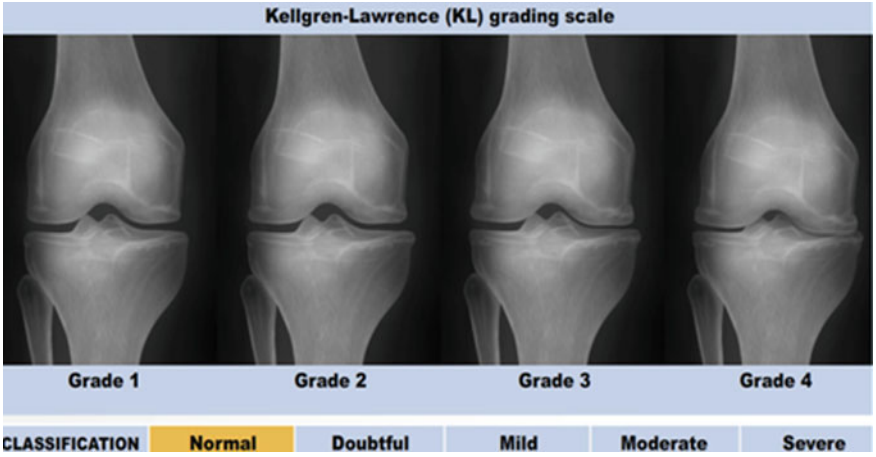

Fig. 2 Kellgren-Lawrence grading. *Source* LNMIA 10358, p. 376

Types of chronic knee injuries are categorized as given below [7]:

1. *Patellar Tendinitis* is the inflammation of patellar tendon (ligament tear).
2. *Patello Femoral Pain Syndrome* (PFPS) is caused by degeneration or stress between the kneecap (patella) and articular cartilage.
3. *Osteoarthritis* (OA) occurs due to cartilage wear between joints.
4. *Prepatellar Bursitis* is the Inflammation to the bursa in front of the kneecap may cause anterior knee pain. It causes friction and also increases pressure on the bursa.
5. *Tibial Plateau Fractures* are bone tear.
6. Knee bone is dislocated from its original position known as *Knee dislocation.*

The knee injuries are identified using radiography imaging techniques like MRI, CT, X-ray. The knee osteoarthritis (KOA) is the most commonly occurring knee injury between 22 and 65 years of age. It occurs due to the obese, elderly, and those with a sedentary lifestyle. The OA is classified using Kellgren and Lawrence (KL) grades. Grade-0, 1, 2, 3, and 4 represents normal, doubtful, minimal, moderate, and severe OA, respectively. Figure 2 shows the KL grading system [8].

The aim of orthopaedic devices is to reduce pain while loading and unloading of the knee. Orthopaedics suggest sleeves, braces, and implants depending on the osteoarthritis grading [9].

1.1 Capturing Patient Geometry

The different knee poses are analyzed using anthropometry and then the 3D scans of knee shape are collected. The SCAPE model of leg is prepared and the data is

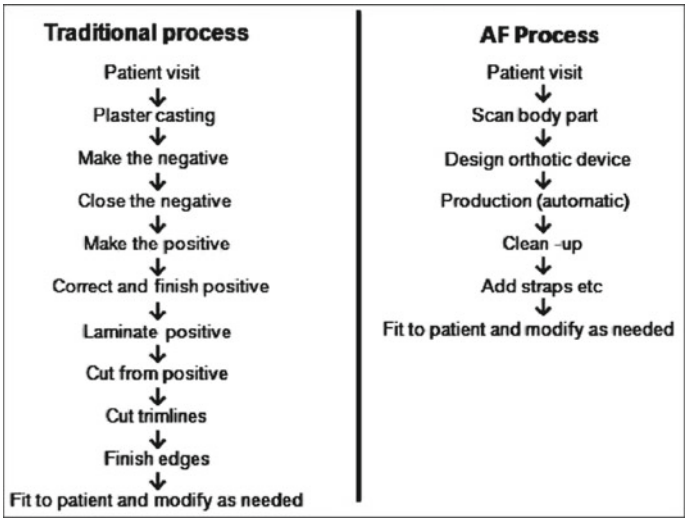

Fig. 3 Comparison of traditional manufacturing process and additive manufacturing process. *Source* J. Plos. One. l.13.1, p. e0190585

collected for standing and bent knee shape. It is found that kneeling position has high internal stresses [10].

Traditional method of modeling protective pads is to collect the data of the body using reverse engineering technology plaster casts, foam impressions, or manual measurement [11]. As shown in Fig. 3, it is clear that the use of 3D scanners in the manufacturing process has reduced the steps of preparing patient-specific devices [12].

1.2 Knee Analysis

Most of the knee injuries occur due to instability [11]. The functional purpose of knee is tested with sleeve, knee braces, and bare knee. The knee flexion is observed using iso-kinetic dynamometer. The jump height and distance of the person is observed using a vertical jump measuring device. The dynamic balance test is measured using biodex balance system which is used to observe the stability of a person [13]. The stair descents are tested to identify the knee joint angle based on the continuous steep descent and sensors, infrared camera is used [14].

2 Knee Pad Analysis

Most of the injuries occur due to impact forces, so the protective equipment is tested using impact testing machines and strain gauge sensors. The pads made of different materials and with different thicknesses are tested for shock absorption [15–17]. Sometime cadaver specimens are used to know the damage (impulse) in drop test [17]. The force distribution of knee can be observed while kneeling. The kneepad of hard polyethylene shell and soft foam material is tested and peak force is observed using flexiforce sensor. The impact test and penetration test is used to identify the strain energy at peak forces [6]. The polyurethane foam, LDPE foam, and viscoelastic material are tested. The hard outer shell absorbs maximum energy and the foam deforms easily to reduce the impact energy [18].

The penetration test on leg pads made of non-linear viscoelastic materials is tested for different mass, velocity, and stiffness of the ball. The cannon uses pressurized air to project the ball. The coefficient of restitution, peak force, deformation is observed. The force transducer transfers output voltage which is used to obtain peak force. Analysis based on recorded video of inbound velocity, outbound velocity, contact time, and de-formation of the pad is observed for different impact velocities [19]. The Image Pro Analyser software is used to identify the central impact and side-impact which is used to obtain an equation based on deformation in terms of position of inbound and penetration velocity.

3 Additive Manufactured Knee Pads

Fused Deposition Modeling (FDM) or Fused Filament Fabrication (FFF) machines are low-cost 3D printers that work on simple principle of extruding a thin filament of molten material through nozzle heated nozzle [20]. The most common 3D printing polymer materials are PolyLactic Acid (PLA), Acrylonitrile Butadiene Styrene (ABS), Polyethylene Terephthalate (PETT), nylon, etc. The low cost and ease of use material are PLA and the strongest one is ABS [21].

The additive manufactured (AM) method is used to create complex shapes, lightweight geometries in less time and cost. The CAD model is prepared using lattice structure. FDM is used to print the external rigid shell component with polypropylene material [20]. The internal foam is made using material 85% EVA and 15% polyethylene. The shin pad and the commercial pads are tested under impact force. It is observed that AM pads have a more constant stress slope, which implies a stiffer pad.

The AM pads are evaluated in terms of their position, shape, area, thickness, weight, flexibility, and ease of use. In general, polyester 51%, nylon 36%, and polyurethane 13% are used. The commercial pads are not custom specific. AM pad is prepared using a fused filament fabrication (FFF) method. The flexible thermoplastic

polyurethane contributes to ease of motion and chloroprene rubber foam is used. The percentage of force attenuation was calculated under impact testing [22].

4 Conclusion

Most of the injuries occur due to the instability of the knee. Radiographic images are used to identify the type of injury and helps the orthopaedic surgeon in the diagnosis. Several studies suggest the use of orthopaedic devices depending on the Kellgren-Lawrence grading. The ergonomics study of leg is helpful in designing the knee braces and implants. The kinematics of knee in forward motion has a major chance of ACL injury occurrence. The orthopaedic devices are used to reduce the forces acting on the knee. Different postures of the knee are studied and maximum stress acting on plateau is observed while kneeling. This emphasizes the need to design knee pad and other orthopaedic devices so as to have reduced internal stresses. 3D scanners provide better accuracy and repeatability than manual measurements for capturing knee dimensions while modeling a patient-specific device. Protective knee pads are used to protect the knee from a sudden impact force. Polyethylene shell and polyurethane foam has better energy absorption properties. AM process has reduced the steps in the preparation of customized patient-specific devices. AM is preferred than traditional methods because of low-cost production, lightweight, and ease of design. PEEK is found to be the strongest polymer material used for 3D printing. Thermoplastic polyurethane has more percentage of force attenuation when compared with ABS, PLA, ABS, PETT, and nylon.

References

1. Smith CC (2004) Acute knee injury: evaluating the painful knee: a hands-on approach to acute ligamentous and meniscal injuries. Sports Med Adv Stud Med 4:362–369
2. Bruno F, Barile A, Arrigoni F, Laporta A, Russo A, Carotti M, Splendiani A, Di Cesare E, Masciocchi C (2018) Weight-bearing MRI of the knee: a review of advantages and limits. J Acta Bio Med 89(Suppl 1):78
3. Sureshbabu P, Ashok C (2010) Two dimensional motion analysis on angle of knee joint bend during long jump take-off. Br J Sports Med 44(Suppl1):i47–48
4. Bacon CE, Van Lunen BL, Hankemeier DA (2018) Postprofessional athletic training students' perceptions concerning the health care competencies. J Athletic Training Educ 4:309–323
5. Liu Y (2013) Doctoral dissertation: a study of warp-knitted spacer fabrics as cushioning materials for human body protection. Polytechnic University, Hong Kong
6. Dahm DL, Curriero FC, Camp CL, Brophy RH, Leo T, Meister K, Paletta GA, Steubs JA, Mandelbaum BR, Pollack KM (2016) Epidemiology and impact of knee injuries in Major and Minor League Baseball players. Am J Orthop 45(3):E54–62
7. Majewski M, Susanne H, Klaus S (2006) Epidemiology of athletic knee injuries: a 10-year study. Knee 3:184–188

8. Antony J, Guinees M, Moran K, O'Connor NE (2017) Automatic detection of knee joints and quantification of knee osteoarthritis severity using convolutional neural networks. In: Machine learning and data mining in pattern recognition. INT. LNMAI 10358. Springer, Cham, p 376
9. Brooks KS (2014) Osteoarthritic knee braces on the market: a literature review. JPO 1:2–30
10. Li P, Corner B, Hurley M, Powell C, LaFleur A (2015) Three-dimensional (3D) analysis of knee shape for designing a knee-pad. J Procedia Manuf 3:3689–3693
11. Dessery Y, Pallari J (2018) Measurements agreement between low-cost and high-level handheld 3D scanners to scan the knee for designing a 3D printed knee brace. J Plos One 13(1):e0190585
12. Milošević P, Slavica B (2018) 3D technologies in individualized chest protector modelling. J Orig Sci Ar 1(2):46–55
13. Ochi A, Ohko H, Ota S, Shimoichi N, Takemoto T, Mitsuke K (2018) Custom-made hinged knee braces with extension support can improve dynamic balance. J Exerc Sci Fitness 16(3):94–98
14. Zhang C, Sun W, Song Q, Gu H, Mao D (2018) Performance of older adults under dual task during stair descent. J Exerc Sci Fitness 16(3):99–105
15. Tatar Y, Ramazanoglu N, Camliguney AF, Saygi EK, Cotuk HB (2014) The effectiveness of shin guards used by football players. J Sports Sci Med 13(1):120
16. Xu H, Jampala S, Bloswick D, Zhao J, Merryweather A (2017) Evaluation of knee joint forces during kneeling work with different kneepads. J Appl Ergonomics 58:308–313
17. Schwarze M, Hurschler C, Welke B (2019) Force, impulse and energy during falling with and without knee protection: an in-vitro study. Sci Rep Nat 9(1):1–6
18. Duncan O, Foster L, Senior T, Allen T, Alderson A (2016) A comparison of novel and conventional fabrication methods for auxetic foams for sports safety applications. ISEA 147:384–389
19. Walker PJ (2014) Representative testing of personal protection equipment. Loughborough University
20. Williams JM, Adewunmi A, Schek RM, Flanagan CL, Krebsbach PH, Feinberg SE, Hollister SJ, Das S (2005) Bone tissue engineering using polycaprolactone scaffolds fabricated via selective laser sintering. J Bio Mater 26(23):4817–4827
21. Farbman D, McCoy C (2016) Materials testing of 3D printed ABS and PLA samples to guide mechanical design. Am Soc Mech Eng Digital Collect, IMSEC
22. Cazón-Martín A, Iturrizaga-Campelo M, Matey-Muñoz L, Rodríguez-Ferradas MI, Morer-Camo P, Ausejo-Muñoz S (2019) Design and manufacturing of shin pads with multi-material additive manufactured features for football players: a comparison with commercial shin pads. J Sci Technol 233(1):160–169

Augmented Reality Based Collaborative Product Enhancement

Ravi Kumar Gupta

Abstract The paper presents an application of Augmented Reality to support collective product development among members of different domains across the product development including end-users. Portable software tool that works on smart devices (smartphones, tablets, laptops, PCs) is developed for collaborative product development using Augmented Reality to nurture, maintain and increase a company's market share by fulfilling consumer's demand. Portable software tool is presented with the proposed methodology for a collaborative platform to work on mobile devices to capture the synergistic dynamics and to customize and interrelate with the product in customer(s) own environment. The product shown to the customer using the developed tool maybe customizable as per the customers' requirement in his/her own environment remotely and to record comments. The recorded customization and comments are then stored in the database and used in the product development and enhancement of the product.

Keywords Augmented reality · Distant collaborative · Product development · AR-based mobile device application

1 Introduction

New product development approaches look at refining present products to investigate a present market or create new products that the market pursues. Product development is a series of steps that include the conceptualization, design, development and marketing of newly created or newly rebranded goods or services. In the early stages of product development, product and user experience concepts are typically envisioned and shaped through sketching and CAD modelling. Designers are very active in using such kind of tools to create, but on paper or on the computer screen, their

R. K. Gupta (✉)
Mechanical Engineering Department, SAMM, Manipal University Jaipur, Jaipur-Ajmer Express Highway, Jaipur 303007, India
e-mail: ravikumar.gupta@jaipur.manipal.edu; rkgmuj@gmail.com

N. Gascoin and E. Balasubramanian (eds.), *Innovative Design, Analysis and Development Practices in Aerospace and Automotive Engineering*, Lecture Notes in Mechanical Engineering, https://doi.org/10.1007/978-981-15-6619-6_55

thoughts are disengaged from realities of scale, spatial context and fit to the user's use situation and environment. The decisions taken at this level are vital and affect the cost and the success of the complete product [1].

Augmented Reality (AR) permits to pull the knowledge out of the screen and drop it into the real world. One can imagine in higher faithfulness much earlier in the process, with an intensely lower level of investment when compared to other forms of rapid prototyping techniques. Augmented Reality-based design environment is a semi-immersive design atmosphere in which the users/operators can see the real world while execution on a virtual product [2]. The requirements of AR in the product development for distant collaboration is explained in literature [3–5]. The greatest impact we'll see from AR, its competence to reform the way that people actually interact with the technology in their lives. AR to support the assembly of product and production re-scheduling is presented by Mourtzis et al. [6]. There is a need to develop solution based on AR for collaborative product development activities and also to integrate different stakeholders irrespective of their locations. The innovative aspect of this paper is to propose a software tool for collaborative product development using AR to nurture, maintain and increase a company's market portion by satisfying a consumer's requests. The AR-based approaches for product development are reviewed first and then the requirement of the development of software tools for Product Development using AR is identified. The proposed methodology and implementation details along with case studies are presented.

2 Augmented Reality and Product Development: State of the Art

Product development necessitates the involved stakeholders [7] to have the essential level of knowledge and a good insight into the product design. For example, using AR supported design assessment process, design errors that could possibly lead to postponements or even disappointment in the final assembly of the radio-controlled car that can be early diagnosed and modified [8]. It includes the integration of target market views and particularity, research on the current technologies, assessment of the available manufacturing resources and requires the collaboration of a group of people, usually with diverse backgrounds, so as to achieve the anticipated result [9, 10]. Literature [11, 12] reviews the use of AR in design and manufacturing including the hardware and software tools associated with AR. Virtual Reality (VR) structures have already been established for computer-aided design and simulation applications in which the users are fully immersed in a virtual environment and interact with the 3-dimensional virtual models. Whereas AR technology is comparatively novel technology that includes the superposition of computer graphics over real objects/scenes [13]. AR delivers more pragmatism to the users and makes the users feel safer and more relaxed while working on the product design [13]. AR-based environment is easy and low-priced to set up, which is a major advantage of using AR as compared

to VR [14]. Moreover, AR-based setting would permit the users to move around in a real three-dimensional settings to imagine the products and interact with and adapt these virtual products using virtual interfaces [2]. Therefore, there is a need to develop a solution based on AR for collaborative product development activities and also to integrate different stakeholders irrespective of their locations. The proposed solution with the development of AR-based software tool for collaborative product development is presented in the following sections.

3 AR-Based Software Tool for Product Development

In the proposed AR-based software for collaborative product development, the basic idea of AR is to superimpose graphics, audio and other sense improvements over a real-world environment in real-time. There are three components required to work namely, smartphone/computer, tracking system (3D model and/or image target), and AR-based software tool (can be viewed in Android devices by installing developed .apk file). Unity3D software development framework [15] is used for the development and generation of .apk for Android devices. The proposed AR-based solution works on mobile devices (i.e. smartphone, tablet, laptop) with operating system as Android and Windows OS and allows the end-user to customize and interrelate with the product in his/her own environment. The following section explains the development of the proposed AR-based software tool.

4 Development of AR-Based Software Tool

Flow chart of the development of the AR-based software tool for collaborative product development is presented in Fig. 1. It starts with the initial configuration in the Unity3D software development environment [15] and then integrating with the Vuforia developer environment [16] which are then configured with the required setting for the development. C# plugin is used for the programming to customize the interactions required for the end-user and real environment. Vuforia developer portal used in the development is shown in Fig. 2. The required object(s) (3D model of the product/parts as base model) can be designed in Unity3D and can also be designed in CAD modeling packages, i.e. AutoCAD, Cero, SolidWorks which are then imported into Unity3D development environment. It is also possible to import the model from the asset store or from any other design software or it can be imported from company catalogue. Rendering the objects are done in Unity3D by adding textures and materials to the 3D models. 3D textures or 2D sprites can be added by creating a material for the object. The required animations are added using the Animator tool in Unity3D. The animations once added have to be added to the legacy animator to prevent bugs.

Virtual buttons are created using C# and Microsoft Visual Studio for end-user intractability and for the selection from the available options against part/product (a

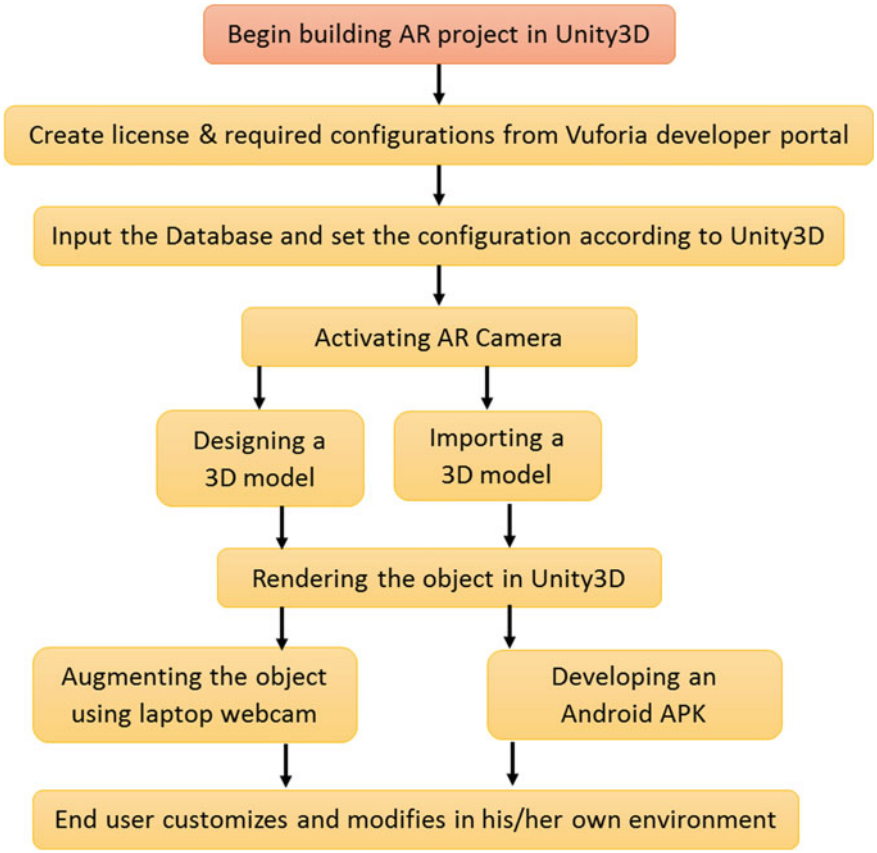

Fig. 1 Flow chart for the AR-based software tool for product development

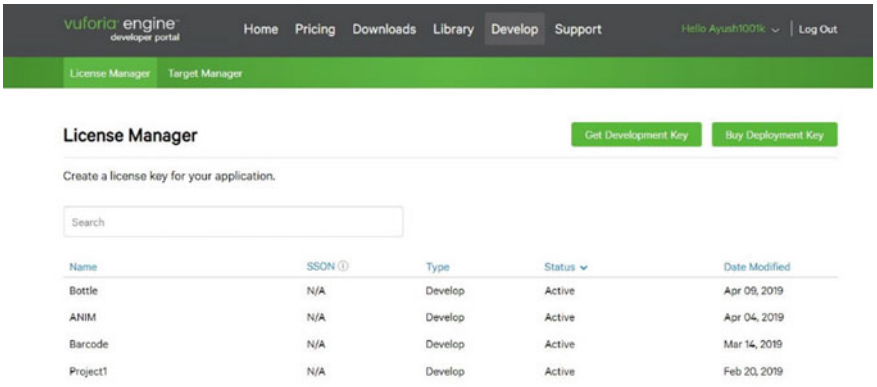

Fig. 2 Vuforia developer portal for AR application

solution). The IVirtualButtonEventHandler in Unity3D initiates the virtual button. OnButtonPressed VirtualButtonBehavior in Unity3D defines the action for the virtual button when the button is pressed. OnButtonReleased VirtualButtonBehaviours defines the action for the virtual button when the button is released. GetComponent<Animation> allocates the animation again to the Virtual button after the button is released. Screenshot for this AR-based interactivity for the end-user is presented in Fig. 3. The object (3D model of the product/parts of which evaluation need to be studied with reference to the base model and working environment) is then augmented using the laptop webcam and template. This step is required as the developed application can be first tested using the webcam and then converted into an Android application to work with the smartphone camera. Installing Android Studio and Android Software Development Kits (SDKs) for different versions of Android in the Unity3D and confirm the required settings in Unity3D to interact with the Android APKs. Designing an Android app and converting the format of Unity3D to Android APK is required to work on Android mobile devices by the end-user(s). This is to be done using Android Studio as it provides the SDKs along with the Android SDKs of Vuforia. The developed tool is used to record customers' preferences and

```
using System.Collections;
using System.Collections.Generic;
using UnityEngine;
using Vuforia;

public class Cap1Script : MonoBehaviour, IVirtualButtonEventHandler

{
    private GameObject vbButtonObject;
    private GameObject Cap1;


    void Start()
    {
        vbButtonObject = GameObject.Find("actionButton1");
        Cap1 = GameObject.Find("Cap1");

        vbButtonObject.GetComponent<VirtualButtonBehaviour>().RegisterEventHandler(this);

    }


    public void OnButtonPressed(VirtualButtonBehaviour vb)
    {
        Debug.Log("Button Down!!!!");
        Cap1.GetComponent<Animation>().Play();


    }

    public void OnButtonReleased(VirtualButtonBehaviour vb)
    {
        Cap1.GetComponent<Animation>().Stop();


    }
}
```

Fig. 3 Screen shot for the AR-based interactivity for the end-user

satisfaction levels on a product, attributes and modules considered using the AR-based developed tool which can be run on customers' smartphone. The information thus recorded is analysis and connected to the company's database in-order to use the recorded information in the product development. This ensures to include the customers' interactions with the digital product in his/her environment of use of the product.

5 Implementation Case Study: Superimposition-Based AR Application for Customer Interaction, Recording Preferences (Seat)

Superimposition based augmented reality either partially or fully replaces the original view of an object (template (2D or 3D) or real physical object) with a newly augmented view of the same object (digital model created in AR tool). The implementation of this is explained with the following example. Three stock seats were imported into Unity3D as shown in Fig. 4. These seats were selected keeping in mind the colour variations along with the overall design. Textures and materials were assigned to each of the seats and colour variations were added. Different animations for each seat was developed using the Unity3D animator and then added to each seat. Furthermore, virtual buttons were coded using Microsoft Visual Studio and Unity3D editor and then allotted to each seat. The virtual buttons and animations were first tested using the image template and laptop webcam. Further, an Android application was developed for the same setup.

Figure 4 showcases three seats with different materials and textures in a Unity3D scene on windows platform. Figure 5 shows the target image as well as the augmented seat models in the smartphone using the developed application. These augmented seats are 3D in nature along with high polygon 4K textures. The superimposed view

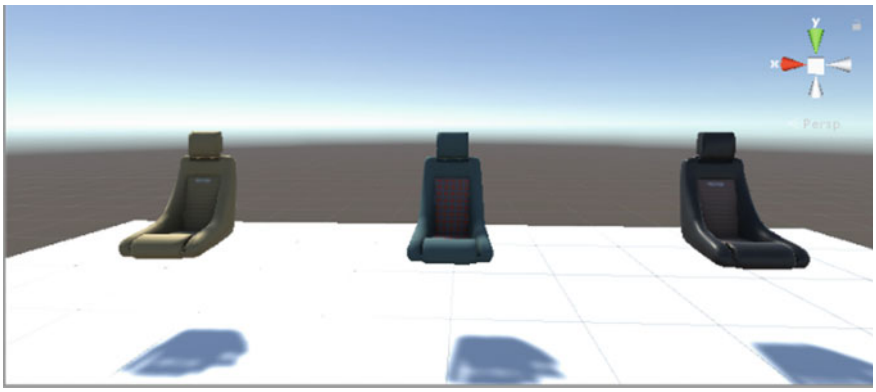

Fig. 4 Scene of seats in Unity3D

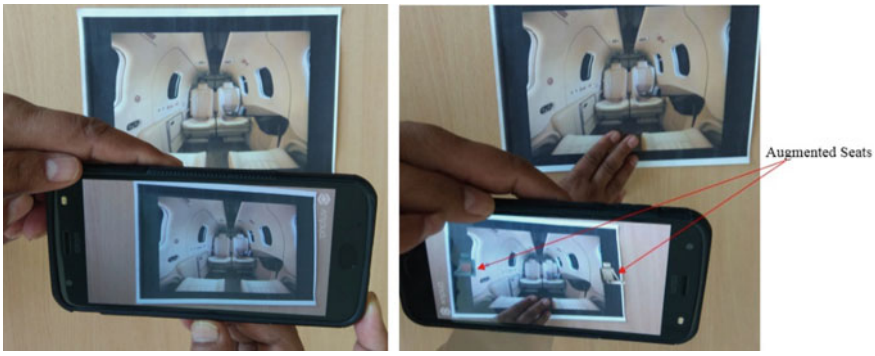

(a) Smartphone camera as AR camera **(b)** Augmented Seats with a target image

Fig. 5 AR application: augmented seats on the cabin

of the seats is shown in Fig. 6 which takes place after the virtual buttons are pressed according to the customer preference. This application can be used by the customer for selecting his preferred type of seat for his/her automobile as per his/her need in his/her environment.

The designed applications were successfully running on Windows PC as well as Android platform devices. The virtual buttons were working when pressed and animations were performed accordingly. The developed AR application can be used by anyone having an Android phone or Windows PC at his/her convenience in his/her own working environment. It is a beneficial add-on to the current product development process as the design, prototyping as well as customer feedback process is improved and fastened. It helps in reducing the errors which are made during the development process as the errors can be easily seen in real-time and then by initiating the correction procedures.

6 Conclusion

Augmented reality is a combination of a real scene viewed by the user and a virtual scene/object produced by a computer/smartphone which augments the scene with supplementary information. AR software tool for collaborative product development is successfully developed and tested with multiple case studies. The working of the AR software tool is explained using a case study as superimposition-based AR application. The developed AR software tool is implemented on Android mobile devices for the end-user interactions in end user's working environment. With the help of the developed AR software tool, we would like to give the user the control to customize an object as per his/her requirement in his/her own working environment. The AR software tool will also play a major part in helping the prototyping phase. Through the AR application, a customer can select his/her preferred design at his/her convenience

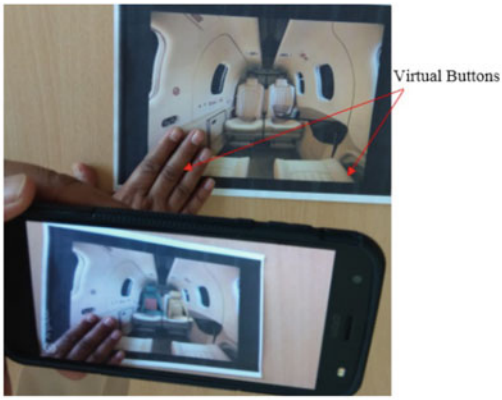

(a) Superimposition of the required object (e.g. seats) on the target object (e.g. Cabin)

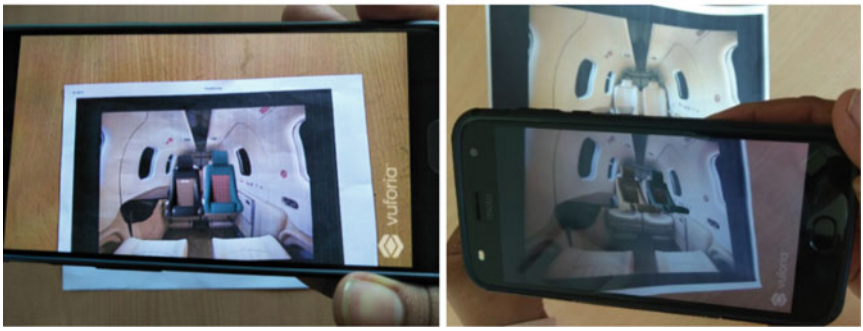

(b) Visualization of the augmented objects (e.g. seats on target object) by rotating the smartphone: Different views.

Fig. 6 Superimposed view of the seats on the target image and visualization in different orientations: smartphone as working device

in his/her environment. The developed AR software tool can further be enhanced by combining marker-less augmented reality in addition to the superimposition-based AR in-order to configure geographical preferences for a product and/or market.

References

1. Boothroyd G (1994) Product design for manufacture and assembly. Comput Aided Des 26(7):505–520
2. Shen Y, Ong SK, Nee AYC (2010) Augmented reality for collaborative product design and development. Des Stud 31:118–145
3. Buergin J, Belkadi F, Hupays C et al (2018) A modular-based approach for just-in-time specification of customer orders in the aircraft manufacturing industry. CIRP J Manuf Sci Technol 21:61–74

4. Gupta RK, Ucler C, Bernard A (2018) Extension of the virtual customer inspection for distant collaboration in NPD. In: 2018 IEEE International conference on engineering, technology and innovation (ICE/ITMC), Stuttgart, Germany
5. Gupta RK, Belkadi F, Buergy C et al (2018) Gathering, evaluating and managing customers' feedback during aircraft production. Comput Ind Eng 115:559–572
6. Mourtzis M, Zogopoulos V, Xanthi F (2019) Augmented reality application to support the assembly of highly customized products and to adapt to production re-scheduling. Int J Adv Manuf Technol 105(9):3899–3910. https://doi.org/10.1007/s00170-019-03941-6
7. Robin V, Rose B, Girard P (2007) Modelling collaborative knowledge to support engineering design project manager. Comput Ind 58(2):188–198
8. Mourtzis D, Zogopoulos V, Vlachou E (2018) Augmented reality supported product design towards industry 4.0: a teaching factory paradigm. Procedia Manuf 23:207–212
9. Morris R (2016) The fundamentals of product design. Bloomsbury Publishing. ISBN: 9781472578242
10. Gupta RK, Belkadi F, Bernard A (2017) Evaluation and management of customer feedback to include market dynamics into product development: satisfaction importance evaluation (SIE) model. In: DS 87-4 Proceedings of the 21st international conference on engineering design (ICED 17), Canada
11. Ong SK, Yuan ML, Nee AYC (2008) Augmented reality applications in manufacturing: a survey. Int J Prod Res 46(10):2707–2742
12. Nee AYC, Ong SK, Chryssolouris G et al (2012) Augmented reality applications in design and manufacturing. CIRP Ann 61(2):657–679
13. Kaufmann H, Schmalstieg D (2003) Mathematics and geometry education with collaborative augmented reality. Comput Graph 27(3):339–345
14. Lu SCY, Shpitalni M, Gadh R (1999) Virtual and augmented reality technologies for product realization. Ann CIRP 48(2):471–495
15. Unity 3D https://unity.com/
16. Vuforia https://developer.vuforia.com/

Influence of Different Abrasives Mixtures on Abrasive Water Jet Drilling of Die Steel

K. Balaji and N. Yuvaraj

Abstract Abrasive Water Jet Machining (AWJM) is a non-traditional machining process used for cutting an extensive range of materials by means of a mixture of water and an abrasive substance. The present study describes the effect of abrasive materials and stand-off distance on AWJ drilling of die steel. Different abrasives namely Silicon Carbide, Garnet, and abrasive mixtures of silicon carbide and garnet in the ratio of (60:40) were used in this study. The Output responses, namely cylindricity, circularity, and surface roughness of the drilled surfaces were analyzed. The experimental results showed that the mixture of the different abrasives increases the cutting ability of AWJ performance as compared to single type abrasives, namely, garnet or Silicon Carbide in die steel.

Keywords Abrasive water jet machining · Cylindricity · Surface roughness and roundness

1 Introduction

The Abrasive Water Jet Machining (AWJM) process provides a high-quality cutting with a great surface finish, therefore it is advantageous in the manufacturing of several components in various industries such as the automotive, aerospace and defence sector Natarajan et al. [1]. It is an environmentally friendly process. Water jet cutting requires no cooling or lubricating oils, so there are no chemically contaminated chips to dispose of. It generates no noxious fumes during the cutting process. The AWJM process utilizes a mixture of water and abrasive to erode material from

K. Balaji (✉) · N. Yuvaraj
Department of Mechanical Engineering, Vel Tech Rangarajan Dr. Sagunthala R&D Institute of Science and Technology, Chennai, India
e-mail: kbalaji.me@gmail.com

N. Yuvaraj
e-mail: yuvaceg09@gmail.com

N. Gascoin and E. Balasubramanian (eds.), *Innovative Design, Analysis and Development Practices in Aerospace and Automotive Engineering*, Lecture Notes in Mechanical Engineering, https://doi.org/10.1007/978-981-15-6619-6_56

the target surface. It uses the kinetic energy of water particles to erode the material by microchipping action. The AWJM process has several predominant process parameters, i.e., water jet pressure, transverse speed, abrasive mass flow rate, standoff distance, abrasive grit size, etc., which affect the performance characteristics (i.e., surface roughness, kerf top width, taper angle, cylindricity, and material removal rate). Materials commonly cut with a water jet include textiles, rubber, foam, plastics, leather, composites, stone, tile, glass and mainly, metals. This process does not require secondary operations to smooth the edge finish. Abrasive is one of the effective process parameters in AWJM process. Abrasive type and size play a crucial role in the production of better surface finish. Recently researchers have attempted or adopted various techniques for the improvement in AWJM performance features on hard materials. In this study, mixing of two abrasives has been used for the AWJM operations. The technical content of this study has not been studied to date. Khan and Haque [2] used different types of abrasives for AWJM namely garnet, aluminum oxide, and silicon carbide. Performance analysis of three types of abrasive has been analyzed and it is observed that cutting ability of silicon carbide was higher than aluminum oxide and garnet. Verma et al. [3] have been conducted abrasive water jet experiments on AA2014 aluminium alloy using aluminium oxide as an abrsasive material. The following parameters namely traverse speed, standoff distance, pressure, and mass flow rate have been considered for the study. Experimental values were compared with a predictive model that was established using the fuzzy logic technique. Shibin et al. [4] conducted abrasive water jet machining process on aluminium alloy. Silicon carbide was used as an abrasive particle and the following process parameters have been considered in the study pressure, traverse speed, standoff distance, and mass flow rate. Pressure was identified as the most influencing factor on the depth of cut followed by the traverse speed and mass flow rate. Yuvaraj and Kumar [5, 6] have investigated the abrasive water jet machining of die steel by varying the garnet abrasive mesh sizes and the jet impingement angles. They reported medium-mesh size of garnet abrasive and oblique jet impingement angle produced a better cutting performance in terms of machinability and surface features. Aydin et al. [7] investigated the performances of different abrasives during AWJM process on marbles. Various abrasives considered in the study are garnet, white fused alumina, brown fused alumina, silicon carbide, glass beads, and emery powder. The performance has been measured and analyzed for the following parameters namely the cutting width, cutting depth, kerf angle, and surface roughness. Natarajan et al. [1] have reported the comprehensive literature survey on abrasive water jet process. It is observed that various investigations were carried with different features of abrasives namely, types of abrasives, abrasive flow rate, and size of the abrasive. It is also observed that there is a scope on mixing of various abrasives for improving the performance of abrasive water jet process. Perec [8] experimented AWJM process on titanium alloy, grade 5 using various abrasive particles namely garnet, olivine, and crushed glass abrasive, the study was conducted to find the solution for replacing predominant usage of garnet in AWJM process. Price of the Garnet keeps on increasing in the global market recently. Alternate abrasives which are cheaper than garnet is a much-needed one and also this will reduce the production

cost. Change in the abrasives also brings about changes in the features of the hole. From the literature survey, it is observed that the mixing of two abrasives and their respective output responses have never been attempted.

2 Materials and Methods

In this study, AISI D2 steel was chosen as work material due to its toughness and hardness properties. It has high wear and abrasion-resistant properties. D2 steel has the following mechanical properties namely, hardness 260 HV, poor toughness, and machinability [6]. The size of the work material is 290 mm × 190 mm × 39 mm. In this study, three types of abrasives were used for drilling operations. First, Garnet is the most widely used abrasive. It has a significant hardness, cost-effective abrasive, Options for recycling, environmentally friendly cutting, and cleaning. Second, Silicon Carbide (SiC) has higher hardness and sharp crystal edges. The reason behind the selection of SiC and Garnet abrasives are suitable for AWJM of hard materials. Third, the mixing of garnet and SiC abrasives was chosen with a ratio of 60:40 (Garnet-Silicon Carbide) which is shown in Fig. 1. This mixture ratio was chosen based on the pilot studies.

In this study, stand-off distance was a variable parameter and the levels were chosen as 1, 3, and 5 mm. The other experimental parameters and their levels are given in Table 1. Also, mixture ratio was kept constant for all experiments. Figure 2 shows the experimental setup for the AWJ drilling operations. A hole is made on the D2 steel with a diameter of 40 mm. The output responses considered in this work,

Fig. 1 60:40 abrasives mixture

Table 1 AWJM process parameters and their levels

Item	Description
AWJM system	Injection type nozzle
Type of pump	Intensifier pump
Abrasive feeding system	Automatic type vibratory conveyor
Abrasive particle shape	Angular (random)
Pressure	3200 bar
Mesh number	#80
Orifice diameter	0.25 mm
Nozzle diameter	0.75 mm
Jet impact angle	90°
Thickness of the work material	30 mm
Feed rate	20 mm/min
Abrasive flow rate	0.45 kg/min
Mixture ratio	60:40 (garnet: SiC)

Fig. 2 AWJ drilling operation

such as surface roughness, circularity, and cylindricity. The surface roughness was taken using the contact type roughness tester. A roughness measurement was made with a cut-off length of 0.8 mm and a traverse length of 4 mm. Hole geometrical features, namely, circularity and cylindricity were examined using the coordinate measuring machine (CMM).

3 Results and Discussion

3.1 Surface Roughness

Table 2 shows the Ra values for the various machining conditions with different stand-off distances. The comparison of Ra values is shown in Fig. 3. From the results, it is noticed that lowest surface roughness was found at SiC with a stand-off distance of 1 mm was employed. These results happened due to the impingement of hard abrasives which erode the material with uniform amount of material removal rate. Lower surface roughness was also observed in 60:40 abrasives and is found to be 1.56 µm. The combined action of both angular and spherical shaped grains in 60:40 mixtures which results in the good surface finish when a stand-off distance of 1 mm was used. In contrast, garnet abrasive shows a higher roughness due to the major involvement of spherical shaped abrasives. Also, it is observed that lower stand-off distance plays

Table 2 Ra of drilled holes

S. No.	Abrasive	Standoff distance	Ra, µm
1	Silicon carbide	5	2
2		3	1.98
3		1	1.23
4	Garnet	5	2.28
5		3	2.20
6		1	1.73
7	Garnet-silicon carbide (60:40)	5	2.23
8		3	1.98
9		1	1.56

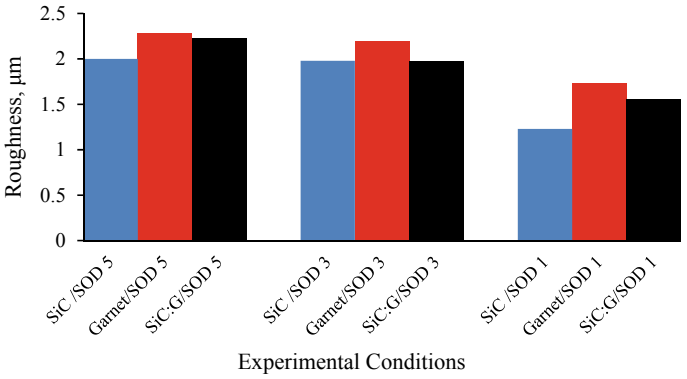

Fig. 3 Surface roughness of AWJ drilled holes

a vital role in affecting surface roughness. Lower stand-off increases the velocity of the abrasives which makes strong erosion in the die steel. It is concluded that spherical shaped abrasives are not suitable for machining die steel.

3.2 Circularity

Table 3 shows the Circularity values for the various machining conditions with different stand-off distances. The comparison of circularity values is shown in Fig. 4. This measurement has been taken at three regions of the machined hole namely top, middle, and bottom. From that, average circularity was taken for the experimental analysis. The results indicate that SiC abrasive has produced the least circularity in the hole at a stand-off distance of 5 mm. These combined parameter settings allow

Table 3 Circularity of drilled holes

S. No.	Abrasive	Standoff distance (mm)	Top (mm)	Middle (mm)	Bottom (mm)	Circularity (mm)
1	Silicon carbide	5	0.027	0.040	0.038	0.035
2		3	0.081	0.094	0.182	0.119
3		1	0.110	0.172	0.149	0.143
4	Garnet	5	0.098	0.127	0.129	0.118
5		3	0.087	0.107	0.142	0.112
6		1	0.334	0.378	0.461	0.391
7	Garnet-silicon carbide (60:40)	5	0.092	0.113	0.142	0.115
8		3	0.083	0.091	0.076	0.083
9		1	0.327	0.359	0.438	0.374

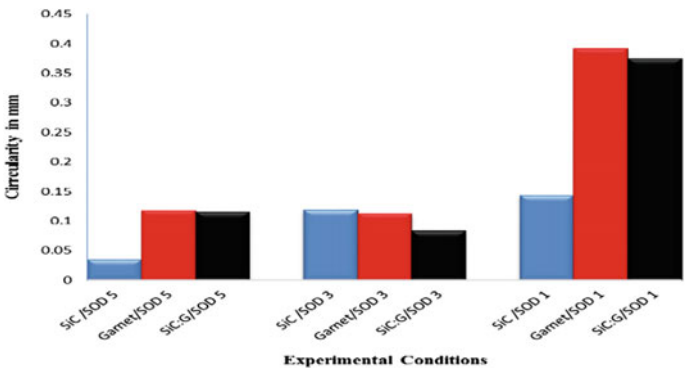

Fig. 4 Circularity values of AWJ drilled holes

the jet to produce the sufficient material removal rate at top, middle, and bottom cutting regions. Similarly, a lower circularity was found in 60:40 abrasive mixture rather than garnet abrasives. This was obtained while the stand-off distance of 3 mm employed. Mixed type abrasives cause the uniform rate of material removal in the cutting regions as a result of angular and spherical shaped particles maintains the cutting energy throughout the depth of target material. Among the experimental conditions, the highest circularity variation was found with the garnet abrasives. It is also observed that stand-off distance influences the circularity of the holes. Lower stand-off distance has produced a higher circularity variation in all types of abrasive conditions. This was due to the employment of a lower stand-off distance produced higher kinetic energy which removes the more volume of material at the entry region compared to the other regions.

3.3 Cylindricity

Table 4 shows the cylindricity values for the various machining conditions with different stand-off distances. The comparison of cylindricity variations is shown in Fig. 5. These values were measured at entry and exit regions of the drilled holes. This geometrical tolerance measures that govern the overall form of a cylindrical feature to confirm that it is circular and straight along with the hole axis. The results reported that 60:40 abrasive mixture produced a least cylindricity variation in the AWJ drilled holes. In addition, the angular shaped abrasives maintain the cutting energy of the jet which results in drilled hole round variations are significantly reduced. These results confirmed that 60:40 abrasives mixture maintains the circularity through an entire cylinder length.

Table 4 Cylindricity of drilled holes

S. No.	Abrasive	Standoff distance (mm)	Cylindricity (mm)
1	Silicon carbide	5	0.169
2		3	0.202
3		1	0.282
4	Garnet	5	0.304
5		3	0.416
6		1	0.542
7	Garnet-silicon carbide (60:40)	5	0.231
8		3	0.032
9		1	0.346

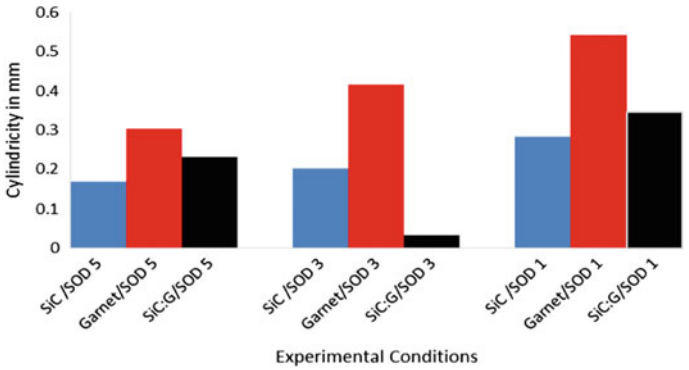

Fig. 5 Cylindricity values of AWJ drilled holes

4 Conclusions

Drilling investigations have been carried out on AISI D2 steel using Abrasive Water Jet Machining (AWJM) process by varying the stand-off distance and abrasive conditions. The experimental results revealed that SiC abrasive influences the surface roughness and circularity features of the drilled holes. However, a least cylindricity variation was found while the employment of 60 (Garnet):40 (Silicon Carbide) abrasives mixture ratio. This result confirmed the circular profile was maintained throughout the hole with a stand-off distance of 3 mm is employed. From the limited results, it is found that 60:40 abrasive mixture ratio plays an important role in surface finish as well as hole geometrical features, which is far better than garnet abrasive and better than SiC abrasive in the hole geometrical features. While the use of abrasives mixture, the selection of stand-off distance is a predominant role such that the AWJM process can minimize/maximize the performance features based on its desirability.

References

1. Natarajan Y, Murugesan PK, Mohan M, Khan SALA (2020) Abrasive water jet machining process: a state of art of review. J Manuf Process 49:271–322
2. Khan AA, Haque MM (2007) Performance of different abrasive materials during abrasive water jet machining of glass. J Mater Process Technol 191(1–3):404–407
3. Verma K, Anandakrishnan V, Sathish S (2019) Modelling and analysis of abrasive water jet machining of AA2014 alloy with Al_2O_3 abrasive using fuzzy logic. Mater Today Proc
4. Shibin R, Anandakrishnan V, Sathish S, Sujana VM (2019) Investigation on the abrasive water jet machinability of AA2014 using SiC as abrasive. Mater Today Proc
5. Yuvaraj N, Kumar MP (2017) Investigation of process parameters influence in abrasive water jet cutting of D2 steel. Mater Manuf Process 32(2):151–161
6. Yuvaraj N, Kumar MP (2017) Surface integrity studies on abrasive water jet cutting of AISI D2 steel. Mater Manuf Process 32(2):162–170

7. Aydin G, Kaya S, Karakurt I (2019) Effect of abrasive type on marble cutting performance of abrasive waterjet. Arab J Geosci 12(11):357
8. Perec A (2018) Experimental research into alternative abrasive material for the abrasive water-jet cutting of titanium. Int J Adv Manuf Technol 97(1–4):1529–1540

Rarefied Flow Field Analysis on a Re-entry Vehicle

M. Abhay, Vinod Kumar, Aaditya Chaphalkar, and Jiju Justus

Abstract Rarefied flow field analysis has been carried out on a re-entry vehicle (REV) for an altitude of 105 km. DSMC-based solver was used to calculate pressure, drag, temperature and heat-flux. A blunt nose re-entry vehicle (REV) was used for the analysis in a rarefied flow field. The flow was considered to be in chemical and thermal non-equilibrium. 11 species (N_2, O_2, NO, N_2^+, O_2^+, NO^+, N, N^+, O, O^+ and e^-) model for gas composition was used with total of 47 chemical reactions. Observations were also made for the existence of shockwave, change in shock thickness and its properties. It was observed that there is a small variation in chemically non-reacting and reacting (chemically non-equilibrium) flow. The existence of shockwave can only be predicted by means of observations of properties such as temperature, pressure and density as the rarefaction is more. No clear distinct region of discontinuity was seen in the flow field and temperature and pressure field shows sudden variations in properties. Drag profile is fairly constant for both the conditions. Although the temperature is very large, the heat-flux to the body was found to be very less.

Keywords Shockwave · DSMC · Rarefied region · Chemical reactions · Heat-flux · Chemical reaction (CR) · Non-chemical reaction (NCR)

M. Abhay
Defence Institute of Advanced Technology (DIAT), Pune, India
e-mail: abhaymeshram111@gmail.com

V. Kumar (✉) · A. Chaphalkar (✉) · J. Justus (✉)
CFDD/AERO, ISRO (VSSC), Thiruvananthapuram, India
e-mail: vinodkgul@gmail.com

A. Chaphalkar
e-mail: aaditya.chaphalkar@gmail.com

J. Justus
e-mail: jiju6justus@gmail.com

N. Gascoin and E. Balasubramanian (eds.), *Innovative Design, Analysis and Development Practices in Aerospace and Automotive Engineering*, Lecture Notes in Mechanical Engineering, https://doi.org/10.1007/978-981-15-6619-6_57

1 Introduction

Macroscopic approach uses the set of continuity, momentum and energy equation for the calculation of properties such as pressure, temperature, velocity, etc. Same set of equations can also be used for microscopic analysis but requires incorporation of transport and heat-flux equations too. It is the use of these set of deterministic equations which accurately models rarefied flow. Use of these additional equations in an analysis breaks the assumption of macroscopic approach rather than the increase in mean free-path between two molecules. Basically, Knudsen number gives the degree of rarefaction and is defined as

$$Kn = \frac{\lambda}{l} \tag{1}$$

where l is the characteristic length, λ is the mean free-path and ρ is the density of gas (air). For the flow to be considered as the rarefied flow, Kn should be more than 0.1 and molecular approach needs to be incorporated. Macroscopic approach starts to yields inaccurate results as rarefaction increases. At Kn equal to 0.2 it becomes important to use the molecular approach and macroscopic model no longer can be used.

In this paper, the analysis was carried out for an altitude of 105 km from the mean sea level with the flow velocity $\sim$ 8050 m/s. At an altitude of 105 km pressure, temperature, density and Knudsen number are 0.01182 N/m^2, 196.0 K, 2.006×10^{-7} and 0.31193 respectively. As the Knudsen number at this altitude is more than 0.2, molecular approach can be used to get accurate results. Direct Simulation Monte Carlo (DSMC) method [1], based on molecular kinematics, is used in this paper to study the flow field around and on a blunt nose re-entry vehicle (REV) using DSMC openFOAM platform.

2 Geometry and Mesh

The configuration used for analysis is the blunt spherical double conic section of 20° and 25°, respectively and the representative sketch of the same is shown in Fig. 1. Length to Diameter ratio (Aspect ratio (AR)), is 0.6. A sector of 5° in the Z-direction is used for the analysis. DSMC uses three-dimensional body to carry out analysis since 2D analysis is not possible owing to the fact that molecular approach is used which considers random scattering of molecules in all directions. 3D configuration with the sector of less than or equal to 5° is a good approximation of 2D axisymmetric body. The base of the configuration is flat.

3D mesh was created by revolving the structured mesh by an angle of 5°. Fine mesh was created near the body and a gradual growth rate of 1.2 times from the first cell height was given towards the outer domain. In Fig. 2, isometric views is shown

Fig. 1 Geometry

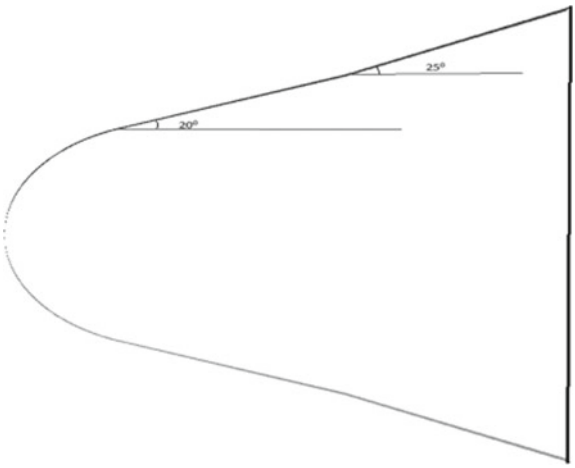

Fig. 2 Mesh

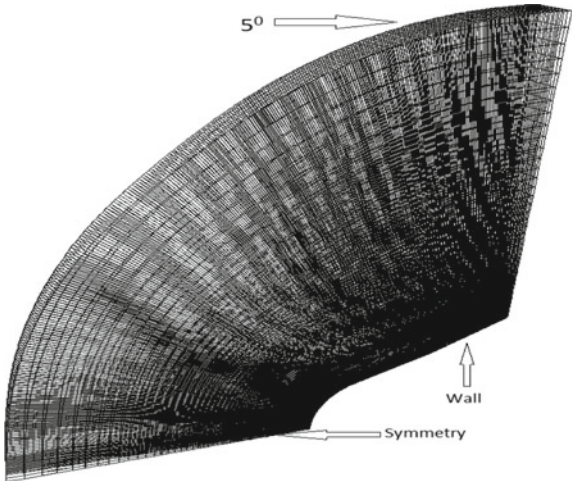

with the 5° sector. ~44,000 cells were created with the domain of twice the base diameter of the configuration.

3 Setup for DSMC

In DSMC time interval and setting of number of packets of molecules in each cell is very important for the flow initialization. The time interval for simulation should be smaller than or equal to the time between successive collisions of two molecules and can be defined as:

$$\mathrm{d}t = \frac{\text{mean free path}}{\text{Thermal Velocity}} = \frac{\lambda}{c'} \tag{2}$$

where

$$c' = \sqrt{3kT}/\sqrt{\bar{m}} \tag{3}$$

For the current case, the interval time was set to be 5×10^{-6} which is smaller than the time calculated by the above formula. For the current case, a large number of molecule were set and are equal to 497,833 in each cell. It is required to set number of equivalent particles in order to get the desired number of molecules in each cell. Number of equivalent molecules can then be calculated as

$$\text{equivalent molecules} = \mathcal{V}n/\wp \tag{4}$$

$$n = n(\mathrm{O}_2) + n(\mathrm{N}_2) + n(\mathrm{NO}) + n(\mathrm{O}) + n(\mathrm{N}) \tag{5}$$

where $\wp$, $\mathcal{V}$ and n are the number of parcels in each cell, volume of largest cell and total number density of gaseous molecules. For the analysis, the reference temperature was considered to be 273 K, and the adiabatic wall temperature as 300 K.

4 Numerical Formulation

The effective temperature of a species p after the collision with species q can be given by

$$T_p = \left(E_t + \varepsilon_{i,p}\right)/k \times \frac{1}{5/2 - w_{pq} + \zeta_{rot}/2 + \sum_{j=1}^{jp} \frac{\theta_{v,p,j}/T_q}{\exp\left(\frac{\theta_{v,p,j}}{T_q}\right)-1}} \tag{6}$$

As a result of increase in temperature, the internal energy of the gas molecules also changes. This results in increase in heat-flux which can be given in x-direction as

$$q_x = \frac{1}{2}\rho'^2 u' + n\varepsilon_{\text{int}} u' \tag{7}$$

where E_t = translational energy, ε_{int} = internal energy, k = Boltzmann constant, ω = angular velocity, ζ = degree of freedom, θ = vibration temperature, n = number density, c' = thermal velocity, u and v are the velocities in x and y directions and superscript ($'$) denotes properties after collision.

5 Chemical Model

The continuous collision of air molecules with the REV increases the temperature of the order of thousands of degree Kelvin in its vicinity. This temperature causes dissociation of gas molecules (O_2, N_2 and NO). Considering chemical reactions in an analysis, gives more realistic behaviour of gas molecules. Quantum Kinematic (Q-K) model by Bird [2] incorporates dissociation and recombination reactions. Reference [2] by Bird does not consider for the charged particles and hence is applicable for neutral gas molecules only. Reference [3] considers the importance of implementing charged reactions and is given for reactions in charged particles. 'Modified Q-K' model incorporates these both qualities and is implemented in dsmcFOAM + which is used for the current study with air as the combination of 11 species (N_2, O_2, NO, N_2^+, O_2^+, NO^+, N, N^+, O, O^+ and e^-).

6 Validation

The validation case was evaluated on a 70° spherically blunt cone configuration. The DSMC results carried out by Moss and their comparison with LENS facility experimental results are given in Ref. [4] for the same configuration. The current DSMC analysis was performed using Nitrogen (N_2) as a test gas and the results are given in Figs. 3 and 4. Figure 3 shows the variation of pressure on the wall of the configuration. It can be seen that pressure is nearly constant on the forebody followed by the sharp expansion at the corner. The pressure on base of the model and sting region is very small. Figure 4 shows pressure colour pallet over the entire domain and thick shockwave can be observed just before the configuration at the normalized axial location of ~0.45.

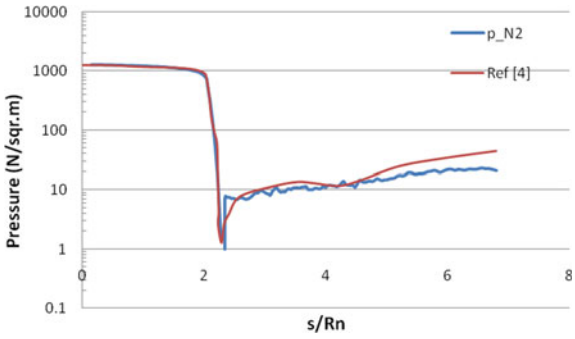

Fig. 3 Pressure variation on wall

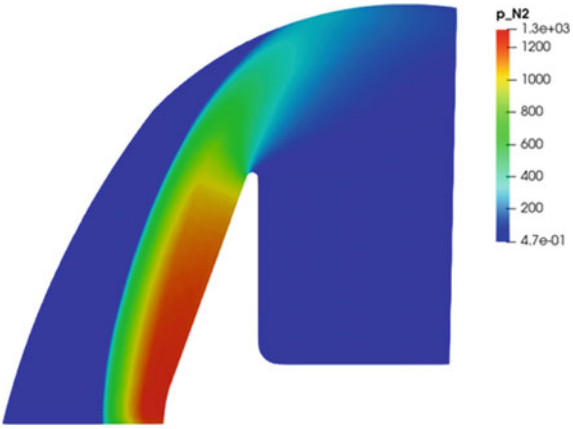

Fig. 4 Pressure variation

7 Results

Figures 5, 6, 7, 8, 9 and 10 show the results for blunt double conic configuration. Variation in temperature along the symmetry line is given in Fig. 5 for chemically and non-chemically reactive cases. Higher values of temperature in the shock region can be observed for chemically reactive gases as compared to non-reactive gas and are in the range of 16,000 to 17,000 K for this case. Temperature pallet for the same is given in Fig. 6, where a small region of thick shock wave can be seen. Figures 7, 8, 9 and 10 show the variation in heat-flux, pressure, shear stress and drag, respectively on the wall of the configuration. Addition of chemical reactions shows reduction in heat-flux, pressure and shear stress. Drag (Fig. 10), remains the same for both cases as very small variation in pressure and shear forces is observed.

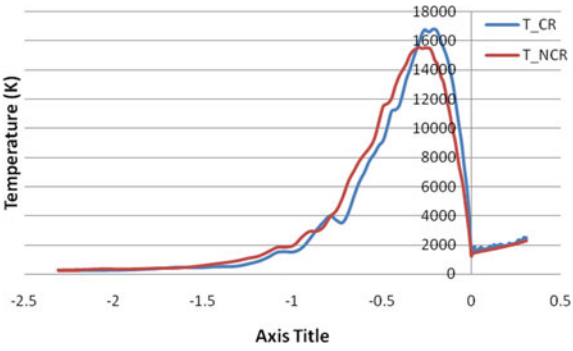

Fig. 5 Variation in temperature along the length of domain

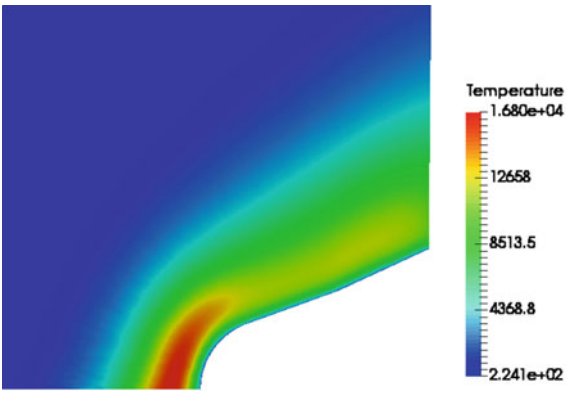

Fig. 6 Temperature variation

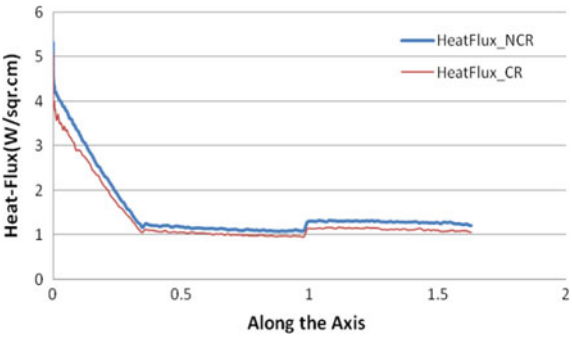

Fig. 7 Variation in heat-flux on the surface

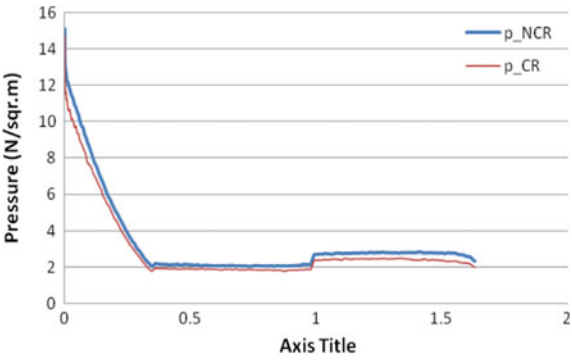

Fig. 8 Variation in pressure on the surface

8 Conclusion

- Modified Q-K model is implemented successfully with the implementation of charged particles in the analysis of the chemically reacting gases using the dsmcFOAM+.

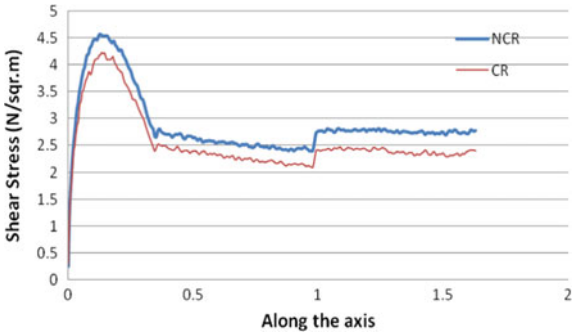

Fig. 9 Variation in shear stress on the surface

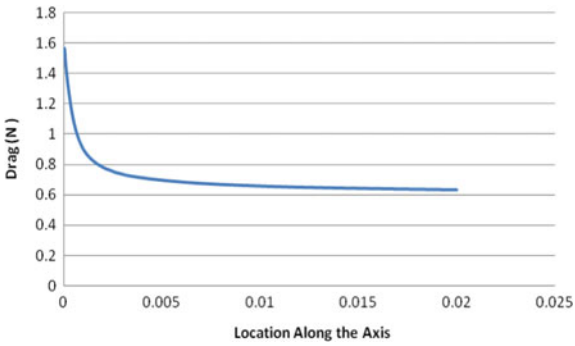

Fig. 10 Variation in drag on the surface

- Validation case based on the data available from Ref. [4] is found to be in good agreement with the current DSMC simulation results.
- Simulation on the blunt cone configuration shows reduction in heat-flux and shear stress with the addition of chemically reactive model. However, variation in pressure is considerably small.
- Thick shockwave is the characteristic of the rarefied region. As the degree of rarefaction increases the shockwave becomes more thick and merges with the boundary layer (Fig. 4) and as the rarefaction decreases shock wave starts to move away from the body (Fig. 6).

References

1. White C, Borg MK, Scanlon TJ, Longshaw SM, John B, Emerson DR (2017) dsmcFoam+, An OpenFOAM based direct simulation monte carlo solver
2. Bird GA (2011) The Q-K model for gas-phase chemical reaction rates
3. Liechty DH, Lewis MJ (2011) Extension of a kinetic theory approach for computing chemical-reaction rates to reactions with charged particles
4. Moss JN, Dogra VK, Hash DB, Price JM (1995) Comparison of DSMC and experimental results for hypersonic external flows

Computation of Drag of a Ballistic Reentry Body at Various Mach Numbers

S. Balasubramanian, G. Vidya, and Ganapati Joshi

Abstract It is necessary to dissipate the kinetic and potential energy of a reentry object from Earth orbit and recover it on the ground with small impact point dispersion without exceeding thermal and structural limits. This can be accomplished either through aerodynamics or propulsion or both. The entry can be ballistic, semi-ballistic or lifting entry. In a non-propulsive ballistic entry, drag is the important aerodynamic parameter that influences the trajectory design other than the mass and entry flight path angle. While re-entering into the atmosphere, deceleration is very high because of Earth gravitational force, to reduce the deceleration rate drag of the configuration should be very high. To increase the drag reentry configuration has to be blunt. In this paper, the flow field around a typical ballistic reentry body has been investigated using RANS CFD simulations. *Ansys-Fluent, CFD++* with *Spalart-Allmaras* and *realizable k-ε* turbulence models have been used in the present analysis. In this paper, various drag properties for a spherically blunt cone flare configuration, code-to-code comparison of drag and Cp distribution on the body have been discussed for various Mach numbers.

Keywords Blunt cone flare configuration · CFD · C_D · Fluent · CFD++

1 Configuration Details

The model is a spherically blunt with a 20° cone angle and a 25° flare angle. The base diameter is D, the length of the configuration is $0.8D$ and the nose radius is $0.25D$ as shown in Fig. 1. The configuration has been generated using the *ANSYS-SpaceClaim*

S. Balasubramanian (✉) · G. Joshi
Department of Aerospace Engineering, Defence Institute of Advanced Technology (DIAT), Pune, India
e-mail: scientistbala1103@gmail.com

G. Vidya
VSSC, ISRO, Thiruvananthapuram, India
e-mail: g_vidya@vssc.gov.in

N. Gascoin and E. Balasubramanian (eds.), *Innovative Design, Analysis and Development Practices in Aerospace and Automotive Engineering*, Lecture Notes in Mechanical Engineering, https://doi.org/10.1007/978-981-15-6619-6_58

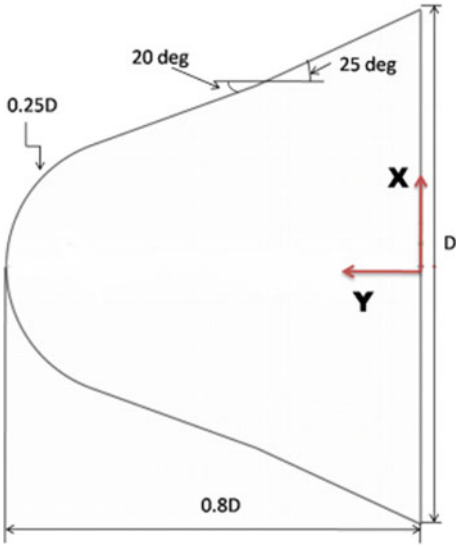

Fig. 1 Spherically blunt cone flare

tool. The origin is fixed at the base of the configuration in the symmetry plane. And the flow direction is $-Y$-axis. The configuration detail has been reproduced from reference [1].

2 CFD Simulation Details

The flow domain is created using *ANSYS-DesignModeler.* The size of the domain is 37*D*, as shown in Fig. 2. An unstructured grid with the size of 38 lakhs (21 inflation layer and density box to capture near-body gradients) is generated using *ANSYS-Meshing* tool over the configuration as shown in Figs. 3 and 4. Boundary conditions applied for the current analysis are inlet, pressure far-field, walls, pressure outlet as shown in Fig. 2. The flow simulation conditions have been taken from reference [2]. CFD simulations are carried out at Mach numbers ranging from 0.3 to 6 at a 0° angle of attack. *ANSYS-Fluent* is the data generation tool and *CFD++* software is used for code-to-code comparison for typical Mach numbers. Finite volume pressure-based coupled solver with the *Spalart-Allmaras* turbulence model is used for Mach number $\leq$1.2. And the density-based solvers are mostly utilized for high-speed compressible flows. So density-based *AUSM* flux scheme with a *realizable k-ε* turbulence model is used for Mach number >1.2.

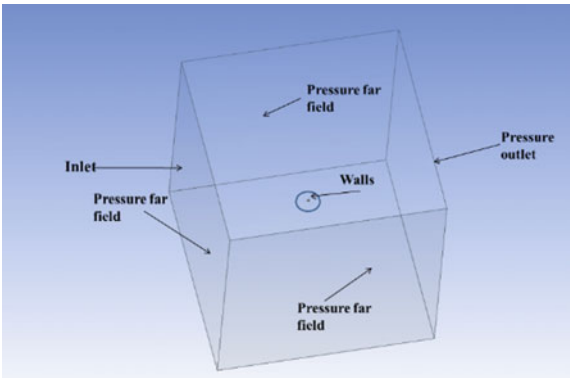

Fig. 2 Flow domain with boundary configuration conditions

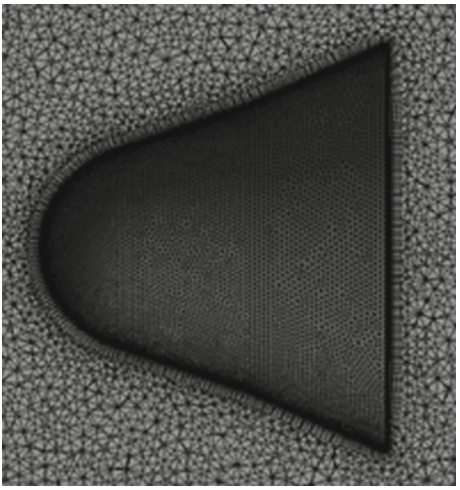

Fig. 3 Unstructured grid with 21 inflation layers

3 Results and Discussions

All drag coefficient data presented in this paper are normalized with the maximum value. Figure 5 shows the drag convergence plot for typical Mach numbers. The analysis has been done for 500 iterations with 1st order upwind scheme and beyond that, the second-order upwind scheme is used. The plot shows good convergence of C_D values for all Mach numbers (maximum of 0.001). Figure 6 shows forebody drag and base drag comparison in percentage for the various range of Mach numbers at a 0° angle of attack. It is observed that for a bluff body, while increasing Mach number from subsonic to hypersonic, the percentage of forebody contribution to drag coefficient is increasing and the contribution of base drag is decreasing. At $M = 0.3$

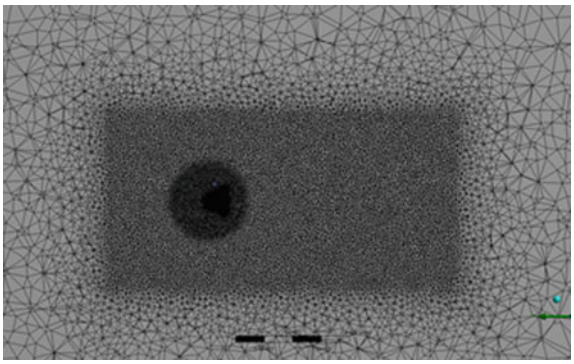

Fig. 4 Unstructured grid with density box (32 lakhs cells)

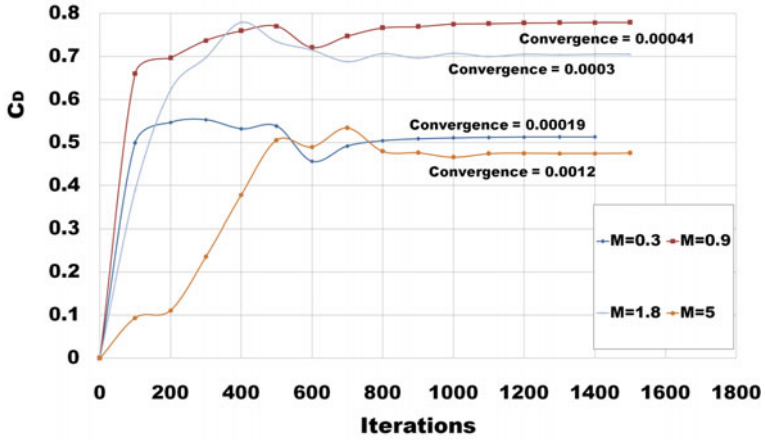

Fig. 5 Convergence plot for drag coefficients at various Mach numbers

base drag coefficient percentage is very high, $M = 1.2$ both forebody and base drag coefficient contribution is equal and $M = 6$ the forebody drag coefficient percentage is high. More details related to base flow and base pressure are presented in [3]. Figure 7 shows the variation of forebody drag and base drag coefficients with Mach numbers and it is observed that both forebody and base drag coefficients are increasing from subsonic to transonic Mach numbers, beyond that base drag coefficient is decreasing drastically whereas forebody drag coefficients remain more or less constant.

Figure 7 also shows the pressure and viscous drag coefficient contribution for the total drag coefficient. It is observed that pressure drag is dominant for a blunt cone configuration; the viscous drag part is very low/negligible as compared to the pressure drag coefficient. Figure 8 shows surface Cp palette over the configuration typical subsonic, transonic, supersonic and hypersonic Mach numbers. It is observed that the Cp stagnation value is increasing with an increase in Mach numbers. Lower

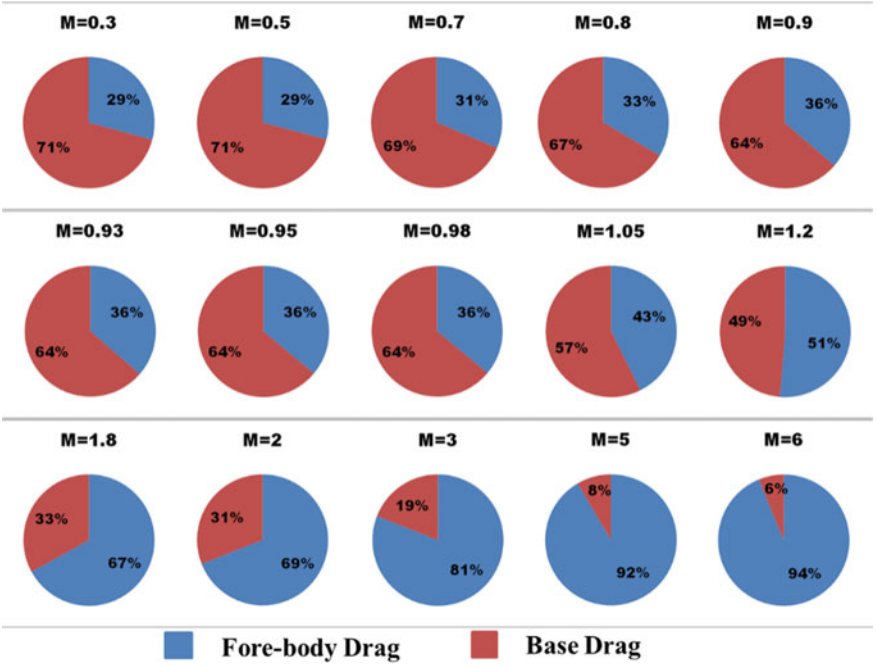

Fig. 6 Fore-body drag and base drag coefficient comparison in percentage

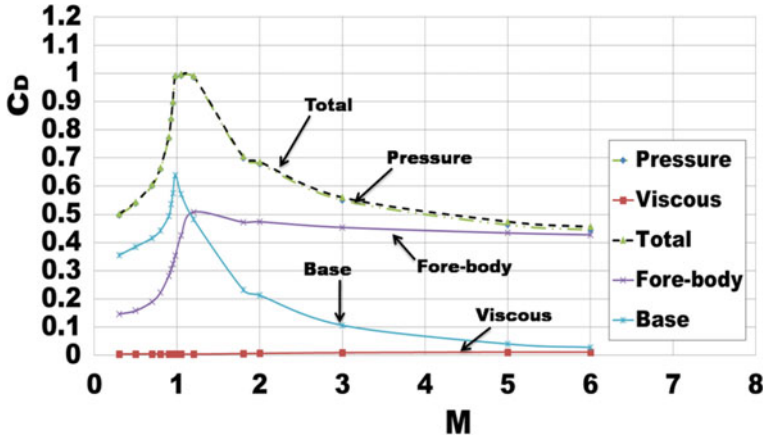

Fig. 7 Components of the drag coefficient and its variation

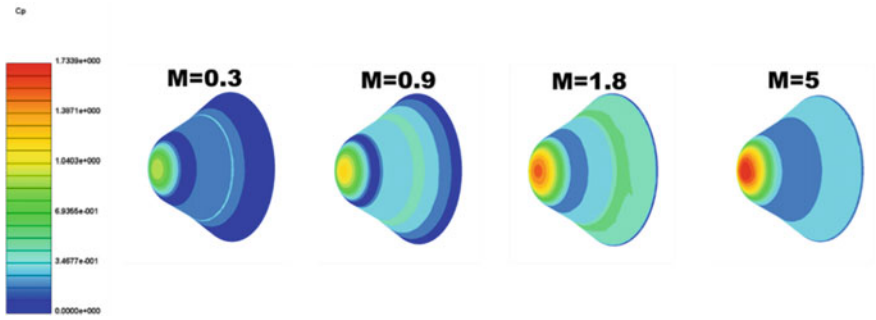

Fig. 8 Surface Cp palette over the spherically blunt cone flare configuration

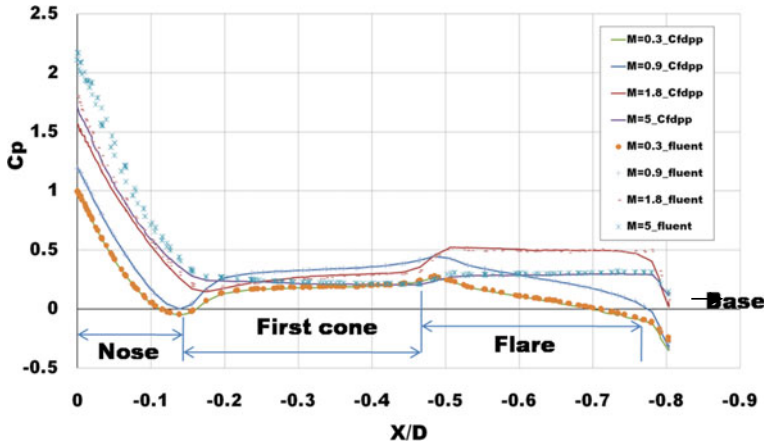

Fig. 9 Cp distribution along the surface meridian of the configuration at '0' AOA

stagnation Cp occurs at $M = 0.3$ and higher stagnation Cp occurs at $M = 5$. Figure 9 shows a variation of Cp along the surface from *Fluent* as well as *CFD++*. From the figure, we can observe that subsonic and transonic Mach numbers result from both software match well, whereas there is a slight mismatch in the stagnation Cp at supersonic and hypersonic Mach numbers. The Cp data estimated using *CFD++* at $M = 5$ matches with data available in [4], whereas *the Fluent* result is higher. It is observed that the Cp is decreasing from the nose and there is an increase in the Cp value near cap-cone and cone flare junction for subsonic and transonic Mach number, in supersonic and hypersonic Mach numbers Cp jump is seen at cone flare-junction only.

In subsonic and transonic Cp is reducing after the slight increase in the flare region, whereas Cp remains constant over flare region at higher Mach numbers. Figure 10 shows the cumulative drag coefficient for typical Mach numbers for the spherically blunt cone flare configuration. It is observed cumulative drag coefficient is increasing

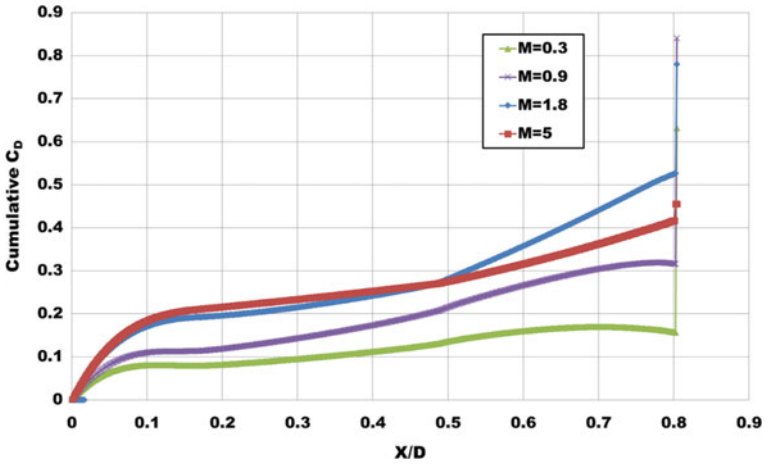

Fig. 10 Cumulative C_D distribution for typical Mach numbers

in the nose and the first cone from subsonic to hypersonic Mach numbers. The drag due to flare is very low in subsonic Mach number. The flare contribution to drag initially increases with Mach number reaches a maximum at $M = 1.8$ and falls at hypersonic Mach number. The base drag is indicated as a vertical jump at the vehicle end. The deceleration level of a ballistic reentry body is a function of drag and mass of the object. Table 1 shows the deceleration levels for various Mach numbers in 'g' Mass of the configuration is taken as 508 kg [5]. It is observed that the deceleration level is the highest at hypersonic Mach number. It is also observed that the standards are less than one at $M = 0.8$ to 0.5.

Table 1 Decelaration variation for various Mach numbers

Mach	Deceleration in 'g'	Mach	Deceleration in 'g'
0.3	1.13	1.05	2.29
0.5	0.921	1.2	2.98
0.7	0.85	1.8	2.99
0.8	0.889	2	3.59
0.9	1.31	3	4.87
0.93	1.52	5	7.36
0.95	1.69	6	8.81
0.98	1.99		

4 Conclusion

The flow simulations over a ballistic reentry configuration have been done carried out from low subsonic to hypersonic Mach numbers using *Ansys-Fluent* with *Spalart-Allmaras and realizable k-ε* turbulence models. Code-to-code comparison has been carried out using *CFD++*. The percentage contribution of forebody drag increases with Mach number, and that of base drag decreases with Mach number. Base drag is dominant from subsonic to lower supersonic (transonic) and forebody drag is dominant from higher supersonic to hypersonic Mach number. The total contribution of viscous drag is very less as compared to pressure drag. The stagnation Cp increases with an increase in Mach number. Flare part of the configuration contributes to a large extent in drag generation in transonic and supersonic/hypersonic Mach numbers.

Acknowledgements I express my sincere thanks to Mr. K. Manoharan Sci/Engr'SG', for reviewing my paper and giving me the right guidance to correct my mistakes. I would like to specially thanks to Dr. Dipankar Das Sci/Engr'G' (Head of the Department), Dr. M. M. Patil Sci/Engr' H' (Group Director), Dr. V. Ashok Sci/Engr' O.S' (Deputy Director) who's given me a constant motivation. Special thanks to APCF computing facilities, which are allowing me to use the facilities in VSSC.

References

1. Mehta RC (2011) Computations of flowfield over reentry modules at high speed. In: Computational simulations and applications. IntechOpen
2. Mehta RC (2007) Three-dimensional inviscid flowfield computation over various re-entry configurations. In: Aerospace sciences meeting and exhibit, AIAA paper
3. Balasubramanian S, Vidya G (2019) Base flow characterisation of blunt cone flare configurations at various Mach numbers. Paper got accepted in FMFP conference 2019, PSG College, Coimbatore
4. Patil MM, Swaminathan S, Kalimuthu R, Mandal JC (2004) Three-dimensional hypersonic flow computations over reentry capsule using energy relaxation method. J Spacecraft Rockets 41
5. https://web.archive.org/web/20131224103000/http://www.aprsaf.org/data/aprsaf14_data/day1/SEU10_SRE%20slides%20for%20web.pdf

Laser Machining of AISI 304: An Experimental Study of Influence of Process Parameters on Dross Height Formation

Aniket Jadhav and Shailendra Kumar

Abstract This paper presents an experimental study on influence of process parameters of laser machining of AISI 304 material on dross height formation. Laser power, cutting speed and gas pressure are process parameters which are considered during present work. Design of experiments is implemented using response surface methodology, and analysis of variance is carried out in order to find out significance and influence of process parameters for dross properties. It is identified that cutting speed acts as the most important significant parameter accompanied by laser power and gas pressure. Dross height increases with the enhancement in cutting speed and decreases with the reduction in laser power and gas pressure. Further, optimization of process parameters is also carried out to reduce dross height formation. Based on the experimental analysis, second-order mathematical model is formulated for the prediction of dross height. Model predictions and experimental results are found in reasonable agreement.

Keywords Laser machining · AISI 304 · Process parameters · Dross height · Optimization

1 Introduction

AISI 304 is an austenitic stainless steel. It has wide range of applications including architectural, nuclear, consumer, ships manufacturing, transportation firms, etc. [1]. Thick austenitic stainless steel is hard to cut sheet material and widely used in production industries due to excellent mechanical properties. Cutting of this material by using conventional machining process is difficult due to excessive friction, tool

A. Jadhav · S. Kumar (✉)
Department of Mechanical Engineering, Sardar Vallabhbhai National Institute of Technology, Surat, India
e-mail: skbudhuwar@gmail.com

A. Jadhav
e-mail: jadhavaniketb@gmail.com

N. Gascoin and E. Balasubramanian (eds.), *Innovative Design, Analysis and Development Practices in Aerospace and Automotive Engineering*, Lecture Notes in Mechanical Engineering, https://doi.org/10.1007/978-981-15-6619-6_59

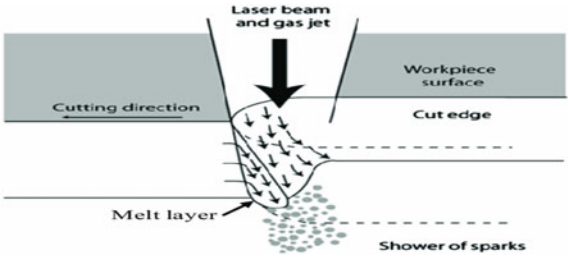

Fig. 1 Schematic view of laser cutting [6]

wear, heat-affected zone, vibration, and poor surface quality [2]. Laser machining of austenitic stainless steel is economical as the laser beam can be controlled by automation, mechanized, and incorporated into manufacturing lines [3]. It is widely used in fabrication industries. Figure 1 shows laser cutting mechanism. Laser beam machining is a high-heat thermal energy process where the generated thermal energy first heats the sheet workpiece material, and then, it transforms the incontact volume of the sheet workpiece material into liquified state that can be easily removed with the help of assist gas pressure. Thermal energy for the process is obtained from intense source of laser light [4]. The non-contact process of laser machining signifies that there is absence of tool storage and tool wear, less cost, very less tool setup time, and less plastic deformation of cut surfaces [5]. During laser machining operations, kerf volume changes into liquid state and blows out with the help of assist gas pressure. The height of dross is formed which involves metal droplets of various sizes. It adheres at lower part of the cut. The dross height formation and its thickness changes based on the process parameters are used. Formation of dross affects the properties and surface finish of machined material [6]. Major process parameters of laser machining consist of laser power, cutting speed, and pressure of gas are used. Selecting optimum values from significant process parameters is essential to minimize dross height formation during cutting of steels.

Some researchers have made efforts to improve cutting performance of laser machining for stainless steel material. Tessier et al. [7] conducted experiments on a lubricant system which is inserted between the inner part of specimen material before and during laser machining. The dross generated due to lubricant solidifies and is thrown out of the specimen along with the lubricant. Chen and Yo [8] used a hybrid approach to optimize process parameters for cutting stainless steel using pulsed fiber laser. It is investigated that dross height enhances since rise of laser power at maximum speed of machining. During low speed, laser power has little effect on dross formation. Kleine et al. [9] concluded that cutting speed along with laser power are significant parameters for the improvement in dross formation for fiber laser machining of stainless steel workpiece. Yilbas and Aleem [10] analyzed regarding the size of fumes discharged had a analog relation with the amount of dross height formation. Its formation depends on laser machining parameters. It was reported that the dross height formation thickness enhances due to the rise weof the laser output por. It reduces because of rise in assisting pressure of gas used. Salem et al. [11] studied fiber laser cutting for thick carbon steel sheets. It is concluded

that width of heat-affected zone was affected importantly due to gas pressure by the generation of adhering dross height on the lower part of cut material. Ahn et al. [12] observed the higher amount of dross formed at the lower part because of excessive material melting. Muhammad et al. [13] experimented on fiber laser machining for stainless steel circular tube and its effects by allowing water to flow through tubes for dross height formations. Yan et al. [14] have investigated striation and dross-free cutting on alumina sheet using fiber laser machining. Baxter et al. [15] developed oxygen gas system for the introduction of gas throughout the workpiece to oxidize dross height formation during laser cutting. Oxygen gas cools the dross as well as workpiece while at the same time oxidizes it. Teixidor et al. [16] analyzed dross height formation for the energy balances during fiber laser machining. Jarosza et al. [17] experimented that rise in occurrence of dross height and molten material metal along with a rough surface on the lower part of workpiece is due to lower cutting speed. Furthermore, occurence of burnt metal had been investigated at the lower part of workpiece with the lowest speed. Madhukar et al. [18] found that dross height varies with power of laser and cutting speed. Bara et al. [19] investigated the effects on process input parameters for drilled characteristics of stainless steel on 1.5 mm thickness sheet workpiece with fiber laser process. Rahimia et al. [20] studied on composite material for laser-engraving performance characteristics.

From the literature review, it can be concluded that most of the researchers have tried out efforts for the investigation of influence on input process parameters for laser machining on responses, namely kerf top-bottom width, kerf taper angle and kerf deviation, heat-affected zone, surface roughness, striations, dross, etc. However, very limited researchers had investigated the experimental results of input process parameters on dross properties in laser machining of thick steel material. This experimental study is concentrated for investigation of influence of input process parameters on laser machining of thick AISI 304 stainless steel on dross height. This paper has been integrated as follows: Sect. 1 describes introduction, Sect. 2 gives experimental work, and results and discussion part is presented in Sect. 3, Sect. 4 discusses optimization of process parameters, and finally, concluding remarks are given in Sect. 5.

2 Experimental Work

For present study, Bystronic fiber laser machine is used for conduction of experiments available at M/s Kakade Laser, Narhe, Pune, India. It produces 1.06 μm wavelength, and 6000 W is the highest laser output power. During performance of experiments, 128 mm was the focal length of the lens and 4 mm nozzle diameter that was maintained constant throughout. 1.5 mm was nozzle stand-off distance maintained during the experiments. A thick AISI 304 stainless steel of 20 mm thickness plate is considered as workpiece material. The maximum chemical composition and mechanical properties for AISI 304 material are depicted in Tables 1 and 2, respectively. For experimentation, 17 workpiece samples of size 20 × 20 mm are cut.

Table 1 Maximum chemical composition for AISI 304 material

C	Ni	Cr	Si	Mn	P	S	Fe
0.08	0.1	18–20	0.75	2.0	0.045	0.030	Balance

Table 2 Mechanical properties for AISI 304 material

Mechanical properties	Values
Density (kg/m^3)	8.03
Yield strength (N/mm^2)	215
Tensile strength (N/mm^2)	505
Hardness (HRC)	70
Elongation (%)	70

Table 3 Levels of laser cutting parameters

Symbol	Parameters	Level 1	Level 2
A	Laser power (W)	5000	5500
B	Cutting speed (mm/min)	210	230
C	Gas pressure (bar)	8	12

For the current study, process parameters considered are laser power (LP), cutting speed (CS), and gas pressure (GP). Table 3 shows levels of laser cutting parameters which are considered based on literature review. To identify the experimental conditions, some trial runs were executed out to identify range of input process parameters. To avoid material surface melting, proper precaution was taken. Experimental design includes two levels and five center points. A total of 17 experiments are carried out according to design suggested by design expert software V11. To design experiments, response surface methodology (RSM) using two levels Box-Behnken (BBD) design is used. BBD provides modelling of the response surface. It is selected due to the shorter range of input process parameters as compared to central composite design (CCD). In this, all involved parameters are simultaneously at their highest and lowest stage. Due of this experiments underneath very extreme conditions can be avoided.

After experimentation, the dross height at the bottom of surface of all samples is measured. Images of the top side surface are captured using high resolution camera (Canon DCC, Model-242S821), and mean average of three measurements readings for every run is noted. Then, dross height is measured using commercial software "Image J." Experimental design data and the measured values of dross height are listed in Table 4.

Table 4 Experimental design data and measured values of dross height

Standard	LP (kW)	CS (mm/min)	GP (bar)	Dross height (mm)
1	−1	−1	0	2
2	1	−1	0	1.25
3	−1	1	0	0.95
4	1	1	0	1.7
5	−1	0	−1	2.15
6	1	0	−1	0.85
7	−1	0	1	2
8	1	0	1	1.85
9	0	−1	−1	1.5
10	0	1	−1	1
11	0	−1	1	2.1
12	0	1	1	2.35
13	0	0	0	1.75
14	0	0	0	1.8
15	0	0	0	1.95
16	0	0	0	0.75
17	0	0	0	2.25

3 Results and Discussion

Table 5 shows the analysis of variance (ANOVA) for dross height. Using 95% confidence level analysis is carried out. The significance of model can be verified by F-value of 26.22. From ANOVA for dross height, it has been identified that cutting

Table 5 Analysis of variance for dross height

Source	Sum of squares	df	Mean square	F-value	p-value	
Model terms	4.13	9	0.4593	26.22	0.0001	Significant
A	0.0153	1	0.0153	0.8741	0.0018	
B	3.38	1	3.38	192.95	<0.0001	
C	0.4753	1	0.4753	27.13	0.0012	
B^2	0.2108	1	0.2108	12.03	0.0104	
Residual	0.1226	7	0.0175			
Lack of fit	0.0856	3	0.0285	3.09	0.1524	Not significant
Pure error	0.0370	4	0.0093			
Cor total	4.26	16				

speed was important and significant factor before laser power assists gas to minimize dross height. Interactions between them are also significant. A quadratic value of cutting speed is other significant parameter.

The predicted and adjusted R^2 value of 0.6645 and 0.9341 reveals reasonable agreement. It is concluded that predicted and the experimental value of results as presented in Fig. 2 are in good agreement with each other.

Influences of laser power and speed along with gas pressure are shown in Fig. 3a and b. It was identified that dross height enhances with rise in the cutting speed. This is because rise in cutting speed causes higher rate of high temperature oxidation reactions. It causes increase in liquid layer thickness which enhances the droplet

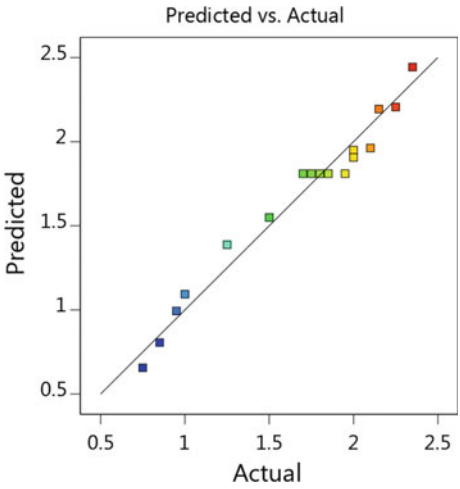

Fig. 2 Predicted versus actual values of dross

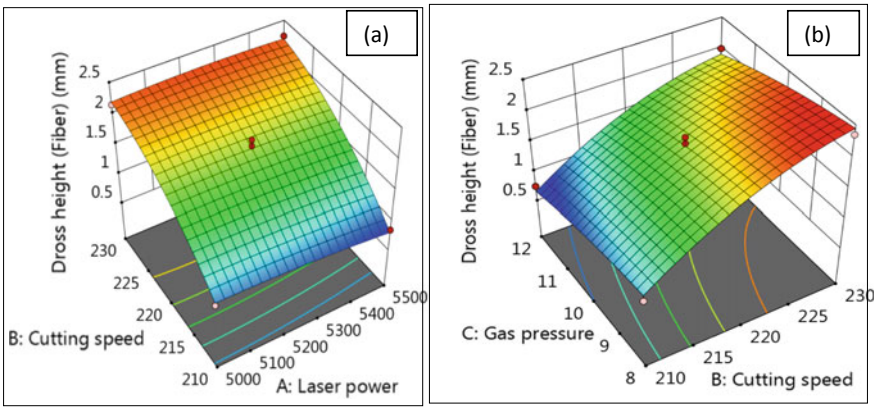

Fig. 3 **a** and **b** Effect of LP, CS, and GP on dross formation

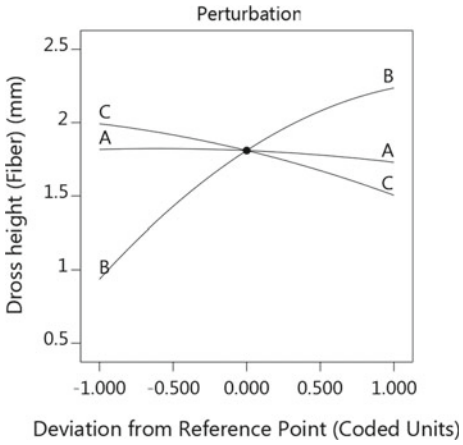

Fig. 4 Perturbation plot for dross height

diameter of molten workpiece. The droplet formed adheres to the workpiece and solidifies in the formation of dross height. It is also observed that dross height lowers with the decrease of laser power and gas pressure. It is because sufficient power, and assist gas pressure is produced for easy removal of molten liquid material through the workpiece.

The perturbation plot showing representation of input process parameters on dross height formation are depicted in Fig. 4. Influence of dross height is plotted keeping other remaining parameters at the centre values at zero level. The role of cutting speed is higher compared to other parameters. The reason behind this is by increasing cutting speed results in more melting of material along its edges. Due to this, dross does not get removed and it settles at the lower part of the workpiece. It results in increase in the height of dross height formation.

Using significant terms, the regression model is developed. For dross height, the final regression equation in terms of coded values are represented in Eq. (1)

$$\begin{aligned}\text{Dross height} = {} & 1.81 - 0.04375A + 0.65B - 0.24375C + 0.05A \times B \\ & - 0.0375A \times C - 0.025B \times C - 0.03625A^2 - 0.22375B^2 - 0.06125C^2 \end{aligned} \quad (1)$$

4 Optimization of Input Process Parameters

For minimizing dross height, a set of process parameters is optimized. Desirability function is used for the performance of optimization. It is the method which simultaneously optimizes a series of response. The optimization for every process parameter response variable is defined in terms of minimum, maximum, in range, or target

Table 6 Criteria for Optimization

Factor	Goal	Lower limit	Upper limit	Optimized value
A (W)	In range	5000	5500	5031.721
B (mm/min)	In range	210	230	210.025
C (bar)	In range	8	12	11.980
Dross height (mm)	Minimize	0.75	2.35	0.749

values. The measured values of input process parameter response variables are transformed to a free scale value between zero and one. It causes improvement in the corresponding response value to becomes more desirable [21]. Table 6 shows criteria for optimization and its optimized values.

5 Conclusion

An experimental study on laser machining of AISI 304 has been performed to minimize dross height formation. The following are the findings of the present work

(i) Cutting speed is most important input process parameter followed by laser power along with the gas pressure to minimize dross height.
(ii) Dross height increases due to enhancement of cutting speed, and it decreases as decrease in power of laser and gas pressure.

Further, a mathematical model has been developed for the prediction of dross height. It has identified that model predictions have good agreement with experimental result values. Optimization of laser power, cutting speed, and gas pressure has also been carried out to reduce dross height formation.

References

1. Parthibana A, Chandrasekaran M, Muthuraman V, Sathish S (2018) Optimization of CO_2 laser cutting of stainless steel sheet for curved profile. Mater Today Proc 5:14531–14538
2. Akkurt A (2009) Surface properties of the cut face obtained by different cutting methods from AISI 304 stainless steel materials. Indian J Eng Mater Sci 16:373–384
3. Ion JC (2005) Laser processing on engineering materials (principles procedure and industrial application). Elsevier Butterworth-Heinemann, Burlington
4. Ghany KA, Newishy M (2005) Cutting of 1.2 mm thick austenitic stainless steel sheet using pulsed and CW Nd-YAG laser. J Mater Process Technol 168:438–447
5. Sharma A, Yadava V (2018) Experimental analysis of Nd-YAG laser cutting of sheet materials—a review. Opt Laser Technol 98:264–280
6. Juptner WP (2002) LIA handbook of laser materials processing. Optics Lasers Eng 38:608–610
7. Tessier, Brown W (1991) United States Patent No. US5073694
8. Chen K, Yao YL (2000) Process optimization in pulsed laser micromachining with applications in medical device manufacturing. Int J Adv Manuf Technol 16:243–249

9. Kleine K, Whitney B, Watkins K (2002) Use of fiber lasers for micro cutting applications in the medical device. ICALEO, Scottsdale, USA, pp 1–10
10. Yilbas BS, Aleem BJA (2006) Dross formation during laser cutting process. J Phys D Appl Phys 39:1451–1461
11. Salem HG, Mansour MS, Badr Y, Abbas WA (2008) CW Nd-YAG laser cutting of ultra low carbon steel thin sheets using O_2 assist gas. J Mater Process Technol 196:64–72
12. Ahn DG, Byun KW, Kang MC (2010) Thermal characteristics in the cutting of Inconel 718 superalloy using CW Nd-YAG laser. J Mater Sci Technol 26:362–366
13. Muhammad N, Whitehead D, Boor A, Li L (2010) Comparison of dry and wet fibre laser profile cutting of thin 316L stainless steel tubes for medical device applications. J Mater Process Technol 210:2261–2267
14. Yan Y, Li L, Sezer K, Whitehead D, Ji L, Bao Y, Jiang Y (2012) Nano-second pulsed DPSS Nd:YAG laser striation free cutting of alumina sheets. Int J Mach Tools Manuf 53:15–26
15. Baxter W, Mackiewicz D (2014) United States Patent No. 0312005 A1
16. Teixidor D, Ciurana J, Rodríguez C (2014) Dross formation and process parameters analysis of fibre laser cutting of stainless steel thin sheets. Int J Adv Manuf Technol 71:1611–1621
17. Jarosza K, Loschnera P, Niesłonya P (2016) Effect of cutting speed on surface quality and heat-affected zone in laser cutting of 316L stainless steel. Procedia Eng 149:155–162
18. Madhukar YK, Mullick S, Nath AK (2016) An investigation on co-axial water-jet assisted fiber laser cutting of metal sheets. Opt Lasers Eng 77:203–218
19. Bara A, Sahoo SK, Naik SS, Sahu AK, Mahapatra SS (2018) Multi response optimization of Nd:YAG laser micro drilling characteristics of 304 stainless steel using desirability function approach. Mater Today Proc 5:18975–18982
20. Rahimia MH, Shayganmanesha M, Noorossanab R, Pazhuheianb F (2019) Modelling and optimization of laser engraving qualitative characteristics of Al-SiC composite using response surface methodology and artificial neural networks. Opt Laser Technol 112:65–76
21. Myer RH, Montgomery DC, Anderson Cook CM (2016) Response surface methodology: process and product optimization using designed experiments. Wiley

Development of Analytical Method for Mass Flow Measurement in a Porous Channel

Hussain Najmi, Eddy El-Tabach, Nicolas Gascoin, Khaled Chetehouna, and François Falempin

Abstract Porous channels are used in scramjet to perform transpiration cooling in order to reduce thermal load in the combustion chamber. Therefore, it is important to analyze fluid flow in the porous channel. Prior to this, it is important to estimate the mass flowrate, pressure, and temperature precisely inside as well as outside the porous channel. In the present work, permeation cells are specifically designed and fabricated for the permselectivity test bench. This allows the user to measure the mass flowrate, temperature, pressure, and composition of outlet flow along the length of the porous tube. In order to measure the mass flowrate correctly, an analytical method is developed. To validate the method, Nitrogen is used as a fluid.

Keywords Porous channel · Mass flowrate · Analytical method · Porous stainless steel tube

1 Introduction

The porous tube is used in various field of research engineering such as fuel cell, aerospace, gas separation, petroleum, and ground water [1–6]. In most of the studies, the more attention is given to the membrane characterization but not to the flow dynamics (such as boundary layer) along the axial direction [7, 8]. It can be due to the experimental configuration which is of shell and tube type. In case of real applications, flow occurs in axial and radial directions. Hence, the flow dynamics can play a very important role in permeation through the porous media [9].

There are various fluid flow properties which can affect the permeation such as velocity of the main flow, V_z (i.e., axial flow), momentum in the main flow, M_z (i.e., in axial direction), momentum in radial direction, M_y, fluid density, ρ and fluid

H. Najmi (✉) · E. El-Tabach · N. Gascoin · K. Chetehouna
University Orléans, INSA-CVL, PRISME EA 4229, 18022 Bourges, France
e-mail: hussain.najmi@ensma.fr

F. Falempin
MBDA, 1 Avenue Réaumur, 92358 Le Plessis-Robinson Cedex, France

N. Gascoin and E. Balasubramanian (eds.), *Innovative Design, Analysis and Development Practices in Aerospace and Automotive Engineering*, Lecture Notes in Mechanical Engineering, https://doi.org/10.1007/978-981-15-6619-6_60

viscosity, μ [10]. To determine the most of the above properties, mass flowrate is required.

It is important to determine fluid properties (such as velocity, viscosity, density etc.) axially as well as radially. In order to determine such properties, it is important to measure fluid flow parameters correctly. In case of porous tube, flow occurs in two directions (axially and radially). It is difficult to measure all the above-described parameters axially. In order to measure the temperature, pressure, and mass flowrate axially, the sensors have to be placed inside the porous tube which can affect the fluid flow and leads to change in flow dynamics. Therefore, all the fluid parameters should be measured radially and eventually with the help of that axial parameters should be determined. Practically, it is not very easy to measure all these parameters radially but it is less complex compare to the axial measurements.

To attain the above objective, a permselectivity bench is developed in which 1 m long porous tube is placed inside the assembly of permeation cells that isolates the porous tube radially and axially. It is seen earlier that out of all fluid parameters, mass flowrate is the most important. Therefore, in the present work, two methods are tried to measure radial mass flowrate. The first method is the traditional one as described in [11] and the second method is a new analytical method developed for this work. Measurements from both the methods are compared and discussed in the next part of this study.

2 Materials and Methods

The developed test bench (Fig. 1) is composed of a porous stainless steel tube (316L SS). The porous tube has one inlet and two outlets (one primary outlet which is divided into eight with the help of permeation cells and one secondary outlet which is at the end of the tube).

The design of different permeation cells is considered and modeled in 3D using CATIA. The feasibility of each designed model is checked. The optimum design has been selected and fabricated. The cells are manufactured in the mechanic department of INSA Center Val de Loire—Bourges campus (Fig. 1). It is made up of INOX-316L because it can withstand high pressure (up to 100 bar) and high temperature (up to 800 °C). In total, eight cells (each of the length 10.00 cm, inner diameter of 5.40 cm, and outer diameter of 6.20 cm) are manufactured. All the eight cells are connected in a series using a rubber seal in non-porous polymer support in order to isolate the porous tube axially as well as radially.

When the fluid enters the tube from one end (inlet), a part of fluid continues into the channel and goes out through the main outlet (secondary outlet) and the rest filtrates through porous media and go into the respective permeation cell along the length. All the eight cells are isolated from each other. Each cell has two outlets (holes), the first one for the thermocouple and the second for pressure and mass flowrate measurement. A three-way valve is connected to second hole in such a way that it allows the measurement of pressure even if the valve is closed.

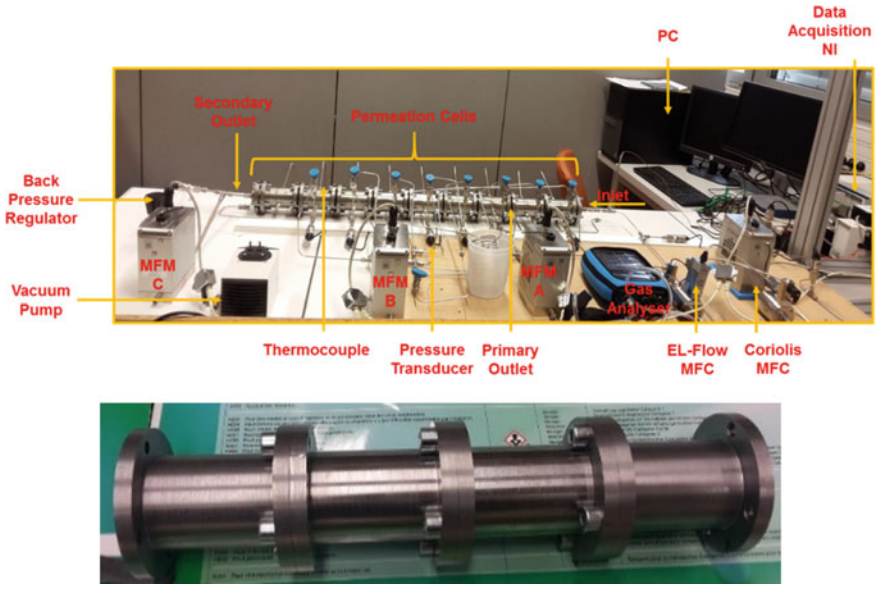

Fig. 1 A photograph of developed permselectivity test bench and manufactured permeation cell [3]

In this study, Nitrogen is used as a fluid, supplied by Air Liquide with purity of 99.99%. The real-time monitoring of all the input parameters (mass flowrate, pressure, and temperature) and their control during the experiments is facilitated by the LabVIEW program that has been developed. Three Coriolis mass flow meters are used to monitor the outflow. In addition, two mass flow controllers are placed at the inlet in order to measure the mass flowrate of the fluid entering into the porous tube. Moreover, pressure transducers and thermocouples are connected to a NI data acquisition system to measure the transient variation of parameters at inlet and outlets. More details regarding the test bench can be found in the previous article [9, 10].

3 Results and Discussion

As described above, three mass flow meters are placed at outlets in order to measure the flow through primary and secondary outlets. The aim is to determine the mass flowrate from each cell (i.e., eight primary outlets) and secondary outlet. In this method, the mass flowrate from each cell is measured one by one by changing the position of the mass flow meters along the length of the porous tube. It can be achieved by repeating the same test four times in which position of the mass flow meters will be changed after each test. A series of tests are performed using this method and it is found that the recovered flow for 0.30 g/s case is 37% (see Table 1). This may

Table 1 Outlet mass flowrate and recovery percentage

Mass flowrate (g/s)										Recovered (%)
Inlet	Cell 1	Cell 2	Cell 3	Cell 4	Cell 5	Cell 6	Cell 7	Cell 8	S.O	
0.30	0	0.002	0	0.002	0.010	0.011	0.008	0.009	0.068	37.09
0.69	0.028	0.037	0.031	0.029	0.025	0.035	0.034	0.024	0.191	63.50
0.90	0.039	0.049	0.042	0.042	0.035	0.050	0.048	0.040	0.263	68.05
1.11	0.049	0.060	0.054	0.056	0.046	0.065	0.058	0.055	0.335	70.45
1.28	0.062	0.069	0.064	0.066	0.057	0.077	0.067	0.067	0.394	72.42
1.50	0.075	0.081	0.077	0.080	0.065	0.091	0.079	0.081	0.445	71.80

be due to uncertainty of the mass flow meter because the mass flowrate measured at cell outlet is very small. Even for higher mass flowrates (more than 1.00 g/s), the recovered flow is about 60–70% which means 40–30% of mass is lost (see Table 1).

Few more tests are performed by changing the position of two mass flowmeter whereas one is permanently placed at secondary outlet (i.e., MFM C see Fig. 1). It is found that whenever the mass flowmeter position is changed, the mass flowrate through the secondary outlet and cells also varies (See Fig. 2).

The above results suggest that the position of the flow meter affects the flow through the porous tube. After analyzing the obtained results, it is confirmed that the reason behind this is the Coriolis mass flow meter which offers a small resistance to the incoming flow. Therefore, if one mass flow meter is connected at cell 1 and other at cell 5, the fluid will take the easiest path and will escape from the outlets (2, 3, 4, 6, 7 or 8) open to the atmospheric pressure. Hence, this method is not reliable and cannot be used for the measurement of the mass flowrate through primary and secondary outlets. A new method is required in order to determine the mass flowrate accurately through various outlets.

In this work, a new method has been developed to measure the mass flowrate from each cell precisely without changing the position of the mass flow meter. It works on mass balancing technique. The two mass flow meters at the primary outlet are named as MFM A and MFM B. The last mass flow meter is named as MFM C and placed at secondary outlet permanently. After that, all the primary outlets are connected to both the mass flow meters, i.e., MFM A and MFM B. This is facilitated by a three-way valve attached to each permeation cell as described above. It also ensures that all the outlets offer the same resistance to the outflow.

During the experiments, it is made sure that at a time, only four outlets are connected to each mass flow meter, i.e., MFM A and MFM B. It means if the primary outlet 1, 5, 7, and 8 are connected to MFM A, the reaming outlets, i.e., 2, 3, 4, and 6 will be connected to MFM B whereas the MFM C will always remain at secondary outlet.

To determine the accurate mass flowrate from each outlet for a given inlet mass flowrate, MFM A and MFM B are required to measure the primary outlet mass flowrate seven times using different combinations of the outlets (see Table 2).

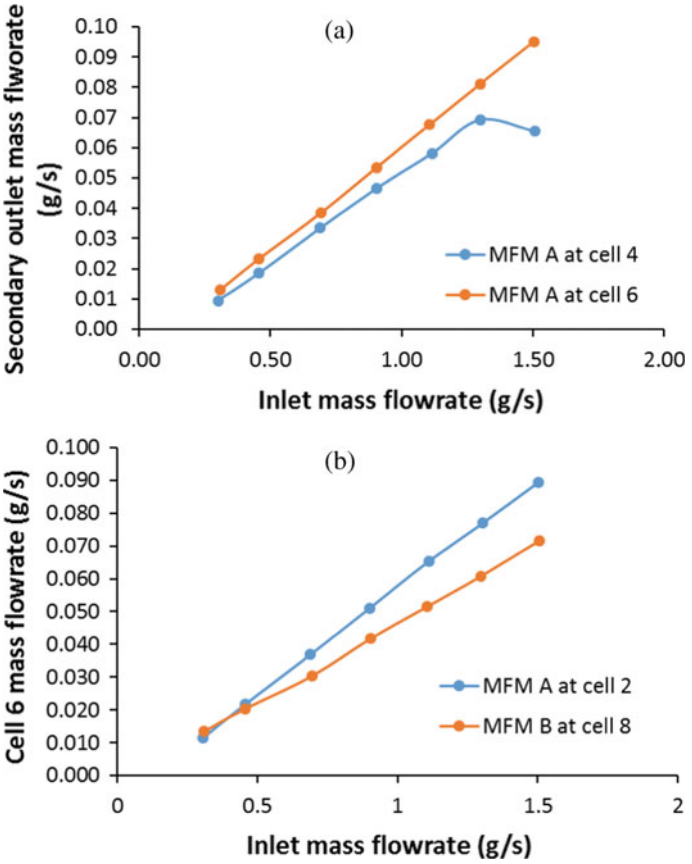

Fig. 2 Comparison between the measured mass flowrate at **a** secondary outlet and **b** cell 6 when the mass flowmeters positions are changed

Table 2 Configuration of primary outlets with respect to mass flowmeter A and mass flowmeter B

Configuration	MFR A	MFR B
1	1 + 2 + 3 + 4	5 + 6 + 7 + 8
2	1 + 2 + 4 + 6	3 + 5 + 7 + 8
3	1 + 2 + 3 + 6	4 + 5 + 7 + 8
4	2 + 3 + 4 + 6	1 + 5 + 7 + 8
5	1 + 3 + 4 + 6	2 + 5 + 7 + 8
6	1 + 2+3 + 5	4 + 6 + 7 + 8
7	1 + 2 + 3 + 7	4 + 5 + 6 + 8

Table 3 Total mass flowrate through the outlets and recovered percentage

Configuration	Inlet MFR (g/s)	Total outlet MFR (g/s)	Flow through S.O (%)	Recovered (%)
1	1.50	1.50	60.26	100.00
2	1.49	1.51	62.08	101.21
3	1.49	1.52	62.61	101.88
4	1.50	1.52	61.93	101.40
5	1.50	1.53	62.33	101.87
6	1.51	1.53	61.92	101.39
7	1.50	1.51	61.00	100.80

These seven different configurations give 14 linear equations in terms of mass flowrates and solving these equations gives the primary flowrates from the respective cell outlets.

To validate the above method, a test is performed for an inlet mass flowrate of 1.50 g/s. This inlet flowrate is selected because it is seen that the uncertainty is very less for the higher mass flowrates. It can be seen from Table 3 that the recovery is near 100% for all the configurations. Hence, it can be concluded that the fluid flow inside the porous tube is not affected by this method and recovery is also equal to 100%. It is also important to note that even when the configuration is changed (i.e., 1 to 2 or 3… and so on), the mass flowrate through the secondary outlet does not varies much. This further suggest that the fluid dynamics inside the tube is not affected as it is seen in the previous method. Table 4 gives the mass flowrate from each cell after solving the equations.

The reliability of the developed method is further ensured by the obtained results presented in Table 5. It can be clearly seen from the table that the recovered flow obtained standard for the cases 3, 4, and 5 is 100%. Whereas, for the first two cases, it is 80% and 95%, respectively. This is due to the uncertainty offered by the mass flow meter in the measurement of the mass flowrate below 0.20 g/s.

The clear advantage of the developed analytical method can also be seen by the fact that in case of 0.25 g/s (see Table 5), it allows to measure the mass flowrate from each cell whereas in case of secondary method, even for the inlet mass flowrate of 0.30 g/s, it is difficult to determine the mass flowrate from cell 1 and 3.

Table 4 Mass flowrate along the length of the tube

Cell	Cell 1	Cell 2	Cell 3	Cell 4	Cell 5	Cell 6	Cell 7	Cell 8
Length (z) in meters	**0.11**	**0.22**	**0.33**	**0.44**	**0.55**	**0.66**	**0.77**	**0.88**
MFR (g/s)	0.059	0.06	0.062	0.061	0.063	0.065	0.062	0.161

Table 5 Flow distribution at primary and secondary outlets with total recovered flow

S. No.	Inlet mass flowrate ($\dot{m}_{in}$)	Total primary flow from cells ($\dot{m}_{cells}$)	Secondary outlet flow ($\dot{m}_{out}$)	Total flow recovered ($\dot{m}_{cells} + \dot{m}_{out}$)
	g/s	g/s	g/s	%
1	0.25 ± 0.001	0.0780 ± 0.045	0.124 ± 0.004	80.3
2	0.49 ± 0.001	0.1933 ± 0.006	0.282 ± 0.004	95.5
3	1.00 ± 0.003	0.4040 ± 0.008	0.605 ± 0.006	100.9
4	1.50 ± 0.002	0.6040 ± 0.009	0.921 ± 0.009	101.5
5	1.98 ± 0.008	0.7780 ± 0.010	1.228 ± 0.012	100.9

4 Conclusion

In this study, permeation cells are designed and fabricated which allow the determination of fluid properties such as pressure, temperature, and mass flowrate axially as well as radially. In order to measure the radial mass flowrate, two different methods are tried. In the traditional method, the mass flow meter positions are changed four times in order to determine the mass flowrate from all the cells. In none of the test case, mass flowrate recovery is 100% which is due to the variable back pressure. This back pressure is caused by the use of the Coriolis mass flow meter that results in change in fluid dynamics. While in the analytical method, all the cells are connected to the mass flow meter that results in identical exit condition that does not change the fluid dynamics inside the porous tube and results in 100% mass flow recovery.

References

1. Dahm K, Virk P, Bounaceur R, Battin-Leclerc F, Marquaire P, Fournet R, Daniau E, Bouchez M (2004) Experimental and modelling investigation of the thermal decomposition of n-dodecane. J Analyt Appl Pyrol 71:865–881
2. Najmi H, El-Tabach E, Chetehouna K, Gascoin N, Falempin F (2015) Effect of flow configuration on Darcian and Forchheimer permeabilities determination in a porous composite tube. Int J Hydrogen Energy 41:316–323
3. Najmi H (2018) Selectivity of porous composite materials for multispecies mixtures: application to fuel cells. Ph.D. Dissertation, University of Orleans, France
4. Shamsabadi A, Kargari A, Babaheidari M, Laki S, Ajami H (2013) Role of critical concentration of PEI in NMP solutions on gas permeation characteristics of PEI gas. J Ind Eng Chem 19:677–685
5. Tanaka D, Tanco M, Niwa S, Wakui Y, Mizukami F, Namba T, Suzuki T (2005) Preparation of palladium and silver alloy membrane on a porous α-alumina tube via simultaneous electroless plating. J Membr Sci 247:21–27
6. Chi Y, Yen P, Jeng M, Ko S, Lee T (2010) Preparation of thin Pd membrane on porous stainless steel tubes modified by a two-step method. Int J Hydrogen Energy 35:6303–6310
7. Abdollahi M, Yu J, Liu P, Ciora R, Sahimi M, Tsotsis TT (2012) Ultra-pure hydrogen production from reformate mixtures using a palladium membrane reactor system. J Membr Sci 390–391:32–42

8. Zhao Q, Wang J, Chu N, Yin X, Yang J, Kong C, Wang A, Lu J (2008) Preparation of high-permeance MFI membrane with the modified secondary growth method on the macroporous α-alumina tubular support. J Membr Sci 320:303–309
9. Najmi H, El Tabach E, Gascoin N, Chetehouna K (2018) Falempin F, Axial distribution of permeance and of ideal selectivity of a porous cylindrical tube. Chem Eng Sci 183:295–305
10. Najmi H, El Tabach E, Gascoin N, Chetehouna K, Falempin (2019) Experimental determination of fluid flow parameters to study permeation process inside a porous channel, Innovative Design, Analysis and Development Practices in Aerospace and Automotive Engineering (I-DAD 2018), Lecture Notes in Mechanical Engineering
11. Najmi H, El-Tabach E, Chetehouna K, Gascoin N, Akridiss S, Falempin F (2017) Flow configuration influence on darcian and forchheimer permeabilities determination. In: Bajpai RP, Chandrasekhar U (eds) Innovative design and development practices in aerospace and automotive engineering. Springer, Lecture Notes in Mechanical Engineering, Singapore, pp 87–94

Experimental Investigation on Thermal Degradation of Multilayer Honeycomb Core Laminate Sandwich Composite in a Cone Calorimeter

Hussain Najmi, Jocelyn Luche, and Thomas Rogaume

Abstract There are a number of composites available but cannot be used in the aircraft because they do not possess the required fire-resistant properties. The fire norms set by the aviation regulatory bodies are very stringent, in order to use any material in aircraft interiors, it should comply with FAR 25.853 norms. This regulation demands that each material in a multilayer material as well as its assembly should comply with the regulation. Therefore, in the present study, a multilayer composite material consisting of four layers is tested in an ISO 5660 cone calorimeter at the incident heat flux of 50 kW/m^2. At first, all the constitute layers (i.e. paint, laminate, and honeycomb) are tested separately at the same heat flux (i.e. 50 kW/m^2) to identify the thermal decomposition process of each material individually. Thereafter, step by step layers are added and three different assemblies are formed and tested under the same heat flux to identify the thermal interaction between each layer. The obtained results confirm that the time to attain the maximum surface temperature increases with an increase in the layers of materials. However, the peak surface temperature attained by the materials increases while the CO emission for the first 300 s decreases with the increase in the material layers.

Keywords Multilayer composite · Aircraft interiors · Fiber-reinforced composites · Phenolic resins · Cone calorimetric tests

1 Introduction

Previously, composite materials were considered only for light structural pieces or cabin components but now they have extended their reach into true functional components—wing and fuselage skins, engines, and landing gear. They can be used as a

H. Najmi (✉) · J. Luche · T. Rogaume
Institut Pprime, UPR 3346 CNRS, Département Fluides, Thermique, Combustion, Université de Poitiers, ISAE-ENSMA, BP 40109, Futuroscope, Chasseneuil-du-Poitou 86961, France
e-mail: hussain.najmi@ensma.fr

N. Gascoin and E. Balasubramanian (eds.), *Innovative Design, Analysis and Development Practices in Aerospace and Automotive Engineering*, Lecture Notes in Mechanical Engineering, https://doi.org/10.1007/978-981-15-6619-6_61

one-piece design and eliminate the complex assemblies and joints which are the potential failure points [1, 2].

As part of the fire safety regulations, all the manufactured airplanes must comply with definitive standards (i.e. FAR 25.853). It states that all the materials used in aircraft interiors should have a maximum peak heat release rate of 65 kilowatts per square meter, a maximum total heat release of 65 kilowatt minute per square meter, and the specific optical smoke density of 200 (i.e., the OSU 65/65/200 fire safety standard defined by Ohio State University) [3]. The fire performance of materials used in aircraft interiors is evaluated at an incident flux of 35 kW/m^2 in an OSU/Cone calorimeter [3, 4]. The OSU calorimeter is difficult to access outside of accredited testing laboratories and consequently expensive to use [5]. Therefore, in numerous research works, a cone calorimeter is used [4, 5].

In order to comply with fire norms set by the Federal Aviation Administration (FAA) different types of fire retardants are also used. These flame-retardants can have significant harmful effects too such as invisible toxic gases, release of increased amounts of carbon monoxide and hydrogen cyanide at the time of fire [6]. It is also found that continuous exposure to some of the fire retardants can also cause serious health problems such as cancer [7]. Therefore, in order to overcome all the above drawbacks, the concept of multilayer materials has been brought into picture. The regulation (i.e. FAR 25.853) in case of multilayer materials stipulates that each element must be qualified and certified according to a standardized test, *i.e.* each of the materials of the whole assembly must meet normative requirements, just like the assembly itself [7]. In some cases, the individual materials pass the fire tests but the whole assembly does not because the thermal interaction between the materials is very complex to predict. This results in loss of money as well as time.

In most of the multilayer materials, Nomex honeycomb structure is used as a core material due to its lightweight and flexibility. Typically, a honeycomb is sandwiched between fiberglass-reinforced phenolic resin skins joined with an adhesively [8]. A study on a phenolic glass fiber suggests that a phenolic resin is completely exhausted at 600 °C) [9]. The primary reactive agent in phenolic-based composite is the phenolic resin itself [10]. As per the author's knowledge, there are some studies in which non-destructive evaluation is carried out on a honeycomb structure [11, 12] but no dedicated study concerning thermal degradation of a honeycomb is found. In some previous studies, the thermal decomposition of a multilayer composite in cone and OSU calorimeter at the incident flux of 35 kW/m^2 is studied [8, 13]. It is difficult to identify which material is taking part in the decomposition process at any given instance only by looking at the global decomposition process. These studies are not sufficient to have an insight into the decomposition process and determine the contribution of each layer into the fire. To understand the decomposition process of such complex material, it is important to study the decomposition process of each material separately prior to the multilayer assembly test. Therefore, in the present study, first, the materials are studied separately and then with different assemblies in order to understand how the addition of different layers affects the thermal decomposition process.

The multilayer composite used here consists of 4 layers, in which the honeycomb core is sandwiched between glass fiber phenolic sheets and paint is applied on the sheet at the top. The cone calorimeter experiments help in determining various thermal parameters of each material and the assembly as well. In the first phase of the experimental study, all the materials are tested separately. After that, layer by layer, material is added and tested at the same heat flux. The results obtained in the first phase of the experimental study are used to identify different stages of decomposition in the second phase of this experimental study.

2 Materials and Methods

The fire characterization is carried out with the three parameters (Heat Release Rate (HRR), Mass Loss (ML), and gaseous emissions) using a cone calorimeter. The cone calorimeter (as per ISO 5660 [14]) is equipped with data acquisition boxes, flowmeters, and quartz tubes according to the fire regulation (see Fig. 1). There are two types of gas analyzers (i.e. Fourier transformed infrared (FTIR) spectrometer Nicolet 6700 and SIEMENS Ultramat/Oxymat 6) used to determine the evolution of gaseous emissions and to understand the thermal behavior of the materials while under thermal attack. More details regarding the experimental setup and methods of HRR determination by oxygen depletion can be found in previous works [15].

In the above setup, an insulated sample holder is used with a specimen of dimensions 10 cm × 10 cm and an exposed surface of 100 cm^2 (Fig. 2). The constituting material of the sample holder is calcium silicate (supplied by Distrisol, France). Except for the sample holder, the cone calorimeter tests are performed as per ISO

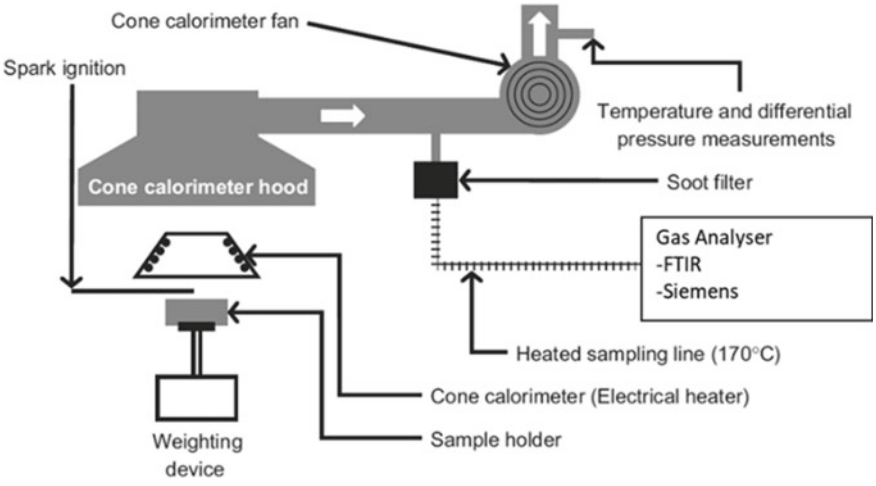

Fig. 1 Schematic layout of the Cone calorimeter bench [10]

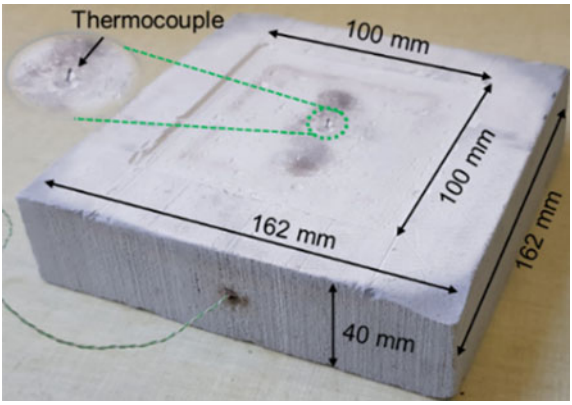

Fig. 2 A picture presenting dimension of an insulated sample holder and the position of a thermocouple

5660 fire norms [14]. In order to measure the back face temperature, a K-type thermocouple (0.2 mm diameter) is passed through the sample holder and placed at the center in such a manner that it touches the center of the sample when the sample is placed upon it. The thermocouple is connected to a data acquisition card which records the transient variations of temperature during the test.

The multilayer composite (thickness 13 mm) used in the study consists of four layers (see Fig. 3) and it is primarily used in aircraft seats and interior panels. In this composite, the honeycomb structure (thickness 12 mm) is sandwiched between two laminate sheets. Each laminate sheet (thickness 0.5 mm) is composed of two layers of glass fiber/phenolic weaved in one another. Laminate sheets are fixed on both sides of the honeycomb structure using an adhesive and paint is applied on the laminate at the top. Please note that in Fig. 3, composite without paint and with paint is shown in order to present different layers clearly. This study does not include the results concerning composite without paint.

The experimental investigation is divided into two phases (see Table 1). In the first one, each layer (i.e. laminate, honeycomb and paint) is tested separately at the incident heat flux of 50 kW/m^2. In order to observe the thermal decomposition of paint, it is applied on an aluminum plate (thickness 1.2 mm) which being an inert material does not take part in fire, and then tested under cone calorimeter. The results from the first phase help in understanding the decomposition process of each material individually. Phase 1 study will also help in identifying different stages of

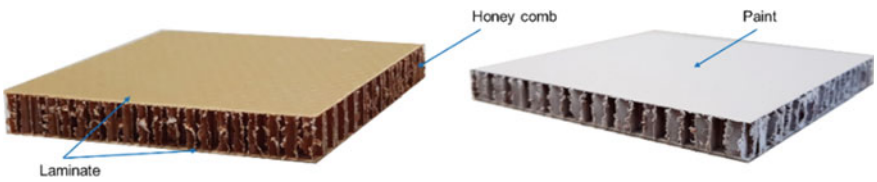

Fig. 3 Picture of multilayer composite without paint (left) and with paint (right)

Table 1 Description of materials and assemblies used in two different phases of an experimental study

S.No	Heat flux	First phase	Second phase
		Materials	Assemblies
1	50 kW/m^2	Paint	Paint + Laminate (P.L)
2		Laminate	Paint + Laminate + Honeycomb (P.L.H)
3		Honeycomb	Paint + Laminate + Honeycomb + Laminate (Composite)

decomposition in the case of different assemblies (i.e. Phase 2 study). After that, in the second phase, three different assemblies (Cf. Table 1) are made by using phase one materials (i.e. laminate, honeycomb, and paint) and tested at the same heat flux. The results of the second phase demonstrate how the thermal decomposition gets affected with the addition of layers (i.e. material) and also allows the comparison of various decomposition parameters in case of different assemblies.

3 Results and Discussion

At first, as described above, in order to understand the decomposition process of materials separately, each constitutes of the multilayer material (i.e. paint, laminate, and honeycomb) is tested individually at the incident flux of 50 kW/m^2. It is evident from Fig. 4 that thermal decomposition of paint and laminate occurs in one step while the honeycomb structure decomposes in two steps (see HRR curves in Fig. 4). In case of all three materials (i.e. paint, laminate, and honeycomb), CO_2 emission coincides with the HRR curve due to the method used in HRR calculations which is primarily based on the CO_2 emission during the combustion [14]. In order to compare different gaseous emissions with respect to HRR and back surface temperature, some of the lower emission values are multiplied by the factor of 10 and 100. The modified gaseous emissions are indicated in the respective legends of the figure. In case of paint, CH_4 and CO emissions are observed at the same time. Whereas in the case of laminate, CO is observed at the time of ignition and at the end of the decomposition process while a single peak of CH_4 is observed at the end of the HRR peak. In the case of laminate, CH_4 emission corresponds to the decomposition of methylene bridges while release of CO_2 and CO at the start of the ignition represents the decomposition of the resin. Sudden rise in CO emission at the end of the decomposition corresponds to the char decomposition which is usually observed at 600 °C. In the case of honeycomb structure, the CH_4 emissions are very negligible and observed after the end of the primary decomposition for a very brief time. CO emissions are observed corresponding with HRR peak and as peak back surface temperature is attained, the sudden increase in CO emission corresponds to char decomposition.

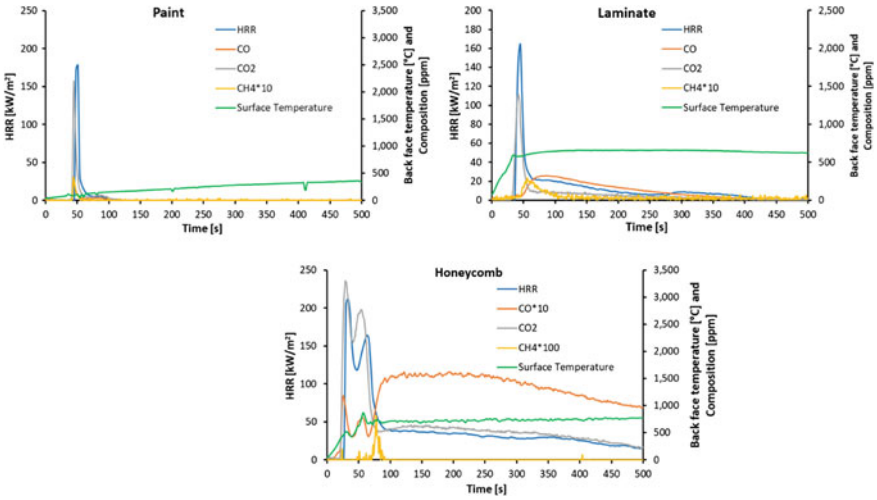

Fig. 4 Evolution of heat release rate, gaseous product of combustion and back face temperature for paint, laminate and honeycomb structure

The decomposition parameters tabulated in Table 2 confirm that the honeycomb structure is completely destroyed by the end of the test. The honeycomb has shrunk by the end of the test and its final dimension is found to be 4×4 cm^2. The mass loss percentage of laminate indicates the amount of phenolic resin present in it and the remaining mass is roughly equal to the glass fiber content. In previous studies, it is found that the phenolic resin is completely decomposed at 600 °C [9] while the glass fiber remains intact up to 1000 °C [16]. Hence from the first phase of the study, the decomposition of single materials and gases emitted during their decomposition process are well understood. This will help in identifying which materials are taking part in the thermal decomposition process when different assemblies are studied at the same incident flux.

In the second phase, different assemblies are made by using phase one materials (i.e. paint, laminate, and honeycomb) in order to study the change in the thermal decomposition process due to the addition of one material to another. To do so,

Table 2 Experimentally determined thermal decomposition parameters of paint, laminate and honeycomb structure

Materials	PHRR	THR	CO_2	I.T	PBT	M.L
	kW/m^2	kJ/m^2	g/g	s	°C	%
Paint	177.7	1488.9	12.6	36–42	580.7	61.5
Laminate	164.1	4828.5	3.8	21–42	664.0	28.5
Honeycomb	218.2	15669.5	1.8	15–495	864.7	99.2

*PHRR-peak heat release rate, THR-total heat release rate (for first 300 s), I.T-ignition time (flame in and flame-out), PBT-peak back surface temperature, M.L-mass loss

step by step layers of materials are added and tested inside the cone calorimeter. In total, the evaluation of the fire characteristics of three different assemblies and their interaction with each other during the fire is attempted. First, assembly of paint and laminate is made and its thermal decomposition is evaluated under a cone calorimeter. After that, in the second assembly, honeycomb structure is added to the first assembly (i.e. P.L) and studied at the same incident flux. In the end, one more laminate sheet is added at the back of the P.L.H assembly and various decomposition parameters are evaluated.

It can be seen from the ignition time data (cf. Table 3) that the flame in time (time at which ignition occurs) in case of all the three different assemblies is the same (i.e. 15 s) which means that the addition of any number of materials to P.L assembly does not impact the time to ignition. Similarly, there is no big difference in PHRR value. In the case of the composite, the extra layer of laminate present at the back of the honeycomb structure disallows the honeycomb from decomposing completely (as observed in the honeycomb test case) and gives rigidity to the structure (see Fig. 5). Therefore, the mass loss percentage and THR are lower in case of the composite compared to the P.L.H assembly. Addition of layers results in an increase in mass (i.e. solid fuel) of the assembly which should cause an increase in CO_2 yield. However, CO_2 yield decreases with the increase of layers.

In order to further understand the thermal decomposition process of these three assemblies, heat release rate curves are plotted with respect to time (see Fig. 6). It can be seen that in all three cases, the primary HRR peak is composed of two simultaneous peaks. In which the 1st peak corresponds to paint and the 2nd corresponds to the laminate decomposition. In order to confirm the above statement in inset (see Fig. 6), HRR curves of paint and laminate are superimposed on the HRR curve of

Table 3 Experimentally determined thermal decomposition parameters of three different assemblies

Materials	Mass	PHRR	THR	CO_2	I.T	PBT	M.L
	g	kW/m^2	kJ/m^2	g/g	s	°C	%
P.L	10.3	155.3	6046.9	2.9	15–55	649.1	33.0
P.L.H	17.4	146.7	11946.8	1.2	15–150	732.5	59.3
Composite	26.1	148.6	11618.8	1.1	15–234	714.2	45.8

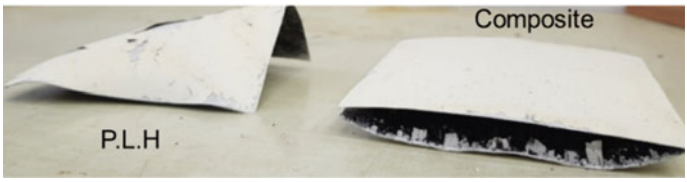

Fig. 5 Residue left after the cone calorimeter test, **a** Paint + Laminate + Honeycomb (P.L.H) and **b** Composite

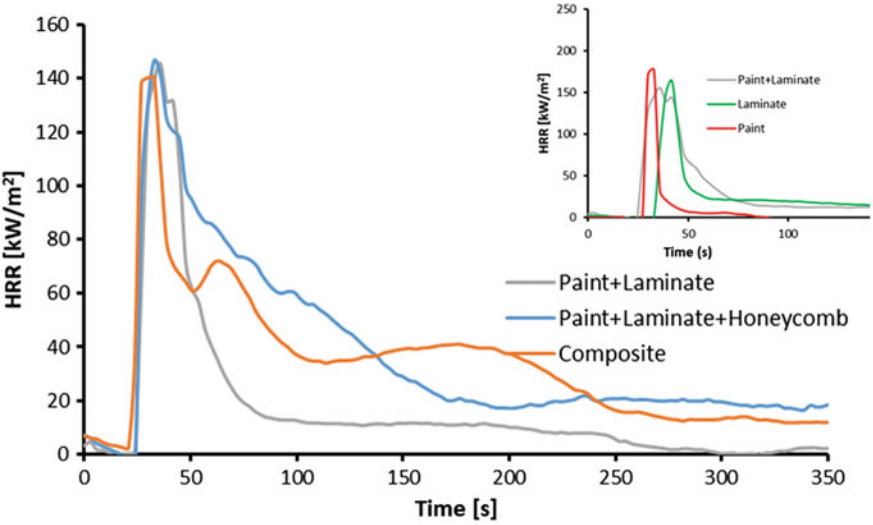

Fig. 6 Heat release rate (HRR) of three different assemblies

P.L assembly which fits quite well. In order to confirm this further, the HRR peak duration is estimated which is about 10, 30, and 40 s for paint, laminate, and P.L assembly, respectively. The HRR peak duration of P.L assembly is 40 s which is the addition of HRR peak duration obtained in case of a separate test of paint (i.e., 10 s) and laminate (i.e. 30 s). This further confirms that the primary peak corresponds to the paint and laminate decomposition. It is also evident from the figure (Fig. 6) that the first decomposition peak which corresponds to paint and laminate decomposition starts and terminates at the same time in case of all the three assemblies (i.e. P.L, P.L.H, composite). This means the addition, of honeycomb in case of P.L.H assembly and of honeycomb and laminate in case of the composite, does not impact the primary decomposition process. In the present multilayer composite, the peak heat release rate is characterized by paint and laminate present at the top of the composite.

If the decomposition in all three assemblies starts with the decomposition of paint then the time to ignition should be similar to the paint test (i.e. 36 s) which is not the case here. It is probably due to the use of an aluminum plate in the paint test which consumes some amount of energy when the paint is heated up and hence the ignition time is slightly delayed.

In order to have more clarifications with the decomposition process, gaseous emissions captured during the combustion are compared (see Fig. 7). The CO emission of a separate test of paint and laminate matches well with the CO emission of the P.L assembly test case. This further confirms that the primary HRR peak corresponds to paint and laminate decomposition. In the case of P.L assembly, the first peak of CO emission is due to decomposition of both (i.e. paint and laminate) while the second CO peak uniquely corresponds to the thermal degradation of laminate. This can also

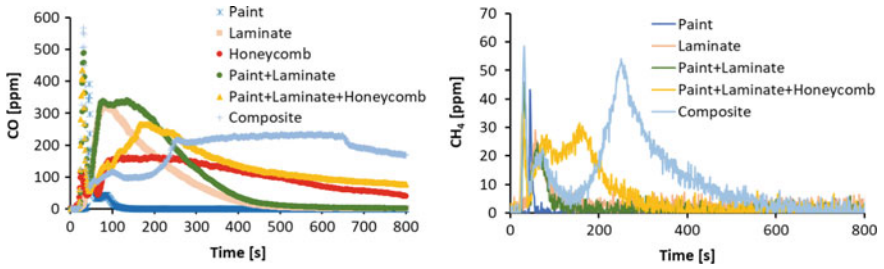

Fig. 7 CO and CH_4 concentrations for different materials and assemblies

be validated by CH_4 concentration as it is observed earlier that CH_4 is produced at the end of the laminate decomposition (cf. Figure 4).

In case of the second assembly (i.e. Paint + Laminate + Honeycomb (P.L.H)), the primary HRR peak (see Fig. 6) corresponds to the decomposition of paint and laminate as discussed above. Here, the 2nd consecutive HRR peak representing decomposition of laminate is slightly lower compared to the P.L case. This is because of loss of heat due to the additional honeycomb structure. Therefore, in the case of second assembly, the rise in back surface temperature is not as rapid as observed in P.L test case (cf. Figure 8). As it is seen earlier the decomposition of methylene bridges occurs at 450–550 °C. This temperature is achieved in the later part of the test in case of the second assembly compared to P.L test case due to which release of methane is also delayed (Fig. 7). After the primary decomposition (primary peak) the honeycomb structure decomposition starts (52 s), which can be confirmed by CO emissions of P.L.H and the honeycomb (Fig. 7).

In the final test case, a complete composite (with a laminate sheet at the back of P.L.H assembly) is tested inside the cone calorimeter. In this case of composite, after

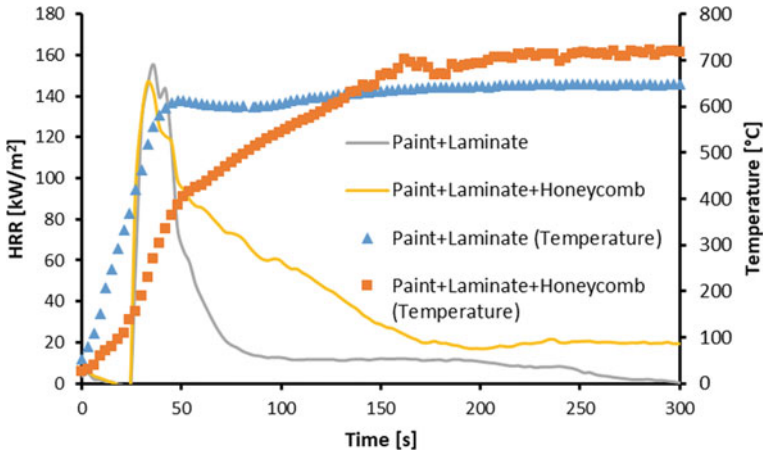

Fig. 8 Heat release rate (HRR) and back surface temperature of different assemblies

the primary HRR peak, two additional HRR peaks are observed (Fig. 6). The peak observed just after the primary peak represents thermal degradation of the honeycomb structure. In order to describe the final HRR peak in case of composite, CH_4 concentration and HRR are plotted in Fig. 9. In the first phase of this experimental study, it is confirmed that the amount of CH_4 released during the honeycomb decomposition is negligible. It (CH_4) is mainly observed in case of laminate and paint decomposition therefore CH_4 concentration is used in Fig. 9. The first two CH_4 peaks represent the decomposition of paint and laminate present at the top of the composite. While the final peak of CH_4 concentration rises just after the final HRR peak similar to the laminate decomposition case. Also, the back face temperature measured at that time corresponds to the decomposition of methylene bridges. This confirms that the final HRR represents the decomposition of laminate present at the bottom of the composite. At the end of the final test, thickness of the composite is reduced to 7 mm from the initial thickness of 13 mm.

It should be noted that in all the test cases, a major part of CO emission is observed after the flame out, representing char decomposition. This occurs at a sufficiently high temperature which is about 580–650 °C. It seen that with the addition of a layer the CO emission is delayed (see Fig. 7). This is probably due to the increase in thickness which retards the increase in back surface temperature (Fig. 10) and hence char decomposition is delayed.

The total mass loss percentage in composite is about 45% (see Table 3). If the average mass loss percentage of P.L.H (59%) and laminate (29%) is estimated, it is around 44% which is very similar to the total mass loss of the composite. This allows us to conclude that the addition of a laminate at the back of P.L.H assembly does not

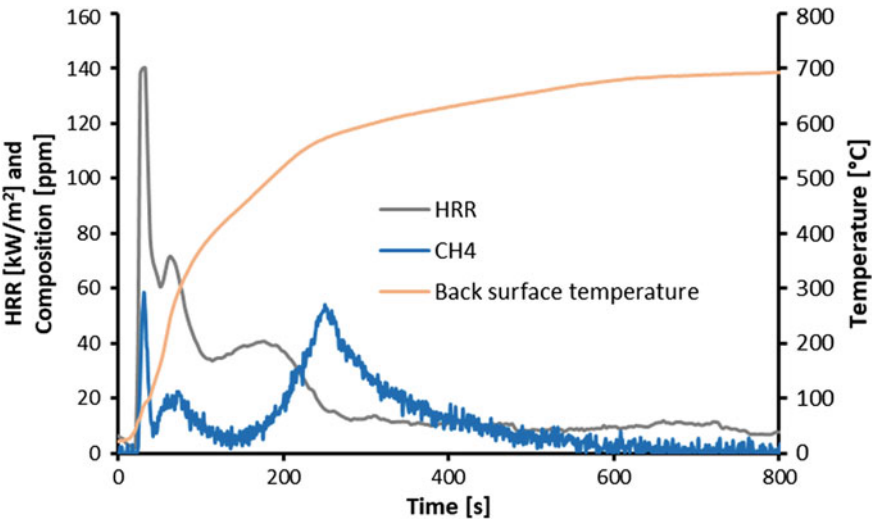

Fig. 9 Evolution of heat release rate, CH_4 concentration and back face temperature for composite

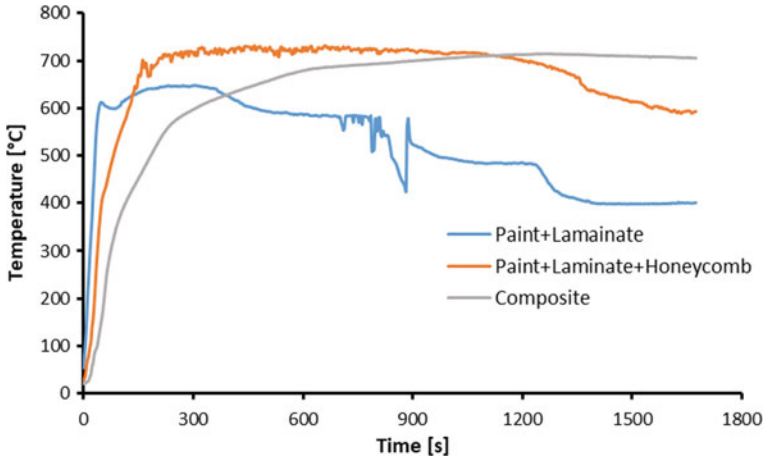

Fig. 10 Evolution of back face temperature in three different assemblies

affect the total mass loss percentage of the composite but surely gives the rigidity to the assembly which seems to be missing in case of P.L.H (see Fig. 5).

In case of the second assembly (P.L.H), the mass loss percentage is estimated using the separate mass loss of honeycomb (99%) and P.L (33%) which is about 66%. This value is higher than the mass loss percentage obtained for the assembly test of P.L.H (59%). This suggests that the addition of honeycomb to the P.L assembly results in a decrease in mass loss. Similarly, the estimated average value for P.L is 45% while the actual mass loss percentage of P.L assembly is 33%. Here also the assembly of paint and laminate results in a decrease in the mass loss percentage.

4 Conclusion

In the present work, the thermal degradation of a multilayer composite is studied under the cone calorimeter at the incident flux of 50 kW/m^2. The experimental campaign is divided into two phases. In the first phase, each constitutes of the multilayer material (i.e., paint, laminate, and honeycomb) is studied separately and in the second phase, 3 different assemblies (P.L, P.L.H, and composite) are formed and various thermal decomposition parameters are determined. The first phase of the experimental study confirms that during the decomposition, CO emissions are more dominant in the case of laminate and honeycomb while CH_4 is observed only in case of paint and laminate. The emission patterns of CO and CH_4 observed in the first phase of the study helps in identifying the different stages of decomposition in the second phase of the experimental study in which three different assemblies are used.

The second phase of this study allows us to conclude that the primary decomposition is governed by paint and laminate. After the primary phase is over, the

decomposition of the honeycomb starts and in the end, the laminate present at the back of the composite is decomposed. In all the cases, a large amount of CO emission is observed after the flame out. The analysis of mass loss percentage suggests that the addition of laminate at the back of the honeycomb structure does not help in reducing the total mass loss but surely helps in providing rigidity to the complete assembly.

Acknowledgements This work was supported by the CPER FEDER project of Région Nouvelle Aquitaine. The authors deeply appreciate the technical support of Mr. Marc Poisson (assistant engineer). This work pertains to the French Government program "Investissements d'Avenir" (LABEX INTERACTIFS, reference ANR-11-LABX-0017-01). We also give many thanks to the "Institut des Risques Industriels Assurantiels et Financiers" of the University of Poitiers for its technical support.

References

1. Marsh G (2011) Bombardier throws down the gauntlet with Cseries airliner. Reinf Plast 55(6):22–26
2. Shi Y, Swait T, Soutis C (2012) Modelling damage evolution in composite laminates subjected to low velocity impact. Compos Struct 94(9):2902–2913
3. FAR 25.853 a-1. Heat release test for cabin materials. Compiled by April Hornor, Aircraft Materials Fire Test Handbook, FAA report DOT/FAA/AR-00/12, April 2000
4. Mouritz A. Fire safety of advanced composites for aircraft. ATSB Research and Analysis Report Aviation Safety Research Grant—B2004/0046 2006 April
5. Kandola BK, Horrocks AR, Padmore K, Dalton J, Owen T (2006) Comparison of cone and OSU calorimetric techniques to assess the flammability behaviour of fabrics used for aircraft interiors. Fire Mater 30:241–255
6. Congleton J, Sharp R, Lunder S (2014) No escape: tests find toxic fire retardants in mothers—and even more in toddlers. Environmental Working Group, Duke University, 7 Aug 2014
7. Babich MA (2006) CPSC staff preliminary risk assessment of Flame Retardant (FR) chemicals in upholstered furniture foam. Consumer Product Safety Commission, US
8. Lyon R (1997) Fire-resistant materials: research overview. U.S. Department of Transportation Federal Aviation Administration, Final report
9. Kim M, Choe J, Lee DG (2016) Development of the fire retardant glass fabric/carbonized phenolic composite. Compos Struct 148:191–197
10. Chen R, Xu X, Zhang Y, Lo S, Lu S (2018) Kinetic study on pyrolysis of waste phenolic fibre-reinforced plastic. Appl Therm Eng 136:484–491
11. Perez MA, Gil L, Oller S (2011) Non-destructive evaluation of low velocity impact damage in carbon fiber-reinforced laminated composites. Ultrasound 66(2):21–26
12. Wong BS (2013) Non-destructive evaluation (NDE) of composites: detecting delamination defects using mechanical impedance, ultrasonic and infrared thermographic techniques, Non-destructive evaluation (NDE) of polymer matrix composites, Woodhead Publishing Limited, pp 279–308
13. Parker W, Filipczak R (1993) Modelling the heat release rate of aircraft cabin panels. U.S. Department of Transportation Federal Aviation Administration, Final report
14. ISO 5660-1: reaction-to-fire tests: heat release, smoke production and mass loss rate: part 1: heat release rate (cone calorimeter method) and smoke production rate (dynamic measurement). Geneva: International Organization for Standardization, 2015

15. Luche J, Rogaume T, Richard F, Guillaume E (2011) Characterization of thermal properties and analysis of combustion behavior of PMMA in a cone calorimeter. Fire Safety J 46:451–461
16. Garay A, Heck V, Zattera A, Souza J, Amico S (2011) Influence of calcium carbonate on RTM and RTM light processing and properties of molded composites. J Reinforced Plastics Compos 30(14):1213–1221

Author Index

N. Gascoin and E. Balasubramanian (eds.), *Innovative Design, Analysis and Development Practices in Aerospace and Automotive Engineering*, Lecture Notes in Mechanical Engineering, https://doi.org/10.1007/978-981-15-6619-6